The Application of Neutron Scattering to Investigate Hydrocarbon Conversion Over Zeolite Catalysts

Alexander Paul Hawkins
MChem

Submitted in fulfilment of the requirements for the degree of
Doctor of Philosophy (PhD) by research.

School of Chemistry
College of Science & Engineering
University of Glasgow

Deposited to the library in June 2021

Abstract

The use of acid zeolites as catalysts for the conversion of hydrocarbons is widespread due to their ability to catalyse both bond-breaking and formation reactions and their shape-selectivity. This selectivity arises from steric interactions with the pore structure which increase the stability of some intermediates and reactions, favouring given products. In this way, yields of high-value products can be increased by use of the correct zeolite structure, such as H-ZSM-5 which optimises the production and utilisation of light olefins. The ways in which olefins interact with, and diffuse through, zeolite frameworks are therefore matters of considerable academic and industrial interest due to the possibility of providing targets for the development of improved catalysts.

Neutron scattering methods are a family of related techniques which are uniquely suited to studying hydrocarbon catalysis in zeolites due to factors arising from the properties of the neutron and how scattering events occur at a sub-atomic level. This thesis enumerates these advantages and seeks to apply them to model compound systems for olefin conversion reactions of industrial interest in a commercial H-ZSM-5 powder-form zeolite. Studies are made of how C_3 and C_8 hydrocarbons react with and diffuse through the zeolite at low temperatures, and the effect of catalyst aging on these processes. The work is then extended to higher temperature studies of olefin isomerisation and cracking reactions under realistic conditions, and the examination of the diffusion of other small-molecule hydrocarbons in zeolites. The results demonstrate the ability of neutron techniques to complement techniques more conventionally used for catalytic reaction studies and to provide new insights into catalytic processes.

Preface

All scientific work is to some extent collaborative, and this is especially true of work performed at Central Facilities such as the ISIS Neutron Source. The work reported here therefore involved a number of close collaborations in the experimental aspects which should be delineated so that the contributions of other individuals should be clearly understood.

This work was carried out as part of one of two simultaneous projects funded by the EPSRC and Johnson Matthey which were conceived as complementary. It has therefore been run in parallel with the work of Ms Andrea Zachariou, also of the Lennon group at the University of Glasgow, resulting in some degree of overlap. Due to the need for 24-hour operation the experimental work for all Central Facilities experiments in both projects was performed jointly, with the sample loading and measurement tasks being shared according to the most efficient resource allocation rather than which project the sample contributed to. Processing and analysis of the resulting data was the responsibility of the student whose project the sample related to. Andrea was also responsible for the QENS analysis of methane reported in Chapter 7, the data collection (although not the analysis) for the GCMS results included in Chapter 6 and the assessment of zeolite acid site populations by quantitative INS in Section 3.1.2.4.

Experiments at ISIS are assigned a local contact familiar with the relevant instrument who is responsible for training users in, and assisting with, experimental design, sample preparation, instrument operation, and data collection and analysis for the duration of the experiment. For the inelastic neutron scattering experiments this role was filled by Professor Stewart Parker, in addition to his position as my second supervisor. For the quasi-elastic neutron scattering beam times the local contact was Dr Ian Silverwood. In addition, Professor Russell Howe of the University of Aberdeen was a collaborator on multiple papers related to propene chemistry, was present for the experimental

portion of some of the beam time experiments which generated data used in Chapters 3, 5 and 6 and collected the ^{29}Si NMR data analysed in Section 3.1.2.3.

Collaborators were also involved in the collection and analysis of some of the data used to characterise the zeolite samples. Data collection for the solid state NMR measurements of zeolites reported in Chapters 3 and 5 was performed by Dr Nathan Barrow at the Johnson Matthey Technology Centre, Sonning Common. The neutron diffraction data in Chapter 3 was collected by the POLARIS instrument team at ISIS and analysed by Dr Jan Skakle of the University of Aberdeen.

Finally, several people have assisted with training in the advanced techniques employed in this thesis. Dr Alex O'Malley of the University of Bath assisted greatly with training in the techniques and principles of QENS analysis; as part of this training the analysis of octene oligomer mobility reported in Section 4.1.2 is partially his work. Similarly, the assistance of Dr Chin Yong and Dr Ilian Todorov of the STFC Daresbury Laboratory was essential in my being able to successfully implement the molecular dynamics simulations reported through this work. Dr Yong's addition of zeolite force-field parameters to the DL_FIELD software library from version 4.6 onward was particularly helpful in this regard and greatly simplified the preparation of simulation inputs.

Except in the specific instances noted above all data collection and analysis was my own work, and the conclusions drawn from the experimental data are my own throughout.

The dataset behind the work reported here has been deposited to the University of Glasgow repository Enlighten: Research Data and is available at (DOI:10.5525/gla.researchdata.1129). Additionally, the full collected datasets from all neutron beam time experiments are publicly available in accordance with the ISIS policy on open-access research: links to these archives are provided in Appendix 1.

Publications

The work reported in this thesis has resulted in the following publications:

- A.P. Hawkins, A.J. O'Malley, A. Zachariou, P. Collier, R.A. Ewings, I.P. Silverwood, R.F. Howe, S.F. Parker and D. Lennon; Investigation of the Dynamics of 1-Octene Adsorption at 293 K in a ZSM-5 Catalyst by Inelastic and Quasielastic Neutron Scattering, *J. Phys. Chem. C,* **2018,** *123* (1), 417-425.
- A.P. Hawkins, A. Zachariou, S.F Parker, P. Collier, R.A. Ewings, R.F. Howe and D. Lennon; Low-temperature studies of propene oligomerization in ZSM-5 by inelastic neutron scattering spectroscopy, *RSC Adv.*, **2019**, *9* (33), 18785-18790.
- A.P. Hawkins, A. Zachariou, S.F Parker, P. Collier, I.P. Silverwood, R.F. Howe and D. Lennon; Onset of propene oligomerization reactivity in ZSM-5 studied by Inelastic Neutron Scattering spectroscopy, *ACS Omega*, **2020**, 5 (14), 7762-7770.
- A.P. Hawkins, A. Zachariou, S.F. Parker, P. Collier, N. Barrow, I.P. Silverwood, R.F. Howe and D. Lennon; Effect of steam de-alumination on the interactions of propene with H-ZSM-5 zeolites, *RSC Adv.*, **2020**, 10 (39), 23136-23147.
- A.P. Hawkins, A. Zachariou, S.F. Parker, P. Collier, R.F. Howe and D. Lennon; Studies of propene conversion over H-ZSM-5 demonstrate the importance of propene as an intermediate in methanol-to-hydrocarbons chemistry, *Catal. Sci. Technol.,* **2021**, 11 (8), 2924-2938.

In addition, work carried out in the course of this project has contributed to these further papers which are published or under review:

- A. Zachariou, A.P. Hawkins, D. Lennon, S.F. Parker, A. Suwardiyanto, S.K. Matam, C.R.A. Catlow, P. Collier, A. Hameed, J. McGregor and

R.F. Howe; Investigation of ZSM-5 catalysts for dimethyl ether conversion using inelastic neutron scattering, *Appl. Catal. A*, **2019**, 569, 1-7.

- A. Zachariou, A.P. Hawkins, P. Collier, R.F. Howe, D. Lennon and S.F. Parker; The Methyl Torsion in Unsaturated Compounds, *ACS Omega*, **2020**, 5 (6), 2755-2765.
- A. Zachariou, A.P. Hawkins, S.F. Parker, D. Lennon and R.F. Howe; Neutron spectroscopy studies of methanol to hydrocarbons catalysis over ZSM-5, *Catal. Today*, **2020**, (DOI:10.1016/j.cattod.2020.05.030).
- A. Zachariou, A.P. Hawkins, P. Collier, R.F. Howe, S.F. Parker and D. Lennon; The Effect of Co-Feeding Methyl Acetate on the H-ZSM-5 Catalysed Methanol-to-Hydrocarbons Reaction, *Top. Catal.*, **2020**, 63 (3-4), 370-377.
- A. Zachariou, A.P. Hawkins, A. Suwardiyanto, P. Collier, N. Barrow, R.F. Howe, S.F. Parker and D. Lennon; New Insight into the Hydrocarbon Pool in a ZSM-5 Methanol-to-Hydrocarbons Catalyst, *ChemCatChem*, **2021**, Accepted Author Manuscript (DOI:10.1002/cctc.202100286).
- A. Zachariou, A.P. Hawkins, R.F. Howe, N. Barrow, J. Bradley, P. Collier, D. Lennon and S.F. Parker; A Spectroscopic Paradox: Methanol Interaction with ZSM-5 at Room Temperature, *Top. Catal.*, Under Review.

Table of Contents

List of Tables **14**
List of Figures **17**
Acknowledgements **30**
Author's Declaration **32**
Definitions of Common Abbreviations **33**
Chapter 1: Zeolites as Hydrocarbon Conversion Catalysts **35**
1.1 An Introduction to Zeolite Structures 36
1.1.1 The MFI Structure and Zeolite ZSM-5 39
1.2 Shape-Selective Catalysis in Zeolites 41
1.2.1 Selective Hydrocarbon Cracking Reactions 43
1.2.2 The Methanol-to-Hydrocarbons Reaction 46
1.3 Studying Interactions and Dynamics in Zeolites 49
1.3.1 Neutron Methods as Tools for Studying Zeolites 50
1.3.2 Studying Adsorbate Dynamics in Zeolites 51
1.3.3 Computational Modelling as a Supplement to Neutron Methods 52
1.4 Project Objectives 53
Chapter 2: Materials and Methods **57**
2.1 Neutron Spectroscopy; Theory, Techniques and Analysis 58
2.1.1 Basic Theory of Neutron Scattering 59
2.1.1.1 Energy and Momentum Transfer 60
2.1.1.2 Coherent and Incoherent Scattering 62
2.1.1.3 Neutron Sources 64
2.1.1.4 Neutron Detectors 69
2.1.2 Inelastic Neutron Scattering 70
2.1.2.1 Overtones, Combinations and Phonon Wings 71
2.1.2.2 Indirect Geometry Spectrometers 72
2.1.2.3 Direct Geometry Spectrometers 74
2.1.2.4 Multiple Scattering 76
2.1.2.5 General Procedure for INS Measurements 77

2.1.3 Quasielastic Neutron Scattering 78
2.1.3.1 Implementation of the QENS Technique 82
2.1.3.2 The Elastic Fixed Window Scan Method 83
2.1.3.3 QENS Instrumentation 84
2.1.3.4 General Procedure for QENS Measurements 86
2.1.4 Neutron Diffraction 88
2.1.4.1 Neutron Diffractometers 89
2.1.4.2 Procedure for Neutron Diffraction Measurements 91
2.1.5 Neutron Data Analysis Tools 92
2.2 Computational Chemistry Methods: Applications to Zeolite-Hydrocarbon Systems 93
2.2.1 Density Functional Theory 93
2.2.1.1 DFT Simulation Procedure 95
2.2.2 Molecular Dynamics Simulations 96
2.2.2.1 Velocity and Temperature Control in MD Simulations ... 99
2.2.2.2 A Molecular Force-Field for Simulating Zeolites 101
2.2.2.3 MD Simulation Procedure 107
2.2.2.4 Deriving Scattering Predictions from MD Data 108
2.3 Catalyst Preparation Reactors and On-Line Analysis 109
2.3.1 The UK Catalysis Hub Microreactor 109
2.3.2 The ISIS Catalyst Preparation Apparatus 110
2.4 Zeolite Pre-Treatment Procedures 112
2.4.1 Calcination of As-Received Zeolite 113
2.4.2 Drying Procedure for Zeolite Samples 113
2.4.3 Steaming Procedure for Partial De-Alumination 114
2.5 Zeolite Characterisation Methods 115
2.5.1 Nuclear Magnetic Resonance Spectroscopy 115
2.5.2 Gas Adsorption Isotherm Analysis 116
2.5.3 X-ray Diffraction Analysis 116
2.5.4 X-Ray Fluorescence Analysis 116
2.5.5 Ammonia Temperature-Programmed Desorption 117
2.6 Ex-situ Reaction Analysis – Methods and Apparatus 117
2.6.1 Optical Spectroscopy Methods 118
2.6.2 GCMS Analysis 119
2.6.3 Temperature Programmed Oxidation 119

Chapter 3: Characterisation of H-ZSM-5 and Model Compounds..... 121

3.1 Properties of H-ZSM-5 122

3.1.1 Structure and Framework Properties 122

3.1.1.1 Determining Crystallite Size 124

3.1.1.2 Measuring the Accessible Pore Area 125

3.1.1.3 The Vibrational Spectrum of ZSM5-FR 128

3.1.2 Measuring the Brønsted Site Population in ZSM5-FR ..131

3.1.2.1 Elemental Composition Analysis..... 131

3.1.2.2 Measurement by Ammonia Desorption 132

3.1.2.3 Measurement by NMR Methods 133

3.1.2.4 Measurement by Inelastic Neutron Scattering..... 136

3.1.2.5 Summary 137

3.1.3 Identifying Brønsted Site Locations by Neutron Diffraction.....138

3.2 Spectra of Model Compounds.....140

3.2.1 Propene Studied by INS 140

3.2.2 1-octene Studied by INS.....142

3.3 Self-Diffusion Dynamics of Model Compounds 148

3.3.1 QENS Analysis of Bulk 1-octene 148

Chapter 4: Olefin Interactions in H-ZSM-5 153

4.1 Octene Interactions in ZSM5-FR.....154

4.1.1 Vibrational Spectra of ZSM5-FR + 1-octene 155

4.1.2 Mobility of 1-octene Oligomers 158

4.2 Propene Interactions in ZSM5-FR 168

4.2.1 Vibrational Spectra of Propene Oligomers 168

4.2.2 Observation of Pre-Reaction Propene in ZSM5-FR.....171

4.2.2.1 Observing Propene Oligomerization In-Progress..... 173

4.2.2.2 A Reaction Mechanism for Linear Propene Oligomerization 178

4.2.3 Propene Dynamics Studies 182

4.3 Determining Dynamics in ZSM5-FR by Alternative Methods..184

4.3.1 Models for C_3 Movement 185

4.3.1.1 Propane QENS in ZSM5-FR 185

4.3.1.2 C_3 MD Simulations in ZSM-5 Framework 192

4.3.2 Models for C_8 Movement 196
4.3.2.1 Octane QENS Literature 196
4.3.2.2 C_8 MD Simulations in ZSM-5 Framework 197
4.4 Summary.....199
Chapter 5: The Effect of Catalyst Aging on Zeolite-Olefin Interactions.... 201
5.1 Effects of Hydrothermal De-Alumination on ZSM-5 202
5.1.1 Characterisation of Steamed Catalysts 204
5.2 Propene Behaviour in Steamed ZSM-5.....210
5.2.1 Changes in Oligomerization Activity.....211
5.2.2 Propene Dynamics in Steamed ZSM-5 214
5.2.2.1 Comparison with Dynamics of Propane 220
5.3 1-Octene Behaviour in Steamed ZSM-5 223
5.3.1 1-Octene Oligomerization Activity 223
5.3.2 1-Octene Dynamics 224
5.4 Summary.....228
Chapter 6: Neutron Spectroscopic Studies of Olefin Conversions..... 231
6.1 Olefin Reaction Testing 232
6.2 Propene Oligomerization Reactions 232
6.2.1 Propene Reaction Testing.....233
6.2.2 Analysis of Propene Reaction Products 234
6.2.2.1 Propene Vapour Phase Products – 473 K.....240
6.2.2.2 Propene Vapour Phase Products – 573 K.....241
6.2.2.3 Propene Vapour Phase Products – 673 K.....241
6.2.2.4 Propene Condensable Products 242
6.2.3 Analysis of Propene Coked Catalysts 245
6.2.3.1 Propene Reacted Catalyst – 473 K 248
6.2.3.2 Propene Reacted Catalyst – 673 K 251
6.2.3.3 Propene Reacted Catalyst – 573 K 252
6.2.3.4 Acid Site Effects 253
6.2.4 Reaction Mechanisms in ZSM-5 Propene Conversion ..254
6.2.4.1 Cycle 1 – Alkyl Production 254
6.2.4.2 Cycle 2 – Aromatic Production 256
6.2.4.3 Overall Reaction Scheme.....258

6.3 Octene Cracking Reactions 261
6.3.1 Octene Reaction Testing 262
6.3.2 Octene Thermal Cracking at Reaction Temperatures 264
6.3.3 Analysis of Octene Reaction Products 266
6.3.3.1 Octene Vapour Phase Products – 473 K 268
6.3.3.2 Octene Vapour Phase Products – 573 K 269
6.3.3.3 Octene Vapour Phase Products – 673 K 269
6.3.3.4 Octene Condensable Products 270
6.3.4 Analysis of Octene Coked Catalysts 273
6.3.4.1 Octene Reacted Catalyst – 473 K 275
6.3.4.2 Octene Reacted Catalyst – 573 K 277
6.3.4.3 Octene Reacted Catalyst – 673 K 279
6.3.5 Reaction Mechanisms in ZSM-5 Octene Cracking 280
6.3.5.1 Reactions at 473 K 280
6.3.5.2 Reactions at 573 K 282
6.3.5.3 Reactions at 673 K 284
6.3.6 De-Alumination Effects on Octene Cracking 286
6.4 Comparison of Propene and Octene Chemistry 287
6.5 Summary 290
Chapter 7: Molecular Dynamics Studies of Methane Diffusion in ZSM-5 ... 291
7.1 Introduction 292
7.2 Experimental Procedure 293
7.3 Elastic Fixed Window Scan Analysis 294
7.3.1 QENS Results 294
7.3.2 MD Results 295
7.4 Analysis of Diffusion Behaviour 297
7.4.1 QENS Results 297
7.4.2 Molecular Dynamics Results 299
7.5 Summary 302
Chapter 8: Conclusions and Future Work 305
8.1 Conclusions and Key Findings 306

8.2 Ongoing and Proposed Further Investigations.....308
8.2.1 Extensions to 1-Octene Cracking Analysis 308
8.2.2 Determining Proton Locations in Zeolites 309
8.2.3 QENS Analysis of Slow-Moving Systems.....309
8.2.4 Improving the Accuracy of MD Force Fields 310
Appendix 1: List of Central Facilities Beam Time Allocations 311
Appendix 2: Diffusion and Interactions of Olefins in Non-protonated Zeotype Structures 313
A2.1 Non-Protonated MFI Frameworks 314
A2.1.5Silicalite Characterisation 314
A2.2 QENS Investigations Using Silicalite 317
A2.3 MD Simulations in Silicalite 320
A2.4 Summary.....321
Appendix 3: Additional Mass Spectrometry Data for Reaction Tests 323
References 333

List of Tables

Table 2-1: Coherent, incoherent and total scattering cross sections, absorption cross sections and natural abundance of selected isotopes. Adsorption cross sections given for neutrons with E = 25.30 meV. Data taken from Sears.[79] 64

Table 2-2: Data range specifications for detector banks of the Polaris neutron diffractometer at the ISIS Neutron and Muon Source. Data taken from Smith, et al.[95] 90

Table 2-3: Potential parameters for intramolecular zeolite interactions. H_b and O_b represent the Brønsted acid proton and its associated bridging oxygen respectively. Potentials taken from Jackson and Catlow[116] and Schröder, et al.[117] 103

Table 2-4: Intramolecular potential parameters for interactions in adsorbed hydrocarbons as implemented in OPLS_2005.[119] 105

Table 2-5: Potential parameters for interactions between molecules of adsorbed hydrocarbons in multiple-adsorbate simulations as implemented in OPLS_2005.[119] 106

Table 2-6: Intermolecular pair potentials describing hydrocarbon-framework interactions derived from Kiselev, et al.[120] 106

Table 2-7: Analysis columns and column temperatures in the GC used for on-line analysis of reactions in the ISIS catalyst preparation apparatus. .112

Table 2-8: Short designations used to refer to treated zeolite materials used in this thesis. 115

Table 3-1: Lorentzian peak parameters for fitting of peaks (c) - (e) in Figure 3-9. 134

Table 3-2: Populations of different O-H sites in a sample of ZSM5-FR as determined by quantitative INS analysis. 136

Table 3-3: Summary of acid site populations of ZSM5-FR as measured by different techniques. 137

Table 3-4: Vibrational assignments for the INS spectrum of solid propene at ≤ 30 K. Assignments based on data from Fateley and Miller,[149] Ghosh and Kydd,[150] and Lennon *et al.*[151] 142

Table 3-5: Vibrational assignments for the INS spectrum of solid 1-octene at ≤ 30 K. Assignments based on data from Bower and Maddams,[154] Braden et al.,[155] Lennon et al.,[151] and DFT simulations. 147

Table 3-6: Parameters for the self-diffusion of liquid 1-octene derived from fitting the data in Figure 3-20. 151

Table 4-1: Summary of dynamical parameters derived from QENS data fitting for the combined ZSM5-FR / 1-octene system. 167

Table 4-2: Summary of dynamical parameters derived from QENS data fitting for the combined ZSM5-FR / propene system. 183

Table 4-3: Comparison of values for the diffusion parameters of propane in MFI-structured zeolites taken from the literature. $r2$ represents mean jump distance, τ residence time between jumps.....186

Table 4-4: Summary of diffusion parameters derived from QENS data fitting for propane in ZSM5-FR. 190

Table 4-5: Self-diffusion coefficients (D_s) and activation energies (E_a) for propene and propane in H-ZSM-5 calculated from MD results. Values for propene marked (*) are above the minimum temperature for oligomerization in real systems and so the reported D_s values will not be observable experimentally. The ratio of the propane MD values to the propane in ZSM5-FR QENS data in Table 4-4 is provided for comparison. 194

Table 4-6: Comparison of values for the self-diffusion constants of octane in MFI-structured zeolites taken from the literature.....197

Table 4-7: Self-diffusion coefficients (D_s) and activation energies (E_a) for 1-octene and octane in H-ZSM-5 calculated from MD results. Fitting for E_a and D_0 values excludes the 170 K data point due to melting point issued with 1-octene. 197

Table 5-1: Comparison of the structural and acid properties of ZSM5-FR, ZSM5-ST(873K) and ZSM5-ST(1073K) as established by zeolite characterisation measurements. 204

Table 5-2: Lorentzian fit parameters for NMR spectra in Figure 5-2 used to derive relative intensities for each ^{27}Al environment. 205

Table 5-3: Comparison of porosities of ZSM5-FR, ZSM5-ST(873K) and ZSM5-ST(1073K) as calculated from isotherm data. 209

Table 5-4: Summary of diffusion parameters derived from QENS data fitting for propene in ZSM5-ST(873K). 218

Table 5-5: Summary of diffusion parameters derived from QENS data fitting for propane in ZSM5-ST(1073K). Ratios show relationships to the QENS results for propane in ZSM5-FR (Section 4.3.1.1) and propene in ZSM5-ST(873K) (Section 5.2.2). 221

Table 5-6: Rotational constants derived from QENS data fitting for 1-octene in ZSM5-ST(1073K). 227

Table 6-1: Sample details and reaction conditions for propene conversion reactions performed on the ISIS catalysis preparation reactor. ...234

Table 6-2: Assignment of mass spectroscopy signals in Figure 6-2 to associated molecules. All alkene signals should be interpreted as also including contributions from fragmentation of larger molecules in the mass spectrometer.....237

Table 6-3: Properties of ZSM5-FR and reacted catalysts determined by TGA and BET surface area assessment. 247

Table 6-4: Sample details and reaction conditions for 1-octene conversion reactions performed on the UK Catalysis Hub micro-reactor. 263

Table 6-5: Sample reaction times and coke content of octene catalysts determined by thermogravimetric analysis.....274

Table 7-1 Self-diffusion coefficients (D_s), residence times (τ) and mean square jump lengths ($\langle r^2 \rangle$) calculated by fitting the experimental QENS data to the model in Equation (8.1). 298

Table 7-2: Self-diffusion coefficients (D_s) and activation energies (E_a) for methane in silicalite and H-ZSM-5 calculated from MD results. Calculated MD:QENS ratios are for H-ZSM-5 simulations. 300

List of Figures

Figure 1-1: The effect of framework substitutions in zeolites: silicon T-atoms are charge-balanced but aluminium substitutions require a charge-compensating cation located at an adjacent oxygen bridge. 37

Figure 1-2: Comparison of the structures of STI, FAU and MFI-type zeolite frameworks, showing T-atom sites only with oxygen bridges as straight links for clarity. STI and FAU viewed in the [110] plane, MFI in [010]. Structural data taken from the IZA structural database [8] and visualised using Aten v1.8.[15] 38

Figure 1-3: View of an MFI-structured zeolite framework along all three axes. Figure shows eight unit cells arranged as a 2×2×2 supercell. Examples of the 10-MR windows defining the straight (green) and sinusoidal (blue) pores are highlighted. Visualisation generated using Aten.[16] 39

Figure 1-4: General reaction scheme for olefin cracking over zeolite catalyst by bimolecular (a), ß-scission (b) and protonated cyclopropane (c) mechanisms. R groups may be CH_3, alkyl chains or H depending on the specific reactant molecule. Mechanisms taken from den Hollander et al.[18] and Guo et al.[30] 45

Figure 1-5: Dual-cycle hydrocarbon pool mechanism for the methanol-to-hydrocarbons reaction under steady state conditions. Figure adapted from Olsbye, et al.[40] 48

Figure 1-6: Infrared spectrum of H-ZSM-5 measured by ATR-IR (i) and DRIFTS (ii). The locations in each spectrum of the O-H stretching bands (*) and framework Si-O and Al-O modes (†) are highlighted. Spectra collected using the procedures in Section 2.6.1. 49

Figure 2-1: Schematic representation of a simple scattering event. Figure adapted from Mitchell, et al. with modifications.[57] 59

Figure 2-2: Momentum vectors in a scattering event and the associated scattering triangle in reciprocal space showing derivation of the momentum transfer, Q. Figure adapted from Mitchell, et al.[57] 61

Figure 2-3: Layout of the ISIS Neutron and Muon Source, Oxfordshire, UK showing the synchrotron used for proton acceleration, the extracted proton beam lines and the neutron instruments clustered around the two spallation targets. Image credit: STFC. 66

Figure 2-4: Simplified layout of an indirect geometry neutron spectrometer such as TOSCA. L_0 and L_1 are incident and scattered flight path lengths. Figure adapted from Colognesi, et al. with modifications.[84] 73

Figure 2-5: Simplified layout of a generic direct geometry neutron spectrometer. 74

Figure 2-6: $S(Q,\omega)$ Mitre plots of 1-octene measured on MAPS at incident energies of 5244 cm^{-1} (a) and 2017 cm^{-1} (b). Line (c) shows the trajectory in (Q,ω) space measured by the forward-scattering detectors on TOSCA, which may be taken as typical for indirect geometry instruments. 75

Figure 2-7: Representation of the low energy transfer region of an ideal scattering spectrum showing neutron intensity due to elastic scattering (a), quasielastic scattering (b) and the lowest energy Stokes (right) and anti-Stokes (left) INS bands (c). Note that relative peak heights are not to scale. Figure based on data in Mitchell et al.[57] 79

Figure 2-8: Simulated Lorentzian line width (Γ) vs Q^2 relationships for scattering from a molecule undergoing Fickian (a) and Chudley-Elliot jump (b) diffusion with $D_s = 5 \times 10^{-9}$ m^2s^{-1}. Chudley-Elliot jump distance is 2.5 Å. 81

Figure 2-9: Components of a theoretical quasielastic scattering function under realistic conditions. The instrumental resolution function (a), quasielastic broadening (b) and background intensity (c) combine to give the spectrum which is observed experimentally (d). Figure based on data in Telling.[86] 82

Figure 2-10: Layout of the inverted-geometry near-backscattering QENS spectrometer IRIS located at the ISIS Neutron and Muon Source, Oxfordshire, UK. Image reproduced from García-Sakai, et al.[90] ... 85

Figure 2-11: Examples of QENS sample cells: (a) standard cell; (b) single-port gas handling cell with copper blocks for temperature control installed; (c) top view with upper end cap removed showing annular internal geometry and perimeter groove for installation of indium wire gasket. Background grid is 5 mm for scale. 86

Figure 2-12: Nomenclature used for describing the atoms involved in force field potential terms illustrated for 1-octene. 104

Figure 2-13: Layout of the UK Catalysis Hub microreactor setup. 110

Figure 3-1: XRD pattern recorded for ZSM5-FR (a) compared with theoretical patterns calculated for calcined ZSM-5 (b), and H-mordenite (c). λ = 1.5406 Å. Patterns offset in *y*-axis for clarity. Peaks marked with (†) indicate the presence of a low level of contamination in the ZSM5-FR sample. 123

Figure 3-2: SEM images of ZSM5-FR collected at 5000× (i), 12,000× (ii) and 75,000× (iii) magnification. 124

Figure 3-3: Adsorption (a) and desorption (b) isotherms for nitrogen on ZSM5-FR showing hysteresis due to sample microporosity. 126

Figure 3-4: Statistical thickness plot for the adsorption isotherm of nitrogen in ZSM5-FR (a) showing the linear fits used to derive the micropore (b) and mesopore (c) volumes according to the method of de Boer.[130] 127

Figure 3-5: Infrared spectrum of ZSM5-FR after drying at 623 K recorded by DRIFTS at that temperature. 128

Figure 3-6: INS spectrum of ZSM5-FR recorded at $T \leq 30$ K on the MAPS spectrometer at incident energies of 2017 cm^{-1} (*left*) and 5244 cm^{-1} (*right*) and integrated over the momentum transfer range $0 \leq Q \leq 10$ $Å^{-1}$. Insets show × 10 expansions of selected regions to make the O-H modes more apparent. 129

Figure 3-7: INS spectrum of ZSM5-FR recorded at $T \leq 30$ K on the TOSCA spectrometer. 130

Figure 3-8: Weight-normalised ammonia desorption vs temperature trace for ZSM5-FR Peaks represent the desorption of ammonia molecules chemisorbed to silanol groups from 400-600 K and those bound to Brønsted acid sites from 650-900 K.[132] 133

Figure 3-9: ^{29}Si NMR spectrum of ZSM5-FR (a) and fit result (b) for deconvolution into contributions from nuclei in a purely siliceous environment (c), nuclei adjacent to an aluminium substitution (d) and nuclei bonded to a silanol group (e). 134

Figure 3-10: ^{27}Al NMR spectrum of ZSM5-FR. 135

Figure 3-11: Neutron diffraction patterns for deuterated ZSM5-FR as recorded on POLARIS. The plot numbering indicates the detector bank which recorded each trace; technical details of each bank are given in Table 2-2. 139

Figure 3-12: INS spectrum of propene recorded at $T \leq 30$ K on the MAPS spectrometer at incident energies of 2017 (*left*) and 5244 (*right*) cm^{-1} and integrated over the momentum transfer range $0 \leq Q \leq 10$ $Å^{-1}$. 141

Figure 3-13: INS spectrum of propene recorded at $T \leq 30$ K on the TOSCA spectrometer. Peaks due to phonon wing modes are highlighted (†). 141

Figure 3-14: INS spectrum of 1-octene recorded at $T \leq 30$ K on the MAPS spectrometer at incident energies of 2017 (*left*) and 5244 (*right*) cm^{-1} and integrated over the momentum transfer range $0 \leq Q \leq 10$ $Å^{-1}$. 143

Figure 3-15: INS spectrum of 1-octene recorded at T ≤ 30 K on the TOSCA spectrometer (a) compared to a simulated spectrum for 1-octene (b) and the simulated spectrum without overtones or phonon wings (c). 143

Figure 3-16: Partially-staggered geometry of 1-octene identified as corresponding to the conformation of the experimental sample recorded by INS. 144

Figure 3-17: C-H stretching region of the 1-octene INS spectrum (a) compared with the results of peak fitting analysis (b) to deconvolute the contributing modes. Fit components are a linear background due to multiple scattering (c) and peaks due to sp^3 νC-H modes (d), sp^2 νC-H modes (e) and a combination of simultaneous sp^3 νC-H modes and a transverse acoustic mode (f). The degree of uncertainty in the reduction of the experimental data is shown. 145

Figure 3-18: Elastic fixed window scan data for 1-octene from 10 to 370 K recorded on IRIS. Energy transfer window for integration of elastic peak is ± 8.75 μeV. Temperatures where high resolution data was collected for additional analysis are highlighted. 149

Figure 3-19: $S(Q,\omega)$ functions at selected values of Q for 1-octene at 220 K (i) and 320 K (ii) showing deconvolution into resolution function (a), Lorentzian (b) and linear background (c) contributions. $S(Q,\omega)$ axis scale is identical between graphs. 150

Figure 3-20: Variation of Lorentzian linewidth (Γ) as a function of Q^2 for the self-diffusion of 1-octene at 220 K (a), 270 K (b) 320 K (c) and 370 K (d). Dotted lines represent best fit of the data to Fickian diffusion. ..150

Figure 4-1: MAPS INS spectrum of 1-octene following adsorption in ZSM5-FR (a) compared with the spectra of the empty zeolite (b) and pure 1-octene (c). Spectra recorded at incident energies of 2017 cm^{-1} (left) and 5244 cm^{-1} (right) and integrated over the momentum transfer range $0 \leq Q \leq 10$ $Å^{-1}$. Intensities scaled to correct for different sample sizes and offset in y-axis for clarity. 155

Figure 4-2: TOSCA INS spectra of 1-octene in ZSM5-FR (a), ZSM5-FR (b) and pure 1-octene (c). Intensities scaled to correct for different sample sizes. 155

Figure 4-3: C-H stretching region of the INS spectrum of 1-octene in ZSM5-FR (a) and results of peak fitting analysis (b) to deconvolute into a linear background (c), sp^3 νC-H modes (d) and a sp^3 νC-H modes / transverse acoustic mode combination (e). The degree of uncertainty from reduction of the experimental data is shown. ..156

Figure 4-4: INS spectrum of 1-octene adsorbed in ZSM5-FR (a) compared with reference spectra of polyethylene (b), tetracosane ($C_{24}H_{50}$) (c) and hexadecane ($C_{16}H_{38}$) (d). All spectra recorded on TOSCA; reference spectra are taken from work by Parker and co-workers,[155, 160] and sourced from the ISIS INS database.[159] 158

Figure 4-5: Elastic fixed window scan data for ZSM5-FR (a) and 1-octene adsorbed in ZSM5-FR (b) from 5 to 373 K recorded on OSIRIS. Energy transfer window for integration of elastic peak is ± 12.5 μeV. Temperatures where high resolution data was collected for additional analysis are highlighted. 159

Figure 4-6: $S(Q,\omega)$ functions at selected values of Q for 1-octene adsorbed in ZSM5-FR at 373 K showing the resolution function (a) and Lorentzian (b) contributions to the overall fit. 160

Figure 4-7: Experimental EISF values for 1-octene in ZSM5-FR at 273 K (a), 323 K (b) and 373 K (c) compared to the predicted EISF values for jump (d) and continuous (e) methyl rotation using the models described in the text.....161

Figure 4-8: Derivation of the radius of hydrogen movement for methyl rotation in 1-octene from DFT-optimised geometry data. 163

Figure 4-9: Derivation of the radius of hydrogen movement for uniaxial rotation of an alkyl chain from DFT-optimised geometry data. 164

Figure 4-10: Experimental EISF values for 1-octene in ZSM5-FR at 273 K (a), 323 K (b) and 373 K (c) compared with the calculated EISF resulting from continuous uniaxial rotation of the alkyl chain, assuming all hydrogens participate (d). The dotted lines represent the results of a partially-immobile modification of this rotation as described in the text using the p_m values in Table 4-1.....164

Figure 4-11: Variation of Lorentzian linewidth (Γ) with Q for 1-octene in ZSM5-FR at 273 (a), 323 (b) and 373 K (c). Dotted lines represent linear fits to the data used to derive the Γ values reported in Table 4-1.....166

Figure 4-12: Arrhenius plot of the rotational diffusion constants of 1-octene oligomers in ZSM5-FR at 273, 323 and 373 K showing a linear relationship across this temperature range. Line of best fit to the experimental data shown as the dotted line, giving an activation energy of 5.1 kJ mol^{-1} for this motion.....167

Figure 4-13: MAPS INS spectrum of propene following adsorption in ZSM5-FR at 293 K (a) compared with the spectra of the empty zeolite (b) and pure propene (c). Spectra recorded at incident energies of 2017 cm^{-1} (left) and 5244 cm^{-1} (right) and integrated over the momentum transfer range $0 \leq Q \leq 10$ Å^{-1}. Intensities scaled to correct for different sample sizes and offset in y-axis for clarity. 169

Figure 4-14: TOSCA INS spectra of propene in ZSM5-FR (a), ZSM5-FR (b) and pure propene (c). Intensities scaled to correct for different sample sizes. 169

Figure 4-15: INS spectrum of propene adsorbed in ZSM5-FR (a) compared with that of 1-octene adsorbed in ZSM5-FR (b) showing the production of similar product oligomers from each reaction. 170

Figure 4-16: INS spectrum of pure propene (a) and propene adsorbed in ZSM5-FR (b) compared with reference spectra of atactic polypropene (c), isotactic polypropene (d) and polyethylene (e) showing that spectrum (b) primarily exhibits spectral features associated with linear alkyl chains. All spectra recorded on TOSCA; reference spectra are taken from work by Parker and co-workers[160, 170] and sourced from the ISIS INS database.[159] 171

Figure 4-17: INS spectrum of propene following adsorption in ZSM5-FR at 140 K (a) compared with empty zeolite (b) and pure propene (c) spectra. Spectra recorded on TOSCA (i) and MAPS (ii); MAPS incident energy is 5244 cm^{-1} and integration range $0 \leq Q \leq 10$ $Å^{-1}$. Intensities scaled to correct for different sample sizes and offset in y-axis for clarity. 172

Figure 4-18: Elastic fixed window scan data for propene in ZSM5-FR from 20-300 K after dosing at 140 K. Data recorded on OSIRIS with energy transfer window for integration ± 12.5 μeV. Intensity values normalised against T = 20 K. 174

Figure 4-19: TOSCA INS spectra of propene after absorption into ZSM5-FR at 140 K (a) then following further heating to the indicated temperatures: (b) = 200 K; (c) = 215 K; (d) = 225 K; (e) = 240 K; (f) = 255 K; (g) = 270 K and (h) = 293 K. Spectra are offset in the *y*-axis for clarity. The positions of the methyl torsion (*), vinyl scissors (§) and unbonded and bonded vinyl torsions (†,‡) in the 200 K spectrum and the in-phase methylene rock (¶) in the final oligomer spectrum are highlighted. 175

Figure 4-20: Difference plots of selected spectra from Figure 4-19 relative to the spectrum at 200 K (a): (b) = 240 K; (c) = 255 K; (d) = 270 K and (e) = 293 K. All spectra reproduced at the same scale. 178

Figure 4-21: Reaction scheme showing 3-step mechanism for oligomerization of propene over ZSM-5 at exterior active sites producing branched oligomers (a) and interior sites producing linear oligomers (b). Exterior mechanism adapted from Spoto, *et al.*,[48] interior mechanism from Chen and Bridger.[26] 179

Figure 4-22: Elastic fixed window scan data for propene in ZSM5-FR from 20-300 K after dosing at 293 K. Data recorded on OSIRIS with energy transfer window for integration ± 12.5 μeV. Temperatures where higher resolution spectra were recorded are highlighted. 183

Figure 4-23: QENS fit results for propene in ZSM5-FR at 273 K (a) and 323 K (b). (i): Variation of Lorentzian linewidth (Γ) with Q. (ii): Variation of EISF with Q. Dotted lines represent fits to a model of partially-immobile uniaxial chain rotation; Γ, D_r and p_m values derived from these fits are given in Table 4-2.....184

Figure 4-24: Elastic fixed window scan data for propane in ZSM5-FR from 20-370 K (a) compared with the EFWS for propene in ZSM5-FR from Figure 4-18 (b). Propane data recorded on IRIS with energy transfer window for integration ± 8.75 μeV; relative intensities normalised against values at the lowest temperature to allow comparison. Temperatures where higher resolution propane spectra were recorded are highlighted. 187

Figure 4-25: $S(Q,\omega)$ functions at selected values of Q for propane in ZSM5-FR at 170 K (i), 220 K (ii) and 270 K (iii) showing deconvolution into resolution function (a), quasielastic Lorentzian (b) and linear background (c) contributions. $S(Q,\omega)$ axis scale is identical between graphs. 188

Figure 4-26: Variation of Lorentzian linewidth (Γ) as a function of Q^2 for propane in ZSM5-FR at 170 K (a), 220 K (b) and 270 K (c). Dotted lines represent best fit of the data to the Singwi-Sjölander model using the parameters given in Table 4-4. 189

Figure 4-27: Arrhenius plot of the self-diffusion coefficients of propane in ZSM5-FR at 170, 220 and 270 K showing a linear relationship across this temperature range. Line of best fit to the experimental data shown as the dotted line, giving an activation energy of 0.86 kJ mol^{-1} for this motion. 191

Figure 4-28: Average mean squared displacement versus time for propene in H-ZSM-5 at a loading of 4 molecules per unit cell calculated at simulation temperatures of 170 K (a), 220 K (b), 270 K (c), 300 K (d), 320 K (e), and 370 K (f).....192

Figure 4-29: Arrhenius plot comparing diffusion constants derived from MD and QENS methods. Simulations of propane (a) and propene (b) in H-ZSM-5 framework are compared to QENS results for propane in ZSM5-FR (c). Literature values of propane diffusion in different environments from Table 4-3 are included for comparison: QENS measurements of diffusion in H-ZSM-5 at a high but undefined loading level by Silverwood and Sakai[174] (d), of diffusion in Na-ZSM-5 at more comparable loading levels by Jobic *et al.*[69] (e) and the results of comparable MD simulations of diffusion in silicalite by Nowak *et al.*[175] (f). Dotted lines represent linear fits of the MD data in the 170 – 270 K region to determine E_a (g,h) and in the 300 – 370 K region to make the different relationship in this region more apparent (i,j). 193

Figure 4-30: Centre of mass positions for a molecule of propene diffusing in ZSM-5 at 270 K as simulated by MD showing preferential positioning outside pore intersections. Positions logged at 5 ps intervals over 1 ns simulation time. 195

Figure 4-31: Arrhenius plot comparing simulations of octane (a) and 1-octene (b) in H-ZSM-5 framework to literature results for octane measured in H-ZSM-5 by MD (c) and QENS (d). Literature MD results taken from O'Malley and Catlow,[74] QENS results from Jobic.[72].....198

Figure 5-1: Reaction scheme for the breaking of an Al-O(H)-Si bridge in an acid zeolite by hydrolysis. Mechanism adapted from Silaghi et al.[179] ..203

Figure 5-2: ^{27}Al NMR spectra of ZSM5-FR (a), ZSM5-ST(873K) (b) and ZSM5-ST(1073K) (c) showing changes due to loss of framework aluminium in the steamed samples. 205

Figure 5-3: Infrared spectra of ZSM5-FR (a), ZSM5-ST(873K) (b) and ZSM5-ST(1073K) (c) recorded by DRIFTS. Spectral intensities normalised with respect to the silanol framework peak at 1875 cm^{-1}. 206

Figure 5-4: Ammonia desorption vs temperature trace for ZSM5-FR (a), ZSM5-ST(873K) (b) and ZSM5-ST(1073K) (c). Peaks represent the desorption of ammonia molecules chemisorbed to silanol groups from 400-600 K and those bound to Brønsted acid sites from 650-900 K.[132].....207

Figure 5-5: XRD pattern recorded for ZSM5-ST(873K) (a) compared to that of ZSM5-FR taken from Figure 3-1 (b). λ = 1.5406 Å.....208

Figure 5-6: Adsorption (▽) and desorption (△) isotherms for nitrogen on ZSM5-FR (a), ZSM5-ST(873K) (b) and ZSM5-ST(1073K) (c) showing increased hysteresis in steamed materials. 209

Figure 5-7: TOSCA INS spectra of propene after absorption into ZSM5-ST(873K) at 140 K (a) then following further heating to the indicated temperatures: (b) = 260 K; (c) = 270 K; (d) = 280 K; (e) = 290 K; (f) = 300 K and (g) = 325 K. Spectra are offset in the *y*-axis for clarity. 211

Figure 5-8: INS spectra of the final product of propene oligomerization in ZSM5-FR (a) and ZSM5-ST(873K) (b) showing evidence of increased average chain length in ZSM5-ST(873K). Both spectra normalised to correct for differing sample masses and zeolite contributions subtracted. Positions of methyl torsion (†) and (-CH_2-) in-phase rock (‡) highlighted. Spectra offset in y-axis.....213

Figure 5-9: Elastic fixed window scan data for propene in ZSM5-ST(873K) from 20 – 370 K (a) compared with equivalent data in ZSM5-FR taken from Figure 4-22(b). Relative elastic intensities normalised against the value at 20 K to allow comparison between samples. 214

Figure 5-10: $S(Q,\omega)$ functions at selected values of Q for propene in ZSM5-ST(873K) at 170 K (i), 220 K (ii) and 270 K (iii) showing deconvolution into resolution function (a), first Lorentzian (b) and linear background (c) contributions. The 170 K data includes a second Lorentzian parameter (d). $S(Q,\omega)$ axis scale is identical between graphs. 216

Figure 5-11: Variation of Lorentzian linewidth (Γ) as a function of Q^2 for propene in ZSM5-ST(873K) at 170 K (a), 220 K (b) and 270 K (c). Dotted lines represent best fit of the data to the Singwi-Sjölander model using the parameters given in Table 5-4. 217

Figure 5-12: Arrhenius plot of the self-diffusion coefficients of propene in ZSM5-ST(873K) at 170, 220 and 270 K showing a linear relationship across this temperature range. Line of best fit to the experimental data shown as the dotted line, giving an activation energy of 1.86 kJ mol^{-1} for this motion. 218

Figure 5-13: Variation of Lorentzian linewidth (Γ) as a function of Q^2 for the second Lorentzian observed for propene in ZSM5-ST(873K) at 170 K showing Q-independent behaviour. Dotted line represents the line of best fit. 219

Figure 5-14: Comparison of EFWS data for: propene in ZSM5-FR (a); propene in ZSM5-ST(873K) (b); propane in ZSM5-FR (c); propane in ZSM5-ST(1073K) (d). Relative elastic intensities normalised against the value at 20 K. 220

Figure 5-15: Lorentzian linewidth (Γ) *vs* Q^2 for propane in ZSM5-ST(1073K) at 170 K (a), 220 K (b) and 270 K (c). Dotted lines represent best fit of the data to the Singwi-Sjölander model using the parameters given in Table 5-5. 221

Figure 5-16: Arrhenius plot comparison of diffusion constants for: propene in ZSM5-ST(873K) (a); propane in ZSM5-FR (b); propane in ZSM5-ST(1073K) (c). 222

Figure 5-17: Spectrum of 1-octene following adsorption into ZSM5-ST(873K) at 200 K (a) and the same sample after heating to 293 K (b) compared with the spectrum of pure 1-octene (c). Spectra normalised to the amount of octene in each sample and offset in *y*-axis. 224

Figure 5-18: EFWS data for 1-octene in ZSM5-ST(1073K) (a) compared with bulk 1-octene (b) and the oligomer formed by 1-octene in ZSM5-FR at room temperature (c). Intensities normalised against the value at 10 K for comparison. 226

Figure 5-19: Lorentzian linewidth (Γ) *vs*. Q^2 for 1-octene in ZSM5-ST(1073K) at 270 K (a), 320 K (b) and 370 K (c). Dotted lines linear fits of each dataset to give the rotational constants in Table 5-6. 226

Figure 6-1: Percentage conversion versus time for the reaction of propene over ZSM5-FR at 473 K (□), 573 K (○) and 673 K (◇). Values calculated from the concentration of propene in the reactor effluent as determined by gas chromatography relative to that when the reactor is bypassed. 235

Figure 6-2: Relative ion intensities from the analysis of the gas phase products by mass spectrometry during operation at 473 K (i), 573 K (ii) and 673 K (iii) over the 6 hour duration of sample preparation. Numbers on the plots indicate the atomic mass numbers of each trace; assignments are given in Table 6-2. Intensities are normalised against the signal for 4 amu (He) to allow comparison between samples. 236

Figure 6-3: Intensities of selected mass spectrum signals from the traces shown in Figure 6-2 after 1 (i) and 6 (ii) hours on-stream. Intensities are averaged over 10 minutes up to and including the indicated time. 237

Figure 6-4: GC traces of samples collected at 6 hours on-stream for the reaction of propene over ZSM5-FR at 473 K (a), 573 K (b) and 673 K (c). Separation columns are: (i) PoraPLOT Q; (ii) CP-Wax 52CB. The identities of significant peaks are highlighted. 238

Figure 6-5: Concentration of methylated benzenes in the gaseous products versus time measured by gas chromatography at 473 K (i), 573 K (ii) and 673 K (iii). Measured components are benzene (□), toluene (○), o-xylene (◇), m-xylene (△) and p-xylene (▽). Concentrations below 3×10^{-7} mmol/cm^3_{He} are not consistently resolvable from the GC baseline. The pattern in xylene selectivity at each temperature is discussed on Page 260. 239

Figure 6-6: Infrared spectra of the condensable product fraction from reactions at 473 K (a), 573 K (b) and 673 K (c) collected by ATR-IR. Spectra offset in *y*-axis for clarity. Inset shows the methyl bending modes of the 473 K products in greater detail.....242

Figure 6-7: GCMS traces of the condensable product fraction for the reaction of propene over ZSM-5 at 573 K (a) and 673 K (b). Identities of significant peaks are highlighted.....243

Figure 6-8: UV-Vis spectra of the condensable product fraction for the reaction of propene over ZSM5-FR at 473 K (a), 573 K (b) and 673 K (c). Analysed samples were 100 ppm solutions in cyclohexane. The absorption ranges associated with typical mono-, bi- and tricyclic polyaromatics are highlighted. 245

Figure 6-9: DRIFTS infrared spectra of ZSM-5 catalysts after reaction at 473 K (a), 573 K (b) and 673 K (c) compared with ZSM5-FR (d). The allyl stretching modes of adsorbed cyclopentadienyl cations (†) and aromatic C-C ring quadrant stretch (‡) are highlighted. Intensities normalised on the zeolite framework combination mode at 1870 cm^{-1} (*) to allow direct comparison between samples. Traces offset in *y*-axis for easier interpretation. 246

Figure 6-10: INS spectra of ZSM-5 catalysts after reaction at 473 K (a), 573 K (b) and 673 K (c) compared with the spectrum of ZSM5-FR (d). Spectra collected on TOSCA and normalised to correct for differences in sample mass. 247

Figure 6-11: Rate of weight decrease during thermogravimetric analysis in 10% oxygen of samples after reaction at 473 K (a), 573 K (b) and 673 K (c) showing the temperatures required for oxidation of coke species in each sample. 248

Figure 6-12: INS spectrum of ZSM-5 catalyst after reaction at 473 K (a) compared with reference spectra of solid atactic polypropene (b)[56] and hexane (c).[153] Modes indicating the presence of adjacent methylene groups (*) and the asymmetric allyl stretch of cyclopentadiene (†) in the experimental spectrum have been highlighted. All spectra collected on TOSCA and offset in *y*-axis for clarity. Reference spectra obtained from the ISIS INS database.[157] 249

Figure 6-13: INS spectra of coke species formed by reaction at 573 K (a) and 673 K (b) after subtraction of spectrum of ZSM5-FR compared with reference spectra of glassy carbon (c),[193] graphite (d)[194] and diamond (e).[194] All spectra collected on TOSCA and offset in *y*-axis for clarity. Reference spectra obtained from the ISIS INS database.[157] 251

Figure 6-14: Scheme for alkoxide intermediate reactions of propene over H-ZSM-5: (i) alkene protonation and initial oligomerization; (ii) alkene product release and acid site regeneration or further oligomerization; (iii) ß-scission of bonded alkoxide; (iv) partial acid site regeneration involving immobile hydrocarbon molecule. Reaction mechanisms derived from References 26, 48-49 and 148. 255

Figure 6-15: Scheme for cyclic and aromatic ring based reactions over H-ZSM-5: (i) alkoxide cyclisation; (ii) hydrogen transfer and cyclopentadienyl formation; (iii) conversion to aromatic products; (iv) elimination of light olefins from substituted cyclopentadienyl cation. Mechanisms derived from References 45, 190 and 194-195. 257

Figure 6-16: Schematic representation of the linked alkyl and aromatic reaction cycles occurring in the conversion of propene over ZSM5-FR. Species released as products are highlighted in green. 258

Figure 6-17: Intensities of selected mass spectrum signals from passing 1-octene over a SiO_2 blank at 473 K, 573 K and 673 K. Intensities are normalised against the signal for the reaction flow gas (4 amu for He, 28 amu for N_2) to allow comparison between samples and averaged over the period + 01:00:00 to + 02:00:00 with errors shown. 264

Figure 6-18: GC traces of the eluent gas flow from flowing octene over SiO_2 blanks at 473 K (a), 573 K (b) and 673 K (c) collected at 3 hours-on-stream showing thermal cracking of the octene at 673 K. 266

Figure 6-19: Intensities of selected mass spectrum signals from the reaction of 1-octene after 1, 12 and 24 hours on-stream. Reactions performed over ZSM5-FR at 473 K (i), 573 K (ii) and 673 K (iii) and ZSM5-ST(1073K) at 473 K (iv), 573 K (v) and 673 K (vi). Intensities are normalised against the signal for the reaction flow gas and averaged over ± 0.5 hours from the indicated time with errors shown. 267

Figure 6-20: Infrared spectra of the condensable product fraction from 1-octene reactions over ZSM5-FR (i) and ZSM5-ST(1073K) (ii) at 573 K (a) and 673 K (b). A spectrum of pure 1-octene is included for comparison (iii). Spectra collected by ATR-IR and offset in *y*-axis. 271

Figure 6-21: GCMS traces of the condensable product fraction from 1-octene reactions over ZSM5-FR (i) and ZSM5-ST(1073K) (ii) at 573 K (a) and 673 K (b). Identities of significant peaks are highlighted. 272

Figure 6-22: Rate of weight decrease during thermogravimetric analysis in 10% oxygen of samples of ZSM5-FR (i) and ZSM5-ST (ii) catalysts after reaction at 473 K (a), 573 K (b) and 673 K (c). 274

Figure 6-23: Infrared spectra of samples of ZSM5-FR (i) and ZSM5-ST (ii) after reaction at 473 K (a), 573 K (b) and 673 K (c) compared with the spectrum of the catalysts pre-reaction (d). Spectra normalised on the zeolite mode at 1870 cm^{-1} and offset in *y*-axis for easier interpretation. 275

Figure 6-24: INS spectra of ZSM5-FR (i) and ZSM5-ST (ii) after reaction with 1-octene at 573 K (a) and 673 K (b) compared with the spectrum of the catalysts pre-reaction (c). Modes associated with $-CH_3$ (†), $-CH_2-$ (‡) and polyaromatic (*) groups are highlighted. Spectra collected on MAPS and normalised to correct for differences in sample mass..278

Figure 6-25: INS spectra of ZSM5-FR after reaction with propene (i) and 1-octene (ii) at 573 K (a) and 673 K (b) compared with the unreacted zeolite (c). Propene spectra collected on TOSCA, 1-octene spectra on MAPS; peak intensities are therefore not comparable between plots. 288

Figure 7-1: Pre-equilibration starting configurations for MD simulations of methane in MFI zeolite frameworks at loadings of 4 molecules per unit cell (i) and 9 molecules per unit cell (ii). Zeolite shown is the H-ZSM-5 protonated framework. 294

Figure 7-2: Experimental elastic intensity vs temperature for unloaded ZSM5-FR (a) and methane in ZSM5-FR at a calculated loading of 4.70 molecules per unit cell (b).....295

Figure 7-3: Comparison of the experimental EFWS of CH_4 in ZSM5-FR (a) with simulated relative elastic intensities for methane in H-ZSM-5 (b) and silicalite (c) derived from molecular dynamics calculations. All values normalised against elastic intensity at T = 5 K.....296

Figure 7-4: Mean squared displacement versus time for methane in H-ZSM-5 at a loading of 4 molecules per unit cell, calculated at simulation temperatures of 95 K (a), 130 K (b), 170 K (c), 225 K (d), 270 K (e), 325 K (f) and 375 K (g).....299

Figure 7-5: Arrhenius plot comparison of: diffusion in H-ZSM-5 calculated by MD at 4 molecules per unit cell (a) and 9 molecules per unit cell (b); experimental QENS values at 4.70 mol/u.c. in ZSM5-FR as determined above (c); experimental QENS value at 4 mol/u.c. in Na-ZSM-5 as reported by Jobic, et al.[67] (d).....301

Figure 7-6: Arrhenius plot comparison of: diffusion in silicalite calculated by MD at 4 (a) and 9 (b) molecules per unit cell; literature values for diffusion in silicalite at 4 (c) and 8 (d) molecules per unit cell as reported by Leroy, et al.[176] 302

Acknowledgements

It would have been impossible to complete this thesis without the help and support of numerous people over the course of the last four years. My first thanks must, of course, go to Prof. David Lennon for giving me the opportunity to undertake this project and for his invaluable guidance and support. Similar appreciation goes to Dr Paul Collier, both as my industrial supervisor and for encouraging me to undertake this project in the first place, and to Prof. Stewart Parker, who as my Central Facilities supervisor both ensured I could get to grips with the arcane mysteries of the ISIS Facility and helped make completing a PhD over three hundred miles from my home institution a less daunting prospect than it could have been.

Prof. Russell Howe, Dr Chin Yong, Dr Ilian Todorov and Dr Alex O'Malley are all thanked for their collaboration, advice and discussions which have assisted in numerous ways. The contributions of Andrea Zachariou as the only fellow Glasgow student at Harwell to provide a sounding board and collaborator have also been invaluable.

This work would not have been possible without the funding support of Johnson Matthey and the Engineering and Physical Sciences Research Council, the access to neutron facilities provided by the STFC and the ISIS Neutron and Muon Source and the lab facilities of the UK Catalysis Hub at the Research Complex at Harwell: the contribution of all these organisations is gratefully acknowledged. I am grateful to Dr Ian Silverwood, Dr June Callison, Dr Josie Goodall and many others for their assistance with ensuring my work at these institutions was a success.

My fellow students at the UK Catalysis Hub have been invaluable in creating a fantastic working environment that it has been a pleasure to be a part of. I particularly thank my fellow 2016 alumni Andrea (again), Emma Campbell, Rachel Blackmore and George Tierney but I am grateful to everyone I had the opportunity to work alongside while I was there. My thanks also to Emily Braiden for putting

up with the last 12 months of me working from home and for helping me avoid lockdown cabin fever.

Last but never least, I thank my mother, father and sister for their love, support and convincing me I could do this. Thanks for everything.

University of Glasgow
College of Science and Engineering
Statement of Originality to Accompany Thesis Submission

Name: Alexander Paul Hawkins
Registration Number:

I certify that the thesis presented here for examination for a PhD degree of the University of Glasgow is solely my own work other than where I have clearly indicated that it is the work of others (in which case the extent of any work carried out jointly by me and any other person is clearly identified in it) and that the thesis has not been edited by a third party beyond what is permitted by the University's PGR Code of Practice.

I declare that the thesis does not include work forming part of a thesis presented successfully for another degree.

I declare that this thesis has been produced in accordance with the University of Glasgow's Code of Good Practice in Research.

I acknowledge that if any issues are raised regarding good research practice based on review of the thesis, the examination may be postponed pending the outcome of any investigation of the issues.

Signature: …….

Date: ……30th March 2021…….

Definitions of Common Abbreviations

amu..... Atomic mass unit, 1 amu = 1.661×10^{-27} kg.

b ..... Barn, 1 b = 10^{-28} m^2.

BET Surface Area .... Material surface area calculated from gas adsorption isotherm data using the method of Brunauer, Emmett and Teller [m^2g^{-1}].

CCR ..... Closed-cycle refrigerator.

DFT ..... Density functional theory, quantum mechanical simulations for the modelling of the structural and electronic properties of molecules.

EFWS ..... Elastic fixed window scan, a method of QENS analysis which quantifies changes in overall sample mobility with temperature. See Section 2.1.3.2.

eV..... Electron volt, 1 meV = 1.602×10^{-22} J = 8.066 cm^{-1}.

INS ..... Inelastic neutron scattering, herein referring specifically to inelastic *incoherent* neutron scattering unless otherwise specified.

PFG NMR ..... Pulsed field gradient nuclear magnetic resonance spectroscopy.

MD ..... Molecular dynamics, force field-based simulations for the modelling of diffusing systems.

MTH..... The methanol-to-hydrocarbons reaction.

Q..... When discussing neutron scattering, used to refer to the momentum transfer component of the overall scattering function [$Å^{-1}$].

QENS ..... Quasielastic neutron scattering, herein referring specifically to quasielastic *incoherent* neutron scattering unless otherwise specified.

SS NMR ..... Solid-state nuclear magnetic resonance spectroscopy.

ZSM-5..... 'Zeolite Socony Mobil-5', the common short designation for a type of MFI-structured microporous zeolite which is the primary catalyst material studied in this project.

σ ..... Used in neutron scattering to represent the cross section of a given atomic nucleus. Depending on application this may be the coherent (σ_{coh}), incoherent (σ_{inc}) or total (σ_{tot}) scattering cross sections or the absorption cross section (σ_a) [b].

ω..... When discussing neutron scattering, used to refer to the energy transfer component of the overall scattering function [cm^{-1} or eV].

Chapter 1: Zeolites as Hydrocarbon Conversion Catalysts

Acid zeolites have found widespread applications as catalysts for hydrocarbon conversions, including both C-C bond formation and bond breaking reactions. Commercial applications include the selective cracking of high molecular weight hydrocarbons to commercially valuable light molecules and the oligomerization of simple reactive species to larger molecules of industrial relevance. Zeolites may also catalyse the conversion of simple alcohols and other hydrocarbons which may be obtained from non-fossil-fuel sources to aromatic and light olefin hydrocarbon mixtures, offering a renewable route to the production of these valuable chemicals. The bulk nature of these processes in industrial use and the potential value of any optimisations to the catalytic process has led to an extensive literature on how zeolite frameworks interact with hydrocarbons and catalyse their reactions. Fundamental studies into these interactions and the resulting adsorbate dynamics and reaction mechanisms can provide new insight into these systems. This includes potential routes towards improving their catalytic activity and lifetime, an approach which forms the reasoning behind the work performed in this thesis.

This chapter introduces protonated zeolites and their related structures. It reviews what is presently known about their catalytic mechanisms, particularly the importance attributed to the role of the pore structure in enabling selective catalysis. The nature of the MFI-structured family of zeotype materials based on H-ZSM-5 as catalysts of particular industrial relevance is also examined. The scope and objectives of the work performed, how it relates to the existing literature and the structure of its presentation within this thesis are summarised.

1.1 An Introduction to Zeolite Structures:

Zeolites are crystalline materials formed of a silicate-based framework enclosing pores ranging from 5-12 Å in diameter which can be formed naturally through the action of alkaline environments on volcanic minerals.[1] The first such mineral was discovered in 1756 and many species of naturally occurring zeolites exist including mordenite, faujusite, and analcime depending on the nature of the volcanic source material, which results in subsequent differences in the framework structure of the zeolite. All such materials have a high surface area and resulting capability to adsorb small molecules like water and hydrocarbons due to their microporous nature; the name *zeolite* derives from the Greek for 'boiling stone' in reference to this property which leads to the release of large quantities of water vapour from heated samples of zeolites which have been exposed to air.

Zeolite frameworks consist of tetrahedral atomic sites, referred to as T-atoms, liked to four adjacent T-atoms by oxygen bridges. Conventional zeolites are aluminosilicate structures, with Si and Al T-atoms. Structures with alternative compositions such as aluminophosphates,[2] siliconaluminophosphates,[3] and various non-aluminium substituted silicates[4-6] also exist. Although these have historically been distinguished from zeolites, this was mainly for commercial reasons and since the expiry of the relevant patents, they have generally been considered subtypes of zeolytic materials.[1] In aluminosilicate zeolites the majority of T-atoms are silicon up to the obvious limiting case of purely siliceous structures such as silicalite.[7] Silicon:aluminium ratios more commonly fall in the range 2-300, with different framework types having different levels of aluminium substitution for optimum stability. Substitution of framework silicon atoms by aluminium results in a negatively charged oxygen adjacent to the substitution site which is offset by the incorporation of extra-framework cations. These may be metal ions such as sodium or potassium that are incorporated loosely within the pore structure or may be hydrogens which bind to the framework at the negative Si-O-Al bridges to form Brønsted acid sites as shown in Figure 1-1: the properties of the resulting hydrogen-exchanged zeolites vary depending on the properties of the zeolite framework, but tends to result in a high level of acidity.[1]

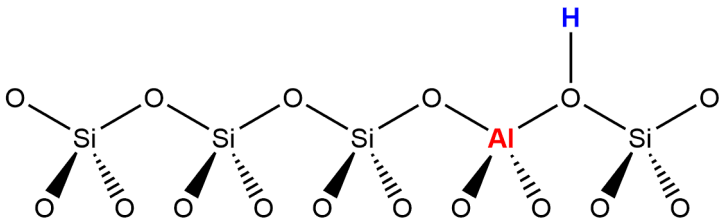

Figure 1-1: The effect of framework substitutions in zeolites: silicon T-atoms are charge-balanced but aluminium substitutions require a charge-compensating cation located at an adjacent oxygen bridge.

Regardless of the specific element occupying the tetrahedral site, the T-atoms are linked together into composite building units, which in turn form the ring structures which define the pore network. These ring structures are referred to according to their number of T-atoms, thus an 8-membered ring (8-MR) structure will, in actuality, have 16 atoms along the circumference of the ring described due to the presence of the oxygen bridges. A large number of possible T-atom arrangements are possible, leading to a correspondingly large number of possible zeolite frameworks possessing different pore sizes and geometries; over two hundred zeolite framework types are currently recognised by the structural commission of the International Zeolite Association (IZA),[8] with the newest unique structure being synthesised and identified as recently as September 2020.[9] Zeolites are broadly separated into small, medium and large-pore types depending on whether they have 8-MR, 10-MR or 12-MR rings as the smallest window size in their pore network, although zeolites with up to 20-MR pores are known. In addition to being the most common ring sizes for zeolite structures, this classification is useful because of the differing adsorption behaviour of each pore type. While large-pore zeolites can accommodate branched paraffins and aromatic rings, small pore zeolites exclude them, being only able to accommodate linear *n*-paraffins and small molecules. Zeolites are therefore a type of molecular sieve and this role forms the primary application for natural zeolites.

Although natural zeolites can be, and are, used commercially, they generally have high levels of structural defects and contaminants, variable Si:Al ratios, and non-uniform compositions. An illustrative example is the case of the very first zeolite discovered: although generally reported to consist of the zeolite subsequently named stilbite a re-examination on the occasion of the 250th anniversary of its

discovery found that the mineral in question actually consists of small stilbite inclusions in stellerite, a closely related zeolite with the same structure but different Si:Al ratio and crystal symmetry.[10] These uncertainties mean that synthetic zeolites see greater use in most applications, particularly as catalytic materials. By controlling the synthesis conditions and the ratio of silica and alumina precursors, zeolites can be created with extremely consistent structural and chemical properties that render them more suitable for industrial use.[11] Furthermore, the development of methods involving the formation of the zeolite framework around an organic template showed that it was possible to create zeolites with structures not found in nature. These templates take the form of small species such as tetraalkyl ammonium ions which are removed *via* calcination after the formation of the zeolite.[12] Synthetic zeolites are named by their inventors and therefore typically receive names that are based on internal references (e.g. zeolite ß, zeolite Y) or on the institution or corporation responsible for the initial synthesis (e.g. SSZ-13 after Standard Selective Zeolite). In order to allow unambiguous references the IZA assigns a three-letter code to each framework structure, derived from the type material for that framework.[13] For example the FAU structure code is shared by, among others, both naturally occurring faujusite (which as the type material supplies the structure code) and the synthetic zeolite Y, which refers specifically to a FAU structure synthesised with a Si:Al ratio between 3.5 and 5.5.[14] Figure 1-2 demonstrates the wide variety

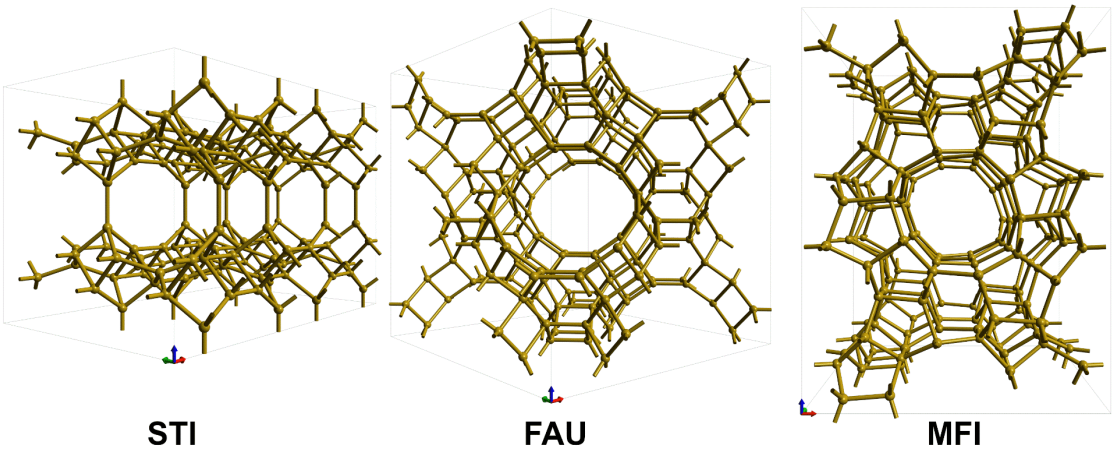

Figure 1-2: Comparison of the structures of STI, FAU and MFI-type zeolite frameworks, showing T-atom sites only with oxygen bridges as straight links for clarity. STI and FAU viewed in the [110] plane, MFI in [010]. Structural data taken from the IZA structural database [8] and visualised using Aten v1.8.[15]

of zeolite framework types by comparing three examples: the STI structure of stilbite and stellerite, the FAU structure of faujusite and zeolite Y, and the MFI structure of the synthetic zeolites ZSM-5 and silicalite.

1.1.1 The MFI Structure and Zeolite ZSM-5:

The MFI structure is a non-naturally occurring zeolite framework formed by synthesis around a tetrapropylammonium ion.[12] This results in a system based on 10-MR windows that form a system of intersecting pores normal to each other which are straight in the [010] direction and sinusoidal in the [100] direction, as shown in Figure 1-3. The pores are elliptical, having dimensions of 5.3 × 5.6 Å in the straight channels and 5.1 × 5.5 Å in the sinusoidal channels. As a medium-pore zeolite, the resulting materials are therefore capable of adsorbing small and intermediate hydrocarbons, including moderately branched chains and single-ring aromatics, but not large hydrocarbon molecules such as naphthalenes.[15] The type material for the MFI structure is ZSM-5, originally developed and patented by Mobil in the 1960s.[12] It is a conventional aluminosilicate zeolite, but is notable in that its stable range of Si:Al ratios is considerably higher than for other framework structures, ranging from 20:1 all the way up to effectively infinity as opposed to the < 10:1 ratios typical for zeolites based on FAU and CHA frameworks.[1] These properties are exploited in a number of applications for industrial hydrocarbon conversion reactions, particularly in the hydrogen-exchanged H-ZSM-5 form which functions as a microporous solid acid.

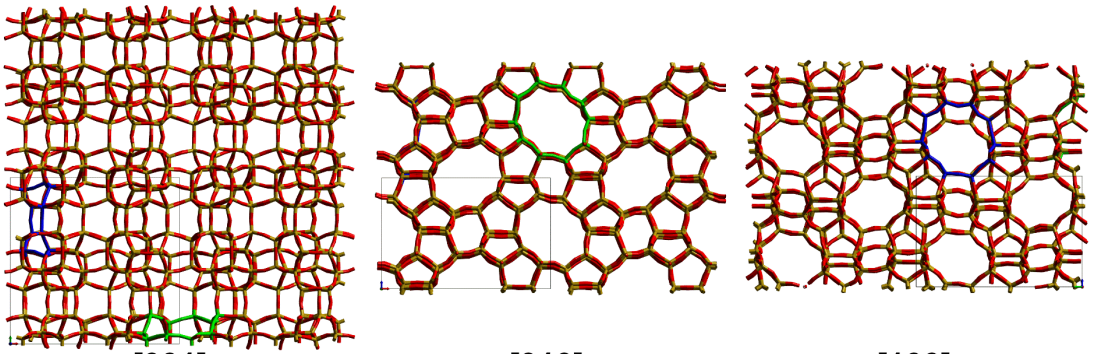

Figure 1-3: View of an MFI-structured zeolite framework along all three axes. Figure shows eight unit cells arranged as a 2×2×2 supercell. Examples of the 10-MR windows defining the straight (green) and sinusoidal (blue) pores are highlighted. Visualisation generated using Aten.[16]

The most widespread commercial use of ZSM-5 is as an additive catalyst in Fluidised Catalytic Cracking (FCC) units, which are used to convert heavy petrochemical fractions such as vacuum gasoil to more profitable fractions such as gasoline. In FCC use, solid acid zeolites protonate hydrocarbon reactants to carbocations, enabling subsequent isomerisation or bond cleavage reactions to generate shorter-chain or more highly branched hydrocarbons that have greater commercial value. In such reactions, the aromatic or olefinic components of the reactant feed are the most actively converted by the zeolite, due to being easier to protonate: saturated paraffins may be cracked or isomerised but this requires the use of zeolites with high levels of acidity.[17-18] Industrial cracking units use a fluidised bed system in order to deal with the carbonaceous 'coke' species which build up on the zeolite during use and which reduce its activity through pore blocking. The catalyst is continually cycled between the reactor and a separate regenerator unit where the coke is oxidised before being returned for reuse; allowing continual operation of the reactor despite coke buildup.[1, 19]

Although first synthesised by Mobil in the 1960s and patented in the 1970s, ZSM-5 was not successfully commercialised as a cracking catalyst until a decade later due to changing market conditions and difficulties with commercial synthesis scale-up.[12, 20] At this time the primary driver for the use of ZSM-5 was due to its ability to increase the octane number of FCC gasoline by promoting isomerisation and cracking of the mid-range *n*-olefin fractions to produce more light olefins. This raised the 'quality' of the gasoline at the cost of reducing the overall quantity of product, a trade-off rendered economically viable by the contemporary requirement to increase the octane of consumer gasoline to compensate for the removal of tetraethyl lead anti-knocking additives. More recently, interest in H-ZSM-5 from the petrochemical sector has been due to the increased light olefin yield itself.[18, 20] Light olefins (referring to alkenes in the C_2-C_5 size range), and particularly propene/propylene (C_3H_6), are valuable hydrocarbon products both due to demand from the polymers industry and due to their use as feedstock chemicals for a wide range of chemical processes including production of acrylic acid, cumene and acrylonitrile.[21] Historically the majority of global propene production has been as a by-product of the steam cracking (SC) of light alkane fractions to produce ethene: SC units accounted for 57% of global propene

production in 2011.[22] However, while the market for propene continues to increase, global production actually fell from 2008-2010 and continues to lag behind demand by an increasing margin. The reason for this shortfall is changes to the steam cracking sector: commercial SC units are increasingly shifting to input streams from shale gas sources and are also improving in overall conversion efficiency, resulting in decreased output of products other than their target ethene. SC is also an inherently inflexible process whose output composition is determined almost purely by the feedstock used; this offers little scope to tune the product distribution catalytically, as can be done with FCC. Given these facts, increasing olefin yields from the FCC cracking of gasoline through more selective catalysis is an area of current industrial interest, with H-ZSM-5 being the main zeolite used in this application.[18, 21-23]

In addition to FCC-related applications, the high activity and selectivity of H-ZSM-5 catalysts lead to other potentially useful reactions. They are capable of catalysing the inverse reaction to hydrocarbon cracking, acid oligomerization, which can be used in the production of synthetic fuels and high quality lubricating oils.[24-26] In addition, the methanol-to-hydrocarbons (MTH) series of reactions uses zeolite catalysts to convert methanol to industrially useful hydrocarbon mixtures such as light olefins and synthetic gasoline: this has been the subject of extensive research due to the ability to supply the necessary feedstock from alternative sources such as biomass, making it a potential replacement route to important chemicals which are currently dependant on fossil fuel sources.

1.2 Shape-Selective Catalysis in Zeolites:

In all of these industrial applications, although the high activity that can be achieved by zeolite catalysts is useful, it is their nature as selective catalysts which is their most attractive property for industrial users. When used in reactions such as FCC, zeolite catalysts shift the composition of the pool of product species to favour some components at the expense of others; the source of this selectivity arises from the ‘shape-selectivity’ of the catalytic process. Because the reactions take place at sites located inside the zeolite framework they occur in a series of linked nanometre-scale reactors whose geometry, size and accessibility all affect

the reaction mechanism through interactions between the framework and the adsorbates. Effectively, the molecular sieving properties of the zeolite framework also apply to reactions which occur within it and modify the products of said reactions accordingly.

Shape-selectivity mechanisms in zeolites may be broadly divided into three different catagories.[27] Reactant shape selectivity occurs in cases where multiple possible reactant species are available in the reactor, such as in the majority of cracking reactions where the feedstock is usually a hydrocarbon distillate fraction containing multiple individual species with similar boiling points. In this case, larger reactants may diffuse through the zeolite considerably slower than smaller molecules due to steric hindrance, or may be excluded from the zeolite entirely and thus be unable to access the catalytic active sites. The products resulting from the reaction of the smaller reactant species will therefore predominate. This type of selectivity is dependent on the diffusional characteristics of the reactants between zeolite pores and is also temperature dependant; since high temperatures result in increased flexibility of large molecules and the 'breathing' of the zeolite pore network; reactant shape selectivity effects may be to some extent relaxed at higher reaction temperatures.[27]

Product shape selectivity occurs when a reaction may produce multiple possible isomers and operates through similar mechanisms. Many zeolite structures contain regions of the pores which are larger than the limiting radius for inter-pore diffusion. H-ZSM-5 is an example of this, with the maximum diameter of the pore intersections being 6.36 Å, larger than the size of the 10-MR windows which form the pore channels.[15] In such cases, reactions in these regions may produce species which are either unable to diffuse through the zeolite to be released as products or which may only do so slowly, increasing the odds of them undergoing further reactions or isomerisations before they escape. These effects result in the preferential production of smaller, more mobile products or of specific isomers which are less subject to hindered diffusion. In an example of the latter effect, methylation reactions of toluene over H-ZSM-5 produce a product mixture where *p*-xylene is the major product, despite being less thermodynamically favourable due to the size of the zeolite pores being small enough to hinder the movement of *o*- and *m*-xylene products.[28]

Finally, transition state shape selectivity occurs where a reactant may undergo multiple possible reaction mechanisms, one of which involves a transition state which is too large for the available space within the zeolite or otherwise disfavoured by the pore geometry, leading the products of the other mechanisms to predominate. Alternatively, interactions with the zeolite pore walls or chemisorption onto the catalytic acid sites may stabilise charged transition states, allowing previously minor reactions with unstable intermediates to make a larger contribution to the overall reaction and, hence, increasing the prevalence of their products. Selectivity due to transition state effects may be distinguished from product selectivity due to being unaffected by the size of the zeolite crystallite, since diffusion through and residence time within the zeolite plays no role in transition state selectivity but is critical to the operation of product selectivity mechanisms.[27]

It can be seen that in all cases it is the geometry of the zeolite pores which determine the shape selectivity of the reaction. It follows that it is possible to adjust the selectivity of a zeolite-catalysed reaction toward desired groups of products through selection of a zeolite with a suitably sized and arranged pore network. The medium-pore nature and intersecting channels of H-ZSM-5 lead to a number of useful shape selectivity effects and result in it being a widely used industrial catalyst. We will now briefly consider two of the most important of these applications: its use as a selective cracking catalyst and in the methanol-to-hydrocarbons reaction.

1.2.1 Selective Hydrocarbon Cracking Reactions:

As noted in Section 1.1.1 above, ZSM-5 in cracking operations operates mainly as a selective catalyst for the conversion of gasoline-range olefins to light olefins in the C_2-C_5 range. For this reason, it is primarily used as an additive catalyst since most FCC columns are designed to operate on low-demand heavy hydrocarbon fractions. Zeolite Y based cracking catalysts convert vacuum gasoil to a large range of products of approximately C_{12} and lighter. The ZSM-5 catalyst, either mixed into the cracking column or in a downstream 'riser' column, further cracks and isomerises the C_6-C_{10} gasoline fraction to more desirable products.[29]

Comparative testing of the cracking ability of ZSM-5 using feedstock typical of FCC column outputs has shown that ZSM-5 is able to double the yield of propene from 1.6 to 3.4 wt% when compared to additional second-stage cracking with zeolite Y.[18]

The primary mechanism behind this increased propene production is a transition state shape-selective effect. Cracking reactions of olefins over zeolite catalysts occur via protonation of the double bond by Brønsted sites to form a bound carbenium ion, as shown in Figure 1-4. This ion may then undergo either a bimolecular reaction involving the addition of another olefin followed by further isomerisation and hydrogen transfer steps (a), or monomolecular cracking reactions proceeding through either ß-scission (b), or protonated cyclopropane (c) intermediates.[18, 30] In ZSM-5, due to the restricted pore diameter, olefins larger than C_4 have insufficient space to react via the bimolecular mechanism; an effect made more significant because the hydrogen transfer reactions which play an important role in the further steps in this reaction pathway require the participation of yet further reactant molecules as hydride donors or acceptors. Therefore, larger FCC reactants react exclusively through the monomolecular mechanisms involving scission, resulting in a higher production of small molecules such as light olefins. This effect is magnified by the fact that in the ß-scission mechanism (b) the post-scission primary carbocation may be stabilised by one of two routes: an isomerisation to a secondary carbocation, optionally followed by a desorption of that carbocation as a disubstituted alkene (d); or by a further bond cleavage resulting in release as two separate, smaller olefin molecules (e).[18] Under ordinary conditions it is the isomerisation pathway which is energetically favoured. However, in ZSM-5 the dimensions of the pores mean that interactions between the closely located framework oxygens and the carbocation act to stabilise the intermediates in the bond cleavage mechanism, further driving the product balance toward the smaller olefins.[18]

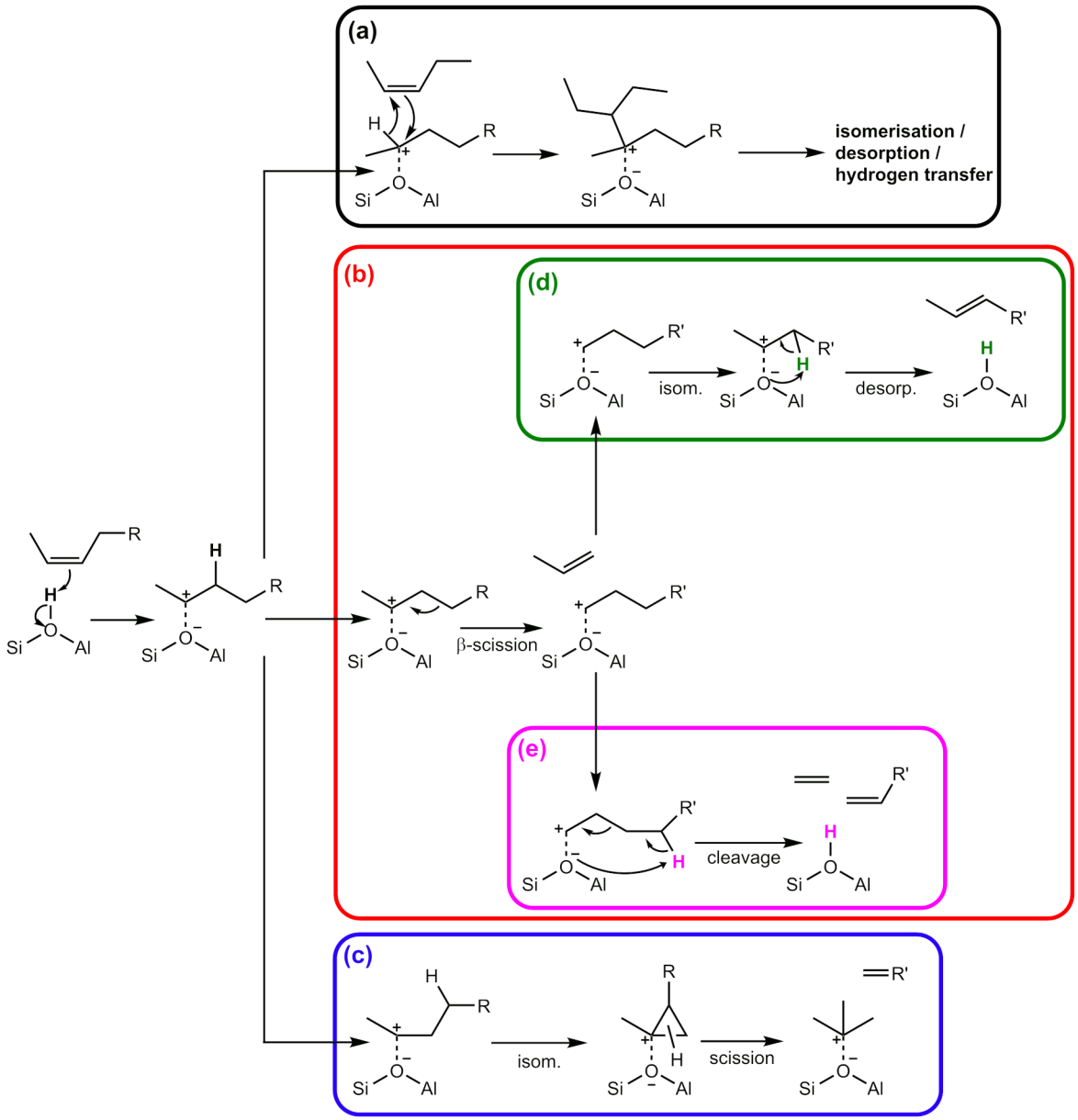

Figure 1-4: General reaction scheme for olefin cracking over zeolite catalyst by bimolecular (a), ß-scission (b) and protonated cyclopropane (c) mechanisms. R groups may be CH_3, alkyl chains or H depending on the specific reactant molecule. Mechanisms taken from den Hollander et al.[18] and Guo et al.[30]

While the shape selectivity explanation for the catalyst selectivity is well established, there are additional aspects to the zeolite cracking chemistry which are not always considered. The physical and chemical properties of the zeolite, including its levels of acidity and mesoporosity, are by no means constant throughout the lifetime of the catalyst. Hydrothermal conditions in catalytic use result in partial de-alumination of the zeolite framework at a rate determined by both the reactor temperature and the concentration of aluminium substitutions within the zeolite.[31] The partial pressure of steam within the reactor also affects

the rate of aluminium loss, but the magnitude of this effect is considerably less than the effects of temperature or zeolite composition.[32] This leads to a corresponding reduction in the number of acid sites, since removing an aluminium atom also removes its associated Brønsted O-H acid group, and possibly increases in mesoporosity depending on the aluminium level of the zeolite and, thus, what proportion of the framework atoms are removed.[31, 33] Effects of this loss of acidity can be dramatic: while even quite severe steaming conditions result in minimal changes to the zeolite crystallinity, and therefore its overall structural integrity, large increases in mesoporosity and decreases in micropore area are found, together with decreased acidity levels.[18, 34-35] While some studies report that these changes merely reduce the overall activity of the catalyst and do not significantly affect its selectivity,[34] others report that hydrothermal de-alumination preferentially removes stronger acid sites from the zeolite, disfavouring reactions such as hydrogen transfer and aromatization, and increasing the production of light olefins.[35] Similar effects are thought responsible for the observation that ZSM-5 cracking is capable of cracking and isomerising paraffins when fresh but that in steady-state operation nearly all reactivity involves changes to the more reactive olefin components, and paraffin fractions of the feed remain inert.[18] The degree to which increased mesoporosity in de-aluminated zeolites affects the diffusion of adsorbates within the framework is also largely unknown, and has obvious ramifications for its reactant and product shape-selectivity effects as the catalyst ages. As proven by the increased propylene yield effect reported by Ibáñez, et al.,[35] new insight into these processes and their potential applications has obvious industrial relevance.

1.2.2 The Methanol-to-Hydrocarbons Reaction:

The methanol-to-hydrocarbons (MTH) reaction, sometimes split into the related methanol-to-olefins and methanol-to-gasoline processes, allows production of a wide range of hydrocarbons from methanol feed. Since methanol is available from biomass sources, or can be made from syngas (itself easily generated from the reforming of natural gas, coal or tar sands), MTH chemistry offers an important route to a supply chain of petrochemicals and petrochemical derivatives that does not involve crude oil.[36] The ability of acidic catalysts to form C-C bonds from

methanol was first reported by Chang and Silvestri in 1977,[37] and the process was commercialised in New Zealand at the 600 kton.yr^{-1} level as early as 1986. However, the drop in oil prices throughout the subsequent decade led to the subsequent closure of that plant. Academic interest in the process has nevertheless remained high to the present day, due to the need to provide a hedge against further oil price shocks and to increase the range of products and commercial value of petrochemicals from unconventional sources.[36, 38-40]

ZSM-5 was the acid zeolite catalyst used by Chang and Silvestri in their initial measurements,[37] and it remains an important catalyst for MTH processes due to producing a product mix which makes high quality gasoline. As with many zeolite processes, the final product composition of the MTH reaction is influenced by shape selective effects from the channel dimensions. The 10-T-atom ring structure of ZSM-5 (Figure 1-3) means that the largest product molecules which can form within the structure and diffuse out are polymethylated aromatics. Extensive studies of the MTH reaction over the 40 years since it was first commercialised have established that it proceeds via a 'hydrocarbon pool mechanism', initially proposed by Dahl and Kolboe for reactions over SAPO-34.[41] Under this mechanism, an internal population of alkenes and aromatics act as co-catalysts, undergoing a continuous process of addition, isomerisation and cracking reactions to give the final products, which are primarily light olefins and methylated aromatics.[39-42] As shown in Figure 1-5, the reactions within the pool can be split into two cycles depending on whether the participating co-catalyst is an olefin or aromatic molecule. In the olefin cycle, unsaturated straight chain hydrocarbons are methylated to longer chain lengths and cracked back down to shorter chains. In the aromatic cycle, benzene rings are repeatedly methylated and de-alkylated. Transfer of carbon between the two cycles is possible either by the cyclisation of alkene molecules, with an associated hydrogen transfer to another alkene to absorb the excess hydrogen, or by the cracking of alkyl groups from substituted aromatics. Since any of the pool species present can be released from the catalyst as product instead of undergoing further reactions, it can be seen that the composition of the final MTH product stream is dependent on the relative rates of the various reaction processes occurring in these cycles.[39-40]

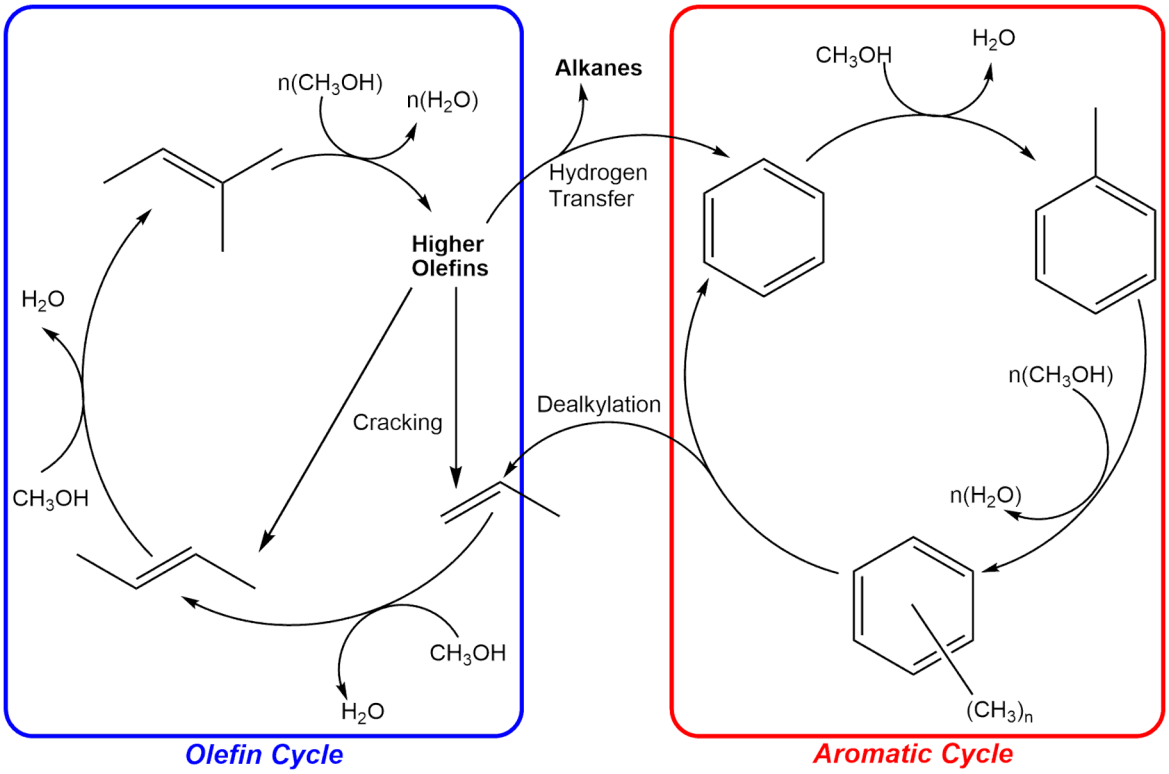

Figure 1-5: Dual-cycle hydrocarbon pool mechanism for the methanol-to-hydrocarbons reaction under steady state conditions. Figure adapted from Olsbye, et al.[40]

The MTH reaction is an important industrial reaction and is therefore a broad area of research with its own extensive literature.[40] In the context of this project, we are mainly concerned with the formation of the hydrocarbon pool during the conditioning period of the catalyst, and the reactions responsible for forming the first carbon-carbon bonds, which is a matter of ongoing debate.[40, 42] It is known that the methanol feed is initially dehydrated to form dimethyl ether (DME), and studies have suggested that the initial C-C bonded species produced by the subsequent reaction of the DME are propene and other light olefins.[43-44] It is the reactions of these olefin products which form the starting population of the hydrocarbon pool, the establishment of which completes the conditioning of the MTH catalyst.[45-47] Studying how light olefins react within zeolites under MTH reaction conditions and comparing this reactivity with olefin chemistry in cracking reactions may provide new insight into both these important processes.

1.3 Studying Interactions and Dynamics in Zeolites:

From the background given in Section 1.2, it is evident that both olefin cracking and MTH processes possess several areas of ongoing research that can be best addressed by spectroscopic investigations of the zeolite catalyst, both under *operando* conditions and by *ex situ* methods. Infrared spectroscopy has been widely applied to the study of reactions in zeolites,[48-52] but its application possesses some inherent limitations. The Si-O and Al-O bonds lead to strong framework modes which dominate the infrared spectrum as shown in Figure 1-6(i) and mask any modes from adsorbed species at wavenumbers of 1350 cm^{-1} and below. This problem is magnified by the fact that, in order to avoid unnecessary mass transport effects, it is best to study zeolite behaviour in the pelletized or powder form it is usually used in; diffuse reflectance infrared Fourier transform (DRIFTS) spectroscopy is the best technique for studying materials in this state, but it leads to the framework bands extending as high as 2000 cm^{-1} (Figure 1-6(ii)). This means that while infrared spectroscopy can provide excellent detail on the C-H and O-H stretching modes located above 2500 cm^{-1}, it is less capable of resolving the C-H deformations and C-C modes which lie in the 'fingerprint region' below 1500 cm^{-1} and which are important to the specific identification of hydrocarbon species. Raman spectroscopy does not suffer from this masking effect but is instead hindered by sample fluorescence which obscures the modes of interest unless advanced techniques such as temporal Kerr-gating are employed.[53]

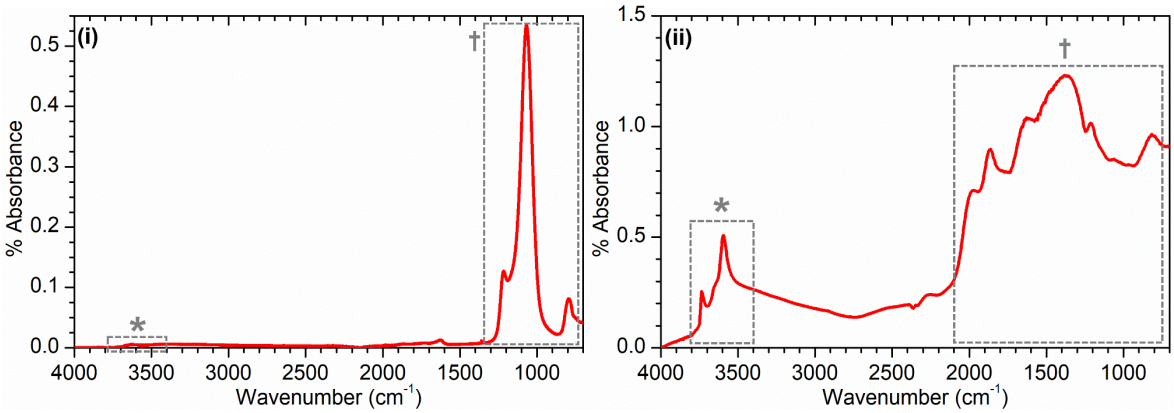

Figure 1-6: Infrared spectrum of H-ZSM-5 measured by ATR-IR (i) and DRIFTS (ii). The locations in each spectrum of the O-H stretching bands (*) and framework Si-O and Al-O modes (†) are highlighted. Spectra collected using the procedures in Section 2.6.1.

In both cases, spectroscopic investigations are further complicated by the fact that these reactions also involve side-reactions that lead to the build-up of immobile 'coke' species within the zeolite over the course of the reaction. These species have a tendency to be highly carbonaceous in form and strongly coloured, leading to progressive darkening of the catalyst with increasing time on-stream.[52] This increased absorbance leads to infrared spectroscopy having problems with achieving useable signal:noise ratios at later stages of the reaction and greatly complicates the use of difference spectroscopy methods; thereby magnifying the inherent difficulty in observing modes masked by the zeolite framework bands. In addition, the nature of the coke species is itself of interest as coke formation rates determine the amount of time the catalyst can operate before it requires regeneration, and therefore indirectly the total useful lifetime of the catalyst. While some information on coke species can be obtained by infrared spectroscopy, and methods such as nuclear magnetic and electron spin resonance spectroscopies are unaffected by either absorbance or the zeolite framework, a method of accessing the full vibrational spectrum of the coke without resorting to destructive methods like Guisnet analysis is desirable.[54-55]

One technique which has potential to address these requirements is neutron scattering spectroscopy, specifically inelastic incoherent neutron scattering (IINS), which is seeing increasing use as a tool for catalytic science investigations.[56] Neutrons are also useful to this study in that a related technique, that of quasielastic neutron scattering (QENS), represents a useful method for measuring the microscopic diffusion of sorbates which occurs within zeolite channels.

1.3.1 Neutron Methods as Tools for Studying Zeolites:

Inelastic neutron scattering (INS) techniques can access a wide range of energies times and lengths from microsecond and micrometre to femtosecond and sub-Ångstrom scales.[57] From a catalytic perspective, the application of greatest interest is in the higher energy region of the inelastic energy transfer range from 20 – 4000 cm^{-1}. In this region INS spectroscopy produces vibrational spectra similar in many ways to those generated by infrared or Raman spectroscopy but with some important differences. Because neutron methods involve interactions with atomic

nuclei, they are highly penetrating and the strength of the scattering from a given nucleus is dependent on its scattering cross-section. This is a property of the specific isotope of the nucleus and is not related to its atomic number; indeed ^{1}H has an exceptionally high scattering cross section for INS while the cross sections of ^{2}H, Si, Al and O nuclei are all low. For hydrocarbon systems in zeolites therefore the INS spectrum is dominated by the modes of the adsorbates and the O-H catalytic groups; masking of the fingerprint region is not a concern. INS spectroscopy also lacks selection rules, meaning that all vibrational modes are present in the spectrum for analysis. INS intensities are also quantitative, being directly proportional to the population of the group responsible for a given vibrational mode without any extinction coefficients or resonance enhancement complicating the quantification of the contents of a catalytic sample. Finally, INS is a bulk technique and while its relative insensitivity does require large sample sizes in comparison to IR or Raman methods (on the order of 10-20 g of catalyst),[58] this means that the resulting spectrum is well averaged, an important consideration when attempting to simulate large-scale industrial processes. For a more detailed consideration of the principles behind INS spectroscopy and their implications for its use in catalysis the reader is referred to Section 2.1.2 below.

Advances in the sensitivity and resolution of INS spectroscopy have led to its increasing application to investigate heterogeneously catalysed systems; this field has been reviewed by Parker and co-workers on multiple occasions as it has developed.[56, 59-61] Most notably for this thesis, recent studies by Howe, et al.[62] and Suwardiyanto, et al.[63] have successfully applied the technique to investigate the MTH reaction. These studies were successful in observing the retained species within the used zeolite and detecting changes in the resulting spectra based on differences in reaction conditions, thus proving the suitability of INS as a technique for investigating zeolite catalysts since applications to FCC-type reactions should yield equal success.

1.3.2 Studying Adsorbate Dynamics in Zeolites:

Diffusion measurements of sorbate molecules in zeolites can be broadly divided into macroscopic and microscopic techniques. Macroscopic measurements use

methods such as sorption uptake, chromatography and steady-state permeation measurements and measure the movement of molecules in the presence of a concentration gradient.[64] Microscopic measurements have more immediate bearing on the catalytic properties of a zeolite catalyst because they involve time and length scales corresponding to the movement of molecules in the interior of zeolite pores.[64-65] Pulsed field gradient (PFG) NMR measurements can access molecular displacements on the order of 0.1-1 μm with timescales of 1 ms and have been successfully applied to the measurement of movements at the larger end of the microscopic scale.[66-67] However, the technique of quasielastic neutron scattering (QENS) can extend these scales down to the level of Ångstroms and picoseconds; this is sufficient to allow observation of essentially the full range of motions which can occur within zeolite pores including small pore zeolites. For this reason, QENS has become the preferred technique for providing detailed, molecular-level experimental information on zeolite-adsorbate systems, particularly with hydrogenated adsorbates, which can exploit the high scattering cross section of the ^{1}H nucleus to achieve high signal strengths. An extensive literature exists on the diffusion of small molecules[67-68] and the normal hydrocarbons from C_3-C_{16} within zeolites,[69-72] together with considerations of the effect of chain branching on diffusion.[72-73] However, information on the diffusion of reactive species like alkenes in zeolites is much less prevalent, furthermore, the effect of catalyst de-alumination remains almost unstudied. The dynamics studies in this thesis are an attempt to address these areas.

1.3.3 Computational Modelling as a Supplement to Neutron Methods:

An additional advantage of neutron spectroscopic methods is that their distinctive properties mean that they possess excellent synergies with computational chemistry methods. Both INS and QENS techniques can benefit from this, with each being complemented by different simulation techniques.

For INS spectra, the lack of any selection rules or extinction coefficients and the simple relationship between the scattering intensity and the vibrational modes (see Section 2.1.2) means that it is possible to generate a model spectrum of a

molecule of interest from computational data. The only information required is the amplitudes of the atomic motions in the various vibrational modes, which may be generated computationally from an optimised electronic structure simulation.[57, 59] Even simulations of isolated single molecules can produce data useful to spectral analysis, and by using methods such as density functional theory (DFT), as described in Section 2.2.1, the resulting calculations can be performed on desktop-level computing hardware, rendering them eminently accessible.

For QENS, the time and length scales of motion accessible for measurement correspond to those which are practical to simulate using force-field based or 'classical' molecular dynamics (MD) simulations, namely up to the nanometre and nanosecond level.[64-65] Both methods produce measures of molecular movement which are directly comparable; as described in Chapter 2, this means that QENS measurements can be used to validate the parameters used to describe molecular interactions in MD simulations, and conversely that results from MD simulations can be used to guide the fitting and analysis of QENS data.[74] Advances in computational hardware mean that MD simulations at the all-atom flexible-zeolite level of realism, which provides for close agreement with experimental data,[74-75] are performable in reasonable time frames without requiring the use of supercomputer-level processing resources, rendering them accessible to the non-specialist.

1.4 Project Objectives:

It is clear from the overview given above that applying inelastic neutron scattering spectroscopy and the combined use of quasielastic neutron scattering and molecular dynamics simulations to the reactions of olefin molecules in zeolites offers the possibility of new insights into the mechanisms of these important reactions. These insights are particularly likely to be industrially relevant if they are used to address fundamental questions about the effect of zeolite aging through de-alumination on the interactions and dynamics of active olefin sorbates. INS also offers the possibility of more detailed study of the processes which build up the coke species responsible for the temporary deactivation of zeolite catalysts by allowing collection of vibrational spectra of the catalyst after longer reaction

times. This thesis seeks to systematically apply these advanced techniques, in combination with conventional micro-reactor studies and optical spectroscopy, to address these questions.

The zeolite used throughout the study was a commercial material grade H-ZSM-5 zeolite supplied in powder form without binder by our industrial partners, Johnson Matthey plc. ZSM-5 was chosen as being the zeolite of greatest use for selective cracking and MTH chemistry, as described in Section 1.1.1. The use of a commercial zeolite was decided on to more closely link the results obtained with chemistry of industrial interest, to increase sample reproducibility across the breadth of the project, and to simplify the process of preparing the large sample sizes necessary for neutron measurements by using a catalyst procurable in bulk. In order to reduce the complexity of the large number of simultaneous reactions which occur in hydrocarbon pool type reactions over zeolites, the hydrocarbon testing was done in the form of model compound studies using pure hydrocarbon feeds. Propene was used as it is the light olefin of greatest commercial interest as a cracking product and is of interest as an intermediate in MTH chemistry.[22, 47] Studies of the dynamics of this system also made use of propane as an inert analogue of similar size and diffusivity. Investigations into cracking chemistry used 1-octene, which is commonly employed as a model compound for the type of linear and branched C_7-C_{12} olefins which are the active fraction for FCC reaction over ZSM-5.[30, 76-77]

Chapter 3 covers the results of a comprehensive characterisation of this ZSM-5 catalyst by both conventional and neutron methods, together with a brief consideration of how the model compounds appear when examined by neutron methods. How the model compounds and the fresh ZSM-5 catalyst interact at low temperatures is examined in Chapter 4. Building on these baseline measurements, the effect of the de-alumination of the acid H-ZSM-5 in a manner consistent with aging in catalytic use on these low temperature interactions is studied in Chapter 5. Finally, Chapter 6 turns to reaction studies of olefin conversions at temperatures more representative of catalytic use in MTH and FCC reactions.

In a separate study to the olefin conversion reactions described in Chapters 4-6, the molecular dynamics methods developed as part of this thesis were applied to study the motions of methane adsorbed in ZSM-5 as an inert analogue for the movement of methanol in MTH systems. This work was performed in partnership with another PhD student at the University of Glasgow, Ms Andrea Zachariou, and the portions of that work relevant to this thesis are presented in Chapter 7. For a more detailed discussion of the division of labour in this study please see the Preface to this thesis.

Before presenting these studies, it is necessary to consider the theoretical background underpinning the neutron and computational methods employed and the techniques and tools used in their analysis. These concepts, together with the experimental apparatus and procedures used in the rest of this project, are introduced in Chapter 2.

Chapter 2: Materials and Methods

Neutron scattering spectroscopic methods are a unique tool for studying the structure and dynamics of materials at scales which are of relevance to catalysis. An overview of neutron scattering theory is necessary to show how it leads to techniques which have both advantages and disadvantages relative to more 'conventional' spectroscopic methods. The technical aspects of neutron sources and instruments are here briefly outlined to demonstrate how the use of different instrument types is necessary to obtain a clear picture of the entire energy-transfer region of interest. A discussion is made of the principles used to analyse neutron scattering data, with particular emphasis on the technique of quasi-elastic neutron scattering (QENS), which allows the direct determination of diffusion characteristics through fitting analysis.

The theory behind neutron vibrational spectroscopy renders its results particularly amenable to comparison with results from ab initio molecular simulations. The size of zeolite-hydrocarbon systems of interest is such that simulations of the motions within the system on QENS timescales can be performed by classical molecular dynamics. The steady increase in widely available processing power, together with development of improved software tools, means that the entry barrier to computational chemistry simulations has decreased to the point where these techniques are accessible to non-specialists. Both of these techniques have been used as tools to aid in the analysis of experimental results: the specific simulation methods utilised and their underlying theory is examined here.

In addition to these neutron- and computer-based investigations, a large number of techniques have been employed to characterize the ZSM-5 catalyst in both used and unused states. Micro-reactor testing has been employed to investigate the catalytic activity of ZSM-5 under varying conditions; additional reactions using a 10 g-scale reactor have been performed to enable product analysis by neutron methods and to prepare aged materials for investigations of the effect of zeolite de-alumination. The apparatus and instruments employed in these investigations are described.

2.1 Neutron Spectroscopy; Theory, Techniques and Analysis:

Neutron scattering techniques make use of the properties of the neutron (^1_0n), namely that it is an elementary particle with zero charge but possessed of both a mass and a magnetic moment. Its rest mass is 1.0087 atomic mass units, approximately that of a hydrogen atom, and its magnetic moment is spin ½. As a quantum mechanical entity, the neutron displays wave-particle duality, with both particle-like and wave-like behaviour depending on how it is viewed. Neutrons with an energy of approximately 25 meV, referred to as 'thermal' neutrons, have a de Broglie wavelength of *ca.* 1-5 Å, on the order of intermolecular and interatomic distances, and an energy expressed in wavenumbers of *ca.* 30-700 cm^{-1}, comparable to those of molecular vibrations. Therefore, investigations using neutrons in this energy range can yield information on both the structure and dynamics of a system from which they scatter. This investigation focuses primarily on the use of neutron scattering spectroscopy, where treating neutrons from a particle-like perspective is often more intuitive, however, wave-like behaviour is also exploited for energy selection or analysis as well as in neutron diffraction measurements.[57, 59-60, 78]

These properties give rise to a number of effects governing the interaction of a neutron flux with matter that are useful for spectroscopy:

- Because neutrons are uncharged, they do not interact with the electron cloud and scatter solely from atomic nuclei. Neutrons are therefore much more penetrating than photon- or electron-based spectroscopic methods, which allows easier probing of the bulk processes of samples where these may differ from surface chemistry.
- Since neutrons do not interact with the electron cloud, the intensity of scattering is determined by nuclear and isotopic effects rather than by the number of electrons. Neutron spectra are therefore not necessarily dominated by heavier components, and in fact certain methods are highly selective towards hydrogenous species as detailed below.

- The above two factors mean that design of sample environments is considerably simplified since a few millimetres of aluminium is functionally transparent to neutrons.
- Neutron spectroscopy has no selection rules as the scattering events involve measurable levels of momentum transfer due to the mass of the neutron, thus the entire vibrational spectrum is measurable.
- Due to the lack of selection rules and electro-optical parameters, neutron spectra are readily and accurately calculated from computer simulations. Spectral intensities are related solely to the displacement of scattering centres and the quantities of scatterers so displaced.
- The energy range of neutrons is extremely wide and may be set by moderation of the incident neutrons down to thermal temperatures. Transitions with energies as low as 25 μeV (0.2 cm^{-1}) can be observed by using extremely slow neutrons allowing observation of translational and rotational modes,[57] while use of higher energy neutrons allows ready access to vibrational regions of the spectrum.

2.1.1 Basic Theory of Neutron Scattering:[57, 59-60, 78]

Neutron scattering techniques are relatively intuitive in their application but involve some specialised concepts that affect the analysis of the resulting data and which it is therefore necessary to define. In the following sections we will discuss the concepts of: energy and momentum transfer, coherent and incoherent scattering and the ways in which the ways to generate a usable neutron flux affect the design and operation of neutron instruments.

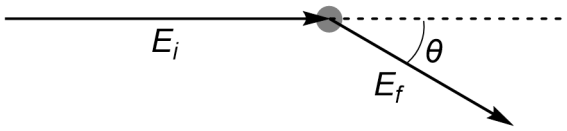

Figure 2-1: Schematic representation of a simple scattering event. Figure adapted from Mitchell, et al. with modifications.[57]

In its simplest form, neutron scattering occurs when an incident neutron encounters an atomic nucleus in the sample and is scattered from it as a result of that collision, as represented in Figure 2-1. An incident neutron with energy E_i is

scattered through angle θ onto a new vector with energy E_f by the nuclear strong force. Because the range of the nuclear interaction potential is very small relative to the wavelength of the neutron, the nucleus may be regarded as a point scatterer and the scattering occurs isotropically. This simple picture is complicated by the fact that not all scattering events are the same. A neutron may scatter in *coherent* or *incoherent* modes and may do so *elastically* or *inelastically*. An additional possibility is that the neutron may be absorbed by the nucleus, resulting either in an isotopic transmutation, the radioactive decay of the now-unstable nucleus or nuclear fission. However, while neutron absorption plays an important role in the design of neutron sources and instruments, its relevance to spectroscopy is relatively small for most samples other than the handling considerations resulting from the induced radioactivity that inevitably occurs in any material investigated by neutron methods.

2.1.1.1 Energy and Momentum Transfer:

The energy of a neutron refers to its kinetic energy, which from a particle perspective is given by:

$$E = \frac{1}{2}mv^2 \tag{2.1}$$

Alternatively, the wave perspective treats the neutron as having a wavevector, k, (which includes both its velocity and direction of travel) and wavelength, λ. From a particle perspective, the momentum of the neutron is given by $\hbar k$.

$$k = \frac{2\pi}{\lambda} = \frac{mv}{\hbar} \tag{2.2}$$

When the neutron scatters from an atomic nucleus it may do so elastically, where no energy transfer between the neutron and the sample takes place; scattering of this type forms the basis of techniques which are used to study material structure such as neutron diffraction, small-angle neutron scattering (SANS) and reflectrometry. Alternatively, the collision may involve a transfer of energy between the neutron and the atom from which it scatters, exciting or de-exciting one of the modes of the molecule that includes the scattering atom and resulting in an inelastic scattering event. All modes are in principle accessible from

molecular translations and rotations upward, limited solely by the incident energy of the specific neutron in the scattering event. The energy transfer which occurs, ω, is the difference between the incident and final neutron energies.

$$\hbar\omega = E_i - E_f = \frac{\hbar^2}{2m}\left(k_i - k_f\right) \tag{2.3}$$

Inelastic neutron scattering therefore has similarities to Raman scattering in that both involve a change in the incident energy of the scatterer which may be exploited spectroscopically. There is, however, one major difference; neutron scattering events involve a significant transfer of momentum from the neutron to the sample by virtue of a change in the direction of its travel and/or its energy. This momentum transfer, Q, is the product of the vectors of the incident and scattered neutrons and its value may be calculated from the wavevectors and scattering angle by applying the cosine rule for triangles. Momentum transfer is not a factor in optical spectroscopy methods due to the momentum of photons being insignificant at energies below the X-ray level. This means that only transitions which occur at zero momentum transfer can be excited, leading to the selection rules in both infrared and Raman spectroscopy, that only transitions at zero wavevector are observable. This is not the case with neutron scattering: all neutron spectroscopic methods are inherently two-dimensional, with ω and Q being linked, and thus transitions at all wavevectors are permitted.

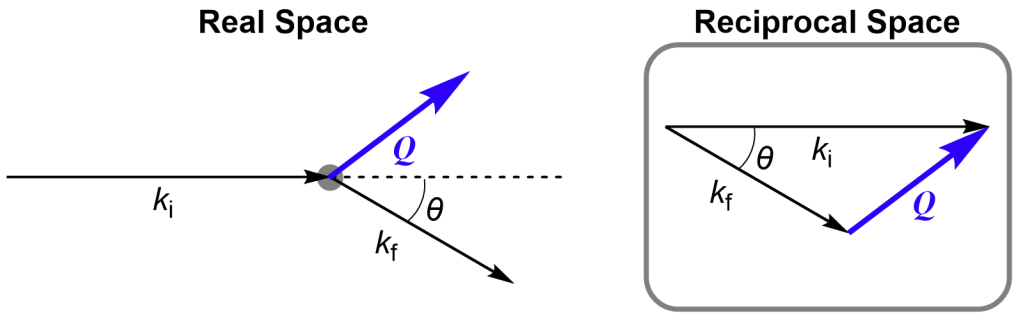

Figure 2-2: Momentum vectors in a scattering event and the associated scattering triangle in reciprocal space showing derivation of the momentum transfer, Q. Figure adapted from Mitchell, et al.[57]

For historical reasons, the neutron scattering literature usually expresses lengths in Ångstroms and Q in $Å^{-1}$. Similarly, neutron energies and energy transfer values are usually expressed in wavenumbers (cm^{-1}) for vibrational spectroscopy

applications and in electron volts (eV) for matters related to instrumental design and in QENS applications. Neutron spectra are conventionally presented as horizontal-step traces or individual data points in order to make the energy resolution of the data more readily apparent, since this can vary within a single spectrum due to instrumental design effects. This thesis will follow these conventions throughout.

2.1.1.2 Coherent and Incoherent Scattering:

The split between coherent and incoherent scattering arises from the wave-particle duality of the neutron. Coherent scattering derives from the wave-like view of neutron behaviour, under which it interacts simultaneously with multiple centres across the entirety of the sample giving rise to new neutron wavefronts. These simultaneously generated wavefronts are in phase and therefore interfere constructively if the sample possesses long-range order, resulting in interference patterns of varying intensity depending on θ. Since the neutron interacts with multiple centres the momentum and energy transfer of the scattering event is likewise distributed across the sample. Coherent scattering is therefore a probe of structure and of collective motions such as phonon modes in crystal structures and magnetic transitions.

In contrast, treating the neutron as a particle involves it only interacting with a single scattering centre. Since the scattered neutron only emanates from a single location there is no possibility of interference and thus the scattering is incoherent. Similarly, the associated momentum and energy transfers involve only the scattering nucleus and its associated bonds, meaning that incoherent scattering is a probe of local structure properties such as bond vibrations and the movement of individual molecules.

The strength of scattering from an atom is expressed in terms of its scattering cross-section, σ, which has units of cross-sectional area, conventionally given in barns (b) where $1\ b = 10^{-28}\ m^2$. The scattering cross section is linked to the scattering length, *b*, a measure of the strength of the neutron-nucleus interaction by the relation:

$$\sigma = 4\pi b^2 \tag{2.4}$$

The number of neutrons scattered out of a beam by a sample depends on the quantity of the scatterer(s) in the sample and the corresponding scattering cross section(s) by a law similar in form to the Beer-Lambert law for optical adsorption; if effects from neutron adsorption are ignored, it may be expressed as:

$$J_f = J_i e^{(-d_s C\sigma)} \tag{2.5}$$

Here d_s is the sample thickness, C its concentration and J_i and J_f the neutron flux before and after the sample respectively. There is no known way to calculate the scattering cross section or length of a nucleus from its fundamental properties, so published lists of such parameters are always derived from experimental measurements.[79]

Any given sample will scatter both coherently and incoherently, but the relative degree to which it does each is a function of its composition. The greater degree of long-range order in a sample the more significant the level of coherent scattering due to the increased scope for constructive interference. Theoretically, this will result in totally coherent scattering in the case of a regularly spaced lattice of a single nuclear type. However, this theoretical limit is never achieved in reality due to the possibility of different isotopes being present and the neutron's sensitivity to sample spin incoherence. It therefore follows that each isotope has its own characteristic coherent and incoherent scattering cross sections.

Table 2-1 presents the adsorption and scattering cross sections for a variety of nuclei relevant to catalysis or the design of neutron instrumentation. A number of consequences for the use of neutron scattering can be derived from these values. Firstly, there is no overall trend which links scattering intensity to the atomic number of the atom, which is the case for techniques such as X-ray fluorescence, and therefore neutron scattering results are not dominated by the heavier elements. The effect of spin incoherence leading to an exceptionally high σ_{inc} value for ^{1}H is also readily apparent, leading to the observation that inelastic neutron scattering is dominated by modes involving hydrogen centres in systems where they are present. In contrast, deuterium is primarily a coherent scatterer

with a much lower incoherent cross section meaning that selective deuteration is a useful tool in neutron scattering to mask or highlight parts of the system which are of interest. The extremely low cross section of other components of the zeolite catalytic system (Si, Al, O and C) means that, as previously noted, they do not significantly contribute to the overall spectrum and masking effects are avoided. Finally, experimental design for neutron experiments is dramatically simplified by the fact that thin windows of vanadium (especially for coherent applications) or aluminium (for incoherent applications) are functionally transparent to neutrons due to their low scattering cross sections and the manufacture of sealed, neutron-transparent sample environments is feasible

Table 2-1: Coherent, incoherent and total scattering cross sections, absorption cross sections and natural abundance of selected isotopes. Adsorption cross sections given for neutrons with E = 25.30 meV. Data taken from Sears.[79]

Isotope	Abundance (%)	σ_{coh} (b)	σ_{inc} (b)	σ_{tot} (b)	σ_{abs} (b)
^{1}H	99.985	1.7583	80.27	82.03	0.3326
^{2}H	0.015	5.592	2.05	7.64	5.19×10^{-4}
^{3}He	1.4×10^{-4}	4.42	1.6	6.0	5333
^{4}He	99.99986	1.34	0.0	1.34	0
^{6}Li	7.5	0.51	0.46	0.97	940
^{10}B	20	0.144	3.0	3.1	3835
^{12}C	98.90	5.559	0.001	5.551	3.53×10^{-3}
^{16}O	99.762	4.232	0.0	4.232	1.9×10^{-4}
^{27}Al	100.0	1.495	8.2×10^{-3}	1.503	0.231
^{28}Si	92.23	2.120	0.0	2.120	0.177
^{51}V	99.75	2.03×10^{-2}	5.07	5.09	4.9
^{113}Cd	12.22	12.1	0.3	12.4	20600
^{157}Gd	15.7	650	394	1044	259000

2.1.1.3 Neutron Sources:

All neutron experiments require a suitable source of neutrons with an appropriate energy distribution. While it is possible to generate weak neutron beams from radioisotopes or fusors, the high levels of neutron flux necessary for spectroscopic

investigations are only available from two types of source: research fission reactors and spallation sources. This in turn means that investigations using neutron methods can only be carried out at dedicated facilities, available instrument time is a limited resource and is usually allocated to researchers through a competitive proposal submission process.

Reactor sources use the slow-neutron-induced fission of ^{235}U to generate further neutrons. Under steady state conditions reactors generate surplus neutrons for each ^{235}U fission event in addition to those necessary to sustain the nuclear chain reaction and these escape the reactor core and are available for scientific use. The neutrons released by fission have extremely high energies and these are brought down to useable energy levels through moderation, a process of repeated inelastic collisions with a hydrogen-containing material, usually water. This results in a Maxwell-Boltzmann distribution of neutron energies around the temperature of the moderator fluid. Moderation in water at room temperature produces a neutron distribution with a peak at around 200 cm^{-1} and very little flux above 1200 cm^{-1}. Production of 'cold' neutrons, which are useful for diffraction applications, may be achieved through the use of moderators at temperatures down to 25 K. Reactors have historically been the most common neutron sources worldwide and offer the advantage of constant neutron production with the flux level determined by the size and power of the reactor core, which is in turn limited by the ability to cool the fuel elements. The most powerful research reactor in operation as of 2021 is located at the Institut Laue-Langevin, Grenoble, France and operates at 58.3 MW (thermal) with a neutron flux of 1.5×10^{15} cm^{-2} s^{-1}.[80]

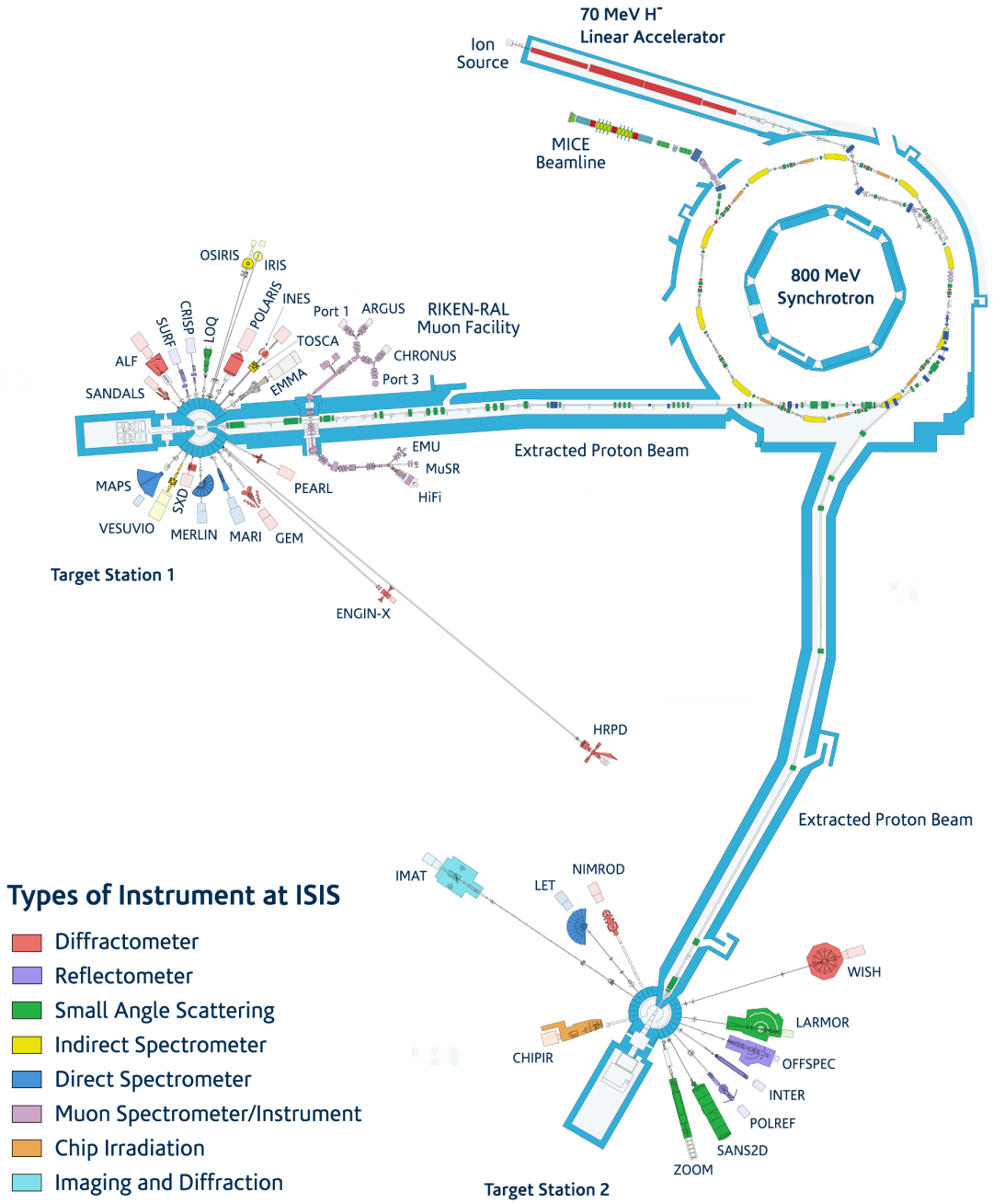

Figure 2-3: Layout of the ISIS Neutron and Muon Source, Oxfordshire, UK showing the synchrotron used for proton acceleration, the extracted proton beam lines and the neutron instruments clustered around the two spallation targets. Image credit: STFC.

Spallation sources generate neutrons by striking a heavy-metal target (usually tungsten or mercury) with a beam of relativistic protons. Collisions between the proton beam and the target generate excited nuclei which decay through the release of subatomic particles, including neutrons. These released particles are sufficiently energetic to generate further excited nuclei in a cascade sequence should they collide with a nucleus before they escape the target, magnifying the

number of neutrons generated; an average of 15 neutrons are released for each proton delivered to the target. This internuclear cascade results in high neutron flux with much lower waste heat production than in an equivalent reactor source. The majority of neutron sources use a synchrotron to accelerate the proton beam and operate in a pulsed mode with bunches of protons being injected into the synchrotron, accelerated to the target velocity (> 80 % *c*) and fed into an extracted beam line leading to the target station. Figure 2-3 shows the layout of the ISIS Neutron and Muon Source located at the Rutherford Appleton Laboratory, Oxfordshire, UK.[81] ISIS was the first high power spallation neutron source, achieving operation in 1984, and is unusual in having two separate spallation targets. The proton synchrotron operates at 50 Hz with 80 % of the resulting pulses being directed to the first target station and the remaining 20 % passed to the newer Target Station 2 (commissioned in 2008) which is optimised for cold-neutron applications.

As with reactor sources, the neutrons produced by spallation require moderation down to useful energies before they are passed to the neutron instruments. Unlike at reactors, the moderator tanks are small enough that the neutron pulse does not achieve thermal equilibrium with the moderator. This is essential in order to preserve the narrow pulse width which is necessary for good energy resolution. This also means that the neutron pulse contains a significant proportion of epithermal neutrons with energies above 1200 cm^{-1}. Therefore, when comparing reactor and spallation sources, spallation offers higher peak neutron flux and higher levels of epithermal neutrons, while reactors generally have higher time-averaged flux and greater levels of cold and thermal neutrons. This means that spallation sources are generally more useful for vibrational spectroscopy due to offering a wider range of accessible energy transfer values.[57]

An important aspect of neutron facility design is the need to shield the source, beamlines and instruments, both for the health of the operators and to prevent the contamination of experimental results by stray neutrons. This is achieved through the use of materials containing isotopes with extremely high adsorption cross sections. Boron is commonly used due to the 20 % ^{10}B content (Table 2-1); this adsorption is most efficient at thermal neutron energies so is often employed in the form of boronated plastics and waxes which moderate any high-energy

neutrons and increase the level of adsorption. Cadmium is often used for shielding and for items such as neutron beam shutters and collimators where the bulk of boronated materials would be problematic. Gadolinium is even more adsorbing than cadmium and works better at higher energies, but its expense limits it to applications where space is at an absolute premium. Other forms of radiation are also emitted during operation from the relaxation of excited nuclei and the decay of radioisotopes generated by neutron activation of components of the source, instruments or samples. This radiation is dealt with by the use of concrete and heavy metal shielding where appropriate.

Once generated and moderated, from whatever source, the neutrons must be transported to the instrument. Since neutrons are uncharged they cannot be focussed or redirected and will travel in a straight line after leaving the moderator tank. Neutron facilities therefore have their instruments clustered around the source with a neutron beam tube, usually evacuated to avoid scattering from air, leading from the moderator to the instrument, as can be seen in Figure 2-3. Lining the beam tube with optically flat nickel guides can increase the flux of low energy neutrons at the instrument by total external reflection of neutrons which strike the guide below its critical angle: the use of layered supermirrors extends the energy range where this can achieve useful increases in flux into the region which is useful for neutron spectroscopy.[82]

Despite these measures, the major limitation of neutron scattering, other than limited availability of facilities and instrument time, is that flux levels remain quite low in comparison to those achievable by even benchtop optical spectrometers. This means that neutron spectroscopy is not particularly sensitive and large sample sizes with long collection times are required to achieve useable signal:noise ratios in the final spectra. While spectra of pure hydrocarbon compounds can be collected using sub-gram samples on sub-hour timescales sample sizes in the 5 – 15 g range and collection times in hours are more realistic for investigations of dosed or reacted zeolites.

2.1.1.4 Neutron Detectors:

The uncharged and penetrating nature of neutrons means detecting them is extremely difficult. All practical detector designs make use of neutron-initiated nuclear reactions which generate charged particles which can be detected. The primary design of detector used in most spectrometers is the helium gas tube. This consists of a high voltage anode surrounded by helium−3 at high pressure. Helium−3 has a high adsorption cross section and on adsorption undergoes the reaction:

$$^{1}_{0}\mathrm{n} + {}^{3}_{2}\mathrm{He} \longrightarrow {}^{3}_{1}\mathrm{H} + {}^{1}_{1}\mathrm{H} + 0.77\ \mathrm{MeV} \tag{2.6}$$

With the resulting charged particles setting off an ionisation cascade which can be detected electronically. He tubes are sensitive and have low background but are relatively bulky, can be saturated by high levels of neutron flux and require an isotope which is both scarce and increasingly expensive. For high count rate applications, or those where high position sensitivity is desirable, an alternative is scintillator detectors. These use the reaction of lithium-6 by:

$$^{1}_{0}\mathrm{n} + {}^{6}_{3}\mathrm{Li} \longrightarrow {}^{3}_{1}\mathrm{H} + {}^{4}_{2}\mathrm{He} + 4.79\ \mathrm{MeV} \tag{2.7}$$

The lithium is embedded in a ZnS phosphor which emits a detectable flash when energised by the adsorption event. High position sensitivity is achieved through the use of fibre optic photosensors, which can be positioned to observe the scintillator with a high pixel density.

One important feature of both gas tube and scintillator detectors is that while they are capable of resolving the momentum transfer component of the scattering event, by arranging multiple detectors into a position-sensitive detector bank, they are incapable of discriminating between different neutron energies due to the insignificance of these energies relative to the nuclear reaction which generates the detected charge. Resolving the energy transfer component of inelastic scattering events is therefore a function of the design of the neutron spectrometer itself (see Sections 2.1.2.2 and 2.1.2.3). Spallation sources have an important advantage in this regard; since all neutrons in a pulse are generated simultaneously when the proton beam strikes the target their energy at any point

downstream may be derived easily from the time taken to reach the detector and the distance travelled. All spectrometers at spallation sources exploit this property and utilise time-of-flight methods to determine energy transfer.

2.1.2 Inelastic Neutron Scattering:[57, 59-61]

Coherent inelastic neutron scattering is, as noted above, a probe of bulk motions like phonon motions and magnetic dispersion in crystals. Its application to the systems of interest to this thesis is limited, particularly as the high incoherent scattering cross section of hydrogen appears as background noise in the coherent spectra of any hydrogenous system. This technique has therefore not been used in this thesis and will not be discussed further.

Incoherent INS is a probe of bond vibrations and rotations and the movement of single molecules. The intensity of the scattering from a given atom l in the ν^{th} mode at energy transfer ω is given by:[59]

$$S^n(Q,\omega_\nu) \propto \frac{\sigma_l}{4\pi}\frac{[(Q\cdot {}^\nu u_l)^2]^n}{n!}\exp\left(-\left(Q\sum_\nu {}^\nu u_l\right)^2\right) \qquad (2.8)$$

where Q is the momentum transfer, σ_l the incoherent scattering cross section of l, ${}^\nu u_l$ the amplitude of motion of l in mode ν and n the order of the transition, with $n = 0$ being elastic scattering, $n = 1$ the fundamental mode and $n \geq 2$ corresponding to overtones (see Section 2.1.2.1). This is conventionally referred to as the *scattering law* for the scattering from a sample (also called the scattering function or the dynamic structure factor) and is the most common way of reporting INS data. $S(Q,\omega)$ is usually reported as a scaled value in arbitrary units of relative intensity since measuring the absolute intensity in the correct units ($b(cm^{-1})^{-1}$) introduces considerable experimental difficulties without tangible benefits.[57] The scaling factor used is consistent between experiments so comparability between samples is maintained.

Equation (2.8) has some important consequences for INS. The dependence of scattering strength on the amplitude of motion further increases the degree to which hydrogen modes dominate the spectrum and means that torsions, bends and

C-C deformations often give intense peaks in INS due to their involving large movements of the associated hydrogens. Secondly, the exponential term in Equation 2.8 is the Debye-Waller factor, which leads to suppression of the INS peak at a level dependant on a sum over all modes. This can be potentially quite significant, and necessitates that as few modes as possible should be populated during the measurement. In practice, this means that INS experiments must be performed at temperatures lower than *ca*. 30 K to return reasonably defined peaks, which is accomplished by incorporating a closed cycle refrigerator (CCR) into the instrument sample environment. The sample is sealed inside an aluminium sample can and suspended inside the CCR which is evacuated to a pressure of *ca*. 30 mbar and cools the sample to these cryogenic temperatures. It is therefore obvious that INS is not suitable as an *operando* spectroscopy technique, and in most cases measurements of reacted samples must be performed *ex situ*. It is however possible to introduce gaseous adsorbents to the sample *in situ* through the use of cans equipped with gas-tight fittings attached to heated lines extending outside the CCR. Finally, the simple dependence of scattering intensity on the amplitude of the vibrational motion can be exploited for simulation of vibrational systems as detailed in Section 2.2.1.

The spectrometers used in INS measurements can be separated into three types. *Triple-axis* spectrometers are the most common type of INS instrument but they are best suited for measurements of coherent scattering at reactor sources; their applicability to the study of catalytic systems is limited and they will not be considered here. The remaining classes of INS instrument are split into *indirect* and *direct geometry* spectrometers depending on whether they determine energy transfer by fixing the final or incident neutron energy respectively.

2.1.2.1 Overtones, Combinations and Phonon Wings:

In addition to the fundamental modes INS results have multiple other features which appear in the final spectrum and can complicate its analysis. The simplest of these features is overtone modes. Unlike in optical spectroscopy, in INS spectroscopy, transitions where $\Delta v \neq 1$ are allowed within the harmonic approximation and contribute significantly to the spectrum. Therefore, in addition to the fundamental ($1 \leftarrow 0$) transitions overtone modes ($2 \leftarrow 0$, $3 \leftarrow 0$ … $n \leftarrow 0$) also

appear; a common rule of thumb is that overtone contributions out to n = 10 are significant enough to be considered when analysing neutron data.[57] The second possibility is combination modes, where two motions of the same atom (e.g. a C-H stretching mode and a bending mode of the same C-H bond) are excited simultaneously, resulting in a peak at the sum of the energies of the two contributing modes. The final possibility is the presence of phonon wing modes. These are formed by coupling between a mode and the external density of states of the sample and are mostly observed for crystalline materials.

2.1.2.2 Indirect Geometry Spectrometers:

Indirect geometry instruments, typified by the TOSCA spectrometer at the ISIS Facility,[83] have historically been the preferred instrument for INS studies of catalytic systems due to their ease of use. A simplified layout of an indirect geometry instrument designed for use at a pulsed source is shown in Figure 2-4. In these instruments the sample is exposed to an unmodified beam of neutrons from the moderator, referred to as a 'white' beam since it contains the full range of moderated neutron energies. Due to separation as they travel down the beam path from the moderator, neutrons with high energies will arrive at the sample first, with the energy of the incident neutron decreasing with increasing time after pulse generation. Neutrons scattered from the sample are filtered so that only those of a specific energy are passed to the detector banks. On TOSCA this is accomplished by scattering from a pyrolytic graphite crystal which is positioned at an angle so that the [002] plane reflects neutrons with the low energy of 32 cm^{-1} onto the detector bank through Bragg scattering. A cooled beryllium filter (which is transparent to neutrons with an energy lower than 40 cm^{-1}) removes higher-order reflections from the final spectrum. The total flight time, t, of a detected neutron in this arrangement is given by:

$$t = \frac{L_0}{v_0} + \frac{L_1}{v_1} \tag{2.9}$$

where v_0 and v_1 are the velocities of the incident and scattered neutrons respectively and L_0 and L_1 the neutron path lengths before and after the sample. Both L values are known and constant due to the design of the spectrometer. The

value of ν_1 is always 32 cm^{-1} since it is set by the crystal analyser and Be filter combination. It therefore follows that as t increases ν_0 decreases, and thus the magnitude of the energy transfer necessary to convert ν_0 to ν_1 as a consequence of the scattering event also decreases. It can therefore be seen that the indirect geometry instrument sweeps across the possible spectrum of ω values with increasing t after the proton beam triggers a neutron pulse.[84]

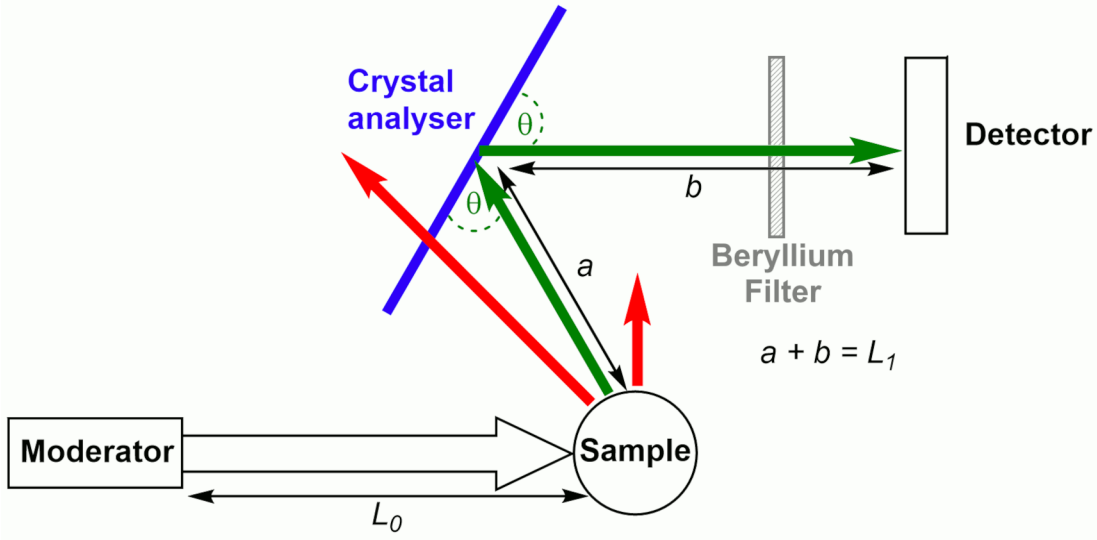

Figure 2-4: Simplified layout of an indirect geometry neutron spectrometer such as TOSCA. L_0 and L_1 are incident and scattered flight path lengths. Figure adapted from Colognesi, et al. with modifications.[84]

Indirect geometry offers (relatively) high neutron flux due to the white incident beam, high resolution at low ω and extremely simple data collection that outputs spectra similar to those collected for IR or Raman techniques. However, it does have some drawbacks due to the fact that the data collection method means ω and Q are inherently linked; scattering intensity collected at high energy transfer values is automatically collected at high momentum transfer values as well. This means that above ~1200 cm^{-1} spectra collected on indirect geometry instruments shows increasing contributions from overtones and broadening which hides all but the largest peaks. If accurate spectra at these energies is required, direct geometry instruments have recently been shown to provide better results.[60]

2.1.2.3 Direct Geometry Spectrometers:

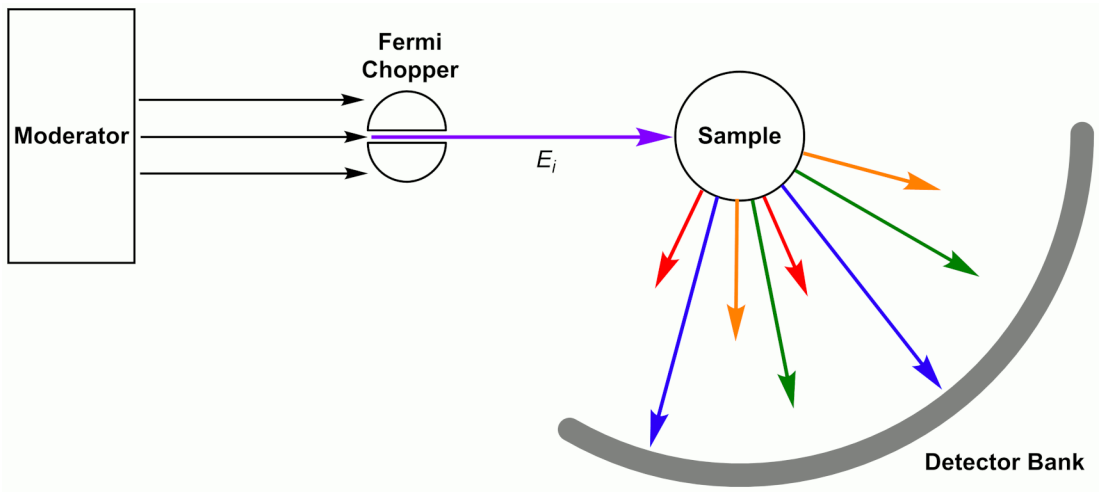

Figure 2-5: Simplified layout of a generic direct geometry neutron spectrometer.

A direct geometry instrument in some ways operates in the opposite fashion to an indirect geometry instrument. As shown in Figure 2-5, instead of bombarding the sample with a white neutron beam and selecting a single scattered energy the direct geometry instrument sets a single incident neutron energy by passing the moderated neutron pulse through a Fermi chopper, a rotating cylinder with curved gaps through the centre which filters out all neutrons whose velocity is not in phase with its rotation rate. Varying the phase of the chopper relative to the pulse generation allows setting the incident energy to any value within the range available in the moderated neutron pulse by determining at what point in the pulse the chopper slits become parallel to the incident beam path. This monochromatic neutron pulse then strikes the sample and is scattered into multiple energies that are picked up by a wide bank of detectors. The detector array is curved, allowing determination of Q for the detected neutron from the angle of the detector relative to the incident beam, and the post-scattering energy is determined by time-of-flight methods as before. This results in a 3-dimensional plot of neutron intensity *vs* both ω and Q known as a mitre plot which presents the full $S(Q,\omega)$ scattering law, an example of which is included in Figure 2-6. This may be reduced to the more familiar 2D spectrum of intensity *vs* energy transfer by integration with respect to Q.

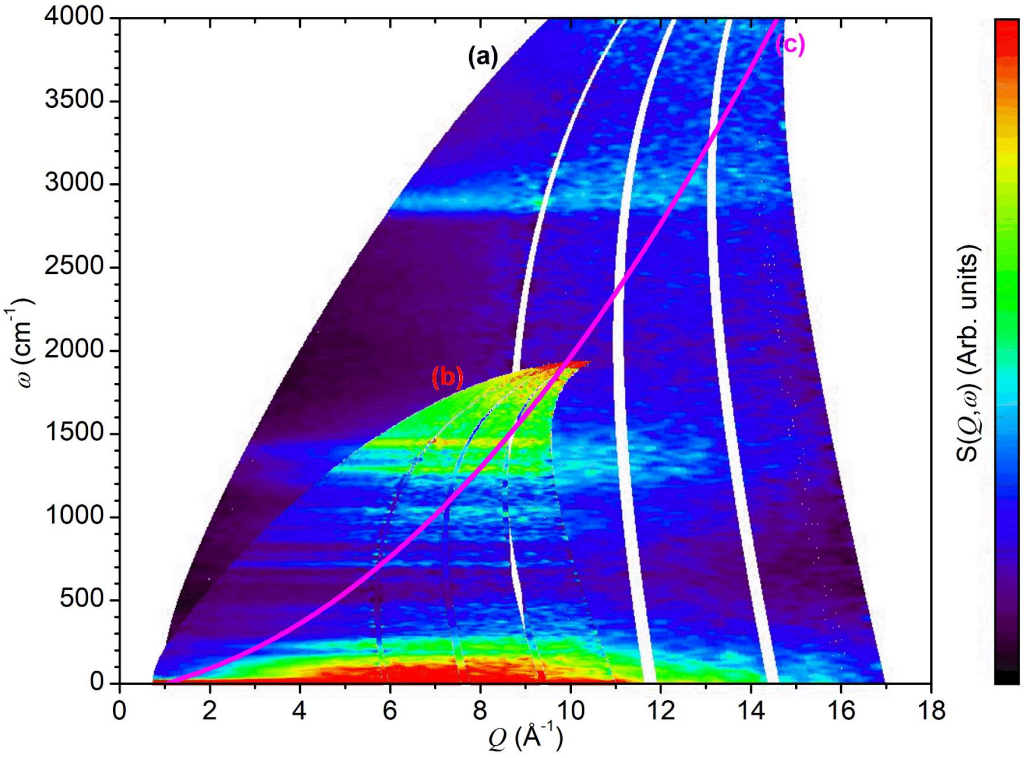

Figure 2-6: $S(Q,\omega)$ Mitre plots of 1-octene measured on MAPS at incident energies of 5244 cm^{-1} (a) and 2017 cm^{-1} (b). Line (c) shows the trajectory in (Q,ω) space measured by the forward-scattering detectors on TOSCA, which may be taken as typical for indirect geometry instruments.

Figure 2-6 presents mitre plots for a sample of 1-octene recorded at two different incident energies. It can be seen how at low values of Q the scattering peaks are sharply defined, corresponding to fundamental transitions, while at higher momentum transfer values the responses become broader and fuzzier as overtone contributions predominate. The fact that the energy resolution of the instrument is a percentage of the incident energy is also apparent, since Figure 2-6(b) recorded at the lower E_i of 2017 cm^{-1} offers much narrower response peaks than Figure 2-6(a) (recorded at 5244 cm^{-1}) in the areas where the two spectra overlap.

Direct geometry instruments have inherently lower resolution than indirect instruments at low ω since a chopper is a less discriminating filter than Bragg scattering from an analyser crystal. In practice the actual energy resolution is a fixed percentage of the selected incident energy depending on the design of the chopper. Additionally, filtering the incident neutron pulse results in lower incident flux and attenuated signal:noise, this is compensated for by direct geometry instruments generally having large areas of detectors. These instruments do offer

the option of directly trading off flux against resolution to meet the needs of the test in question by the choice of chopper and its speed. The advantage of direct geometry instruments is that it is possible to deliberately exclude the high-*Q* portions of the spectrum when integrating the mitre plot, resulting in a spectrum with less contributions from overtone modes, enabling access to the C–H and O–H stretch regions. It can be seen from Figure 2-6 that limiting the integrated Q range to values of 10 $Å^{-1}$ and below eliminates the majority of the overtone modes from the spectrum. Comparison with the $S(Q,\omega)$ trajectory of an indirect instrument (Figure 2-6(c)) demonstrates how this will lead to lower levels of overtone contributions in date collected on a direct geometry instrument if the area of interest is above *ca.* 2000 cm^{-1}. Additionally, by varying the incident energy it is possible to shift the region of the energy transfer spectrum which corresponds to low *Q* values. Essentially, a direct geometry instrument has lower overall resolution but can reposition the region of optimum resolution as needed, while the indirect geometry has higher peak resolution, but this is fixed at low energies. The two designs are therefore complementary.

2.1.2.4 Multiple Scattering:

One additional factor which requires consideration in experimental design is the possibility of a scattered neutron undergoing an additional scattering event before escaping the sample. This presents a problem for instruments that resolve the *Q* dimension of the scattering function, including direct geometry INS spectrometers, because it destroys the linkage between the energy and momentum transfer values of the scattered neutron. For this reason, sample sizes and compositions for direct geometry measurements are set so that the sample will scatter approximately 10 % of the incident neutron intensity. This level keeps the contribution of multiple scattering low enough to not significantly affect the final results while still allowing timely collection of sufficient scattered neutrons for a usable spectrum. *Q*-insensitive measurements are less affected by multiple scattering: since the majority of scattering events are elastic, the odds of a neutron undergoing two inelastic collisions in succession are in most cases negligible and the final recorded energy transfer will be the same as if the elastic collisions had not occurred. Experiments on TOSCA at the ISIS Facility have shown that indirect geometry instruments can tolerate up to 25 % multiple scattering

without significant degradation of spectral quality allowing the use of larger samples to reduce collection time.[57]

2.1.2.5 General Procedure for INS Measurements:

INS data collection is relatively straightforward and similar procedures were followed for the majority of measurements performed. Samples were loaded into appropriately sized aluminium sample cells with indium wire gaskets to create a cryogenic gas-tight seal. These cells present a flat plate profile in order to make maximum use of the incident neutron beam without multiple scattering. In the case of zeolite-based samples, or other hygroscopic materials samples, they were first dried (see Section 2.4.2) and loading carried out in an argon glovebox (MBraun UniLab MB−20-G, [H_2O] < 1 ppm, [O_2] < 1 ppm) in order to prevent re-contamination from atmospheric water.

Once loaded, each sample cell was attached to a 'centre stick'; this forms the part of the INS sample environment which holds the sample in the correct position relative to the neutron beam and ensures it does not contact the walls of the sample chamber. Samples were quenched to 77 K by immersion in liquid nitrogen then inserted in the INS spectrometer and cooled below 30 K using the integrated CCR which forms part of the sample environment. The quenching procedure was followed to reduce the duration of the sample cooling period, which otherwise represents a substantial unproductive use of limited instrument time. Once cooled to a suitable temperature, spectra were collected until signal:noise levels were increased to a suitable level for analysis; the exact duration of each collection therefore varied depending on sample size, level of hydrogen content and the needs of the experiment.

All INS measurements were performed using instruments at the ISIS Facility. For measurements in the low energy (50 – 1200 cm^{-1}) region the preferred instrument was the indirect geometry spectrometer TOSCA due to its higher low energy resolution.[82-84] Typical collection times on this instrument were 1−2 hours for pure model compounds, 3-5 hours for adsorbate-loaded zeolites and 8−10 hours for reacted catalyst samples. For samples where data at higher energies was desirable use was made of the direct geometry spectrometer Multi-Angle Position Sensitive

(MAPS) using the high resolution A-chopper package selecting incident energies of 5244 and 2017 cm^{-1}, with chopper frequencies of 600 and 400 Hz respectively. The higher of these two incident energies provides energy transfer information up to 4000 cm^{-1}, allowing observation of C-H and O-H stretching modes, while the lower energy provides spectra from *ca* 200 – 2000 cm^{-1} with less peak broadening in the 1200 – 2000 cm^{-1} region than is achievable on TOSCA. Collection times on MAPS were approximately 2.5 – 3 times as long as for equivalent samples on TOSCA due to the need to collect two spectra per sample and the lower flux available on direct geometry instruments.

A full list of the INS beam times performed as part of this thesis, together with a listing of the samples measured in each case, is presented in Appendix 1 for reference purposes. Digital object identifier (DOI) links to the archived raw datasets collected in each beam time, which are publicly accessible after three years from the completion of the relevant experiment in accordance with the ISIS Facility's open access policy, are provided in the same location.

2.1.3 Quasielastic Neutron Scattering:[64, 85-86]

Quasielastic neutron scattering (QENS) may be regarded as a special case of INS concerning inelastic scattering events with energy transfers lower than 2 meV (16.1 cm^{-1}), down to μeV levels. These energies correspond to rotational energy levels and the translational motions of whole molecules with timescales in the picosecond to nanosecond range. The low value and close spacing of these energy transfers means that they do not appear as separate resolvable peaks but instead manifest as a broadening of the peak due to elastic scattering at an energy transfer value of zero, as shown in Figure 2-7.

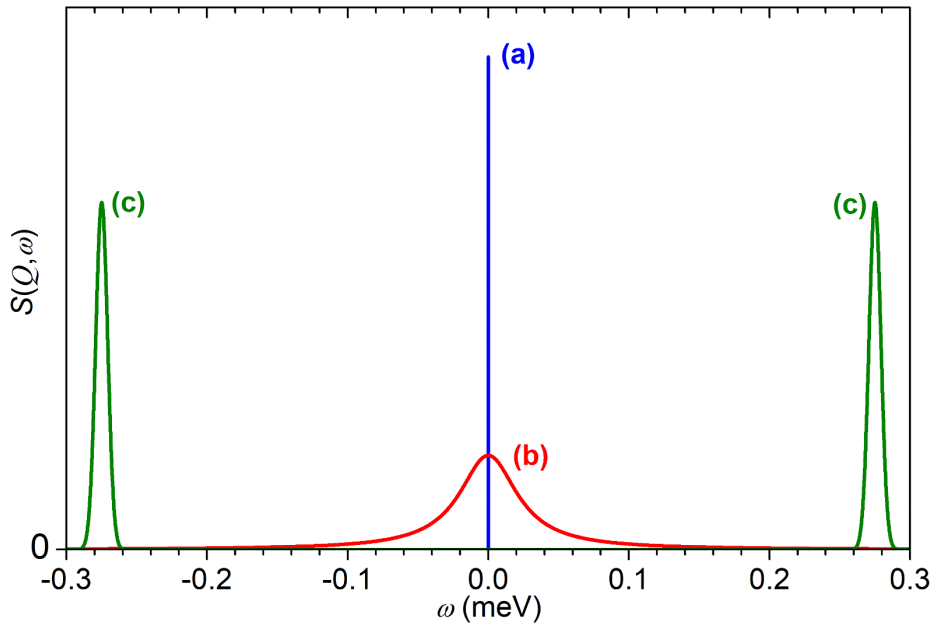

Figure 2-7: Representation of the low energy transfer region of an ideal scattering spectrum showing neutron intensity due to elastic scattering (a), quasielastic scattering (b) and the lowest energy Stokes (right) and anti-Stokes (left) INS bands (c). Note that relative peak heights are not to scale. Figure based on data in Mitchell et al.[57]

As with INS, QENS involves both coherent and incoherent scattering, each of which probes different aspects of the system dynamics. Specifically, when implemented on a real system, coherent QENS probes transport diffusion while incoherent QENS measures molecular self-diffusion parameters. The properties of hydrogen mean that incoherent scattering dominates the spectrum of zeolite-hydrocarbon systems and therefore QENS measurements of these systems are probing the self-diffusion of the adsorbed hydrocarbon molecules.

The self-diffusivity of a species adsorbed into a zeolite describes its motion in the absence of a concentration gradient and when the system is at a thermal equilibrium. It can be defined from the slope of the mean squared displacement of its molecules by means of the Einstein relation, namely:[87]

$$D_s = \lim_{t\to\infty}\left\{\frac{1}{6t}\langle[r(t)-r(0)]^2\rangle\right\} \tag{2.10}$$

where r is the displacement of the molecule. Since mean squared displacement values are independent of particle index at equilibrium, the D_s value for one molecule of the adsorbate should be the same as that of the average over all

molecules provided that the timescale of the measurement is sufficiently large. A more comprehensive description of the self-diffusion of the adsorbate molecules is given by the self-part of the van Hove correlation function, $G_s(r,t)$, which is the three-dimensional probability density that a molecule will be displaced by vector r at time t.[88] At the long times and large displacements where self-motions become diffusive this takes the form:

$$G_s(r,t) = \frac{1}{(4\pi D_s t)^{\frac{3}{2}}} \exp\left[\frac{r^2}{4D_s t}\right] \tag{2.11}$$

The four-dimensional Fourier transform of this correlation function in both space and time corresponds to the incoherent scattering function, $S_{inc}(Q,\omega)$.

$$S_{inc}(Q,\omega) = \frac{1}{2\pi}\int \mathrm{d}t\, \exp(-i\omega t)\int \mathrm{d}r\, \exp(iQ\cdot r)\, \mathrm{G}_s(r,t) \tag{2.12}$$

Similarly, the total scattering function (both coherent and incoherent) corresponds to the full van Hove correlation function. However, for hydrogen containing systems incoherent scattering dominates to such an extent that it is a reasonable simplification to consider only the self-diffusion behaviour. This relationship means that Q and ω are therefore the Fourier transformed variables for r and t respectively; Q relates to reciprocal distance and ω to inverse time.

Since each possible motion of an adsorbate has a characteristic correlation function, it follows that the derived quasielastic scattering function will also be distinctive. In the simplest case, that of diffusion according to Fick's second law, this takes the form:

$$S(Q,\omega) = \frac{1}{\pi}\frac{D_s Q^2}{\omega^2 + (D_s Q^2)^2} \tag{2.13}$$

This equation gives a Lorentzian energy profile in the energy transfer dimension and it is evident that the shape of the scattering function is Q-dependant. Specifically, in this case the half-width at half-maximum (HWHM, Γ) of the Lorentzian is related to Q^2 by the linear relationship:

$$\Gamma(Q) = D_s Q^2 \tag{2.14}$$

Thus as the momentum transfer value increases, the $S(Q,\omega)$ profile becomes broader and it is possible to exploit the two-dimensional nature of neutron scattering measurements to determine the diffusion constant by measuring the quasielastic broadening at multiple values of Q.

While Fickian diffusion is conceptually simple, it is rarely the case for molecules in zeolites because of the effect of the pore network constraining the diffusion. A more common scenario is jump diffusion between low energy sites within the pores. Multiple models to describe jump diffusion exist: the model developed by Chudley and Elliot, originally to describe motions in semi-crystalline liquids, is used here as a representative example.[89] It assumes the molecule undergoes a series of jumps between low-energy sites separated by distance d with residence time between jumps τ and produces broadening with the profile:

$$\Gamma(Q) = \frac{1}{\tau}\left[1 - \frac{\sin(Qd)}{Qd}\right] \tag{2.15}$$

Figure 2-8 shows how the Lorentzian broadening varies with Q^2 for examples of Fickian and Chudley-Elliot jump diffusion with the same self-diffusion constant. It can be seen that at low Q values, corresponding to long distances, the relationship is the same in both mechanisms, but the jump mechanism deviates from Fickian behaviour as the probed length scale approaches the size of the jump distance.

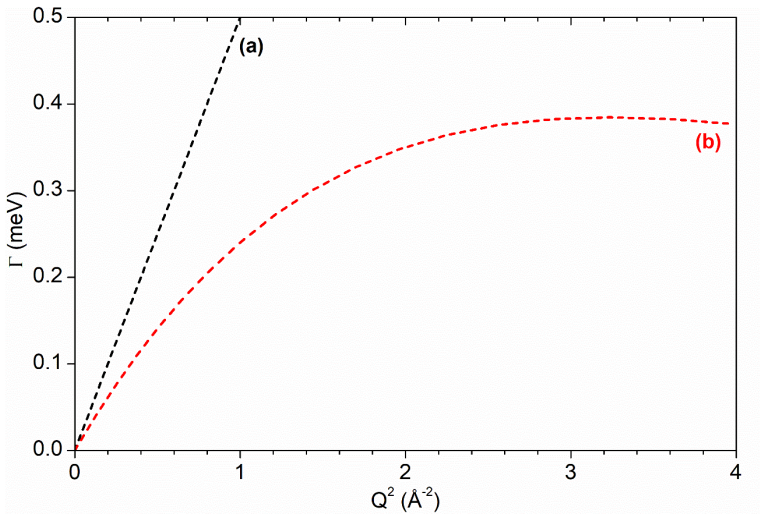

Figure 2-8: Simulated Lorentzian line width (Γ) vs Q^2 relationships for scattering from a molecule undergoing Fickian (a) and Chudley-Elliot jump (b) diffusion with $D_s = 5 \times 10^{-9}$ m^2s^{-1}. Chudley-Elliot jump distance is 2.5 Å.

2.1.3.1 Implementation of the QENS Technique:

Although, theoretically, the elastic scattering from a sample takes the form of a delta function (Figure 2-7), actually observing it as such would require an ideal instrument of infinite resolution. In practice, any real instrument will have a finite energy resolution which will also contribute to the observed peak broadening. Similarly, any instrument will also have a maximum energy transfer value which it can resolve and any motions which occur faster than this limit will appear as a flat background intensity in the final spectrum. The measured scattering function will therefore be a convolution of the scattering due to elastic and quasielastic contributions with the instrument resolution function, while a linear background may or may not be present depending on the dynamics of the sample (Figure 2-9). Since ω corresponds to inverse time, it being the Fourier transformed value of t, it follows that the resolution of a QENS instrument limits the maximum time window of a motion which can be detected by it. Similarly, the minimum and maximum Q values which can be measured by an instrument's detector bank determine the longest and shortest length scales which can be observed by it, respectively.

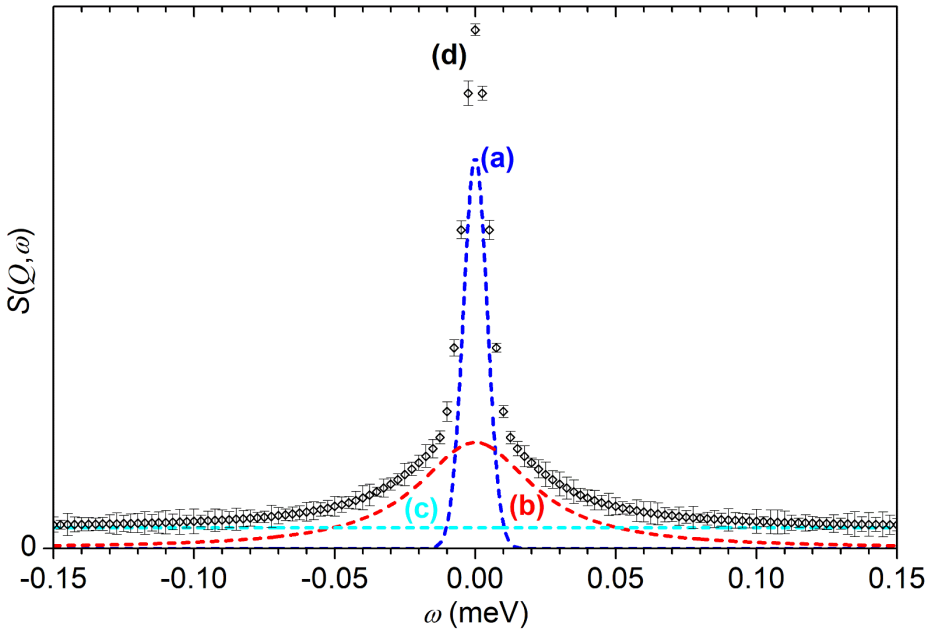

Figure 2-9: Components of a theoretical quasielastic scattering function under realistic conditions. The instrumental resolution function (a), quasielastic broadening (b) and background intensity (c) combine to give the spectrum which is observed experimentally (d). Figure based on data in Telling.[86]

Since the $S(Q,\omega)$ relationships described above refer solely to scattering from molecules in motion, it is necessary to extract the quasielastic component of the recorded scattering spectrum before it can be analysed to determine the type of motion it describes. Experimentally, both the elastic scattering and instrument resolution functions can be combined and modelled by use of a scaled spectrum of the sample collected at low temperatures (< 10 K) where the motion in the sample is assumed to be zero. The recorded spectrum is convoluted with a scaling delta function to give the final resolution function because the degree of elastic scattering within a sample changes with temperature and decreases at high values of Q even though the resolution remains constant. Use of this technique also means that any degree of coherent scattering from the zeolite framework is also embodied in the resolution function and is effectively cancelled out, allowing the use of the approximation that the quasielastic spectrum arises solely from the uncorrelated motions of the hydrocarbon adsorbates. This allows the collected experimental scattering function to be modelled by the equation:[86]

$$S(Q,\omega) = S^{quasi}(Q,\omega) \otimes R(Q,\omega) + B(Q,\omega) \qquad (2.16)$$

where $R(Q,\omega)$ is the recorded resolution function and $B(Q,\omega)$ the linear background. Fitting the experimental data at a temperature where motion is occurring to Equation (2.16) allows the extraction of the quasielastic contribution to the scattering, which takes the form of one or more Lorentzian functions with each function corresponding to an individual molecular motion which is resolvable in the collected data. These Lorentzian functions can then be analysed to determine the type of motion they describe and to extract the corresponding diffusion parameters, as detailed above.

2.1.3.2 The Elastic Fixed Window Scan Method:

Fitting analysis of QENS data requires high resolution spectra at multiple Q values. While the signal:noise ratio of a spectrum can be improved by combining the results from adjacent detectors, this can only be taken so far before the resolution in the Q dimension becomes too low to draw reasonable conclusions. This means that acquisition of QENS spectra suitable for this type of analysis takes considerable time, on the order of 6-8 hours per temperature point. If a measure

of the overall mobility of a sample over a wide range of temperatures is desired without the need to quantify the specific motions, results can be achieved in much shorter time frames by integrating over the full collected Q range to improve the statistics of the integrated spectrum. Since in QENS spectra the amount of movement in the sample determines the degree of inelastic broadening of the elastic peak, the relative overall mobility of the sample at a given temperature can be quantified by determining the intensity of the elastic scattering at each temperature $I_i^{el}(Q,T)$ (taken as the integrated intensity which lies within 50 % of the instrumental resolution from $\omega = 0$) and normalising that value against the intensity at < 10 K where it is assumed that the entire sample is immobile and all scattering intensity is elastic.[85] This provides a measure of relative overall mobility versus temperature, referred to as an elastic fixed window scan (EFWS), and suitable data may be collected in as little as 15 minutes per temperature point, allowing mobility data across a wide range of temperatures to be collected in a single beam time allocation. The bulk mobility data provided by EFWS analysis is useful for identifying phase changes and reaction points as well as for preliminary surveys, identifying temperature ranges of interest for more detailed investigation.

2.1.3.3 QENS Instrumentation:

QENS requires spectrometers with a combination of high energy resolution and the ability to quantify the momentum transfer component of the scattering event and is therefore usually performed on dedicated instruments. The low energy transfer values of interest mean that cold neutrons from moderators at around 20–30 K, usually liquid hydrogen, are employed. The most widely used design on pulsed neutron sources is the inverted geometry spectrometer which uses the same principle of energy selection through Bragg scattering as the indirect geometry INS instruments discussed in Section 2.1.2.2 above. Due to the uncertainty in the energy selection varying with scattering angle being proportional to $(\cot\theta\ \Delta\theta)$ the highest energy resolution is achieved when the Bragg scattering occurs at 90°. Since this is impossible to achieve in practice, the instrument is instead laid out so that the detector bank is positioned below the sample position and scattered neutrons are reflected onto it by *near*-backscattering reflections from the analyser crystals (Figure 2-10). The use of a curved crystal array and parallel

position-sensitive detector bank allows the *Q* dimension of the scattering function to be resolved. Since the *Q* dimension is important, sample sizes must be restricted so that scattering from the sample is kept below 10 % of the incident neutron intensity to prevent multiple scattering, in the same manner as described for direct geometry INS instruments above.

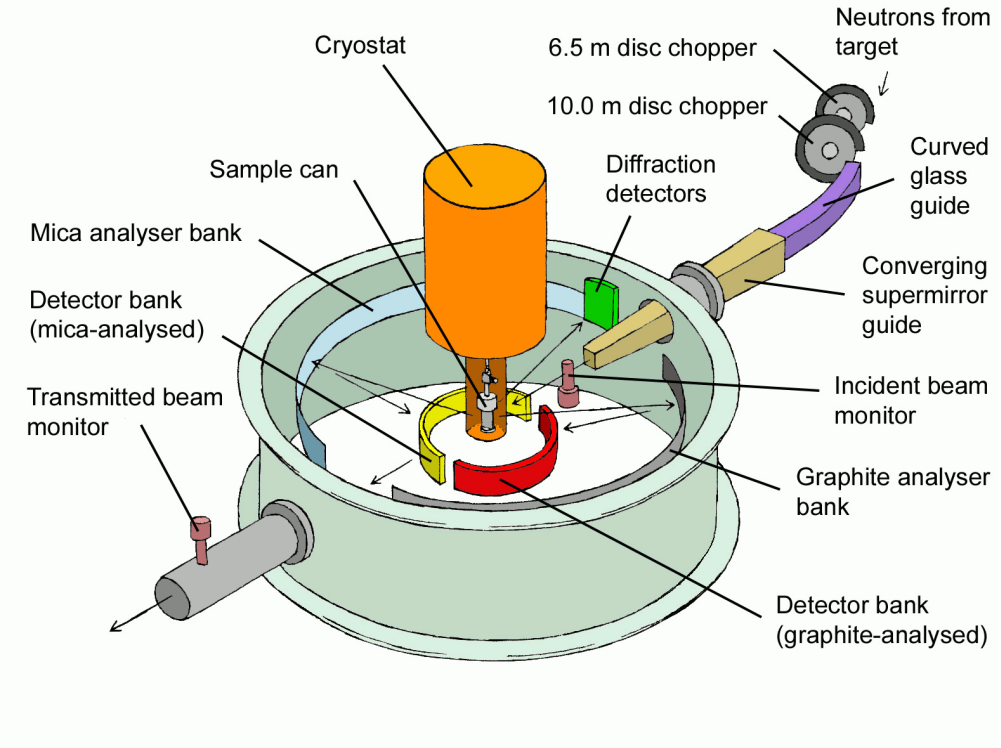

Figure 2-10: Layout of the inverted-geometry near-backscattering QENS spectrometer IRIS located at the ISIS Neutron and Muon Source, Oxfordshire, UK. Image reproduced from García-Sakai, et al.[90]

Backscattering instruments vary in the lowest energy transfer events they can detect, however, resolutions in the 10–25 μeV range are typical. This means that the slowest motions which are observable on these instruments occur on timescales of *ca* 30-60 picoseconds (1 μeV = 1.519×10^{-3} ps^{-1}, therefore 10 μeV = 1.519×10^{-2} ps^{-1} = 65.8 ps). In order to observe slower motions an alternative means of detecting the energy transfer is required. Neutron spin-echo (NSE) spectrometers achieve this by utilising a polarised neutron beam and determining the time of flight by measuring changes in polarisation due to precession from the neutron spins. NSE spectrometers can resolve timescales up to tens to hundreds of nanoseconds and generally have a wider accessible *Q* range than backscattering instruments, at the cost of significantly increased measurement times due to the loss in neutron intensity from beam polarisation.

This technique has not been used in the work reported in this thesis, so it will not be considered in detail beyond noting that it provides the possibility of analysing slow movements, with upper limits in the single-microsecond range depending on the instrument, that elude analysis by QENS experiments on backscattering instruments.

2.1.3.4 General Procedure for QENS Measurements:

Figure 2-11: Examples of QENS sample cells: (a) standard cell; (b) single-port gas handling cell with copper blocks for temperature control installed; (c) top view with upper end cap removed showing annular internal geometry and perimeter groove for installation of indium wire gasket. Background grid is 5 mm for scale.

QENS measurements can be performed with relatively small sample sizes for neutron techniques due to utilising the intensity in the elastic peak; sample sizes for loaded zeolite systems were *ca* 2.5 g. Zeolite samples were dried, and in the case of liquid-loaded samples dosed *ex situ* (Section 2.4.2) and loaded into aluminium sample containers. The containers used for QENS are of annular geometry with the sample sitting in the space between two concentric hollow aluminium cylinders (Figure 2-11(c)). This geometry means that sample thickness remains constant as a function of scattering angle, resulting in isotropic scattering, while making use of a greater proportion of the neutron beam area

than would be the case for a cylindrical sample container of the same internal volume. The cells are identically sized but have different annular spacing to ensure that the amount of sample approximates that necessary for 10 % scattering of the incident beam. In cases where it was intended to introduce gaseous adsorbents to the system the top end plate was equipped with gas handling fittings (Figure 2-11(b)). Cells were sealed with indium wire gaskets and equipped with copper blocks for the installation of electrical cell heaters and temperature sensors at both ends of the cell.

The loaded cells were mounted on appropriate centre sticks for measurement. In the case of the gas handling cells, the sticks were equipped with a trace heated gas line connecting the cell to a gas handling panel outside the instrument CCR and equipped with containers of known volume for accurate gas dosing. Heaters and Rh/Fe resistance-based temperature sensors were installed in the copper blocks and wired to the instrument for temperature control. For each zeolite tested, background spectra of the unloaded material were collected first. The sample was inserted into the instrument CCR and cooled to < 5 K to collect a 'base temperature' spectrum to serve as the instrument resolution function. The sample was then heated to three other temperatures previously identified as being of interest and spectra taken at these temperatures. Spectral collection time was 6-9 hours in each case.

Following completion of this background collection process, the zeolite was loaded with the adsorbed molecule under investigation and returned to base temperature for collection of a loaded resolution function. The sample was then heated from base temperature to 370 K in steps of 10 or 20 K. At each temperature the sample was allowed to equilibrate and a short (*ca.* 20 min collection time) spectrum collected. When the sample reached one of the temperatures where background collection had been performed the collection process was extended to the same length as the background spectrum. This procedure gives an EFWS overview of the diffusion over a wide range of temperatures while recording high resolution data for fitting analysis at three temperature points, allowing whether the diffusion constants follow an Arrhenius relationship to be established. In certain cases, it was found that fitting analysis was simplified by the removal of the contributions from the zeolite framework. In such cases this could be

accomplished by the subtraction of the previously recorded background spectrum at the corresponding temperature.

All QENS measurements reported here were performed on the ISIS Facility's two backscattering QENS spectrometers, IRIS and OSIRIS. For the purposes of this work the two instruments are essentially identical save that IRIS has an energy resolution of ± 17.5 μeV and an accessible momentum transfer range of 0.42−1.85 $Å^{-1}$, whereas OSIRIS has an energy resolution of ± 25.4 μeV and a *Q* range of 0.18−1.8 $Å^{-1}$.[91-92]. A full list of the QENS beam times performed as part of this thesis, together with a listing of the samples measured in each case, is presented in Appendix 1 for reference purposes. Links to the archived raw datasets collected in each beam time, which are publicly accessible after three years from the completion of the relevant experiment in accordance with the ISIS Facility's open access policy, are provided in the same location.

2.1.4 Neutron Diffraction:

In contrast to the spectroscopic methods considered above, neutron diffraction derives its information from neutrons which scatter elastically without energy transfer. It is a probe of structure, similar in many respects to X-ray diffraction (XRD), and therefore measures coherent scattering from a sample lattice.[78] Scattering waves radiating from atomic nuclei constructively interfere at angles determined by Bragg's law:

$$\mathrm{n}\lambda = 2\mathrm{d}\sin\theta \tag{2.17}$$

which relates to the measured scattering law S(*Q*) by the relationship:

$$Q = \mathrm{n}\left(\frac{2\pi}{d}\right) \tag{2.18}$$

resulting in peaks occurring only at those angles which satisfy these constraints. It should be noted that since neutron diffraction involves elastic scattering, the scattering law does not include the energy transfer term, ω. Since this project is concerned with zeolites as they are utilised in industrial catalysis, the ZSM-5 studied is composed of small crystallites in the form of a polycrystalline powder

with crystal dimensions of approximately 0.5 × 0.1 × 0.1 μm. We are therefore concerned with powder diffraction measurements of the zeolite rather than single crystal studies.

Neutron diffraction has a number of important differences when compared to X-ray diffraction due to the same factors which distinguish INS from optical spectroscopy.[93] The point nature of the scattering means that there is no angular dependence (form factor) of S(*Q*) and the relative intensity of high-θ peaks in neutron diffraction is greater than their XRD equivalents. Scattering intensity also varies according to the coherent scattering cross section of a given nucleus rather than according to its atomic number, meaning that heavy atoms do not dominate the diffraction pattern as is the case for XRD. Since the range of σ_{coh} found in most materials at natural abundance is *ca*. 0-15 b, even 'weak' coherent scatterers typically make detectable contributions to the scattering pattern in a way which light elements do not in XRD patterns. This means that neutron diffraction has potential applications in determining the location of protons within acid zeolites, which cannot be done by XRD due to the hydrogen contributions being masked. This method has seen some limited use in previous studies, including a determination of the proton positions in zeolite Y by Czjzek and Jobic,[94] but data on its application to other systems like ZSM-5 is more limited.

One complication in neutron diffraction is that incoherent scattering from the sample appears in the diffraction pattern as an elevated level of background noise. This is particularly a problem for samples involving hydrogen due to the high σ_{inc} of ^{1}H, which has already been discussed at length. In many cases neutron diffraction measurements are therefore performed on deuterated samples. This reduces the level of noise in the results and increases the relative intensity of coherent scattering from the hydrogen portions of the system since the σ_{coh} of ^{2}H is approximately three times larger than that of ^{1}H.

2.1.4.1 Neutron Diffractometers:

Neutron powder diffractometer design varies considerably between reactor and spallation sources. Reactor sources expose the sample to a monochromatic neutron beam (usually generated by a crystal monochromator) and measure the

scattering from the sample using a curved, position-sensitive detector bank which records the complete 2θ range simultaneously. The sample environment and detector assembly can often be moved on a curved track centred on the location of the monochromator in order to change the incident neutron wavelength by varying the angle between the monochromator's input and output beam lines.

In contrast, powder diffractometers at spallation sources expose the sample to the full range of energies in the moderated neutron pulse and have discrete detector banks located at fixed angles. At a given detector, this results in a plot of neutron intensity *vs* time-of-flight; since time-of-flight is dependent on the neutron energy, which also determines its wavelength as per Equation (2.2), this can be converted to a plot of intensity *vs d*-spacing by means of Bragg's law just as easily as the intensity *vs* 2θ data generated by the reactor instrument. Since the accessible range of *d*-spacings is limited by the energies in the neutron pulse, diffractometers at spallation sources have multiple detector banks at different angles, the diffraction patterns from which can be combined to cover a larger range of length scales. The Polaris diffractometer at the ISIS Facility is a fairly typical example of such an instrument and the parameters of its various detector banks are given in Table 2-2 as an example. As noted above for QENS instruments, the energy resolution of the instrument varies with scattering angle and is highest for (near)-backscattering detectors, corresponding to short *d*-spacings.

Table 2-2: Data range specifications for detector banks of the Polaris neutron diffractometer at the ISIS Neutron and Muon Source. Data taken from Smith, et al.[95]

Detector Bank	Bank Description	2θ range (°)	Δ*d*/*d* resolution (%)	d_{max} (Å)
1	Very Low Angle	6.7 - 14.0	2.7	>40
2	Low Angle 1	19.5 – 34.1	1.5	13.5
3	Low Angle 2	40.4 – 66.4	1.85	7.0
4	90°	75.2 – 112.9	0.51	4.1
5	Back Scattering	134.6 – 167.4	0.30	2.65

In addition to dedicated diffractometers, many indirect-geometry INS and QENS spectrometers also include detector banks to collect neutron diffraction data since both types of measurement may be performed simultaneously. The range of

d-spacings measurable on these detectors tends to be quite limited since the diffraction detectors are limited to locations where they will not interfere with the primary purpose of the instrument, which often also precludes placement for optimum resolution. Nevertheless, this capability can provide useful structural data on samples used for vibrational or diffusional investigations.

2.1.4.2 Procedure for Neutron Diffraction Measurements:

As part of the structural characterisation of the ZSM-5 catalyst used in this thesis neutron diffraction measurements were made in order to attempt to experimentally determine the location of the acid sites within the zeolite framework. Measurements were made of both the dry (activated) H-ZSM-5 material and a deuterated D-ZSM-5 equivalent for the reasons described above.

Two samples of H-ZSM-5 were dried according to the method in Section 2.4.2. One of these was then deuterated by passing a saturated stream of D_2O in helium through the sample using a sealable container and a bubbler arrangement. The sample was heated to 573 K during the deuteration process, this temperature having been found to be high enough to promote exchange of the Brønsted acid sites in the zeolite with deuterium from the heavy water without being high enough to cause significant steam de-alumination of the zeolite framework.[96] The deuteration process was continued for 5 hours, followed by the sample being sealed and cooled. The D-ZSM-5 was then dried to remove adsorbed D_2O at 523 K under vacuum, since it was found that even the minute quantities of water present in the 99.999 % helium available on the ISIS catalysis apparatus was sufficient to cause significant back-exchange of the deuterated zeolite.

Following preparation, *ca*. 1.1 g of each zeolite was transferred to cylindrical vanadium sample containers with indium wire gaskets designed for neutron diffraction measurements. Vanadium is used for diffraction sample cells as it has a negligible σ_{coh} value. These samples then had their diffraction patterns measured on the Polaris diffractometer at the ISIS neutron source. These samples were submitted under the ISIS 'Xpress' access route, designed for simple one-off measurements which do not require a full beam time allocation. This means that

the measurement itself was performed entirely by the Polaris instrument team, who collected the sample and returned it together with the collected dataset.

2.1.5 Neutron Data Analysis Tools:

All the neutron instruments used in this work output data as raw neutron intensity *vs* time-of-flight data for the individual detectors, which requires processing in order to reduce it to the $S(Q,\omega)$ data used for analysis. This data reduction process also involves correction for such factors as background scattering from portions of the instrument which reaches the detectors, non-uniform detector efficiency and the energy profile of the incident neutron beam.[57, 86] For direct geometry and QENS instruments, this is accomplished by normalisation of the collected data against a calibration file created from the spectrum of a vanadium sample, used because vanadium is effectively a purely incoherent scatterer. For diffraction measurements a similar process is performed using a measurement of pure silicon, whose cubic lattice parameter is known to a high degree of accuracy. These processes were carried out for all neutron measurements reported in this thesis using Mantid, a software package jointly developed by several neutron scattering facilities, including ISIS, as a standardised framework for manipulating and analysing neutron data.[97] In addition to data reduction Mantid provides tools for analysis and comparison of reduced datasets which were also used throughout.

Direct geometry INS measurements require additional processing in order to present the $S(Q,\omega)$ mitre plots and integrate data in the Q dimension. This was carried out using MSlice, originally a standalone analysis tool which has been integrated into Mantid from version 1.2.0 onward.[98]

Background subtraction and fitting analysis of high resolution QENS spectra was carried out using the programme Data Analysis and Visualisation Environment (DAVE), a QENS analysis software suite developed by the NIST Centre for Neutron Research.[99]

Neutron diffraction data was converted to a format compatible with standard diffraction analysis tools using Mantid and analysed by Rietveld refinement using GSAS-II.[100]

2.2 Computational Chemistry Methods: Applications to Zeolite-Hydrocarbon Systems:

Computational chemistry techniques can provide useful information to assist in the interpretation of vibrational and diffusion experiments and are exceptionally well suited to being used in combination with neutron methods. This work has made use of both DFT-based simulations of vibrational data and molecular dynamics simulations of hydrocarbon motion.

2.2.1 Density Functional Theory:[57]

Density functional theory (DFT) is one of several approaches to applying the laws of quantum mechanics to solve the energy of a system as a function of atomic coordinates, referred to as electronic structure methods. All such methods are ultimately an attempt to approximate the solution to the Schrödinger equation for the system:

$$\hat{\mathrm{H}}\Psi(r,t) = \frac{ih}{2\pi}\frac{\partial\Psi(r,t)}{\partial t} \tag{2.19}$$

differing in the assumptions they make in order to simplify the problem sufficiently that it can be solved for multi-electron systems.

All electronic structure methods use the Born-Oppenheimer approximation, which states that the timeframes of nuclear and electronic movements are sufficiently different that the Schrödinger equation may be separated into equations for the electronic and nuclear motions and that the energy of a given molecular configuration can be calculated while assuming that the positions of the nuclei are fixed.[101] Where DFT differs from *ab initio* calculation methods is that rather than modelling the system as a series of individual atomic orbitals which are combined to describe the electronic structure of the whole system, it instead considers the system in terms of its electron probability density, $\rho(r)$. Doing this considerably reduces the computational difficulty of a calculation because only the three spatial dimensions need be considered, so the complexity of the

calculation scales according to the number of atoms at N^3 as opposed to $N^{(4-7)}$ for *ab initio* methods.

DFT parameters are *functionals* because they are functions of the electron density, which is itself a function of the molecular coordinates. The Hohenberg-Kohn theorem states that there is a functional that relates the ground state energy to the electron density.[102] However, the exact form of this functional is unknown and DFT instead approximates it through the use of model functionals which are fitted to the results of experimental data or higher order *ab initio* simulations. These functionals may be atom-centred or calculated as plane-waves across the entire molecule being simulated; this work has exclusively employed the atom-centred approach. The calculations in this thesis have been performed using the B3LYP functional, which includes corrections for electron energy exchange and the gradient of the electron density.[103-104] This is a well-established functional and produces accurate simulations for systems which do not involve heavy atoms at low computational cost.[105]

The other parameter which affects DFT simulations is the choice of the basis set, which is the function used to describe the electron density around the nucleus. For computational simplicity electron density is described in terms of Gaussian functions, but this does not provide a perfect match to the Slater-type distribution that quantum mechanics predicts as the actual electron density. Multiple Gaussian terms are therefore combined into a basis function in order to bring the model electron density more closely in line with theory. Due to their greater importance, it is conventional to use more complex basis functions to model the valence shell electrons. The basis set used in these calculations was the 6-311+-G* set, which uses a combination of six Gaussians for the basis function of the core shell electrons and models the valence electrons with a triple basis function consisting of three, one and one Gaussian respectively. The splitting of the valence basis function in this way allows adjustment of the spatial distribution of the valence electron density depending on molecular environment in a way which is not possible for single basis function models. This basis set also includes polarization (*) functions to model orbital mixing, and bonding and dispersion (+) functions to model charge distribution in the molecule. The choice of a Pople basis

set of this type was made for simplicity and their well-tested nature and greater compatibility with DFT methods than correlation-consistent type basis sets.

The DFT simulation provides the energy of a given molecular configuration. This can then be used to generate an optimised geometry for the molecule by adjusting the atomic coordinates until the energy converges to a minimum. The vibrational modes of this minimum energy configuration can then be calculated. This provides the eigenvalues (vibrational frequencies) and eigenvectors (atomic displacements) of the vibrations; as noted in Section 2.1.2 above, this is all that is necessary to predict the scattering intensity at a given energy transfer from Equation (2.8), allowing creation of a simulated INS spectrum. Although computationally straightforward, the large number of modes in molecules of any significant size means that the process is simplified by the use of dedicated tools. Historically, the aCLIMAX software package has been used to convert data from DFT simulations to simulated spectra.[106] This was developed at the ISIS Facility specifically to provide simulated spectra corresponding to experimental data collected on the TOSCA indirect geometry spectrometer. More recently this software has been superseded by a new tool, AbINS, which offers the advantages of ongoing development and integration into the Mantid neutron scattering analysis package.[107] Both programs have been used at various points in the work reported here.

2.2.1.1 DFT Simulation Procedure:

DFT modelling for optimisation and frequency calculations of molecular structures was carried out using the molecular simulation software suite GAUSSIAN.[108] Initial molecular structures were generated by hand which were then written in z-matrix format and submitted to the software for geometry optimisation. Energy calculations for optimisation were performed using the B3LYP functional carried out on a 6−311-G* basis set.[103-104, 109] Geometry optimisation was carried out until the energy converged to a minimum, followed by the vibrational modes of the resulting optimised geometry being calculated using the same functional and basis set. All geometric parameters were unrestricted and no symmetry-based shortcuts were used in the DFT energy calculations to prevent limitation of the final optimised geometry.

Once optimised structures and frequency modes were calculated, they were converted to simulated INS spectra using the aCLIMAX or AbINS simulation packages.[106-107] While the resulting simulations are generally reported to be highly accurate, one exception is that simulations derived from single-molecule calculations have a tendency to overestimate the intensity of contributions from lattice modes due to lacking information on intermolecular interactions resulting in correspondingly oversized lattice overtones which affect the spectrum across the full energy range. To mitigate this the intensities of the predicted lattice modes in the simulated spectra were scaled down by a factor of 0.75: this is a standard technique for the treatment of simulations of this type and produces a more representative spectrum in the region above 200 cm^{-1}.[57]

2.2.2 Molecular Dynamics Simulations:[64-65, 110-111]

Molecular dynamics (MD), sometimes referred to as *classical* molecular dynamics, apply Newton's laws of motion and allow simulation of much larger systems than *ab initio* methods by by-passing the calculation of the electronic properties of the system. Instead, the energies arising from the interactions of particles in the simulation are parameterised as equations which describe how the energy of each contribution varies as a function of atomic position. The Born-Oppenheimer approximation is applied but in the opposite manner to electronic structure methods, here only the motions of the nuclei are considered. The total energy of the system simulation is given by the sum of all the contributing equations.[111]

$$E_{tot} = E_{bond} + E_{angle} + E_{dihedral} + E_{elec} + E_{VdW} \qquad (2.20)$$

The complete set of parameters which describes all interactions in the simulation is referred to as the *molecular force field*. Since force-field calculations model the system at a much simpler level than quantum mechanical calculations, they are considerably less computationally expensive and simulation sizes involving thousands of atoms are easily achievable.

The size of system which can be practically simulated by MD is still far too small to provide a realistic model for diffusion at the scale of a zeolite crystal. To provide a more representative environment, periodic boundary conditions are

employed. In this arrangement the simulation box is treated as being located at the centre of an infinite array of identical boxes. Movements by any atom in the simulation are mirrored by its counterparts in adjacent boxes. Interatomic interaction potentials are allowed to cross the boundaries but the simulation is given a cut-off distance beyond which interactions between atom pairs are not calculated; the maximum value for this cut-off is always less than ½ the shortest dimension of the simulation box, thus ensuring that an atom will interact with only one instance of any other atom, which may lie in an adjacent box, and cannot directly affect its equivalents in the other boxes. Atoms which leave the box are immediately replaced by an equivalent atom with the same velocity entering on the opposite side, conserving the number of atoms in the simulation. By these means surface forces are eliminated and the constraints of the maximum simulation size are largely relaxed at no additional computational expense, since the cut-off radius means that the number of interactions which must be calculated for each timestep are not increased relative to the non-periodic system.

The functions which constitute the force field are all simple relationships between potential energy and atomic position. For example, a bond between two atoms *a* and *b* may be described by a harmonic potential where the potential energy of the bond varies with bond length r_{ab} by:

$$E(r_{ab}) = \frac{1}{2}k(r_{ab} - r_0)^2 \tag{2.21}$$

Where *k* is the force constant of the bond and r_0 the equilibrium bond length. Similarly, the valence angle between atoms *a*, *b* and *c* may also be described by a harmonic potential:

$$E(\theta_{abc}) = \frac{1}{2}k(\theta_{abc} - \theta_0)^2 \tag{2.22}$$

All parameter functions will include one or more terms such as *k* in the above examples which determine the value of the potential energy profile. The values of these terms are set by fitting to experimental data or the results of quantum mechanical simulations to give a function which accurately describes the interaction the parameter embodies. The overall force field will include a function

for each bonded pair of atoms, each valence angle and so on, the sum of which gives the overall E_{bond}, E_{angle}, etc.

The bond, angle and dihedral interactions are all *intramolecular* potentials which embody the interactions within individual molecules in the simulation and are concerned with maintaining that molecule in a chemically accurate geometry, given its structure and interactions with the surrounding environment. The van der Waals forces and electrostatic interactions form the intermolecular non-bonding interactions which apply between molecules, including between adsorbate molecules and surrounding framework structures in the case of simulations of zeolites. Van der Waals forces are typically modelled by the Lennard-Jones potential which relates the potential energy at a given distance to the minimum energy distance, σ, and the depth of the potential energy well, ϵ.

$$E(r_{ab}) = 4\epsilon\left[\left(\frac{\sigma}{r_{ab}}\right)^{12} - \left(\frac{\sigma}{r_{ab}}\right)^{6}\right] \tag{2.23}$$

This potential is zero at long distances, repulsive at short distances and slightly attractive at distances around σ, accurately describing the behaviour due to induced dipole-dipole interactions.

The potential for electrostatic interactions is more complex. The basic form is that the electrostatic interaction between two atoms is given from their charge, q, by the Coulomb potential:

$$E(r_{ab}) = \frac{q_a q_b}{4\pi\epsilon_0\epsilon\, r_{ab}} \tag{2.24}$$

Charge values are assigned to the atoms in the simulation based on their electronegativity, although modification and the use of partial charges may be necessary to fit experimental observations in some systems. The problem with this implementation is that the range of electrostatic interactions is considerably greater than other potentials and in periodic systems such as zeolites can still be significant even at the simulation cut-off radius. This leads to a significant jump in the potential energy between two atoms occurring whenever they move within the cut-off boundary of each other. This problem is addressed by use of the Ewald

sum method, which splits the electrostatic interaction into real-space and reciprocal-space components.[112] Long range interactions in real space are ignored and calculated instead in reciprocal space as a series of Gaussians which can be solved as a Fourier series across the whole simulation, avoiding cut-off effects.

At the start of a molecular dynamics simulation, the initial configuration may be supplied from experimental data or set according to a theoretical model. The initial velocities of the atoms in the system are randomly assigned from a Maxwell-Boltzmann distribution based on the target temperature of the simulation and adjusted so that the overall momentum of the system is zero. These positions and velocities are then used to calculate the starting forces on each atom from the force field parameters.

2.2.2.1 Velocity and Temperature Control in MD Simulations:[111]

Calculating the trajectory of a system in a molecular dynamics system requires solving Newton's equations of motion for interacting bodies. Since all atoms in the system affect all others in ways embodied by the force field parameters, the entire system is coupled together. Solving this interrelationship as a continuous potential is impractical, and instead the simulation is performed using a finite difference approach through the velocity Verlet algorithm.[113] The simulation is divided into extremely short timesteps, on the order of femtoseconds. To advance time t by timestep Δt, the forces on each atom ($\underline{f}$) are calculated from the force field, while the atomic positions ($\underline{r}$) and velocities ($\underline{v}$) at t are already known. These are used to calculate the values of $\underline{v}$ at (t + ½Δt) by integration of the forces.

$$\underline{v}\left(t+\tfrac{1}{2}\Delta t\right) \longleftarrow \underline{v}(t)+\frac{\Delta t}{2}\frac{\underline{f}(t)}{m} \tag{2.25}$$

These updated velocities are used to calculate the atomic positions at (t+Δt);

$$\underline{r}(t+\Delta t) \longleftarrow \underline{r}(t)+\Delta t\,\underline{v}\left(t+\tfrac{1}{2}\Delta t\right) \tag{2.26}$$

the new positions are used to recalculate the atomic forces;

$$\underline{f}(t + \Delta t) \longleftarrow \underline{f}(t) \tag{2.27}$$

and finally, the new forces are used to update the half-step velocities to their values after the full timestep:

$$\underline{v}(t + \Delta t) \longleftarrow \underline{v}\left(t + \tfrac{1}{2}\Delta t\right) + \frac{\Delta t}{2}\,\frac{\underline{f}(t + \Delta t)}{m} \tag{2.28}$$

The velocity Verlet algorithm provides the positions and velocities, and thus the system energies, at each timestep. However, because of the extremely short length of Δt these are usually sampled for output at a much lower rate, usually every few picoseconds, to avoid excessively large results files.

The velocity Verlet algorithm alone is capable of maintaining the correct system conditions when the simulation is operating in the microcanonical (NVE) ensemble. In order to operate under the canonical (NVT) ensemble it is necessary to couple the energies in the system to an 'external heat bath' which modifies the velocities at each timestep in order to push the average kinetic energy of the system toward that corresponding to the target simulation temperature. NVT simulations in this work use the Nosé-Hoover thermostat which operates by introducing a friction coefficient, χ, which is defined as:

$$\frac{d\chi(t)}{dt} = \frac{2E_{kin}(t) - 2\sigma}{2\sigma\ \tau_T{}^2} \tag{2.29}$$

where E_{kin} is the system kinetic energy, τ_T a simulation-specified time constant for thermal energy exchange and σ is the target thermostat energy, given from the target temperature, T_{ext}, and the total degrees of freedom in the system, f, by:

$$\sigma = \frac{f}{2}\ k_B\ T_{ext} \tag{2.30}$$

χ(t) is updated at (¼Δt) intervals and used to scale the system velocities before and after each iteration of the velocity Verlet algorithm (Equations (2.23) to (2.26)). The Nosé-Hoover thermostat was chosen because it avoids the 'flying ice cube' problem associated with the more commonly employed Berendsen thermostat, where the energy of high frequency fundamental vibrations can

transfer to the translational energy of the whole molecule resulting in rigid molecules with unrealistically high velocities.[114]

The initial stage in any MD simulation is an equilibration process which is continued until the constant parameters for the ensemble under which the simulation is to be run (number of atoms, volume and total energy for the microcanonical ensemble, number of atoms, volume and temperature for the canonical ensemble) reach stable values. Once this process is complete the system is allowed to evolve and the molecular trajectories collected. Only the trajectories in this post-equilibration 'production' run are representative and usable for the determination of diffusion properties.

2.2.2.2 A Molecular Force-Field for Simulating Zeolites:

The specific characteristics of the force field model used to simulate the diffusion of hydrocarbons in H-ZSM-5 will now be described. In order to quantify the effect of framework acid sites on diffusion of adsorbed molecules simulations were performed of both H-ZSM-5 and its purely siliceous analogue silicalite. Both alkene and alkane adsorbates were simulated in order to investigate how the additional rigidity and charge density introduced by the C=C double bond affects molecular movement through the zeolite. The specific adsorbates chosen were propene, propane, 1-octene and *n*-octane for direct comparability with model compound experimental studies.

The zeolite framework in all simulations used the orthorhombic MFI structure with *Pnma* symmetry. The simulation box was a 2 × 2 × 2 supercell with overall dimensions of 40.18 × 39.48 × 26.28 Å containing 2304 framework atoms in the silicalite structure and 2328 atoms in the ZSM-5 due to the addition of charge-compensating protons. Periodic boundary conditions were employed to simulate a realistically sized zeolite environment without increasing computational expense. Aluminium substitutions and their associated Brønsted acid protons were included in the ZSM5 framework at a level of three acid sites per unit cell (Si:Al 31:1) to match the pre-steaming experimental catalyst as closely as possible without the complication of fractional numbers of acid sites. These were distributed to maximise acid site separation in accordance with Dempsey's rule, which predicts

that zeolites will exhibit ordering during synthesis to maximise Al-Al separation, and the Brønsted groups positioned to point into the pore channels.[115]

The zeolite model in both cases used a flexible framework with potentials taken from work by Jackson and Catlow[116] and expanded on by Schröder, et al.[117] based on fitting to the properties of α-quartz and alumina with the properties of the hydroxyl groups modified based on *ab initio* simulations. These potentials are well established and have been found to accurately describe the properties of both zeolites and SiO_2 structures.[116] They have also been used to accurately describe the behaviour of adsorbed molecules within zeolite frameworks.[73, 75, 118] Full ionic charges were assigned to the framework T-atoms and non-hydroxyl oxygens while partial charges were assigned to the atoms of the hydroxyl groups (designated O_b and H_b) as per Schröder; these were used to generate the long-range Coulombic interactions *via* the Ewald method. Rather than using bond potentials, short range framework pair interactions were described by a Buckingham potential for the Si-O, Al-O and O-O pairs; these interactions may be modelled in the form:

$$E(r_{ij}) = A \exp\left(\frac{-r_{ij}}{\rho}\right) - \frac{C}{{r_{ij}}^6} \tag{2.31}$$

where A and C are constants and ρ the minimum energy distance. The O_b-H_b bond required a more complex function and was modelled by a Morse potential, which has the capacity to describe behaviour such as dissociation. This potential considers the depth of the potential energy minimum (E_0), frequency of the bond vibration (ω), reduced mass of atoms i and j (μ) and the equilibrium bond distance (r_0) with the relationship:

$$E(r_{ij}) = E_0\left[\left\{1 - exp\left(-k(r_{ij} - r_0)\right)\right\}^2 - 1\right] \tag{2.32}$$

where

$$k = \omega\sqrt{\frac{\mu}{2E_0}} \tag{2.33}$$

Since this value does not change during the course of the simulation, *k* is the parameter supplied to the simulation engine to reduce computational overhead. The interactions between T-atoms are regarded as having a negligible contribution and are discounted and all pair interactions were calculated with a cut-off radius of 10 Å. A harmonic three-body potential was used to describe and accurately constrain the geometry of the O-Si-O and O-Al-O triads; this is identical to the harmonic valence angle potential described by Equation (2.20) above, but differs in how it is treated; three-body potentials are considered as being partially *inter-*

Table 2-3: Potential parameters for intramolecular zeolite interactions. H_b and O_b represent the Brønsted acid proton and its associated bridging oxygen respectively. Potentials taken from Jackson and Catlow[116] and Schröder, et al.[117]

Atomic Charges			
Atom	Charge (a.u.)		
Si	+ 4.000		
Al	+ 3.000		
O	- 2.000		
O_b	- 1.426		
H_b	+ 0.426		
Buckingham Potentials			
Atoms	A (eV)	ρ (Å)	C (eV Å^6)
O-O/O_b	22764.0	0.14900	27.8800
Si-O	1283.91	0.32052	10.6616
Si-O_b	983.557	0.32052	10.6616
Al-O	1460.30	0.29912	0.0
Al-O_b	1142.68	0.29912	0.0
O-H_b	311.970	0.25000	0.0
Morse Potentials			
Atoms	E_0 (eV)	r_0 (Å)	k (Å^{-1})
O_b-H_b	7.0525	0.9485	2.1986
Three-Body Potentials			
Atoms	k (eV rad^{-2})	θ_0 (°)	
O-Si-O/O_b	2.09724	109.470	
O-Al-O/O_b	2.09724	109.470	

molecular and therefore van der Waals interactions and other intermolecular pair potentials between atoms linked by a three-body term are not excluded from the overall calculation.[111] This is important in maintaining an accurate simulation over large molecules such as zeolite structures. The values of the parameters for these potentials are given in Table 2-3.

The properties of the carbons and hydrogens and the intermolecular interactions between adsorbate molecules were parameterised using OPLS_2005, a generalised all-atom force field for the simulation of organic molecules.[119] OPLS parameters are derived from both experimental data and quantum chemical simulations and can predict small molecule behaviour in both gas and condensed phases across a wide range of temperatures with good accuracy. In describing the potentials used for this model, it is important to distinguish between the terminal and chain-bonded sp^2 carbons, the sp^3 carbons in the alkyl chain and the hydrogen atoms associated with each. The abbreviated nomenclature used for each type of atom in the parameter tables is illustrated for 1-octene in Figure 2-12.

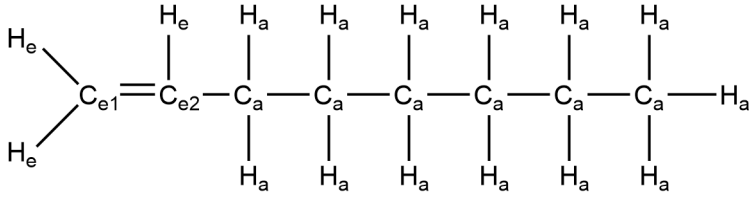

Figure 2-12: Nomenclature used for describing the atoms involved in force field potential terms illustrated for 1-octene.

In the OPLS implementation all hydrogens bonded to sp^2 carbons are assigned a charge of + 0.115 atomic units and the hydrogens bonded to sp^3 carbons a charge of + 0.060 a.u. The charges of the carbon atoms are set to neutralise the combined charge from their bonded hydrogens to create an overall charge-neutral molecule. All bonds and bond angles are described by harmonic potentials (Equations (2.19) and (2.20)). The dihedral angles used triple cosine potentials to allow for asymmetric energy profiles with respect to dihedral angle: the formula used was:

$$E(\phi) = \frac{1}{2}\{A_1(1 + \cos(\phi)) + A_2(1 - \cos(2\phi)) + A_3(1 + \cos(3\phi))\} \qquad (2.34)$$

A scaling factor of 0.5 was applied to the electrostatic and van der Waals interactions between atoms 1 and 4 in any specified dihedral sets. The

intermolecular pair interactions for van der Waals forces between hydrocarbon molecules are modelled as Lennard-Jones potentials (Equation (2.21)). All parameters are given in Table 2-4 and Table 2-5.

Table 2-4: Intramolecular potential parameters for interactions in adsorbed hydrocarbons as implemented in OPLS_2005.[119]

Harmonic Bond Potentials		
Atoms	k (eV Å^{-2})	r_0 (Å)
C_{e1}=C_{e2}	47.6148	1.340
C_{e2}-C_a	27.4929	1.510
C_a-C_a	23.2431	1.529
$C_{e1/e2}$-H_e	29.4876	1.080
C_a-H_a	29.4876	1.090
Harmonic Angle Potentials		
Angle	k (eV rad^{-2})	θ_0 (°)
C_{e1}=C_{e2}-C_a	6.0710	124.000
C_{e2}-C_a-C_a	6.0710	112.027
C_a-C_a-C_a	5.0606	112.700
C_e=C_e-H_e	3.0355	120.000
C_{e2}-C_a-H_a	3.0355	109.500
C_a-C_{e2}-H_e	3.0355	117.000
C_a-C_a-H_a	3.2523	110.700
H_e-C_{e1}-H_e	3.0355	117.000
H_a-C_a-H_a	2.8620	107.800
Dihedral Potentials		
Dihedral	A_1 (eV)	A_2 (eV)	A_3 (eV)
C_{e1}=C_{e2}-C_a-C_a	8.543×10^{-3}	1.323×10^{-2}	-4.393×10^{-2}
C_{e2}-C_a-C_a-C_a	2.983×10^{-2}	8.196×10^{-3}	9.627×10^{-3}
C_a-C_a-C_a-C_a	4.652×10^{-2}	-6.548×10^{-3}	1.735×10^{-2}
H_e-C_{e1}=C_{e2}-C_a	0.0	0.6071	0.0
H_a-C_a-C_a-$C_{a/e2}$	0.0	0.0	1.301×10^{-2}
H_e-C_{e1}=C_{e2}-H_e	0.0	0.6071	0.0
H_e-C_{e2}-C_a-H_a	0.0	0.0	2.871×10^{-2}
H_a-C_a-C_a-H_a	0.0	0.0	1.301×10^{-2}

Table 2-5: Potential parameters for interactions between molecules of adsorbed hydrocarbons in multiple-adsorbate simulations as implemented in OPLS_2005.[119]

Lennard-Jones Pair Potentials		
Atoms	ε (eV)	σ (Å)
$C_{e1/e2}$-$C_{e1/e2}$	0.31798	3.550
$C_{e1/e2}$-C_a	0.29633	3.525
C_a-C_a	2.8620×10^{-3}	3.500
$C_{e1/e2}$-$H_{e/a}$	0.19978	2.931
C_a-H_e	0.18618	2.910
C_a-H_a	1.9296×10^{-3}	2.958
H_e-$H_{e/a}$	0.12552	2.450
H_a-H_a	1.3009×10^{-3}	2.500

Table 2-6: Intermolecular pair potentials describing hydrocarbon-framework interactions derived from Kiselev, et al.[120]

Lennard-Jones Pair Potentials		
Atoms	ε (eV)	σ (Å)
O-C_e	0.80702	2.958
O_b-C_e	0.80702	2.958
O-C_a	7.083×10^{-3}	2.923
O_b-C_a	8.280×10^{-3}	3.150
O/O_b-H_e/H_a	4.987×10^{-3}	2.557
H_b-C_e	0.37632	2.806
H_b-C_a	2.990×10^{-3}	2.806
H_b-H_e/H_a	8.510×10^{-4}	1.784

The framework-adsorbate interactions were taken from the work of Kiselev, et al.[120] on deriving potential energies of interaction from atom electronic properties as implemented for hydrocarbons in zeolites by Vetrivel, et al.,[121] Catlow, et al.[122] and O'Malley, et al.[123] All interactions were modelled as Lennard-Jones potentials using the parameters in Table 2-6; interactions involving the framework T-atoms were once again discounted as negligible.

2.2.2.3 MD Simulation Procedure:

All molecular dynamics simulations presented in this thesis were performed using the DL_POLY 4 code.[124] Calculations were carried out on the University of Glasgow high performance computing cluster (HPCC) using eight cores per simulation with 2 GB RAM per core; average processing speed was approximately 20 hrs simulation time per ns_{sim}.[125] Configuration files for the zeolite frameworks were prepared from CIF files of the MFI structure obtained from the IZA structural database.[8] These were modified with an appropriately-distributed level of aluminium substitutions and Brønsted sites using the Aten visualisation software package, v1.8, which was also used to introduce the adsorbate molecules for study.[16] For the initial configuration, the adsorbate molecules were placed in the centre of the zeolite pore channels equidistant throughout the zeolite supercell. Adsorbate loadings were chosen to match experimental loadings from equivalent QENS measurements.

The DL_FIELD toolset was used to convert the resulting .XYZ format system configuration to the native file format for DL_POLY (.CONFIG).[126] DL_FIELD also considerably simplifies the preparation of the input file used to describe the molecular force field (.FIELD) by being able to detect relevant intramolecular interactions in the input structure and add the relevant parameters to the output .FIELD file. Intermolecular interaction parameters were added manually using standard text editing tools, which were also used to create the control file which sets the simulation parameters.

All simulations were performed in the canonical (NVT) ensemble using a Nose-Hoover thermostat with a 1 ps thermal exchange time constant to maintain the desired temperature for each simulation.[127] The simulation timestep was 0.5 fs throughout. All systems were initially equilibrated for 1 ns at 270 K in order to ensure that low-temperature simulations began from a stable distribution of the molecules within the zeolite. They were then equilibrated for a further 1 ns at the target temperature for the simulation followed by a production run of 5 ns, this was chosen based on examination of the earliest simulations as being sufficient to achieve true diffusive motion for the adsorbed molecules, as evidenced by the mean squared displacement (MSD) of the molecules becoming

linear with respect to time. The atomic coordinates and velocities for the system were saved every 2000 steps (1 ps) for analysis. The resulting trajectory files were analysed using the MDANSE software with visualisations prepared using Aten.[128]

2.2.2.4 Deriving Scattering Predictions from MD Data:

The parameter measured in QENS experiments is the incoherent scattering function or dynamic structure factor, $S_{inc}(Q,\omega)$, which as described above can be related to the van Hove self-correlation function, $G_s(r,t)$ by Equation (2.11). In the same paper where he established this relationship, van Hove also defined an additional parameter, the self-intermediate scattering function $I_s(Q,t)$, which relates to the dynamic structure factor by:

$$S_{inc}(Q,\omega) = \frac{1}{2\pi}\int_{-\infty}^{+\infty} \mathrm{d}t\; I_s(Q,t)\; e^{-i\omega t} \tag{2.34}$$

This in turn can be related to the positions of the nuclei in a sample by the relationship:

$$I_s(Q,t) = \frac{1}{N}\sum_{\alpha} {b_{inc}}_{\alpha}{}^{2} \langle \exp\left[-iQ\cdot \hat{\mathrm{R}}_{\alpha}(t_0)\right] \exp\left[-iQ\cdot \hat{\mathrm{R}}_{\alpha}(t_0+t)\right]\rangle \tag{2.35}$$

where $b_{\mathrm{inc},\alpha}$ and $\hat{\mathrm{R}}_{\alpha}$ are the incoherent scattering cross length and position operator for nucleus α. The angle brackets denote a quantum thermal average over the length of the time period considered.[88]

It is possible to calculate the position operator for a given nucleus over the course of a simulation from its recorded positions in a molecular trajectory file. Therefore, using these relationships, it is possible to calculate the theoretical QENS scattering results that would be produced by a system which has been simulated by molecular dynamics with the calculated energy transfer window determined by the length of the simulation. The MDANSE package includes tools to simplify the process of implementing this calculation.[128]

2.3 Catalyst Preparation Reactors and On-Line Analysis:

Investigations of the activity of ZSM-5 as a catalyst require the capability to undertake reaction testing under conditions of relevance to industrial catalysis. Two test reactor setups were utilised, a micro-scale reactor located at the UK Catalysis Hub, Oxfordshire, and a larger scale reactor at the ISIS Facility.

2.3.1 The UK Catalysis Hub Microreactor:

This apparatus comprises a vertically oriented fixed-bed tube micro-reactor with an internal diameter of 10 mm; catalyst masses used were approximately 0.5 g giving a bed length of 10 mm when using ZSM-5 zeolites. A diagram of the reactor design is shown in Figure 2-13. Gas flow control is provided by three independently supplied mass flow controllers with a maximum flow rate of 100 cm^3 min^{-1} each. Liquid reagents are supplied by a HPLC pump (minimum flow rate 0.1 cm^3 min^{-1}) or syringe pump (minimum flow rate 0.001 cm^3 min^{-1}) injecting into a silica-packed mixing volume heated to 423 K and located immediately upstream of the reactor tube to ensure complete vaporization of the injected liquid prior to entering the reactor. The reactor is heated by a tube furnace mounted around the fixed bed; a separate bypass system allows routing gas flows around the reactor if required. All pipework downstream of the heated mixing volume and outside region heated by the tube furnace are insulated and equipped with trace heating to maintain them at 423 K, preventing condensation of any hydrocarbon products on the interior of the gas lines.

In order to provide on-line analysis of the reaction products the eluent gas flow from the reactor can be sampled by both gas chromatography (GC) and mass spectrometry (MS). GC analysis is provided by a GC-FID (Shimadzu GC-2014 fitted with a BP20 column of dimensions 30 m x 0.25 mm x 0.5 µm) drawing from a 150 µl heated sample loop. MS analysis is provided by an ESS EcoCat drawing from immediately downstream of the GC sample loop using a differentially pumped heated capillary. All pipework between the reactor and the analysis instruments is equipped with trace heating and maintained at 423 K to prevent condensation of any products within the pipework. Zero percent conversion data for reactions

can be collected by initially bypassing the reactor using the installed bypass system.

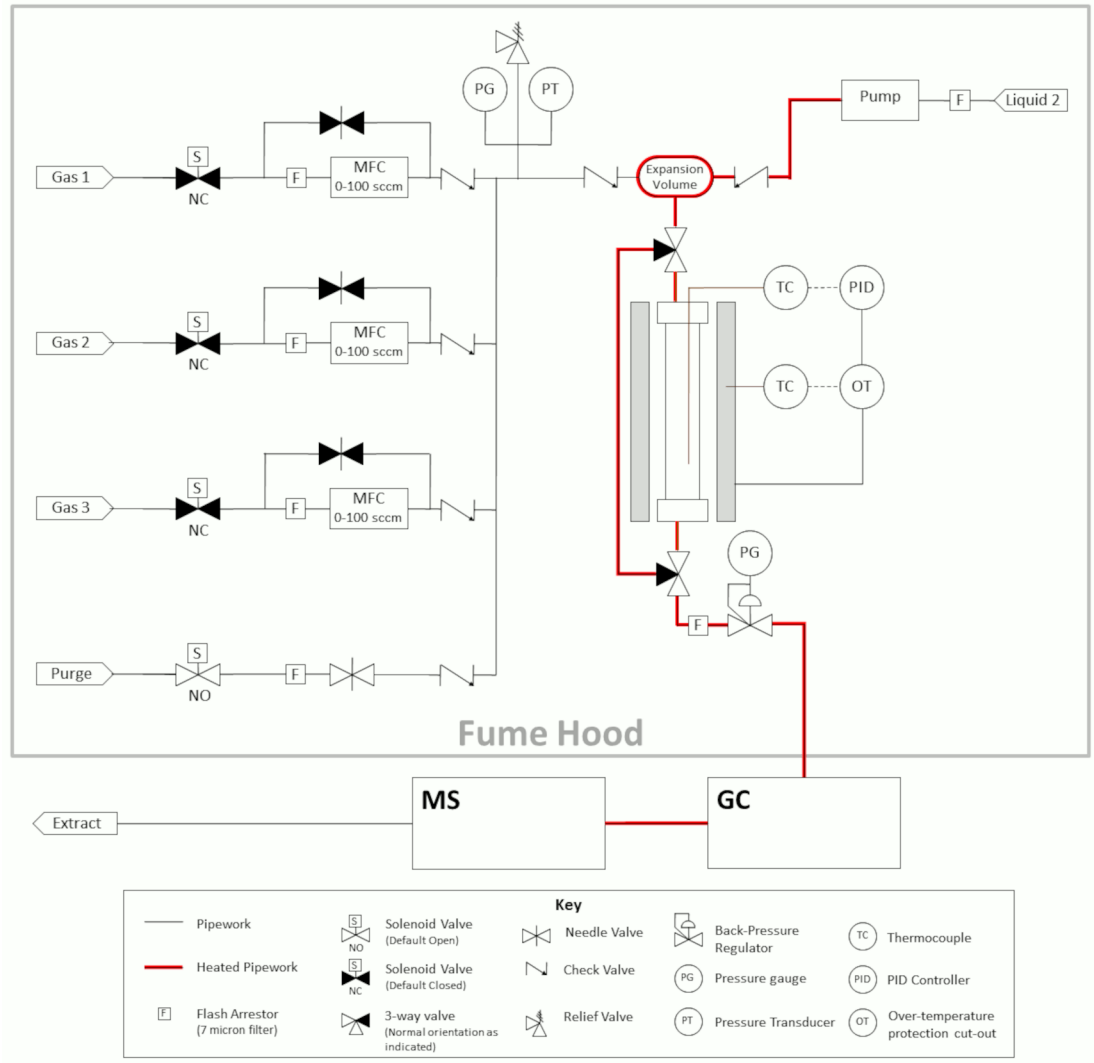

Figure 2-13: Layout of the UK Catalysis Hub microreactor setup.

2.3.2 The ISIS Catalyst Preparation Apparatus:

Neutron experiments require larger quantities of sample than the *ca.* 0.5 g samples which can be prepared on microreactor setups. For this reason, the ISIS Facility's sample preparation laboratory possesses a gas handling reaction system designed for the testing of catalyst systems at a scale of approximately 15 g per reaction. The layout and development of the majority of this system is described by Warringham, et al.[58] . However, since the publication of that report, the system has been modified by the addition of a micro GC for additional analysis of the reaction products (see below) and the addition of a HPLC pump (Teledyne, model

M1010SNN1C) feeding into the inlet gas stream immediately upstream of the reactor to allow the introduction of liquid reagents and a downstream catch-pot. The reactor is in the form of a cylindrical steel sample cell equipped with gas handling fittings which is loaded with the zeolite giving a cylindrical fixed bed reactor with the bed having a diameter of 35 mm and a length of 45 mm. This geometry minimises bed length effects and maximises the homogeneity of the reacted catalyst samples. The reactor is mounted so that a tube furnace can be raised around it to provide temperature control of the reaction and the gas flow enters the reactor at the bottom, ensuring that any liquid reagents are vaporized during their passage through the inlet pipework.

The rig is equipped with a catch pot located downstream of the reactor vessel and maintained at 293 K which collects any condensable reaction products. The composition of the remaining gas stream is analysed by a Hiden Analytical HPR-20 mass spectrometer and an Agilent 490 micro-GC, with both instruments drawing from the outlet of the reaction rig via differentially pumped capillaries heated to 423 K. MS analysis was used to monitor all operations performed on the rig; micro-GC analysis was only used in reaction testing experiments due to its greater complexity of operation.

The micro-GC is equipped with four parallel analysis columns, as detailed in Table 2-7, each analysed by a thermal conductivity detector with an injection volume of 5 cm^3 per analysis. Testing of GC analysis methodologies showed that five minutes is sufficient for the elution of all detectable products from the GC columns, meaning that GC sampling takes place approximately every 7 minutes with minor variations due to the need for the instrument to equilibrate prior to injection. During reaction tests, sampling was performed at maximum rate for the first hour to maximise data collection during the initial catalyst run-in period but was then interrupted for 45 minutes every 8 cycles in order to re-condition the columns at higher temperature. The apparatus is equipped with a reactor bypass system to permit the collection of zero percent conversion data for the on-line analysis methods.

Table 2-7: Analysis columns and column temperatures in the GC used for on-line analysis of reactions in the ISIS catalyst preparation apparatus.

Column	Temperature (°C)	Make-up gas	Details (Detected Product Types)
1	50	He	5 Å molecular sieve, 20 m column with backflush (O_2, N_2, CO, CO_2)
2	55	He	PoraPLOT Q, 10m column (CO_2, water, light alkyl hydrocarbons)
3	65	He	CP-Wax 52CB, 10m column (heavy alkyl hydrocarbons, aromatics, alcohols)
4	50	N_2	5 Å molecular sieve, 20 m column with backflush (He, H_2)

2.4 Zeolite Pre-Treatment Procedures:

The catalyst used for the majority of this thesis was a powder form commercial material grade H-ZSM-5 zeolite supplied by our industrial partners, Johnson Matthey plc. The material as it was originally supplied will be referred to as ZSM5-AR for short. This material was not utilised as-is but was subjected to one or more treatment procedures prior to its use in any experiments. The rest of this section outlines these procedures and defines the abbreviations which will be used to unambiguously refer to each treated zeolite in the remainder of this work. These designations are summarised in Table 2-8 for easy reference.

Appendix 2 attempts to investigate the effect of Brønsted acid groups in the zeolite on adsorbate diffusion through the use of a non-protonated silicalite-type MFI framework. For these investigations a second ZSM-5 material with only nominal levels of aluminium substitution was sourced from Johnson Matthey. This was calcined and dried in the same manner as described for ZSM5-FR below to generate the material used experimentally, which will be referred to as ZSM5-SIL.

2.4.1 Calcination of As-Received Zeolite:

IR spectroscopy shows ZSM5-AR contains residual tetrapropyl ammonium hydroxide template material from the zeolite synthesis process which must be removed before it can be used. This was done by calcination in static air using a muffle furnace. ZSM5-AR was loaded into ceramic boats holding *ca.* 10 g each, placed in the furnace and heated to 773 K at a rate of ≤ 5 K min^{-1} in order to allow adsorbed water to be driven out of the zeolite matrix without causing steam de-alumination. The zeolite was then held for 12 hours at temperature and allowed to cool. This was sufficient to remove all template material, evidenced by a colour change of the zeolite from pink to white and confirmed by infrared characterisation of the calcined material. The zeolite which has undergone this treatment is the baseline fresh catalyst for the work reported here and will be referred to as ZSM5-FR (fresh). A full characterisation of the properties of this material is given in Chapter 3, Section 3.1.

2.4.2 Drying Procedure for Zeolite Samples:

Zeolites are hygroscopic and will adsorb water from the atmosphere if not stored in a moisture-free environment. To prevent this affecting the results, the ZSM-5 catalysts used were dried immediately prior to use in any experiment. A sample of the zeolite sufficient for the experiment at hand was heated to 623 K under flowing helium (100 cm^3 min^{-1}, BOC, >99.999%) at a rate of ≤ 5 K min^{-1} and held at that temperature to remove all water from the sample. The heating was continued until either analysis of the eluent gas stream showed no remaining water being released from the zeolite or, where such analysis was unavailable, for 6 hours at temperature to ensure complete drying. In situations where this was possible, the process was carried out on the instrument itself *in situ* prior to commencing the experiment. Where this could not be done, zeolite batches were dried on the ISIS catalyst preparation apparatus and the dried zeolite sealed inside its reactor and transferred to an argon glovebox (MBraun UniLab MB-20-G, [H_2O] < 1 ppm, [O2] < 1 ppm) for storage until required. Samples were loaded into the relevant experimental apparatus inside the glovebox,

sealed where apparatus design made this practical and used immediately on removal from the glovebox.

2.4.3 Steaming Procedure for Partial De-Alumination:

Steam treatment of the fresh catalyst to generate the artificially aged material used in Chapter 5 was carried out by two methods. Method #1 was performed using the ISIS catalyst preparation rig (Section 2.3.2). 15 g batches of ZSM5-FR were loaded into an Inconel reaction vessel equipped with gas-handling fittings and mounted on the rig. The reactor was heated to 873 K under flowing helium (100 cm^3 min^{-1}, BOC, >99.999%) at a rate of ≤ 5 K min^{-1}. Once at temperature, steaming was initiated by the introduction of 1 g/g_{cat}/hr of deionised water into the inlet gas stream using the rig HPLC pump. Steam treatment was carried out for 48 hours, with these conditions being chosen to generate a de-aluminated end product with similar properties to steady-state industrial cracking catalysts.[33, 96] Following water shut-off, the temperature of the reactor was reduced to 623 K and helium flow maintained for a further 6 hours to remove all adsorbed water from the sample. The reactor was then sealed using the integrated fittings, cooled to room temperature and transferred to an argon glovebox to permit preparation of the experimental samples without contamination from atmospheric water. This material will be referred to as ZSM5-ST(873K).

In order to prepare larger quantities an alternative method was employed, with the ZSM5-FR held in a static atmosphere of steam-saturated helium at 1073 K for 12 hours. Material prepared by this method is designated ZSM5-ST(1073K). Preparation of ZSM5-ST(1073K) was performed by Dr Iain Hitchcock at the Johnson Matthey Technology Centre, Sonning Common, UK and the resulting material transferred to the UK Catalysis Hub by courier. Due to this, the resulting material had adsorbed water and required drying before use in the same manner as ZSM5-FR.

Despite their different preparation methods, ZSM5-ST(873K) and ZSM5-ST(1073K) were found to have essentially similar final properties. For details the reader is referred to Section 5.1.1, below.

Table 2-8: Short designations used to refer to treated zeolite materials used in this thesis.

Designation	Description
ZSM5-AR	Untreated zeolite as received from Johnson Matthey
ZSM5-FR	'Fresh' zeolite calcined to remove synthesis template.
ZSM5-ST(873K)	ZSM5-FR following partial de-alumination by steam treatment at ISIS.
ZSM5-ST(1073K)	ZSM5-FR following partial de-alumination by steam treatment at JMTC Sonning Common.
ZSM5-SIL	Vary low aluminium 'silicalite' material used for non-protonated MFI studies in Appendix 2.

2.5 Zeolite Characterisation Methods:

Characterisation measurements of the zeolite forms used were carried out in order to establish their structural and chemical properties and how they are affected by the various treatment processes used to prepare the different materials in Table 2-8. This section details the methods and equipment used in these measurements.

2.5.1 Nuclear Magnetic Resonance Spectroscopy:

Solid state nuclear magnetic resonance (SSNMR) experiments are widely used to study the framework structure of zeolites because both ^{27}Al NMR (100 % abundance) and ^{29}Si (4.67 % abundance) are NMR-active. Aluminium NMR was used to assess the level of aluminium substitution, and thus the number of acid sites, in zeolite samples: spectra were acquired at a static magnetic field strength of 9.4 T ($\nu_0(^1H)$ = 400 MHz) on a Bruker Avance III console using TopSpin 3.5 software. A wide bore Bruker 4 mm MAS probe was used, tuned to 104.27 MHz and referenced to yttrium aluminium garnet at 0.0 ppm. The zeolites were left in a humid environment overnight to hydrate any extra-framework aluminium species,

which results in less distorted aluminium coordination environments and reduces the level of quadrupolar peak broadening in the final spectrum.[129] The samples were packed into zirconia MAS rotors with Kel-F caps, with before and after weight measurements providing the sample mass for normalisation. The rotors were spun at 14 kHz using room-temperature purified compressed air. Nutation tip angle was 22.5°. Relaxation times were 0.1 s. 8192 scans were acquired using a one pulse acquisition program. These measurements were carried out at the Johnson Matthey Technology Centre, Sonning Common, UK in collaboration with Dr Nathan Barrow.

2.5.2 Gas Adsorption Isotherm Analysis:

Surface area analysis was performed using a Quantachrome Quadrasorb EVO/SI gas adsorption instrument. 0.15 g samples of the materials for analysis were degassed to $< 2.67 \times 10^{-2}$ mbar (20 mTorr) at 523 K and gas adsorption and desorption isotherms were collected across a relative pressure (P/P_0) range from 5×10^{-4} – 0.99 using liquid nitrogen as the coolant and N_2 as the adsorbent gas. Isotherm analysis was carried out using the method of Brunauer, Emmett and Teller (BET) using the software supplied with the instrument.[130] Sample microporosity levels were estimated using the *t*-plot method of de Boer.[131]

2.5.3 X-ray Diffraction Analysis:

X-ray diffraction (XRD) analysis was performed at the ISIS Materials Characterisation Laboratory to investigate structural effects on zeolite frameworks. The instrument was a Rigaku Smartlab diffractometer with a 9 kW source using a Cu Kα anode with Ge (220) monochromation giving wavelength of 1.5406 Å. Scans were performed from $5° \leq 2\theta \leq 50°$ at 0.1°/min with sample rotation (6 rpm).

2.5.4 X-Ray Fluorescence Analysis:

The elemental composition of zeolite samples was investigated by X-ray fluorescence (XRF) analysis on a PANalytical Epsilon3 XL energy-dispersive XRF

spectrometer. Samples mere measured as powders using thin film sample pots to allow the beam access to the zeolite material. The resulting fluorescence spectra were fitted to reference spectra of SiO_2, Al_2O_3 and various potential contaminants in order to extract the relative proportions of each elemental component.

2.5.5 Ammonia Temperature-Programmed Desorption:

In order to accurately determine the level of acidity in zeolite samples and how that changes under various treatment conditions it is necessary to be able to quantify the acid site population of zeolite samples. This was achieved by means of ammonia temperature-programmed desorption (TPD), using the experimental methodology described by Niwa and Katada.[132] TPD experiments were carried out using a Quantachrome ChemBET Pulsar instrument equipped with a thermal conductivity detector. Samples were dried at 623 K under flowing helium (15 ml min^{-1}) then cooled to 373 K and saturated with ammonia by passing 10 % NH_3 in He (15 ml min^{-1}) through the sample for 15 minutes. The sample was returned to helium flow and purged for 2 hours at the same temperature; these conditions are reported to remove any physisorbed ammonia from the zeolite pore network leaving only molecules chemisorbed to Lewis silanol or Brønsted acid sites.[132-133] Desorption was then carried out from 373-973 K with a heating rate of 5 K min^{-1} and a 30 minute hold at the highest temperature to ensure full removal of all ammonia. The response of the TCD was normalized against that of ammonia injections of known quantity to enable the determination of the volume of chemisorbed ammonia in each sample.

2.6 Ex-situ Reaction Analysis – Methods and Apparatus:

In addition to the on-line monitoring performed during the reaction itself the products and reacted catalysts from reaction testing experiments were subjected to additional *ex situ* investigations to provide more information on the reaction mechanisms.

2.6.1 Optical Spectroscopy Methods:

Optical spectroscopic methods were employed as a supplement to the use of neutron vibrational spectroscopy as required. Infrared measurements were used for preliminary testing of samples or reaction methods prior to commitment of neutron instrument time, for *operando* tests that would be impractical for neutrons due to temperature or collection time limitations and to collect high-energy vibrational data in cases where beam time on direct geometry INS instruments was unavailable. Ultraviolet-visible (UV-vis) spectroscopy was used to assist in the identification of large aromatic products.

Infrared spectra of solid materials were collected by diffuse-reflectance infrared Fourier transform spectroscopy (DRIFTS) using an Agilent Carey 680 FTIR spectrometer equipped with a Harrick praying mantis beam accessory and heated sample cell with gas flow capability. The flow gas used for cell purging and transport of other reagents was dry N_2 from a liquid nitrogen boil-off source due to the use of bottled gas supplies being found to lead to water contamination of zeolite samples for extended analysis times. Spectra were collected from 4000-700 cm^{-1} using a liquid nitrogen cooled MCT detector with a resolution of 4 cm^{-1} and averaged over 64 scans per spectrum.

Liquid samples, such as catch-pot contents from reaction testing and pure compounds, were analysed using attenuated total reflectance infrared spectroscopy on a Nicolet iS10 instrument equipped with a Smart iTX diamond crystal ATR accessory and a room temperature deuterated triglycine sulphate detector. Spectra were collected from 4000-650 cm^{-1} at a resolution of 1 cm^{-1} and averaged over 64 scans per spectrum.

UV-vis spectroscopy of liquid product mixtures was carried out on Shimadzu UV-1800 spectrophotometer across a wavelength range of 1100-190 nm with a resolution of 1 nm. Two spectra were collected per sample following dilution to 0.1 %v and 0.01 %v in cyclohexane.

2.6.2 GCMS Analysis:

Gas chromatography mass spectrometry (GCMS) was used to analyse the composition of the liquid-phase products of the reactions of propene and octene over H-ZSM-5. The instrument used was an Agilent 7890A gas chromatograph equipped with a series 5975 mass-selective detector. Component separation was achieved using a 60 m DB−1MS nonpolar capillary column which achieved good separation of all product peaks. These measurements were carried out in collaboration with Ms. Andrea Zachariou of the University of Glasgow.

2.6.3 Temperature Programmed Oxidation:

The level of hydrocarbon coke on reacted samples was assessed by thermogravimetric analysis (TGA) performed using a TA Instruments TGA Q50. Samples were first dried at 373 K in an inert atmosphere of 100 % N_2 to remove adsorbed water due to the inability to load samples in a glovebox environment: experiments using DRIFTS analysis proved that this does not significantly alter the composition of the hydrocarbon species. The samples were then heated from 373 – 1000 K in a 10 % O_2 gas stream to oxidise the coke species. The variation of the sample mass with temperature was recorded and used to derive the decomposition temperature of the coke.

Chapter 3: Characterisation of H-ZSM-5 and Model Compounds

Before starting to consider the reaction and diffusion properties of hydrocarbons in ZSM-5 it is important to have a comprehensive understanding of the properties of the initial system. This chapter therefore presents the results of a wide-ranging characterisation of our ZSM-5 catalyst after it has undergone the calcination and drying procedures to prepare it for use, generating the material designated ZSM5-FR. The structure, spectroscopic data and acidity of the zeolite are all determined by a variety of techniques. The INS spectra of our model hydrocarbon species is also considered insofar as these differ from the infrared or Raman data which is widely available in the literature. Aspects of this work were undertaken in collaboration with Andrea Zachariou.

3.1 Properties of H-ZSM-5:

As noted in Chapter 2, the zeolite catalyst used throughout this project is a powder form commercial material grade H-ZSM-5 zeolite. This was supplied in bulk quantities by our industrial partners, Johnson Matthey plc., to simplify the process of acquiring consistent zeolite catalyst in the quantities required for neutron analysis. This also has the useful property of bringing us closer to the type of industrially produced zeolite catalyst which is used commercially, although this material (ZSM5-AR) does differ in being in powder form; industrial catalysts are usually pelletized for easier handling and therefore incorporate binder materials and stabilising agents in addition to the zeolite itself.

The catalyst as-supplied included residual synthesis template and required calcination according to the procedure in Section 2.4.1 in order to produce ZSM5-FR, the 'fresh' zeolite which forms the initial-state catalyst for our investigations. Since we did not synthesise this material ourselves it is important to fully characterise it in order to gain a complete understanding of its physical and chemical properties as they are relevant to catalysis. These measurements also allowed us to establish that the material supplied was consistent in its properties across the entire volume of material supplied.

3.1.1 Structure and Framework Properties:

The first and most essential test is to establish that ZSM5-FR possesses the correct framework type with high crystallinity and is therefore not contaminated by inclusions of other zeolite frameworks or amorphous silica, both of which will significantly degrade the catalyst selectivity. Powder X-ray diffraction (PXRD) analysis is capable of determining the overall arrangement of the zeolite framework by scattering from the Al and Si atoms in the zeolite: it is incapable of resolving the position of the acid sites due to their negligible electron density, but this may be left as a problem for later consideration at this stage. A PXRD pattern of ZSM5-FR was collected by the procedure in Section 2.5.3 and is reproduced in Figure 3-1. It is compared with theoretical diffraction patterns for a template-

free H-ZSM-5 framework and H-mordenite, a zeolite with a different structure type which is often found as a contaminant in ZSM-5 samples prepared with poor control of synthesis conditions.[134] The theoretical patterns were sourced from the International Zeolite Association's online structural database.[8]

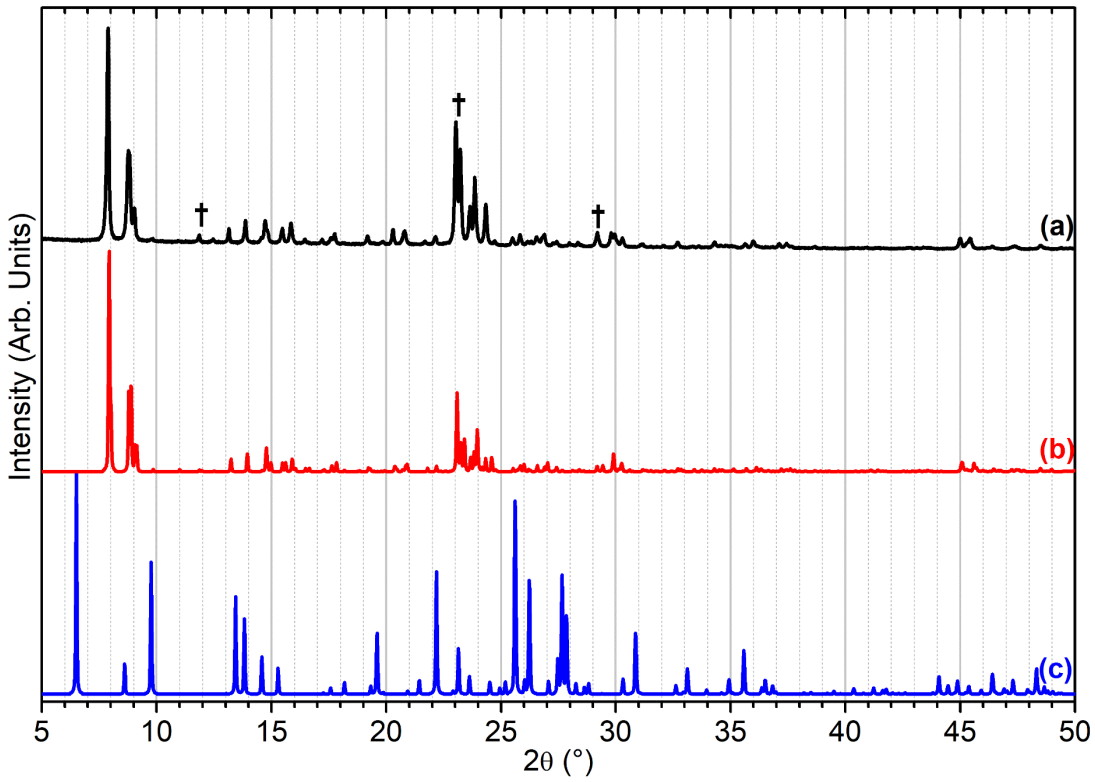

Figure 3-1: XRD pattern recorded for ZSM5-FR (a) compared with theoretical patterns calculated for calcined ZSM-5 (b), and H-mordenite (c). λ = 1.5406 Å. Patterns offset in *y*-axis for clarity. Peaks marked with (†) indicate the presence of a low level of contamination in the ZSM5-FR sample.

It can be seen that ZSM5-FR closely matches the expected pattern for the desired MFI structure and definitely does not include mordenite inclusions. A minor degree of peak broadening indicates that the structure is not a perfect MFI crystal but includes a very low level of amorphous material. This is attributed to the presence of minor quantities of aluminium compounds present outside the zeolite framework. The nature and source of these extra-framework aluminium species is considered in greater detail in Sections 3.1.2.3 and 3.1.2.4 below. The strengthening of certain peaks which are highlighted in Figure 3-1 (†) is suggestive of a degree of contamination, which does not correspond to H-mordenite. The use of a rotating stage during measurement eliminates the possibility of preferred orientation effects. The identity of this contaminant is unknown, but levels are low.

3.1.1.1 Determining Crystallite Size:

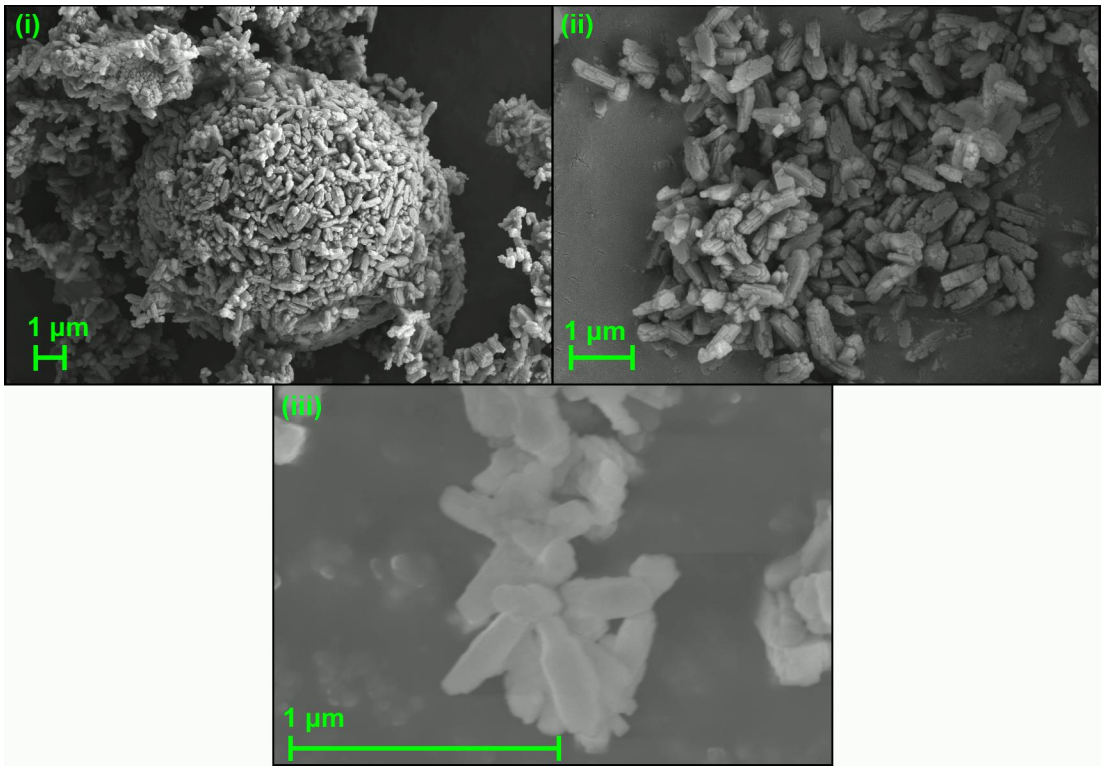

Figure 3-2: SEM images of ZSM5-FR collected at 5000× (i), 12,000× (ii) and 75,000× (iii) magnification.

The crystallite size is important to the catalytic activity of the zeolite because of how it affects the internal volume available for diffusion and the relative proportions of interior and surface acid sites. Zeolite crystals are usually large enough that attempting to size them by Scherrer analysis of the peak broadening in X-ray data does not produce useful results and crystallite sizing is therefore usually done by examination of the material using scanning electron microscopy (SEM).[135] A sample of ZSM5-FR was examined by SEM on a Zeiss SEM300 in collaboration with Professor Russell Howe of the University of Aberdeen; Figure 3-2 presents a representative sample of the images produced. Analysis of the structures in these images revealed that crystal sizes were in the 0.2 – 1.0 µm range with typical crystallite dimensions being 0.5 × 0.1 × 0.1 µm. It can also be seen that the individual crystallites have a tendency to stick together into larger agglomerations; in order to prevent this having an effect on the reaction data all zeolite samples were crushed and sieved prior to drying to ensure consistent particle sizes in the 200 – 500 µm range.

3.1.1.2 Measuring the Accessible Pore Area:

The pore area of a zeolite sample provides a relative measure of the degree of microporosity within the zeolite, and therefore allows quantification of effects such as pore blockage in reacted samples and the relative quantity of different pore sizes within the sample. It is assessed by gas adsorption experiments, measuring how the quantity of gas adsorbed in a sample varies with relative pressure (P/P_0) at the triple point of the adsorbate to produce an isotherm plot. The shape of this plot may then be analysed to determine the gas adsorption behaviour, which relates to the surface area available for adsorption. The most widely used method is that of Brunauer, Emmett and Teller (BET theory), which uses a number of assumptions to extend the Langmuir adsorption model of ideal gas behaviour at isothermal conditions to multilayer systems.[130] Under this model the weight of gas adsorbed at a given relative pressure, W, can be related to the weight of a single monolayer adsorbed on the entire sample surface, W_m, by the equation:

$$\frac{1}{W([P/P_0]-1)} = \frac{1}{W_m C} + \frac{C-1}{W_m C}\left(\frac{P}{P_0}\right) \tag{3.1}$$

The term C is the BET constant which is derived from the adsorption energies of the first (E_1) and subsequent (E_L) gas layers.

$$C = exp\left(\frac{E_1 - E_L}{R\,T}\right) \tag{3.2}$$

At sufficiently low relative pressures a plot of the left hand term in Equation (3.1) *vs* P/P_0 is linear, allowing W_m to be calculated from the slope and intercept of this plot. W_m may then be easily converted to the surface area of the monolayer using the cross-sectional area and molar mass of the adsorbate and this is assumed to be the same as the surface area of the sample.

Zeolites are microporous materials; therefore it is useful to know what proportion of the overall surface area is found within the micropore channels and from that to derive the micropore volume. This is done by statistical thickness or t-plot methods, of which we use that developed by de Boer.[131] This plots the volume of

adsorbed gas against the statistical thickness of the adsorbed film, t, calculated from the inverse relative pressure by the de Boer equation:

$$t(\text{Å}) = \sqrt{\frac{13.99}{\log(P_0/P) + 0.034}} \tag{3.3}$$

The slope of this plot provides the total surface area of all pores, S_t. In non-microporous samples this is the same as the BET surface area; microporous samples will have a t-plot with a positive intercept, representing the external surface area not accounted for in the statistical thickness measurement.

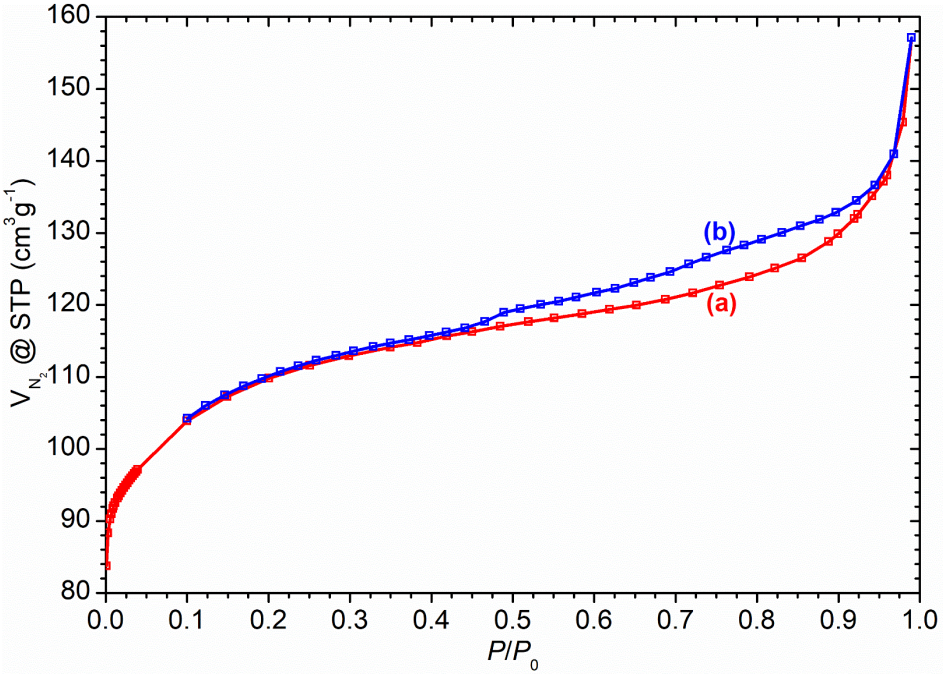

Figure 3-3: Adsorption (a) and desorption (b) isotherms for nitrogen on ZSM5-FR showing hysteresis due to sample microporosity.

ZSM5-FR was analysed to produce the isotherm shown in Figure 3-3 by the method in Section 2.5.2. The measurement was repeated three times to allow estimation of the degree of accuracy in the measurement. The hysteresis visible between the adsorption and desorption isotherms is due to condensation of the nitrogen in mesopore-sized gaps between the zeolite crystals, evidenced by the lack of a sharp onset in the hysteresis region and its location at high relative pressures. The formation of multiple layers and subsequent condensation is also responsible for the fact that the isotherm does not attain a plateau value at high relative pressures.[136] BET analysis of this isotherm shows ZSM5-FR to have a total surface

area of 370 ± 11 m^2g^{-1} as an average and standard deviation based on three measurements. It should be noted that the adsorbate gas used was nitrogen which has a cross-sectional area of 16.2 $Å^2$; this is close to the cross-sectional areas of the zeolite channels which are 23.3 $Å^2$ for the straight channels and 18.0 $Å^2$ for the sinusoidal channels. This therefore means that these values represent a 'nitrogen-accessible' surface area and micropore volume which can be used for relative comparisons between samples but which is lower than the true properties of the zeolite.

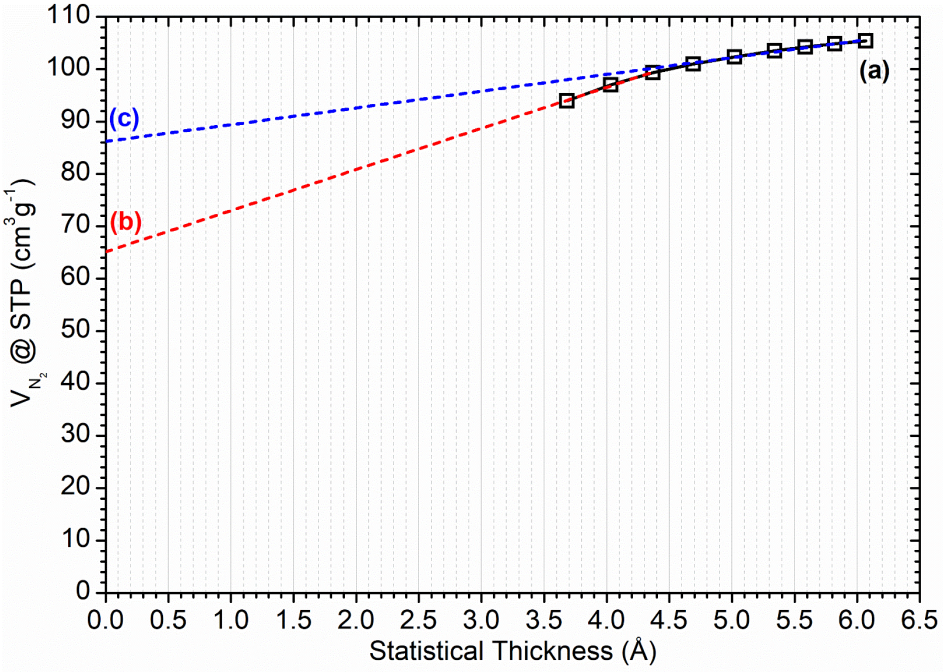

Figure 3-4: Statistical thickness plot for the adsorption isotherm of nitrogen in ZSM5-FR (a) showing the linear fits used to derive the micropore (b) and mesopore (c) volumes according to the method of de Boer.[130]

The t-plot (Figure 3-4) shows an inflection in the curve located at a statistical thickness value of *ca.* 4.5 Å, which indicates the presence of two types of pore sizes. The data points located below this value correspond to adsorption in the micropores: t-plot analysis cannot be used below a statistical thickness of 3.5 Å due to the size of the nitrogen molecule, but the linear trend of the data available suggests a micropore surface area of 248 ± 9 m^2g^{-1} with a volume of 0.101 ± 0.003 cm^3g^{-1}. The points above this value but below the region of hysteresis in Figure 3-3 correspond to adsorption in mesopores of 9 – 10 Å in diameter, formed by defects in the MFI structure. These have a surface area of

72 ± 2 m^2g^{-1} and a volume of 0.032 ± 0.001 cm^3g^{-1}. The remaining surface area in the total BET measurement, amounting to 50 m^2g^{-1}, is the external surface area, which comprises both adsorption on the exterior surface of the crystals and condensation in the intercrystalline voids. These properties closely match those reported for commercially produced ZSM-5 zeolites in the literature.[137]

3.1.1.3 The Vibrational Spectrum of ZSM5-FR:

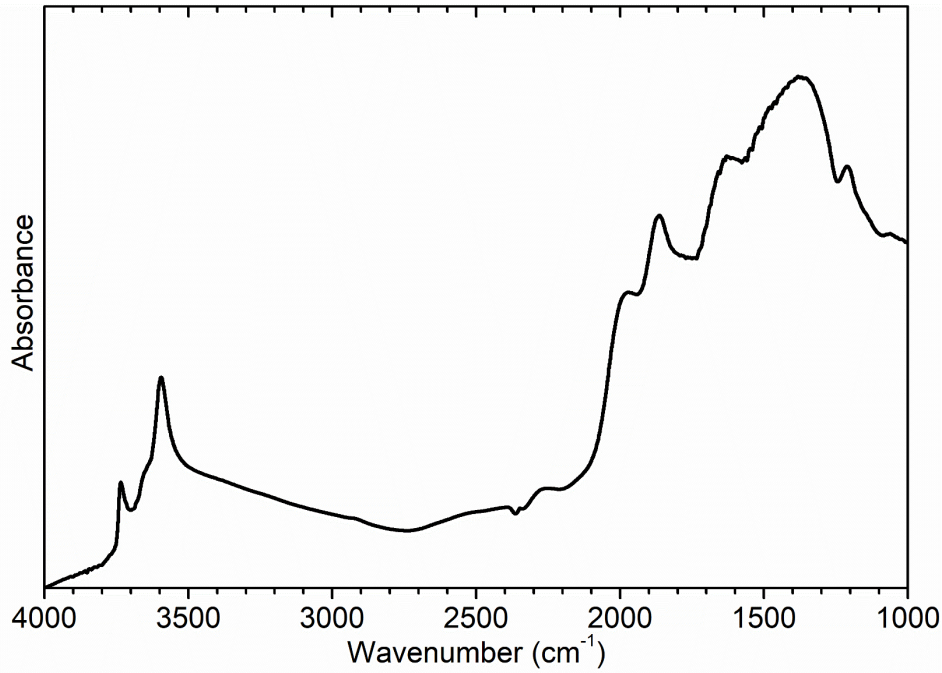

Figure 3-5: Infrared spectrum of ZSM5-FR after drying at 623 K recorded by DRIFTS at that temperature.

Figure 3-5 presents the infrared spectrum of ZSM5-FR, which was recorded by DRIFTS using the procedure in Section 2.6.1. The spectrum is dominated by the Si-O and Al-O framework stretch modes below 2000 cm^{-1} which are not associated directly with the active sites. However, it does provide good information on the O-H stretch modes located above 3500 cm^{-1}. The strongest of these is at 3595 cm^{-1} and is assigned to Brønsted acid groups within the zeolite. The weaker separate peak at 3736 cm^{-1} is due to the silanol Si-O-H groups which terminate the zeolite framework at its exterior surfaces. The peak between these two modes at 3650 cm^{-1} is due to the presence of extra-framework aluminium species which are considered in more detail in Section 3.1.2.3 below.

The corresponding spectra as measured by INS is given in Figure 3-6 for data recorded on MAPS and Figure 3-7 for TOSCA. The low intensity of the zeolite spectra due to the low scattering cross sections of the framework atoms are immediately apparent. The lowest energy feature in both spectra is the edge of the elastic scattering peak, which will always be the largest feature in an INS spectrum since elastic scattering events are the most common outcome of a neutron-nucleus collision. The peak is very narrow in the TOSCA spectrum due to the instrument's higher resolution, but extends as high as 1000 cm^{-1} in the MAPS spectrum and therefore overlaps with the lower energy modes. Fortunately, it's nature as a broad Gaussian peak means that it is easy to discount its contributions and the low energy modes remain visible. Other than this feature, the zeolite INS spectra are essentially flat, meaning that any modes from adsorbed hydrocarbons will be clearly visible in the spectra of loaded systems. It can also be seen from these graphs how TOSCA provides considerably higher energy resolution at low wavenumbers but that this advantage becomes less significant as the energy transfer increases due to the linkage between energy and momentum transfer in indirect geometry instruments, as described in Section 2.1.2.2, hence the need for MAPS to provide information on the spectrum above 2000 cm^{-1}.

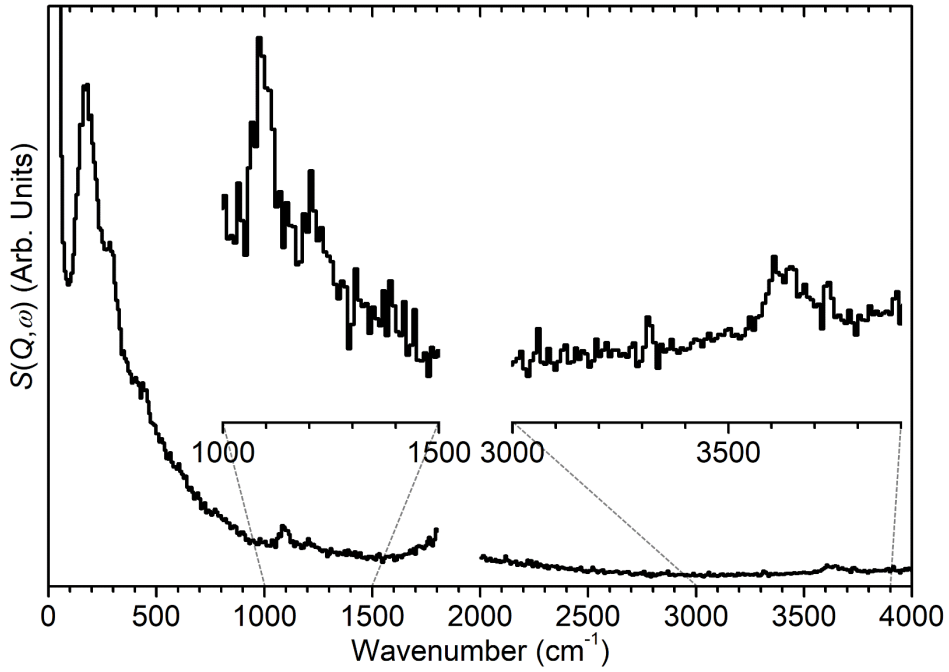

Figure 3-6: INS spectrum of ZSM5-FR recorded at T ≤ 30 K on the MAPS spectrometer at incident energies of 2017 cm^{-1} (*left*) and 5244 cm^{-1} (*right*) and integrated over the momentum transfer range $0 \leq Q \leq 10$ $Å^{-1}$. Insets show × 10 expansions of selected regions to make the O-H modes more apparent.

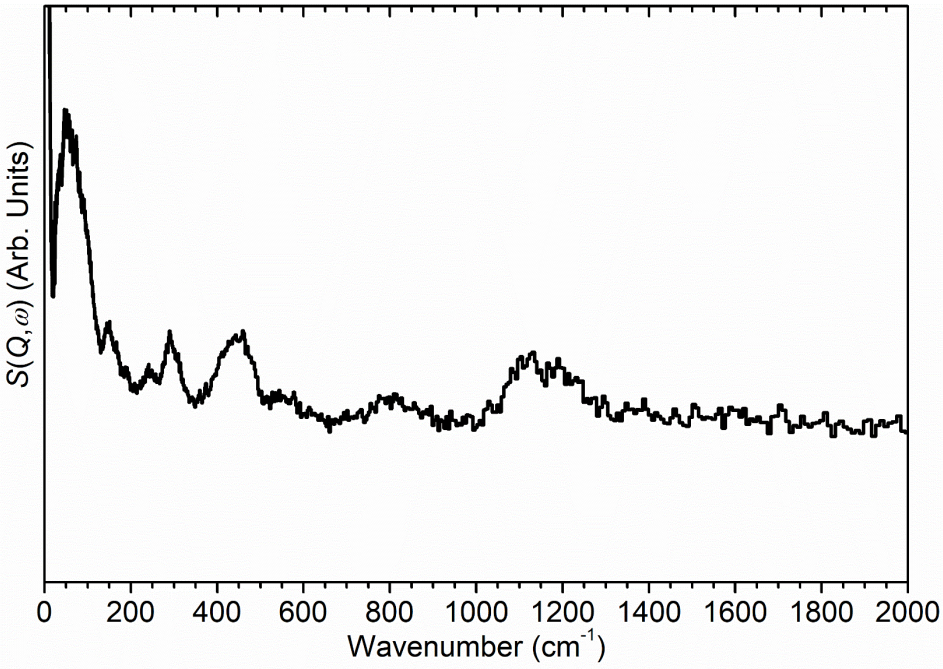

Figure 3-7: INS spectrum of ZSM5-FR recorded at T ≤ 30 K on the TOSCA spectrometer.

Although weak due to their low population several O-H modes can still be distinguished from the baseline in the INS data. The modes at 50 and 300 cm^{-1} are associated with the aluminium sample environment and are only significant because the sample in this case is almost as transparent to neutrons as the container. Modes at 445, 800, 1100 and 1190 cm^{-1} are all due to O-H deformations. The O-H stretching modes are also observed by MAPS, although the resolution is insufficient to distinguish the different O-H groups as can be done by infrared analysis. It is also notable that the νO-H peak appears to be centred around 3625 cm^{-1} rather than the 3595 cm^{-1} value recorded in Figure 3-5, a difference which may be explained by the relatively broad nature of the INS peak. This discrepancy between infrared and INS measurements is observed for all ZSM-5 samples we have investigated and also applies to measurements made on TOSCA, insofar as the poor resolution of TOSCA at these high ω values allows determination of the peak centre with any precision. It is not, however, observed for other zeolites or siliconaluminophosphates we have tested by INS. The source of this discrepancy is presently unknown and is the subject of ongoing investigations, however, it is considered to be mainly a curiosity and not to meaningfully affect the results of our experiments.

3.1.2 Measuring the Brønsted Site Population in ZSM5-FR:

After the framework structure, the number and distribution of acid sites within the zeolite is the most important factor affecting its catalytic activity. It is especially important to determine the acid properties of ZSM5-FR because of the fact that catalytic use results in these parameters changing due to steam de-alumination, something which will be the subject of further study in Chapters 5 and 6. While the catalyst as-supplied has a target acidity level of 3 acid sites per unit cell, as set by the ratio of precursors during synthesis (see Section 3.2.1.1), this is only an approximate value for the final state of the zeolite framework. A number of measurements have therefore been performed to gain the most complete possible overview of the acid site levels in the zeolite. The related question of how these acid sites are distributed is more complex and is considered in Section 3.1.3 below.

3.1.2.1 Elemental Composition Analysis:

The simplest way to measure the acidity of a zeolite is by determining the level of aluminium substitution within the framework. ZSM-5 has the molecular formula $H_n[Al_nSi_{(96-n)}O_{192}]$;[12] since every Brønsted site is associated with, and adjacent to, an aluminium atom, the aluminium content should correspond directly with the level of acidity. This is also the method used to set the target level of acidity during zeolite synthesis by controlling the level of silica and alumina precursors. This extends far enough that it is common to express the acidity of a zeolite in terms of its Si:Al ratio rather than the number of acid sites per unit cell.

X-ray fluorescence (XRF) analysis allows the easy determination of the relative quantities of elements within a sample. Analysis of ZSM5-FR (procedure as per Section 2.5.4) indicates its composition to be 95.10 wt% SiO_2 and 4.85 wt% Al_2O_3; this gives a weight ratio of 19.6:1, a molar SiO_2:Al_2O_3 ratio of 33.3:1 ($M(SiO_2)$ = 60.08 g mol^{-1}, $M(Al_2O_3)$ = 101.96 g mol^{-1}) and a final molar Si:Al ratio of 16.6:1. Since a single ZSM-5 unit cell contains 96 T-atoms, this equates to the zeolite possessing 5.45 Brønsted acid sites per unit cell (for n Al substitutions/Brønsted acid sites the Si:Al ratio$= \mathrm{Si/Al} = [96 - n]/n$ and therefore

$n = 96/[\text{ratio} + 1]$). Therefore XRF analysis predicts a significantly higher level of framework acidity than the zeolite was believed to possess.

3.1.2.2 Measurement by Ammonia Desorption:

An alternative means for quantifying acidity is to measure it directly by determining the amount of a base which can be chemisorbed onto the acid sites. Ammonia is a commonly used probe molecule for these experiments because as a small gas it is capable of accessing the majority of acid site locations, something which is not the case for larger bases such as pyridine.[138] Care must be taken when using ammonia, since it is also capable of binding to the zeolite by physisorption onto the framework, in addition to those molecules which chemisorb at active sites. To counteract this, we implement the method suggested by Niwa and Katada, which uses extended purging at 373 K to remove the majority of the physisorbed ammonia prior to starting data collection.[132] Full experimental details are provided in Section 2.5.5.

Figure 3-8 presents the rate of ammonia desorbed from a sample of ZSM5-FR as a function of temperature. Two desorption peaks are observed, indicating the presence of at least two environments for ammonia chemisorption within the zeolite. The lower temperature population of adsorbed ammonia is assigned to chemisorption at silanol sites, potentially with additional contributions from adsorption on extra-framework species or residual physisorbed ammonia. Of more immediate interest is the population which is desorbed at temperatures greater than 650 K, which represents binding to the Brønsted sites.[132, 138] Comparison of the integrated intensity of this desorption peak with peaks recorded for ammonia injections of known volume and averaging over multiple experiments, allows the determination that ZSM5-FR contains 381 ± 19 μmol of Brønsted-bonded ammonia per gram of zeolite as an average and standard deviation of 3 measurements. Since the sample mass is for dried zeolite, this may be converted to the number of acid sites per unit cell, *n*, by choosing an estimated value for *n*, using that to generate an estimated molar mass from the formula of a single unit cell, $H_n[Si_{(96-n)}Al_nO_{192}]$, and from there calculating the estimated number of moles of zeolite in the sample. Normalising the TPD measurement against this value gives the number of moles of ammonia per mole of zeolite, and thus a new value for *n*. This process

then can be repeated until *n* converges to the correct value. Since the Al and H atoms constitute a relatively low percentage of the overall molar mass this process only requires a few iterations for convergence to occur. In this case this gives a final value of 2.31 ± 0.12 acid sites per ZSM-5 unit cell and a molar Si:Al ratio of 40.6:1. This is a dramatically lower level of acidity than that derived from the XRF composition analysis, and it is therefore necessary to perform further measurements to resolve this discrepancy.

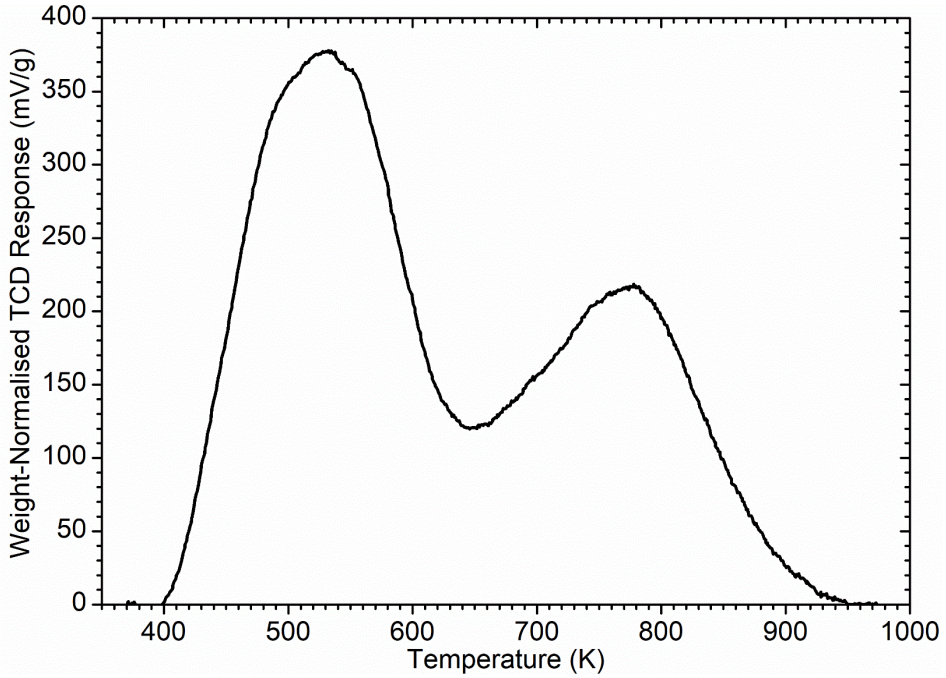

Figure 3-8: Weight-normalised ammonia desorption vs temperature trace for ZSM5-FR Peaks represent the desorption of ammonia molecules chemisorbed to silanol groups from 400-600 K and those bound to Brønsted acid sites from 650-900 K.[132]

3.1.2.3 Measurement by NMR Methods:

Solid-state NMR measurements are widely used for studying zeolites and have the advantages of being able to distinguish framework from extra-framework species, unlike XRF, and of being unaffected by diffusion concerns blocking access to the Brønsted sites, unlike ammonia adsorption. ^{29}Si NMR is capable of resolving the signals of Si T-atoms surrounded exclusively by other silicon sites, those bonded to a Si-O-Al bridge and those bonded to silanol groups; these have chemical shifts relative to tetramethylsilane of *ca.* -113, -107 and -103 ppm respectively.[139] The ^{29}Si NMR spectrum of a sample of ZSM5-FR and the results of a peak fitting to

extract the individual peak areas is shown in Figure 3-9. NMR data collection was carried out by Professor Russell Howe of the University of Aberdeen, while data fitting and analysis has been performed in-house. The data was fit to a combination of three Lorentzians, one for each Si environment, with the peak centres allowed to move freely; all peaks converged to locations closely matching their literature values. Peak widths were constrained to be the same for all three environments, since it was found that allowing these parameters to float freely led to consistent, large overestimations of the silanol site population. Table 3-1 reports the final fit parameters.

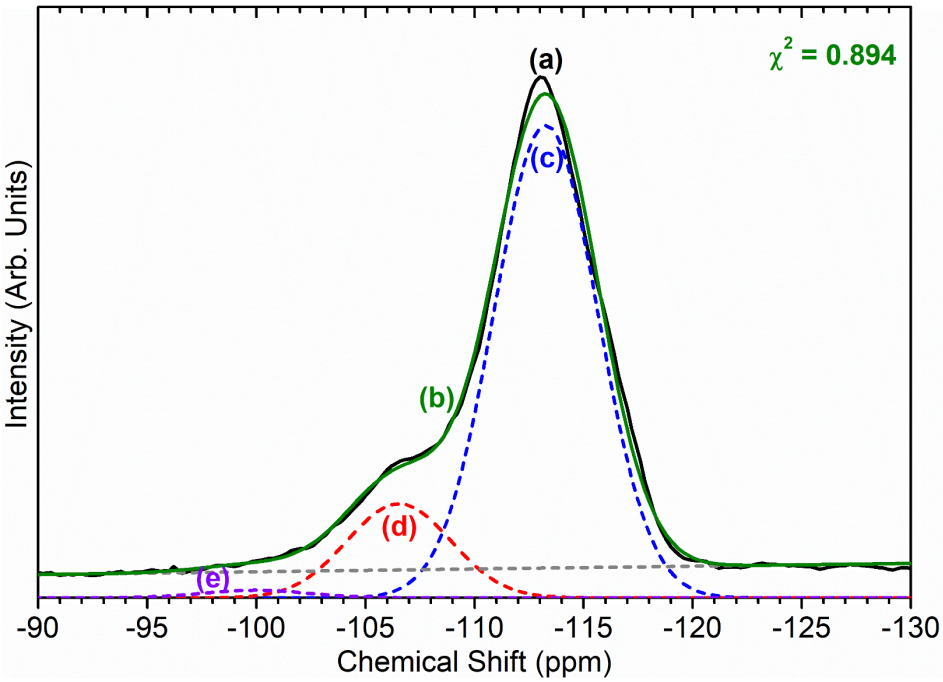

Figure 3-9: ^{29}Si NMR spectrum of ZSM5-FR (a) and fit result (b) for deconvolution into contributions from nuclei in a purely siliceous environment (c), nuclei adjacent to an aluminium substitution (d) and nuclei bonded to a silanol group (e).

Table 3-1: Lorentzian peak parameters for fitting of peaks (c) - (e) in Figure 3-9.

Environment	Γ (ppm)	Centre (ppm)	Area
$Si(OSi)_4$	2.376	-113.3	523.8 ± 1.7
$Si(OSi)_3(OAl)$	2.376	-106.6	100.6 ± 1.7
$Si(OSi)_3(OH)$	2.376	-103.0	7.4 ± 1.6

Because each Al substitution results in four Si nuclei in the $Si(OSi)_3(OAl)$ environment the Si:Al ratio in the sample is found by dividing the total area of all peaks by ¼ the area of the $Si(OSi)_3(OAl)$ peak, giving a ratio of 25.5:1 and an acid population of 3.68 ± 0.06 sites per unit cell, intermediate between the results found by XRF and TPD analysis.

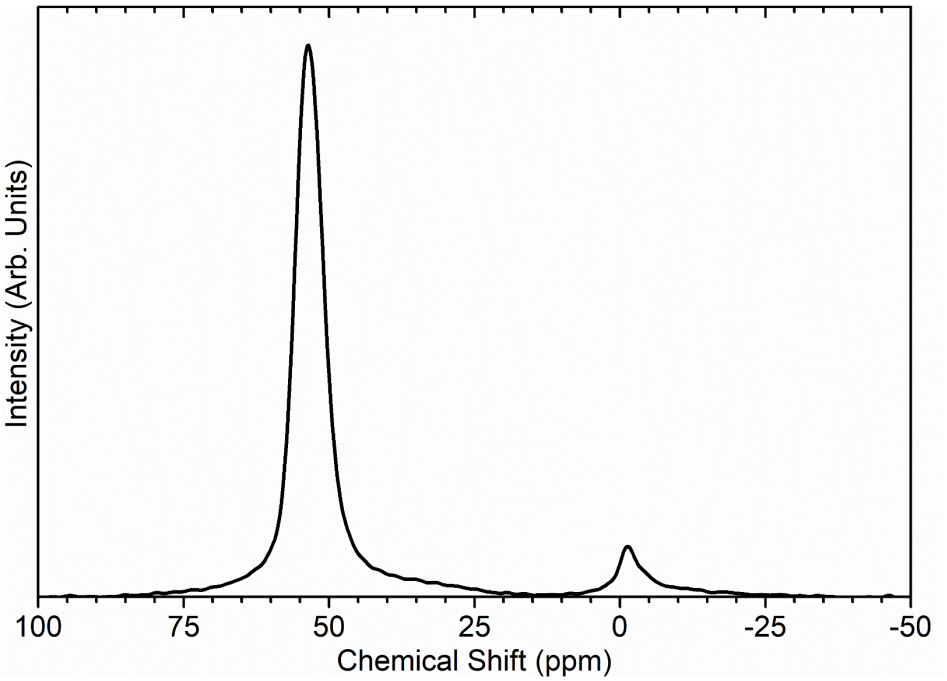

Figure 3-10: ^{27}Al NMR spectrum of ZSM5-FR.

^{27}Al NMR is also widely used in the study of zeolites. In the absence of a suitable calibration curve to relate the peak intensity in each environment to the number of aluminium nuclei present it cannot be used to quantify the number of acid sites as the ^{29}Si results were, however, it does provide additional insight into the state of the aluminium ions within the sample, which helps explain the results observed. The ^{27}Al NMR spectrum of ZSM5-FR is shown in Figure 3-10; the peak at 53.4 ppm corresponds to the 4-coordinated AlO_4 species which constitute the framework aluminium sites, however it is apparent that there is also an additional aluminium environment within the sample represented by the peak at -1.2 ppm. This peak is due to the presence of octahedral aluminium nuclei of the type which are found in species such as alumina.[33, 140] These extra-framework aluminium (EFAl) species have two possible sources; they may be residual, unused aluminium precursor left over from the zeolite synthesis or, more likely, may indicate that despite the efforts taken to prevent it, the calcination process used to generate ZSM5-FR from

ZSM5-AR has resulted in a small degree of framework de-alumination. This de-alumination would also result in the mesoporosity detected in the analysis of the zeolite pore volumes in Section 3.1.1.2 above. Both potential sources involve octahedral alumina species of the type detected here.

These results mean that ZSM5-FR contains additional aluminium which is not associated with the zeolite framework: while this will not affect the acidity levels obtained by TPD or NMR analysis and is unlikely to affect the sample reactivity significantly it has serious implications for the bulk elemental analysis performed by XRF.

3.1.2.4 Measurement by Inelastic Neutron Scattering:

Table 3-2: Populations of different O-H sites in a sample of ZSM5-FR as determined by quantitative INS analysis.

Species	Brucite Equivalent (mg/g_{zsm-5})	OH Sites per Unit cell
Brønsted	9.8 ± 1.3	3.3 ± 0.4
EFAl	4.0 ± 1.9	1.1 ± 0.5
Silanol	1.0 ± 0.4	0.6 ± 0.2

Since INS peak intensities are quantitative it is also possible to derive the number of acid sites in the zeolite by examining the intensity of the O-H stretching peak. This type of direct analysis rarely features in zeolite characterisation strategies and represents a further benefit of applying INS to investigate heterogeneous catalysts. Although the relationship between peak intensity and population is linear, it does depend on specific factors in the design and setup of the neutron spectrometer used. Conversion between the two is therefore most conveniently done by comparison against a calibration curve created by the measurement of samples containing known quantities of the group of interest. The results of an analysis of ZSM5-FR using this method carried out on the MAPS spectrometer at ISIS by Ms. Andrea Zachariou are reproduced in Table 3-2. Detailed fitting of the O-H stretching region shows the presence of three different peaks of which the Brønsted sites in the zeolite form the majority; peak intensities were converted to acid site populations by comparison against the spectra of known masses of brucite ($Mg(OH)_2$).[141] The relatively high level of uncertainty in the final data

derives from the weak intensity of the zeolite O-H peaks resulting in background noise, which increases the uncertainty in the spectral peak fitting.

3.1.2.5 Summary:

Table 3-3: Summary of acid site populations of ZSM5-FR as measured by different techniques.

Technique	Si : Al Ratio	Brønsted sites per unit cell
X-ray Fluorescence	16.6 : 1	5.45
Ammonia TPD	40.6 : 1	2.31 ± 0.12
^{29}Si NMR	25.1 : 1	3.68 ± 0.06
Quantitative INS	27.9 : 1	3.3 ± 0.4

Table 3-3 summarises the predicted levels of acidity in ZSM5-FR from all the methods considered above. Although there is considerable variation in the results, it can be seen that the two bulk techniques (NMR and INS) agree to within the degree of accuracy of each measurement. They are also likely to be the methods which provide the most accurate measure of the actual Brønsted site population of ZSM5-FR despite the uncertainty in the quantitative INS results. The fact that XRF detects much higher levels of aluminium than the other methods can be explained by reference to the presence of EFAl species which will not be detected by the other methods, which only consider the framework aluminium or measure acid sites directly. The fact that XRF measurements were taken in powder form without dilution or additional support also has been reported to increase the significance of matrix effects from differing X-ray penetration depths, reducing the accuracy of the final composition analysis.[142] Lower levels of acidity as measured by ammonia TPD can be attributed to some combination of inaccessible acid sites, residual ammonia bonding at the end of the desorption temperature ramp and the sensitivity of the TCD detector; all combining to reduce the accuracy of the TPD experiment and the level of acidity measured.

Based on these results it can be stated with some degree of confidence that ZSM5-FR exhibits a Si: Al ratio of 27:1 and contains *ca.* 3.5 ± 0.4 Brønsted acid sites per unit cell. It is this level of acidity that has been used to inform the models used for computational simulations of the zeolite reported below. Although

ammonia TPD has not proven completely accurate in assessing the absolute acidity level of the zeolite structure, it is much more accessible than the other quantification methods reported here and should still prove sufficient to measure the relative changes in acidity which occur on undergoing the steam-treatment procedures investigated in Chapter 5.

3.1.3 Identifying Brønsted Site Locations by Neutron Diffraction:

While these methods allow the determination of the level of acidity within the zeolite, they cannot provide information on the location of these sites within the zeolite framework. The experimental determination of hydroxyl distributions in zeolites is a significant challenge and the subject of ongoing research. Methods employed have included: drawing conclusions from the lattice parameters which are detectable crystallographically,[115] investigating Si and Al coordination patterns by solid state NMR,[139] observing the spatial distribution of aluminium in zeolite samples by atom probe tomography[143] and simulating multiple possible zeolite structures to determine which are most energetically favourable.[144-145] These studies have allowed the development of a number of 'rules of thumb' which can be used to guide the preparation of zeolite structures for simulations, while remaining consistent with the experimental data. Lowenstein's rule forbids the presence of Al-O-Al triads, while Dempsey's rule extends this to predict that zeolites will exhibit ordering to achieve the maximum possible Al-Al distance attainable for a given Si:Al ratio. These have been applied in the preparation of the simulated zeolite structures used in later chapters of this thesis, however, obtaining direct experimental measurements of proton location in our specific zeolites remains a useful goal.

In principle, neutron diffraction is capable of resolving contributions from the hydrogen atoms in a zeolite framework in a way which is not possible for equivalent X-ray measurements, for the reasons discussed above. This property has previously been successfully applied to studies of proton locations in zeolites, although the body of work in this area is limited.[94, 146] For this reason the decision was made to attempt a neutron diffraction measurement of ZSM5-FR and the determination of its structure by Rietveld refinement. The resulting data,

collected as described in Section 2.1.4.2, is shown in Figure 3-11. The data presented is that recorded on 4 separate detector banks (bank 1 provided no additional information and has been omitted); it can be seen how each detector provides higher resolution over a narrower range as the scattering angle relative to the incident beam moves closer to backscattering.

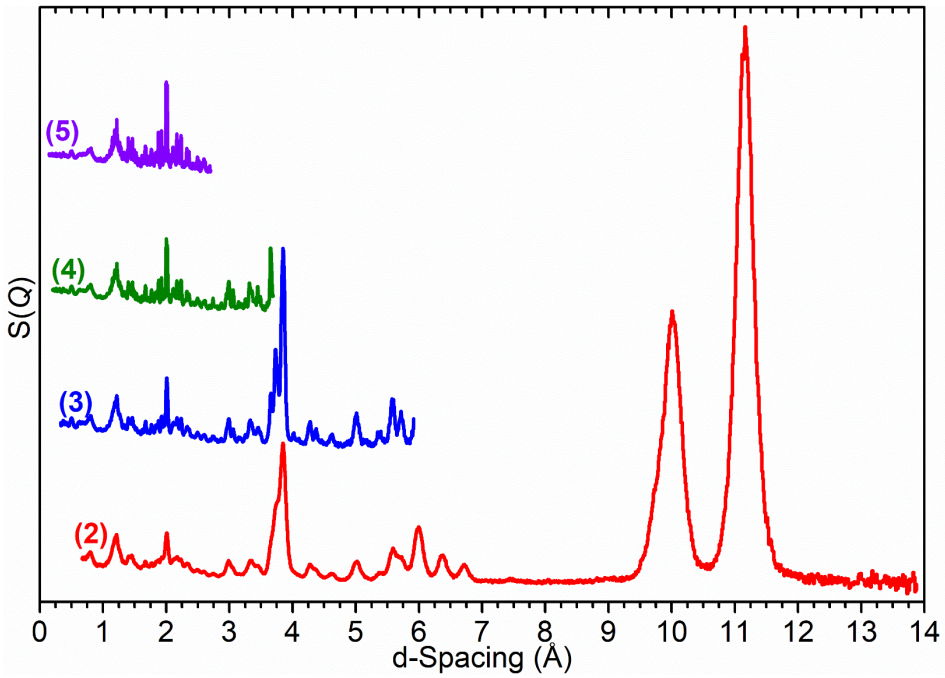

Figure 3-11: Neutron diffraction patterns for deuterated ZSM5-FR as recorded on POLARIS. The plot numbering indicates the detector bank which recorded each trace; technical details of each bank are given in Table 2-2.

The diffraction pattern was analysed using GSAS-II.[100] Due to the specialised nature of this analysis and the complexity of the data, the diffraction results were analysed by Professor Jan Skakle of the University of Aberdeen as part of a wider collaboration on zeolite structural studies. Unfortunately, the data has so far proven extremely difficult to refine and has eluded structural determination. These difficulties have been attributed to the effect of EFAl species on the dataset and motional averaging between the Brønsted sites complicating the analysis. Analysis remains on-going, however, it is evident that determining proton locations in commercial zeolites remains a considerable technical challenge.

3.2 Spectra of Model Compounds:

Although the vibrational spectra of our selected model compounds, propene and 1-octene, are fully assigned and readily available from a number of literature sources, it is still useful for us to briefly consider how the pure compounds appear to INS analysis. INS spectra are richer than infrared or Raman equivalents due to the lack of selection rules, and a firm grounding on the assignment of the vibrational modes will be important later, as these are changed by their interactions with zeolite frameworks after being adsorbed.

3.2.1 Propene Studied by INS:[147-148]

Since INS data collection is carried out at ≤ 30 K the collected spectra are those of propene in its solid state. Measurements were performed on both MAPS and TOSCA in order to provide the best possible resolution across the full energy region from 0 – 4000 cm^{-1}; these are shown in Figure 3-12 and Figure 3-13 respectively. It can also be seen that the MAPS data exhibits non-linear baselines as the energy transfer value approaches the incident neutron energy for each collected spectrum. This effect is due to a degree of multiple neutron scattering occurring within the sample, resulting in what is effectively a large Gaussian peak centred at the incident neutron energy values (2017 cm^{-1} for the low energy spectrum and 5244 cm^{-1} for the high energy spectrum.)

The INS spectra contain all the expected modes which are assigned to the vibrations given in Table 3-4 with this process being guided by previous investigations of propene vibrations by Fateley and Miller,[149] Ghosh and Kydd,[150] and Lennon *et al.*[151] Key modes are the methyl torsion mode at 221 cm^{-1}, the vinyl scissors at 429 cm^{-1}, the vinyl torsion at 584 cm^{-1} and the nature of the C-H stretching modes as a broad peak centred on 3000 cm^{-1} with equal intensity on either side of this value due to the equal number of sp^2 and sp^3 hydrogens. The broad modes at 287, 496 and 652 cm^{-1}, highlighted in Figure 3-13 (†), are not fundamental vibrations, but are phonon wing modes of the peaks immediately below them in energy, formed by coupling between these modes and the external density of states. This is proven by the lower intensity of these modes in

Figure 3-12; due to wing modes mainly scattering at high values of Q, the limited range of Q values used for the MAPS data integration removes much of the intensity of wing mode peaks, without affecting the fundamental transitions.

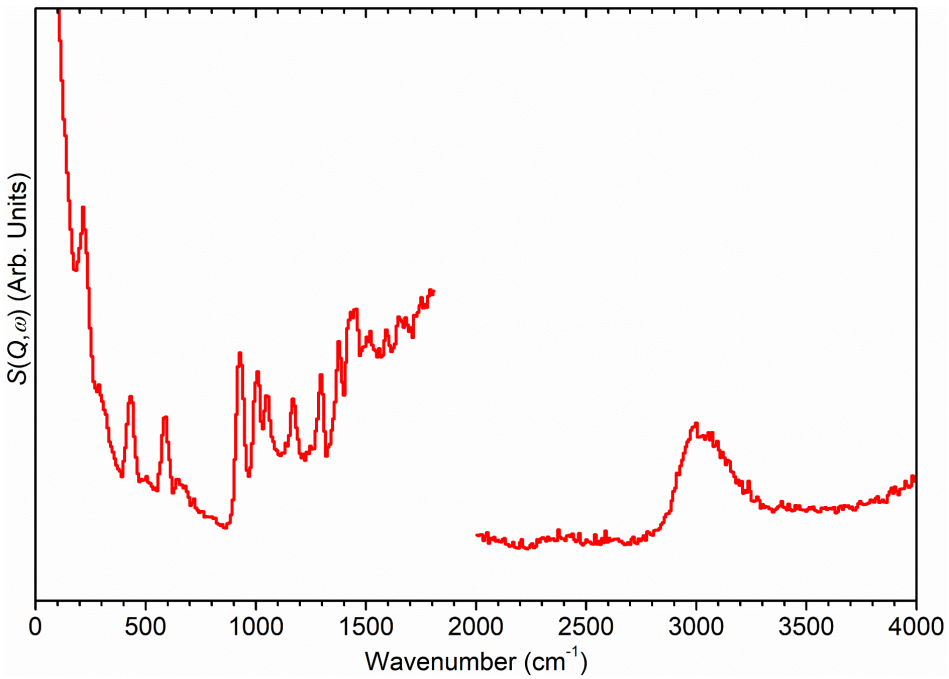

Figure 3-12: INS spectrum of propene recorded at T ≤ 30 K on the MAPS spectrometer at incident energies of 2017 (*left*) and 5244 (*right*) cm^{-1} and integrated over the momentum transfer range $0 \leq Q \leq 10$ $Å^{-1}$.

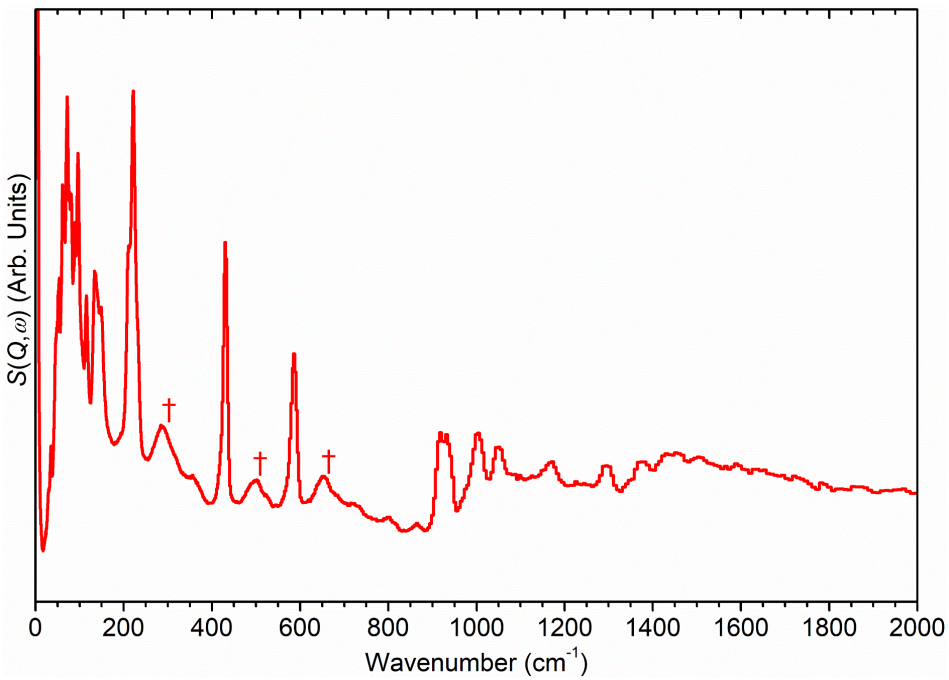

Figure 3-13: INS spectrum of propene recorded at T ≤ 30 K on the TOSCA spectrometer. Peaks due to phonon wing modes are highlighted (†).

Table 3-4: Vibrational assignments for the INS spectrum of solid propene at ≤ 30 K. Assignments based on data from Fateley and Miller,[149] Ghosh and Kydd,[150] and Lennon *et al.*[151]

Peak	Wavenumber (cm^{-1})	Assignment
-	0-150	Multiple overlapping lattice modes
1	221	-CH_3 torsion
2	*287*	*Wing mode of Peak 1*
3	429	C=C-C scissors
4	*496*	*Wing mode of Peak 3*
5	584	C=CH_2 torsion
6	*652*	*Wing mode of Peak 5*
7	915	=CH_2 in-plane rock
8	929	=CH_2 out-of-plane wag
9	1002	-CH- out-of-plane wag
10	1048	-CH_3 out-of-plane rock
11	1169	-CH_3 in-plane rock
12	1291	-CH- in-plane rock
13	1371	-CH_3 symmetric deformation
14	1440	=CH_2 scissors
15	1500	-CH_3 asymmetric deformation
16	3000	Overlapping modes for C-H stretches on sp^2 (< 3000 cm^{-1}) and sp^3 (> 3000 cm^{-1}) carbon centres.

3.2.2 1-octene Studied by INS:[152]

The INS spectrum of 1-octene is considerably more complex, as would be expected from a larger molecule. The collected INS spectra are presented in Figure 3-14 for the MAPS data and Figure 3-15 for TOSCA. The MAPS data exhibits the same non-linear baseline as the spectra approaches the incident neutron energy as was observed in the propene data but to an even higher degree, indicating that the sample may have been slightly too large for optimum scattering levels in MAPS. The indirect geometry spectrum avoids this issue due to its insensitivity to multiple scattering; the increased resolution of TOSCA at low energies and advantages exhibited by MAPS above *ca.* 1200 cm^{-1} are again readily apparent.

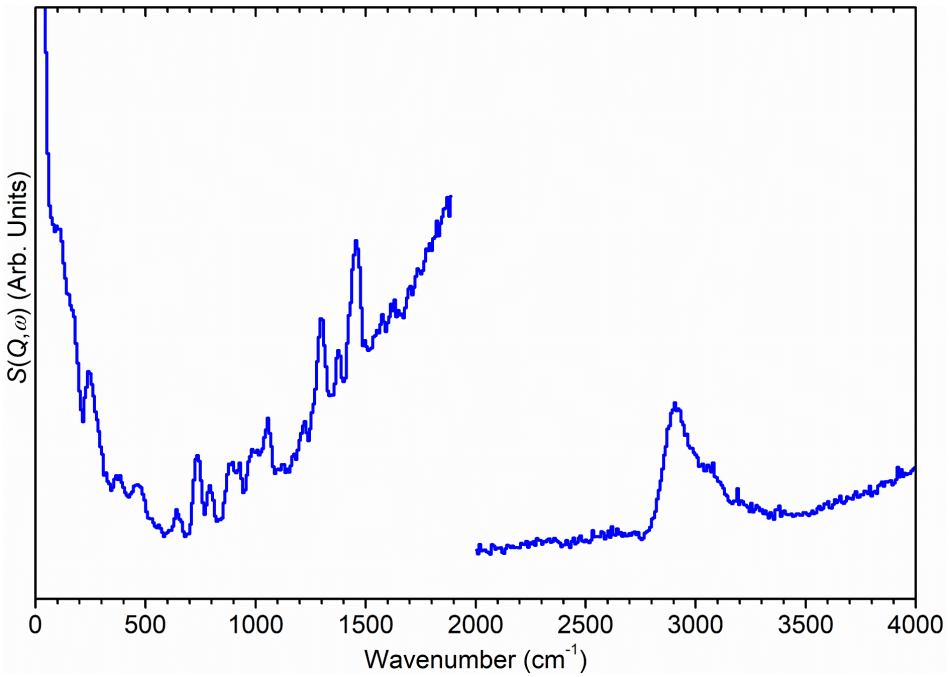

Figure 3-14: INS spectrum of 1-octene recorded at T ≤ 30 K on the MAPS spectrometer at incident energies of 2017 (*left*) and 5244 (*right*) cm^{-1} and integrated over the momentum transfer range $0 \leq Q \leq 10$ $Å^{-1}$.

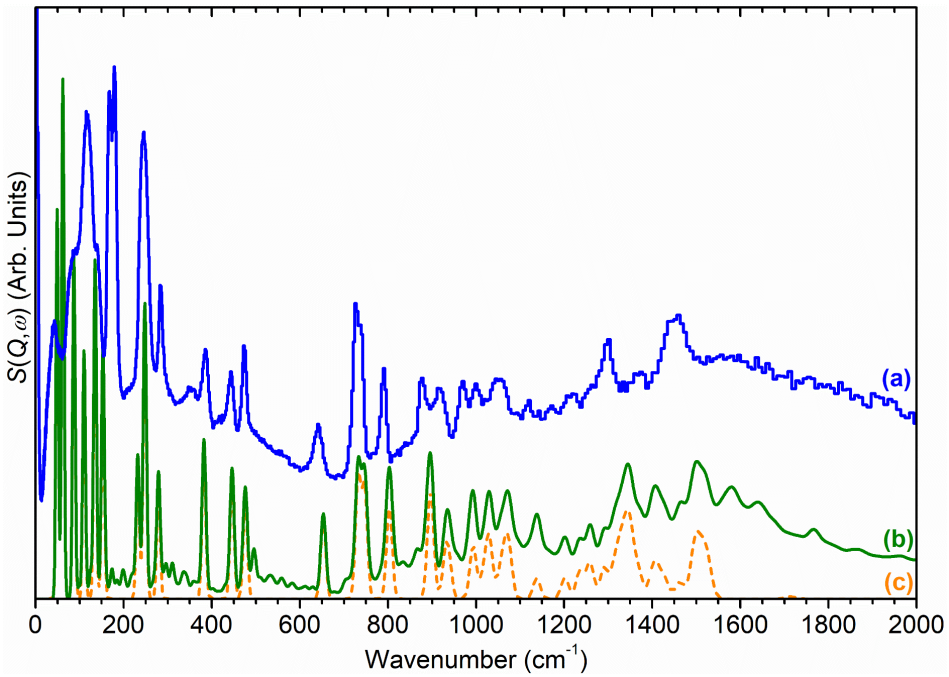

Figure 3-15: INS spectrum of 1-octene recorded at T ≤ 30 K on the TOSCA spectrometer (a) compared to a simulated spectrum for 1-octene (b) and the simulated spectrum without overtones or phonon wings (c).

The vibrational assignment of the peaks in the 1-octene spectra was assisted by computational modelling of the 1-octene system. Multiple potential conformations

of 1-octene were optimised through DFT and converted to simulated INS spectra using the procedures in Sections 2.2.1.1. The results providing the closest fit to the experimental data are reproduced in Figure 3-15; these results correspond to the low energy conformer reported by Fraser et al.[153] In this conformation, the alkyl chain assumes the usual anti-periplanar zig-zag conformation, but the (C=C-C-C) dihedral angle is oriented at ±120º instead of 180º, resulting in the (C=C) bond being staggered out of the plane of the (C-C) bonds. Simulations of conformers where the (C=C) bond is not staggered in this fashion introduce an additional (C=C) torsion mode in the 500 – 600 cm^{-1} region, while those involving a bend in the methylene chain introduce splitting of the peak at 728 cm^{-1}. Since neither of these features is observed in the experimental spectrum it can be accepted that solid 1 octene is in the conformation shown in Figure 3-16.

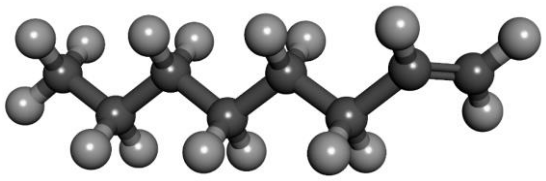

Figure 3-16: Partially-staggered geometry of 1-octene identified as corresponding to the conformation of the experimental sample recorded by INS.

In addition to identifying the conformation, the simulation also assists in identifying which peaks in the experimental spectrum are due to fundamental modes and which, such as the mode visible at 350 cm^{-1} in Figure 3-15, are due to overtones and therefore have no corresponding 0-1 transition in the simulation (Figure 3-15(c)). The application of these results allows the assignment of the peaks in the 1-octene spectra. The slightly broadened peak observed at 1456 cm^{-1} in Figure 3-15 is assigned to the overlap of the asymmetric methyl deformation with the methylene scissors modes, with the narrower peak at 1298 cm^{-1} representing a combination of multiple -CH_2- twisting modes that occur along the axis of the alkyl chain. A smaller peak corresponding to the symmetric methyl deformation is just visible between these peaks at 1371 cm^{-1}. The other peaks of interest are the CH_3 rocking mode at 1118 cm^{-1}, the (C=C) torsion at 639 cm^{-1}, the distinctive peak of the terminal methyl torsion at 245 cm^{-1} and the two transverse acoustic modes located at 167 and 178 cm^{-1}. The alkyl CH_2 rock modes at 728 and 739 cm^{-1} are also of interest since it is known from infrared studies of alkane

systems that the frequency of the methylene rocking modes is dependent on the number of consecutive CH_2 groups, n, making the position of these peaks a marker for the length of the alkyl chain. In *n*-alkanes, the frequency is observed to vary from a maximum of 815 cm^{-1} for n = 1 to a final value of 722 cm^{-1} for all n ≥ 5.[154] The fact that the frequency of the 1-octene peak is shifted to a slightly higher value than its chain length would suggest from this series is tentatively attributed to the effect of the adjacent sp^2 carbon on the final methylene group in the chain.

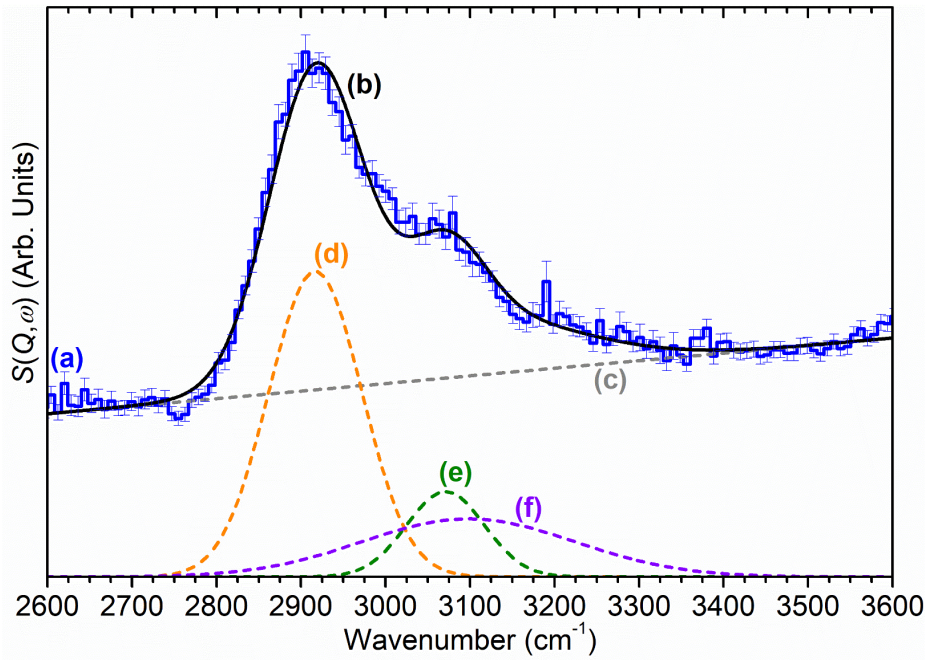

Figure 3-17: C-H stretching region of the 1-octene INS spectrum (a) compared with the results of peak fitting analysis (b) to deconvolute the contributing modes. Fit components are a linear background due to multiple scattering (c) and peaks due to sp^3 νC-H modes (d), sp^2 νC-H modes (e) and a combination of simultaneous sp^3 νC-H modes and a transverse acoustic mode (f). The degree of uncertainty in the reduction of the experimental data is shown.

The high energy portion of the MAPS spectrum (Figure 3-14) clearly shows the splitting of the 1-octene (C-H) stretch region into a peak at 2917 cm^{-1} with a shoulder at 3071 cm^{-1}. The simplest assignment is to attribute these to the (C-H) stretching modes of the sp^3 and sp^2 carbons respectively, however, comparison of the relative peak areas above and below 3000 cm^{-1} shows that they do not correspond to the 13:3 ratio expected, given the number of hydrogens in each environment. Additionally, this hypothesis fails to account for fact that the peak continues with a tail up to energies as high as *ca.* 3200 cm^{-1}. Deconvolution of the

2400-3600 cm^{-1} region of the 1-octene spectrum by peak fitting indicates the presence of an additional contribution in this region centred at 3095 cm^{-1}. The positioning of this peak, together with the fact that it is more broadened than the other modes in this region, marks it as being due to a combination of the sp^3 (C-H) stretching modes from the $-CH_2-$ groups in the alkyl chain with the transverse acoustic mode of the same groups at 178 cm^{-1}. Other peaks in the spectrum represent various internal modes and wags and are assigned as detailed in Table 3-5. These assignments are guided by data taken from Bower and Maddams,[154] Braden et al.,[155] Lennon et al.,[151] and the DFT calculation described above.

Table 3-5: Vibrational assignments for the INS spectrum of solid 1-octene at ≤ 30 K. Assignments based on data from Bower and Maddams,[154] Braden et al.,[155] Lennon et al.,[151] and DFT simulations.

Peak	Wavenumber (cm^{-1})	Assignment
-	0-150	Multiple overlapping lattice modes
1	167	Transverse acoustic –CH_2- wag
2	178	Transverse acoustic –CH_2- wag
3	245	-CH_3 torsion
4	283	Longitudinal acoustic C-C stretch
5	*350*	*First overtone of peak 1*
6	384	Longitudinal acoustic C-C stretch
7	442	Longitudinal acoustic C-C stretch
8	472	C=C-C scissors
9	639	=CH_2 torsion
10	728	-$(CH_2)_n$- in-phase rock, n ≥ 4
11	739	-$(CH_2)_n$- out-of-phase rock, n ≥ 4
12	789	Mixed –CH_2- rock/twist
13	875	-CH_3 in-plane rock
14	911	=CH_2 wag
15	967	=CH_2 rock
16	997	=CH- rock
17	1052	-CH_2- twist
18	1118	-CH_3 in-plane rock
19	1217	=CH- rock
20	1298	Multiple –CH_2- twist or rock modes along the molecular axis.
21	1371	-CH_3 symmetric deformation + -CH_2- wag
22	1438	-CH_2- scissors
23	1456	-CH_3 asymmetric deformation + -CH_3 scissors
24	2917	sp^3 C-H stretches
25	3071	sp^2 C-H stretches
26	*3095*	*Combination of modes 2 + 24*

3.3 Self-Diffusion Dynamics of Model Compounds:

As with the vibrational data it is useful to establish a baseline level of mobility for our model compounds in their pure state, against which their movements once adsorbed into the zeolite can be compared. This is especially important as accurate information on hydrocarbon self-diffusion in the literature can be quite sparse and rarely covers the complete temperature range of interest for our studies. Unfortunately, the mobility of bulk propene is too high for its self-diffusion constants to be easily obtained due to the energy transfer values for the associated motions lying outside the accessible time window of the QENS spectrometers at the ISIS Facility (from 1.6 to 26-38 ps depending on the instrument).[156] The movements of bulk 1-octene are more amenable to analysis and an appropriate experiment has accordingly been carried out.

3.3.1 QENS Analysis of Bulk 1-octene:

The sample measured consisted of 0.693 g (6.174×10^{-3} moles) of HPLC-grade 1-octene in a cylindrical aluminium sample can of 10 mm radius, with the sample occupying a 0.1 mm annulus at the perimeter of the cylinder. This gives the correct number of nuclei in the beam to achieve optimal 10 % scattering of the incident neutrons. The sample was measured according to the procedure in Section 2.1.3.4 at 10 K intervals from 10 to 370 K, with high resolution spectra being recorded at 5, 220, 270, 320 and 370 K, these temperatures being chosen as lying in the liquid phase for 1-octene and therefore being most likely to exhibit analysable motions. Collection of the data point at 280 K was omitted due to a scripting error. The IRIS spectrometer was the instrument used for this investigation with the PG002 analyser crystal employed, giving an accessible momentum transfer range of $0.42 \leq Q \leq 1.85$ Å^{-1} and an energy transfer resolution of 17.5 μeV.[156] Examination of the results by the EFWS method, shown in Figure 3-18, shows results which are in line with expectations for a bulk sample (the reader is reminded that the estimated elastic intensity at a given temperature, $S(Q, \omega \sim 0, T)$, is inversely proportional to sample mobility). Mobility is initially minimal and increases only slowly while the sample remains in the solid state. On exceeding its melting point (171.5 K) the 1-octene undergoes a rapid increase in mobility as it enters the liquid phase, and the

elastic intensity drops to essentially zero by *ca*. 270 K, indicating that almost the entire sample is undergoing motion at this temperature.

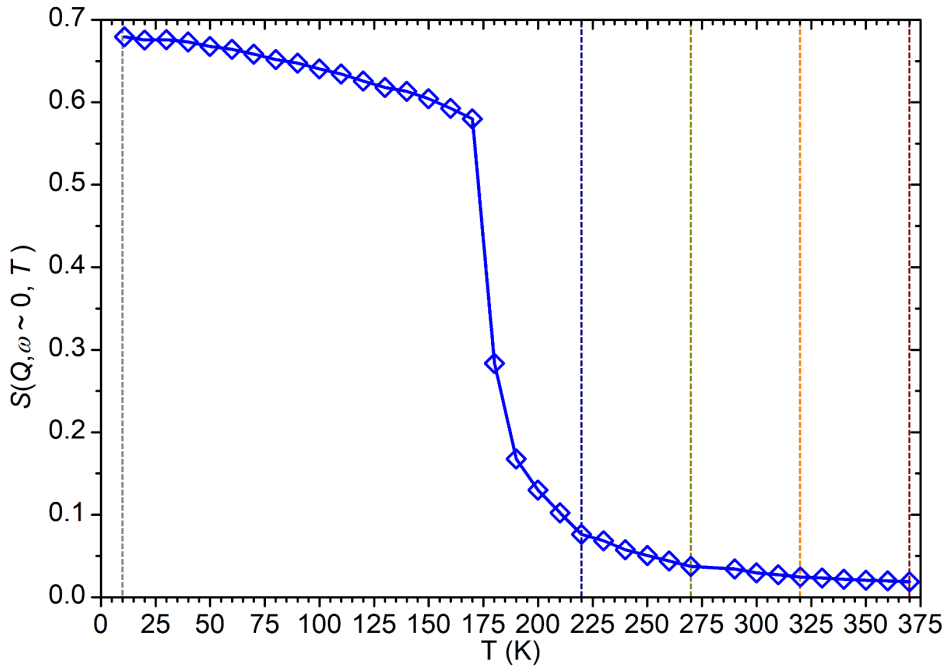

Figure 3-18: Elastic fixed window scan data for 1-octene from 10 to 370 K recorded on IRIS. Energy transfer window for integration of elastic peak is ± 8.75 μeV. Temperatures where high resolution data was collected for additional analysis are highlighted.

Examination of the high resolution data produces results consistent with these observations; the majority of the scattering intensity in each case lies in the quasielastic Lorentzian fit parameter or the linear background, with contributions from the elastic resolution function being much lower due to the fact that the immobile portion of the sample is small. The proportion of the intensity which is elastic further decreases with temperature, and the apparent overall intensity decreases, despite the sample having the same number of molecules in the beam, because of more molecules moving fast enough to lie outside the IRIS energy window. Fitting analysis showed that a single Lorentzian parameter was adequate to describe the observed broadening at all temperatures, meaning that there is one motion occurring within the IRIS time window, while the linear background is high due to the large amount of movement which is too rapid to be resolved. It is also clearly apparent that the Lorentzian broadening increases with *Q*, indicating diffusion. Figure 3-19 shows the scattering functions and fit deconvolutions for a selection of *Q* values at 220 and 320 K to demonstrate these trends.

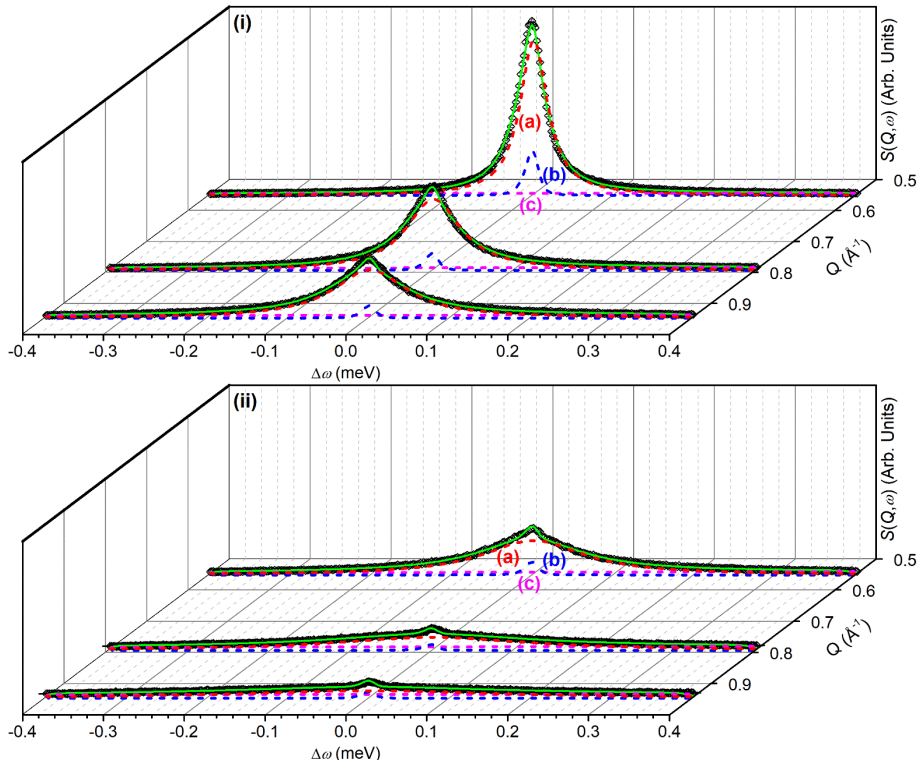

Figure 3-19: $S(Q,\omega)$ functions at selected values of Q for 1-octene at 220 K (i) and 320 K (ii) showing deconvolution into resolution function (a), Lorentzian (b) and linear background (c) contributions. $S(Q,\omega)$ axis scale is identical between graphs.

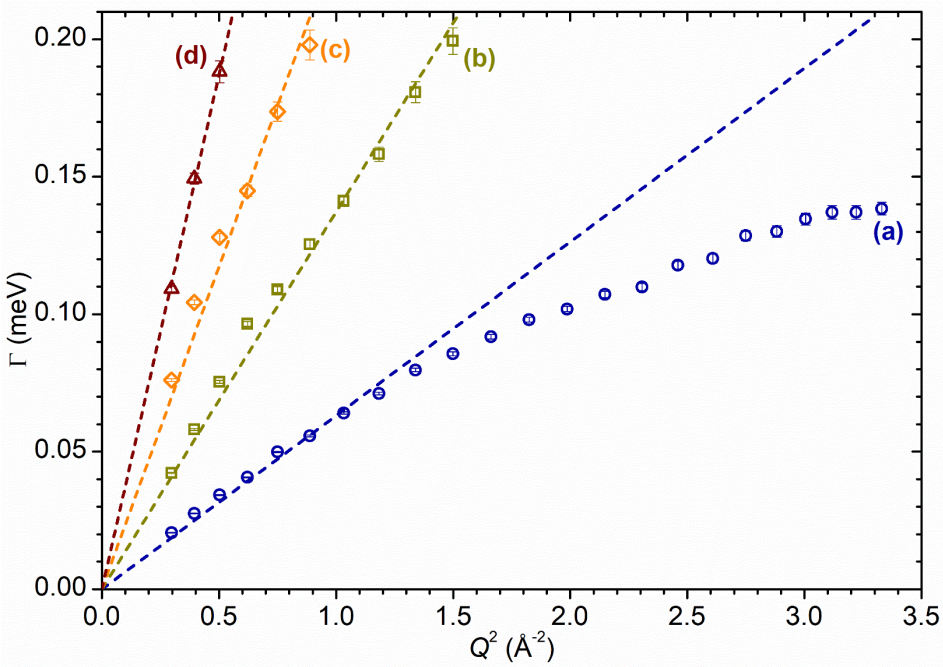

Figure 3-20: Variation of Lorentzian linewidth (Γ) as a function of Q^2 for the self-diffusion of 1-octene at 220 K (a), 270 K (b) 320 K (c) and 370 K (d). Dotted lines represent best fit of the data to Fickian diffusion.

Table 3-6: Parameters for the self-diffusion of liquid 1-octene derived from fitting the data in Figure 3-20.

Temperature (K)	D_s (m^2s^{-1})
220	6.31×10^{-10}
270	1.37×10^{-9}
320	2.35×10^{-9}
370	3.74×10^{-9}
D_0 (m^2s^{-1})	4.37×10^{-8}
E_a (kJ/mol)	7.76

Plotting the Lorentzian linewidth against Q^2 (Figure 3-20) reveals that at the three higher temperatures investigated this relationship is linear and therefore represents broadening due to Fickian diffusion of the 1-octene molecules, allowing the diffusion constants given in Table 3-6 to be derived from the slope of the data. This analysis is complicated by the fact that, although IRIS in theory allows energy transfers up to ± 0.4 meV to be detected, for this dataset is becomes impossible to deconvolute the Lorentzian fit parameter from the linear background once its width exceeds Γ = 0.2 meV. This means that the Q range where we obtain useful data becomes increasingly constrained at higher temperatures, and the diffusion constant at 370 K is based on a very small number of data points. At 220 K, the data can be fit across the full Q range recorded by the instrument but is observed to deviate from this simple Fickian relationship at high Q values. As explained in Chapter 2, this is characteristic of jump diffusion with the deviations occurring at low distances where the scale of the jump lengths becomes significant. The data in this case best fits movement according to the jump diffusion model of Chudley and Elliot,[89] which behaves identically to Fickian diffusion at low Q values allowing the D_s value in Table 3-6 to be derived by limiting the fit to those data points at $Q^2 \leq 1.5$.[64]

The resulting parameters derived from the QENS fit exhibit a linear Arrhenius relationship since they all represent motions within the same phase, allowing the activation energy of the movement to be calculated as *ca.* 7.76 kJ/mol. Although data on the self-diffusion of 1-octene is somewhat sparse, our diffusion constant at 270 K is essentially identical to the value of 1.3×10^{-9} m^2s^{-1} reported by Weber et al. for the diffusion of 1-octene in the in interior of large macropores at room

temperature as measured by PFG-NMR.[157] We can therefore regard this data as representing the dynamic characteristics of 1-octene in their undisturbed state with good confidence and now have access to this information across a temperature range wide enough to accommodate all of our projected measurements of zeolite-hydrocarbon systems.

Chapter 4: Olefin Interactions in H-ZSM-5

Although there is an extensive literature on the mobility of hydrocarbons in zeolites of varying structures, the majority of these studies make use of simple saturated alkanes as their model adsorbates for reasons of simplicity. In contrast, this project is primarily concerned with the interactions of more active unsaturated olefin molecules since it is these species that form the majority of the active fraction in fluidised catalytic cracking and light hydrocarbon valorisation feedstocks. These are also the product species of greater commercial interest. Zeolites can catalyse both C-C bond formation and cleavage reactions, with the balance between the different possible reactions being determined by reaction conditions and the acid strength of the zeolite. This chapter reports the results of a series of investigations of the interactions and mobility of model light and gasoline-range olefin species with a commercial-grade powder-form H-ZSM-5 catalyst at low temperatures. The improved access to the low-energy deformational modes of adsorbed hydrocarbons in zeolites provided by the use of inelastic neutron scattering allows new insights into the mechanism of olefin oligomerization over these catalysts, which have not been previously reported. QENS analysis allows the determination of the mobility of the final product species of these reactions. The easy access to cryogenic studies permitted by the neutron sample environment also permits accurate observations of the onset of reactivity for both model species.

4.1 Octene Interactions in ZSM5-FR:[152]

In this section we will consider the interactions and dynamics of 1-octene, which will later be employed as a model compound for gasoline-range cracking feedstocks, with the fresh catalyst at temperatures up to 300 K; this represents a maximum temperature considerably below those used in typical FCC reaction conditions, a decision taken in order to study the pre-cracking behaviour of the 1-octene. The ability of ZSM-5 to oligomerize short-chain olefins at low temperatures is well reported, however, 1-octene lies within the range of olefin chain lengths which are generally reported as terminal species for this reaction at temperatures < 473 K.[48, 150, 158]

The sample for the INS measurements consisted of 10.78 g of pre-dried ZSM5-FR loaded into an aluminium sample cell (50 × 50 × 10 mm sample geometry) equipped with gas handling fittings. These fittings were used to load the sample with 1-octene without exposure to air by passing a stream of 200 cm^3 min^{-1} of helium through the sample cell after saturating it with 1-octene at 293 K using a bubbler arrangement. Loading was continued until gravimetric analysis indicated no further increase in mass, then the sample was purged with dry helium for 15 minutes to remove any 1-octene not adsorbed into the zeolite. The final 1-octene loading was determined gravimetrically to be 1.03×10^{-3} mol $g^{-1}_{ZSM\text{-}5}$, equating to 5.96 octene molecules per ZSM-5 unit cell. This was analysed on both MAPS and TOSCA using the standard measurement procedures (Section 2.1.2.5).

The sample for QENS analysis consisted of 2.27 g of ZSM5-FR in a 2 mm annular QENS sample cell with gas fittings at both top and bottom, allowing flow-through of gasses. The measurements were taken using the PG002 analyser of OSIRIS, hence the energy resolution was 25 μeV across a momentum transfer range of $0.18 \leq Q \leq 1.8$ $Å^{-1}$.[92] Unloaded spectra of the zeolite/sample cell combination were first collected at base temperature and at 25 K intervals from 23 – 373 K, with high resolution spectra at 5, 273, 323 and 373 K. The sample was then dosed with 1-octene using the same procedure as above; final loading in this case was 1.06×10^{-3} mol $g^{-1}_{ZSM\text{-}5}$ or 6.49 1-octene molecules per unit cell. Data of the loaded sample was then collected using the same protocol as the empty zeolite.

4.1.1 Vibrational Spectra of ZSM5-FR + 1-octene:

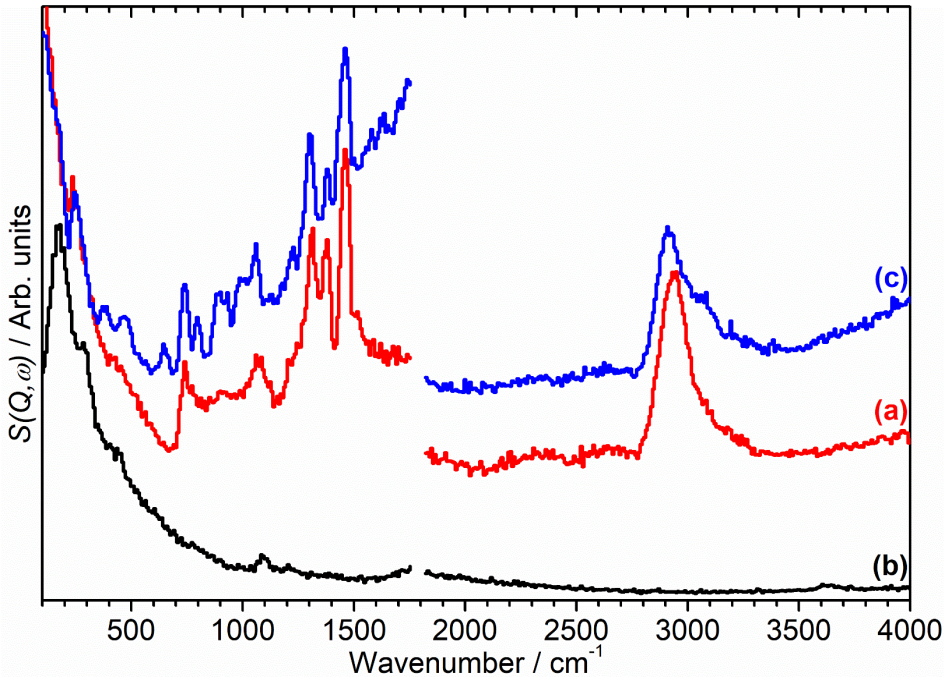

Figure 4-1: MAPS INS spectrum of 1-octene following adsorption in ZSM5-FR (a) compared with the spectra of the empty zeolite (b) and pure 1-octene (c). Spectra recorded at incident energies of 2017 cm^{-1} (left) and 5244 cm^{-1} (right) and integrated over the momentum transfer range $0 \leq Q \leq 10$ $Å^{-1}$. Intensities scaled to correct for different sample sizes and offset in y-axis for clarity.

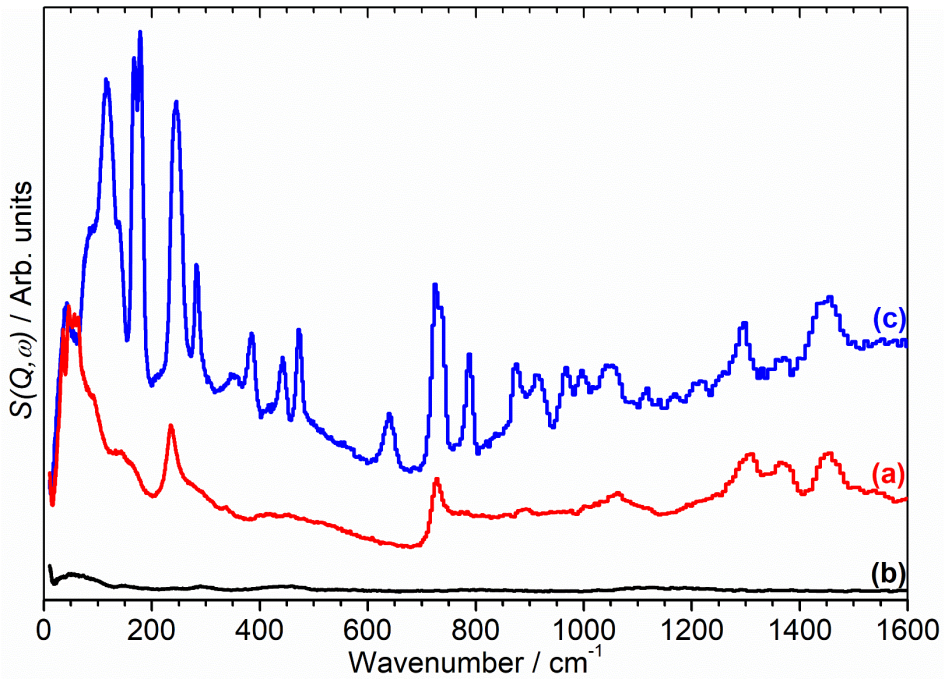

Figure 4-2: TOSCA INS spectra of 1-octene in ZSM5-FR (a), ZSM5-FR (b) and pure 1-octene (c). Intensities scaled to correct for different sample sizes.

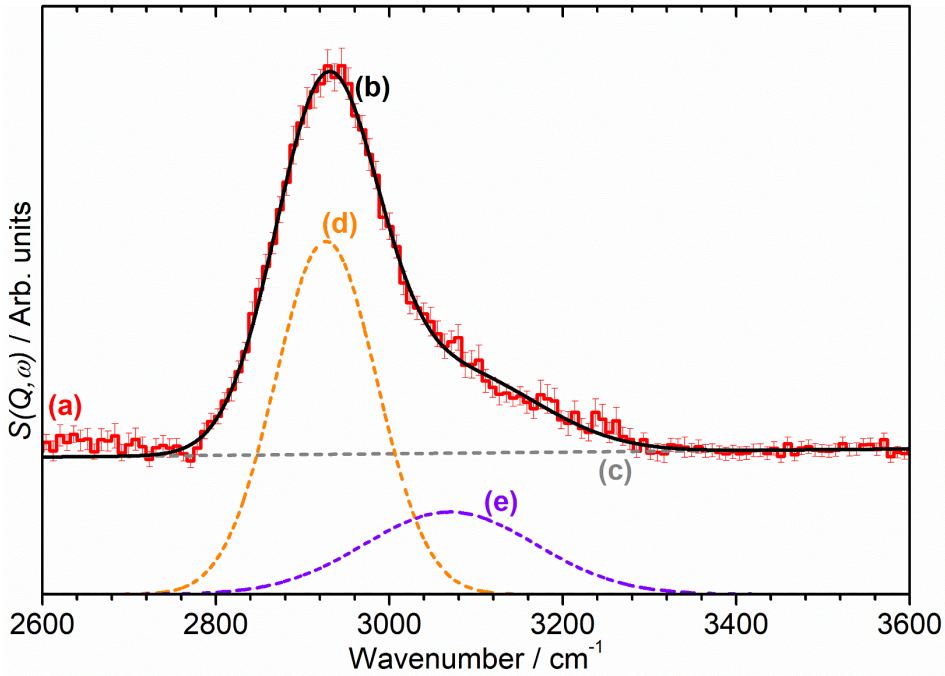

Figure 4-3: C-H stretching region of the INS spectrum of 1-octene in ZSM5-FR (a) and results of peak fitting analysis (b) to deconvolute into a linear background (c), sp^3 νC-H modes (d) and a sp^3 νC-H modes / transverse acoustic mode combination (e). The degree of uncertainty from reduction of the experimental data is shown.

The INS spectra collected are reproduced as Figure 4-1 for MAPS and Figure 4-2 for TOSCA; the corresponding spectra of the individual components, as investigated in Chapter 3, are also included for comparison purposes. The combined 1-octene / ZSM5-FR sample has a lower total quantity of hydrocarbon when compared to the pure 1-octene spectrum, therefore the problem with non-linear baselines in the MAPS spectra due to multiple scattering is less pronounced. The observed spectrum also differs significantly from the spectra of the individual components, indicating that some form of chemisorption involving a degree of molecular rearrangement is occurring. The intensity of the (C-H) stretch region above 3000 cm^{-1} is reduced relative to that observed for pure 1-octene. There is a residual tail of intensity above this value, however, peak fitting of this region (Figure 4-3) shows that this consists entirely of the sp^3 (C-H) stretch / transverse acoustic mode combination previously observed for 1-octene and that the spectrum of the adsorbed system therefore has no contributions from unsaturated carbons. The relevant acoustic mode has undergone a reduction in energy and is visible as a shoulder at 143 cm^{-1} in Figure 4-2, with this being reflected in the energy difference between the centres of the C-H stretch and combination peaks.

The sp^3 ν(C-H) peak has undergone a minor upward shift of 10 cm^{-1}, however, this is too close to the resolution limit of MAPS at this energy transfer to draw meaningful conclusions from this difference.

Together with the complete disappearance of the (=CH_2)-associated peaks at 639, 911 and 967 cm^{-1} this indicates that the change on adsorption involves the carbocation-forming protonation of the octene.[158] This conclusion is further supported by the absence of any peaks corresponding to zeolite (O-H) groups in the loaded spectrum. The lack of an increase in the relative size of the methyl torsion peak supports the assertion by Stepanov et al.[158] that steric hindrance from the zeolite pores means that adsorbed octene within ZSM-5 is mainly present as a linear secondary carbocation with the normally preferred branched tertiary carbocations forming minority species. Further evidence of this is provided by the presence of the -(CH_2)- rocking modes at 727 cm^{-1} in the combined system; the frequency of this mode is dependent on methylene chain length, as mentioned in Section 3.2.2, thus the fact that it has not shifted significantly relative to its position in the free 1-octene spectrum indicates that the average methylene chain length in the system remains ≥ 5 adjacent CH_2 units and that the octene chain is not undergoing any significant degree of rearrangement.

Previous literature suggests that 8-carbon molecules like 1-octene are stable species over ZSM-5 at room temperature and although protonation occurs the resulting carbocations do not react further.[48, 150, 158] However, the extremely broadened nature of the peaks in the 690-1140 cm^{-1} region does not appear consistent with the expected results from a simple molecule such as an octene derivative. This was confirmed through DFT modelling of a secondary octene carbocation, which results in a spectrum with peaks at the correct energies but which do not exhibit the necessary broadening to match the experimental spectrum. Simulations of various other possible C_8 species likewise universally produce predicted spectra with key differences from the experimental results. Taken together, these results indicate that the product species cannot be solely a C_8 carbocation. The experimental spectrum instead more closely resembles the predicted spectra of longer linear alkanes or polyethylene (Figure 4-4), indicating that the protonated 1-octene does in fact undergo oligomerization to longer chain lengths. Comparisons against the extensive library of alkane spectra publicly

accessible in the ISIS INS database does not reveal a molecule which provides an exact match to the peak ratios in the experimental spectrum,[159] particularly the -CH_2 and CH_3 modes in the 1200 – 1500 cm^{-1} range, meaning that the experimental spectrum likely consists of a mixture of multiple chain lengths. Based on the lack of evidence for chain branching as detailed above, it appears that the oligomerization proceeds via a linear end-to-end polymerization reaction due to restriction by the zeolite pore disfavouring branching reactions. The complete absence of sp^2 character in any of the INS spectra indicates that the reaction proceeds to completion even at the comparatively low temperature of 293 K as the 1-octene is loaded into the zeolite, likely due to the high acidity of ZSM5-FR.

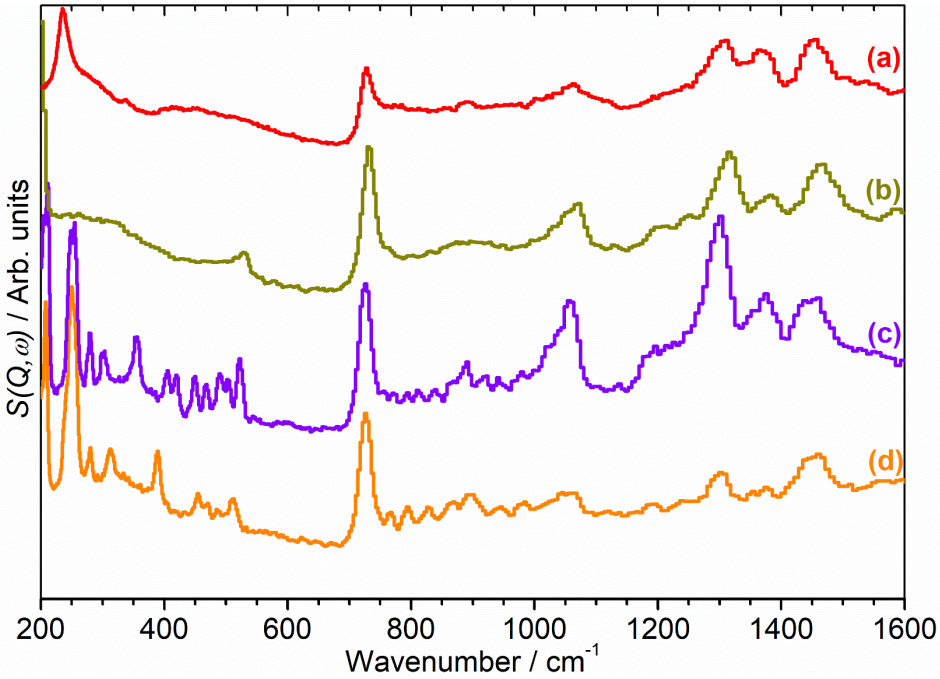

Figure 4-4: INS spectrum of 1-octene adsorbed in ZSM5-FR (a) compared with reference spectra of polyethylene (b), tetracosane ($C_{24}H_{50}$) (c) and hexadecane ($C_{16}H_{38}$) (d). All spectra recorded on TOSCA; reference spectra are taken from work by Parker and co-workers,[155, 160] and sourced from the ISIS INS database.[159]

4.1.2 Mobility of 1-octene Oligomers:

The QENS spectra of the unloaded ZSM5-FR sample reveal no significant changes in the width of the elastic peak across the temperature range investigated and the zeolite is therefore essentially static. This is also clearly demonstrated by the flat nature of the EFWS data for ZSM5-FR (Figure 4-5). Examination of the loaded

sample by the same method shows the considerable increase in scattering intensity resulting from the introduction of a hydrocarbon to the sample. It also confirms that the oligomerization reaction has proceeded to completion during the dosing process; the rate of intensity change with temperature is nearly constant across the temperature range without any phase transitions as were observed for the 1-octene and the overall increase in mobility is much smaller than that observed for the free 1-octene in Section 3.3.1. The small fluctuation observed in the 298 and 323 K data points in Figure 4-5(b) may be due to a slight decrease in mobility associated with the monoclinic-orthorhombic phase transition of ZSM-5, which occurs in the range 300 – 350 K for unloaded samples.[161] However, it is generally reported that adsorption of molecules into the ZSM-5 structure locks it in the monoclinic phase, and the magnitude of the discrepancy in the EFWS data is small enough that it could merely be statistical noise instead.

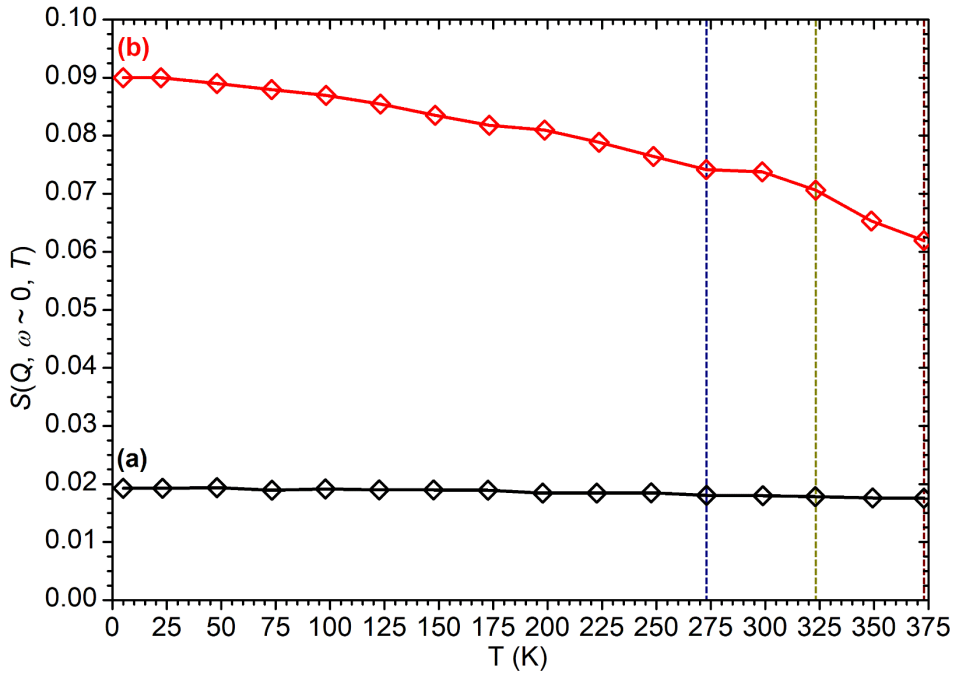

Figure 4-5: Elastic fixed window scan data for ZSM5-FR (a) and 1-octene adsorbed in ZSM5-FR (b) from 5 to 373 K recorded on OSIRIS. Energy transfer window for integration of elastic peak is ± 12.5 μeV. Temperatures where high resolution data was collected for additional analysis are highlighted.

Visualisation and fitting of the high resolution QENS spectra shows results consistent with this low level of mobility. Due to the extremely low levels of mobility indicated by the EISF analysis (see below), the contributions of the zeolite and sample environment to the scattering functions were removed from the

loaded QENS results at each temperature by subtracting the corresponding unloaded spectra. The resulting hydrocarbon-only data fitted best to a combination of the resolution function, a linear background and a single Lorentzian. Even for the highest temperature investigated (373 K) it is immediately apparent that the resolution function remains the major component of the overall scattering function across the entire *Q* range, as shown in Figure 4-6. This is in sharp contrast to the comparable results for the free 1-octene in 3.3.1 and indicates that even at this high temperature the majority of the hydrocarbon in the sample remains immobile. It is also apparent that the Lorentzian function only contributes significantly to the overall scattering function at higher *Q* values: the same pattern is also observed for the spectra at 273 and 323 K. Since *Q* is inversely related to distance, this indicates that the movement of the hydrocarbon is restricted to localised motions and it does not exhibit the long-range translations reported for linear alkanes in ZSM-5.[72, 74] It is therefore clear that the oligomerization reaction has resulted in a product which is sufficiently large to be immobilised (on the OSIRIS timescale) within the pore structure of the zeolite by interactions with the pore walls and with only a limited range of possible movement.

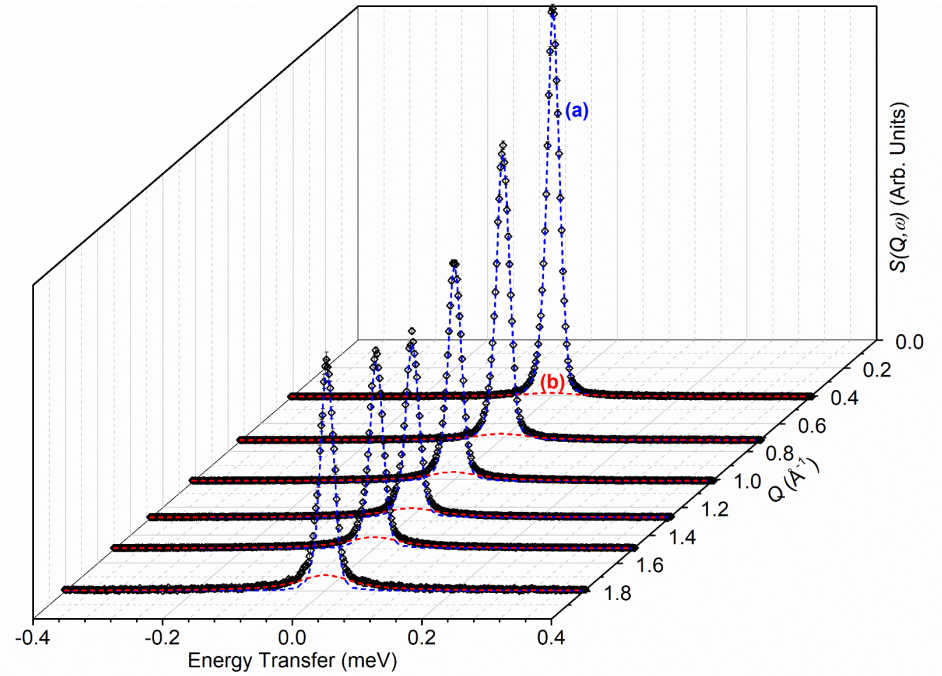

Figure 4-6: $S(Q,\omega)$ functions at selected values of *Q* for 1-octene adsorbed in ZSM5-FR at 373 K showing the resolution function (a) and Lorentzian (b) contributions to the overall fit.

Localised motions in a QENS spectrum may be characterised by deriving the Elastic Incoherent Structure Factor (EISF, $A_0(Q)$) which is the fraction of the total scattering intensity that is elastic, given by:

$$A_0(Q) = \frac{I_{elastic}(Q)}{I_{elastic}(Q) + I_{quasielastic}(Q)} \tag{4.1}$$

The quasielastic contribution is always zero at Q = 0 giving $A_0(Q)$ = 1 and for completely immobile systems this will remain the case at all Q values. Where there is motion, the EISF will initially decrease with increasing Q and the exact shape of the EISF vs Q curve is determined by the geometry of motion.[85]

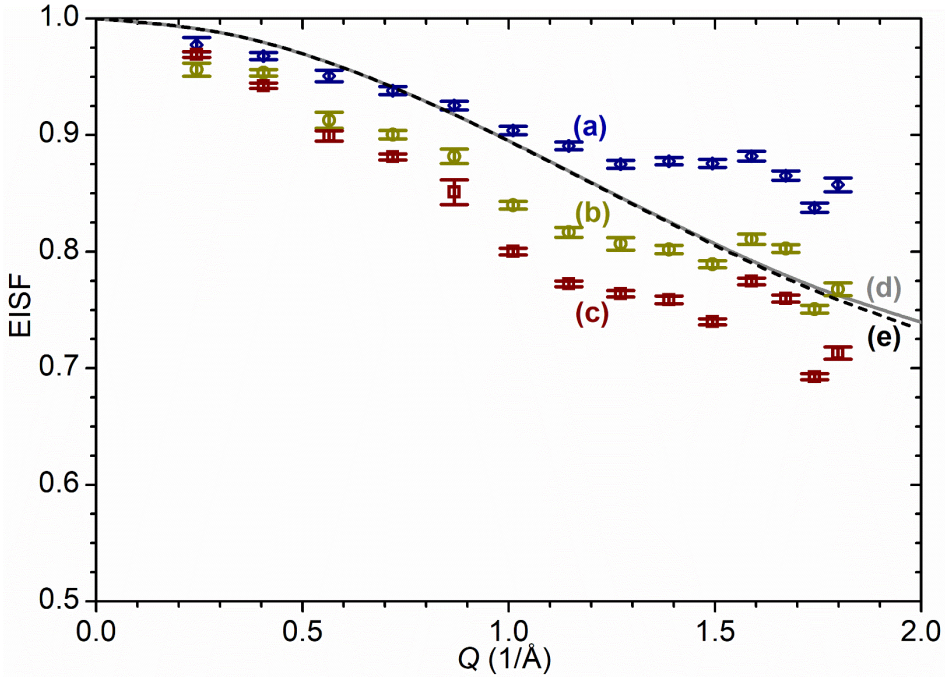

Figure 4-7: Experimental EISF values for 1-octene in ZSM5-FR at 273 K (a), 323 K (b) and 373 K (c) compared to the predicted EISF values for jump (d) and continuous (e) methyl rotation using the models described in the text.

The EISF values of the loaded zeolite QENS spectra are reproduced in Figure 4-7; it can be seen that the overall reduction in EISF magnitude is small at all temperatures and that the motion of the molecules within the zeolite is therefore highly hindered. The fluctuation observed for all three temperatures in the 1.5-1.75 $Å^{-1}$ region is a residual effect of the Bragg peak in that region of Q; expansion of the zeolite structure because the adsorbed 1-octene results in a shift

in the position of the Bragg peaks and results in incomplete cancellation by the baseline subtraction process.

The identification of the exact motion responsible for the quasielastic intensity observed is simplified by the results of the vibrational analysis completed above. Since the hydrocarbon is a long chain constrained within zeolite pores whose diameter is less than the chain length, only a few types of rotation are physically possible, namely the reorientation of the terminal methyl groups around their C-C bond, either continuously or as a series of 120° jumps between equivalent orientations, or the uniaxial rotation of the entire alkyl chain. Distinguishing between these possibilities can be accomplished through fitting of the EISF curves. Just as the Fourier transform of the van Hove autocorrelation function can yield a description of the Γ *vs* Q^2 relationship for translational motions, it can also be used to derive an model for the EISF *vs Q* relationship in localised motions.[64, 85] In the case of a rotation, the generalised scattering law for rotation between *N* equivalent sites on a circle yields the following equation for the EISF:

$$A_0(Q) = \frac{1}{N}\sum_{n=1}^{N} j_o\left[2Qr\sin\left(\frac{\pi n}{N}\right)\right] \qquad (4.2)$$

where *r* is the radius of rotation, and j_0 is the spherical Bessel function of order zero.[85] In the continuous rotation case, the scattering law for true continuous rotation requires knowledge of the angle between the scattering vector and the rotational axis and modelling it is therefore only possible for single crystals. However, a sufficiently accurate approximation for powder samples which is valid for *Q* values $\leq \pi/r$ may be obtained using Equation (4.2) provided the value of *N* is sufficiently large.[85]

For the methyl rotations the value of *r* is 1.03 Å, the radius of the circle circumscribed by the methyl hydrogens, which can be calculated from the C-H and C-C bond lengths and angles given by the DFT simulations in Section 3.2.2 as shown in Figure 4-8. Since in both cases the rotation only involves the terminal methyl hydrogens, the other hydrogens in the molecule do not contribute to the elastic intensity and it is therefore necessary to include a correction factor to reflect this. This can be done by splitting the EISF into mobile (*m*) and immobile (*i*)

contributions, and weighting each by the proportion in each state ($p_{(i,m)}$ where p_i + p_m = 1). The total EISF would then be the sum of each contribution, and since the value of $A_0(Q)_i$ is always 1:

$$A_{0\,eff}(Q) = p_i A_0(Q)_i + p_m A_0(Q)_m$$
$$= p_i + p_m A_0(Q)_m \qquad (4.3)$$

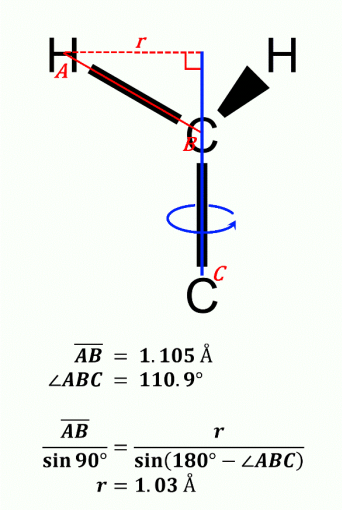

Figure 4-8: Derivation of the radius of hydrogen movement for methyl rotation in 1-octene from DFT-optimised geometry data.

The maximum mobility possible for these rotations will occur with protonation of the adsorbed 1-octene at the terminal carbon but no oligomerization, giving six methyl hydrogens out of seventeen and so p_m = 0.353. The predictions from the model for r = 1.03 Å and p_m = 0.353 are reproduced as Figure 4-7(d) for the jump rotation using N = 3 and Figure 4-7(e) for continuous rotation using N = 50; it is apparent that the influence of N on the EISF is small at the length scales involved with methyl rotation. It can be seen that both models fail to reach the degree of mobility observed experimentally at 373 K across the Q range investigated. Oligomerization of the 1-octene molecules as deduced from the INS data means that the actual proportion of methyl hydrogens in the sample must be lower than the limiting case modelled here, which would result in even higher EISF values than these predictions. The observed quasielastic intensity therefore cannot be solely due to methyl rotation.

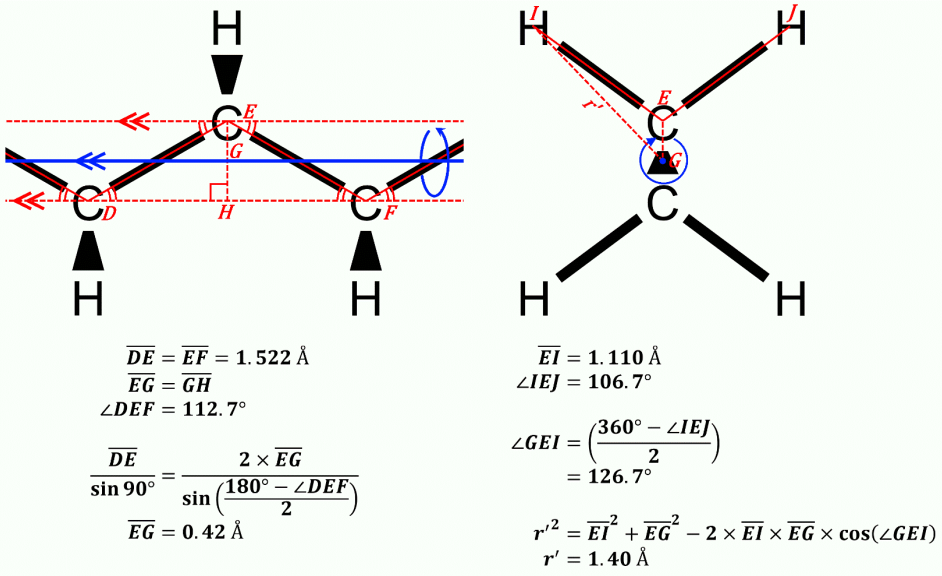

Figure 4-9: Derivation of the radius of hydrogen movement for uniaxial rotation of an alkyl chain from DFT-optimised geometry data.

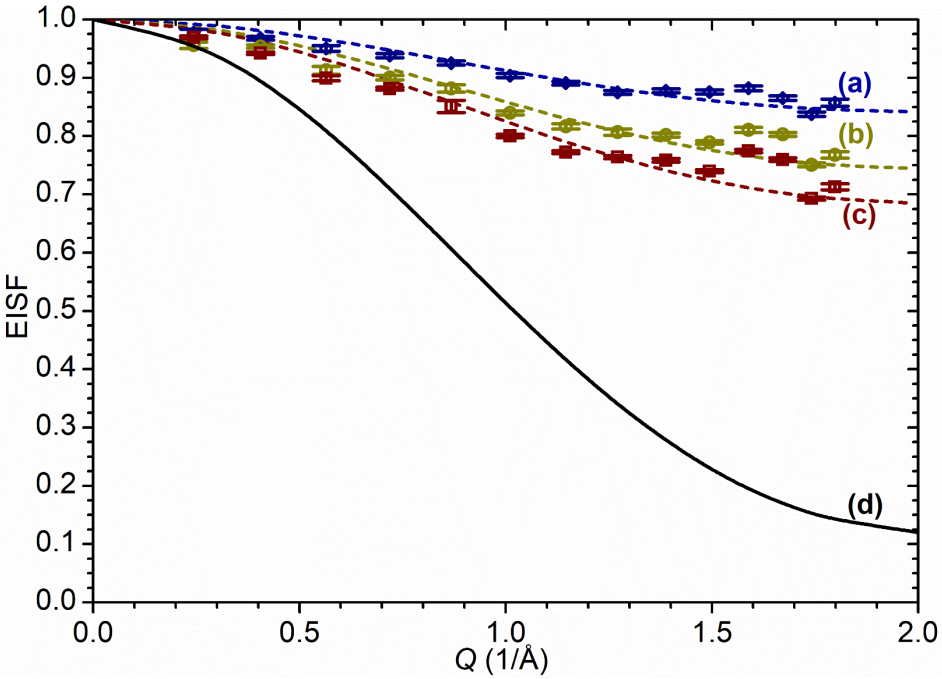

Figure 4-10: Experimental EISF values for 1-octene in ZSM5-FR at 273 K (a), 323 K (b) and 373 K (c) compared with the calculated EISF resulting from continuous uniaxial rotation of the alkyl chain, assuming all hydrogens participate (d). The dotted lines represent the results of a partially-immobile modification of this rotation as described in the text using the p_m values in Table 4-1.

In the case of uniaxial rotation of the alkyl chain, the motion of the CH_2 hydrogens occurs on a circle of 1.40 Å (Figure 4-9). Modelling continuous rotation on this radius while assuming that all hydrogens participate, corresponding to the limiting

case of a chain of infinite length, produces the EISF plot shown as Figure 4-10(d): it can be seen that in this case the maximum mobility case predicts lower-than-observed EISF values across the *Q* range. Close fits for the experimental data can be obtained by assuming partial sample immobility and fitting the model to the experimental data with respect to p_m, shown as the broken lines in Figure 4-10: the final p_m values used to generate these fits are reproduced in Table 4-1 and indicate that the mobile fraction of the hydrogens is temperature dependant, varying from 18.0 % at 273 K to 35.8 % at 373 K.

This degree of immobility is too high to be entirely due to non-participation by the terminal hydrogens in the alkyl chain and indicates that a majority of the oligomers remain completely immobile at these temperatures. This high degree of immobility is likely caused by strong hydrocarbon-zeolite interactions owing to the short distances between the methylene hydrogens and the pore walls in the zeolite channels. Experimental adsorption enthalpies as high as – 79 kJ/mol have been reported for short-chain (C_6) alkanes in MFI-structured zeolites, with computational studies indicating that the effect of hydrogen bonding will lead to even stronger interactions in H-ZSM5.[162-163] Given these high energies, it is possible that at the temperatures investigated, the mobile fraction represents those oligomers which terminate within a pore intersection and therefore have a proportion of the chain which is further from the zeolite pore walls, reducing the overall binding energy which hinders the rotation. Increased temperatures result in a more tightly bound portion of the oligomers, residing within the pore channels, gaining sufficient energy to break the framework-sorbate interactions and participate in rotational movement. Since the temperature range investigated does not reach a point where all CH_2 groups are participating in the rotation and p_m attains a plateau value, it is therefore not possible to use p_m to estimate the average chain length in the sample. While the alteration of the shape of the EISF plot due to the large scaling factor from the low p_m means that the possibility of secondary contributions from methyl rotations to the overall shape cannot be ruled out with complete certainty (as changes to the plot shape due to the addition of a 3-site rotational model would be too insignificant to be noticeable due to the p_m scaling), the close fit of the uniaxial rotation model to the experimental data indicates that it is responsible for the majority of this

quasielastic character and the contributions of other modes are likely to be negligible.

A property of continuous rotations of this form is that the degree of quasielastic broadening remains constant with respect to *Q* and that the half-width at half-maximum (HWHM, *Γ*) of the Lorentzian corresponds to the inverse of the time constant of the rotation (τ) and therefore is the same as the rotational diffusion constant (D_r).

$$D_r = \frac{1}{\tau} = \Gamma \tag{4.4}$$

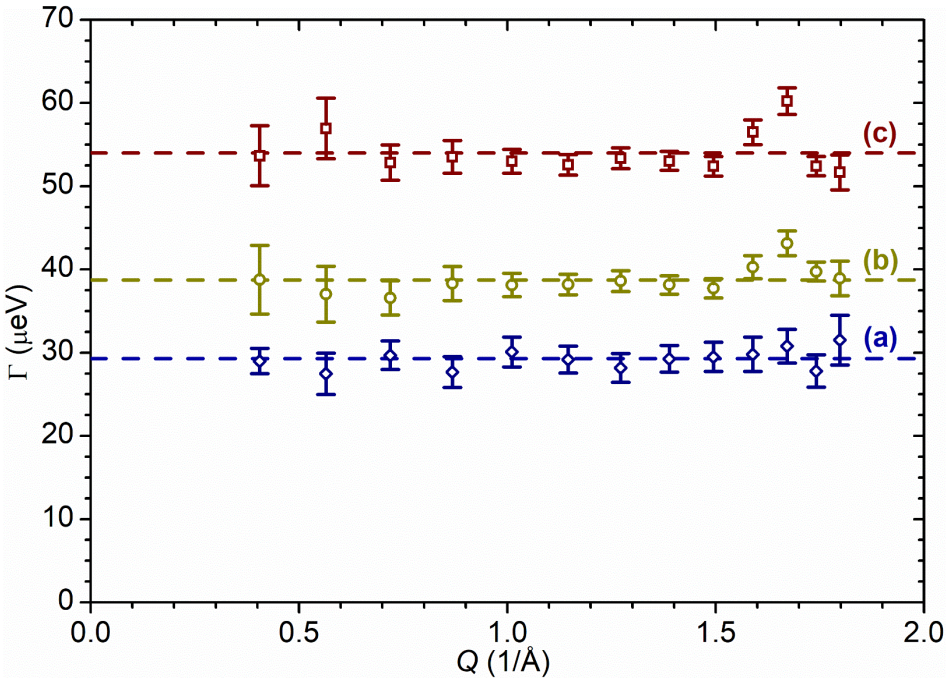

Figure 4-11: Variation of Lorentzian linewidth (Γ) with *Q* for 1-octene in ZSM5-FR at 273 (a), 323 (b) and 373 K (c). Dotted lines represent linear fits to the data used to derive the Γ values reported in Table 4-1.

Figure 4-11 shows that this *Q*-independent relationship holds true at all three temperatures within the limits of experimental accuracy and allows the extraction of D_r values for the rotation at each temperature, reproduced in Table 4-1. It can also be seen that this motion occurs on a considerably longer time scale than the Fickian diffusion observed for free 1-octene, with the level of Lorentzian broadening lying close to the resolution limit of OSIRIS (25 μeV). Over the temperature range studied these values follow an Arrhenius relationship, leading to a calculated activation energy for the rotation of 5.1 kJ mol^{-1}. This is

approximately 27% of the activation energy previously reported for similar oligomer motions in bulk polyethylene.[164] It is likely that the reduction in activation energy is due to the isolated nature of the oligomer chains within the zeolite, with pore wall-oligomer interactions offering a lower barrier to rotation than chain-chain interactions, particularly when the population of oligomers in the pore intersections is considered.

Table 4-1: Summary of dynamical parameters derived from QENS data fitting for the combined ZSM5-FR / 1-octene system.

Temperature (K)	P_m	Γ (μeV)	D_r (s^{-1})
273	0.180	29.3	4.45×10^{10}
323	0.291	38.7	5.89×10^{10}
373	0.358	54.0	8.21×10^{10}

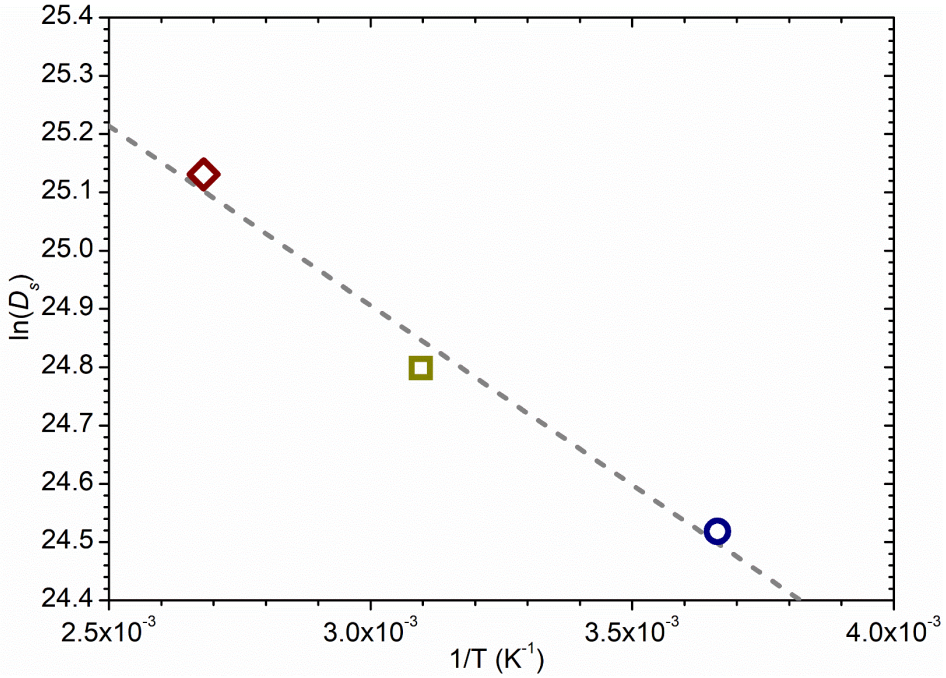

Figure 4-12: Arrhenius plot of the rotational diffusion constants of 1-octene oligomers in ZSM5-FR at 273, 323 and 373 K showing a linear relationship across this temperature range. Line of best fit to the experimental data shown as the dotted line, giving an activation energy of 5.1 kJ mol^{-1} for this motion.

It therefore appears most likely that the 1-octene / ZSM5-FR system consists of long-chain linear hydrocarbons formed by the sterically hindered catalytic oligomerization of the 1-octene, as observed in the INS spectrum, which are large enough to be immobilised within the zeolite pores. A temperature-dependant

fraction of the oligomers are able to break the forces holding them to the pore wall sufficiently to undergo localised rotation; the fact that this rotation is either partially or completely due to free rotation of the alkyl chain around its long axis implies that the mobile hydrocarbons are located along the length of the straight pore channels in the zeolite. The presence of movement on QENS timescales supports the identification of the sorbate as a carbocation rather than a bonded silyl ether.

4.2 Propene Interactions in ZSM5-FR:[147-148]

Based on the high activity towards low temperature oligomerization found for 1-octene in ZSM5-FR above, it is to be expected that propene will exhibit similar levels of activity. This is especially true because while previous studies on 1-octene oligomerization were somewhat ambiguous about the minimum reaction temperature, the literature of propene-zeolite chemistry contains extensive evidence on ZSM-5's capability to catalyse oligomerization at room temperature or below.[46, 165-168] It is nevertheless still worthwhile to investigate this chemistry because it provides a route for the generation of C-C bonds and therefore contributes to a number of important chemical processes. Light olefin oligomerizations are believed to play an important role in the formation and evolution of the 'hydrocarbon pool' in methanol-to-hydrocarbons reactions.[40, 42, 47] They also, as the inverse reaction to the *β*-scission cracking mechanism, are important contributors to the product stream composition in FCC processes.[169] Any additional insights which can be gained *via* neutron methods are therefore of industrial interest.

4.2.1 Vibrational Spectra of Propene Oligomers:

INS analysis of the product of propene oligomerization in ZSM5-FR was carried out using a 11.8 g sample of the pre-dried material. This was contained in an aluminium sample cell of the same design as that used for the 1-octene measurements above and mounted on an INS centre stick equipped with gas dosing lines leading outside the instrument environment. This sample was loaded with

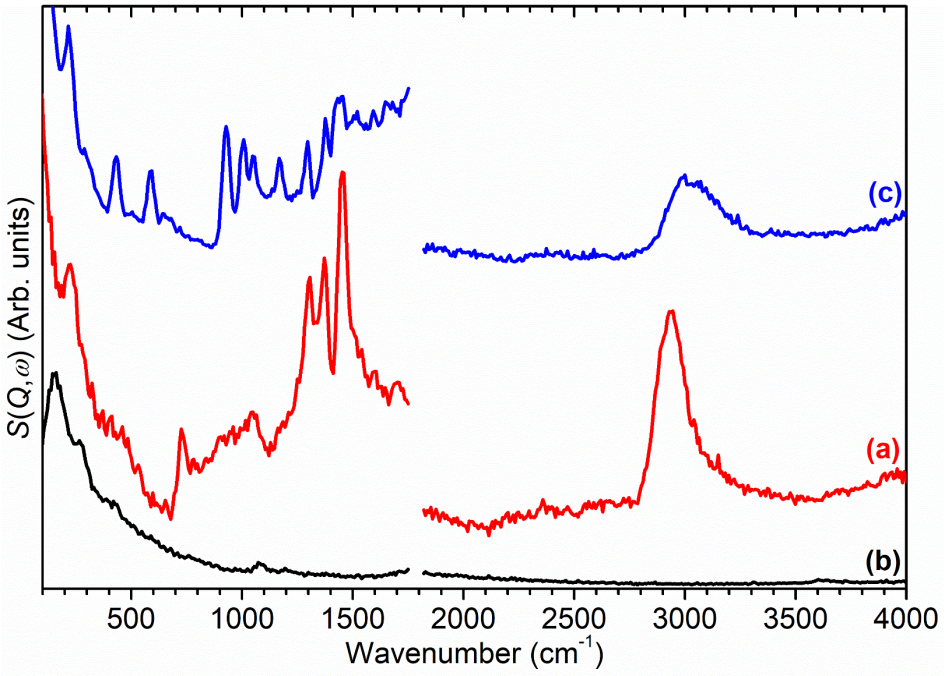

Figure 4-13: MAPS INS spectrum of propene following adsorption in ZSM5-FR at 293 K (a) compared with the spectra of the empty zeolite (b) and pure propene (c). Spectra recorded at incident energies of 2017 cm^{-1} (left) and 5244 cm^{-1} (right) and integrated over the momentum transfer range $0 \leq Q \leq 10$ $Å^{-1}$. Intensities scaled to correct for different sample sizes and offset in y-axis for clarity.

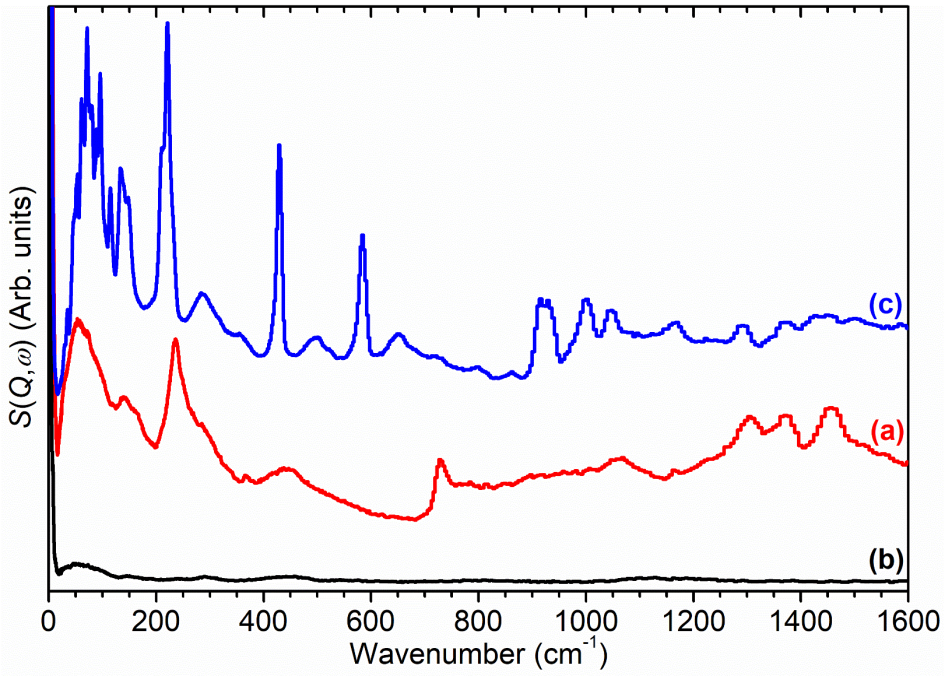

Figure 4-14: TOSCA INS spectra of propene in ZSM5-FR (a), ZSM5-FR (b) and pure propene (c). Intensities scaled to correct for different sample sizes.

1.3×10^{-2} moles of propene (6.6 propene molecules per unit cell) by filling a container of known volume to a pressure equating to that quantity and allowing

the gas to diffuse into the zeolite. The entire propene dose was taken up by the zeolite, as evidenced by there being no residual gas pressure in the gas handling system after equilibration with the zeolite sample. Measurement of the resulting sample on MAPS and TOSCA produced the spectra in Figure 4-13 and Figure 4-14; as before, the relevant pure compound spectra from Chapter 3 have been reproduced here for comparison.

It is apparent from these figures that the combined ZSM5-FR / propene system has undergone a reaction, and an acid oligomerization reaction is the most likely process to have occurred. Comparing the post-adsorption spectrum for the ZSM5-FR / propene system with that of the ZSM5-FR / 1-octene system from Figure 4-2 indicates that the propene has in fact undergone the same type of oligomerization reaction previously observed for 1-octene (Figure 4-15).

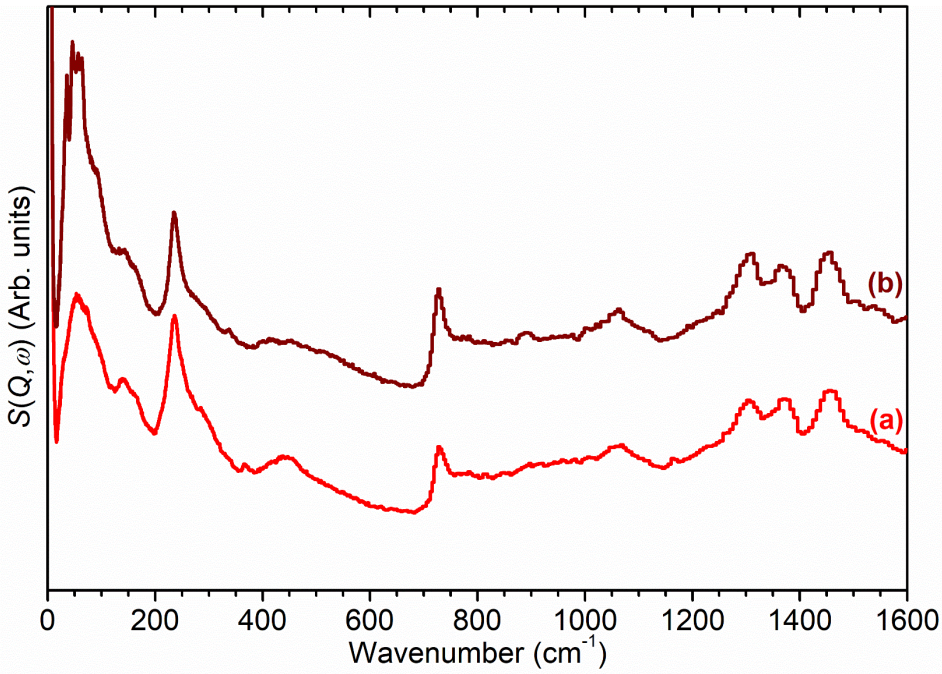

Figure 4-15: INS spectrum of propene adsorbed in ZSM5-FR (a) compared with that of 1-octene adsorbed in ZSM5-FR (b) showing the production of similar product oligomers from each reaction.

Infrared studies by Spoto *et al.* report that room-temperature oligomerizations of propene produce polypropene-type products,[48] but this is not the case in this sample which exhibits spectral features not found in any of the various polypropene tacticities (Figure 4-16) and instead shows peaks characteristic of a primarily linear product mixture as described for the 1-octene oligomerization

product in Section 4.1.1. Heating of the sample to 373 K does not produce any change in the INS spectrum, indicating that the oligomerization reaction has proceeded to completion at room temperature. The INS results have therefore revealed a new type of oligomerization chemistry which is not apparent in the infrared literature and it is necessary for us to further investigate how the reaction proceeds in ZSM5-FR. Of most immediate importance is the requirement to observe propene within the zeolite in its pre-reaction state.

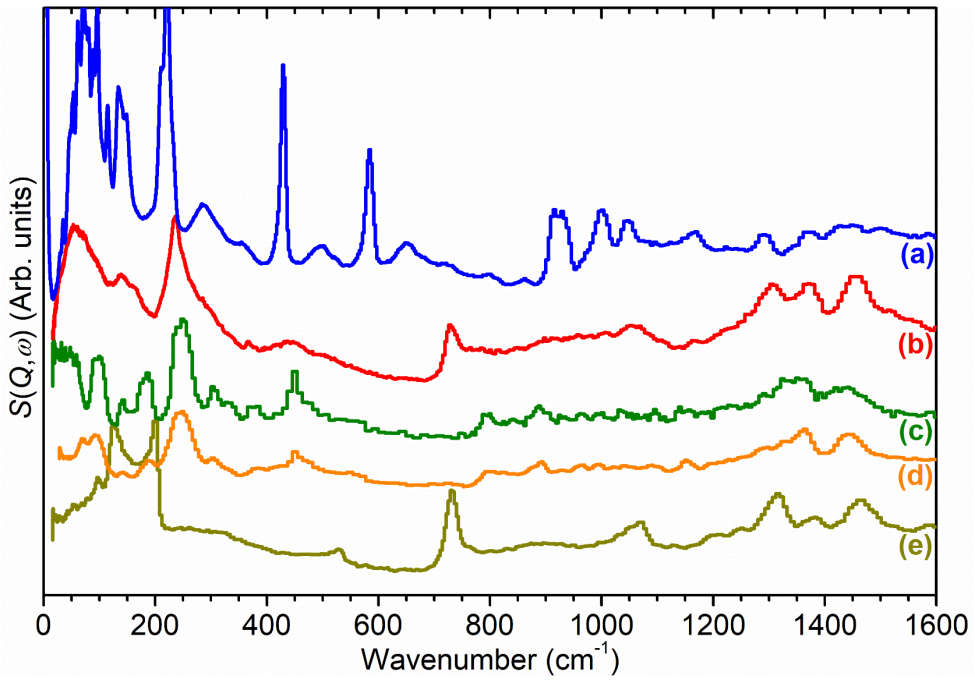

Figure 4-16: INS spectrum of pure propene (a) and propene adsorbed in ZSM5-FR (b) compared with reference spectra of atactic polypropene (c), isotactic polypropene (d) and polyethylene (e) showing that spectrum (b) primarily exhibits spectral features associated with linear alkyl chains. All spectra recorded on TOSCA; reference spectra are taken from work by Parker and co-workers[160, 170] and sourced from the ISIS INS database.[159]

4.2.2 Observation of Pre-Reaction Propene in ZSM5-FR:

Unlike 1-octene, it has proved possible to introduce propene to a sample of ZSM5-FR without triggering oligomerization by a modification of the dosing procedure. By immersing the ZSM5-FR sample cell in liquid nitrogen up to the level of the top of the catalyst bed and introducing the propene through the top gas port it was possible to condense the propene dose into the sample cell. The sample was then inserted into the INS spectrometer and heated to 140 K using a

combination of the instrument CCR environment and cell-mounted resistance heaters similar to those employed in QENS measurements. This melted the condensed propene and allowed it to diffuse into the sample as a liquid; this procedure was chosen as opposed to the alternative of introducing it directly to the sample at 140 K using a trace-heated gas line to prevent any possibility of the sample temperature rising above 140 K during the equilibration process. Following this procedure (on two separate samples due to the impossibility of transferring cells between instruments while maintaining them at cryogenic temperatures) produced the spectra in Figure 4-17.

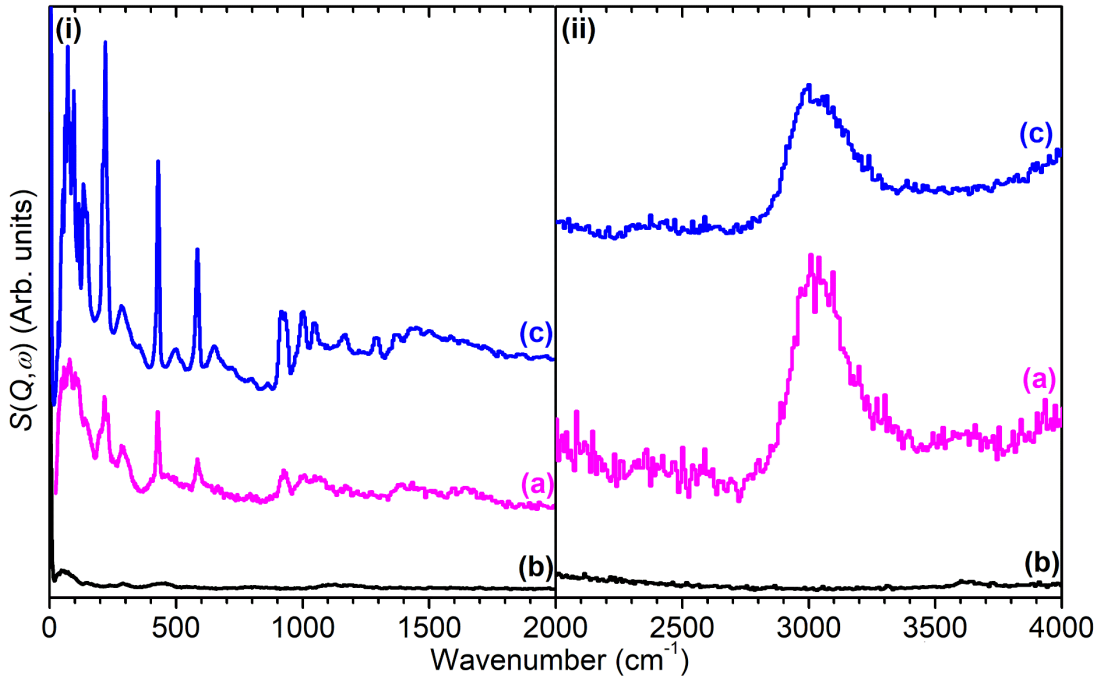

Figure 4-17: INS spectrum of propene following adsorption in ZSM5-FR at 140 K (a) compared with empty zeolite (b) and pure propene (c) spectra. Spectra recorded on TOSCA (i) and MAPS (ii); MAPS incident energy is 5244 cm^{-1} and integration range $0 \leq Q \leq 10$ $Å^{-1}$. Intensities scaled to correct for different sample sizes and offset in y-axis for clarity.

It can be seen that the resulting spectrum (Figure 4-17(a)) retains all the features of the propene reference spectrum with the exception of the phonon wing modes of the methyl torsion, vinyl scissors and vinyl twist modes (discussed in Section 3.2.1), which are absent due to the zeolite preventing the formation of a propene crystal lattice. It is therefore clear that the unreacted propene has been successfully introduced to, and is stable within the zeolite, under these conditions. The zeolite O-H stretch is also still perceptible in the combined

spectrum again indicating that no protonation reactions have occurred, although the centre of the peak (at 3600 cm^{-1}) appears to have shifted to a slightly lower energy: if this is the case it indicates that the hydrogen-bonded olefins which are reported as a precursor to the protonation reaction can still form at this temperature.[48]

4.2.2.1 Observing Propene Oligomerization In-Progress:

Since the propene can be adsorbed without undergoing oligomerization it is therefore also possible to induce the oligomerization reaction *in situ* and observe it by neutron spectroscopy as it occurs. Since this reaction involves the formation of larger molecules, it results in a reduction in the overall mobility of the ZSM-5 / hydrocarbon system since the large oligomer molecules are not able to diffuse freely through the zeolite pores. It is therefore possible to quantify the progression of the reaction with temperature by means of a QENS EFWS analysis; the oligomerization reaction will reverse the trend of increasing mobility with temperature as the small propene molecules are converted to less mobile long-chain species. Once the oligomerization has run to completion, the downward trend in elastic intensity with temperature will resume as the final product mixture moves more with increased thermal energy. The short collection times associated with EFWS analysis allow the collection of data over a wide temperature range, shown in Figure 4-18, and allow the identification of the minimum temperature for the oligomerization reaction to occur being at 225 K. Despite the sample being given time to react and equilibrate at each temperature point the decrease in mobility due to oligomerization is not instantaneous but occurs over a range of temperatures from 225 – 270 K, in contrast to the rapid oligomerization which was noted to occur when the loading took place above this range. This indicates that the reaction is only partially complete in this range of temperatures, which is wide enough that it is possible to observe the reaction in progress by INS methods.

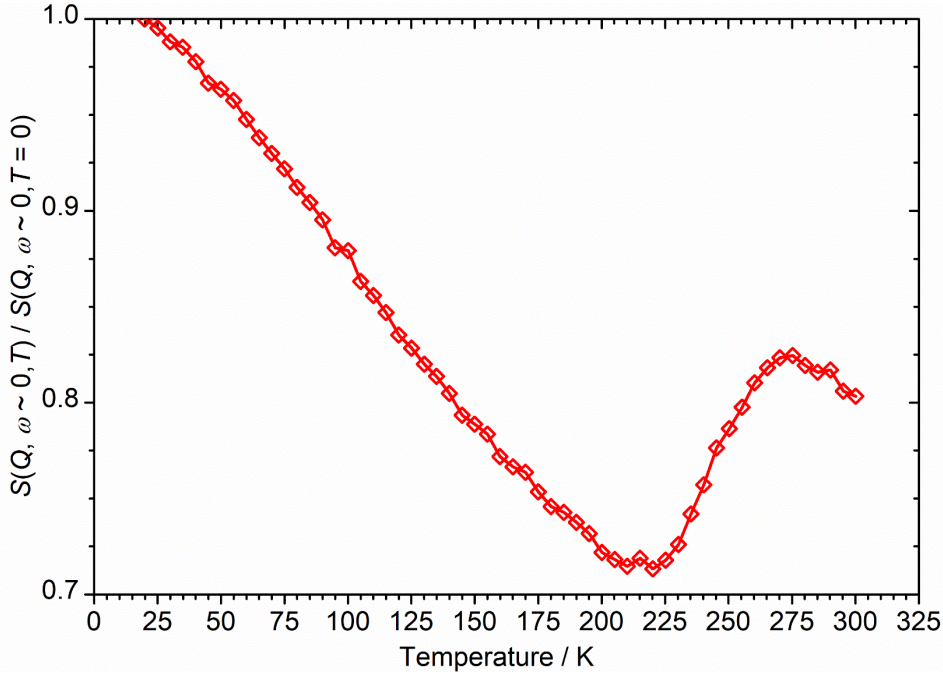

Figure 4-18: Elastic fixed window scan data for propene in ZSM5-FR from 20-300 K after dosing at 140 K. Data recorded on OSIRIS with energy transfer window for integration ± 12.5 μeV. Intensity values normalised against T = 20 K.

Due to the mechanics of INS, specifically the need for low temperature measurements to avoid Debye-Waller effects, it is impossible to perform this investigation as a true *operando* measurement. Instead, a stepwise protocol was adopted, where a cryogenically loaded ZSM5-FR / propene sample is sequentially heated to successively higher temperatures, held for 30 minutes to allow any reactions to take place then returned to ≤ 30 K to allow spectrum collection. The experiment was performed using TOSCA both because it has higher neutron flux and hence lower collection times and because detectable changes from the formation of any reaction intermediates are most likely to lie in the C-H deformation region where TOSCA offers better resolution. This analysis was performed across the temperature range of interest identified by the QENS analysis above, giving the spectra in Figure 4-19.

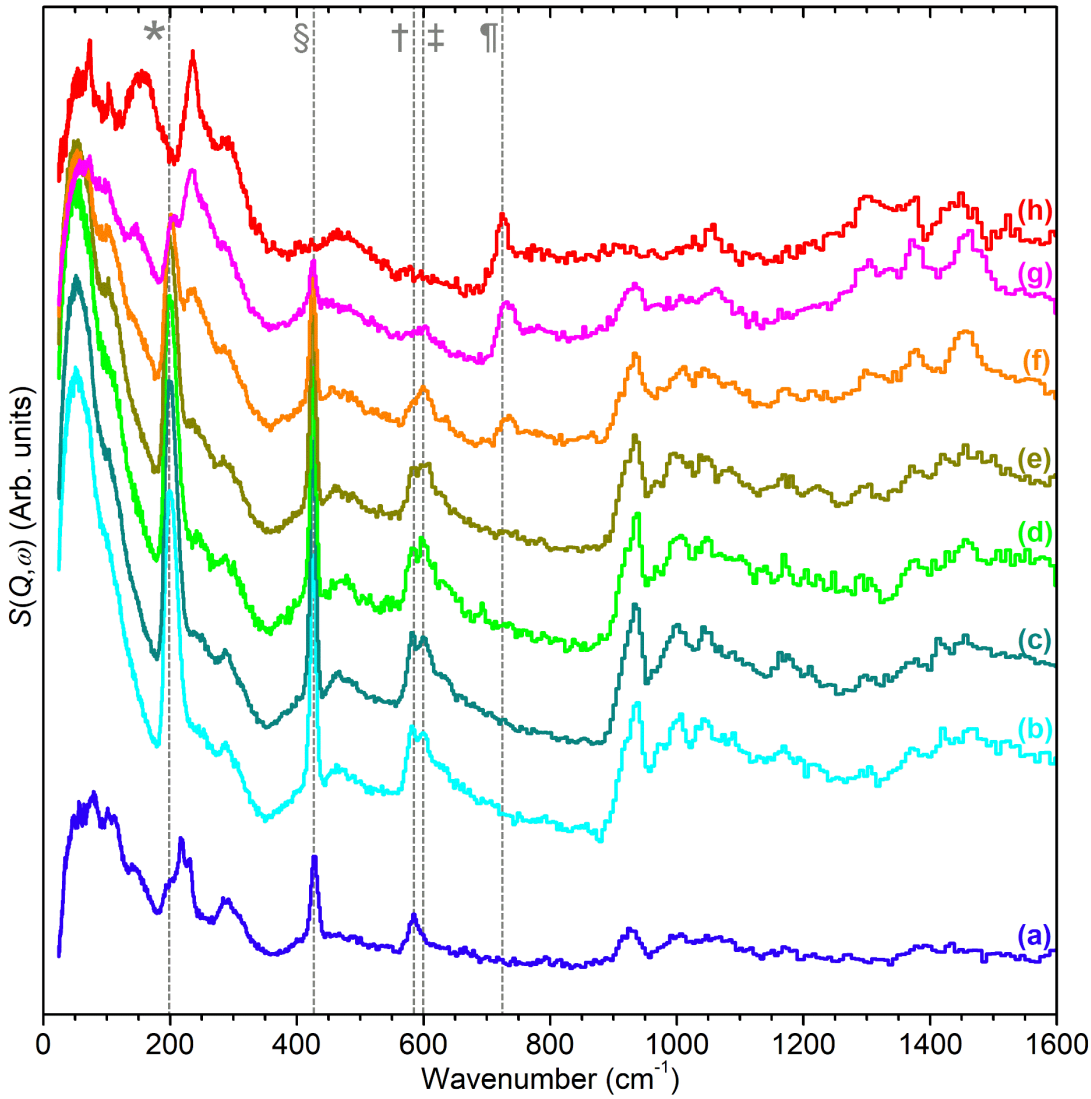

Figure 4-19: TOSCA INS spectra of propene after absorption into ZSM5-FR at 140 K (a) then following further heating to the indicated temperatures: (b) = 200 K; (c) = 215 K; (d) = 225 K; (e) = 240 K; (f) = 255 K; (g) = 270 K and (h) = 293 K. Spectra are offset in the *y*-axis for clarity. The positions of the methyl torsion (*), vinyl scissors (§) and unbonded and bonded vinyl torsions (†,‡) in the 200 K spectrum and the in-phase methylene rock (¶) in the final oligomer spectrum are highlighted.

Examining the 140 K spectrum shows all the modes that are observed in the spectrum of pure propene as before, confirming that the propene adsorption process has been completed successfully without oligomerization. A close examination of the spectrum does show one difference from the free propene data, namely the splitting of the =C-CH_3 torsion mode from a single peak at 221 cm^{-1} to a complex feature with peaks at 200, 216 and 230 cm^{-1}. From the three peaks in the 140 K spectrum, we can deduce that the propene is present in multiple environments in this sample, potentially representing internally and

externally adsorbed propene. Above 250 cm^{-1} differences between the free and 140 K adsorbed propene spectra are minor; peak assignments therefore correspond to those given in Table 3-4. In addition to the methyl torsion, modes of particular importance are the vinyl scissors mode at 429 cm^{-1} (§) and the vinyl torsion at 584 cm^{-1} (†).

After heating the sample to 200 K (Figure 4-19(b)) some changes are visible despite the QENS data suggesting that this temperature lies below the point at which significant changes in sample mobility start to occur. The most notable change is the splitting of the 585 cm^{-1} peak, corresponding to the twisting motion of the propene C=C bond, into a pair of peaks at 581 cm^{-1} (†) and 600 cm^{-1} (‡). This is attributed to the formation of an intermediate consisting of a propene hydrogen-bonded to a Brønsted acid site through the π orbitals of the C=C double bond, with this intermediate being responsible for the higher energy peak in the doublet and the remaining physisorbed propene being responsible for the 581 cm^{-1} signal. The formation of such hydrogen-bonded intermediates as the first step in the oligomerization reactions of light olefins over acid zeolites is reported in the literature.[48-49, 171-172] Although the H-bonded transition states are only observed experimentally in these reactions at low temperatures, this is regarded as a spectroscopic limitation due to their transient nature at higher temperatures. Computational studies confirm that H-bonded π-complexes remain a necessary first intermediate in the oligomerization reaction mechanism at temperatures closer to industrial conditions.[45]

An increase in overall spectral intensity relative to the spectrum at 140 K is also observed, consistent with an increase in the amount of hydrogen nuclei in the neutron beam. Since the sample cell at this point in the experiment is a closed system, the most likely source of the additional hydrogens is from the adsorption of propene previously located in the headspace of the sample cell into the zeolite. No further intensity increases relative to the 200 K spectrum are observed for the following temperature points indicating that all the propene is adsorbed at 200 K and above. Further evidence for this is provided by the shift of all the methyl torsion intensity into the peak at 200 cm^{-1} (*), indicating that all the propene present is now in the same external

environment and that the 200 cm^{-1} peak in the 140 K spectrum represents the fraction of the propene which is within the zeolite pore network at that temperature. Since neither the methyl torsion (*) nor the vinyl $=CH_2$ scissors modes (§) are split in the same fashion as the C=C torsion (†,‡) the hydrogen bonding in the intermediate does not appear to be strong enough to affect modes which do not involve the C=C bond itself.

Further heating to 215 K (Figure 4-19(c)) and 225 K (d) does not result in significant changes, although some transfer of intensity occurs between the 581 and 600 cm^{-1} peaks, indicating a slight increase in the proportion of hydrogen-bonded propene and confirming this entity to be the intermediate responsible for the higher energy peak. Reaching 240 K (e) results in new changes, namely a reduction in the intensity of peaks associated with the vinyl group, most clearly observable with the vinyl scissors mode at 430 cm^{-1} (§), and the shifting of some of the intensity in the methyl torsion peak to a higher value (235 cm^{-1}) consistent with the change in internal effects on the transition energy from being part of a longer chain length.

At 255 K (f) a broad oligomer longitudinal acoustic mode becomes visible above the level of background noise at 155 cm^{-1}. It is also clearly apparent at this temperature that there is now a further reaction step operating which consumes the C=C bond, as evidenced by reductions in the intensities of the vinyl modes (§,†,‡), and leads to the formation of methylene modes, particularly the in-phase rock at 728 cm^{-1} (¶). This confirms the initiation of the oligomerization reaction step; taking difference spectra of the higher temperature data (Figure 4-20) highlights these changes and indicates that the oligomerization has actually begun by 240 K. The growth of peaks in the methylene region of the spectrum continues until the final spectrum is achieved at 293 K. Some propene molecules remain to contribute to the spectrum at temperatures as high as 270 K, although at this temperature the 581 cm^{-1} vinyl peak has been completely suppressed, so the propene is purely present in the hydrogen-bonded intermediate form.

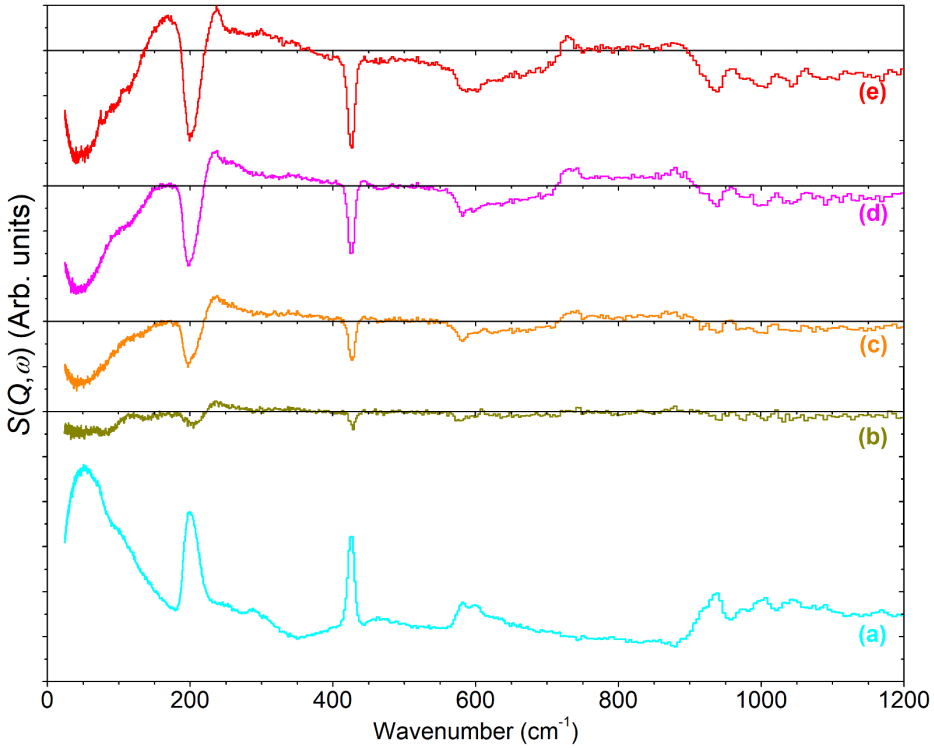

Figure 4-20: Difference plots of selected spectra from Figure 4-19 relative to the spectrum at 200 K (a): (b) = 240 K; (c) = 255 K; (d) = 270 K and (e) = 293 K. All spectra reproduced at the same scale.

4.2.2.2 A Reaction Mechanism for Linear Propene Oligomerization:

Taken together, these results can be interpreted as signifying that the oligomerization reaction proceeds via a three-step mechanism consisting of: (i) initial formation of an olefin hydrogen bonded to an acid site as an intermediate (as signified by the C=CH_2 torsion at 600 cm^{-1}), followed by (ii) protonation of the bonded olefin to form a carbocation and (iii) subsequent oligomerization of that carbocation to form the final product. This mechanism is summarised in Figure 4-21. The large temperature range from 200–240 K where the hydrogen bonded intermediate is stable is consistent with the report that it is the olefin protonation that forms the rate-limiting step in olefin oligomerizations.[48, 169] Although step (ii) of the reaction is observed to commence at a temperature close to the boiling point of free propene (225 K), this is believed to be a coincidence. Other studies of low-temperature propene oligomerization over H-mordenite report temperatures for the initiation of this phase of the reaction which are lower by over 40 K, indicating oligomerization can take place well below the free propene boiling point.[49]

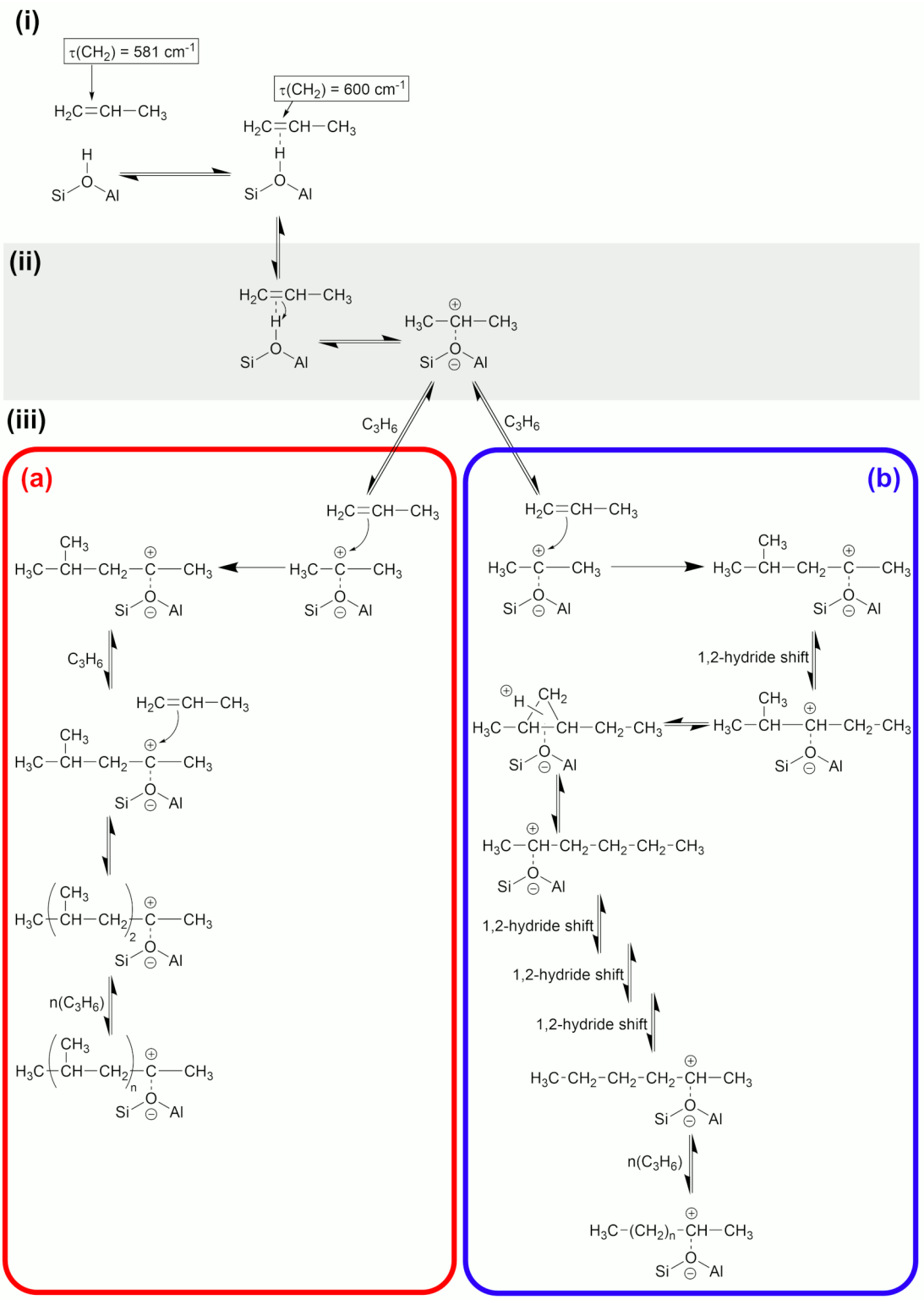

Figure 4-21: Reaction scheme showing 3-step mechanism for oligomerization of propene over ZSM-5 at exterior active sites producing branched oligomers (a) and interior sites producing linear oligomers (b). Exterior mechanism adapted from Spoto, *et al.*,[48] interior mechanism from Chen and Bridger.[26]

It is in step (iii) that we encounter the differences between the oligomerization patterns observed in the literature by infrared methods and by INS in this study.

The formation of the hydrogen-bonded intermediate is a prerequisite in both reactions: the fact that the non-bonded vinyl torsion disappears first proves hydrogen bonding is a necessary first step in our results, while the infrared studies report similarly.[48] The subsequent protonation of the hydrogen-bonded propene to form a carbocation, which forms the reactive centre for the subsequent oligomerization, is likewise common to both. Step (iii) always consists of the addition of additional propene monomers to the carbocation to form the product oligomer. Spoto *et al*. report that this oligomerization produces a product with approximately equal quantities of CH_3 and CH_2 groups based on an analysis of the C-H stretch modes in the infrared spectra. This is consistent with the mechanism being a simple stepwise addition forming polypropene, shown as mechanism (a) in Figure 4-21. However, the strong evidence of long linear chains and lack of countervailing evidence for chain branching in our INS results, indicates that this cannot be what is occurring in our sample and the methyl side chains are instead being incorporated into the oligomer backbone prior to the reaction proceeding to further oligomerization steps. Such primarily linear products have previously been observed using NMR by van den Berg *et al*. at 300 K,[173] and by Chen and Bridger at higher temperatures up to 503 K in ZSM-5 samples where the surface acid sites have been selectively deactivated;[26] they propose a 1,2-hydride shift mechanism which positions the cationic charge adjacent to the methyl branch, allowing its incorporation into the chain backbone through a protonated cyclopropyl intermediate, as shown in Figure 4-21(b). Both of these reactions are driven by the greater heat of adsorption of linear chains in the ZSM-5 pores. The series of three sequential 1,2-hydride shift reactions which are included after the cyclopropyl rearrangement are not necessary for the initial dimer formation but are necessary to reposition the carbocation charge at the accessible C_2 position following the addition of the third and subsequent propene molecules. Hydride shifts of this form are known to contribute to the rearrangement of long aliphatic carbocations and such a mechanism adequately explains our experimental results.

The reason for the difference in mechanisms is not purely an effect of reaction temperature, since the study by Chen and Bridger finds evidence of linear oligomerization at temperatures higher than those reported to cause polypropene formation by Spoto.[47] Instead the evidence appears to suggest that what we are

seeing represents a distinction between zeolite surface chemistry and that taking place in the interior pores. Both previous studies reporting linear oligomerization were NMR-based and in the case of Chen and Bridger involved a zeolite which had its exterior acid sites selectively deactivated by blockage with bulky pyridine adsorbents.[26, 171] In contrast, the study by Spoto *et al*. is likely to over-emphasise effects which occur at the zeolite surface because it utilised zeolite crystals which are unusually small (20-50 nm) with a correspondingly high exterior surface area.[47] It therefore seems likely that propene oligomerization on acid sites at or near the surface of zeolite crystals is unconstrained and produces polypropene-type oligomers, while that which occurs inside the pore structure is subject to steric constraints which favour rearrangement to a linear geometry, which dominates the product observed by bulk techniques such as NMR and INS.

For this experiment, examination of the shape of the positive peaks in the difference spectra indicates that the reacted oligomers exhibit the broadened shape characteristic of the final long-chain alkane product mixture (Figure 4-14(a)) even at the lowest temperature where reaction occurs (Figure 4-20(c,d)). Combined with the continued presence of propene molecules up to 270 K it can be deduced that the propene oligomerization reaction is extremely slow at temperatures below 270 K, but that the reaction proceeds to yield alkoxide oligomers in the same range of final chain lengths regardless of temperature. This hypothesis is consistent with the fact that kinetic studies of alkene oligomerization report carbocation chain length as not having a noticeable effect on the activation energy required for the further addition of an additional alkene onto the carbocation chain.[169] The system being in an equilibrium condition which shifts with increasing temperature is not a suitable explanation since ß-scission reactions are universally reported to become more significant with increasing temperature, which would result in a decrease in average chain length.[48, 168] Systems where ß-scission is a significant contributor are also reported to result in a product stream which is primarily olefinic in character at temperatures lower than 500 K.[172] Since neither of these observations are the case for this system it can be concluded that, for this catalyst, cracking reactions do not make a significant contribution in the temperature range investigated and the intermediate character of the hydrocarbon-zeolite system in the 225-270 K

temperature range is purely due to slow kinetics of the oligomerization reaction at these temperatures. Since the length of the oligomer chains is not temperature-dependent, it is most likely determined by steric effects from the zeolite pores. As previously noted, from the fact that the ratio of peak heights in the final spectrum does not exactly match any available model compound spectrum for linear alkanes, it can be concluded that multiple alkoxide chain lengths are present. While it is possible to obtain an estimate of the average straight chain length in bulk or aqueous linear oligomers from the energy of the longitudinal acoustic mode peak,[173-175] this analysis requires knowledge of the density and Young's modulus of the material in question. The inability to separate the oligomers from the surrounding zeolite framework therefore precludes the application of this technique in this case.

4.2.3 Propene Dynamics Studies:

Accurate investigation of the dynamics of propene in ZSM5-FR is somewhat constrained by data availability. Breakdowns in the ISIS synchrotron and spallation target system prevented the acquisition of high resolution QENS data during the beam time allocation used to collect the dataset presented in Figure 4-18; this means that no QENS data suitable for fitting analysis exists for cryogenically loaded propene prior to oligomerization. Data does exist for propene loaded at room temperature, however, this experiment was performed prior to gaining a full understanding of the oligomerization behaviour of propene in ZSM5-FR; therefore, while the sample was not loaded in such a fashion as to prevent all oligomerisation, it was also not allowed to react at 293 K long enough to proceed to completion before cooling to base temperature. The result of this is that the sample undergoes a second round of oligomerization after heating above 300 K, as visible in the EFWS results (Figure 4-22). The data at 373 K is contaminated by the results of this ongoing reaction which remove any pattern in the QENS data. The data at 273 K is unaffected and that at 323 K also proved amenable to analysis, although Figure 4-22 shows that it still has some degree of contamination and the results at this temperature should be treated cautiously.

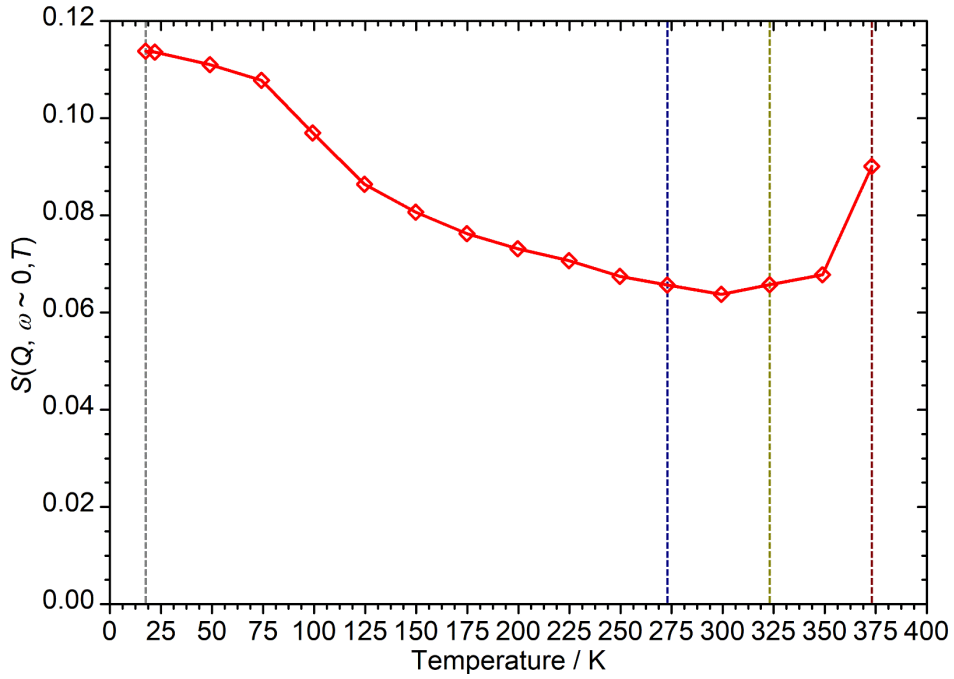

Figure 4-22: Elastic fixed window scan data for propene in ZSM5-FR from 20-300 K after dosing at 293 K. Data recorded on OSIRIS with energy transfer window for integration ± 12.5 μeV. Temperatures where higher resolution spectra were recorded are highlighted.

Both the 273 K and 323 K spectra fit to a single Lorentzian model and produce results similar to those of the 1-octene oligomer in Section 4.1.2, with the broadening being due to partially mobile uniaxial rotation of the oligomer within the zeolite pore channels. Figure 4-23 presents the resulting Γ and EISF *vs* *Q* relationships, with the fit parameters given in Table 4-2. It can be seen that both the speed of rotation and the proportion of oligomers participating is higher than achieved by the 1-octene oligomers at the same temperature. This can be attributed to shorter chain lengths in the sample due to both the incomplete oligomerization and the overall lower number of carbon atoms in the system due to the smaller size of propene.

Table 4-2: Summary of dynamical parameters derived from QENS data fitting for the combined ZSM5-FR / propene system.

Temperature (K)	P_m	Γ (μeV)	D_r (s^{-1})
273	0.236	38.0	5.78×10^{10}
323	0.478	49.5	7.52×10^{10}

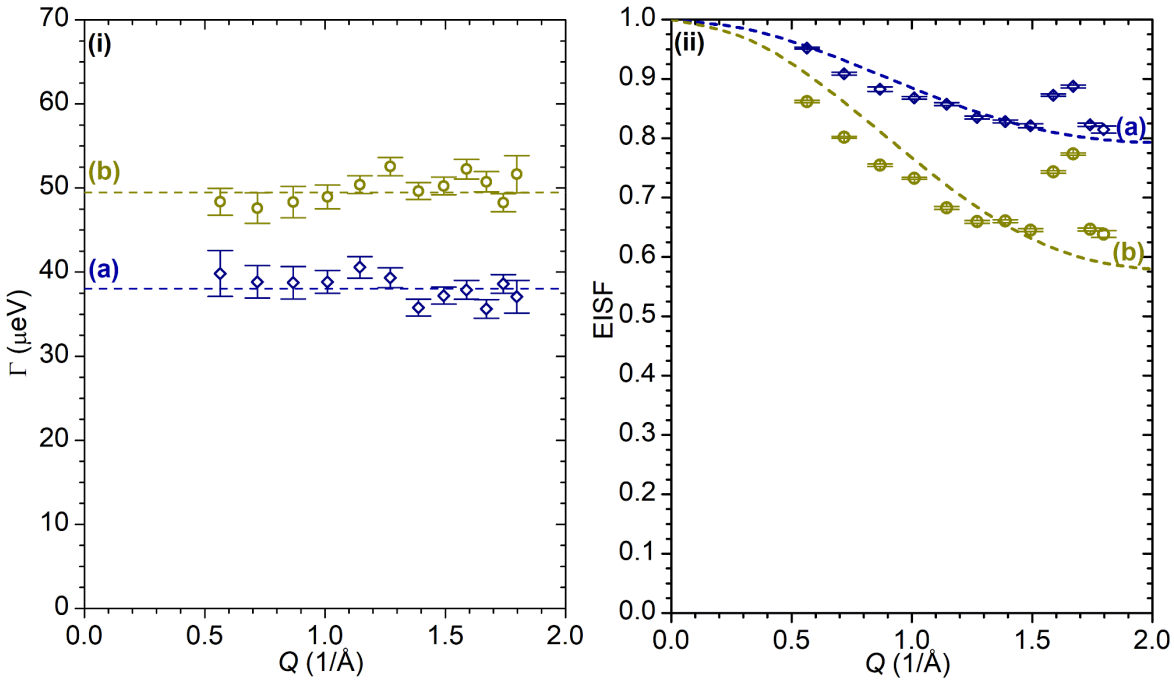

Figure 4-23: QENS fit results for propene in ZSM5-FR at 273 K (a) and 323 K (b). (i): Variation of Lorentzian linewidth (Γ) with *Q*. (ii): Variation of EISF with *Q*. Dotted lines represent fits to a model of partially-immobile uniaxial chain rotation; Γ, D_r and p_m values derived from these fits are given in Table 4-2.

Based on these results it can be assumed that the dynamics of the propene oligomer product are very similar to those observed for 1-octene above, except with a slightly higher degree of movement at each temperature due to shorter average chain lengths. Based on these differences being minor, and the rotation of the oligomer not having any relevance to catalytically interesting chemistry, it was not considered worthwhile to employ limited QENS instrument time to more fully characterise them.

4.3 Determining Dynamics in ZSM5-FR by Alternative Methods:

Due to the various effects outlined above, it has therefore not been possible to directly determine the dynamics of olefin mobility in ZSM5-FR by QENS methods. However, being able to obtain an estimate of these dynamics is still a worthwhile target both to draw conclusions on movement in fresh catalysts directly and to provide a baseline level of mobility for comparison with the mobility in less active zeolite systems considered in later chapters. It is therefore necessary to turn to

methods of investigating movement in ZSM5-FR indirectly by studies of inert models for the olefins under consideration and by computational simulations.

Since the issues with the QENS studies above lie in the complications arising from the reactivity of the alkene group on the olefin molecules used it is possible to obtain an estimate of the mobility of propene and 1-octene in ZSM-5 by investigating the dynamics of the corresponding alkanes. These will, in theory, have higher mobility than the olefins they are standing-in for due to lacking the additional effects of the hydrogen bonding between the vinyl group and the zeolite acid sites, and also being more flexible due to the absence of a C=C bond. These effects will be especially pronounced when comparing propene to propane due to the vinyl group constituting a greater proportion of the overall molecule. As noted in Section 1.3.2, there have been numerous QENS studies of alkane diffusion in zeolites; we have made use of this literature where practicable and employed QENS resources primarily to expand the available datasets to more closely match the temperature and loading ranges employed in the studies above.

Use of the molecular dynamics force field described in Section 2.2.2.2 allows the simulation of the movement of both alkenes and alkanes in the appropriate size range. Since the MD force field contains no provision for reaction, the investigated temperature range will only correspond to the actual behaviour of the alkenes at temperatures below the lower limit for oligomerization, but diffusion constant estimates should prove reasonable approximations within this limitation. As with the inert model QENS studies, the trend will be to overestimate the actual mobility of the alkene systems due to the cumulative effect of the simplifications built into the computational system to render it suitable for processing.

4.3.1 Models for C_3 Movement:

4.3.1.1 Propane QENS in ZSM5-FR:

The QENS literature on the diffusion of propane in MFI structured zeolite frameworks has some inconsistencies in its results. At a temperature of 300 K experiments by Silverwood and Sakai report that propane in ZSM-5 (Si:Al ratio 30:1) is mobile and moves by a jump diffusion mechanism with an average jump

length of *ca.* 2.9 Å and a self-diffusion constant of 5.2×10^{-9} m^2s^{-1}.[174] Unfortunately, this study was performed with a very high (and potentially non-constant) level of propane loading in the sample based on flowing propane through a zeolite bed at 48 cm^3min^{-1} and 1 bar, then stopping the gas flow to collect a 'static' mobility measurement. Exact values for the final propene loading in this study were not provided, so its utility for direct comparisons with our results is somewhat limited since self-diffusion is inversely proportional to sample loading due to congestion effects.[72] A separate study by Jobic et al. has a more representative loading but was performed using Na-ZSM-5, and the larger size of the sodium counter-ion relative to hydrogen likely explains why the measured diffusivity in this study is considerably lower at 1.3×10^{-9} m^2s^{-1}.[69] Both studies do, however, agree on the propane diffusing by a jump mechanism. Molecular dynamics studies report results broadly in line with the first of these QENS experiments;[175-176] although MD involves a considerable number of simplifications, particularly in the case of these studies which simulated a pure SiO_2 silicalite framework without acid sites, they do support the conclusion that propane likely diffuses in H-ZSM-5 by a jump diffusion mechanism with a diffusion constant in the region of 5×10^{-9} m^2s^{-1} at 300 K. These literature results are summarised in Table 4-3 for easier comparison.

Table 4-3: Comparison of values for the diffusion parameters of propane in MFI-structured zeolites taken from the literature. $\sqrt{\langle r^2 \rangle}$ represents mean jump distance, τ residence time between jumps.

Source	Method	Zeolite	Loading (mol / u.c.)	τ (ps)	$\sqrt{\langle r^2 \rangle}$ (Å)	D_s (m^2s^{-1})
Silverwood and Sakai.[174]	QENS	H-ZSM-5	Unknown	3	2.86	5.2×10^{-9}
Jobic, *et al.*[69]	QENS	Na-ZSM-5	4	90	3.84	1.3×10^{-9}
Nowak, *et al.*[175]	MD	Silicalite	8	-	-	4.1×10^{-9}
Leroy, *et al.*[176]	MD	Silicalite	4	-	-	4×10^{-9}

In order to collect comparable EFWS data and mobility at the temperatures of greatest interest, a 2.583 g sample of ZSM5-FR was subjected to QENS analysis from 20 – 370 K with high resolution spectra collected at 20, 170, 220 and 370 K (see Section 2.1.3.4 for method.) The propane loading level was 2.343×10^{-3} moles, equivalent to 4.73 propane molecules per unit cell. Comparison of the

EFWS results with those obtained for the cryogenically-loaded propene / ZSM5-FR system discussed in Section 4.2.2.1 above (Figure 4-24) shows that, as expected, the propane spectrum shows considerably higher mobility than the propene equivalent and exhibits no signs of any reaction chemistry occurring up to the maximum temperature of the test. From 20 – 180 K the rate at which propane gains mobility with increasing temperature is higher than that of the propene trace, likely due to different melting behaviour of the solid propane. From 180 – *ca*. 220 K there is a brief temperature window where both samples appear to be in the liquid phase but the propene oligomerization reaction has not yet begun; comparing the relative elastic intensities in this region indicates that the overall mobility of propane appears to be approximately twice that of propene under the same conditions.

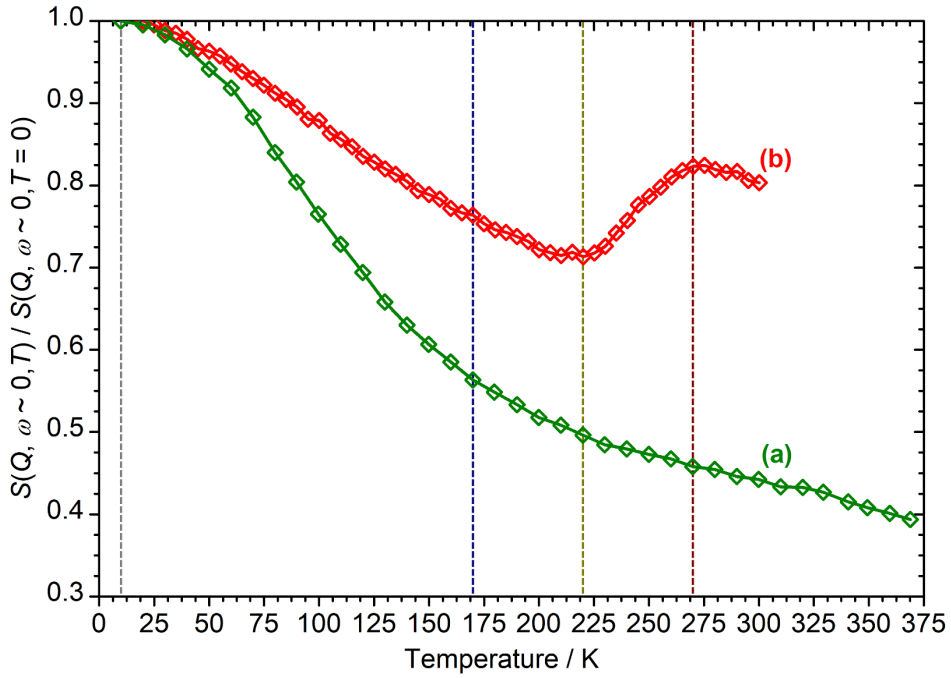

Figure 4-24: Elastic fixed window scan data for propane in ZSM5-FR from 20-370 K (a) compared with the EFWS for propene in ZSM5-FR from Figure 4-18 (b). Propane data recorded on IRIS with energy transfer window for integration ± 8.75 μeV; relative intensities normalised against values at the lowest temperature to allow comparison. Temperatures where higher resolution propane spectra were recorded are highlighted.

The QENS data at 170, 220 and 270 K had the zeolite contributions removed by subtraction of the unloaded spectra and were fitted for analysis. The data at all

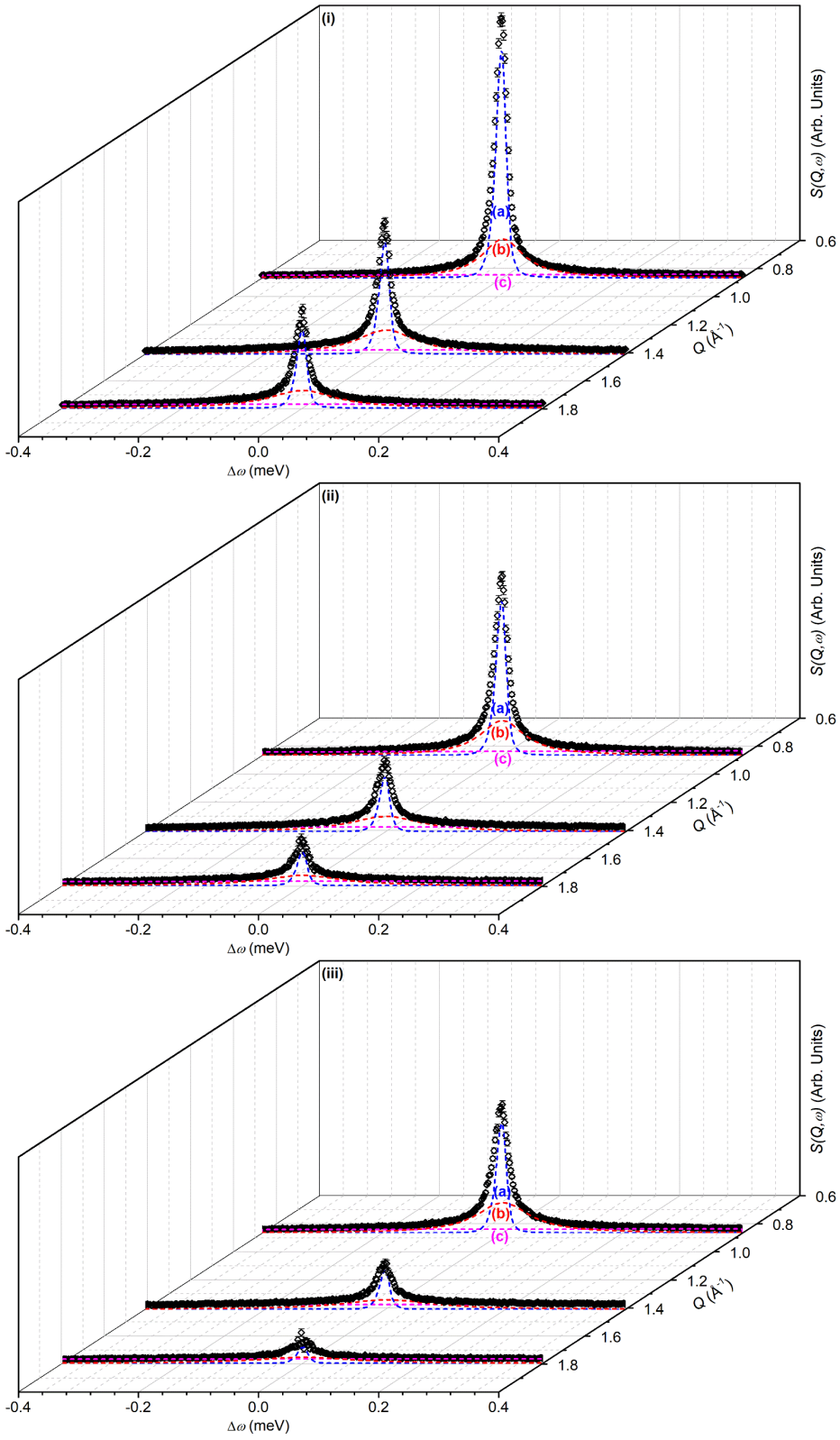

Figure 4-25: $S(Q,\omega)$ functions at selected values of Q for propane in ZSM5-FR at 170 K (i), 220 K (ii) and 270 K (iii) showing deconvolution into resolution function (a), quasielastic Lorentzian (b) and linear background (c) contributions. $S(Q,\omega)$ axis scale is identical between graphs.

three temperatures is best described by a combination of the resolution and background functions with a single Lorentzian as in the oligomer studies above, however, the intensity of the quasielastic contributions, both Lorentzian and linear background, is considerably higher. The resulting S(Q,ω) functions include strong contributions from both immobile propane at low *Q* and moving propane across the entire *Q* range, as shown in Figure 4-25 for selected *Q* values.

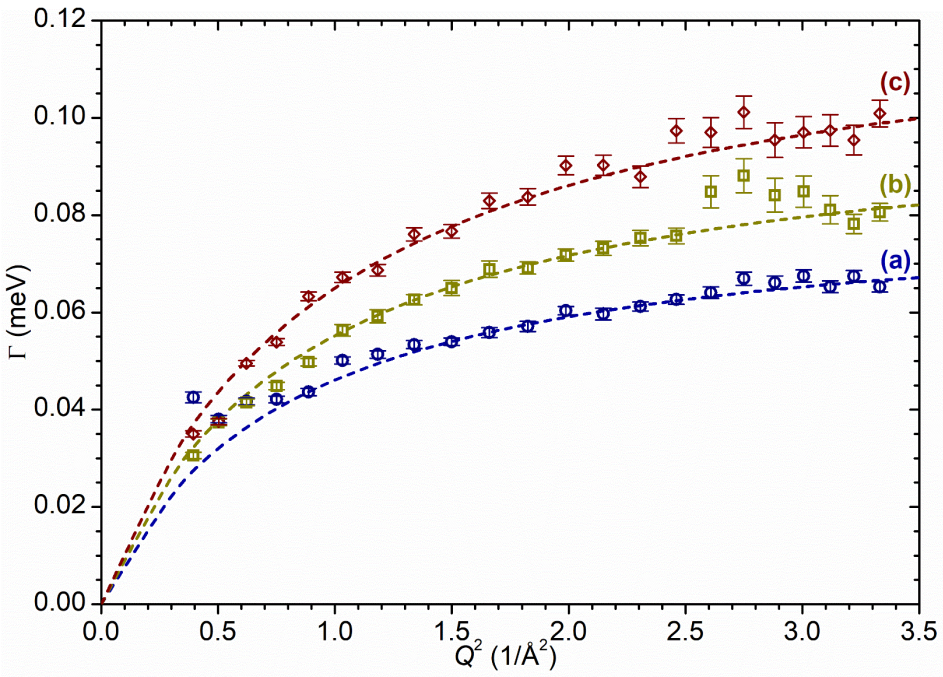

Figure 4-26: Variation of Lorentzian linewidth (Γ) as a function of Q^2 for propane in ZSM5-FR at 170 K (a), 220 K (b) and 270 K (c). Dotted lines represent best fit of the data to the Singwi-Sjölander model using the parameters given in Table 4-4.

Figure 4-26 shows the variation of the Lorentzian HWHM parameter as a function of Q^2; it can be seen that the behaviour is similar at all three temperatures. Although all points lie well clear of the IRIS resolution limit at 17.5 μeV, the Lorentzian fit is unreliable below approximately 0.75 $Å^{-2}$ due to low intensity. The presence of a zeolite Bragg peak in the 2.6 $Å^{-2} \leq Q^2 \leq$ 2.9 $Å^{-2}$ range results in a large decrease in the signal:noise levels in the subtracted propene-only function due to much stronger contributions from the immobile zeolite. This leads to increased noise in the final results and tends to overstate the amount of broadening in this region, resulting in the anomalous values observed in the 220 K data. The type of non-linear Q^2 dependence observed here is characteristic of broadening due to jump diffusion, with the present case most closely

corresponding to the model of Singwi and Sjölander. This proposes a system where the scatterers perform periodic jumps between low-energy positions but are also able to oscillate around those positions between jumps, with the peak width variation given by:

$$\Gamma(Q) = \frac{1}{6\tau} \frac{Q^2\langle r^2\rangle}{1 + \frac{1}{6}(Q^2\langle r^2\rangle)} \tag{4.5}$$

where τ is the residence time between jumps and $\langle r^2\rangle$ the mean square jump length.[177] A least-squares fit of the data to this equation gives the traces shown as the dotted lines in Figure 4-26. Table 4-4 presents the derived values for τ and $\langle r^2\rangle$, together with calculated values for the self-diffusion coefficient. Since the Singwi-Sjölander model involves a range of jump lengths the self-diffusion constant is calculated from the mean square jump length by:

$$D_s = \frac{\langle r^2\rangle}{6\tau} \tag{4.6}$$

Table 4-4: Summary of diffusion parameters derived from QENS data fitting for propane in ZSM5-FR.

T (K)	τ (ps)	$\sqrt{\langle r^2\rangle}$ (Å)	D_s (m^2s^{-1})
170	8.01	2.77	1.60×10^{-9}
220	6.45	2.67	1.84×10^{-9}
270	5.17	2.51	2.03×10^{-9}
D_0 (m^2s^{-1})		3.00×10^{-9}	

The differences in jump length distribution may be regarded as being within the level of experimental error in the fit analysis, meaning that the process which is being modelled by this Lorentzian corresponds to propane diffusing through jumps of approximately 2.7 Å length with the time between jumps decreasing with temperature. This jump length indicates that the jumps in this motion are not occurring between pore intersections in the zeolite framework, which are separated by 9 Å in the straight [010] channels and 12 Å in the [100] channels, but represents movements on a shorter length scale. Since the distance is also less

than the diameter of the 10-ring framework window which forms the limiting radius of the zeolite pores (5.1 × 5.5 Å in the narrower sinusoidal channel) it is likely that propane-propane interactions play an important role in determining the favoured jump length. The values for the diffusion coefficients follow a linear Arrhenius relationship across the temperature range investigated (Figure 4-27) allowing an estimate of 0.89 kJ mol^{-1} to be made for the activation energy of this motion.

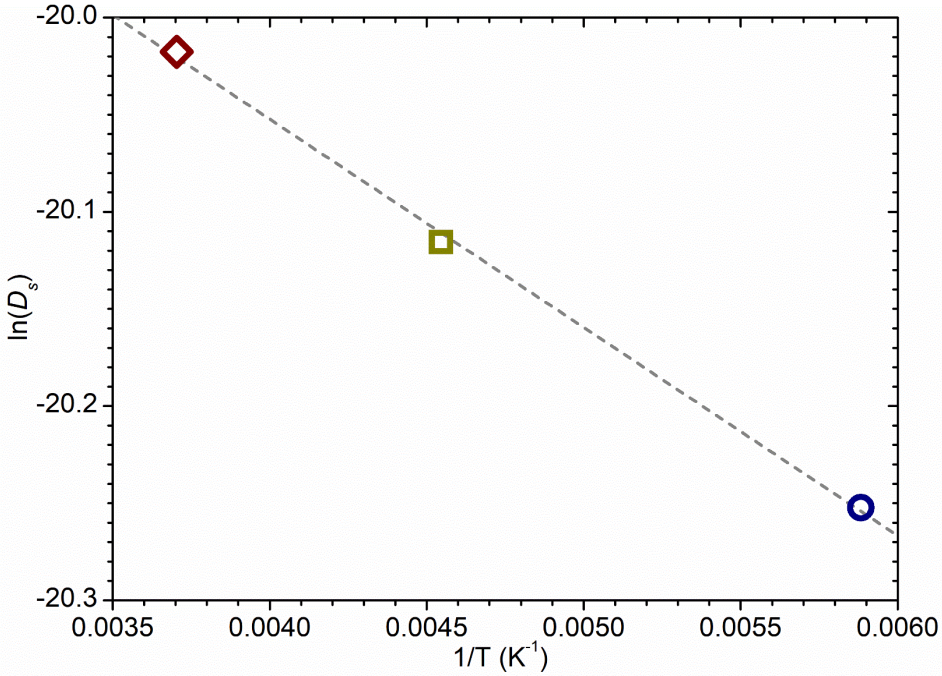

Figure 4-27: Arrhenius plot of the self-diffusion coefficients of propane in ZSM5-FR at 170, 220 and 270 K showing a linear relationship across this temperature range. Line of best fit to the experimental data shown as the dotted line, giving an activation energy of 0.86 kJ mol^{-1} for this motion.

Extrapolating this relationship gives an estimated self-diffusion coefficient at 300 K of 2.10 × 10^{-9} m^2s^{-1}, meaning that these results lie in the middle of the QENS literature values in Table 4-3. This also matches well with the literature computational results, since as noted MD simulations will generally return an upper limit estimate of sample diffusivity. Calculated jump lengths are essentially identical to those reported by Silverwood and Sakai,[174] suggesting that we are observing the same motion as reported in that study, but with a longer residence time between jumps. The reason for the longer residence time is somewhat less clear; it may be connected to differences in the sample loading but in order to develop more detailed theories it is necessary to understand exactly what motion

we are observing and where in the zeolite it occurs, information which can be provided by our own computational simulations.

4.3.1.2 C_3 MD Simulations in ZSM-5 Framework:

Simulations were performed of both propane and propene molecules in a ZSM-5 zeolite framework using the force field parameters and simulation procedure described in Section 2.2.2.2 and 2.2.2.3. The simulated system incorporated 4 adsorbate molecules per ZSM-5 unit cell, with starting positions prior to equilibration in both the straight and sinusoidal channels in order to ensure an even distribution of the adsorbates. Simulations were performed at 170, 220 and 270 K to match the QENS investigations, with additional simulations at 300 K to provide a direct comparison with literature data and at 320 and 370 K to extend the range of information to match that of the EFWS analysis. It should be noted that the propene simulations at 270 K and above lie above the minimum temperature for oligomerization and therefore do not correspond to the system as it will behave in reality. They are included in order to provide a wider range of comparison points between the alkene and alkane dynamics in order to better understand the effect of the double bond on the zeolite-hydrocarbon interactions.

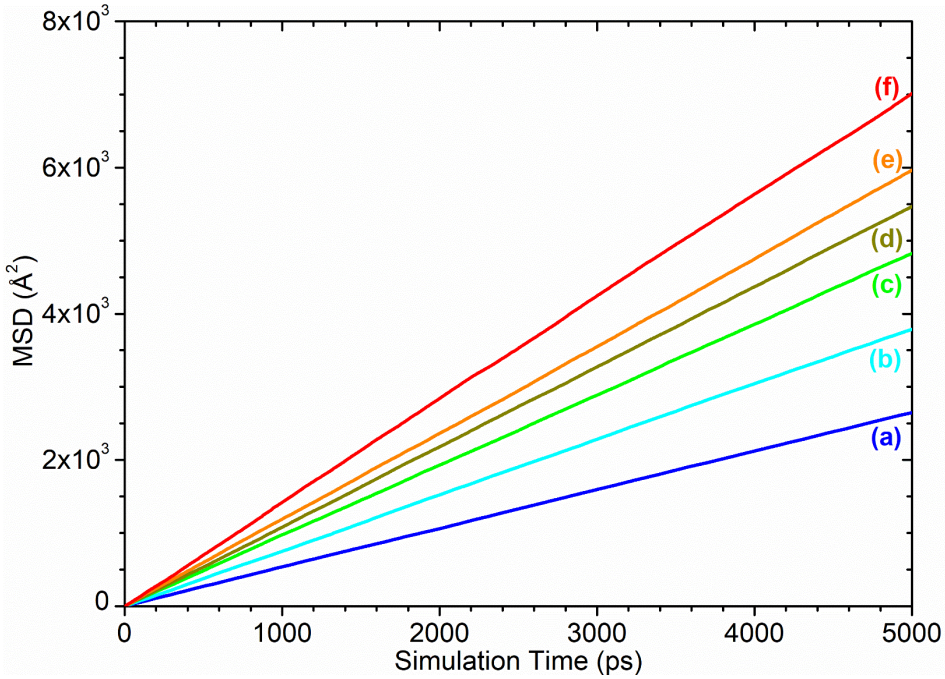

Figure 4-28: Average mean squared displacement versus time for propene in H-ZSM-5 at a loading of 4 molecules per unit cell calculated at simulation temperatures of 170 K (a), 220 K (b), 270 K (c), 300 K (d), 320 K (e), and 370 K (f).

Accurate calculation of diffusion constants from the statistics of molecular dynamics simulations requires simulation lengths long enough that the system achieves true diffusive motion and the mean squared displacement (MSD) of the adsorbed molecules becomes linear with respect to time. As shown in Figure 4-28 for the propene simulation, when averaged over all 32 hydrocarbon molecules the systems studied here achieve this for essentially the entire simulation runtime and the MSD, and hence self-diffusion coefficient, may be calculated from the data in the 1-5 ns region.

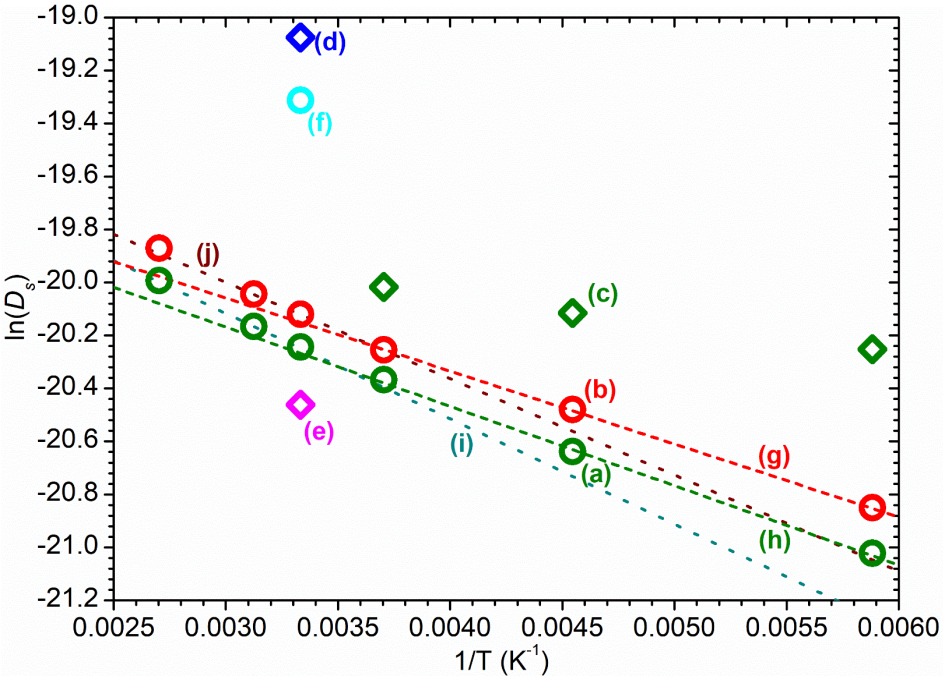

Figure 4-29: Arrhenius plot comparing diffusion constants derived from MD and QENS methods. Simulations of propane (a) and propene (b) in H-ZSM-5 framework are compared to QENS results for propane in ZSM5-FR (c). Literature values of propane diffusion in different environments from Table 4-3 are included for comparison: QENS measurements of diffusion in H-ZSM-5 at a high but undefined loading level by Silverwood and Sakai[174] (d), of diffusion in Na-ZSM-5 at more comparable loading levels by Jobic *et al.*[69] (e) and the results of comparable MD simulations of diffusion in silicalite by Nowak *et al.*[175] (f). Dotted lines represent linear fits of the MD data in the 170 – 270 K region to determine E_a (g,h) and in the 300 – 370 K region to make the different relationship in this region more apparent (i,j).

Examining an Arrhenius plot of the available diffusion data (Figure 4-29), it can be seen that the simulations exhibit a slightly different *T vs.* D_s relationship in the 300 – 370 K region than that in the 170 – 270 K region which aligns with the

availability of QENS data, something likely attributable to the effect of the adsorbates entering the gas phase. Linear fits of the three lower data points have been used to derive the activation energy of the movement in this region for comparison with the QENS results with the values summarised in Table 4-5.

Table 4-5: Self-diffusion coefficients (D_s) and activation energies (E_a) for propene and propane in H-ZSM-5 calculated from MD results. Values for propene marked (*) are above the minimum temperature for oligomerization in real systems and so the reported D_s values will not be observable experimentally. The ratio of the propane MD values to the propane in ZSM5-FR QENS data in Table 4-4 is provided for comparison.

T (K)	D_s (m^2s^{-1})		Ratio MD : QENS (Propane)
	Propene	Propane	
170	8.80×10^{-10}	7.41×10^{-10}	0.46 : 1
220	1.23×10^{-9}	1.09×10^{-9}	0.59 : 1
270	$*1.60 \times 10^{-9}$	1.43×10^{-9}	0.70 : 1
300	$*1.83 \times 10^{-9}$	1.62×10^{-9}	-
320	$*1.97 \times 10^{-9}$	1.75×10^{-9}	-
370	$*2.35 \times 10^{-9}$	2.08×10^{-9}	-
D_0 (m^2s^{-1})	4.44×10^{-9}	4.28×10^{-9}	-
E_a (kJ/mol)	2.29	2.49	2.80 : 1

It can be seen that the diffusion constants for the propane simulation are slower than both the values from the literature and, where equivalent data exists, those derived from QENS analysis. The differential relative to the QENS results is clearly due to the activation energy in the MD simulations being almost three times higher than that estimated by QENS, with the result that the differential between QENS and MD results decreases sharply with temperature. Extrapolation of the Arrhenius trends in Figure 4-29 suggests that the MD predicted mobility would exceed that measured by QENS if data collection was performed above 400 K. The MD simulations performed here also give values considerably below those in Table 4-4.

An additional issue with the MD simulation data can be seen by comparing the values reported for the propene and propane simulations, which shows the propene simulation as having a higher mobility. Although the difference between

the two simulations is small at 10 – 15 %, it is consistent across the temperature range and is also reflected in the activation energies derived for each system. A hypothesis consistent with these results would be that the force field used in these simulations overestimates the magnitude of interactions between the zeolite framework and alkane carbons and hydrogens and underestimates the magnitude of the zeolite-alkene interactions. This results in the diffusion behaviour of the simulation being dominated by overly strong steric effects, resulting in the under-prediction of mobility in both cases, with the slightly smaller propene molecule resulting in a higher level of mobility which outweighs the individually stronger zeolite – alkene potentials. In order to rule out the possibility of the lower mobility being due to the opls2005 force field predicting excessively strong hydrocarbon-hydrocarbon interactions, a simulation was performed where the intermolecular hydrocarbon potentials were replaced with terms taken from work by O'Malley and Catlow that achieved close agreement with QENS measurements of octane (see below);[74] the results of this simulation matched those in Table 4-5 to within 10 %, indicating that this cannot be the cause of the reduced mobility in these simulations.

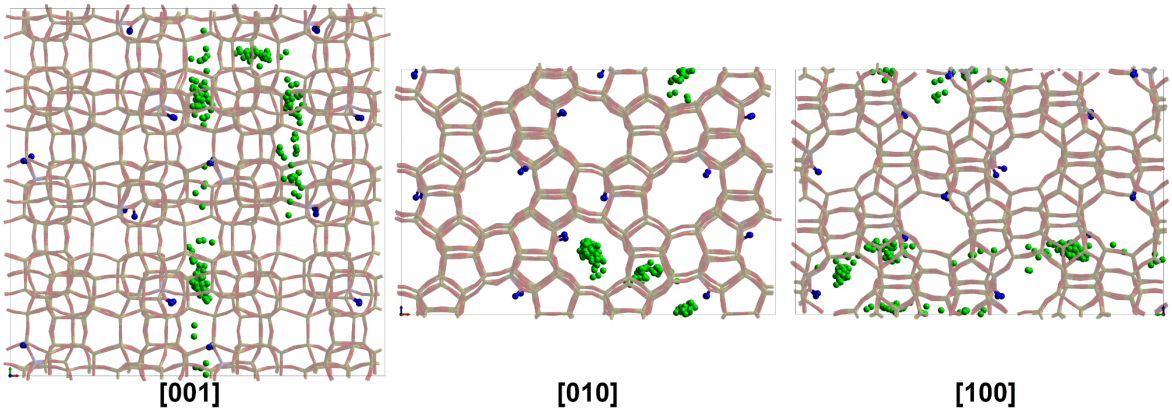

Figure 4-30: Centre of mass positions for a molecule of propene diffusing in ZSM-5 at 270 K as simulated by MD showing preferential positioning outside pore intersections. Positions logged at 5 ps intervals over 1 ns simulation time.

Although the mobility of the MD simulations does not appear to closely match the experimental data at the macro level, examination at the micro level does provide some potential insight into the question raised above concerning the source of the *ca.* 2.8 Å jump length observed in the majority of the QENS experiments considered. Examination of the trajectories of the molecules in the simulation

indicates that they appear to prefer to spend the majority of the simulation time inside the pore channel sections of the zeolite (Figure 4-30). While in these locations the molecule performs small jumps which do not involve it entering the channel intersections or coming into close proximity to the pore walls, and the size of this apparent radius of confinement is approximately 3 Å, corresponding to the jumps observed by QENS. Transitions across the intersections to enable longer-ranged diffusion occur at longer time intervals which would likely not be observable by experiments on IRIS or OSIRIS. It is therefore likely that it is this type of localised motion which is being observed by QENS measurements, and the excessively strong interactions in the MD force field reduce the measured mobility by increasing the residence time between these jumps. The fact that this force field has greater success in describing the movement of C_8 species (see Section 4.3.2.2) may be due to the larger molecules not fitting entirely within a single pore volume, reducing this effect less significant.

4.3.2 Models for C_8 Movement:

4.3.2.1 Octane QENS Literature:

QENS literature on the movement of gasoline-range alkanes in MFI structured zeolites is both more comprehensive and more up-to-date than that available for propane. Of particular note, a 2000 study by Jobic provides information on the movement of octane in H-ZSM-5 with both a range of temperatures and sample loading level that closely match those used in this thesis.[72] The reported self-diffusion constants are approximately 40 times smaller than those measured for the movement of 1-octene in the bulk phase in Section 3.3.1, a difference which seems reasonable given the likely effect of confinement within the zeolite pore network. They are also *ca*. 25 % of those reported for similar movements in silicalite by Jobic and Theodorou,[71] although the degree to which this disparity is due to the acid sites cannot be determined with complete accuracy since the effect of differing sample loadings also contributes. Exact values are reproduced in Table 4-6 together with values derived from MD simulations by O'Malley and Catlow; these simulations are performed under identical conditions to the silicalite QENS study and achieve a close overall agreement by MD standards, being

approximately 3x faster than the experimental values due to the lack of defects, edge effects and silanol nests.[74] This study is also important because it is the source of the flexible zeolite parameters which forms the basis of the force field used in the simulations in this thesis following modification with terms to simulate Brønsted acid groups as described in Section 2.2.2.2. Based on the availability of this data it was decided to forgo additional QENS measurements of the octane - ZSM-5 system to allocate available instrument time to higher-priority measurements.

Table 4-6: Comparison of values for the self-diffusion constants of octane in MFI-structured zeolites taken from the literature.

Source	Method	Zeolite	Loading (mol / u.c.)	D_s (m^2s^{-1})		
				300 K	350 K	400 K
Jobic.[72]	QENS	H-ZSM-5	5	5.2×10^{-11}	8.0×10^{-11}	1.1×10^{-10}
Jobic and Theodorou.[71]	QENS	Silicalite	1.56	2.0×10^{-10}	2.8×10^{-10}	3.9×10^{-10}
O'Malley and Catlow.[74]	MD	Silicalite	1.56	6.0×10^{-10}	8.8×10^{-10}	1.1×10^{-9}

4.3.2.2 C_8 MD Simulations in ZSM-5 Framework:

Table 4-7: Self-diffusion coefficients (D_s) and activation energies (E_a) for 1-octene and octane in H-ZSM-5 calculated from MD results. Fitting for E_a and D_0 values excludes the 170 K data point due to melting point issued with 1-octene.

T (K)	D_s (m^2s^{-1})	
	1-octene	Octane
170	2.91×10^{-10}	2.97×10^{-10}
220	4.35×10^{-10}	4.47×10^{-10}
270	5.90×10^{-10}	5.77×10^{-10}
320	7.55×10^{-10}	7.24×10^{-10}
370	8.92×10^{-10}	8.94×10^{-10}
D_0 (m^2s^{-1})	2.57×10^{-9}	2.72×10^{-9}
E_a (kJ/mol)	3.20	3.42

Simulations were performed for both octane and 1-octene at a loading level of 4 molecules per unit cell; the framework was ZSM-5 using the model described by Section 2.2.2.2 as before. Simulation temperatures were 170, 220, 270, 320 and 370 K. Results are reported in Table 4-7 and Figure 4-31, with the Arrhenius plot including data from Table 4-6 for comparison.

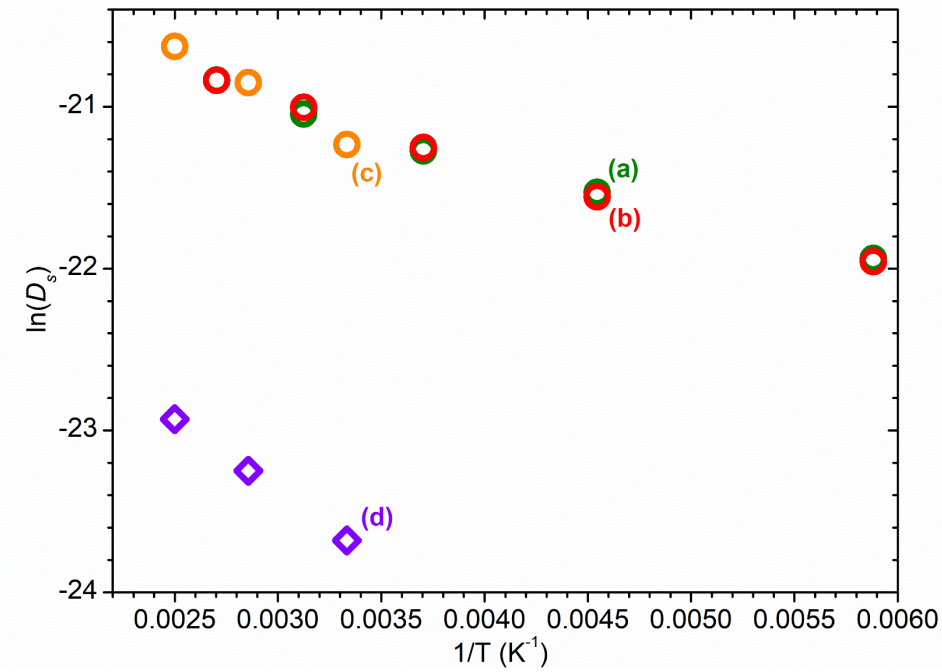

Figure 4-31: Arrhenius plot comparing simulations of octane (a) and 1-octene (b) in H-ZSM-5 framework to literature results for octane measured in H-ZSM-5 by MD (c) and QENS (d). Literature MD results taken from O'Malley and Catlow,[74] QENS results from Jobic.[72]

Two facts are immediately apparent. Firstly, the differences between the 1-octene and octane simulations are much smaller, on the order of 10 % the size of the differences observed between propene and propane. As a result, these differences likely lie within the margin of experimental error as can be seen by the fact that which simulation is more mobile varies between temperature points. This is, as noted above, an expected effect of the fact that 75 % of the adsorbate molecule is identical between the two systems and the effect of the alkene bond will therefore be correspondingly small, even without accounting for the possible over-emphasis on alkane interactions tentatively identified from the propane / propene data. Secondly, the results obtained are in reasonably close agreement with the results of the MD simulations from Table 4-6 in the range where data exists for comparison, validating the results of our C_8 MD simulations against

published data. The lower activation energy which is observed for our simulations is attributed to greater flexibility in the simulated octane chain. The cited study uses a force field with a quite stiff alkyl backbone due to high energy barriers in the C-C-C-C dihedral parameters; this results in channel switching by the octane molecules only being observed at 350 K and above. The parameters used in this study result in higher chain flexibility, with channel switching being observed down to 220 K.

4.4 Summary:

When adsorbed into a fresh zeolite sample the high activity of ZSM5-FR is capable of triggering rapid oligomerization of both propene and octene even at quite low temperatures. In the case of propene this reaction can occur at temperatures as low as 225 K, although the amount of oligomer formation only becomes large enough to be noticeable in the vibrational spectrum at temperatures of 240 K and above. INS investigations have allowed clear observation of the deformation modes of both the final oligomer product and, in the case of propene, the intermediates formed during the oligomerization reaction. These results indicate that the oligomerization reaction proceeds *via* a two-step mechanism with the formation of a hydrogen-bonded intermediate as a first step. This intermediate is then protonated, which forms the rate-limiting step in the reaction, to form a zeolite-bonded carbocation which is the reactive centre for the further addition of alkenes to form the oligomers. At low temperatures the carbocation undergoes rearrangement after each stepwise addition to incorporate side branches into the chain backbone, forming linear oligomer products. The chain growth process is still too rapid to be observed in progress at all temperatures and the ultimate chain termination length is believed to be dictated by pore steric effects, evidenced by the fact that the same product spectrum is produced regardless of the dosing temperature up to 373 K. The resulting bonded alkoxides are in the long oligomer / short polymer length scale.

The effects of the oligomerization reaction prevent the measurement of the mobility of propene or 1-octene in ZSM5-FR but do allow the reaction to be observed in progress through the resulting change in sample mobility and allows

the determination that a temperature-dependant proportion of the product oligomers is able to undergo uniaxial rotation within the zeolite after formation. The use of inert analogues has proven more successful and has allowed the collection of data on the movement of propane in ZSM5-FR, showing that from 170 – 270 K it undergoes short jumps on the order of 2.8 Å with a residence time between jumps determined by temperature. These results are broadly in agreement with previous publications in the literature. MD simulations using the model from Section 2.2.2.2 have proven able to simulate C_8 species with good accuracy but are less accurate in the simulation of smaller C_3 species, possibly due to an improper parameterization of the zeolite-olefin interactions. In order to test this hypothesis, it is necessary to gain an understanding of the effect of the Brønsted acid sites on the hydrocarbon interactions and resulting dynamics; the attempts to address this question were not entirely successful and are therefore presented in Appendix 2. The next chapter moves forward to consider the effect of framework de-alumination on the interactions of zeolites with adsorbed hydrocarbons.

Chapter 5: The Effect of Catalyst Aging on Zeolite-Olefin Interactions

In industrial use, zeolite catalysts undergo progressive loss of acidity over the course of the catalyst lifetime due to hydrothermal de-alumination of the zeolite framework and associated removal of acid sites. This naturally has subsequent effects on reactivity and motion of adsorbed hydrocarbons due to reduced acid-hydrocarbon interactions, with resulting changes to catalytic activity and selectivity. Zeolite samples with equivalent properties to extensively used FCC or oligomerization catalysts may be prepared by accelerated aging of the fresh catalyst by steam treatment at high temperature. We here report the preparation and characterisation of a series of these aged zeolites and the comparison of their olefin interactions with the results for the fresh zeolite considered in Chapter 4. The results obtained illustrate the rapid nature of the initial de-alumination and point toward the poor nature of fresh zeolite samples as models for actual catalysts after any significant degree of time-on-stream.

5.1 Effects of Hydrothermal De-Alumination on ZSM-5:

The acid site density and the mean diffusion path within a zeolite catalyst are the most important factors in determining how it interacts with reactive substrates. This in turn determines its catalytic activity because of the positioning of the reaction within the pore network governing how it is affected by shape selective effects as discussed in Section 1.2. As mentioned there, these acid properties do not remain constant throughout the catalyst's useful lifetime as hydrothermal conditions in catalytic use result in partial de-alumination of the zeolite framework, with a corresponding reduction in the number of acid sites and increased mesoporosity due to removal of portions of the framework.[33] The effects of this loss of acidity in leading to improved selectivity, stability and even activity in steamed zeolites relative to studies performed using fresh materials have been reported in several studies.[34-35, 178]

The rate of de-alumination is first order with respect to the number of aluminium substitutions within the zeolite, meaning that loss of acidity is initially rapid before the catalyst achieves a pseudo steady state level of acidity which it occupies for the majority of its active lifetime.[31] Theoretical studies of the hydrothermal mechanism suggest that it proceeds in a stepwise fashion for each bond of the aluminium T-atom.[179] Water is initially adsorbed onto the Al atom at an anti-position to the Brønsted acid bridge (Figure 5-1(a)). This leads to an Al-O hydrolysis through a 1,2-dissociation of the adsorbed water molecule which converts the Brønsted site to a silanol and protonates one of the remaining Al-O-Si bridges (Figure 5-1(b)). This process may then be repeated to break the remaining three oxygen bridges, generating a silanol nest in the place of the aluminium T-atom and an extra-framework aluminium (EFAl) entity. This stepwise mechanism is important because it means it is possible for an aluminium site in the zeolite to be in an intermediate state, where it is partially removed from the framework. However, the increased flexibility of these partially removed aluminium sites renders the energy barrier to additional hydrolysis reactions lower than that of the first reaction.[179] Therefore, at least in theory, the majority of the aluminium sites in a partially de-aluminated zeolite should be either fully removed

from the framework or unaffected, with partially hydrolysed aluminium atoms being a minority species.

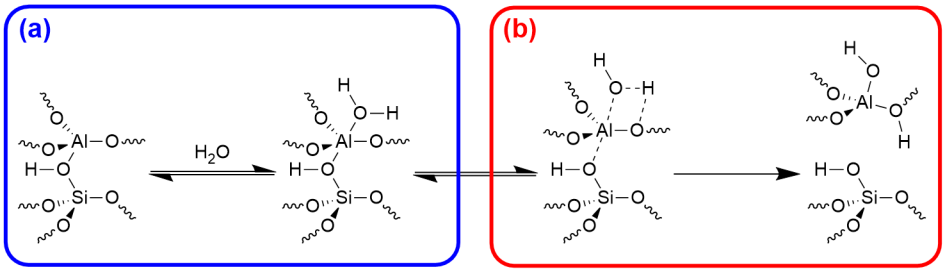

Figure 5-1: Reaction scheme for the breaking of an Al-O(H)-Si bridge in an acid zeolite by hydrolysis. Mechanism adapted from Silaghi et al.[179]

It is evident that knowledge of how these framework changes affect fundamental properties, such as diffusion and acid site bonding in the zeolite, is therefore key to understanding the catalytic activity and the mechanism of zeolites in industrial use at any point in time beyond their initial reactivity. Fortunately, changes due to de-alumination from catalytic use can be simulated by deliberately inducing de-alumination of fresh zeolite by steam treatment. In studies of the MTH reaction, experimental tests have shown that steam treatment of a zeolite under a given set of conditions produces a final material with similar levels of aluminium removal to a sample used catalytically for the same length of time under the same conditions.[180] It is therefore possible to generate model zeolite materials whose properties closely match those of used or partially-deactivated catalysts.[31, 33, 96]

Thus, in order to investigate the effects of acid site loss, a series of partially de-aluminated zeolite samples was prepared in order to compare their properties with the results obtained from investigations of ZSM5-FR as reported in earlier chapters. Since the first order rate of the de-alumination reaction means that catalysts will spend the majority of their catalytic lifetime in a significantly de-aluminated state, steam treatment conditions were deliberately chosen in order to induce a high level of acid site loss. Two steaming protocols were used, depending on the availability and capabilities of sample preparation equipment. As detailed in Section 2.4.3, the resulting zeolites are designated ZSM5-ST(873K) and ZSM5-ST(1073K) for unambiguous reference. The first step is therefore to

characterise the properties of these treated materials and how they relate to those of ZSM5-FR.

5.1.1 Characterisation of Steamed Catalysts:

Table 5-1 summarises the results of the characterisation analyses, which confirm that both steam treatment protocols have resulted in extensive de-alumination of the treated zeolite framework. It is also clear that the properties of both treated materials are remarkably similar despite the differences in steaming temperature and duration. In particular, the key parameters of framework aluminium level and Brønsted acidity are identical to within the limits of accuracy of the characterisation measurements.

Table 5-1: Comparison of the structural and acid properties of ZSM5-FR, ZSM5-ST(873K) and ZSM5-ST(1073K) as established by zeolite characterisation measurements.

Sample	^{27}Al NMR		Ammonia TPD		BET Surface Area	
	Total Relative Intensity (± 0.03)	AlO_4 Relative Intensity (± 0.03)	Silanol (sites /u.c)	Brønsted (sites /u.c)	Micropore (m^2g^{-1})	Total (m^2g^{-1})
ZSM5-FR	1.00	0.91	2.62 ± 0.26	2.31 ± 0.12	248 ± 9	370 ± 11
ZSM5-ST(873K)	0.66	0.21	0.21 ± 0.05	0.12 ± 0.02	221 ± 5	357 ± 22
ZSM5-ST(1073K)	0.74	0.24	0.23 ± 0.06	0.13 ± 0.02	234 ± 13	332 ± 4

When measured by ^{27}Al NMR and compared against the spectrum of ZSM5-FR discussed in Section 3.1.2.3, both steamed samples show the signals assigned to the 4-coordinated AlO_4 species which constitute the framework aluminium located at 53.4 ppm and octahedral extra-framework aluminium (EFAl) species, although the EFAl signal has shifted from -1.8 ppm to being centred at *ca.* 2.5 ppm and has broadened considerably.[33, 140] Fitting of the NMR data to a Lorentzian function for each peak across the range −50 – 100 ppm was carried out in order to determine the peak intensities at each shift value and the overall intensity in each sample; fit parameters are given in Table 5-2.

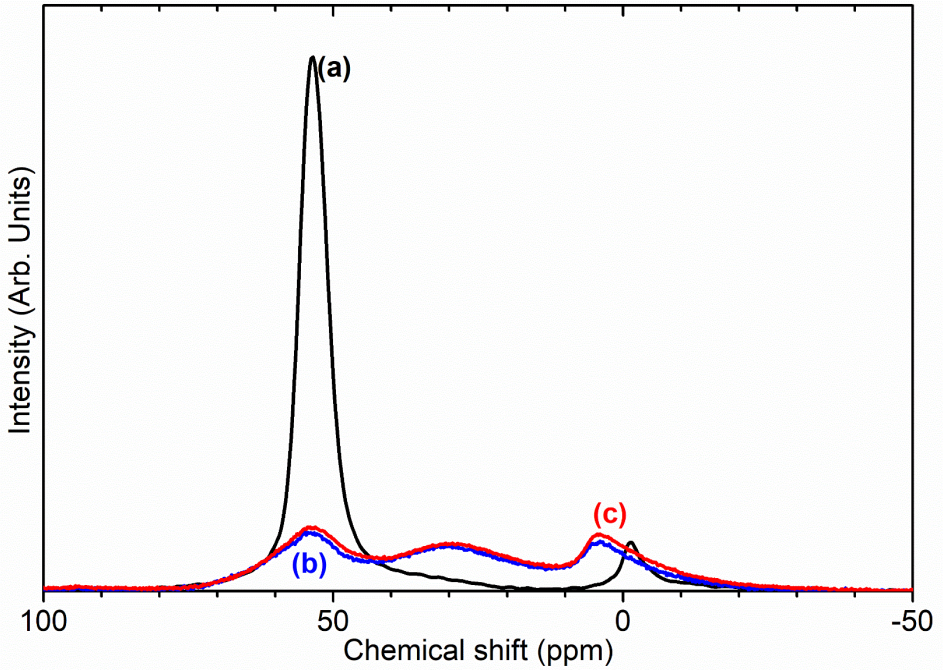

Figure 5-2: ^{27}Al NMR spectra of ZSM5-FR (a), ZSM5-ST(873K) (b) and ZSM5-ST(1073K) (c) showing changes due to loss of framework aluminium in the steamed samples.

Table 5-2: Lorentzian fit parameters for NMR spectra in Figure 5-2 used to derive relative intensities for each ^{27}Al environment.

Sample	Peak 1 (AlO_4)			Peak 2 (AlO_6)			Peak 3 (intermediate)		
	x_0	Γ	Rel. Area	x_0	Γ	Rel. Area	x_0	Γ	Rel. Area
ZSM5-FR	53.4	5.1	1.000	-1.8	5.1	0.080	32.7	7.1	0.017
ZSM5-ST(873K)	54.5	12.8	0.227	2.7	12.8	0.180	29.8	21.9	0.309
ZSM5-ST(1073K)	54.0	13.1	0.259	1.9	14.3	0.230	29.4	21.9	0.320

In the spectrum for ZSM5-ST(873K) the AlO_4 peak shows a reduction in intensity of 77% relative to that of ZSM5-FR, representing a matching percentage reduction in the number of framework aluminium nuclei. The corresponding decrease in framework aluminium for ZSM5-ST(1073K) is 74 %, although the difference between the two samples is smaller than the experimental error. While the steamed spectra show an increase in the intensity of the AlO_6 peak, it is also clear that there is an additional, broad peak centred at *ca.* 30 ppm in both. The exact species responsible for this signal is a matter of debate; it has been assigned to the distorted pentahedral-type geometries generated by the partially removed Al T-atoms described above,[181-182] but also attributed to the presence of EFAl species with distorted tetrahedral geometries.[183] However, regardless of this uncertainty,

it is accepted that both possibilities represent an environment intermediate between the framework and AlO_6 states.[31] Re-fitting of the ZSM5-FR spectrum with the presence of this peak being taken into consideration reveals it to be present at just-detectable levels in the pre-treatment material as well (Table 5-2). However, even accounting for the contributions of all these environments there is a reduction of 25-35 % in the overall signal intensity of the steamed samples relative to the fresh material. Since EFAl species are not reported to be mobile enough to leave the zeolite framework without additional treatment,[33] it can be surmised that the additional EFAl generated by the steam de-alumination process remains present in the sample in a number of different environments, a proportion of which are subject to second-order quadrupolar interactions which render them invisible to NMR detection, despite the high MAS frequency employed. Generally, this 'NMR-invisible' fraction of the EFAl is attributed to the presence of clustered aluminium species containing multiple nuclei.[31, 33, 96]

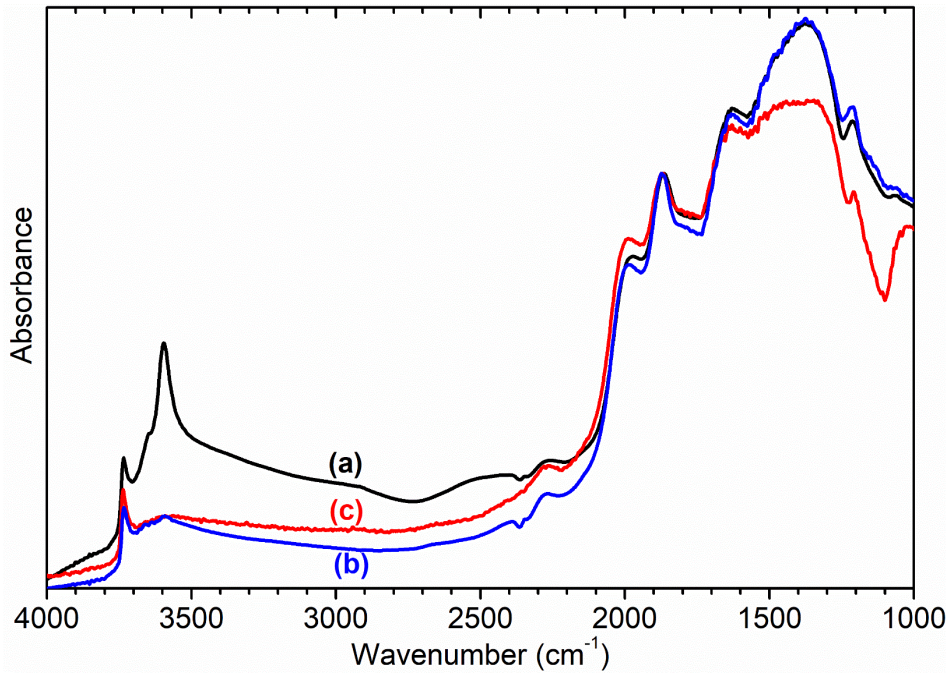

Figure 5-3: Infrared spectra of ZSM5-FR (a), ZSM5-ST(873K) (b) and ZSM5-ST(1073K) (c) recorded by DRIFTS. Spectral intensities normalised with respect to the silanol framework peak at 1875 cm^{-1}.

Further characterisation shows that this de-alumination has had the expected effect of significantly reducing the level of Brønsted acidity. Infrared analysis (Figure 5-3) shows a large reduction in the peak at 3595 cm^{-1}, assigned to the O-H

stretch of the zeolite Brønsted acid groups, with a slightly smaller reduction in the signal for the terminal silanol O-H species on the exterior of the crystals at 3736 cm^{-1} in both steamed zeolites.[31] The signal due to O-H groups associated with extra-framework aluminium (EFAl) species, visible as a shoulder to the Brønsted peak at 3655 cm^{-1} in the ZSM5-FR spectrum and an overlapping peak at the same position for ZSM5-ST(873K) and ZSM5-ST(1073K) does not change significantly between the samples indicating that the EFAl species generated do not contain a significant quantity of O-H groups. These observations, combined with those drawn from the NMR data, are consistent with results in the literature which report that the pore structure of ZSM-5 favours the agglomeration of released aluminium into polymeric aluminium species rather than the octahedral aluminium-oxy-hydrides which make a significant contribution in steam-treated large pore zeolites such as zeolite HY.[96]

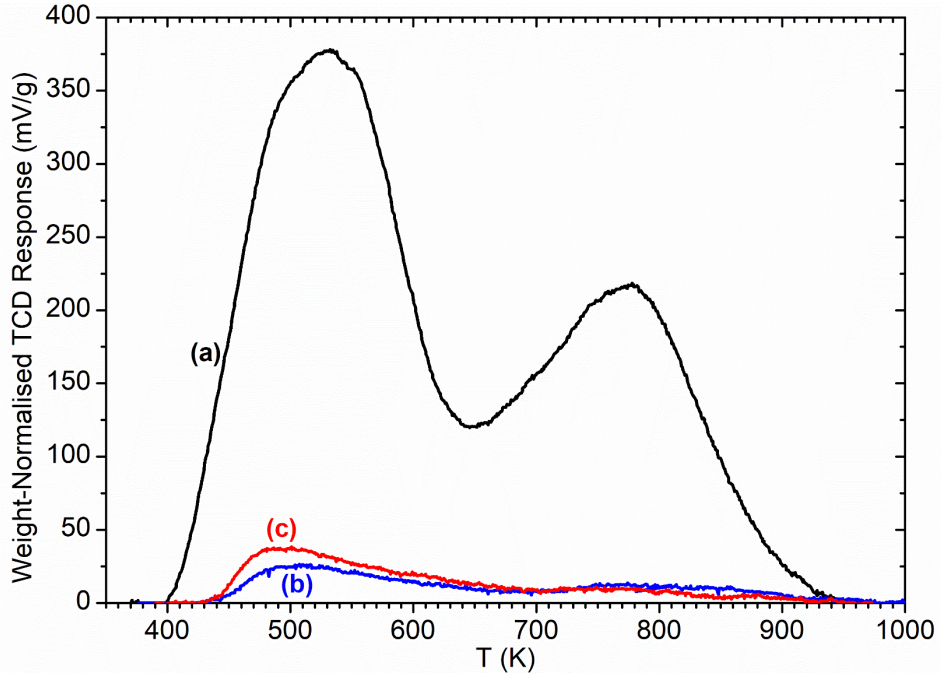

Figure 5-4: Ammonia desorption vs temperature trace for ZSM5-FR (a), ZSM5-ST(873K) (b) and ZSM5-ST(1073K) (c). Peaks represent the desorption of ammonia molecules chemisorbed to silanol groups from 400-600 K and those bound to Brønsted acid sites from 650-900 K.[132]

Ammonia TPD analysis of the samples confirms the results observed in the infrared data, with significant reductions in the population of both Brønsted acid and silanol –OH groups. Both steamed samples show the same pattern of two distinct populations of ammonia, assigned to molecules chemisorbed to silanol and

Brønsted –OH groups, as was observed for ZSM5-FR (Section 3.1.2.2).[132] It can be seen that the final effect of the steam treatment is a 94-95 % reduction in the acid site population relative to ZSM5-FR and a 91-92 % reduction in the number of silanol groups which are active for ammonia chemisorption, with differences between the two steamed samples being too small to be meaningful. It is notable that this reduction in acid sites is considerably higher than the value for the loss of framework aluminium derived from the NMR data. The reduction in the size of the silanol peak also indicates that the silanol nests generated by the de-alumination mechanism in Figure 5-1 are not active for the chemisorption of ammonia, presumably due to steric hindrance around the newly generated silanol sites. Examination of the shape of the ammonia desorption curves, shows that the maximum of the desorption peak assigned to the Brønsted groups lies at 770 K in all cases and that all samples retain chemisorbed ammonia at temperatures up to 950 K, indicating that the peaks represent ammonia interacting with the same type of acid groups in each case and that neither of the peaks in the steamed samples are due to adsorption on EFAl species.

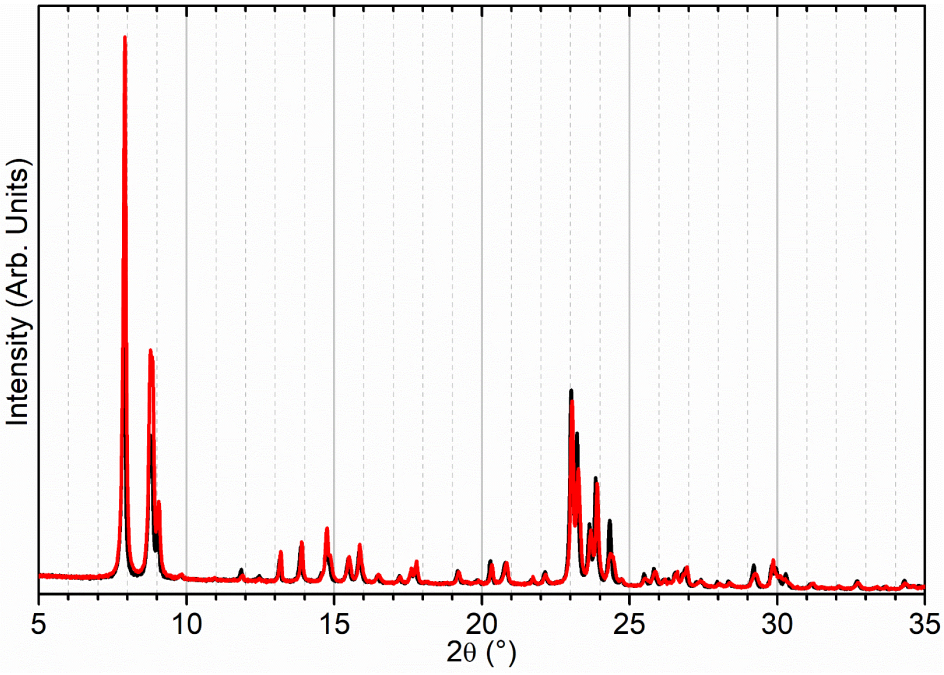

Figure 5-5: XRD pattern recorded for ZSM5-ST(873K) (a) compared to that of ZSM5-FR taken from Figure 3-1 (b). λ = 1.5406 Å.

In contrast to the extensive chemical changes, there is little evidence of changes to the zeolite structure due to steam treatment. Comparing the powder XRD patterns of ZSM5-FR and ZSM5-ST(873K) shows that the steamed material exhibits

some minor broadening of the diffraction peaks but no significant changes in bulk structure (Figure 5-5). XRD data for ZSM5-ST(1073K) is not available at the same high resolution, but screening measurements using a benchtop XRD instrument (Rigaku Miniflex 600) suggest similar properties to ZSM5-ST(873K).

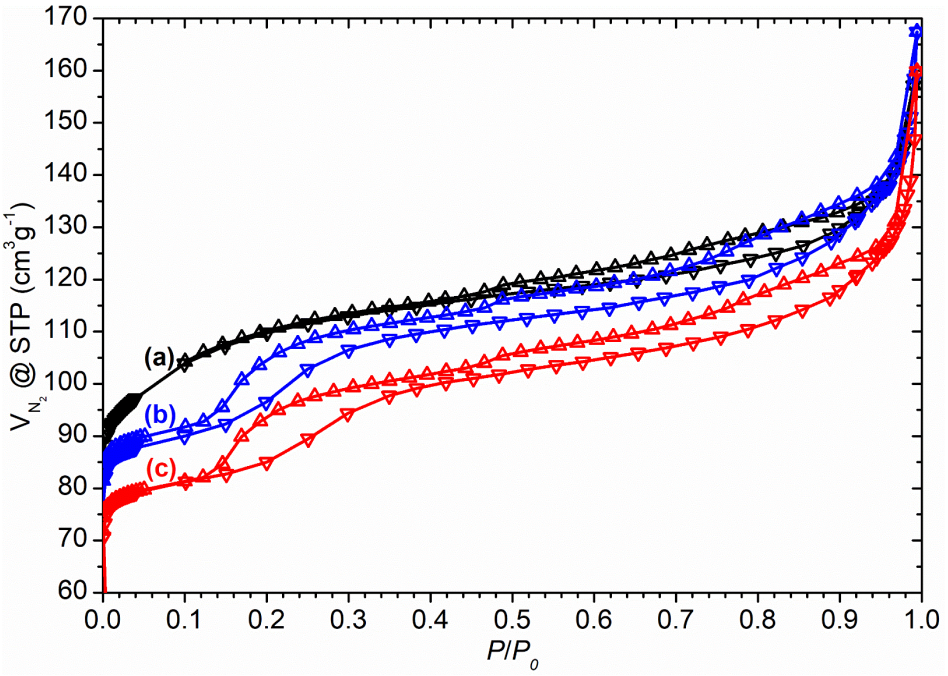

Figure 5-6: Adsorption (▽) and desorption (△) isotherms for nitrogen on ZSM5-FR (a), ZSM5-ST(873K) (b) and ZSM5-ST(1073K) (c) showing increased hysteresis in steamed materials.

Table 5-3: Comparison of porosities of ZSM5-FR, ZSM5-ST(873K) and ZSM5-ST(1073K) as calculated from isotherm data.

Sample	Micropore		Mesopore		External Surface Area (m^2g^{-1})	Total Surface Area (m^2g^{-1})
	Surface Area (m^2g^{-1})	Volume (cm^3g^{-1})	Surface Area (m^2g^{-1})	Volume (cm^3g^{-1})		
ZSM5-FR	248 ± 9	0.101 ± 0.003	72 ± 2	0.032 ± 0.001	50 ± 14	370 ± 11
ZSM5-ST(873K)	221 ± 5	0.085 ± 0.002	90 ± 3	0.044 ± 0.002	46 ± 23	357 ± 22
ZSM5-ST(1073K)	234 ± 13	0.089 ± 0.005	29 ± 2	0.028 ± 0.002	69 ± 14	332 ± 4

BET gas adsorption experiments using N_2 as the adsorbent gas, reveal that the effect of steaming is to increase the hysteresis in the isotherms, an effect which is more pronounced for ZSM5-ST(1073K) than for ZSM5-ST(873K) (Figure 5-6). Both the overall surface area and the proportion of that surface area which represents micropore channels of < 3.5 Å diameter are reduced in the steamed materials relative to ZSM5-FR. In the case of ZSM5-ST(873K), the magnitude of this reduction

lies below the degree of accuracy available, but the overall trend in the isotherms suggests that it is a real effect (Table 5-3). Results for ZSM5-ST(1073K) suggest that loss of surface area is occurring primarily in the mesopore channels, which suggests that it may potentially be due to EFAl species restricting the access of the N_2 to portions of the framework. Analysis of pore size distributions is of limited utility due to the limitations of analysing microporous materials with N_2 as the adsorbent gas, however, the lack of a significant increase in sample mesoporosity indicates that the surface area loss is not caused by breakdown of the zeolite framework, consistent with the XRD results.

Taken together, these results indicate that the zeolite framework, and thus the overall microporous structure, remains intact despite the removal of the majority of the aluminium in both steamed samples due to the fact that these represent only ~2.1 % of the framework T-atoms. The broadening of the XRD pattern for ZSM5-ST(873K) indicates that the removal of aluminium sites occurs essentially at random, increasing the amount of noise in the diffraction pattern. Both steam treatments therefore produce an artificially aged sample, representative of a catalyst towards the end of its steady-state activity in industrial use. The properties of the bulk-treated sample prepared at Johnson Matthey (ZSM5-ST(1073K)) are close enough to those prepared by the smaller scale batch treatment procedure at ISIS (ZSM5-ST(873K)) to allow results from experiments performed using each material to be meaningfully compared.

5.2 Propene Behaviour in Steamed ZSM-5:

The first model compound to be tested with steam-treated zeolite was propene due to its greater ease of handling. Since it was expected that the reaction chemistry would be comparable to that observed for ZSM5-FR in Chapter 4, i.e. oligomerization of the propene once the sample achieved a sufficiently high temperature, the system was investigated by both INS, to observe the oligomerization reaction, and QENS, to check for any changes in sample mobility.

5.2.1 Changes in Oligomerization Activity:

The zeolite sample used for INS measurements consisted of ZSM5-ST(873K) which was loaded with 4.8 propene molecules per ZSM-5 unit cell at 140 K and tested in a repeat of the stepwise heating experiment used to observe the reaction intermediates in ZSM5-FR in Section 4.2.2.1. Owing to the reaction being expected to be less active, the range of temperatures investigated was extended, with additional measurements being performed after heating to 300 and 325 K. The resulting spectra are presented in Figure 5-7.

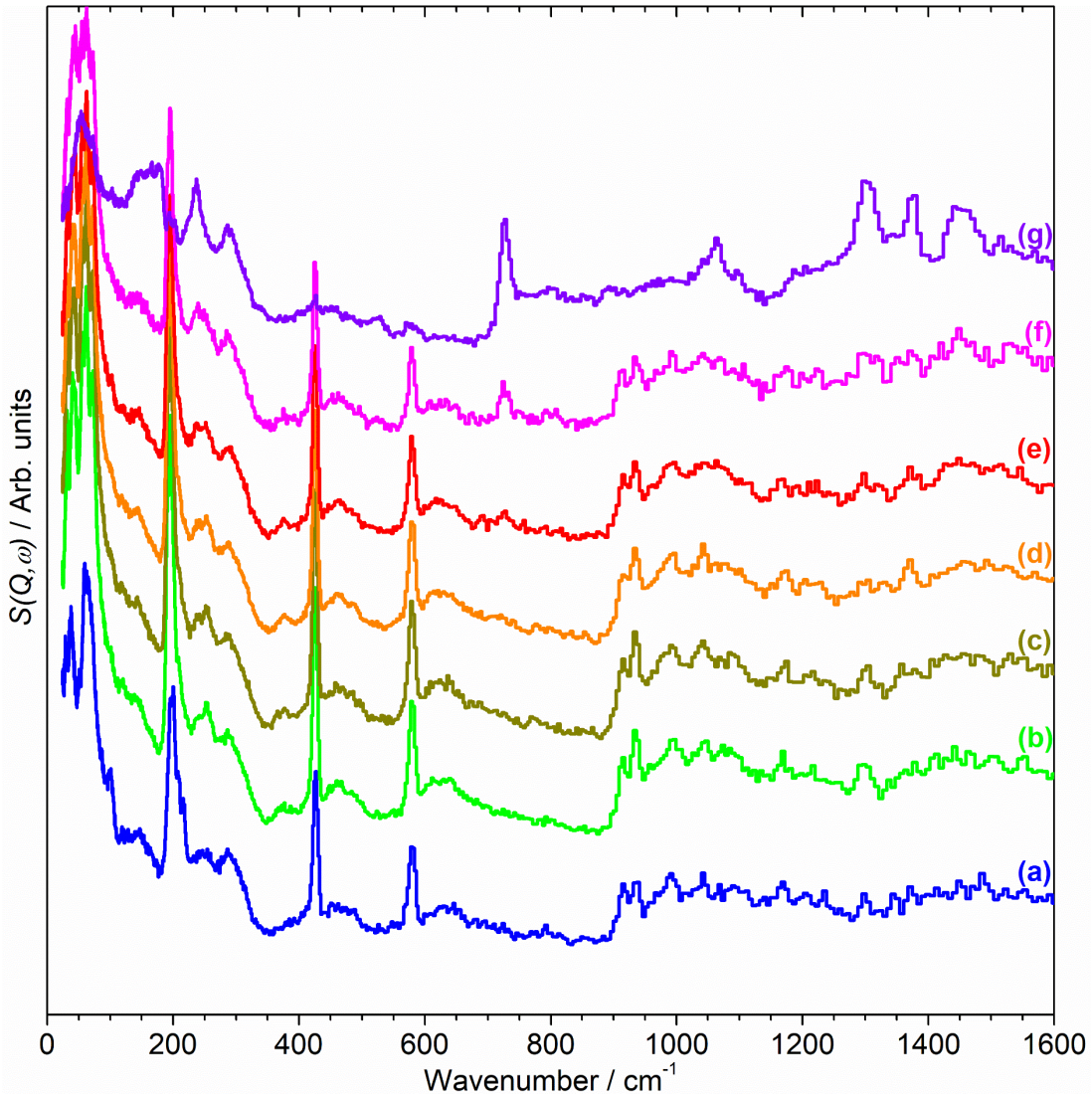

Figure 5-7: TOSCA INS spectra of propene after absorption into ZSM5-ST(873K) at 140 K (a) then following further heating to the indicated temperatures: (b) = 260 K; (c) = 270 K; (d) = 280 K; (e) = 290 K; (f) = 300 K and (g) = 325 K. Spectra are offset in the *y*-axis for clarity.

The INS data collected allows us to follow the oligomerization reaction of propene in progress within ZSM5-ST(873K) in the same manner as Figure 4-19 allows for ZSM5-FR (the reader is cautioned that when comparing Figure 4-19 and Figure 5-7 the assignment of spectrum colour to sample temperatures is different between figures.) The assignment of modes is also identical to the earlier experiment (See Table 3-4).

It is immediately apparent from Figure 5-7 that the reduction in acidity observed in the characterisation of ZSM5-ST(873K) has had the expected effect of reducing its ability to catalyse olefin oligomerization at low temperatures. Whereas the ZSM5-FR reaction was observed to commence at *ca*. 225 K, with temperatures above 270 K resulting in oligomerization occurring fast enough that only the final product is observable if propene is introduced at this temperature, in this case the first unambiguous sign of oligomerization activity is not observed until the sample has been heated to 290 K, when the in-phase rock mode of the oligomer rises above the level of background noise (Figure 5-7(e)). The continued presence of weak contributions from unreacted propene in Figure 5-7(g) suggests that the reaction remains incomplete even at the highest temperature investigated by INS (325 K). The conclusion drawn is that the reduced acidity of ZSM5-ST(873K) means that higher energies are required to initiate the protonation of the propene, which is believed to be the process that represents the rate-limiting step in the oligomerization reaction.[48, 169]

Figure 5-7 also exhibits some differences to the behaviour previously observed for propene oligomerization in the fresh catalyst prior to the initiation of the final oligomer formation. Specifically, the formation of the hydrogen bonded propene intermediate and associated splitting of the propene vinyl torsion peak at temperatures as low as 40 K below the temperature required for propene protonation is not observed in this case. Since the reaction mechanism of the oligomerization in unlikely to have been altered, the most probable explanation is that the reduced number of acid sites means that the population of H-bonded propene in ZSM5-ST(873K) is insufficient for the bonded species to be visible in the INS spectrum even when all acid sites are occupied. These differences in reaction behaviour result in slight differences in the composition of the product

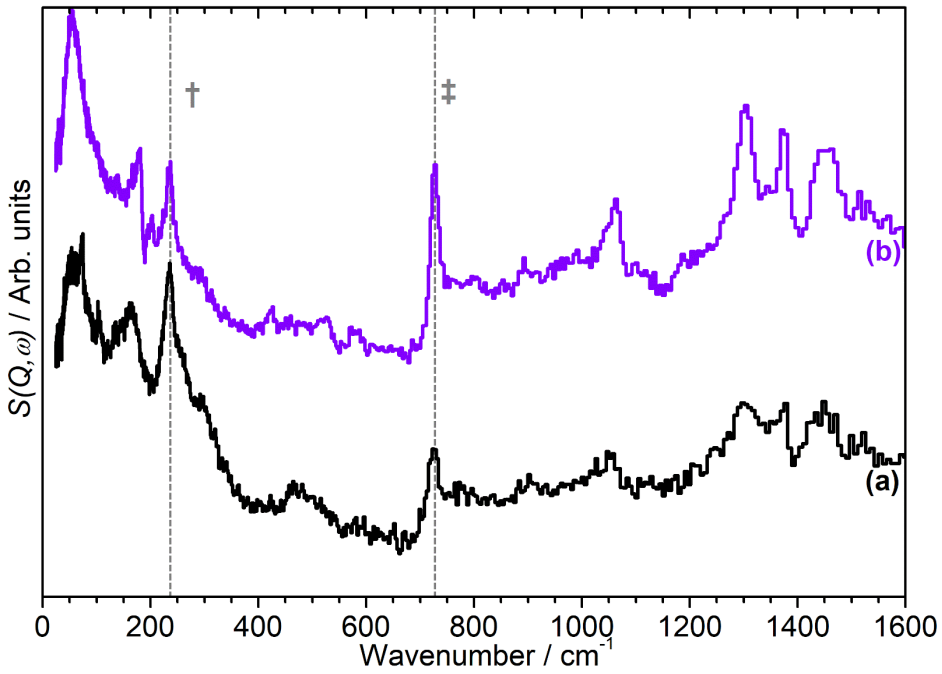

Figure 5-8: INS spectra of the final product of propene oligomerization in ZSM5-FR (a) and ZSM5-ST(873K) (b) showing evidence of increased average chain length in ZSM5-ST(873K). Both spectra normalised to correct for differing sample masses and zeolite contributions subtracted. Positions of methyl torsion (†) and (-CH_2-) in-phase rock (‡) highlighted. Spectra offset in y-axis.

oligomer in each zeolite. As shown in Figure 5-8, although in both cases the final product spectrum has the characteristic shape associated with the formation of a primarily linear series of oligomer chains, the spectra exhibit different relative intensities for the peaks in question. In particular, the reduced relative intensity of the methyl torsion mode and increased contribution from the in-phase methylene rock in the ZSM5-ST(873K) oligomer spectrum is evidence of a greater average chain length than in ZSM5-FR. This is consistent with our previous hypothesis that the average oligomer chain length is determined by steric effects causing termination of the chain formation reaction. This is demonstrated by the fact that the final product spectrum of propene oligomerizations in ZSM-5 samples with the same level of acidity is not temperature dependant. Since the protonated end of the oligomer is fixed in place at the location of the catalytic site, it is the other end of the molecule which moves through the pore network as the chain is extended by propene additions. For the majority of forming oligomers at interior sites, the limitation on maximum length will occur when this end of the chain encounters a pore channel which is already occupied by another molecule, preventing further growth since the oligomer has no further room for expansion.

Since ZSM5-ST(873K) has fewer, more widely spaced active sites, the forming oligomer can extend further before intersecting another oligomer and having its growth blocked, resulting in the observed increase in average chain length.

5.2.2 Propene Dynamics in Steamed ZSM-5:

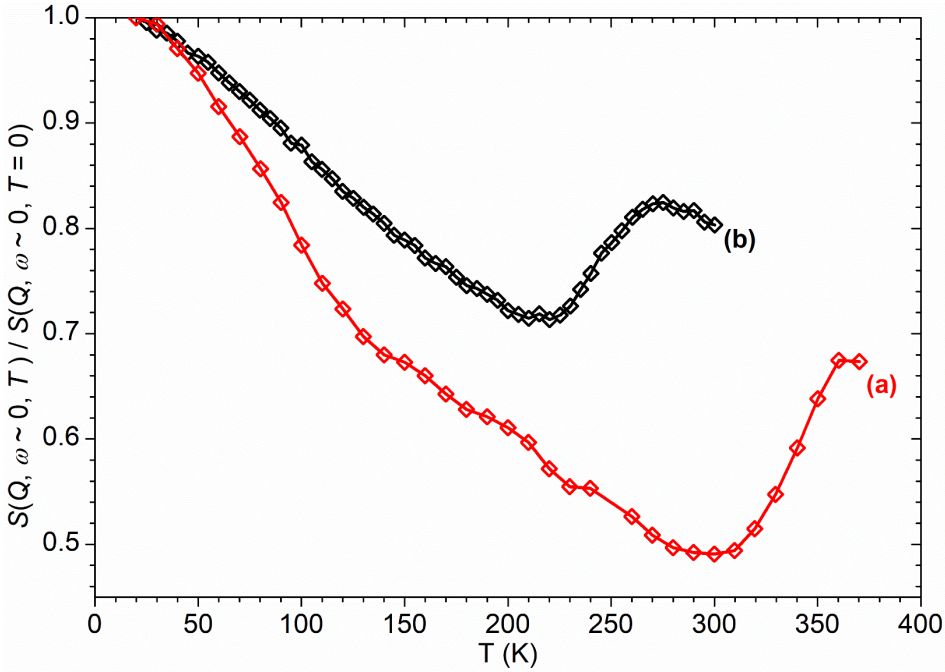

Figure 5-9: Elastic fixed window scan data for propene in ZSM5-ST(873K) from 20 – 370 K (a) compared with equivalent data in ZSM5-FR taken from Figure 4-22(b). Relative elastic intensities normalised against the value at 20 K to allow comparison between samples.

As in the case of the reaction in ZSM5-FR (Section 4.2.2), mobility changes from the oligomerization of the propene will be visible in the QENS data due to generation of a less mobile product. To obtain the same type of data on the oligomerization as was achieved for ZSM5-FR, a 3.3 g sample of ZSM5-ST(873K) was measured by QENS on the OSIRIS spectrometer. The loading level of the sample in this case was 5.06 propene molecules per unit cell, which was loaded into the sample at 200 K using the OSIRIS CCR and a gas handling stick with trace heated gas lines. This temperature is higher than that used for earlier cryogenic loadings, since the results obtained from the ZSM5-FR experiments show that it will still prevent oligomerization while allowing faster diffusion of the propene into the zeolite. EFWS data was collected from 20 – 370 K with high resolution

data at 20, 170, 220 and 270 K. Unloaded spectra at the high resolution temperatures were collected prior to sample loading and used to remove the zeolite contributions to the final spectrum, as was done in the ZSM5-FR studies.

Comparing the EFWS results for propene in ZSM5-ST(873K) with the earlier results (Figure 5-9) confirms the observations about oligomerization requiring higher temperatures for initiation, that were drawn from the INS dataset. The first signs of changes due to oligomerisation, are observed at 290 K with the deviation of the elastic window trace from the linear decrease with temperature observed from 130 – 280 K, matching the first appearance of oligomer modes in Figure 5-7. Due to the shorter data collection time at each temperature allowing continuation of the testing to higher values, we can also confirm the tentative identification of the continued presence of unreacted propene at 325 K in Figure 5-7(g), since Figure 5-9 shows that the system does not achieve its final state with all propene converted until 360 K. In addition to this decreased reactivity, the EFWS plot also allows some examination to be made of the effect of the steam treatment on the overall mobility of the propene in the two zeolites, most prominently that the ZSM5-ST(873K) sample shows considerably higher mobility even at temperatures below 200 K, where the effect of oligomerization does not contribute in either sample. The majority of this difference is due to a more rapid increase in mobility in ZSM5-ST(873K) from 20-140 K, at which point there is a visible inflection in the Figure 5-9(a) trace above which the rate of mobility increase in each sample appears similar.

The linear nature of the ZSM-5-ST elastic window plot from 130 – 280 K suggests that the adsorbed propene is undergoing similar motions across this range and provides the opportunity to characterise these motions in more detail by means of the high resolution spectra collected at 170, 220 and 270 K. All spectra required the inclusion of a linear background in addition to the resolution function. In fitting the 220 K and 270 K spectra, the remaining quasielastic component was adequately described by a single Lorentzian, corresponding to a single motion occurring within the resolvable time window. For the 170 K dataset this model did not produce an acceptably close fit to the experimental data and better results were obtained by use of two Lorentzian functions, one with similar *Q*-dependant behaviour to that observed at higher temperatures and the second considerably broader. Examples of

the fits obtained at each temperature are shown in Figure 5-10 for selected Q values.

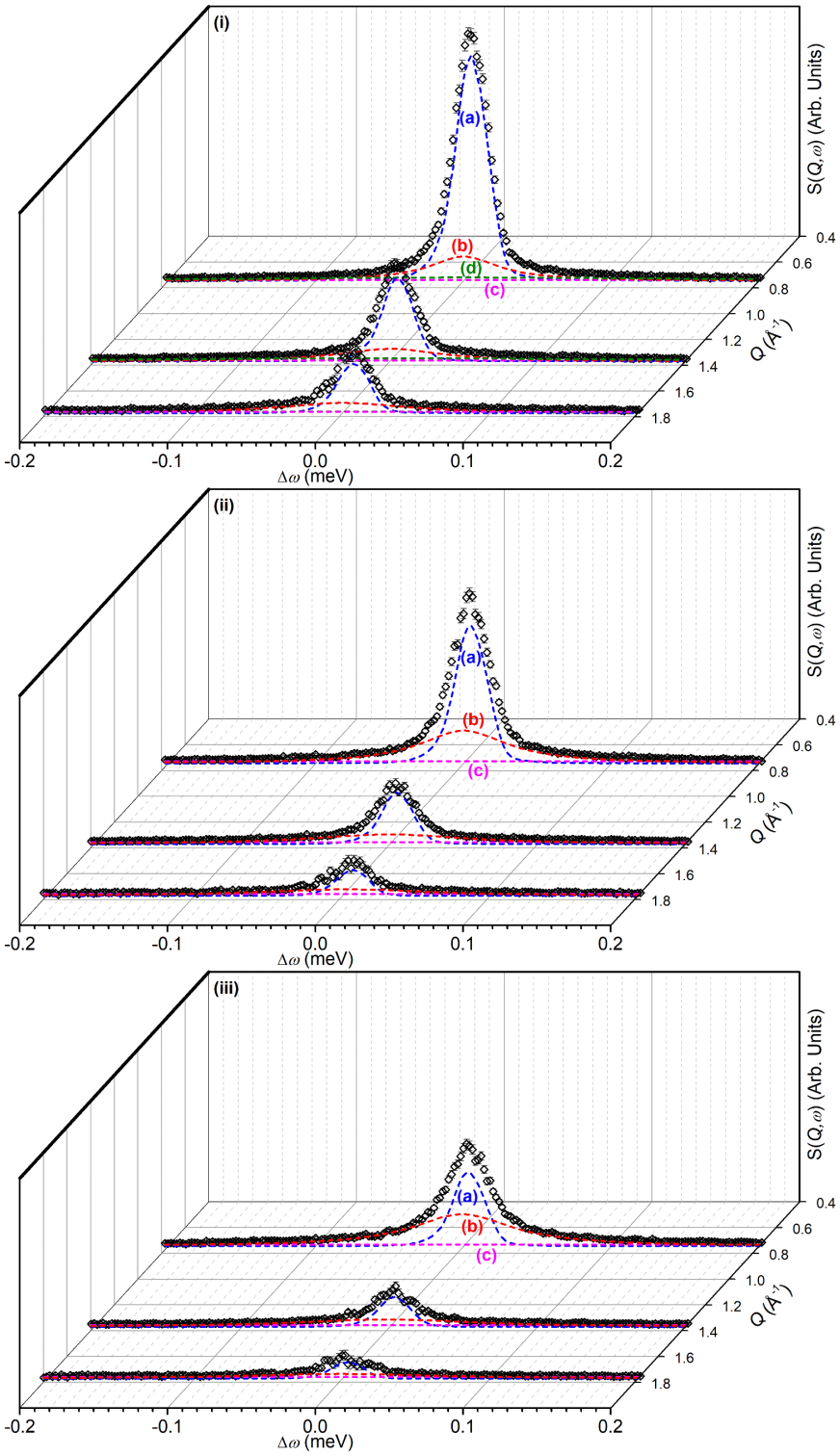

Figure 5-10: $S(Q,\omega)$ functions at selected values of Q for propene in ZSM5-ST(873K) at 170 K (i), 220 K (ii) and 270 K (iii) showing deconvolution into resolution function (a), first Lorentzian (b) and linear background (c) contributions. The 170 K data includes a second Lorentzian parameter (d). $S(Q,\omega)$ axis scale is identical between graphs.

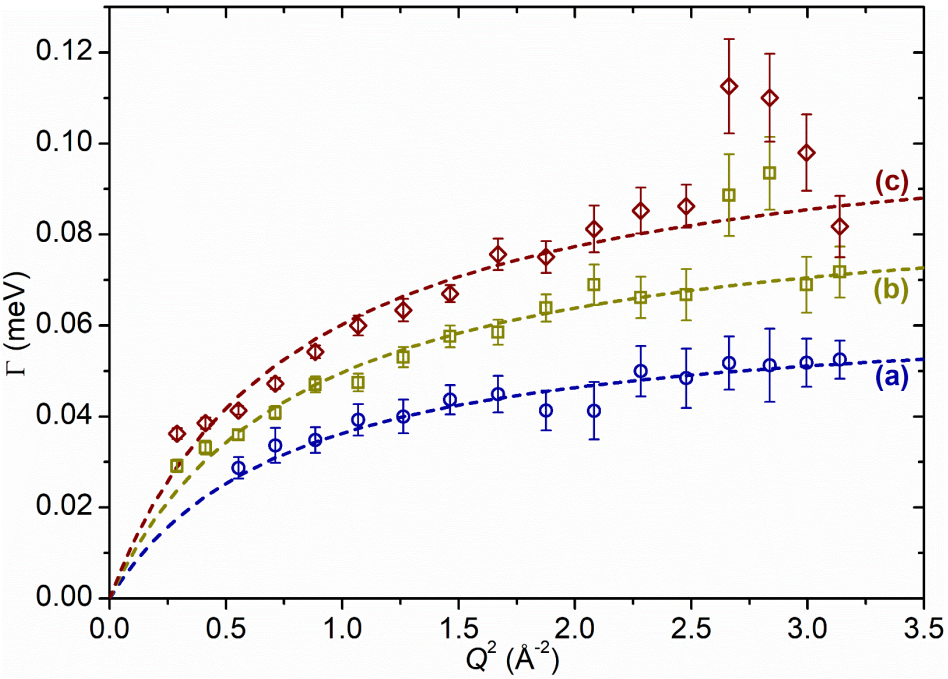

Figure 5-11: Variation of Lorentzian linewidth (Γ) as a function of Q^2 for propene in ZSM5-ST(873K) at 170 K (a), 220 K (b) and 270 K (c). Dotted lines represent best fit of the data to the Singwi-Sjölander model using the parameters given in Table 5-4.

In the case of the Lorentzian which is observed at all temperatures, Figure 5-11 shows the variation of its HWHM as a function of Q^2 displaying similar behaviour at all three temperatures. The energy resolution of OSIRIS (25.4 μeV) means that the Lorentzian is indistinguishable from the elastic peak below 0.5 Å^{-2} at 170 K and below 0.3 Å^{-2} at any temperature resulting in no HWHM points being available below these values. The presence of the Bragg peak from the zeolite in the 2.6 Å^{-2} ≤ Q^2 ≤ 2.9 Å^{-2} range results in the usual anomalous values for the 220 and 270 K data due to the inferior signal:noise levels in the propene-only function once the immobile contributions are subtracted. The Q^2 versus Γ relationship fits to the same Singwi-Sjölander jump diffusion relationship as previously observed for propane in ZSM5-FR in Section 4.3.1.1. Fitting of the data to this equation gives the traces shown as the dotted lines in Figure 5-11 and the diffusion parameters in Table 5-4. As was also the case for propane, the diffusion coefficients follow a linear Arrhenius relationship across the temperature range investigated (Figure 5-12) with the estimated activation energy being 1.86 kJ mol^{-1} in this case.

Table 5-4: Summary of diffusion parameters derived from QENS data fitting for propene in ZSM5-ST(873K).

T (K)	τ (ps)	$\sqrt{\langle r^2 \rangle}$ (Å)	D_s (m^2s^{-1})
170	10.27	2.80	1.28×10^{-9}
220	7.38	2.75	1.71×10^{-9}
270	6.10	2.76	2.08×10^{-9}
D_0 (m^2s^{-1})		4.74×10^{-9}	

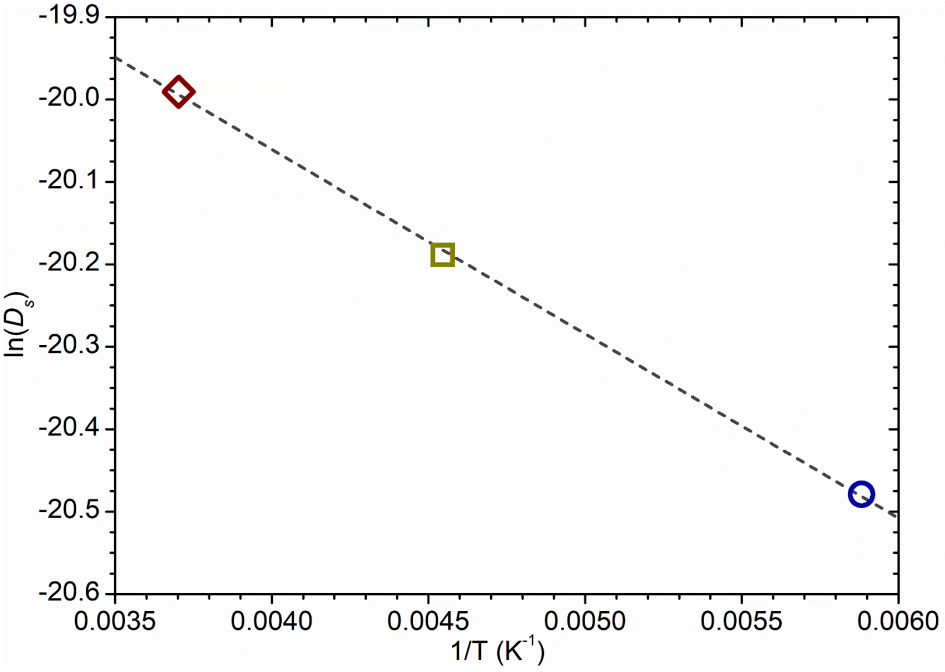

Figure 5-12: Arrhenius plot of the self-diffusion coefficients of propene in ZSM5-ST(873K) at 170, 220 and 270 K showing a linear relationship across this temperature range. Line of best fit to the experimental data shown as the dotted line, giving an activation energy of 1.86 kJ mol^{-1} for this motion.

Examining the fit parameters shows that the propene molecules are also undergoing a very similar motion to that observed for propane in ZSM5-FR, with the typical jump distance remaining *ca.* 2.8 Å and the differences in self-diffusivity arising mainly from differences in residence time. The activation energy for movement is approximately 1 kJ/mol higher than the propane / ZSM5-FR results, presumably due to remaining acid-alkene hydrogen bonding. The propene / ZSM5-ST(873K) system diffuses slower than the propane / ZSM5-FR system at 170 and 220 K but catches up to approximately the same level of mobility at 270 K.

Contextualising these findings requires examination of how steaming also affects propane behaviour and will therefore be discussed in further detail below.

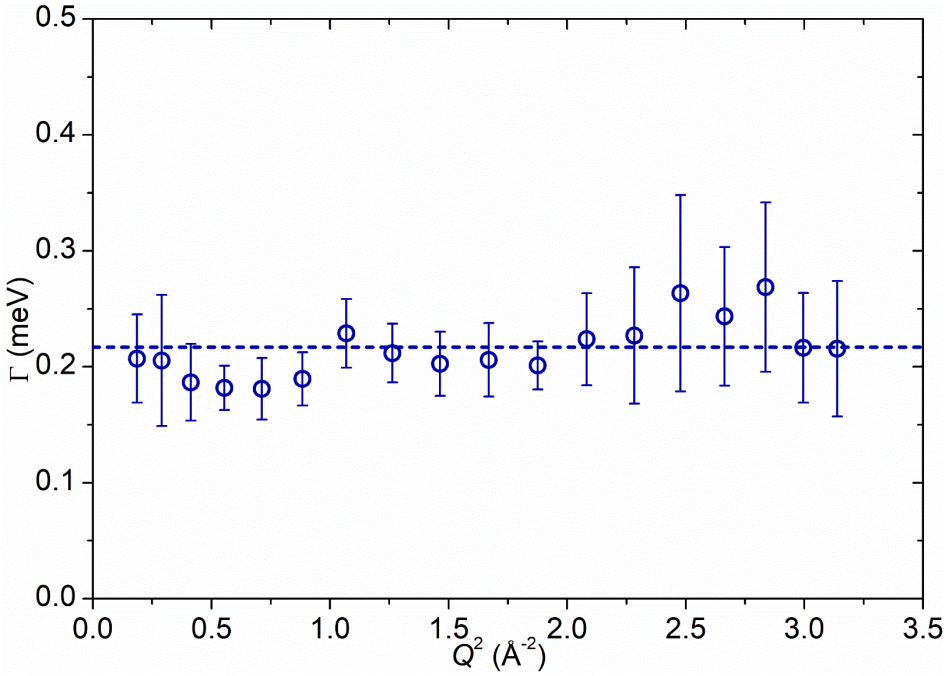

Figure 5-13: Variation of Lorentzian linewidth (Γ) as a function of Q^2 for the second Lorentzian observed for propene in ZSM5-ST(873K) at 170 K showing Q-independent behaviour. Dotted line represents the line of best fit.

In contrast to the first Lorentzian, the second Lorentzian, which is only observed at 170 K, is considerably broader. This leads to some difficulty in separating its contribution from the linear background resulting in the larger degree of uncertainty in the Γ *vs* Q^2 plot shown in Figure 5-13, although the greater magnitude of the energy transfer values in this case means that this Lorentzian is wider and remains resolvable across the full Q range accessible on the instrument. Within the limits of experimental accuracy, the Γ values appear constant and independent of Q, indicative of this Lorentzian corresponding to a rotational movement of the propene. The line of best fit to the experimental values provides an estimate of the rotational constant for the motion of $D_r = 3.29 \times 10^{11}$ s^{-1}. Due to this Lorentzian not being observable at higher temperatures, we can surmise that it represents a rapid rotation of the propene molecule that is only observable at extremely low energies, and at higher temperatures moves quickly enough that it is outside the instrumental dynamic window and so merges into the flat background. This rapidity also explains why similar motions have not been

reported in other studies in the literature, which generally only consider higher temperatures.

5.2.2.1 Comparison with Dynamics of Propane:

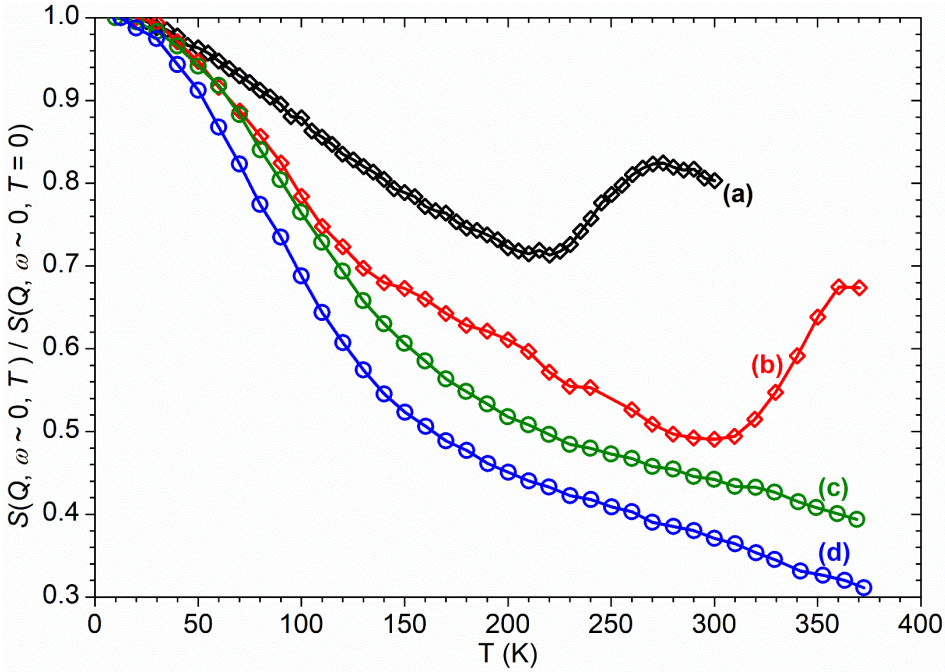

Figure 5-14: Comparison of EFWS data for: propene in ZSM5-FR (a); propene in ZSM5-ST(873K) (b); propane in ZSM5-FR (c); propane in ZSM5-ST(1073K) (d). Relative elastic intensities normalised against the value at 20 K.

Comparing the propene in steamed zeolite mobility values obtained above, with the inert model study of mobility in ZSM5-FR using propane reported in Section 4.3.1.1, requires measurement of propane movement in a steamed zeolite, to baseline the differences which are not due to changes in acid-double bond interactions. Such an experiment was performed on the IRIS spectrometer from 10 – 370 K, with high resolution spectra at 170, 220 and 270 K as before. The steamed zeolite used in this case was ZSM5-ST(1073K) with a sample loading of 5.26 propane molecules per unit cell. The resulting EFWS plot (Figure 5-14(d)) shows the exact same trends observed for propane in ZSM5-FR (c) but with a globally increased level of overall mobility due to the effects of the steam treatment. The high resolution spectra were fit to the same single-Lorentzian model as propane in the fresh zeolite and the resulting broadening conformed to the Singwi-Sjölander jump diffusion model as before (Figure 5-15, Table 5-5). The

average jump distance is marginally (0.1 Å) reduced, but this is likely too small to be meaningful, so the motion being observed likely remains the same in both samples. The activation energy for propane diffusion in ZSM5-ST(1073K) predicted from these measurements is 0.99 kJ mol^{-1}.

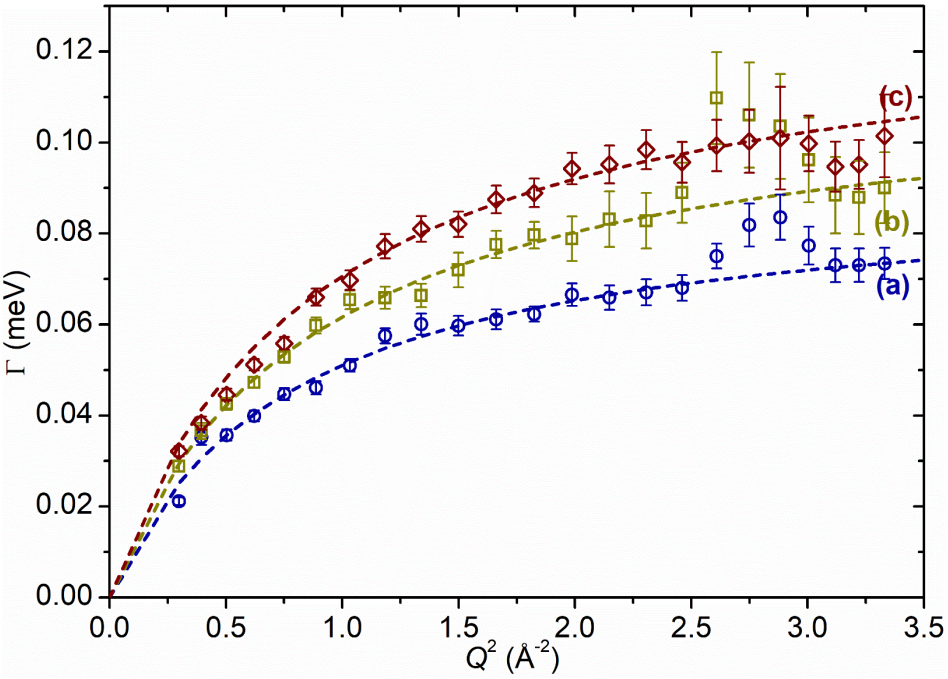

Figure 5-15: Lorentzian linewidth (Γ) *vs* Q^2 for propane in ZSM5-ST(1073K) at 170 K (a), 220 K (b) and 270 K (c). Dotted lines represent best fit of the data to the Singwi-Sjölander model using the parameters given in Table 5-5.

Table 5-5: Summary of diffusion parameters derived from QENS data fitting for propane in ZSM5-ST(1073K). Ratios show relationships to the QENS results for propane in ZSM5-FR (Section 4.3.1.1) and propene in ZSM5-ST(873K) (Section 5.2.2).

T (K)	τ (ps)	$\sqrt{\langle r^2 \rangle}$ (Å)	D_s (m^2s^{-1})	D_s Ratio *vs*:	
				Propane in ZSM5-FR	Propene in ZSM5-ST(873K)
170	7.27	2.79	1.78×10^{-9}	1.11 : 1	1.39 : 1
220	5.73	2.64	2.02×10^{-9}	1.10 : 1	1.18 : 1
270	4.99	2.63	2.31×10^{-9}	1.14 : 1	1.11 : 1
D_0 (m^2s^{-1})		3.54×10^{-9}		1.18 : 1	0.75 : 1

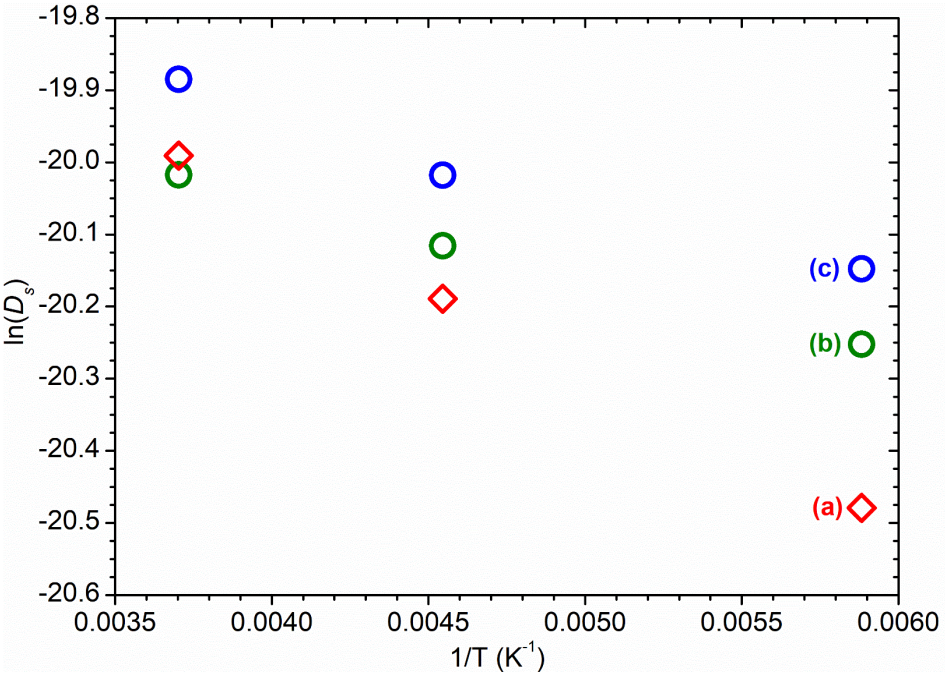

Figure 5-16: Arrhenius plot comparison of diffusion constants for: propene in ZSM5-ST(873K) (a); propane in ZSM5-FR (b); propane in ZSM5-ST(1073K) (c).

Comparing the propane results, the effect of the steaming has been to raise the self-diffusion coefficient of the propane by approximately 10 % relative to its value in the fresh zeolite. This is in agreement with the difference in relative elastic intensity between the two samples in the 170 – 270 K region, indicating that this increased jump diffusion accounts for the entirety of the increased mobility experienced by propane. The activation energy for propane diffusion does not change significantly between the two samples and the magnitude of what change does occur (0.09 kJ mol^{-1}) may lie within the margin of error of the Arrhenius fit of the D_s data; this suggests that hydrogen bonding with the acid sites does not have a significant effect on the mobility of alkane molecules under these conditions and the increased mobility is primarily due to removal of the groups from the pore channels resulting in decreased steric effects.

In comparison to the propane values, propene has lower overall mobility across the temperature range, confirming that the MD simulations in Chapter 4 are mistaken in this respect. The slower diffusivity is due to increased residence times between jumps and the majority of this increased residence time is likely due to hydrogen bonding with the remaining acid sites, as evidenced by the higher activation energy of propene diffusion: as the temperature increases and the

effect of such bonding on mobility becomes less significant the difference between the propene and propane self-diffusion constants decreases. At sufficiently high temperature it appears likely that the lower steric bulk of the propene molecule will allow it to diffuse faster than propane in an equivalent environment, as evidenced by propene having a higher D_0 value, but this does not occur in the temperature range investigated here.

One additional anomaly which requires comment lies in a difference between the trends in specific and overall mobility. Specifically, while the *Ds* value for propene in ZSM5-ST(873K) is higher than that of propane in ZSM5-FR at 270 K (Figure 5-16) the overall mobility of the propane sample, as measured by EFWS analysis, remains higher across the entire temperature range (Figure 5-14). This is due to both propane samples having a considerably higher level of intensity embodied in the linear background fit parameter, representing motions too fast to be resolved on the spectrometer used and, in this case, likely corresponding to molecular rotations. Therefore, the propane samples have additional mobility arising from higher levels of molecular rotations which appears in the EFWS data but not in the Lorentzian fit which measures only the jump diffusion motion.

5.3 1-Octene Behaviour in Steamed ZSM-5:

Studies of the behaviour of 1-octene in steamed zeolite were less extensive due to time constraints favouring the easier-to-handle propene experiments. However, it was possible to collect both INS and QENS data on 1-octene in steam-treated materials.

5.3.1 1-Octene Oligomerization Activity:

The INS sample consisted of 9.37 g of ZSM5-ST(873K) which was dosed with 1-octene to a level of 8.92 octene molecules per unit cell by means of a bubbler arrangement. The sample was held at 200 K by immersion in dry ice during this process in order to prevent any possibility of premature oligomerization. Purging of the sample after loading was carried out with pure helium to remove any 1-octene not adsorbed into the sample. However, examination of the INS spectrum

following installation on TOSCA revealed that the migration of the 1-octene into the zeolite was incomplete at this temperature, as shown by the low spectral intensity (Figure 5-17(a)). The sample was heated to 293 K for one hour which was sufficient to allow the 1-octene to diffuse into the zeolite, as proven by the intensity reaching the levels expected given the quantity of hydrocarbon within the neutron beam. Examination of this spectrum (Figure 5-17(b)) confirms that the steam treatment has reduced the ability of ZSM5-ST(873K) to catalyse the oligomerization of 1-octene in the same manner as observed for propene above, and that 293 K is now an insufficiently high temperature for oligomerization to occur. With the exception of some peak broadening due to interactions with the zeolite pore walls, the adsorbed spectrum at 293 K is therefore identical to the molecular spectrum of 1-octene, with assignments as in Table 3-5.

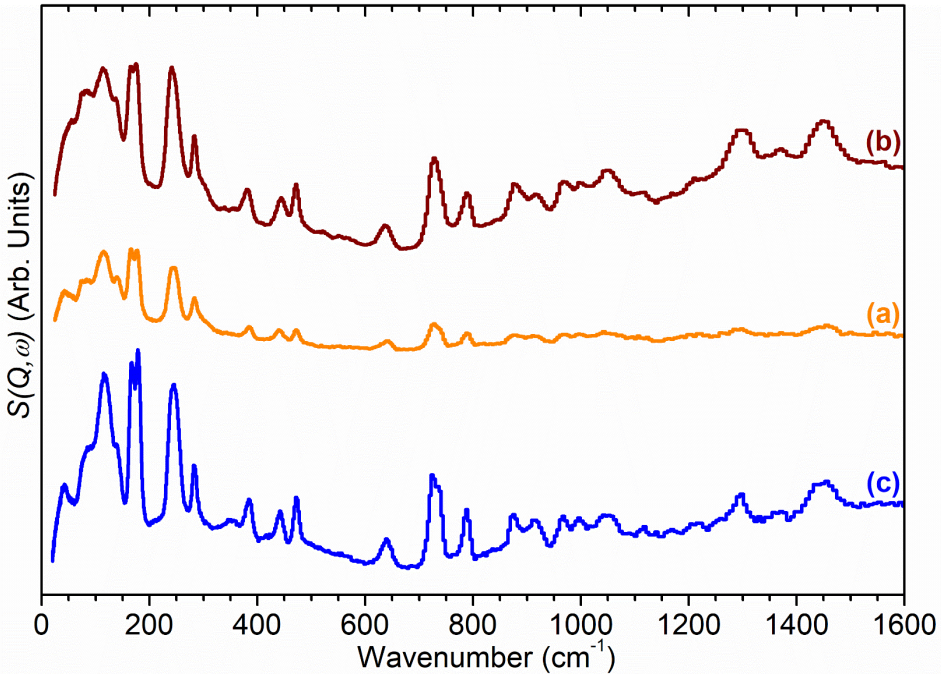

Figure 5-17: Spectrum of 1-octene following adsorption into ZSM5-ST(873K) at 200 K (a) and the same sample after heating to 293 K (b) compared with the spectrum of pure 1-octene (c). Spectra normalised to the amount of octene in each sample and offset in *y*-axis.

5.3.2 1-Octene Dynamics:

A QENS investigation of the 1-octene dynamics was carried out using a 2.73 g sample of ZSM5-ST(1073K) in a QENS sample can with both top and bottom gas

inlets to allow the sample to be loaded with 5 molecules of 1-octene per unit cell using a bubbler arrangement and flowing helium. This was analysed on OSIRIS. Unfortunately, equipment and time limitations prevented the exact duplication of the earlier experimental protocol. The design of the flow-through sample container required the use of PTFE gaskets for sealing; these can be used up to 400 K but will begin to leak if cooled below 150 K and then reheated due to contraction of the gaskets. The test protocol was therefore adjusted to collect data in the temperature range 150 – 370 K first, including high resolution spectra at 270, 320 and 370 K, followed by cooling the sample to base temperature to collect the resolution function and removing it from the instrument while still cold immediately after data collection finished. This means that no EFWS data was collected in the 20 – 140 K temperature range. Limited beam time availability meant that it was also not possible to collect an unloaded background of the sample prior to dosing, since this would cause the sample to amass a level of induced radioactivity which would not decay sufficiently to allow loading within the time available. This prevents the subtraction of the zeolite and cell contributions to the QENS spectrum as was used in previous loaded zeolite experiments; this is not, in principle, a catastrophic problem since the immobile contributions should be embodied in the resolution function regardless, but it did result in noisier data and a more difficult fitting process.

Comparing the EFWS data to that of bulk octene from Section 3.3.1 and the oligomerized octene results from Section 4.1.2 shows that the mobility of the –octene in the liquid phase is sharply reduced by its adsorption into the zeolite (Figure 5-18). Conversely, in the two data points where data exists for both experiments the mobility in the solid phase appears slightly greater in the loaded system, presumably due to interactions with ZSM5-ST(1073K) disrupting the 1-octene crystal lattice and allowing for melting at lower temperatures. It can also be seen that the final temperature of 370 K is just high enough to catalyse some degree of oligomerization of the octene, evidenced by the decrease in mobility in the final data point. This should not affect the validity of the base temperature spectrum as a resolution function since the number of scattering nuclei in the sample remains constant, but will influence the results observed by fitting analysis at 370 K.

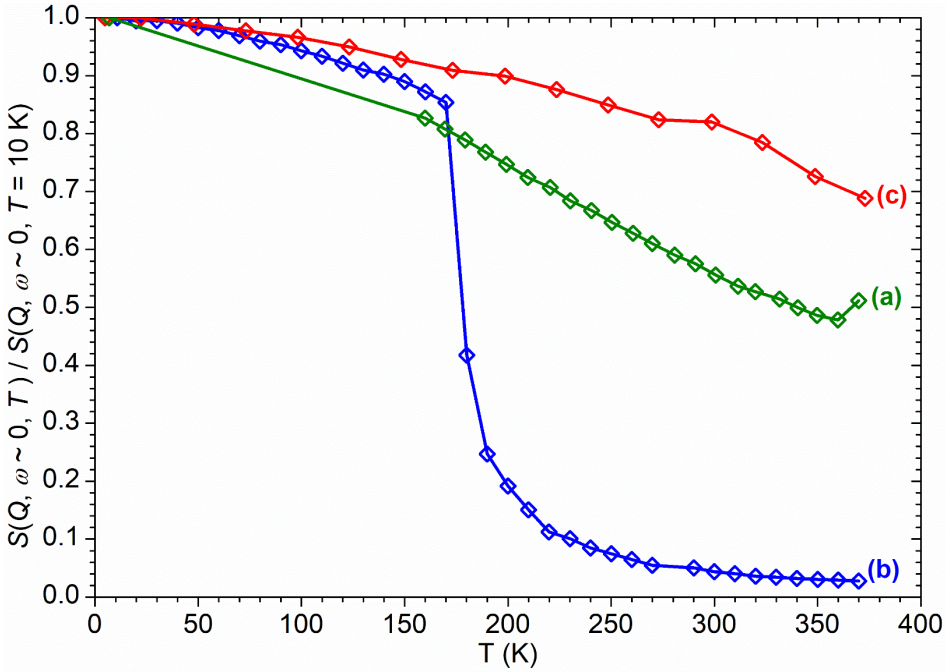

Figure 5-18: EFWS data for 1-octene in ZSM5-ST(1073K) (a) compared with bulk 1-octene (b) and the oligomer formed by 1-octene in ZSM5-FR at room temperature (c). Intensities normalised against the value at 10 K for comparison.

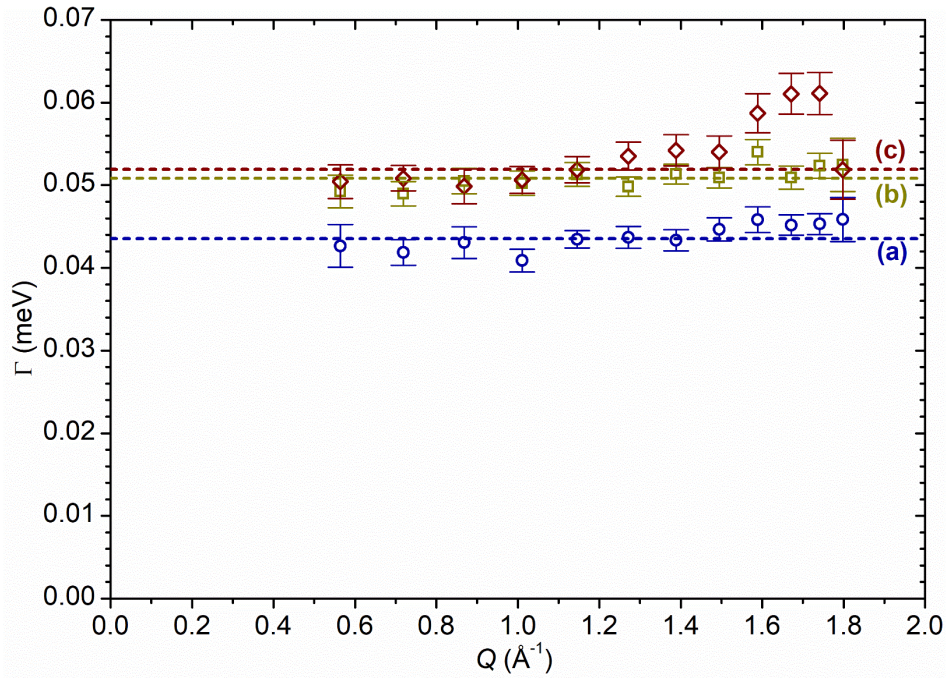

Figure 5-19: Lorentzian linewidth (Γ) *vs.* Q^2 for 1-octene in ZSM5-ST(1073K) at 270 K (a), 320 K (b) and 370 K (c). Dotted lines linear fits of each dataset to give the rotational constants in Table 5-6.

Fitting analysis of the data showed a single resolvable Lorentzian, which exhibited a constant value with respect to *Q* indicating a rotational motion (Figure 5-19). The effect of the oligomerization is also clearly apparent as the speed of rotation at 370 K is barely increased relative to the value at 320 K due to the effect of oligomerization negating the greater kinetic energy due to increased temperature. The EISF data was too noisy to allow a positive assignment of the rotation responsible but it seems likely that it represents the uniaxial rotation of the 1-octene molecules in the manner previously observed for oligomerization products in Sections 4.1.2 and 4.2.3.

If this is the case, the rotation of the 1-octene is occurring approximately 1.5× as fast as that of the 1-octene oligomer and 1.2× as fast as the propene oligomerization product, in both cases due to the 1-octene having a shorter chain length and thus being less strongly bound to the zeolite pore walls. It is not possible to perform an Arrhenius fit of all three data points to extract the activation energy of the rotation due to the contamination of the results at 373 K by the partial oligomerization. Taking the slope between the 273 K and 323 K data points only suggests that the activation energy for the rotation of the unreacted 1-octene in ZSM5-ST(1073K) is approximately 2.2 kJ mol-1, *ca.* 40 % of that of the octene oligomer in ZSM5-FR. One possible conclusion which could be drawn from this is that the mobile proportion of the octene oligomer products observed by QENS in Section 4.1.2 are on average approximately twice as long as the 1-octene chains we are observing rotate here, however the available data is too sparse to assert with confidence.

Table 5-6: Rotational constants derived from QENS data fitting for 1-octene in ZSM5-ST(1073K).

Temperature (K)	D_r (s^{-1})
273	6.62×10^{10}
323	7.72×10^{10}
373	7.89×10^{10}

5.4 Summary:

These results show that the de-alumination of H-ZSM-5 zeolites has considerable effect on its interactions with reactive olefin species. The two steamed zeolite materials created, ZSM5-ST(873K) and ZSM5-ST(1073K), possess extremely similar properties, despite the differences in their preparation methods and have been used interchangeably. The most immediately noticeable effect of the reduction in overall framework acidity in these materials is higher temperatures being required to H-bond and protonate olefins to initiate the oligomerization reaction, something observed for both 1-octene and, in greater detail, for propene. This is despite the fact that characterisation of the acid groups by ammonia TPD suggests that the individual acid sites have the same strength in both ZSM5-FR and the steamed materials. The reaction appears to propagate at a similar rate to that observed for ZSM5-FR, once the higher energies required to initiate it in either of the steamed materials are reached. However, the product oligomer mix for propene in ZSM5-ST(873K) shows evidence that the average chain length is longer in steamed samples due to the greater separation of active sites resulting in less steric restriction of maximum chain length due to intersection of the growing oligomers.

QENS analysis shows that steaming increases the mobility of adsorbed hydrocarbons. In all cases the geometry of the detected motions remains the same as those detected in ZSM5-FR, indicating that the geometry of the motion is dictated by the constraints of the zeolite pore network and these constraints are not changed significantly by steaming. Instead, the effect of the steaming is to reduce hydrogen bonding between the zeolite and the adsorbed molecules, resulting in faster rotation of 1-octene and reduced residence time between jumps for C_3 species. Propene is found to diffuse slower than propane in an equivalent environment due to the effect of interactions between the zeolite and the double bond, although this effect becomes less pronounced at higher temperatures due to the breaking of the remaining hydrogen bonds.

The differences in behaviour observed here illustrate the important distinction between the reactivity of fresh acid zeolites and that of materials which are more

representative of catalysts in industrial use, especially once they have reached steady-state operating conditions. This chapter has only considered relatively mild conditions and only one aspect of the olefin reactivity. The differences in behaviour are likely to become even more pronounced at the higher temperatures associated with cracking and isomerisation reactions, something which will be considered in more detail in Chapter 6.

Chapter 6: Neutron Spectroscopic Studies of Olefin Conversions

Having established a clear dataset on the interactions of hydrocarbons over zeolites and how these affect bond-formation reactions between olefins, consideration is now given to reactions which occur at higher temperatures. The reaction of propene at temperatures between 473 and 673 K is used to investigate its role as an intermediate in methanol-to-hydrocarbons (MTH) chemistry, while the cracking reactions of 1-octene are studied in order to better understand the chemistry of the bond breaking side of cyclic reaction mechanisms in zeolites. In the latter case, the effect of simulated catalyst aging by steam de-alumination on actual reaction chemistry is also investigated. On-stream product analysis and post-reaction testing allows determination of the likely catalytic mechanisms, while INS spectroscopy allows new insights into the nature of the coke species which form on the catalyst in use and the differences in reaction mechanisms involved in the reaction of long and short-chain oligomers over H-ZSM-5 at different temperatures.

6.1 Olefin Reaction Testing:

Having completed our series of model compound studies, we now turn to the application of the techniques developed to the more complex systems of zeolite catalysts undergoing actual catalytic reactions. In order to do this, it is necessary to increase the range of temperatures considered toward the 400 – 700 K range where a number of industrial reactions operate. We still use propene and 1-octene as model reagents, rather than the complex mixtures which are used as catalytic feedstocks in industrial reactions, as this reduces the complexity of the reaction scheme to levels where it can be analysed. The chemistry of 1-octene introduces selective cracking reactions that are important in FCC industrial processes, while the chemistry of propene conversion provides insights into aspects of methanol-to-hydrocarbons chemistry.

6.2 Propene Oligomerization Reactions:

While propene is a target product for cracking of heavier hydrocarbons, its own reactions over ZSM-5 are also of interest. Light olefin oligomerizations are related to the methanol-to-hydrocarbons reaction through the reactions which form the hydrocarbon pool in MTH chemistry. The source of the initial C-C bonds which occur in the pool formation process has been a matter of some debate, and studies suggest that propene, as well as other light olefins such as ethene, are the products of these reactions.[43-44] It is the subsequent reactions of these olefin products which form the starting population of the hydrocarbon pool, the establishment of which completes the conditioning of the MTH catalyst.[45-46, 184]

Howe and co-workers have recently shown that *operando* spectroscopic methods can observe the formation of these transient olefin intermediates within H-ZSM-5 zeolites dosed with methanol even at typical MTH reaction temperatures.[47] The same study also followed the subsequent consumption of the olefins to form higher oligomers and cyclopentadienyl (CPD) cations, both of which are known to form as part of the hydrocarbon pool cycle in MTH reactions,[185] with the cyclopentadienyl ions representing a key intermediate in the formation of

aromatic product and hydrocarbon pool species.[186] It follows that the products of the propene/zeolite reaction system at temperatures typical of MTH reactions (450-700 K)[36] should therefore closely correspond to MTH product mixtures in similar conditions, which are determined by the pore structure of the specific zeolite employed. This study seeks to test this hypothesis and to extend the reaction timeframe studied by an investigation of the reactivity of propene from 473-673 K over ZSM5-FR. On-line and *ex-situ* analysis enables determination of the specific reactions occurring within the zeolite at each temperature and their subsequent comparison with the reactions of methanol in similar zeolites, on which there is an extensive literature. The use of INS allows the characterisation of retained coke species on the catalyst, including those in the interior of the H-ZSM-5 crystallites, in a manner similar to the observations of oligomerization products described in previous chapters.

6.2.1 Propene Reaction Testing:[187]

All reactions used ZSM5-FR as the catalyst and were carried out on the ISIS catalyst preparation reactor (Section 2.3.2). Sample masses of *ca.* 17 g were used to prepare sufficient reacted catalyst for both INS and *ex situ* analysis. Samples were dried *in situ* by the procedure in Section 2.4.2 then reacted under a flow of 50 % propene in helium at a WHSV of 1 h^{-1} for a total of 6 hours on-stream, followed by 10 minutes of purging with helium alone to remove volatile products and residual propene from the reactor. Inlet and outlet pressures were recorded and remained at 1 bar (gauge) for the entirety of the reaction period in all cases. The reaction product fractions that are condensable at 293 K were collected in the reactor catch pot and the remaining products monitored using the reactor's integrated GC and MS analysis instruments (Section 2.3.2). After completion of the test protocol, the reactor was sealed, cooled and transferred to an argon glove box for sample recovery. Reactions were performed at temperatures of 473, 573 and 673 K; full details of each are given in Table 6-1.

The reacted catalyst samples were analysed on TOSCA using the standard INS collection procedure, by gas adsorption isotherm analysis and by TGA (see Sections 2.1.2.5, 2.5.2 and 2.6.3). Infrared spectra of the reacted catalysts were

collected by DRIFTS (Section 2.6.1) at a temperature of 373 K to prevent water adsorption during spectrum collection; monitoring of the infrared spectrum during heating indicated that this temperature was insufficient to affect the composition of the hydrocarbon layer in the samples. The condensable product fractions collected in the reactor catch-pot were analysed to determine composition by attenuated total reflectance infrared spectroscopy, ultraviolet-visible spectroscopy and GC-MS analysis (Sections 2.6.1 and 2.6.2).

Table 6-1: Sample details and reaction conditions for propene conversion reactions performed on the ISIS catalysis preparation reactor.

Sample Designation	Reaction Temperature (K)	Mass Zeolite (g)	Propene Flow (cm^3min^{-1})	Helium Flow (cm^3min^{-1})	Propene WHSV (h^{-1})
ZSM5-FR_Prop_473K	473	16.49	147	147	1.0
ZSM5-FR_Prop_573K	573	17.02	151	151	1.0
ZSM5-FR_Prop_673K	673	17.47	155	155	1.0

6.2.2 Analysis of Propene Reaction Products: [187]

The products of olefin conversion reactions over ZSM-5 are known to vary significantly depending on the reaction temperature employed. Temperatures below 500 K are known to favour the production of paraffins and olefins with linear or partially branched structures,[24, 26] while higher temperatures result in aromatic compounds becoming more significant contributors to the product mixture with temperatures of up to 700 K used in the olefins to gasoline distillate process.[166] The reaction conditions employed here are therefore likely to result in three different reaction regimes: (i) production of primarily linear products the 473 K sample, (ii) a transitional regime in the sample at 573 K and (iii) the final, aromatic-heavy product composition in the 673 K reaction.

The different reactivity of the three samples is readily apparent from the on-line analysis of the products, with marked differences even in the percentage conversion of the reactant. As shown in Figure 6-1 the catalyst is initially highly active at all three temperatures, attaining conversions of greater than 95 % of the propene feed as assessed by GC analysis. However, while the 573 K and 673 K samples maintain this high conversion value for the duration of the test at 473 K

the catalyst rapidly undergoes a progressive deactivation that results in conversion dropping to around 40 % after 6 hours.

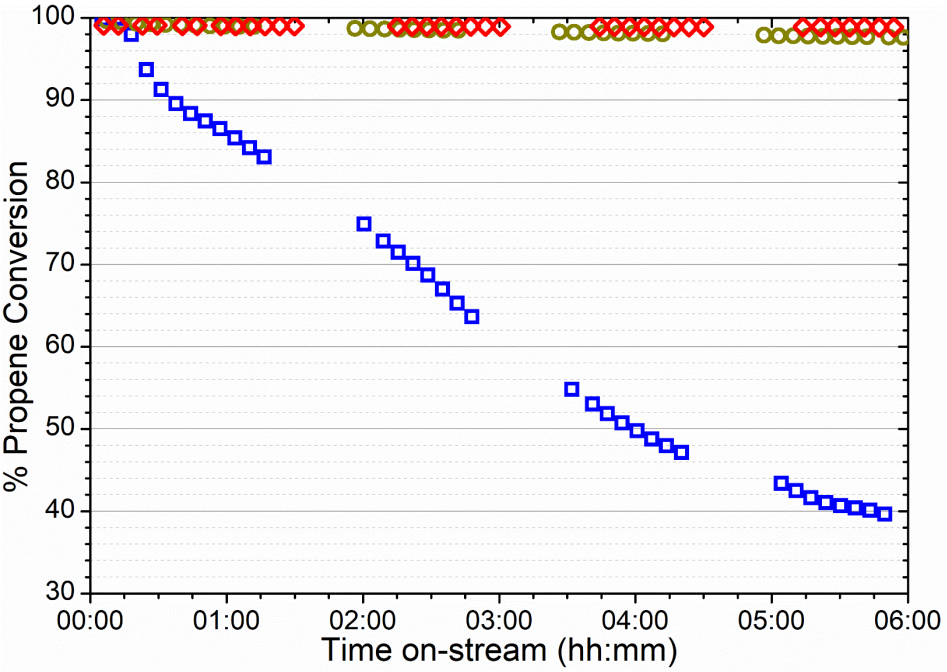

Figure 6-1: Percentage conversion versus time for the reaction of propene over ZSM5-FR at 473 K (□), 573 K (○) and 673 K (◇). Values calculated from the concentration of propene in the reactor effluent as determined by gas chromatography relative to that when the reactor is bypassed.

The on-line analysis of the products of the reaction which remain in the gas phase confirm that the catalyst is operating in a different reaction regime at each temperature studied. Figure 6-2 shows the gas phase reaction products as measured by mass spectrometry. The m/z signals measures are taken to indicate the presence of fragments associated with product species according to the scheme given in Table 6-2 Figure 6-2 shows the mass spectrometry traces across the full length of the reaction period; this allows the identification of trends, but results in complex graphs. To allow for easier comparison between samples, therefore, the signals for the most significant products at time points at the beginning and end of the reaction period are presented as bar graphs in Figure 6-3.

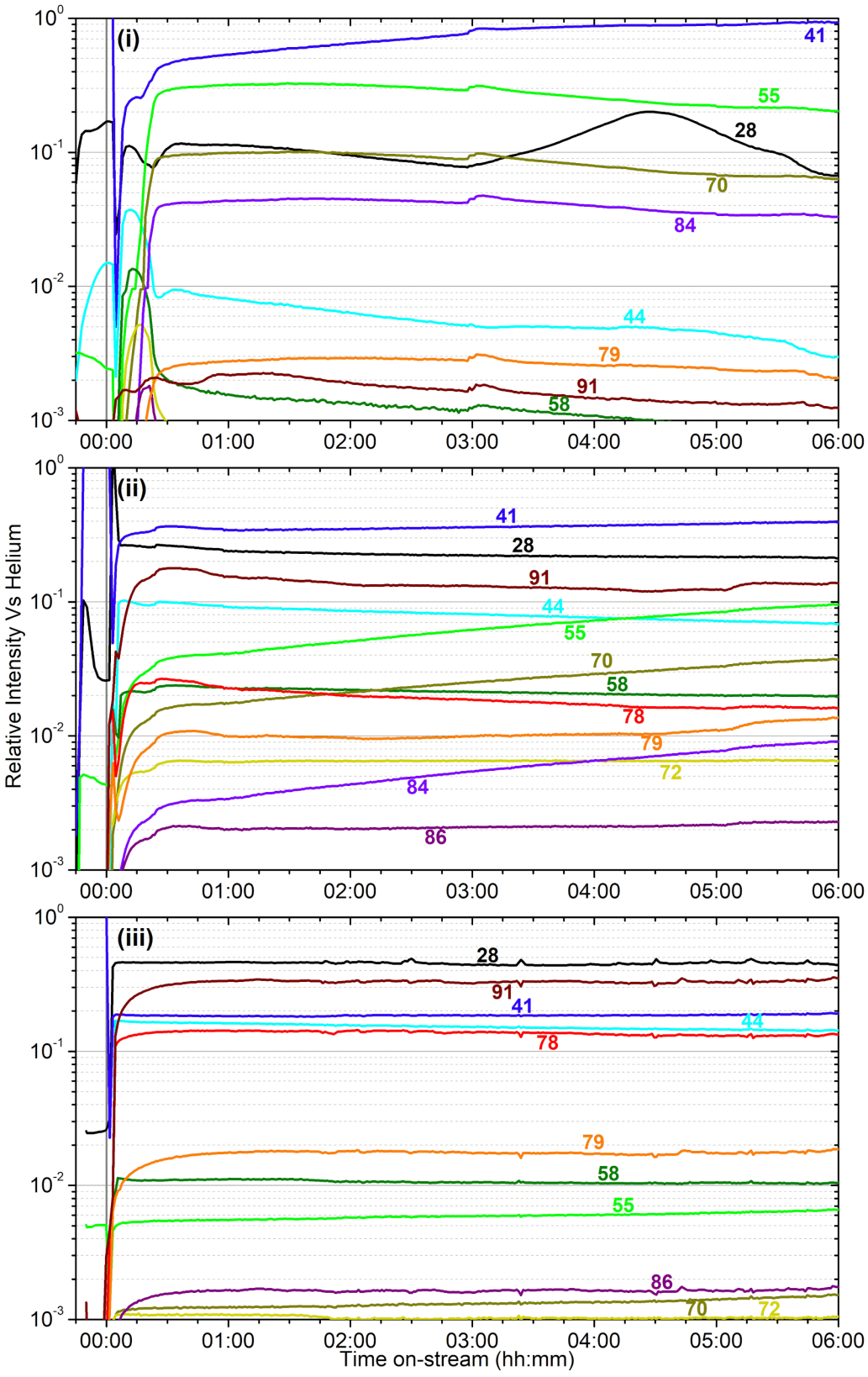

Figure 6-2: Relative ion intensities from the analysis of the gas phase products by mass spectrometry during operation at 473 K (i), 573 K (ii) and 673 K (iii) over the 6 hour duration of sample preparation. Numbers on the plots indicate the atomic mass numbers of each trace; assignments are given in Table 6-2. Intensities are normalised against the signal for 4 amu (He) to allow comparison between samples.

Table 6-2: Assignment of mass spectroscopy signals in Figure 6-2 to associated molecules. All alkene signals should be interpreted as also including contributions from fragmentation of larger molecules in the mass spectrometer.

Signal (amu)	Associated Fragment
28	Ethene
41	Propene
44	Propane
55	Butene
58	Butane
70	Pentene
72	Pentane
78	Benzene
79	Dimethyl cyclopentadiene
84	Hexene
86	Hexane
91	Tropylium (subst. benzenes)
112	Octene (only recorded for octene reactions)

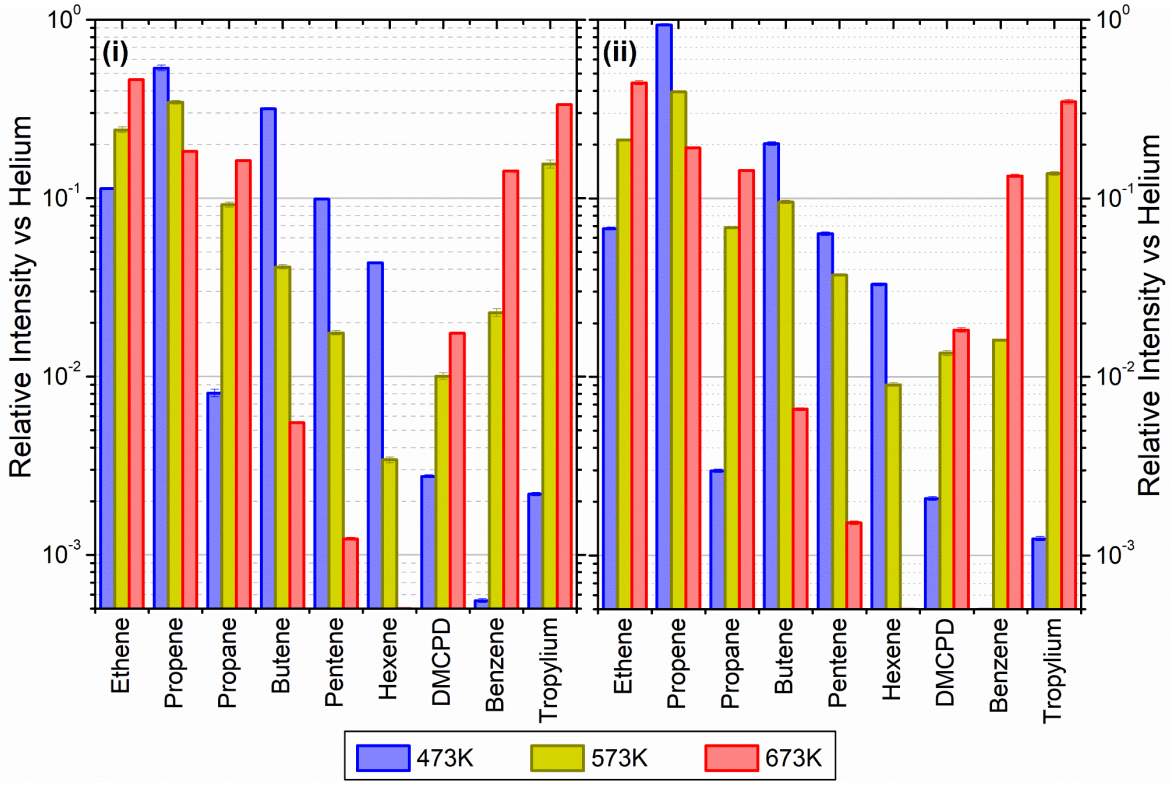

Figure 6-3: Intensities of selected mass spectrum signals from the traces shown in Figure 6-2 after 1 (i) and 6 (ii) hours on-stream. Intensities are averaged over 10 minutes up to and including the indicated time.

An example of the data obtained by GC analysis at each temperature is presented as Figure 6-4; in each case the sample represented is the one taken closest to the 6 hours on-stream mark. It can be seen that we achieve good peak separation of the light olefin components in the Poraplot Q column and of the substituted benzenes *via* the wax column but are unable to resolve the C_4+ alkyl components which emerge as a set of overlapping peaks at short retention time in the wax column trace. Neither of the molecular sieve columns produce data of interest. The GC data therefore complements the MS analysis by providing two important sets of information. Firstly, it provides a measure of the concentration of propene in the product stream that is uncontaminated by fragmentation of larger products, which can be used to accurately determine the percentage conversion of the reactant as already discussed above. Secondly, it allows the contributions of each substituted aromatic species to the overall tropylium signal observed in the MS data (91 amu) to be evaluated. Figure 6-5 shows how the concentrations of benzene and the various methylated benzenes in the product mix vary with time for each reaction temperature.

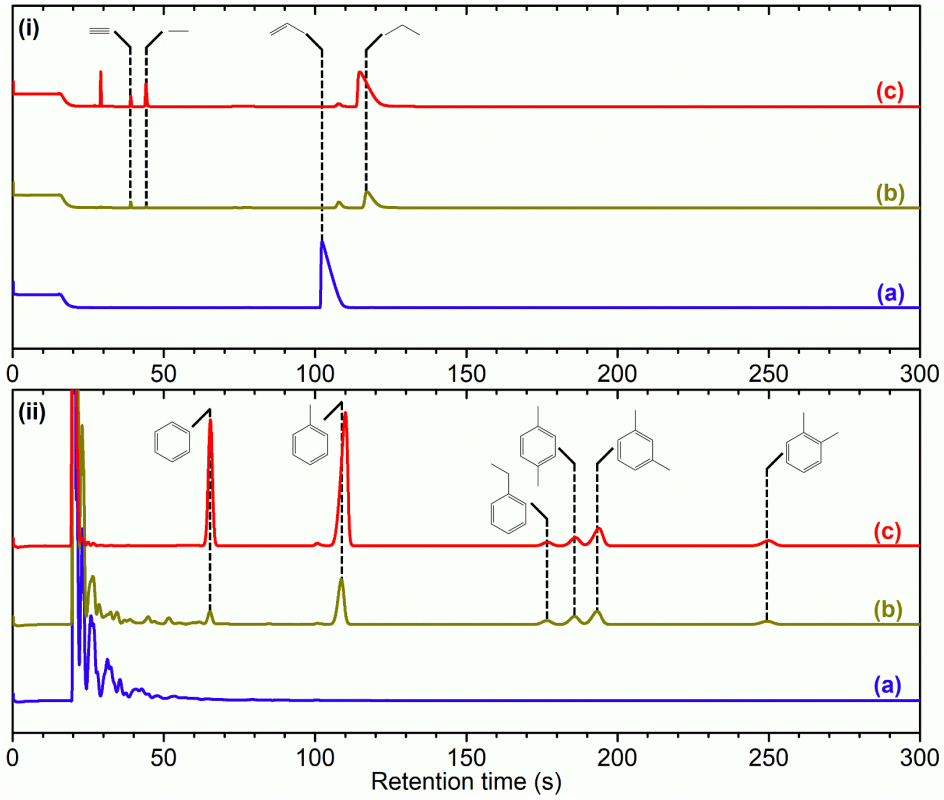

Figure 6-4: GC traces of samples collected at 6 hours on-stream for the reaction of propene over ZSM5-FR at 473 K (a), 573 K (b) and 673 K (c). Separation columns are: (i) PoraPLOT Q; (ii) CP-Wax 52CB. The identities of significant peaks are highlighted.

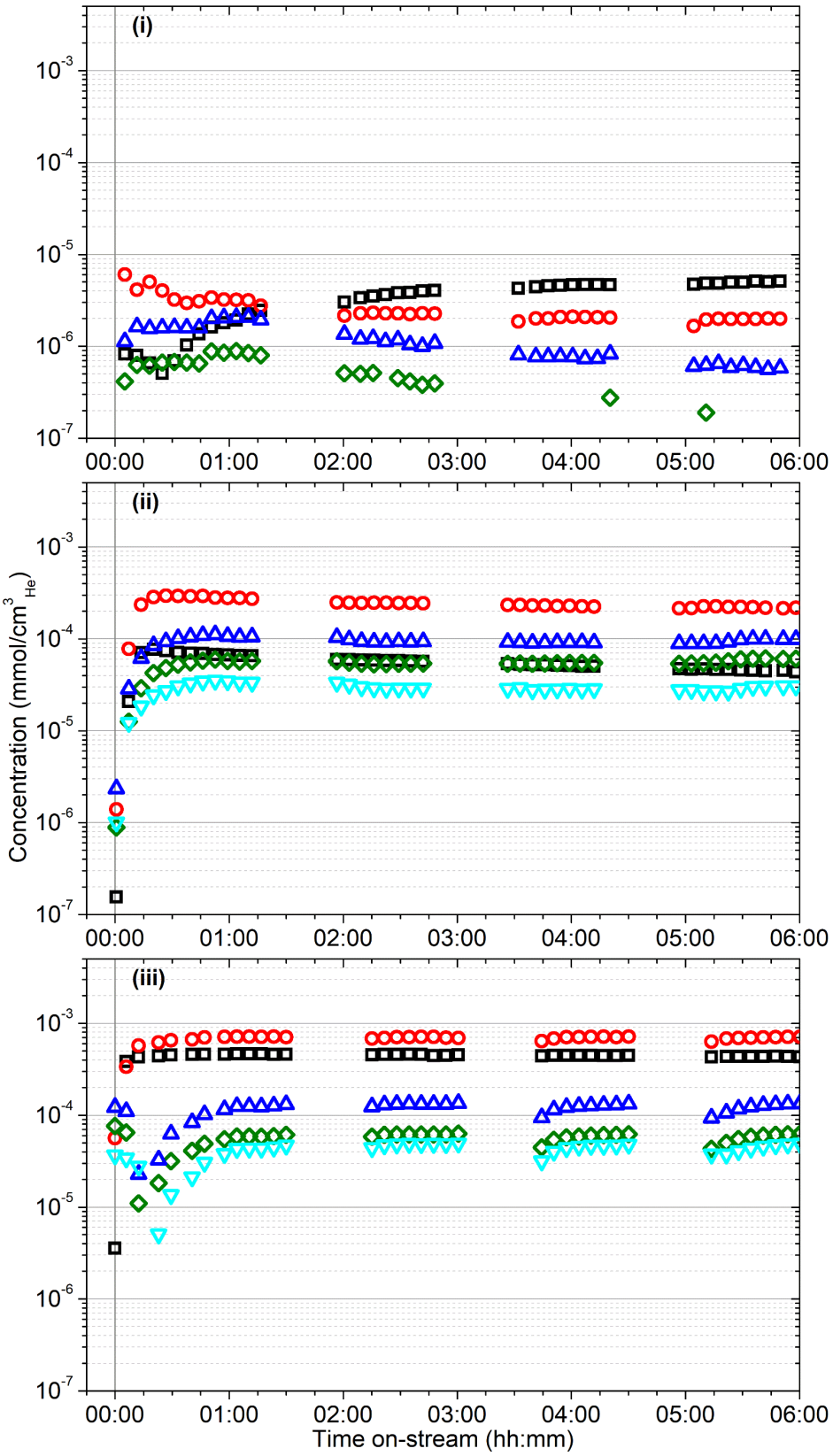

Figure 6-5: Concentration of methylated benzenes in the gaseous products versus time measured by gas chromatography at 473 K (i), 573 K (ii) and 673 K (iii). Measured components are benzene (□), toluene (○), o-xylene (◇), m-xylene (△) and p-xylene (▽). Concentrations below 3×10^{-7} mmol/cm$^3_{He}$ are not consistently resolvable from the GC baseline. The pattern in xylene selectivity at each temperature is discussed on Page 260.

6.2.2.1 Propene Vapour Phase Products – 473 K:

At 473 K the products are dominated by small olefinic fragments. The major MS signal at all points is the 41 amu signal associated with propene and propyl fragments, although the fact that this signal is high throughout the run, even in the initial stages where propene conversion as measured by gas chromatography remains high, indicates that the majority of contributions to this signal come from the fragmentation of larger molecules. The second most significant product in the early stages of the reaction is ethene (28 amu), while production of aromatic products remains negligible throughout. On initial propene contact with the catalyst, MS analysis shows an initial jump in the production of propane (44 amu), which is mirrored at lower values by the signals associated with other alkane molecules (Figure 6-2). However, this alkane production is short-lived and begins a drop-off to negligible levels after 20 minutes time-on-stream, simultaneous with the commencement of the decay in propene conversion observed in the GC data (Figure 6-1). At the same time, there is a significant increase in the production of heavier alkenes, with production of butene and pentene being particularly significant. Since the production of hexene is also significant at this point, this suggests that the catalyst is operating in a regime where propene oligomers (C_6 and C_9) form the major products, with fragmentation of the C_9 product occurring in the mass spectrometer to give the C_4 and C_5 signals observed. The switchover to this chemistry is complete by t + 30 minutes and the catalyst remains in this regime for the remainder of the reaction, with the levels of non-propyl products falling over time in line with the reduced propene conversion.

Although aromatic production is minimal, the GC concentration data shows that the predominant substituted benzene products still vary over time. On initial contact, the major aromatic product is toluene with some production of m-xylene. After the same time period observed for the switch to C_6 and C_9 production in the major alkene products, the level of toluene is observed to decrease and benzene production begins to increase which makes it the major aromatic product by + 90 mins. Xylene production also drops steadily from this point until the end of the reaction run.

6.2.2.2 Propene Vapour Phase Products – 573 K:

The reaction profile at 573 K is markedly different. The activation time after propene contact is reduced to approximately 10 minutes and does not feature the production of saturated alkanes observed initially at 473 K. The zeolite achieves its steady-state distribution of products by 15 minutes on-stream and maximum production by + 30 mins. The 41 amu signal remains the largest, although it is approximately one third as intense as at 473 K. The lack of any significant propene peak in the GC data, means that propene conversion remains high and this MS signal must be due to propyl fragments from larger products. The signal at 44 amu is also considerably stronger, suggesting that some degree of propene hydrogenation may be occurring. Ethene remains a major product, and aromatic production is now significant with large signals for both the tropylium ion (91 amu) and the benzyl ion itself (78 amu); as well as a noticeable population of dimethyl cyclopentadiene (DMCPD), which is produced as an intermediate in the alkene cyclisation process that forms aromatic species within zeolites.[47] The concentration of aromatics in the GC feed is two orders of magnitude higher than at 473 K, with the major constituent being toluene and benzene being produced at a similar rate to the xylenes. Xylene production continues to favour *m*-xylene over *o*- or *p*-xylene, an effect which remains constant throughout the reaction period. There is also a shift in product levels which occurs throughout the reaction: minor decreases in aromatic production levels are accompanied by an increase in the butyl and pentyl signals, suggesting that, while the catalyst does not deactivate significantly over a 6-hour timeframe, it does indeed undergo a change in reaction scheme toward one more similar to that observed at 473 K.

6.2.2.3 Propene Vapour Phase Products – 673 K:

The 673 K reaction reveals yet another product profile. Catalyst conditioning is now a single step process with the product signals rising immediately to their steady-state values. Levels of propyl fragments are significantly decreased and the major products are now aromatics and ethene, while propane levels are increased only slightly relative to 573 K. Similarly, xylene production remains at the same level as at 573 K, and continues to favour *m*-xylene, with the increased aromatic levels being due to increased amounts of toluene and benzene. Levels

of larger alkyl fragments are negligible, indicating that simple propene oligomers are not major products. Product levels remain constant throughout the run with no signs of catalyst deactivation or a shift in reaction scheme occurring at this temperature.

6.2.2.4 Propene Condensable Products:

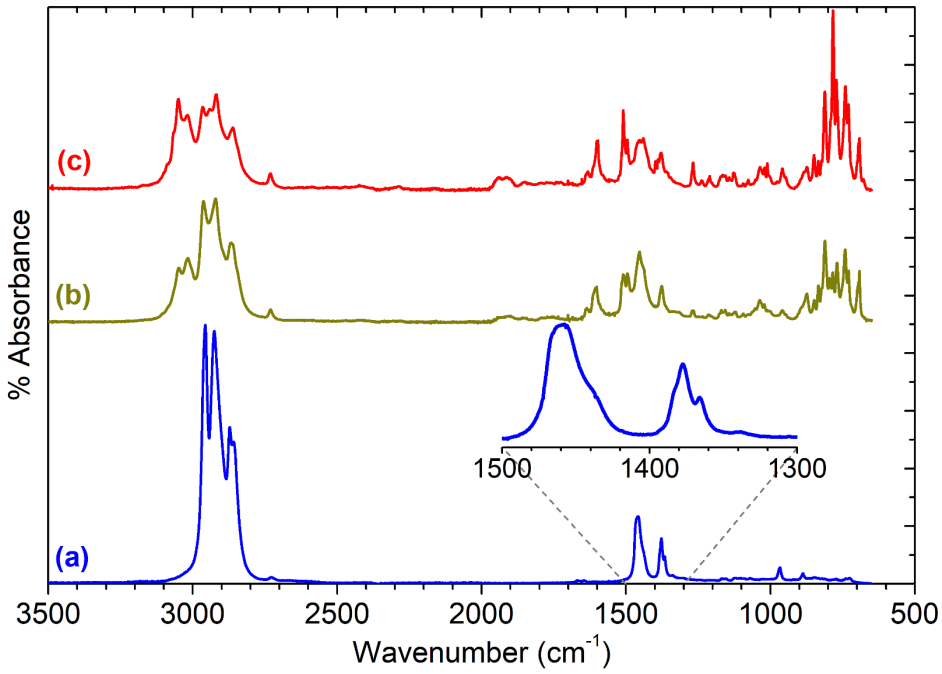

Figure 6-6: Infrared spectra of the condensable product fraction from reactions at 473 K (a), 573 K (b) and 673 K (c) collected by ATR-IR. Spectra offset in *y*-axis for clarity. Inset shows the methyl bending modes of the 473 K products in greater detail.

Analysis of the condensable product fraction collected in the reactor catch-pot confirms the deductions made from the *in situ* monitoring. The infrared spectrum of the condensable product, shown in Figure 6-6, is remarkably simple at 473 K. No distinct peaks are observed above 3000 cm^{-1}, indicating that the product mixture is primarily alkanes with the four visible peaks in the C-H stretch region being the symmetric and antisymmetric stretches of CH_3 (2871, 2956 cm^{-1}) and CH_2 (2857, 2924 cm^{-1}).[188] The methylene scissors mode is present at 1458 cm^{-1} and the antisymmetric methyl bending mode at 1437 cm^{-1}. The fact that the symmetric methyl bending is present both as the isolated mode from R-CH_3 groups at 1377 cm^{-1} and as the characteristic doublet formed by coupling between adjacent groups in R-$CH(CH_3)_2$ at 1365 cm^{-1} and 1383 cm^{-1} (as a shoulder to the R-CH_3 peak)

indicates that the products consist of both straight chain and branched species. Other modes in the spectrum are extremely weak, indicating that no primary alkenes are present in the product mixture, although the presence of a peak at 968 cm^{-1} and very weak absorbances in the 1640-1690 cm^{-1} range indicates that there may be small amounts of dialkyl alkenes. Vinyl groups of this stereochemistry have quite weak peak intensities in infrared spectra and the associated vC-H modes fall in the 2990-3020 cm^{-1} range, so could be concealed by the tail of the alkyl stretching peak.[188] This would be consistent with the condensable products at 473 K consisting of saturated alkanes and quite large alkenes, resulting in a low level of sp^2 character. There is no evidence of appreciable levels of aromatic products, which would result in C-H stretches at energies of 3050 cm^{-1} and above and strong modes in the 900 – 650 cm^{-1} region.

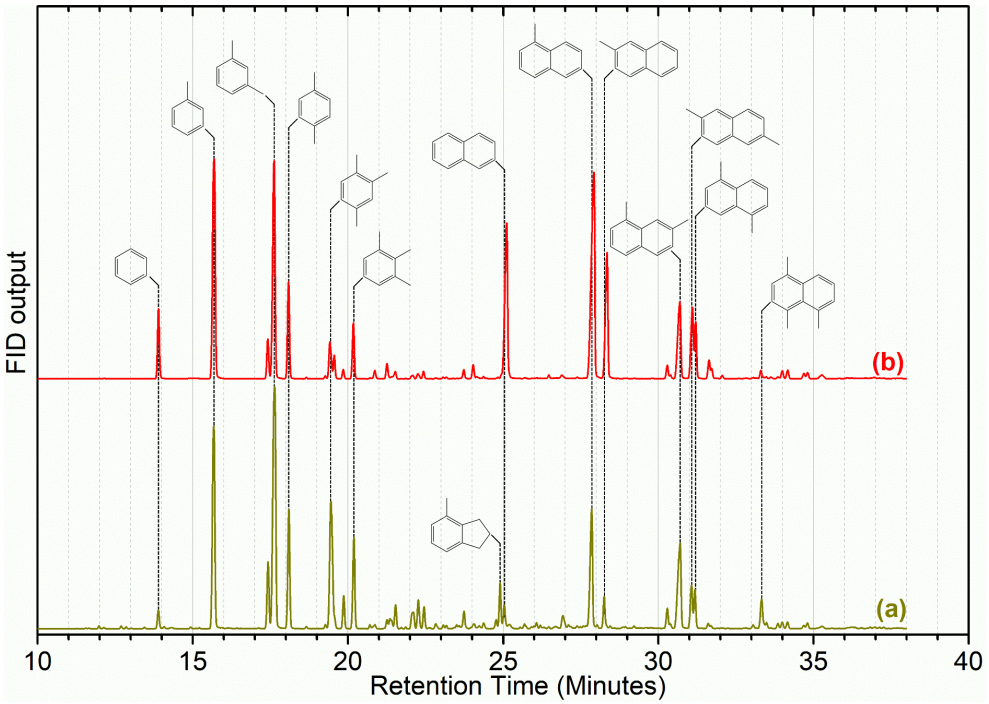

Figure 6-7: GCMS traces of the condensable product fraction for the reaction of propene over ZSM-5 at 573 K (a) and 673 K (b). Identities of significant peaks are highlighted.

The products at 573 and 673 K exhibit all of the alkyl modes present in the 473 K spectrum, but also add additional features due to the presence of aromatic species. This is most clearly demonstrated by the presence of additional vC-H modes at 3050 and 3017 cm^{-1} which are stronger in the 673 K spectrum due to the greater production of aromatics at this temperature. The rich nature of the

aromatic spectra, particularly in the 600-800 cm^{-1} region, confirms that multiple substituted aromatics are present, due to the presence of modes at frequencies associated with mono-, di-, and trisubstituted benzenes, as well as other modes which indicate the presence of multiple isomers or larger species. GCMS analysis (Figure 6-7) confirms the presence of tri-methyl benzenes, naphthalenes and tetralins in significant quantities, although tetra-, penta- and hexa-methyl benzenes are notably absent. These species were not present in the liquid products of the 473 K reaction, which exhibits no significant peaks in the GCMS trace using the column and analysis programme employed and has therefore been omitted from Figure 6-7. UV-Visible spectroscopic analysis of the liquids indicates the presence of trace quantities of polyaromatics as large as tricyclic species, evidenced by the presence of peaks up to 380 nm (Figure 6-8), despite the fact that durene is generally regarded as the largest species capable of diffusing out of the zeolite pore in ZSM-5.[40] Due to their low concentrations, these polyaromatics products may represent propene conversion on exterior acid sites where steric considerations are not relevant. The disappearance of the mode at 968 cm^{-1} and lack of any additional modes in the 1650-1700 cm^{-1} or 3075-4000 cm^{-1} regions in Figure 6-6 indicates that linear or branched alkenes are even less significant contributors to the condensable products at these higher reaction temperatures than was the case at 473 K.

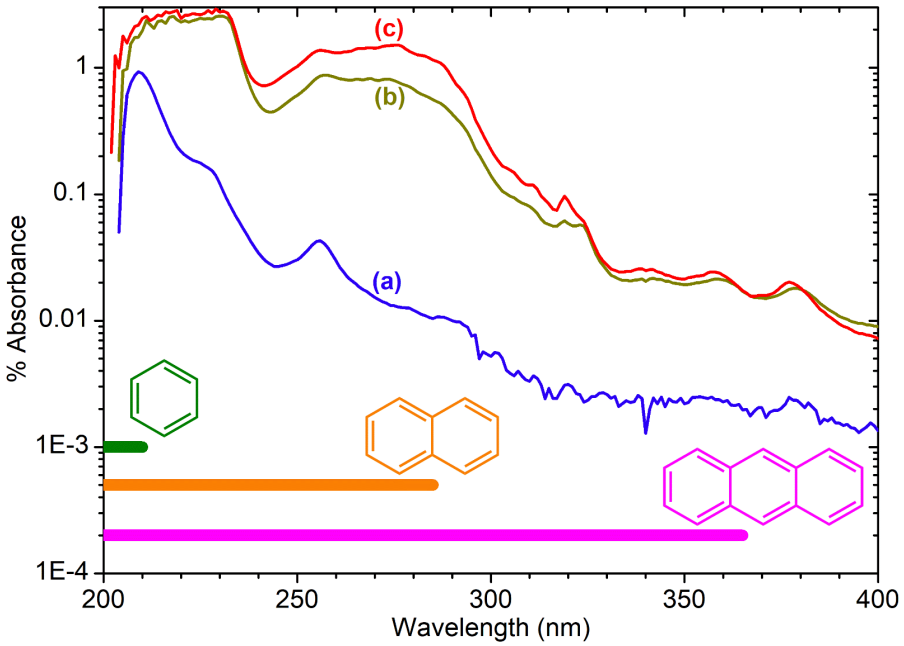

Figure 6-8: UV-Vis spectra of the condensable product fraction for the reaction of propene over ZSM5-FR at 473 K (a), 573 K (b) and 673 K (c). Analysed samples were 100 ppm solutions in cyclohexane. The absorption ranges associated with typical mono-, bi- and tricyclic polyaromatics are highlighted.

6.2.3 Analysis of Propene Coked Catalysts:

Ex situ analysis of the zeolite catalysts following completion of the reaction allows examination of both the state of the catalytic acid sites and any retained species which remain inside the zeolite pores. Due to the fact that the reactor was purged with inert gas at the end of the 6 h reaction run, the non-zeolite species which are observed in these measurements are those which are immobilised within the pore network and which therefore contribute to catalyst deactivation through pore blocking. For brevity, these species will be referred to by the generic designation of ‘coke’ for the remainder of this section.

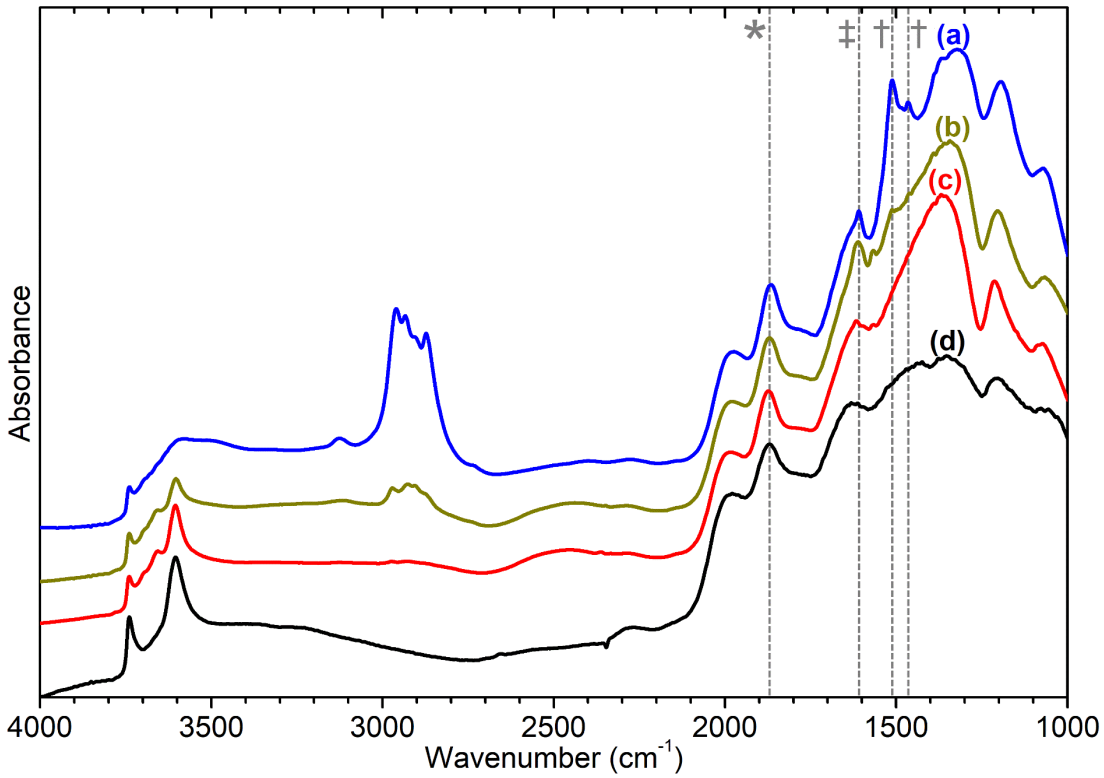

Figure 6-9: DRIFTS infrared spectra of ZSM-5 catalysts after reaction at 473 K (a), 573 K (b) and 673 K (c) compared with ZSM5-FR (d). The allyl stretching modes of adsorbed cyclopentadienyl cations (†) and aromatic C-C ring quadrant stretch (‡) are highlighted. Intensities normalised on the zeolite framework combination mode at 1870 cm^{-1} (*) to allow direct comparison between samples. Traces offset in *y*-axis for easier interpretation.

Infrared analysis of the reacted samples by DRIFTS, shown in Figure 6-9, allows examination of the νC-H and νO-H regions of the vibrational spectrum of the catalysts. However, the usual problem of interference from the zeolite framework means that only the strongest deformation modes of the coke are available for analysis. This holds true even if difference spectra are used since the darkening of the samples due to hydrocarbon build-up results in increased absorbance across the full frequency range and incomplete cancellation of the zeolite modes. The INS spectra collected on TOSCA, presented as Figure 6-10, do not share this limitation, and in combination with the infrared data, provide access to the full vibrational spectrum of the coke species.

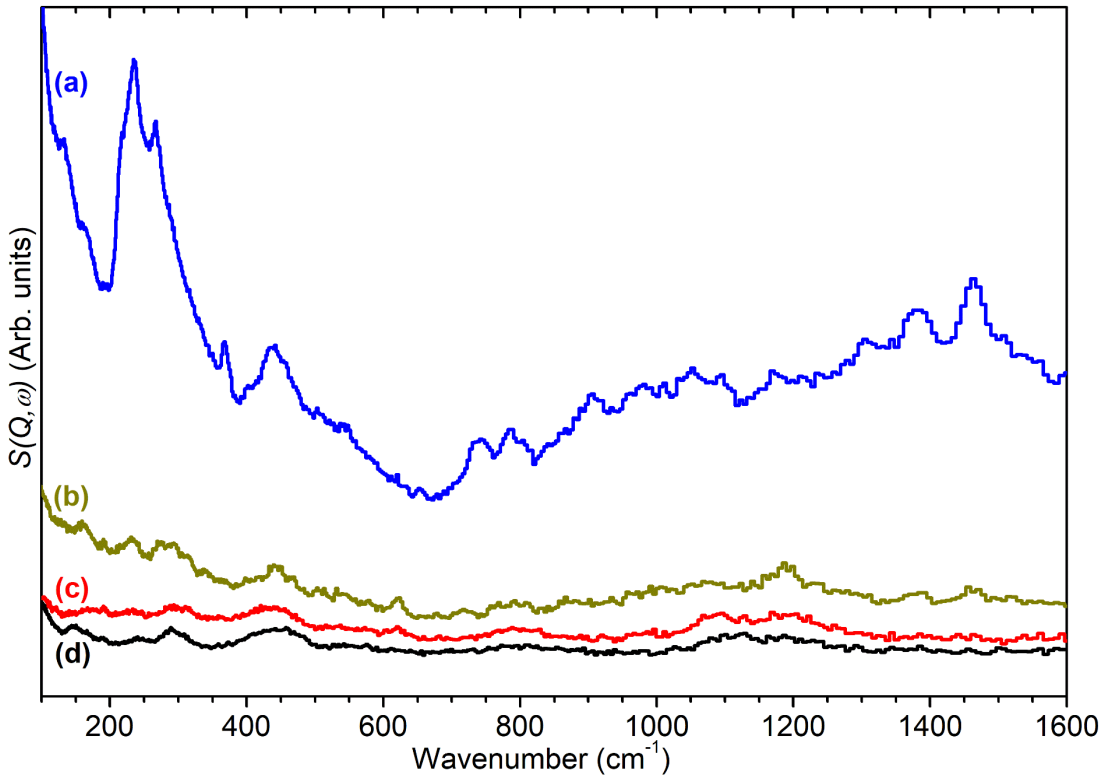

Figure 6-10: INS spectra of ZSM-5 catalysts after reaction at 473 K (a), 573 K (b) and 673 K (c) compared with the spectrum of ZSM5-FR (d). Spectra collected on TOSCA and normalised to correct for differences in sample mass.

Analysis of the reacted samples by TGA and BET methods allow determination of the percentage of the sample which is composed of coke species and the degree to which this coke blocks access to the zeolite pore channels by comparing the accessible surface area to that of the fresh catalyst (Section 3.1.1.2). The results are given in

Table 6-3, while Figure 6-11 shows the temperature dependence of the coke combustion which varies depending on its composition.

Table 6-3: Properties of ZSM5-FR and reacted catalysts determined by TGA and BET surface area assessment.

Sample	Coke Content (wt%)	BET Surface Area (m^2s^{-1})
ZSM5-FR	-	370 ± 11
ZSM5-FR_Prop_473K	9.53	66 ± 1
ZSM5-FR_Prop_573K	5.31	284 ± 6
ZSM5-FR_Prop_673K	2.32	364 ± 8

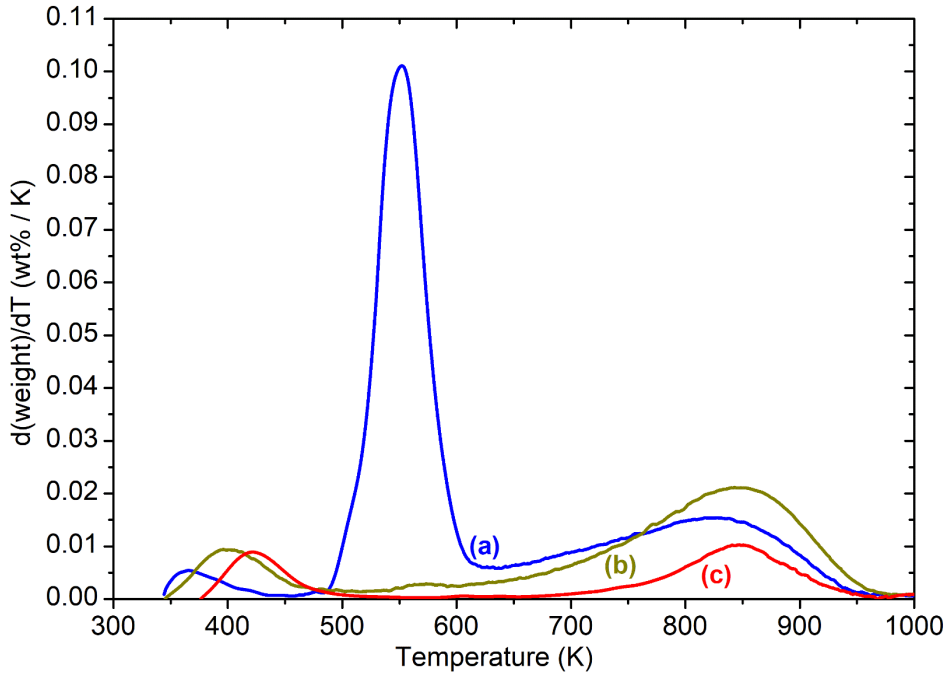

Figure 6-11: Rate of weight decrease during thermogravimetric analysis in 10% oxygen of samples after reaction at 473 K (a), 573 K (b) and 673 K (c) showing the temperatures required for oxidation of coke species in each sample.

6.2.3.1 Propene Reacted Catalyst – 473 K:

As shown by the values in

Table 6-3, at 473 K the ZSM-5 retains a considerable quantity of coke, constituting 9.5% of the sample mass as determined by thermogravimetric analysis (TGA). This high coke content leads to a correspondingly high degree of pore blockage, with over 80% of the BET surface area of the fresh zeolite being rendered inaccessible in the reacted sample. The intensity of the spectrum observed in the INS data at this temperature (Figure 6-10) also makes it clear that the coke is highly hydrogenated. Examination of the rate of coke oxidation with temperature confirms this (Figure 6-11), with approximately two thirds of the total mass of coke in the sample being oxidised between 500 and 600 K, indicating that it is Type I coke with a high hydrogen content.[189] The lack of any potential sources of oxygen in the reaction inputs means that oxygenates cannot form a component of this Type I coke and it must consist primarily of saturated hydrocarbons. From the vibrational data it is evident that these species are similar in form to the mix of saturated alkanes observed in the condensable products, with the νC-H region

showing strong bands from CH_3 and CH_2 groups but no modes associated with the presence of substituted benzenes. The exception is a single broad alkene mode centred at 3125 cm^{-1}, which is considered below. The INS spectrum is considerably richer than the corresponding region of the IR spectrum in Figure 6-9(a) due to the lack of selection rules in INS meaning that more modes are present, confirming that the coke species are primarily alkyl. As shown in Figure 6-12 the spectrum is very

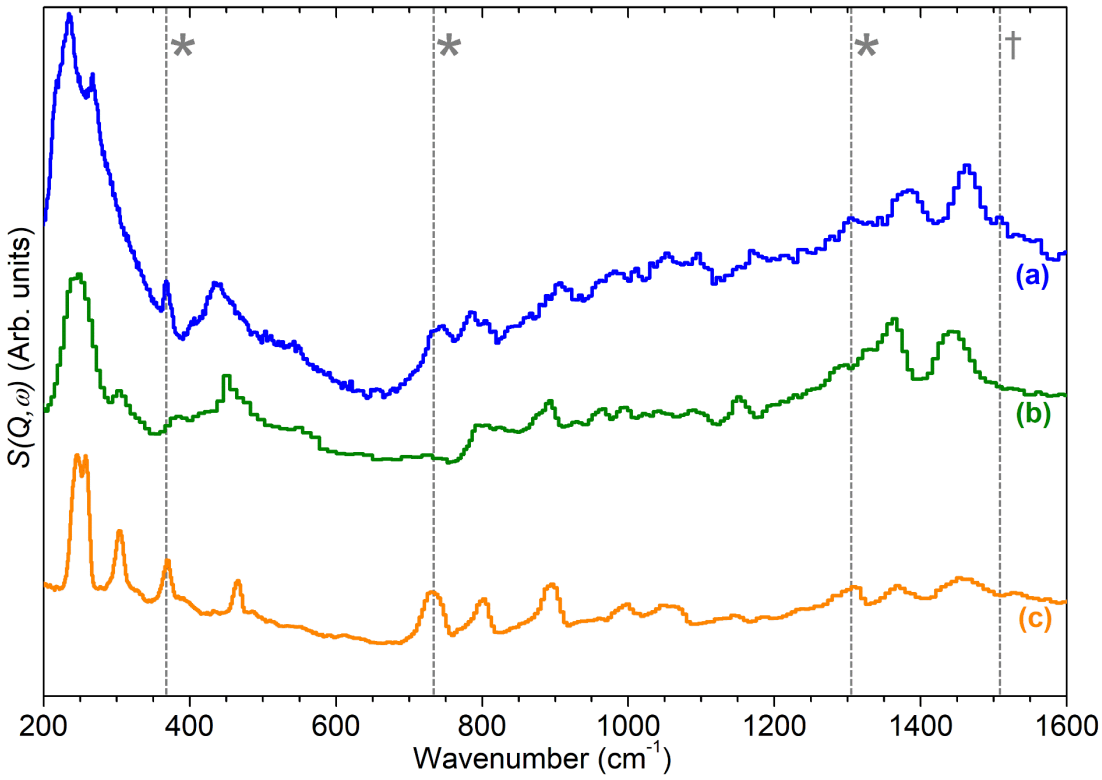

Figure 6-12: INS spectrum of ZSM-5 catalyst after reaction at 473 K (a) compared with reference spectra of solid atactic polypropene (b)[56] and hexane (c).[153] Modes indicating the presence of adjacent methylene groups (*) and the asymmetric allyl stretch of cyclopentadiene (†) in the experimental spectrum have been highlighted. All spectra collected on TOSCA and offset in *y*-axis for clarity. Reference spectra obtained from the ISIS INS database.[157]

similar to that of atactic polypropene, suggesting a highly branched saturated structure. However, the presence of additional peaks at 1304, 730 and 368 cm^{-1} indicates that chains of adjacent methylene groups are also present, these corresponding to the in-phase twist, in-phase rock and in-phase longitudinal acoustic mode of $-(CH_2)_n-$ groups respectively.[188] It can therefore be deduced that the coke species in this sample are not purely polypropene-like but contain regions

where the oligomerization of the introduced propene has proceeded *via* a linear end-to-end mechanism.

The previously mentioned alkene mode at 3125 cm^{-1} visible in addition to these alkyl species in Figure 6-9 has been taken in previous studies of hydrocarbon conversion over zeolite catalysts to be indicative of the presence of cyclopentadienyl (CPD) cations, which form a key intermediate species in the conversion of linear oligomers to alkenes and aromatic species in the hydrocarbon pool mechanism,[47, 185-186] and that are known to be stable in ZSM-5 type zeolites.[190] The associated very strong allyl asymmetric stretching mode at 1510 cm^{-1} and the weaker symmetric counterpart at 1465 cm^{-1} are also visible in the infrared spectrum, being two of the few modes strong enough to be clearly distinguishable from the zeolite contributions below 2000 cm^{-1} and are highlighted in Figure 6-9.[185] The asymmetric stretching mode is also just visible in the INS spectrum, although considerably weaker due to the overall population of the CPD cation being low and the associated hydrogen motions small, but the symmetric mode overlaps with, and is indistinguishable from, the CH_3 asymmetric bending from the more populous alkyl species. The DRIFTS data also shows an additional mode at 1611 cm^{-1}, which is assigned to an aromatic C-C stretching mode (the ring quadrant stretch) from adsorbed toluene or xylenes.[188] The population of these aromatics is quite low, as indicated by the low levels of their production in the on-line analysis and their minimal contributions to the INS data, explaining why their presence cannot be discerned from Figure 6-9 as the associated C-H stretch modes are weak. This indicates that trace aromatic products, and reactive intermediates from the reactions which formed them, remain trapped within the zeolite by the high degree of pore blockage. In the case of the intermediates, this also prevents them from accessing a catalytic site and being converted to one of the final product species. The TGA data also shows the presence of a population of coke with combustion temperatures from 700-950 K, as visible in Figure 6-11. While the trapped aromatics represent some of this material, the relatively high weight of this coke relative to the low levels of aromatics visible spectroscopically, argues for the presence of a quantity of fully carbonaceous material which is not easily detectable by infrared or INS.

6.2.3.2 Propene Reacted Catalyst – 673 K:

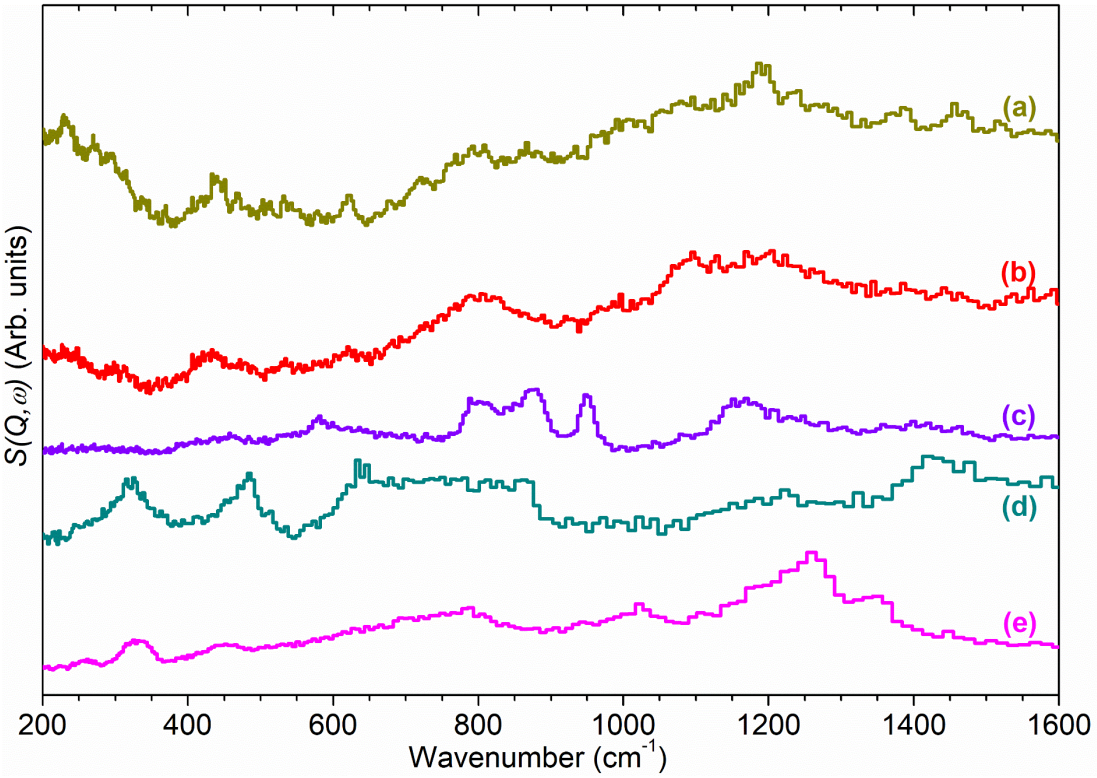

Figure 6-13: INS spectra of coke species formed by reaction at 573 K (a) and 673 K (b) after subtraction of spectrum of ZSM5-FR compared with reference spectra of glassy carbon (c),[193] graphite (d)[194] and diamond (e).[194] All spectra collected on TOSCA and offset in *y*-axis for clarity. Reference spectra obtained from the ISIS INS database.[157]

In contrast to the data at 473 K, the infrared data at 673 K shows no evidence of C-H stretching modes from coke species. Therefore, the 2.3 wt% coke composition of the sample must take the form of primarily carbonaceous material. This is borne out by the extremely low intensity of the INS spectrum, indicating very low levels of hydrogen in this sample and also that all weight loss due to coke oxidation takes place from 750-950 K. Since INS spectra are quantitative, the zeolite contributions can be simply subtracted to give the spectrum of the coke species only. Doing this (Figure 6-13) shows that the coke does not have distinct bands but does exhibit broad regions of increased intensity in the ranges 700-900 cm^{-1} and 1050-1300 cm^{-1}, which correspond to features found in the spectra of pure carbon in its various forms. The coke produced at this temperature is therefore highly carbonaceous, with a composition closer to amorphous coke than graphitic coke, evidenced by the lack of intensity in the 600 – 700 cm^{-1} region of the experimental

spectrum, or glassy carbon (formed of randomly-arranged graphene sheets), evidenced by the missing peak at 950 cm^{-1}. This clear view of the spectrum of the carbonaceous coke also allows the identification of the previously noted high temperature coke material in the 473 K sample, which could not be identified earlier due to blending into the higher level of background intensity from the hydrogenated coke. Since the difference in surface area between the fresh and 673 K reacted samples is below the margin of error in the BET measurements, this coke content does not block the zeolite pores to any appreciable degree. The lack of any CPD in the spectrum indicates that conversion of the intermediate to alkene and aromatic products occurs too rapidly for any significant population of this moiety to accumulate at this temperature. Some evidence of retained toluene and benzene products is found in the 1565-1620 cm^{-1} region of the infrared spectrum (Figure 6-9), although the aromatic CC stretching peaks are difficult to separate from the overall increased baseline level of absorbance caused by darkening of the catalyst sample.

6.2.3.3 Propene Reacted Catalyst – 573 K:

The properties of the sample reacted at 573 K are intermediate between the extremes represented by the 473 and 673 K samples in all respects. The coke content at 573 K is almost exactly halfway between the other two samples and results in a lower, but still noticeable, degree of pore blockage. The IR data shows the same C-H stretching modes as observed at 473 K and the presence of trapped CPD ions but considerably weaker in both cases. In contrast, the signals of aromatic products in Figure 6-9 are stronger than at 473 K, with a weaker lower-frequency ring stretch also being visible at 1567 cm^{-1},[188] which is consistent with the higher level of aromatic production observed at this temperature. The TGA temperature graph similarly shows a small but detectable level of Type I coke, a high level of the carbonaceous coke observed at the other two reaction temperatures and elevated levels of aromatics, evidenced by the loss of mass from 700-800 K. The INS data is somewhat different in that the overall scattering intensity is much closer to the low-hydrogen spectrum observed at 673 K with very little evidence of the CH groups observed by infrared representing a significant proportion of the coke (Figure 6-13). This suggests that the CH containing species are concentrated at or near the surface of the zeolite crystallites and are

therefore over-represented in the DRIFTS spectra compared to the bulk measurement provided by INS. What INS intensity there is, takes the form of a broad region from 600-1200 cm^{-1} which lacks assignable features, suggesting it is formed from a mixture of different coke types. A possible hypothesis is that coke build-up in the catalyst is initially similar to that observed at 673 K, but with the progressive shift towards more alkyl products observed in the on-line reaction monitoring, a population of immobile alkanes begins to build up near the catalyst surface towards the end of the reaction period. This is detectable by DRIFTS and pore blocking by these immobile alkanes leads to higher levels of trapped aromatics.

6.2.3.4 Acid Site Effects:

Examination of the 3400-3800 cm^{-1} region of the infrared spectrum (Figure 6-9) shows the effect of the coke build-up throughout the zeolite on the acid sites in each catalyst. The spectrum of the fresh zeolite shows a strong peak at 3595 cm^{-1}, corresponding to the Brønsted Al-O(H)-Si catalytic sites, and a weaker peak at 3735 cm^{-1} from the presence of silanol groups at the zeolite surface and in silanol nest defects.[191-192] A third mode, visible as an extremely weak shoulder to the Brønsted site peak at 3651 cm^{-1}, is due to the presence of extra-framework AlOH species in the zeolite pores.[96] The corresponding region in the 673 K sample shows minor differences. The intensity of the Brønsted OH peak is slightly reduced, indicating a reduction in the number of acid sites, which is explained by the increase in the intensity of the AlOH site peak, indicating that the reaction conditions at this temperature have led to some de-alumination of the zeolite framework. The intensity of the silanol groups is also decreased and this can be attributed to the presence of a new shoulder at 3696 cm^{-1} which is caused by the shift of the silanol peak in cases where a hydrocarbon is physisorbed onto the Si-OH group.[193] This indicates that at least some of the coke formation is occurring at sites associated with silanol groups. The 573 K spectrum shows similar behaviour, except that the reduction in the Brønsted peak is greater without a correspondingly greater level of AlOH formation, indicating that some of the loss of acid sites is due to the non-regeneration of the catalytic acid groups rather than framework de-alumination in this case. The 473 K spectrum shows yet further loss in Brønsted sites, and notably does not exhibit any increase in AlOH

population, indicating that this temperature is insufficient to cause framework de-alumination. In this case some of the loss in acid sites is due to the formation of physisorbed hydrocarbon – Brønsted site complexes which can be seen as a broad peak centred at 3500 cm^{-1} in a similar fashion to the behaviour observed for the silanol peak.[193]

6.2.4 Reaction Mechanisms in ZSM-5 Propene Conversion:

The reaction data indicates the presence of a wide variety of different product and coke species with quite different profiles at each reaction temperature investigated. However, the presence of all these species can be explained in terms of the zeolite catalysing a hydrocarbon pool series of reactions similar to that extensively studied for methanol-to-olefins chemistry. Two distinct reaction cycles occur within the zeolite, with the predominant cycle varying depending on temperature.

6.2.4.1 Cycle 1 – Alkyl Production:

On initial propene contact, at all temperatures, the reaction occurs according to the mechanism previously identified in Chapter 4, Section 4.2.2.2 with propene at the active site forming a H-bonded intermediate, which immediately protonates to form a bonded alkoxide, and reacts with additional gas-phase propene to form branched oligomers.[48-49, 148] After any given alkene addition, the branched product may optionally undergo rearrangement *via* the method described by Chen and Bridger[26] to give the linear oligomer sections whose modes are observed in the INS data. While the linear product predominates at the lower temperatures investigated in Chapters 4 and 5, the relative intensity of the branched and unbranched modes in the 473 K INS indicates that the branched form predominates at this temperature, due to the faster oligomerization reaction rate, resulting in decreased time for rearrangements between alkene addition steps. Once formed, the alkoxide chains may either be released and diffuse away from the active site, yielding the alkene products observed in the product analysis and regenerating the Brønsted acid group or, alternatively, undergo further chain propagation to

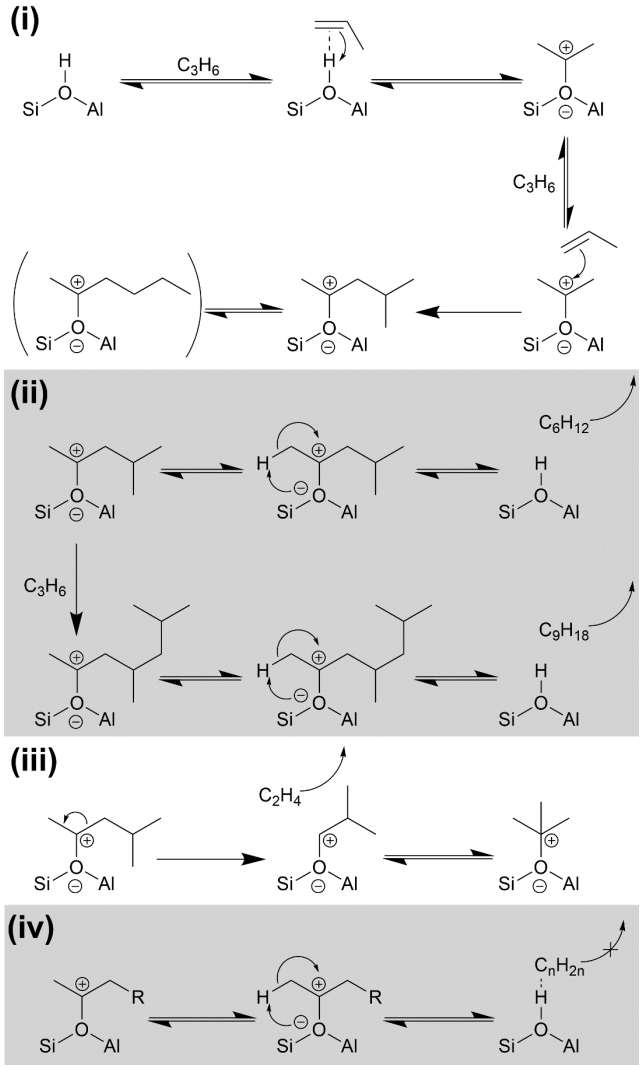

Figure 6-14: Scheme for alkoxide intermediate reactions of propene over H-ZSM-5: (i) alkene protonation and initial oligomerization; (ii) alkene product release and acid site regeneration or further oligomerization; (iii) ß-scission of bonded alkoxide; (iv) partial acid site regeneration involving immobile hydrocarbon molecule. Reaction mechanisms derived from References 26, 48-49 and 148.

give larger products (Figure 6-14(ii)). Due to the positioning of the carbocation charge in the adsorbed alkoxide, the primary alkene products will be di-substituted alkenes, matching the conclusions drawn from the product infrared spectra (Figure 6-6). Sufficiently long oligomers may undergo ß-scission cracking reactions (Figure 6-14(iii)), producing the ethene detected in the non-condensable products and explaining the presence of chains which are not an integer multiple of propene units. However, an alkoxide which undergoes a large number of successive oligomerizations without cracking, will grow large enough that it is

unable to diffuse away from the Brønsted site if it breaks away (Figure 6-14(iv)). This results in the formation of the physisorbed Brønsted-hydrocarbon species observed in the infrared spectrum of the 473 K reacted catalyst (Figure 6-9). The blockage of the zeolite pore network at that location then prevents the associated Brønsted site from participating in further reactions, contributing to catalyst deactivation and the observed reduction in propene conversion at 473 K.

6.2.4.2 Cycle 2 – Aromatic Production:

The reactions shown in Figure 6-14 are able to explain the linear species which form the majority of the products at 473 K, but not the aromatic fraction which is a minor contribution at this temperature and the major products at 573 and 673 K. The production of these products requires a second cycle of reactions which are detailed in Figure 6-15. The presence of cyclopentadienyl ions in both the MS and IR data indicates that the aromatic species are formed *via* a route involving 5-membered rings. Bonded alkoxides in the C_6-C_9 size range formed by the reactions in Figure 6-14 may cyclise to form substituted cyclopentanes in a process which also regenerates the Brønsted site (Figure 6-15(i)).[45] Removal of four hydrogens and the subsequent re-protonation of the resulting diene results in the formation of the cyclopentadienyl cations which Figure 6-9 shows are observed spectroscopically (Figure 6-15(ii)). The hydrogen abstraction reaction is driven by their transfer to alkene species also within the zeolite, explaining the presence of propane in the gaseous products.[45, 194] This also accounts for the high proportion of saturated alkyl molecules in the condensable products: molecules heavy enough to condense in the catch-pot will diffuse through the zeolite slower than the non-condensable alkenes, resulting in a higher probability of their participation in a hydrogen transfer reaction before they escape the zeolite pore. The protonated cyclopentadienyl cation is observed in the coke infrared spectra (Figure 6-9) because it is more stable in H-ZSM-5 than the corresponding diene, even though steric constraints mean that it does not form a framework-bound alkoxide as the linear carbocations do.[190] Once formed, these cyclopentadienyl cations can easily interconvert to the corresponding benzene or methylated benzene through a rearrangement that involves the removal of four more hydrogens (Figure 6-15(iii)), generating further alkane products through hydrogen transfer to alkenes. Alternatively, multiple cyclopentadienyl ions may react in concert through a

disproportionation mechanism, with some of them fragmenting to adsorb the excess hydrogen and forming propene in addition to the aromatic product.[195] Cyclopentadienyl cations with ethyl or longer side chains may release light olefins through an internal rearrangement followed by elimination, as demonstrated for ethene in Figure 6-15(iv).[195]

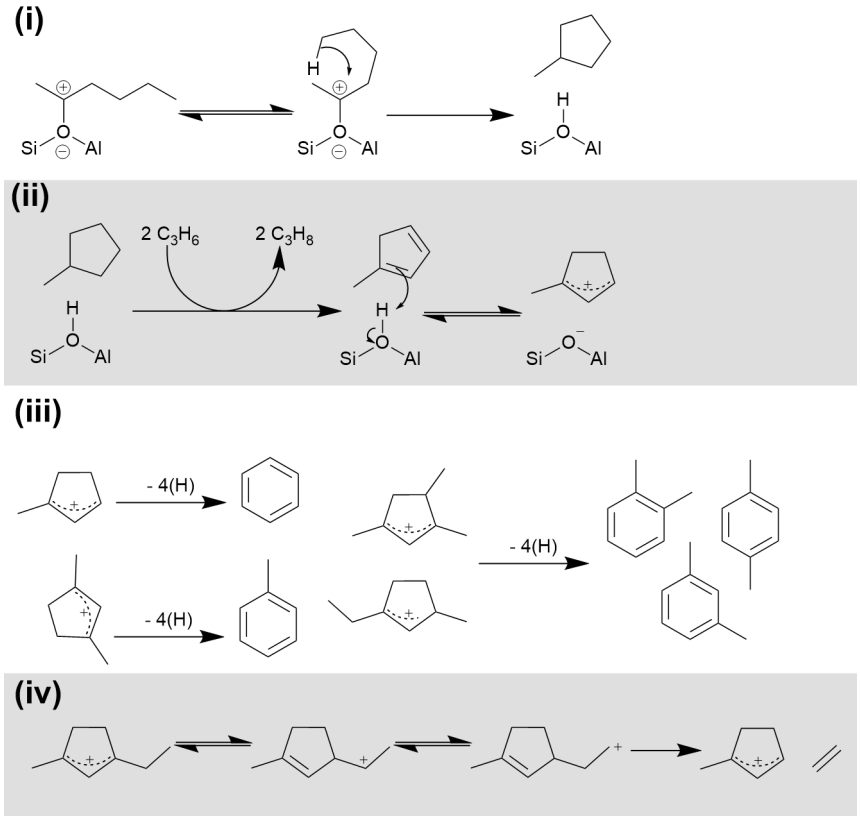

Figure 6-15: Scheme for cyclic and aromatic ring based reactions over H-ZSM-5: (i) alkoxide cyclisation; (ii) hydrogen transfer and cyclopentadienyl formation; (iii) conversion to aromatic products; (iv) elimination of light olefins from substituted cyclopentadienyl cation. Mechanisms derived from References 45, 190 and 194-195.

6.2.4.3 Overall Reaction Scheme:

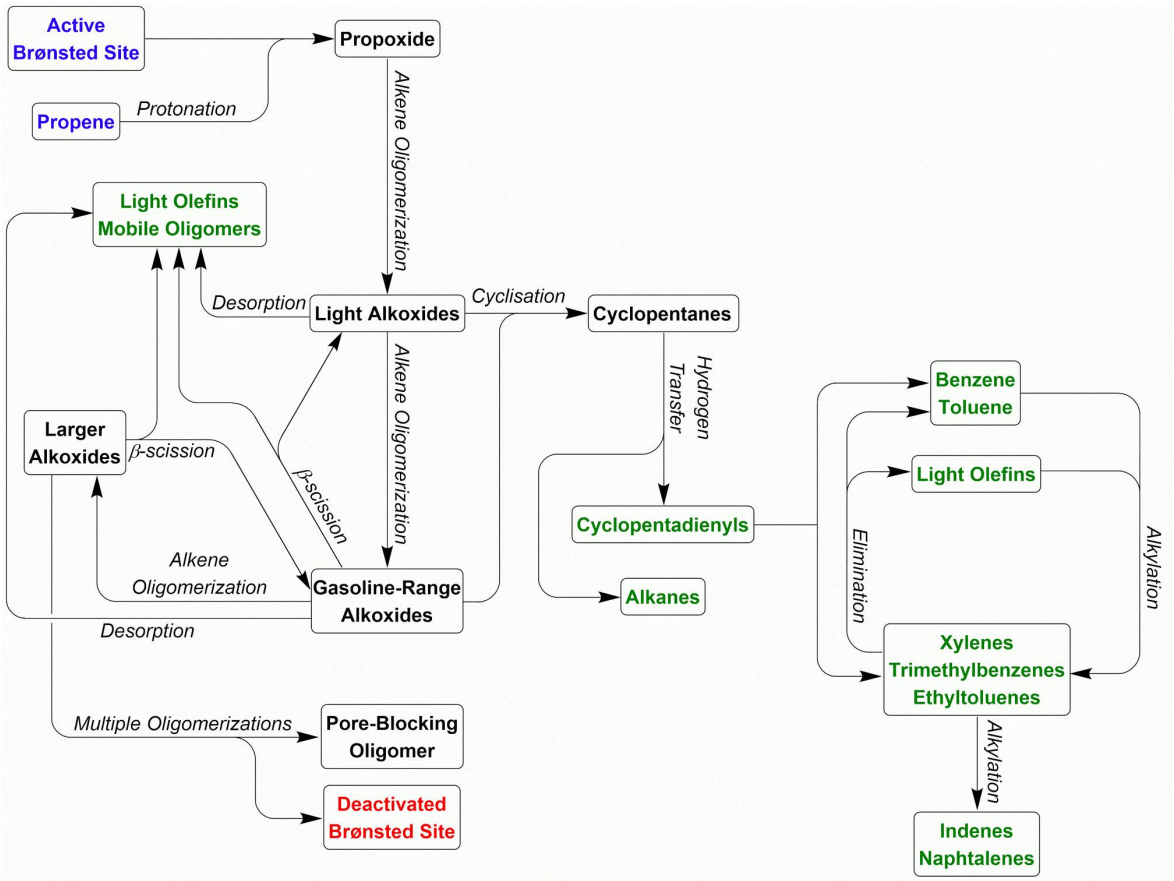

Figure 6-16: Schematic representation of the linked alkyl and aromatic reaction cycles occurring in the conversion of propene over ZSM5-FR. Species released as products are highlighted in green.

These two groups of reactions can therefore account for all the observed products outlined in Section 6.2.2 and all species which are detected within the reacted catalyst described in Section 6.2.3 and form a linked pair of reaction cycles, as summarised in Figure 6-16. While the alkyl reaction cycle is active at all temperatures, it is evident that formation of aromatic species from the cyclopentadienyl cations has a sufficiently high activation energy that the aromatic cycle does not contribute significantly at 473 K. The presence of detectable levels of cyclopentadienyl C-H and C-C vibrations in the infrared and the fact that di-methyl cyclopentadiene is more prevalent in the exit gas stream than aromatic species at this temperature (Figure 6-2(i)) indicates that it is the aromatic ring formation step which is rate limiting in the transfer between cycles. At higher temperatures, it is proposed that this energy barrier is overcome and the aromatic cycle may fully contribute to product formation. The availability of

this additional reaction branch, together with the increased rate of ß-scission at higher temperatures, also means that bonded alkoxides are less likely to undergo multiple successive oligomerization steps and the formation of immobile, branched pore blocking oligomers is not significant at temperatures higher than 473 K, preventing premature deactivation of the catalyst. Instead, what coke species do form at this temperature are amorphous carbon agglomerations which form at the surface of the zeolite crystallites.[52, 196]

Desorbed precursors to the formation of these coke species are the likely source of the signals of polyaromatics observed in the products by UV-Vis spectroscopy (Figure 6-8). Full operation of the aromatic production cycle also increases the number of hydrogen transfer reactions which occur, converting more of the alkene population to alkanes, thereby explaining why levels of condensable alkenes are even lower at 573 K and 673 K than they are at 473 K. However, while the aromatic cycle remains fully operational for the lifetime of the reaction at 673 K, the 573 K reaction seems to progressively shift toward the alkyl cycle becoming more dominant, indicating that there may be a step in the regeneration of the catalytic sites following aromatic production that is not totally efficient at this temperature.

The hydrogen transfer reactions which form the linking steps between the two cycles are well established in the MTH literature,[45, 194-195, 197] and the ability of H-ZSM-5 to catalyse these reactions is proposed as one of the key differentiating factors between aromatic-producing MTH reactions over H-ZSM-5 and the more constrained methanol-to-olefins reaction which occurs over siliconalumino-phosphates such as H-SAPO-34.[194] The rate of hydrogen transfer reactions is strongly influenced by the strength and population of the acid sites within the catalyst framework, as shown by comparative studies of zeolite and SAPO catalysts with identical framework structures.[198-199] It therefore follows that the high aromatic productivity observed at 573 and 673 K is a function of the high acidity of ZSM5-FR, and that aromatic production is likely to decrease over time as the zeolite acid sites are removed through framework de-alumination and production of CPD intermediates is reduced. The decrease in aromatic production observed at 573 K is not believed to be due to this process, since the rate of acid site loss in zeolites is temperature-dependant and no comparable loss in production is

observed at 673 K. The losses at the lower temperature are therefore best explained by incomplete catalytic site regeneration, with permanent acid site losses not being significant on the timescales investigated here. A study by Arora and Bhan[200] also shows a link between the methanol partial pressure and hydrogen transfer reaction rate in MTH chemistry, which by analogy suggests that the high WHSV of propene used here may also play a role in the high aromatic production observed.

The reactions described in Section 6.2.4.2 also explain the distribution of the aromatic products which are observed at each temperature. The identity of the aromatic species initially formed is determined by the length of the alkoxide chain which undergoes cyclisation, which in turn is dictated by the alkenes present in the zeolite to undergo oligomerization. At 473 K, these chains are primarily C_6, hence the increasing dominance of benzene as an aromatic product as the initial pool of other oligomers generated during catalyst conditioning is consumed or converted to pore blocking oligomers (Figure 6-5). At higher temperatures, the quantity of ethene in the zeolite is greatly increased, due to both increased ß-scission and the full participation of the alkene elimination reactions in Figure 6-15(iv). This results in a wider distribution of oligomer lengths and means that the higher stability of 1,3-dimethyl cyclopentadienyl cations relative to other CPD species becomes relevant, resulting in toluene becoming the major aromatic product. In a similar fashion, the increased production of benzene at 673 K relative to 573 K can be explained by ethene elimination from CPD species which would otherwise yield xylenes. Oligomer cyclisation can occur with chains of up to C_9 length, directly generating the trimethyl benzenes and ethyl toluenes observed by GCMS. However, alkylation of these first stage aromatics to produce heavier products can only occur through the addition of ethyl and propyl groups since the reaction systems lacks a source of methyl cations. These additions will directly yield naphthalenes, bypassing the production of polymethylated ($\geq$4 CH_3) benzenes, that form a major component of the products in MTH reactions, but which are not observed in the products here. This lack of significant production of tetra-, penta- and hexa-methyl benzenes and higher-substituted naphthalenes, which are important aromatic-cycle reaction centres and pore blocking species in MTH chemistry, is attributed to the fact that methylation reactions cannot play a

significant role due to the absence of a significant source of methyl cations, resulting in a more restricted population of aromatic products. The greater energy required to alkylate aromatics using ethyl or propyl cations relative to the energy barrier of methylation explains why this reaction requires higher temperatures than comparable MTH processes.

An additional anomaly observed in the aromatic products is the production of higher levels of *m*-xylene than *o*- or *p*-xylene, as observed in the GC analysis for all temperatures and times on-stream (Figure 6-5). This is counter to expectations as ZSM-5 is known to usually favour the production of *para*-xylene due to a product shape-selectivity effect arising from its smaller molecular diameter and easier diffusion through the zeolite micropores.[201-202] The slower diffusion of *o*- and *m*-xylenes results in them spending longer within the catalyst pores and thus increases the likelihood that they undergo an isomerisation reaction before being released as products. The detected products instead exhibit a distribution that closely corresponds to the thermodynamic equilibrium mixture of xylene isomers (26 % *o*-xylene, 51 % *m*-xylene, 23 % *p*-xylene).[202] The most likely reason for this is that the crystal size in ZSM5-FR is too small for this shape-selectivity to significantly affect the product distribution. Studies of toluene disproportionation over ZSM-5 samples with different crystal sizes have shown that *p*-xylene selectivity does not significantly affect the product composition unless the average crystal size is ≥ 5 μm, since below this size the mean path length of products out of the crystallite is low enough that the higher diffusivity of *p*-xylene does not significantly reduce its residence time within the pore network.[202] This crystal size is 10 times larger than the value determined for ZSM5-FR in Section 3.1.1.1 and the *p*-xylene selectivity mechanism is therefore unlikely to contribute in our sample.

6.3 Octene Cracking Reactions:

Using octene as the reagent increases the importance of cracking reactions to the overall reaction profile, as C_8 hydrocarbons are themselves large enough to undergo cracking, rather than such reactions only acting on the product of previous reaction steps and pool species. In industrial FCC use, the hydrocarbon

fraction which is active for cracking by H-ZSM-5 is that constituting the straight and branched olefins in the C_7-C_{12} size range.[18] Model compound studies use 1-octene to study this type of cracking chemistry under controlled conditions.[30, 76-77]

The increased significance of cracking reactions means that the effect of zeolite de-alumination is more relevant in 1-octene studies than in propene reactions. The way in which loss of acidity is reported to lead to improved selectivity, stability, and even activity, in steamed zeolites relative to studies performed using fresh materials has already been considered above.[34-35, 178] For this study, in addition to testing how reactivity over ZSM5-FR varies with temperature, we have also performed reactions using ZSM5-ST(1073K) as the catalyst to compare the zeolite's initial catalytic activity with one which may be viewed as representative of a cracking catalyst in the middle or near the end of its operational lifetime.

6.3.1 Octene Reaction Testing:

The fresh catalyst used was ZSM5-FR, while for testing of de-aluminated catalysts the bulk prepared material ZSM5-ST(1073K) was used due to its greater availability. The reader is referred to Chapter 5 Section 5.1.1 for characterisation of ZSM5-ST(1073K) and how it compares to the fresh material.

Initial reaction testing for the majority of data reported below was carried out on the UK Catalysis Hub micro-reactor setup (Section 2.3.1) at *ca*. 0.5 g_{cat} scale. The reagent used was 1-octene (Sigma-Aldrich, 99%), supplied at a rate calculated to give a weight-hourly space velocity (WHSV) of 1 h^{-1}. Reactions were performed at temperatures of 473 K, 573 K and 673 K for both ZSM5-FR and ZSM5-ST, giving a total of six samples in all. A 50 cm^3 min^{-1} flow of inert gas was used as a carrier gas for the 1-octene and any reaction products. This was helium for the initial two reactions (ZSM5-FR_Oct_673K, ZSM5-ST(1073K)_Oct_673K), following which nitrogen was substituted for reasons of expense. The inlet pressure of the reactor was recorded; on commencement of the flow through the reactor. It rose to 0.6 barg in all cases due to back-pressure from the catalyst bed but, thereafter, was not observed to vary significantly as the reactions progressed. The reaction was

monitored using the GC and MS instruments described in Section 2.3.1. The target reaction period was 72 hours on-stream, however, the reactions at 473 K were terminated early, after exhibiting no significant changes in product concentrations for an extended period after 12 hours. Exact catalyst masses, conditions and times for each reaction are given in Table 6-4. The reacted catalysts generated in the micro-reactor were further characterised by DRIFTS and TGA analysis (Sections 2.6.1 and 2.6.3).

Table 6-4: Sample details and reaction conditions for 1-octene conversion reactions performed on the UK Catalysis Hub micro-reactor.

Sample	Mass Catalyst (g)	Flow 1-octene (cm^3 min^{-1})	Inert Flow Gas	Final Time On-Stream (hh:mm)
ZSM5-FR_Oct_473K	0.504	0.012	N_2	46:20
ZSM5-FR_Oct_573K	0.521	0.012	N_2	72:10
ZSM5-FR_Oct_673K	0.513	0.012	He	72:30
ZSM5-ST(1073K)_Oct_473K	0.483	0.011	N_2	24:00
ZSM5-ST(1073K)_Oct_573K	0.495	0.012	N_2	72:25
ZSM5-ST(1073K)_Oct_673K	0.531	0.012	He	72:00

Following completion and analysis of the micro-reactor dataset, it was decided that the chemistry observed at 573 K and 673 K was sufficiently distinct from that of propene to benefit from the commitment of neutron instrument time to characterise the coke species. In order to prepare samples of sufficient size, additional reactions at 573 K and 673 K were performed on the ISIS catalysis preparation reactor for both ZSM5-FR and ZSM5-ST(1073K) at a scale of *ca.* 5 g_{cat}. Total time on-stream was 24 h for all reactions in this series. These larger samples were then investigated on MAPS using the standard INS analysis procedure (Section 2.1.2.5). An additional advantage was that the larger quantity of catalyst in these reactions allowed the collection of sufficient liquid products for analysis by GCMS and ATR-IR methods (Sections 2.6.2 and 2.6.1).

6.3.2 Octene Thermal Cracking at Reaction Temperatures:

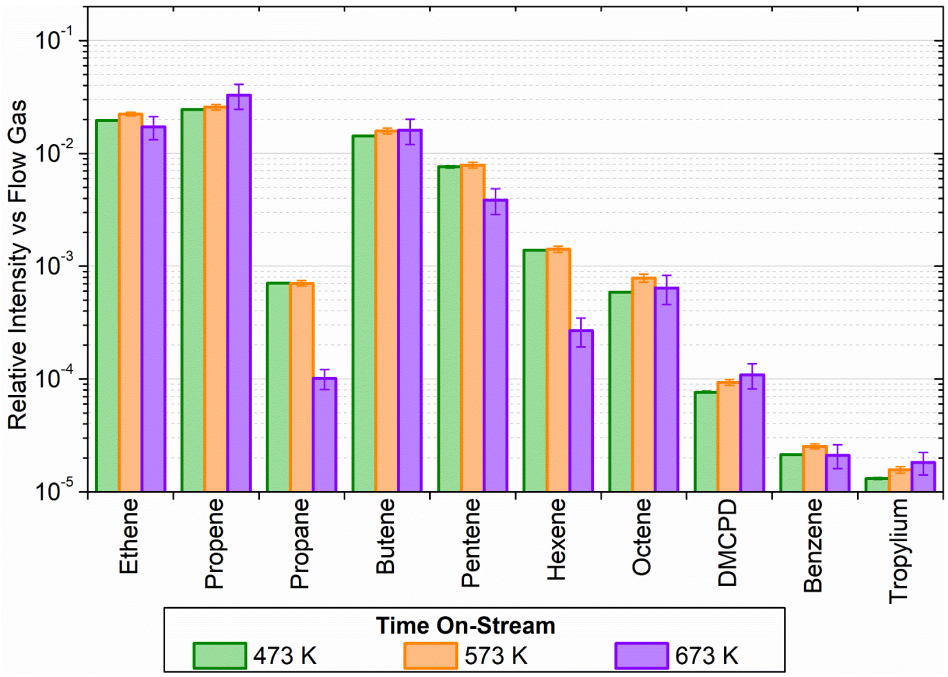

Figure 6-17: Intensities of selected mass spectrum signals from passing 1-octene over a SiO_2 blank at 473 K, 573 K and 673 K. Intensities are normalised against the signal for the reaction flow gas (4 amu for He, 28 amu for N_2) to allow comparison between samples and averaged over the period + 01:00:00 to + 02:00:00 with errors shown.

Due to the large range of products from the octene cracking reaction resulting in extremely complex GC traces for the micro-reactor experiments, on-stream analysis of the reaction products was accomplished by mass spectrometry as the primary method. It is therefore necessary to establish the fragmentation pattern of 1-octene within the mass spectrometer to act as a baseline. Additionally, temperatures at the higher end of the tested range are potentially sufficient for 1-octene to undergo thermal cracking without the presence of active catalytic sites. The products of this reactivity must therefore be established so that they may be distinguished from the effects of the acid and microporous catalysis of the ZSM-5 materials. To this end, blank reactions using ~1.5 g samples of amorphous silica in place of the ZSM-5 catalysts were run at 473, 573 and 673 K. After allowing the system to stabilise, this yielded the ion intensities in Figure 6-17. The assignment of m/z values to molecular fragments remains that given in Table 6-2. The mass of silica used was chosen to give the same bed length as in the catalytic

reaction experiments and the rate of octene injection was also the same as in the reaction tests.

At 473 K the temperature is not high enough for any thermal cracking to occur, as no change in MS intensities was observed when the gas flow was switched from the bypass system to the reactor at t = 0. The resulting pattern is therefore due to fragmentation in the MS and is dominated by light species such as propyl and ethyl fragments. Pentyl and hexyl ions are also present, although their lower levels indicate that breakdown of the C_8 chain into < C_4 units is favoured. It should be noted that the use of N_2 as the flow gas requires that the level of ethyl species must be measured by reference to the less significant 27 amu ion, meaning that the population of ethyl fragments is likely larger than Figure 6-17 would suggest. The molecular octyl ion at 112 amu has sufficient intensity to allow its use in assessing the level of octene conversion in the actual reactions.

At 573 K the system takes approximately 30 minutes to stabilise following the switch to the reactor, suggesting that some adsorption of octene on silanol groups may be occurring, which requires these to be saturated before the octene can pass through the reactor unimpeded. Once this occurs, the fragmentation pattern is essentially the same as that observed at 473 K. In contrast, at 673 K the mass spectrum shows reductions in the levels of larger ions, particularly hexene, with a corresponding increase in the signals for propyl fragments. Examination of the eluent by gas chromatography, with an example trace reproduced as Figure 6-18, confirms that this is due to thermal cracking leading to fragmentation of octene inside the reactor, with the single octene peak being significantly reduced and multiple lighter species including ethane and propene being detectable. Comparison of peak intensities before and after t=0 suggests that approximately 15 % of the octene exits the reactor without having undergone thermal cracking in this instance.

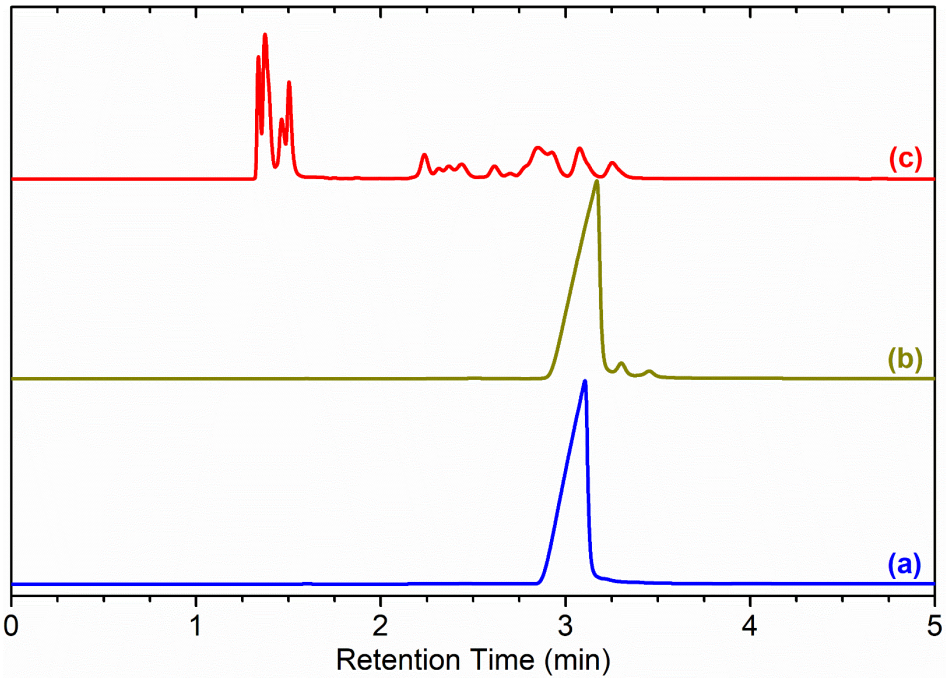

Figure 6-18: GC traces of the eluent gas flow from flowing octene over SiO_2 blanks at 473 K (a), 573 K (b) and 673 K (c) collected at 3 hours-on-stream showing thermal cracking of the octene at 673 K.

6.3.3 Analysis of Octene Reaction Products:

Moving on to the catalytic reaction chemistry, in all the reactions studied the majority of the changes in product composition with time occurred within the first 24 hours on stream, with subsequent changes being the progress of trends established within this initial time frame. Therefore, the MS intensities at selected points over the first 24 hours of reactions over ZSM-5-FR are presented in Figure 6-19 as bar charts to allow easier comparison. To smooth out variations in the MS intensities due to regular fluctuations in the line temperatures and pressures each bar represents a 1 hour average taken over ± 0.5 hours from the indicated time, with the standard deviation of the data presented as error bars in Figure 6-19. The full MS traces for each reaction run are included in Appendix 3 as full page figures to allow their presentation without crowding. All statements about product levels in the following sections are made comparative to their levels in the corresponding baseline fragmentation pattern from Figure 6-18.

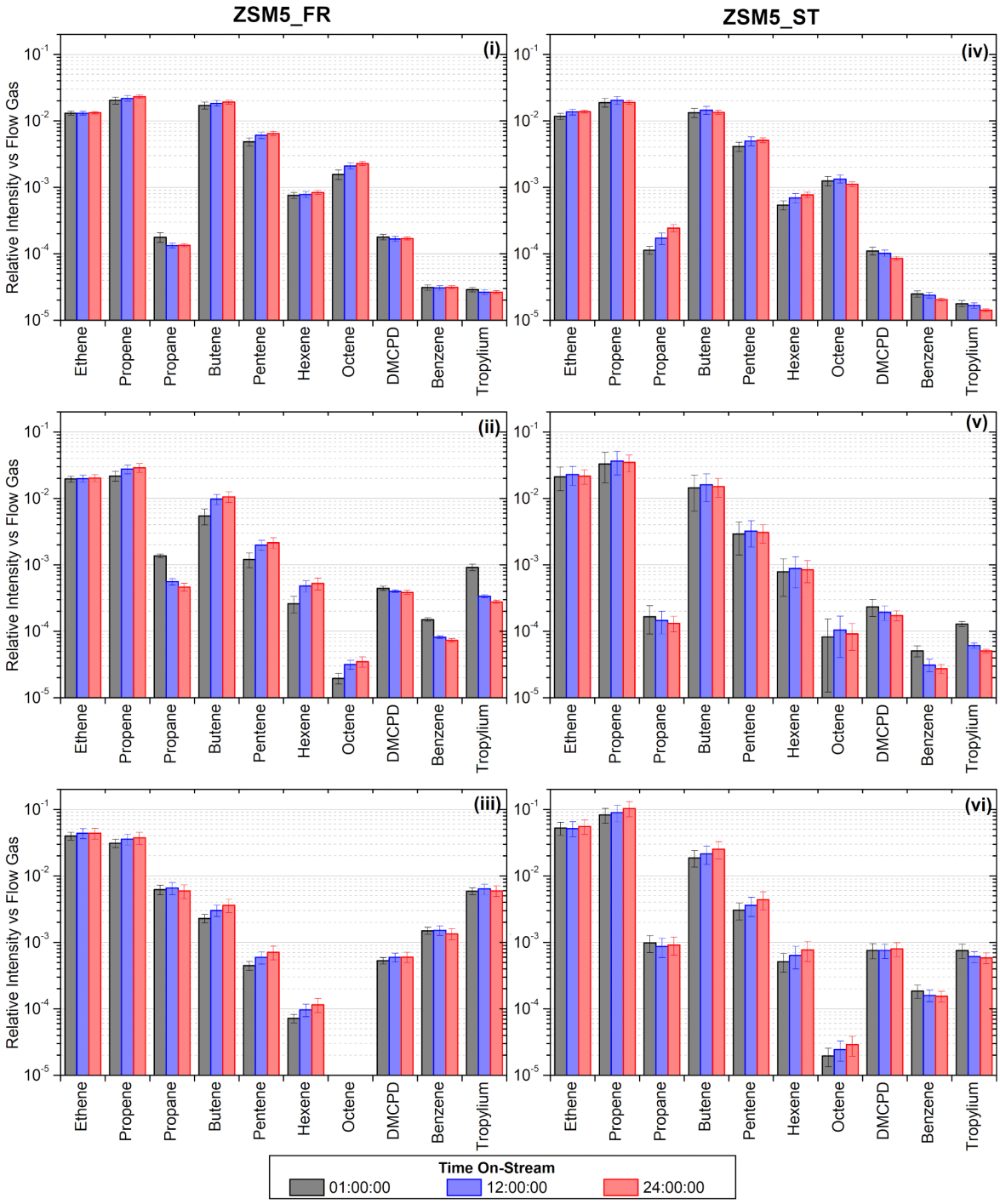

Figure 6-19: Intensities of selected mass spectrum signals from the reaction of 1-octene after 1, 12 and 24 hours on-stream. Reactions performed over ZSM5-FR at 473 K (i), 573 K (ii) and 673 K (iii) and ZSM5-ST(1073K) at 473 K (iv), 573 K (v) and 673 K (vi). Intensities are normalised against the signal for the reaction flow gas and averaged over ± 0.5 hours from the indicated time with errors shown.

6.3.3.1 Octene Vapour Phase Products – 473 K:

At 473 K the reaction of the fresh catalyst is initially characterised by an absence of reaction products, with the concentration of all products dropping to negligible levels following contact with the reactor bed and remaining in this state for the first 30 minutes on stream. Following this run-in period, product breakthrough is rapid, with most signals stabilising at values which they occupy with minimal deviation for the remainder of the time-on-stream: due to the time frames involved, this run-in period lies outside the region averaged for the + 1 hour data point in Figure 6-19(i). Compared to the baseline fragmentation pattern, the products of the reaction exhibit increased levels of propyl and C_4 fragments and the production of trace quantities of aromatics and cyclopentadienyl (CPD) species. These changes are compensated by reductions in the production of C_5 and C_6 ions and propane. Levels of the octyl ion are actually increased relative to the baseline, indicating the presence of alkyl chains longer than C_8 as products, which fragment to give octyl ions in the mass spectrometer. Over the course of the first 24 hours, there is a slight increase in the production of these longer chains and a partial restoration of the production of pentene, matched with a simultaneous reduction in aromatic and CPD levels and a further reduction in propane. This trend reaches a peak at approximately t + 25 hrs, following which production levels remain static.

The ZSM5-ST(1073K)_Oct_473K reaction has similar overall behaviour to that of the fresh catalyst, but is less consistent across the length of the reaction. It exhibits the same initial lack of eluted products, although the time before breakthrough occurs is reduced by approximately 50% relative to ZSM-5-FR. Following breakthrough, the same trends in products are observed; however, in each case the magnitude of the shift away from baseline production levels is lower than in ZSM5-ST(1073K)_Oct_473K. The catalyst run-in period is complete by +01:30 hrs. However, rather than remaining constant, all signals immediately begin a slow, but consistent, drift back toward their baseline levels. While technical difficulties prevented the following of this trend to completion, it appears that this represents a steady deactivation of the catalyst toward being unable to convert octene at 473 K. This trend is slow enough that differences in

the levels of various products between the fresh and steamed catalysts remain on the order of 30 – 50 % at the +24:00 hrs point.

6.3.3.2 Octene Vapour Phase Products – 573 K:

ZSM5-FR_Oct_573K undergoes an initial period without products lasting 15 minutes. The initial product breakthrough has high levels of saturated alkyl species, but this is only momentary and is entirely replaced by a product slate dominated by ≤ C_4 alkene fragments by + 00:30 hrs. Levels of aromatic production are also initially significant, with substituted aromatics predominating. Levels of the octyl molecular ion are much lower than baseline, indicating both high conversion of the reactant and the lack of significant quantities of alkyl products larger than the reactant. Unlike at 473 K, the product slate evolves significantly over the course of the reaction with production of aromatics and alkanes dropping from the start of the post run-in period, with a corresponding increase in the production of alkenes. Additionally, CPD concentrations do not vary significantly and overtake the concentration of the tropylium ion by + 07:00 hrs. The rate of all changes is exponential, and therefore the majority of the shift in concentrations occurs in the first twelve hours on stream. However, all observed trends continue at lower rates to the end of the observed reaction period.

Breakthrough time for ZSM5-ST(1073K)_Oct_573K is on the same order as that for the fresh catalyst at the same temperature. There is no initial pulse of saturated products and the product distribution is dominated by light olefin fragments, a preponderance which becomes more extensive as the reaction proceeds and even the initially low levels of aromatic and alkane production decay away. 1-Octene conversion, as assessed by the 112 amu, signal remains high throughout, although at a lower level than that observed for ZSM5-FR_Oct_573K.

6.3.3.3 Octene Vapour Phase Products – 673 K:

The reactions at 673 K exhibit the largest difference between the fresh and steamed zeolite catalysts. ZSM5-FR_Oct_673K exhibits very high levels of aromatic production, to the point where the tropylium ion is a more significant product than butyl fragments at the start of the reaction. It is also the only reaction where

ethyl fragments are a more significant product than propene at the beginning of the reaction. The catalyst is apparently quite stable in this regime and changes in product distribution are slow, however, the overall trend is still a reduction in aromatic levels and increased production of alkenes, with butene becoming the third most significant product by + 53:00 hrs. This is also the point at which propene becomes the most significant product again. Unlike at 573 K, the rate of change remains constant throughout the reaction once it has achieved steady-state. In contrast, ZSM5-ST(1073K)_Oct_673K exhibits the same pattern observed at lower temperatures, with the major products being propene, ethene, butenes and pentenes in that order, with the major distinguishing factor compared to lower temperatures being that octene conversion is much higher and the concentrations of the light olefins produced being correspondingly increased.

6.3.3.4 Octene Condensable Products:

Analysis of the catch pot contents for the large-scale reactions performed at ISIS was carried out by ATR-IR (Figure 6-20) and GCMS (Figure 6-21). It should be noted that the GCMS analysis used a different temperature profile to that used for the measurements in Figure 6-7 to achieve better peak separation. The retention times are therefore not directly comparable, although the general order of products remains essentially the same due to use of the same chromatographic column.

ATR-IR analysis is presented in Figure 6-20. At 573 K both ZSM5-FR and ZSM5-ST(1073K) produce an alkane-dominated mixture of liquids. ZSM5-FR_Oct_573K contains detectable levels of aromatics, with a shoulder of the C-H stretching peaks extending above 3000 cm^{-1} and the GCMS results (Figure 6-21) containing peaks for mono- and di-substituted benzenes and simple naphthalenes. The spectrum of ZSM5-ST(1073K)_Oct_573K sees these features almost absent, while the GCMS results show a minor growth in the peaks for various cyclic isomers of the 1-octene feed, of which 1,2,3-trimethylcyclopent-1-ene is marked on Figure 6-21 as an example. This is consistent with the results of the on-line analysis, with aromatic production only being significant near the start of the reaction and decreasing with time-on-stream. The catalyst operates in the

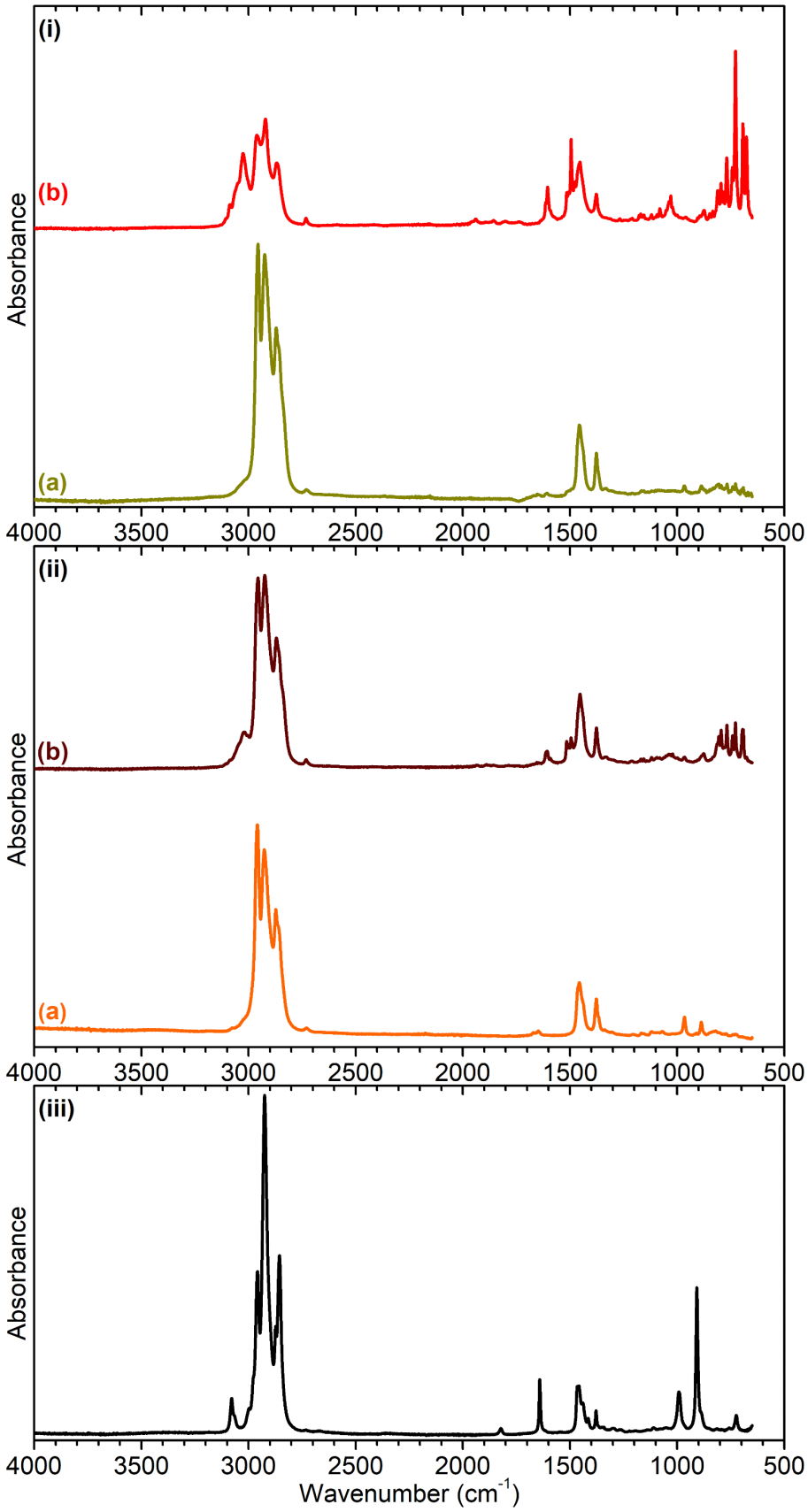

Figure 6-20: Infrared spectra of the condensable product fraction from 1-octene reactions over ZSM5-FR (i) and ZSM5-ST(1073K) (ii) at 573 K (a) and 673 K (b). A spectrum of pure 1-octene is included for comparison (iii). Spectra collected by ATR-IR and offset in *y*-axis.

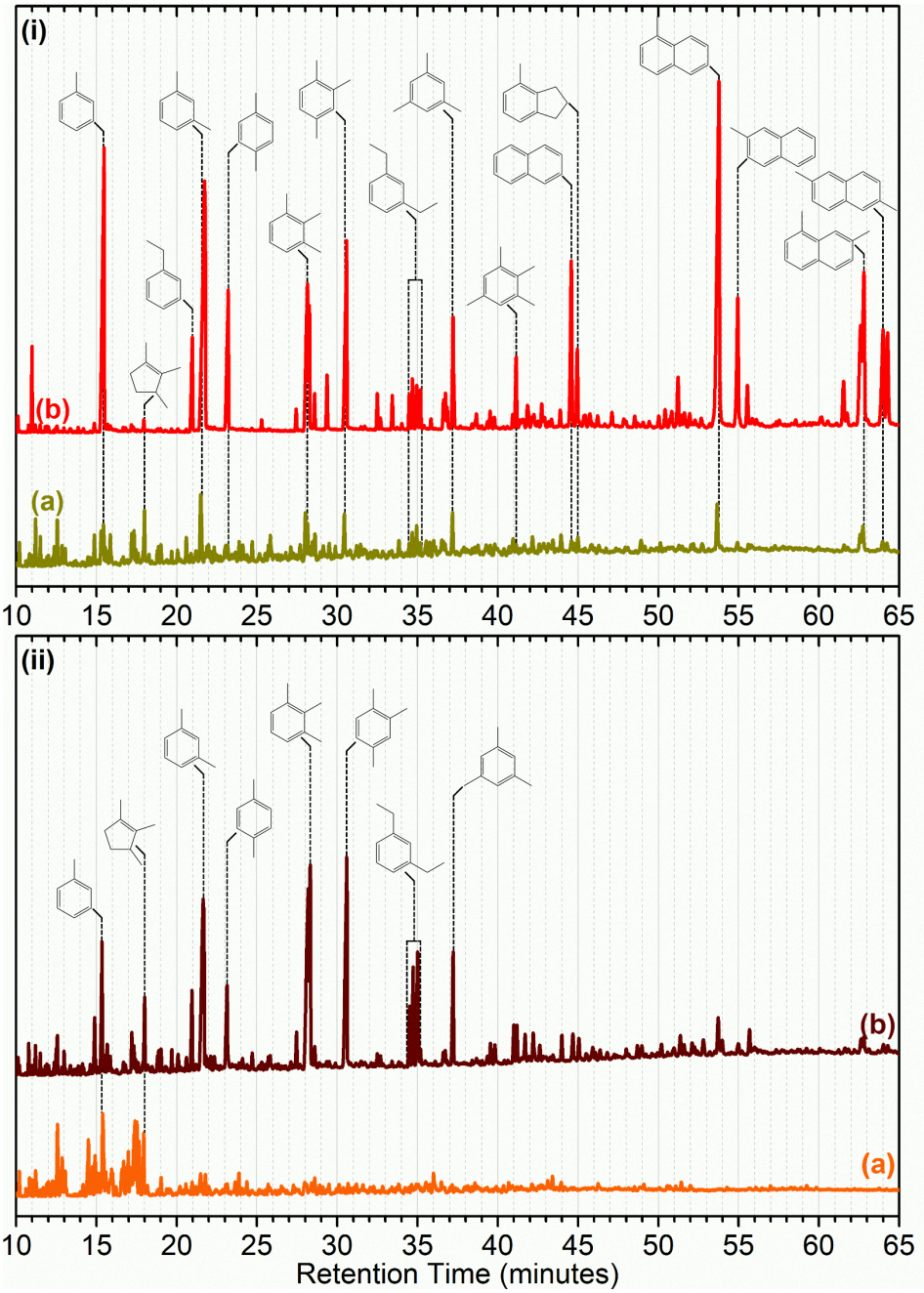

Figure 6-21: GCMS traces of the condensable product fraction from 1-octene reactions over ZSM5-FR (i) and ZSM5-ST(1073K) (ii) at 573 K (a) and 673 K (b). Identities of significant peaks are highlighted.

non-aromatic regime for the majority of the runtime and thus alkanes dominate the liquid products, which represent an average over the entire reaction run. Relative peak intensities in the infrared data appear similar between samples, suggesting that both catalysts are producing a similar mixture of alkanes at this temperature, but lower overall intensity in the ZSM5-ST(1073K)_Oct_573K spectrum suggests reduced production of molecules large enough to condense at 293 K.

At 673 K ZSM5-FR produces a product slate with much higher levels of aromatic products, as evidenced by both IR and GCMS results. Products include both extensively substituted benzenes and multiple naphthalene, species all of which are present in large quantities. In contrast, production of C_8 isomers is low, indicating that the catalyst favours conversion over isomerisation processes under these conditions. In contrast to the behaviour with fresh catalyst, ZSM5-ST(1073K)_Oct_673K does not produce significant quantities of bicyclic aromatics and sees an increase in rearrangement products. Levels of single-ring aromatic production are less than for the fresh catalyst at the same temperature, but higher than the fresh catalyst at 573 K.

6.3.4 Analysis of Octene Coked Catalysts:

The reacted zeolites were retained for *ex situ* analysis by TGA and DRIFTS. As was the case for the propene reactions, these analyses provide information on the end state of the catalyst itself and those hydrocarbon species which are immobilised within the pore network. Mobile products are removed by the reactor purging at the end of the run. The samples were exposed to air during their removal from the microreactor, meaning that only stable species will be observed. The overall coke content of the reacted samples from TGA is given in Table 6-5, while Figure 6-22 shows the temperature dependence of coke oxidation. The DRIFTS infrared spectra are shown as Figure 6-23.

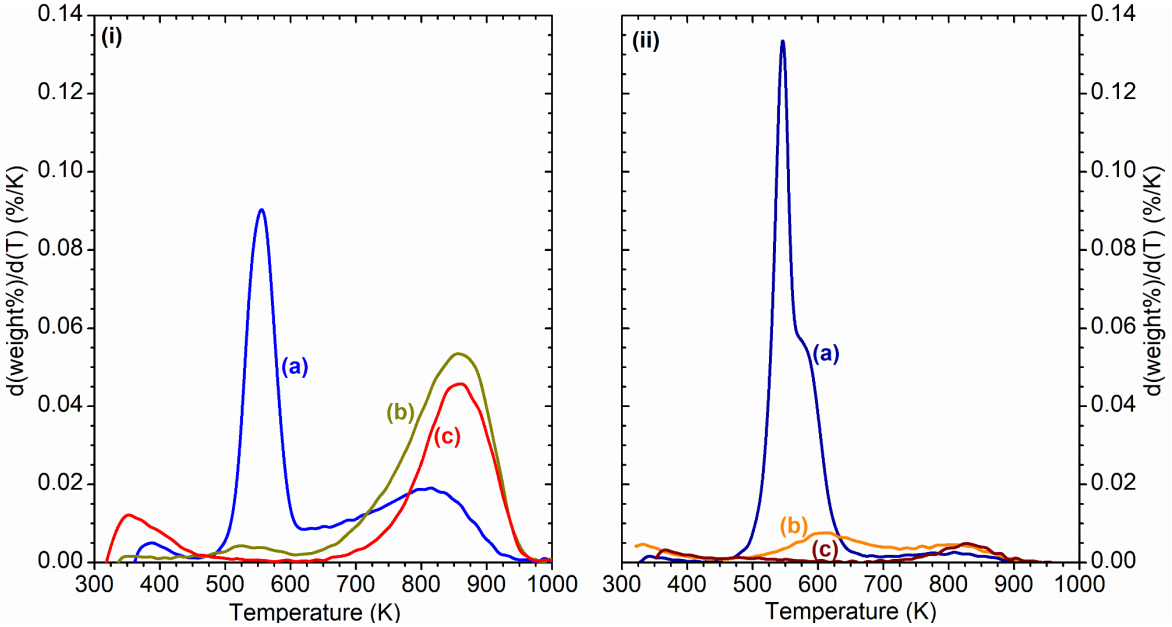

Figure 6-22: Rate of weight decrease during thermogravimetric analysis in 10% oxygen of samples of ZSM5-FR (i) and ZSM5-ST (ii) catalysts after reaction at 473 K (a), 573 K (b) and 673 K (c).

Table 6-5: Sample reaction times and coke content of octene catalysts determined by thermogravimetric analysis.

Sample	Reaction Time (hh:mm)	Coke Content (wt%)		
		Type I	Type II	Total
ZSM5-FR_Oct_473K	46:00	5.54	3.93	9.47
ZSM5-FR_Oct_573K	72:00	0.58	8.70	9.28
ZSM5-FR_Oct_673K	72:30	0.16	6.51	6.67
ZSM5-ST(1073K)_Oct_473K	24:00	6.91	0.44	7.35
ZSM5-ST(1073K)_Oct_573K	72:30	0.81	1.06	1.87
ZSM5-ST(1073K)_Oct_673K	72:00	0.14	0.64	0.78

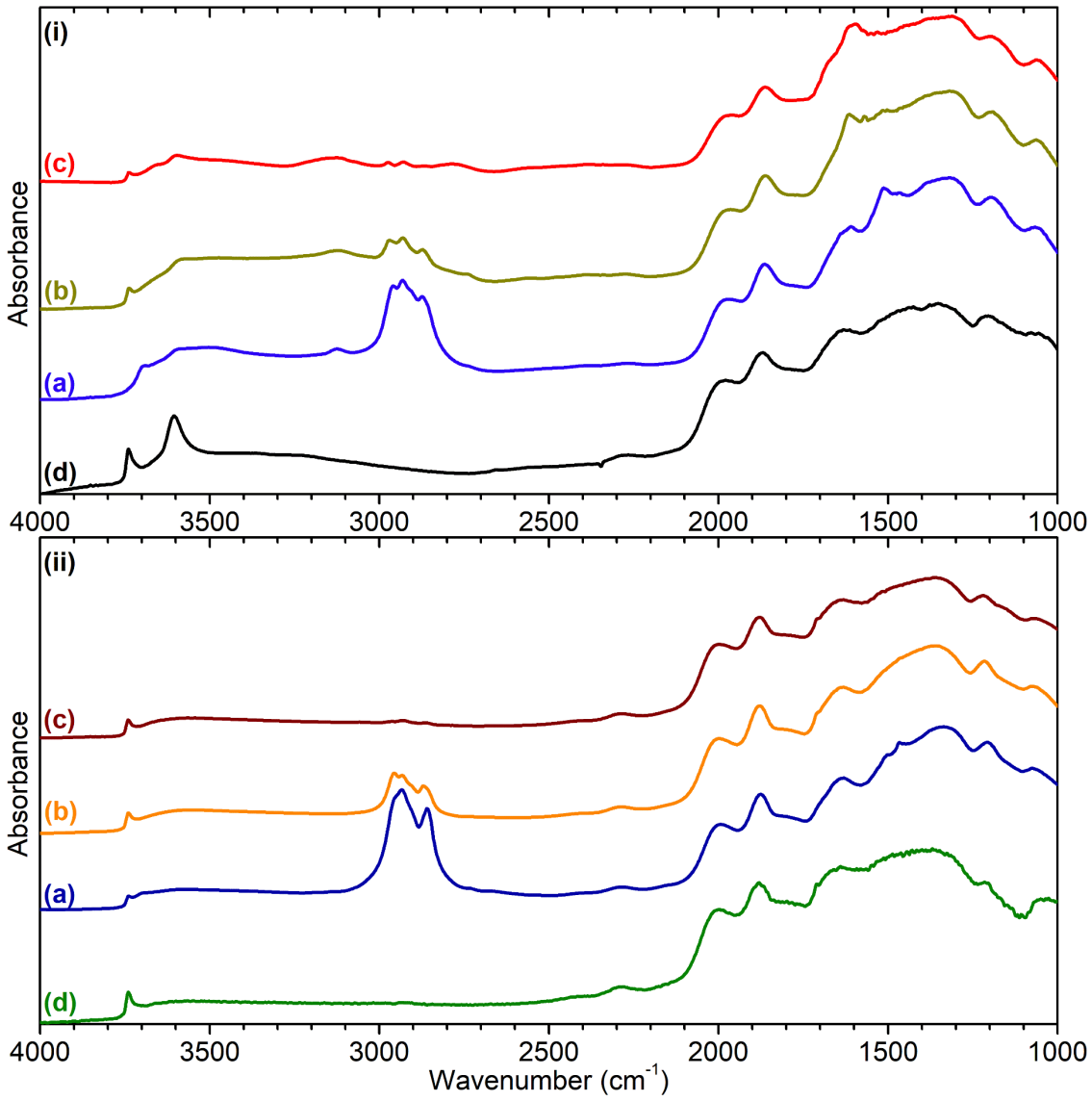

Figure 6-23: Infrared spectra of samples of ZSM5-FR (i) and ZSM5-ST (ii) after reaction at 473 K (a), 573 K (b) and 673 K (c) compared with the spectrum of the catalysts pre-reaction (d). Spectra normalised on the zeolite mode at 1870 cm^{-1} and offset in *y*-axis for easier interpretation.

6.3.4.1 Octene Reacted Catalyst – 473 K:

The ZSM5-FR-473K reaction produces a catalyst which is coked to approximately 9.5 % by weight, a level of hydrocarbon loading which in the propene reactions resulted in the total blockage of the ZSM-5 pore structure through filling of the pore channels with hydrocarbonaceous material. The majority (59 %) of this material is Type I coke with a high hydrogen content which oxidises in the range 450-650 K, and which therefore is thought to consist mainly of saturated hydrocarbons.[189]

The infrared data is consistent with this, with the major feature being the symmetric and asymmetric stretches of sp^3 CH_3 and CH_2 groups at 2960, 2930, 2905 (as a shoulder) and 2870 cm^{-1}.[188] The only mode attributable to C-H stretching in unsaturated hydrocarbons is the clearly separated cyclopentadienyl peak at 3125 cm^{-1}; the corresponding asymmetric and symmetric allyl stretch modes at 1510 and 1465 cm^{-1} are also present.[188] In the O-H stretch region, the intensity of the Brønsted acid peak at 3605 cm^{-1} is significantly reduced and the silanol peak is suppressed entirely due to hydrocarbons physisorbed on the O-H sites resulting in a shift of the νO-H mode as discussed above. In the case of the silanol groups, this produces the new peak observed at 3690 cm^{-1}, while the Brønsted groups with physisorbed hydrocarbons produce the broad peak from 3600-3400 cm^{-1}, which overlaps with the remaining free Brønsted site intensity.

The ZSM5-ST(1073K)_Oct_473K sample is approximately 7.4 % coke by weight, a value which is remarkably similar to that of the fresh catalyst given that the steamed material was reacted for only 50 % of the time on stream used for ZSM5-FR_Oct_473K. Therefore, the majority of the coking process in both cases can be assumed to occur in the initial stages of the reaction. The predominance of Type I coke in this material is even greater than in the fresh catalyst, with only 3.5 % of the mass loss from oxidation occurring above 650 K. In contrast to the relatively homogeneous nature of the Type I coke in ZSM5-FR_Oct_473K, the coke in the steamed catalyst clearly consists of two separate populations: one that oxidises around 550 K, similar to that observed in ZSM5-FR_Oct_473K, and a second type of hydrocarbon, which requires higher temperatures centred around 575 K to oxidise.

The infrared spectrum of ZSM5-ST-473K continues to be dominated by saturated C-H stretching modes, although a direct comparison shows that the intensity of the CH_2-associated modes at 2930 and 2870 cm^{-1} are increased relative to their methyl equivalents. The CPD νC-H stretch mode is much weaker, to the point of near-invisibility, and the corresponding allyl modes likewise reduced. The lack of any discernible peak for the Brønsted sites of the steamed catalyst means that related peaks are not available for analysis in the reacted catalyst either, however silanol νO-H stretches are seen at both 3700 cm^{-1} as in ZSM5-FR-473K and at

3740 cm^{-1} for free silanol groups, indicating that not all silanol sites have associated physisorbed hydrocarbons in ZSM5-ST(1073K)_Oct_473K.

6.3.4.2 Octene Reacted Catalyst – 573 K:

After 72 hours ZSM5-FR_Oct_573K achieves a similar level of coke content to that observed at 473 K despite the differing time on-stream, however, the composition of the coke is markedly different. Type I coke makes only a minor contribution to the overall mass loss, with the majority of the coke oxidising at temperatures greater than 700 K, corresponding to Type II coke consisting mainly of substituted aromatic or polyaromatic species. This is reflected in the DRIFTS spectrum by a significant reduction in the intensity of the sp^3 νC-H modes, although the ratios between these peaks remain similar to those observed for the 473 K reactions. However, the large quantity of Type II coke does not result in similarly significant contributions to the infrared spectrum. Peaks at 1570 and 1615 cm^{-1} in Figure 6-23 may be due to C-C stretching in mono- and di-substituted aromatic rings and are not observed at 473 K, but the only C-H stretch mode observed above 3000 cm^{-1} is the peak at 3125 cm^{-1} associated with CPD ions. The intensity of this CPD peak is slightly increased, which conforms to the higher level of CPD species observed in the on-stream products analysis at this temperature.

The INS data collected for the repeat reactions (Figure 6-24) allows much better information on the low-energy vibrational modes of the coke than is available from the DRIFTS spectra and assists in identifying the Type II coke composition. Strong $-CH_3$ symmetric and antisymmetric deformations are visible at 1381 and 1452 cm^{-1}. The methylene twist located *ca*. 1300 cm^{-1} is comparatively weak indicating that the majority of these methyl groups are not associated with alkane chains. The strong peak at 1185 cm^{-1} is associated with C-H wag modes of the ring hydrogens in aromatics and polyaromatics. However, the fact that this mode is considerably more intense than the associated modes in the 800 – 1100 cm^{-1} region, which are produced by hydrogens of this type in benzene and naphthalene structures, indicates that the majority of the aromatic C-H wag modes are from groups in polyaromatic structures with ≥ 3 rings, up to and including glassy carbon type materials. It is notable that the spectrum observed is extremely similar to that

produced by MTH reactions at similar temperatures after extended reaction periods.[203-204]

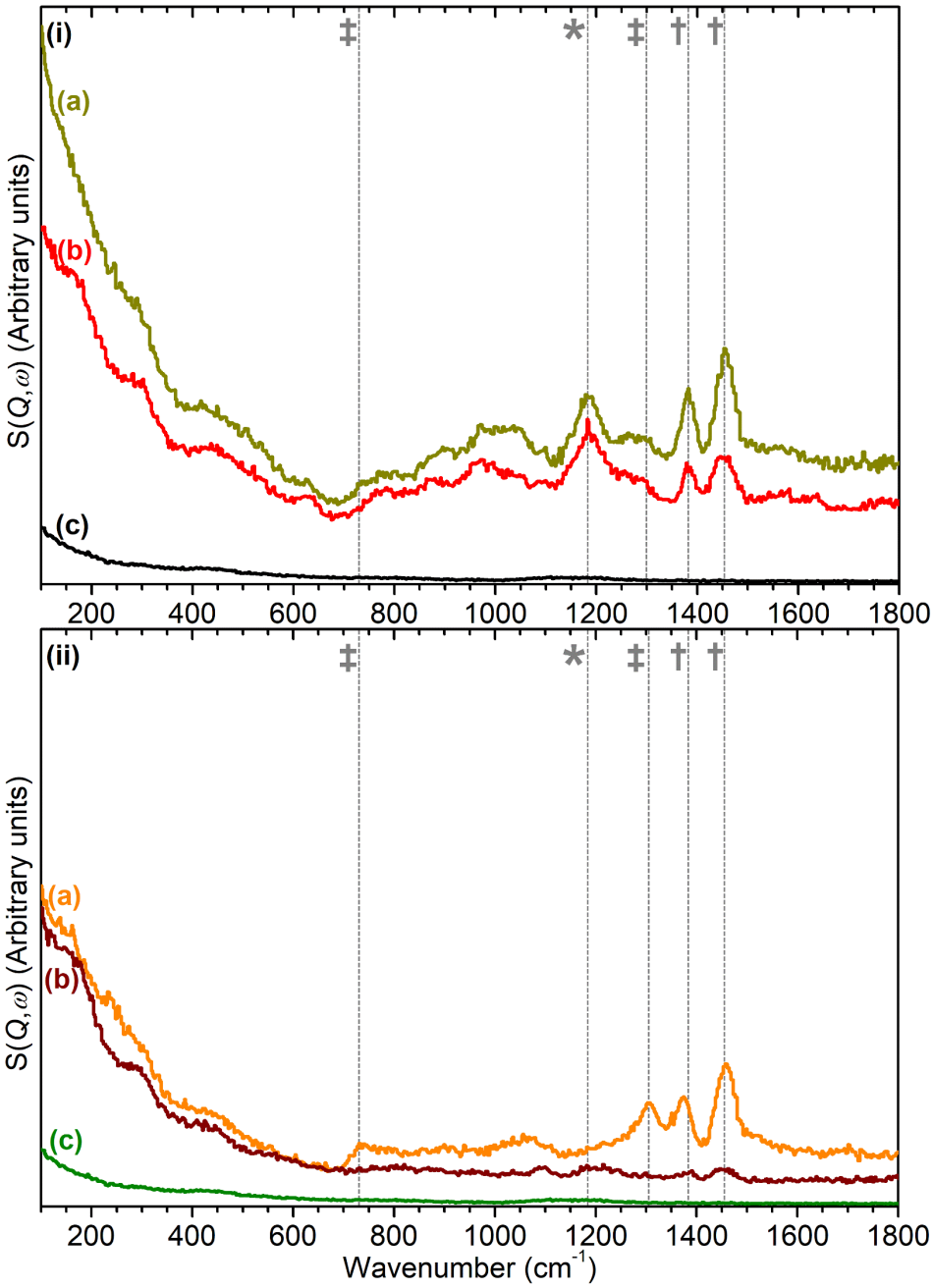

Figure 6-24: INS spectra of ZSM5-FR (i) and ZSM5-ST (ii) after reaction with 1-octene at 573 K (a) and 673 K (b) compared with the spectrum of the catalysts pre-reaction (c). Modes associated with $-CH_3$ (†), $-CH_2-$ (‡) and polyaromatic (*) groups are highlighted. Spectra collected on MAPS and normalised to correct for differences in sample mass.

It can therefore be concluded that the coke produced on ZSM5-FR_Oct_573K consists primarily of highly substituted aromatic and polyaromatic species with very low levels of hydrogen present on sp^2 carbon atoms, leading to the infrared

spectrum being dominated by the limited population of Type I coke. The maximum size of the products visible in the GCMS of the released products suggests that the aromatic coke products have a minimum size corresponding to trisubstituted naphthalenes or tetramethyl benzenes, where the substituents are not adjacent, such as durene. Unlike at 473 K, the silanol vO-H mode is not suppressed fully by adsorbed hydrocarbons in the infrared spectrum, although the Brønsted site peak exhibits a similar pattern with some free sites and a large broadened region of bonded sites.

ZSM5-ST(1073K)_Oct_573K is the first sample to have a significant difference in its level of coking, achieving only 1.9 wt% coke after 72 hours. This is also reflected in a reduction in the overall intensity of the INS spectrum due to lower levels of hydrogen in the neutron beam despite the more hydrogenous nature of the coke. This decrease in coke loading is entirely due to a reduction in the levels of Type II coke; the quantity of Type I coke may even be increased relative to the levels in the fresh catalyst, although the magnitude of this increase is fairly small. The INS spectrum confirms this, with ZSM5-ST(1073K)_Oct_573K returning a classic example of the long-oligomer spectrum observed on multiple occasions in our model compound studies. Aromatic signals appear totally absent, while the relative intensity of the methylene peaks indicates that the oligomer possesses multiple CH_2 units but is not primarily linear as is the case for octene oligomerization at room temperature (Section 4.1.1) due to the 720 cm^{-1} band not being significantly stronger than the other methylene modes in the 700 – 1100 cm^{-1} region. The infrared data also appears to support this, with the intensity of the vC-H modes being increased relative to ZSM5-FR_Oct_573K (Figure 6-23), although the differing levels of background intensity due to greater sample darkening in ZSM5-FR_Oct_573K make direct comparisons difficult. ZSM5-ST(1073K)_Oct_573K shows no evidence of hydrocarbon modes other than the sp^3 C-H stretches, including no visible perturbations of the silanol peak by adsorbed molecules.

6.3.4.3 Octene Reacted Catalyst – 673 K:

The 673 K samples continue the trends observed at 573 K. ZSM5-FR_Oct_673K sees a further reduction in Type I coke deposition to negligible levels but also sees a reduction in Type II coke build-up, indicating a more efficient catalytic process at

this temperature. Figure 6-24(i) is consistent with this, with the spectrum of the 673 K sample having the same polyaromatic characteristics as at 573 K but at a lower overall intensity due to lower coke quantities. The infrared data shows significant reductions in all νC-H modes, and also lower levels of evidence for adsorbed hydrocarbons in the νO-H region due to the absence of immobilised coke species. Despite this, the intensity of the Brønsted and silanol O-H peaks is still reduced relative to the clean zeolite spectrum, suggesting that permanent O-H site loss is occurring.

Coke build-up in ZSM5-ST(1073K)_Oct_673K is even lower than at 573 K and is almost entirely invisible to both the infrared and the INS analysis methods employed. This indicates that the minimal quantities of coke produced in this catalyst are almost entirely carbonaceous; the INS spectrum does exhibit extremely weak modes at *ca*. 1200 and 1100 cm^{-1}, supporting this reasoning.

6.3.5 Reaction Mechanisms in ZSM-5 Octene Cracking:

The observed products of all reactions described above are consistent with the reactions within the zeolite conforming to a dual-cycle hydrocarbon pool mechanism similar to that observed for propene reactions. The individual reactions which occur in the catalyst are the same as those described above and shown in Figure 6-16. The difference is the relative contribution of each reaction to the overall system and how the reactions are affected by the reaction temperature. In particular, the average size of molecules in the hydrocarbon pool is increased due to the larger reactant molecule, resulting in β-scission cracking reactions being of increased importance to the overall reaction scheme.

6.3.5.1 Reactions at 473 K:

At the lowest temperature considered, the hydrocarbon pool reaction is constrained by the same factors as the propene reaction at the same temperature. The rate of β-scission is temperature dependent, and therefore relatively low, and the hydrogen transfer reaction linking the alkyl and aromatic cycles also has a very low reaction rate. This results in similar behaviour, with the cyclic nature of the hydrocarbon pool mechanism breaking down and the catalyst undergoing a

rapid series of successive oligomerization reactions at each active site that consume all of the 1-octene supplied to the catalyst. This effect is clearly demonstrated in ZSM5-FR_Oct_473K by the complete absence of products which is observed for the first 50 minutes of the reaction. As before, these oligomers grow until they occupy the whole of the pore network, generating the large quantities of coke detected by TGA in ZSM5-FR_Oct_473K and the strong saturated vC-H modes in the infrared spectrum. It is only once this oligomer growth reaches an equilibrium state that product breakthrough occurs.

Since, as established above, these oligomers block the catalyst active sites ZSM5-FR_Oct_473K is largely deactivated from the moment that the run-in period is complete and the majority of the detected molecules in the exit stream are octene. The residual deviations from the octene fragmentation pattern observed by MS are due to the minority of Brønsted sites located at, or very near to, the external surface of the zeolite crystallites, which are less vulnerable to blocking by immobile oligomers. These sites continue to produce hexadecane and tetracosane, which are still mobile enough to be released and form the saturated proportion of the liquid products, as well as the very low levels of residual aromatic production due to the cyclisation of octyl alkoxides. The fact that CPD ions predominate over aromatic signals in the MS, is because of the hydrogen transfer reaction being the rate-limiting step in this reaction, leading to a build-up of the intermediate, which is also detectable by infrared analysis as seen in Figure 6-23(i(a)). The external sites are also responsible for the production of the Type II coke which is observed by TGA. The remaining shifts in the products after the first hour are caused by the slow deactivation of these external sites progressing towards a completely deactivated catalyst.

In ZSM5-ST(1073K)_Oct_473K the result is similar, however, the lower initial population of acid sites means that the time taken for the saturation of the catalyst with oligomer is lower. Despite this, the overall quantity of Type I coke is comparable in both systems since it is the pore geometry of the zeolite which determines the amount of space available for filling by oligomer molecules and this remains largely unchanged. The wider separation of the Brønsted sites within ZSM5-ST results in a longer average chain length for the pore blocking oligomer as observed in our model compound studies, which explains the increased intensity

of CH_2 modes observed in Figure 6-23(ii(a)), relative to those in Figure 6-23(i(a)). The separation of the Type I coke into two populations, with one corresponding to that in the fresh catalyst and the other requiring higher temperatures to oxidise, may be due to increased mesoporosity in the steamed zeolite leading to a population of larger, harder to oxidise oligomers. The lower levels of residual production, following catalyst conditioning, and the more rapid decay of even this production towards a completely deactivated catalyst, are explained in terms of a lower level of external, non-blocked active sites.

6.3.5.2 Reactions at 573 K:

At 573 K the hydrogen transfer reactions are rapid enough for the aromatic cycle to contribute meaningfully to the overall reaction, which combined with the increased rate of ß-scission, means that the runaway oligomerization process does not occur in the fresh catalyst. Instead, the initial catalyst conditioning in ZSM5-FR_Oct_573K consists of the build-up of a population of aromatic species within the zeolite, as evidenced by the initial burst of alkanes which are the hydrogen accepting products of the hydrogen transfer reaction. After approximately 30 minutes this aromatic pool has reached a stable level and the catalyst shifts to its main operational regime where both cycles are operating in equilibrium, releasing both mobile monoaromatics from the cyclisation reaction and light olefins from ß-scission in the alkyl cycle. Reduced levels of oligomerization and increased cracking rates account for the fact that non-aromatic products larger than C_3 are observed at considerably lower levels than in ZSM5-FR_Oct_473K.

The rate of production of aromatics is not stable but begins an immediate decay after the catalyst conditioning period. This is linked to a simultaneous decrease in 1-octene conversion which indicates that the aromatic catalytic cycle is not fully efficient at 573 K. The high level of coke content in ZSM5-FR_Oct_573K, together with the primarily Type II nature of this coke, indicates that the problem lies with excessive formation of aromatic coke species. This depletes the pool of aromatic hydrocarbons available for the reaction and block the catalytic sites suitable for the formation of fresh aromatics through cyclisation. The high coke production is likely due to the aromatic formation and alkylation reactions

proceeding at a faster rate than the rearrangement and alkene elimination reactions which form the 'regeneration' arm of the aromatic cycle (Figure 6-19) under the reaction conditions at 573 K. The INS data indicates that the coking process involves the formation of both highly substituted benzenes and naphthalenes, primarily with methyl substituents, as well as amorphous-carbon like coke species, despite the methylated aromatics not being readily apparent to infrared analysis. The inefficiency of the aromatic cycle may be due to slower diffusion of the aromatic products within the zeolite, leading to a high percentage of them undergoing further additions and becoming trapped. This would explain the relatively low levels of di- and tri-substituted benzenes detected by GCMS in the liquid products.

The progressive deactivation of the aromatic cycle leads to the alkyl cycle beginning to dominate the reaction from + 07:00 hrs on-stream, giving the light olefin dominated product distribution that is observed from this point onward and producing the large quantities of alkanes which dominate the liquid products. The continued decay in aromatic product levels indicates that deactivation of the catalyst is continuing even to the end of the reaction period studied. The GCMS results indicate that the reduced activity of the catalyst also means that isomerisation reactions of the octene to other C_8 hydrocarbons also become relevant, since it is possible for molecules to diffuse in, isomerise and diffuse out of the catalyst, without undergoing cracking or encountering another reactive alkoxide for oligomerization. With less of the 1-octene feed to the catalyst being diverted into the aromatic cycle in the late stages of the reaction, the alkyl cycle is able to build-up a small quantity of immobile long-chain oligomers, similar to those observed at 473 K, despite the higher rate of oligomer cracking reactions. These are responsible for the small population of Type I coke which is observed by TGA and INS and that dominates the infrared spectrum. The catalyst is still active enough to promote rearrangements of these oligomers during their formation, resulting in them being relatively branched with INS peaks mostly overlapping with the modes of the Type II coke.

The effect of the steam treatment is to considerably accelerate this suppression of the aromatic cycle. ZSM5-ST(1073K)_Oct_573K exhibits the same behaviour of aromatic product levels reaching a maximum immediately after catalyst

conditioning, followed by a transition to a primarily alkyl-cycle, light-olefin producing regime as the reaction proceeds. However, the peak level of aromatic production is lower than that achieved by ZSM5-FR_Oct_573K, even at the end of the experiment. Levels of alkene production, including the heavier products from C_4-C_8, likewise follow the distribution which would be expected from projecting the trends observed in ZSM5-FR_Oct_573K to a timestamp considerably beyond the end of the experimental period. This reduction in aromatic cycle reactivity also has the effect of preventing the formation of polyaromatic Type II coke, meaning that catalyst deactivation occurs by the formation of large oligomers, similar to lower temperature reactions as observed in the INS spectrum. The levels of this Type I coke are broadly similar to those found in the fresh catalyst but the shape of the INS spectrum suggests a lower level of branching, with the oligomer retaining most of the adjacent CH_2 groups found in 1-octene.

6.3.5.3 Reactions at 673 K:

The increase in temperature to 673 K is sufficient for the restrictions to the aromatic cycle to be overcome. The level of aromatic production in ZSM5-FR_Oct_673K is much higher than at 573 K and remains stable for the first 24 hours on-stream, indicating that no premature deactivation of the catalyst is occurring. This suggests that elimination reactions to remove alkenes from larger aromatics are able to occur, recycling the aromatic ring. This supposition is supported by the significantly increased production of ethene observed, relative to the thermal cracking profile at 673 K, due to elimination of ethyl side-chains. Some deactivation of ZSM5-FR_Oct_673K does occur, but this takes much longer: aromatic product levels do not begin to decrease until 18:00 hours on stream and the rate of deactivation remains low, as reflected by the coke content of ZSM5-FR_Oct_673K being only 70 % of that found in the fully coked catalysts generated at lower temperatures. The final coke content of the ZSM5-FR_Oct_673K catalyst is high enough that the catalyst deactivation may be due to active site blocking, as is the case at lower temperatures. However, the longer time frame over which it occurs, indicates that the permanent removal of acid sites through de-alumination, as observed in the infrared data, may be responsible instead. The fact that Type I coke is essentially absent from the TGA profile, also indicates that the aromatic cycle remains active enough to prevent multiple oligomerizations

until the end of the reaction run. The deactivation which does occur takes the form of a progressive shift towards alkyl cycle reactivity and light olefin products, similar to the behaviour at lower temperatures.

The effect of the steaming at this temperature is again to suppress aromatic production in favour of additional cracking and the production of light olefins, although aromatic levels are still higher than those achieved at lower temperatures except in the earliest stages of the reaction of ZSM5-FR_Oct_573K. The aromatic composition is also changed, with naphthalene production being almost completely suppressed and the production of benzenes with more than two substituent groups also being significantly reduced. This may be due to the greater ease of diffusion in de-aluminated ZSM-5 (Chapter 5) reducing the average residence time of benzene products within the catalyst, lowering the probability of further reactions. Due to the lack of opportunities for the formation of type II coke and the high rate of cracking preventing Type I coke formation, deactivation of ZSM5-ST(1073K)_Oct_673K is minor, resulting in very low final coke content and stable product levels across the entire length of the reaction run.

The coke that does form at 673 K is very similar to that generated in ZSM5-FR_Oct_573K, with a similar mix of mostly aromatic species. This suggests that there are two reactions within the hydrocarbon pool mechanism which have a key effect on the overall cycle chemistry: the hydrogen transfer reaction which links the alkyl and aromatic cycles and the rearrangement/elimination reactions which remove groups from pool aromatic species. Each of these reactions require successively higher temperatures to become active and deactivate in turn as the catalyst ages and cokes. This in turn partitions the hydrocarbon pool into three separate reaction regimes depending on which reaction, if any, is active: (i) the fully operating catalytic cycle observed at 673 K; (ii) the excess polyaromatic coking regime which ZSM5-FR_Oct_673K enters in the later stages of the reaction (and where ZSM5-FR_Oct_573K operates throughout) and (iii) the alkyl-cycle only regime observed for the majority of ZSM5-ST(1073K)_Oct_573K's lifetime and at 473 K.

6.3.6 De-Alumination Effects on Octene Cracking:

Apart from at 473 K, where the temperature is too low for the catalytic mechanisms to cycle properly, the fresh catalyst undergoes a progressive shift away from aromatic-producing chemistry, towards a more olefin-dominated product mixture over the course of the reaction. This process occurs as access to catalytic sites capable of catalysing the hydrogen transfer reactions, which form BTX aromatics from adsorbed alkoxides, is lost due to pore blockage by coke species. The effect of the pre-emptive removal of the majority of these active sites through steam treatment is to accelerate this process for the steam-treated catalyst, resulting in the ZSM5-ST(1073K) samples operating primarily in the olefinic reaction regime from the start of their time on stream. This reduced aromatic production has the additional consequence of substantially reducing the level of coke formation during the course of the reaction, resulting in the steam-treated catalysts having more stable product levels than their fresh counterparts and likely increasing their catalytic lifetime before deactivation. This behaviour is similar to that observed by Ibáñez, et al.[35] for the conversion of butene over mildly steamed ZSM-5. In that study, the suppression of the aromatic cycle was attributed to the selective removal of the strongest acid sites from the zeolite framework. In this case, the harsher steaming conditions employed resulted in a more complete removal of Brønsted acidity and shows no evidence of selective removal of stronger acid groups, suggesting that another mechanism may be responsible.

Therefore, for octene cracking, all catalysts shift from a mixed aromatic-light olefins product mixture, towards a purely olefinic product regime as the reaction proceeds. The temperature of reaction determines how fast this occurs, by influencing what coke formation routes are made available by low reaction rates in key steps in the dual cycle mechanism. The removal of acid sites by steam de-alumination means that the aromatic cycle is pre-emptively suppressed in ZSM5-ST(1073K) and the reaction operates in the primarily light olefin producing regime from the start of the reaction, increasing the overall selectivity of the reaction towards ethene and propene. This ‘Gasoline-to-Olefins’ type chemistry is more similar to the results reported for ZSM-5 catalysts in industrial FCC

reactors, where it is primarily used to increase the yields of propene and ethene.[23, 29] The aromatic-based chemistry of the fresh catalyst is less commonly observed and is attributed to the exceptionally high acidity of ZSM5-FR. The reduction in aromatic cycle chemistry in ZSM5-ST also has the effect of reducing the level of coke formation in the catalyst, particularly at high temperatures, by inhibiting the formation of polyaromatic Type II coke, resulting in increased stability and operating lifetime of ZSM5-ST(1073K) relative to ZSM5-FR. Consequently, for octene cracking reactions catalysed by ZSM-5 zeolites both catalyst selectivity and stability are increased by steam treatment and the resulting behaviour of the treated catalyst is more representative of ZSM-5 catalysts in industrial FCC use.

6.4 Comparison of Propene and Octene Chemistry:

Differences between the results produced for the propene and 1-octene reactions are mainly confined to those reactions performed at temperatures of 573 K and above; at 473 K the reactions primarily produce large oligomers through essentially similar processes, with only minor differences in the degree of oligomer branching due to the different feeds.

At the higher reaction temperatures, the propene reaction produces a higher proportion of aromatics and light olefins and relatively fewer gasoline-range alkenes. The effective absence of hexene from the propene products at 673 K is especially notable, since it means that even C_6 species are not playing a significant role. Nearly all the propene consumed either participates in the aromatic cycle or is cracked back to its starting point. In contrast, the 1-octene reactions produce a wider range of products, as would be expected from the greater number of ways that the 1-octene can react on first introduction to the catalyst. While propene must either oligomerize, alkylate an aromatic or act as a hydrogen acceptor, 1-octene can undergo immediate cracking with multiple possible fragmentation patterns. The greater variety in the 1-octene reaction extends to the products of the aromatic cycle, with tri- and tetra-substituted benzenes and a larger variety of naphthalenes being produced at 673 K.

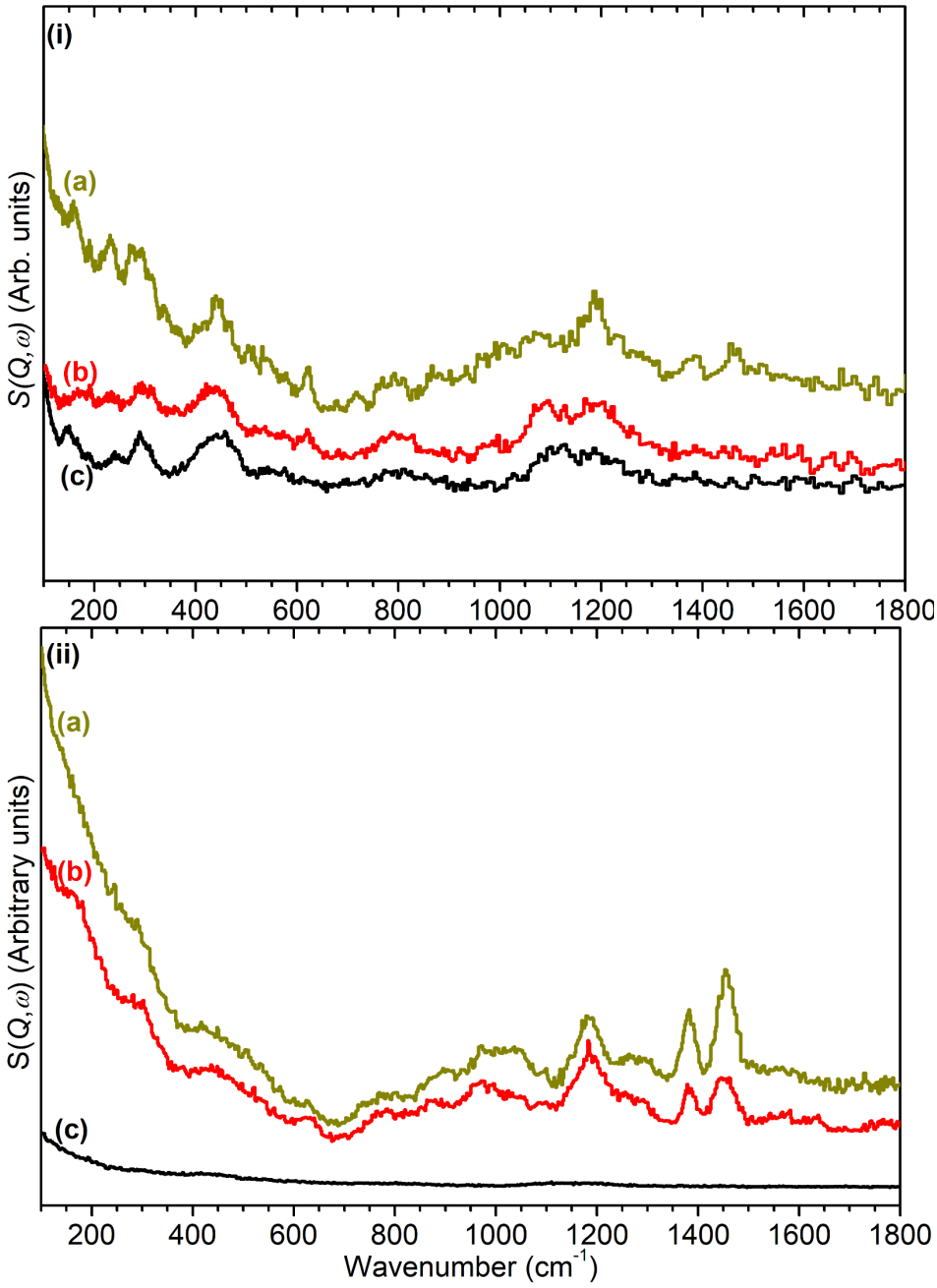

Figure 6-25: INS spectra of ZSM5-FR after reaction with propene (i) and 1-octene (ii) at 573 K (a) and 673 K (b) compared with the unreacted zeolite (c). Propene spectra collected on TOSCA, 1-octene spectra on MAPS; peak intensities are therefore not comparable between plots.

Comparison of the retained coke species between the reactions is complicated by their differing times on-stream, meaning that it is not possible to gain a meaningful comparison of the rate of coke build-up in each reaction. Comparison of the INS results for each sample does allow some conclusions to be drawn on the composition of the coke. The relevant INS results are reproduced as Figure 6-25 for easier reference. They were collected on different instruments so scattering

intensities cannot be meaningfully compared between samples, although mode energies and relative intensities within spectra remain comparable regardless of the INS collection method. The most obvious difference is that the 1-octene coke contains a much higher population of methyl groups, leading to the modes either side of 1400 cm^{-1}. As noted above, these are attributed to the presence of immobilised polymethylated aromatics, the absence of which from the propene coke spectra was the most notable difference between our 'propene-to-hydrocarbons' chemistry and the published mechanisms of MTH catalysis where tetra-, penta- and hexamethyl benzenes play important roles as reaction centres in the aromatic cycle (Section 6.2.4.3). It appears likely that the 1-octene hydrocarbon pool has a more statistical distribution of chain lengths than the propene hydrocarbon pool due to fragmentation of the C_8 chains. Therefore, the aromatic product mixture of 1-octene is less restricted by the availability of suitable fragments and produces a more statistical mixture of products, closer to that of MTH chemistry.

6.5 Summary:

The INS techniques previously developed in our investigations of model compound systems over zeolite at low temperatures have been applied to investigate olefin reaction chemistry over zeolites, in combination with standard microreactor and *ex situ* characterisation methods. The use of INS allows characterisation of the retained coke species which remain within the zeolite in a way not previously possible. Both propene and 1-octene are found to react *via* a two-cycle hydrocarbon pool mechanism, with strong similarities to that reported for methanol-to-hydrocarbons chemistry, supporting the assertion that propene plays an important role as an intermediate species in MTH catalysis.[47] This dual-cycle mechanism requires temperatures of 673 K or higher to function with full efficiency, with lower temperatures deactivating portions of the cyclic mechanism, leading to premature deactivation of the catalyst through overproduction of coke species, which have been observed with INS. Even at full efficiency, the catalyst is found to slowly progress from an aromatic-heavy to an olefin-heavy product schema due to the progressive blockage of active sites by the formation of amorphous carbon-rich coke. Artificial aging of the zeolite,

through steam treatment, is found to shift the catalyst lifetime so that it starts at a later stage in this process, resulting in increased light olefin production; this trend matches results in the literature. The reduced aromatic production also means that deactivation of the catalyst occurs more slowly in steamed catalysts than in fresh ones, after an equivalent time-on-stream

Chapter 7: Molecular Dynamics Studies of Methane Diffusion in ZSM-5

Although developed to assist in the analysis of the motions of molecules in the C_3-C_8 size range by QENS, the molecular force field described in Section 2.2.2.2 is equally applicable to the simulation of other zeolite-hydrocarbon systems, whether differing in zeolite structure or the nature of the adsorbate. Here, it has been used to simulate the movement of methane in MFI zeolite frameworks, for comparison with results obtained by QENS analysis. The motions of this system are of interest as a model for the motion of methanol in zeolites, which plays an important role in the selectivity of the methanol-to-hydrocarbons reaction, but which is hard to study directly due to issues with the reactivity of the methanol molecule in highly acidic zeolites. In addition to comparison with experimental results, this study also investigated the influence of hydrocarbon loading on diffusion behaviour, through the simulation of zeolites with different quantities of methane molecules per unit cell.

7.1 Introduction:

The work reported in this chapter forms part of an ongoing study into the interactions of methanol with zeolites, which is of interest due to the methanol-to-hydrocarbons (MTH) reaction. As discussed in detail in Section 1.2.2 this uses zeolite catalysts to selectively convert methanol to high-value hydrocarbon products through a shape-selective hydrocarbon pool mechanism. As with all such shape-selective reactions, the diffusion of the methanol reagent directly affects the selectivity mechanisms, and therefore the product composition, and applying QENS methods is the best available tool to gain an increased understanding of how this diffusion changes with temperature and zeolite properties.

While direct studies of methanol diffusion in acid zeolites have been performed, these encounter problems with measuring the movement of methanol through the pore network due to the high reactivity of the system. This is particularly the case in investigations using ZSM-5 type zeolites due to their high acidity. While O'Malley et al.[123] were able to successfully determine the self-diffusivity of methanol in zeolite Y, attempts to study the methanol-ZSM-5 system by similar methods encountered extremely low levels of mobility.[205-206] Methanol motions were limited to isotropic rotations of the methyl group, or diffusion within confined spheres the size of a single zeolite pore, owing to the adsorption of the methanol on the Brønsted sites through the –OH group. Avoiding this problem, requires the use of a probe molecule of similar size to methanol but without the reactive centre: methane is the obvious candidate, as has been successfully applied in previous studies.[67-68, 207-208]

The present investigation uses methane as a probe molecule for the diffusion of C_1 hydrocarbons in fresh and reacted ZSM-5 catalysts. This work was performed in partnership with Ms Andrea Zachariou, as described in further detail in the Preface, who performed the QENS data analysis of the methane – ZSM-5 datasets. Since the analysis methods used in this study are the same as those already reported for QENS investigations in previous chapters, the details will not be reported here. Instead, we will only consider the final results obtained and how they compare to the findings from the MD simulations. Since simulations were not

performed for the coked material, only the results obtained for the unreacted catalyst (ZSM5-FR) will be discussed.

7.2 Experimental Procedure:

A 3.13 g sample of ZSM5-FR was prepared according to the procedures in Section 2.4 and loaded into a gas handling QENS sample can. This was then investigated according to the standard QENS measurement procedure (Section 2.1.3.4) on the IRIS spectrometer with methane as the adsorbed hydrocarbon. The full temperature range investigated was 5 – 373 K with EFWS points taken at 25 K intervals from 25 K to 373 K, the final temperature being reduced by 2 K to not exceed the maximum rated temperature of the QENS sample container. High resolution spectra were collected at 5, 225, 275, 325 and 373 K. The methane dosing was carried out by filling a container of known volume with 3.65×10^{-2} moles of methane as determined from the loading pressure by the ideal gas law, opening it to the zeolite sample cell and allowing the system to equilibrate. After removal of the residual methane remaining in the gas handling apparatus this resulted in a sample containing 2.55×10^{-3} moles of methane, equating to a loading of 4.70 methane per ZSM-5 unit cell. This represents the saturation loading of the zeolite at 877 mbar. The evacuated dosing volume was left connected to the zeolite sample during measurement to safely contain any methane desorbed on heating, as required by ISIS gas handling procedures.

MD simulations were performed on both silicalite and ZSM-5 type frameworks using the molecular force field and simulation procedure given in Sections 2.2.2.2 and 2.2.2.3. Loading levels of 4 and 9 methane molecules per unit cell were simulated in order to determine the effect of loading level on the diffusion properties. Simulations were performed at 95, 130, 170, 225, 270, 325 and 375 K in order to match the range of temperatures investigated by detailed QENS analysis and to provide information on the low temperature behaviour of the simulated systems. 270 K was simulated rather than 275 K to provide a universal comparison temperature in common with the C_3 and C_8 simulations reported above. 95 K was chosen as being immediately above the melting point of solid methane and therefore the first temperature where mobility is likely to be observed.

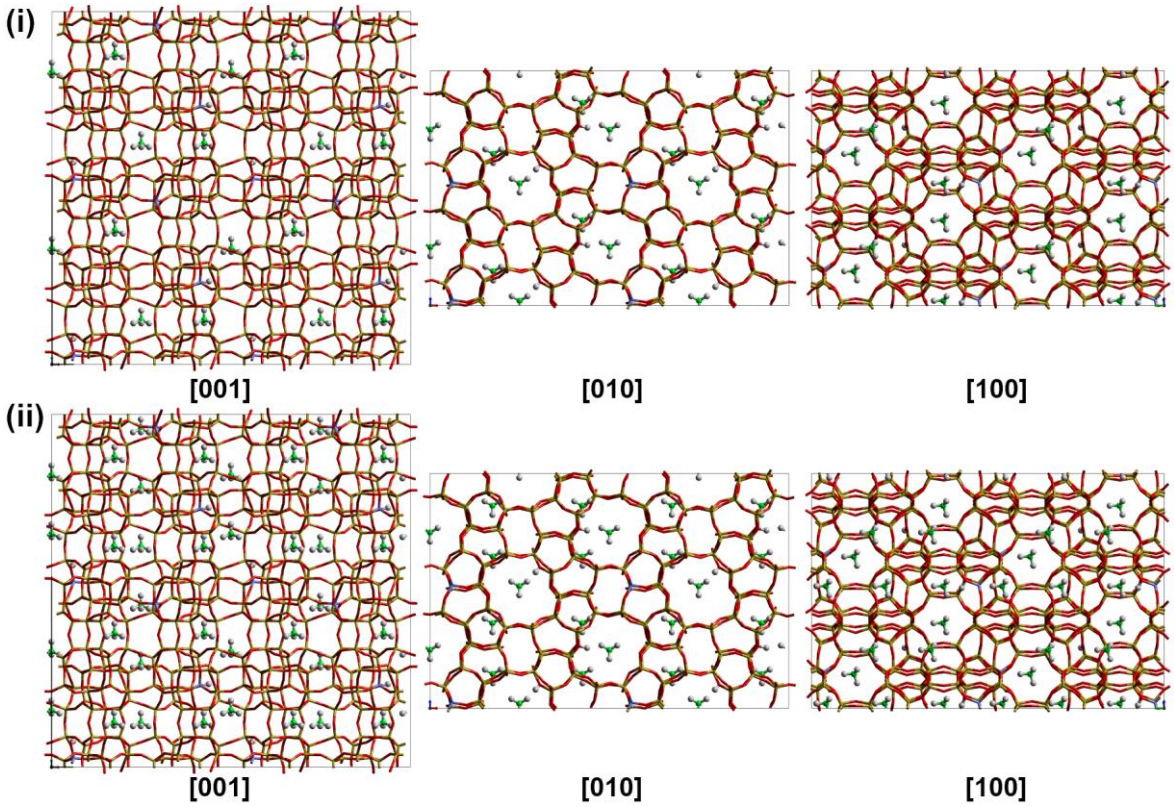

Figure 7-1: Pre-equilibration starting configurations for MD simulations of methane in MFI zeolite frameworks at loadings of 4 molecules per unit cell (i) and 9 molecules per unit cell (ii). Zeolite shown is the H-ZSM-5 protonated framework.

7.3 Elastic Fixed Window Scan Analysis:

As with previous QENS investigations, initial examination of the mobility of the system was through EFWS analysis because of its ease of calculation and ability to provide an overview of the changes in diffusion behaviour with temperature across the full range studied.

7.3.1 QENS Results:

The EFWS of methane in ZSM5-FR shows the expected behaviour of increased mobility with temperature, with the greatest increase in mobility occurring at low temperatures (Figure 7-2). A small inflection in the slope of the EFWS trace occurs between 75 and 100 K due to the methane passing through its melting and boiling points. One notable feature is that at temperatures of 300 K and above the elastic intensity in the loaded sample is essentially identical to that recorded for the

unloaded ZSM5-FR prior to hydrocarbon loading. This shows that at these temperatures, the methane is fully mobile and does not contribute to the measured elastic intensity at all, with the remaining EFWS intensity values being entirely due to scattering from the zeolite framework. The methane still contributes to the quasielastic scattering and may be analysed through fitting, however, such high levels of mobility are likely to complicate this process.

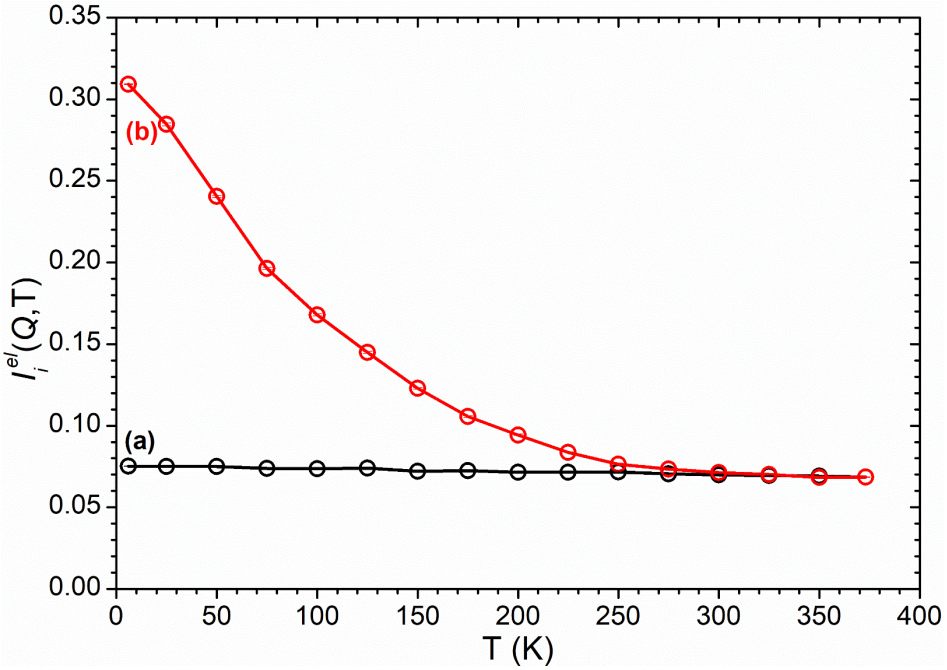

Figure 7-2: Experimental elastic intensity vs temperature for unloaded ZSM5-FR (a) and methane in ZSM5-FR at a calculated loading of 4.70 molecules per unit cell (b).

7.3.2 MD Results:

Simulated EFWS plots were created from the simulation trajectory data by calculating the $S(Q,\omega)$ of each system using the procedure described in 2.2.2.4. Scattering functions were simulated in the range 0.1 Å^{-1} ≤ Q ≤ 5 Å^{-1} at 0.1 Å^{-1} intervals but the integrated intensities used to calculate the theoretical relative elastic intensity were limited to the momentum transfer values which are accessible on IRIS (0.42 – 1.85 Å^{-1}, simulation integration performed from 0.4 - 1.9 Å^{-1}).

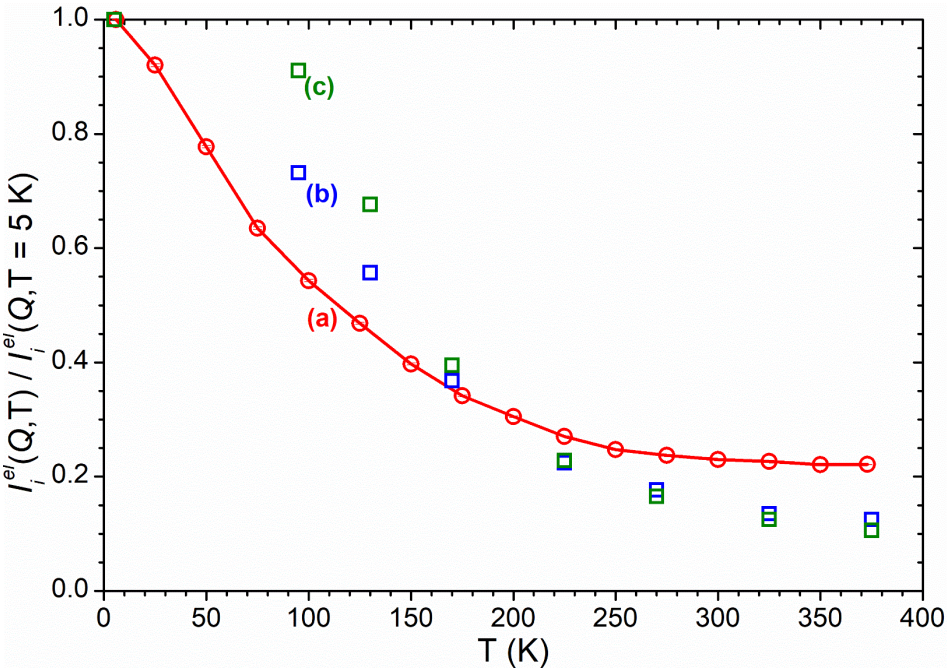

Figure 7-3: Comparison of the experimental EFWS of CH_4 in ZSM5-FR (a) with simulated relative elastic intensities for methane in H-ZSM-5 (b) and silicalite (c) derived from molecular dynamics calculations. All values normalised against elastic intensity at T = 5 K.

The resulting simulated EFWS for simulations in H-ZSM-5 (Figure 7-3(b)) conforms closely to the experimental data in the blank ZSM-5 at temperatures above 200 K, which includes one point (225 K) where the experimental spectrum still possesses some methane-derived elastic intensity. The overall trend is towards a plateau value at approximately 10 % of the initial relative intensity. This confirms that all methane molecules are fully mobile by *ca*. 300 – 350 K and the remaining elastic intensity is due to scattering from the essentially immobile zeolite framework. That the final relative intensity values in the simulated spectra are at a slightly lower level than in the experimental case, can be attributed to the absence of any background intensity in the simulations and that the simulated results can observe all motions which occur during the simulation, not just those which occur within the time window accessible on the spectrometer used.

An anomaly in the simulated data is observed in the simulations performed at 95, 130 and 170 K where the MD simulation persistently underestimates the level of mobility in the sample at these temperatures. Surprisingly, this effect is even more heavily pronounced in the simulation of methane movement in the pure SiO_2 framework (Figure 7-3(c)). This suggests that the problem may be due to an

overestimation of the intermolecular forces between the methane molecules in the simulation force field, caused by the OPLS force field terms being fit to behaviour at higher temperatures and not being optimised for liquid-phase interactions in methane. This would result in the methane in the simulation remaining in the solid and liquid states at higher temperatures than are the case in reality, which would account for the behaviour observed. The decreased magnitude of the effect in the H-ZSM-5 simulation would then be attributable to the acid-methane bonding disrupting the structure of the solid methane and decreasing the energy required for methane molecules to break free into the gas phase.

An alternative explanation is provided by observations made in a molecular dynamics study by López, et al.[209] of a change in the preferred low-energy site of methane in silicalite structures which occurs at 250 K. Below this temperature the methane prefers locations within the straight channels, while above it the lowest energy site lies in the channel intersections, with a corresponding change in the energy barriers to diffusion. While this is a possible explanation for the observed behaviour, the López investigation was carried out at infinite dilution and caution should be used in extrapolating from such studies to systems where methane-methane interactions are significant.[210] Therefore the source of the discrepancy cannot be asigned with certainty.

7.4 Analysis of Diffusion Behaviour:

The region from 200 to 375 K shows good agreement between experimental results and simulation, and contains 4 temperatures where high resolution QENS spectra are available for analysis. We may therefore compare the results obtained by both methods.

7.4.1 QENS Results:

The QENS data was fit to a combination of resolution function, linear background and single Lorentzian, indicating a single resolvable motion and one or more motions too fast to be visible on IRIS. The Lorentzian broadening was found to be

best described by jump diffusion according to a model developed by Jobic.[211] This is similar to the Chudley-Elliot model of jump diffusion as described in Section 2.1.3 and Equation (2.15), but rather than assuming a single length for all jumps, it assumes a distribution of jump lengths described by an average distance d_0 and a parameter describing the variation in molecule position between jump motions, r_0. The relationship of the Lorentzian broadening with Q is then described by the equation:

$$\Gamma(Q) = \frac{1}{\tau} - \left[\frac{\sin Q d_0}{Q d_0} \exp\left(-\frac{Q^2 \langle r_0^2 \rangle}{2}\right)\right] \tag{7.1}$$

and the mean squared jump length, required for the derivation of the diffusion constant *via* the Einstein equation, is given by:

$$\langle r^2 \rangle = {d_0}^2 + 3{r_0}^2 \tag{7.2}$$

Fitting the QENS data to this model produced the results given in Table 7-1.

Table 7-1 Self-diffusion coefficients (D_s), residence times (τ) and mean square jump lengths ($\langle r^2 \rangle$) calculated by fitting the experimental QENS data to the model in Equation (8.1).

Temperature (K)	**τ (ps)**	**$\langle r^2 \rangle$ (Å^2)**	**D_s (m^{2}s^{-1})**
225	13.4	29.6	3.66×10^{-9}
275	10.4	41.9	6.74×10^{-9}
325	8.00	45.0	9.37×10^{-9}
373	8.00	45.0	9.38×10^{-9}

7.4.2 Molecular Dynamics Results:

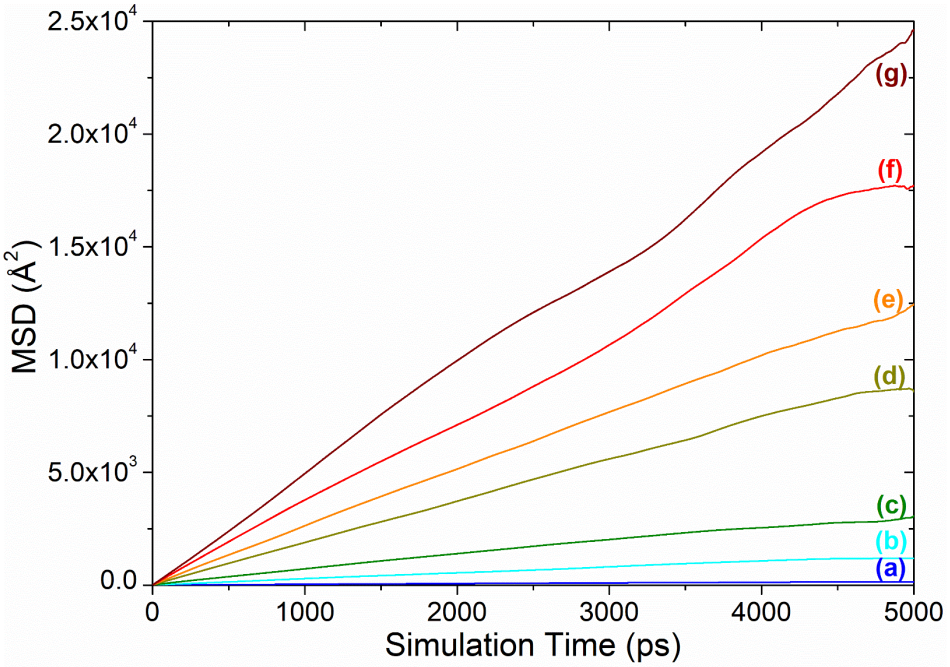

Figure 7-4: Mean squared displacement versus time for methane in H-ZSM-5 at a loading of 4 molecules per unit cell, calculated at simulation temperatures of 95 K (a), 130 K (b), 170 K (c), 225 K (d), 270 K (e), 325 K (f) and 375 K (g).

Accurate calculation of diffusion constants from the statistics of molecular dynamics simulations requires simulation lengths long enough that the system achieves true diffusive motion and the mean squared displacement (MSD) of the adsorbed molecules becomes linear with respect to time. As shown in Figure 7-4, the systems studied here achieve this for the majority of the simulation runtime. The fluctuations at longer time values observed for the higher temperature simulations are because the MSD is calculated as an ensemble average over all possible molecules and origins, with each timestep in the simulation being treated as a 'time zero' for a displacement trajectory. As the length of the time window being considered approaches the full length of the simulation the number of potential origins for averaging is reduced, resulting in less consistent results. By limiting ourselves to the linear portion of the MSD trace the self-diffusion constants at each temperature may be calculated using the Einstein relationship; these calculated values are given in Table 7-2.

Table 7-2: Self-diffusion coefficients (D_s) and activation energies (E_a) for methane in silicalite and H-ZSM-5 calculated from MD results. Calculated MD:QENS ratios are for H-ZSM-5 simulations.

T (K)	D_s (m^2s^{-1})				Ratio MD : QENS	
	Silicalite		H-ZSM-5			
	4 × CH_4 per u.c.	9 × CH_4 per u.c.	4 × CH_4 per u.c.	9 × CH_4 per u.c.	4 × CH_4 per u.c.	9 × CH_4 per u.c.
95	8.22×10^{-11}	5.57×10^{-11}	4.00×10^{-11}	5.64×10^{-11}	-	-
130	4.93×10^{-10}	3.87×10^{-10}	4.00×10^{-10}	4.52×10^{-10}	-	-
170	1.99×10^{-9}	1.50×10^{-9}	1.81×10^{-9}	1.10×10^{-9}	-	-
225	4.97×10^{-9}	3.51×10^{-9}	3.91×10^{-9}	3.10×10^{-9}	1.07 : 1	0.85 : 1
275	7.13×10^{-9}	4.93×10^{-9}	7.11×10^{-9}	4.25×10^{-9}	1.05 : 1	0.63 : 1
325	1.02×10^{-8}	6.43×10^{-9}	9.31×10^{-9}	6.18×10^{-9}	0.99 : 1	0.66 : 1
375	1.34×10^{-8}	7.96×10^{-9}	1.40×10^{-8}	7.95×10^{-9}	1.49 : 1	0.85 : 1
D_0 (m^2s^{-1})	5.15×10^{-8}	3.19×10^{-8}	6.96×10^{-8}	4.04×10^{-8}	-	-
E_a (kJ/mol)	4.39	4.26	5.30	5.01	1.19 : 1	1.07 : 1

These values show a clear disconnect between the diffusion constants at low temperatures and those from simulations performed above 200 K. This is consistent with the results observed in the elastic window scan data above and the same explanation proposed there applies. Comparison of the results above 200 K, which are more in line with experimental observations, shows that the difference in diffusion constants between silicalite and H-ZSM-5 structures is quite small in both the 4- and 9-molecule per unit cell cases. In both structures the difference between the low and high loaded simulations in the same material is more significant. This suggests that the higher loaded simulation in both cases is sufficiently congested that methane-methane interactions are the limiting factor in determining the bulk diffusion through the zeolite pores, with the effect of methane-zeolite interactions being masked by this pore congestion effect. This hypothesis is given further support that at 373 K, even the lower loaded samples see a convergence between their diffusion constants as the methane molecules become more mobile. In the lower temperature region of the 4/u.c. simulations, where differences exist, the methane diffuses slower in H-ZSM-5 as would be expected due to the additional H_b-adsorbate interactions. The activation energies similarly show the expected trend, with the value in H-ZSM-5 being 118 % of that

in silicalite. This compares favourably with the E_a of 4.667 kJ/mol determined experimentally by QENS above, is 109 % of that reported for methane in silicalite by Caro, et al.[68] This suggests that our molecular dynamics force field is accurately describing the effect of the Brønsted acid sites on the overall behaviour of the system.

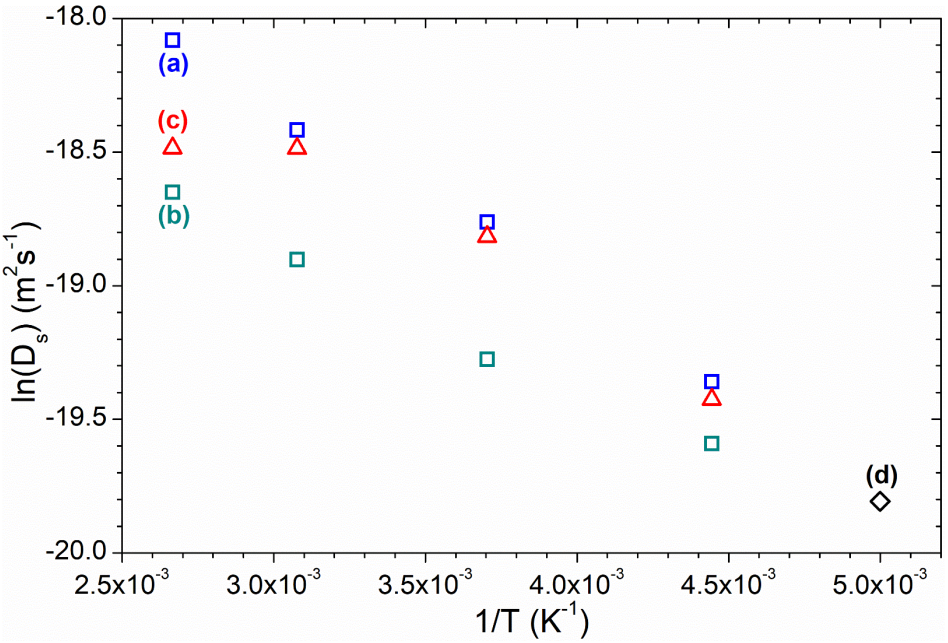

Figure 7-5: Arrhenius plot comparison of: diffusion in H-ZSM-5 calculated by MD at 4 molecules per unit cell (a) and 9 molecules per unit cell (b); experimental QENS values at 4.70 mol/u.c. in ZSM5-FR as determined above (c); experimental QENS value at 4 mol/u.c. in Na-ZSM-5 as reported by Jobic, et al.[67] (d).

Discounting the simulations below 200 K and comparing the values derived at higher temperatures with the QENS results shows close agreement between the simulated and experimental data. For the 4 molecules per unit cell in ZSM-5 simulation, which is the closest match to the experimental data, the calculated diffusion constants match those recorded experimentally to within 10 %, with the exception of the value at 373 K where the QENS result does not follow the trend in the other three data points and may be anomalous in any case. The simulated D_s values are higher than those obtained experimentally as shown in Table 7-2 and Figure 7-5. This is because molecular dynamics predictions of diffusion constants represent an upper limit to the possible mobility of the adsorbed species both due to the use of a slightly lower loading and as a result of the use of a perfect crystal structure, which does not account for the presence of local defects, silanol sites,

crystal edge effects or inhomogeneous Brønsted site locations, all of which will tend to reduce the experimentally observed diffusion values.

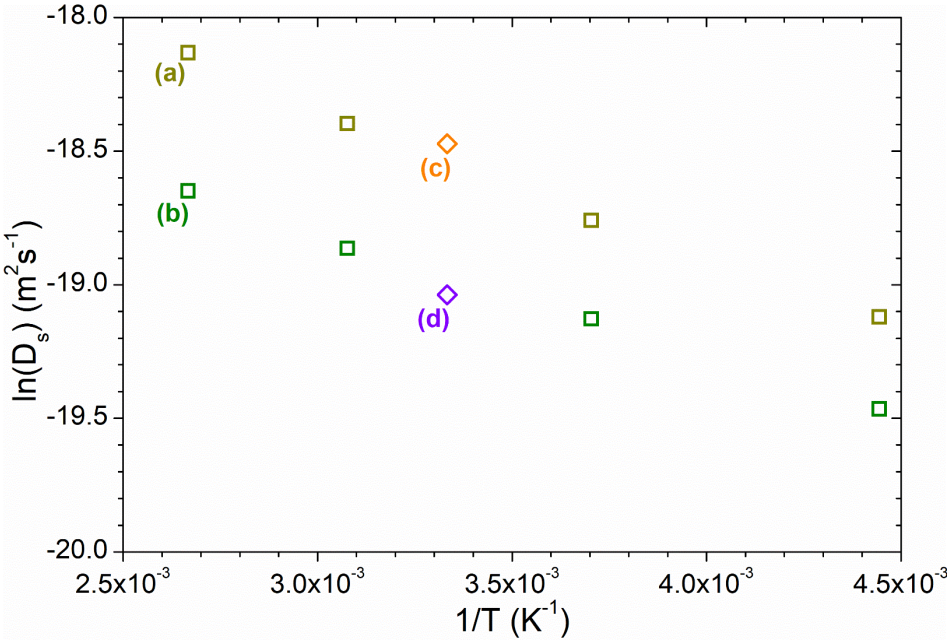

Figure 7-6: Arrhenius plot comparison of: diffusion in silicalite calculated by MD at 4 (a) and 9 (b) molecules per unit cell; literature values for diffusion in silicalite at 4 (c) and 8 (d) molecules per unit cell as reported by Leroy, et al.[176]

In addition to closely matching the experimental data, the molecular dynamics results obtained are consistent with those found in the literature for comparable systems. As shown in Figure 7-6, the simulations in silicalite closely match those reported by Leroy, et al.[176] for comparable loadings at 300 K. It is notable that this paper reports that its molecular dynamics simulations produce diffusion constants *ca*. 2 - 2.5 times larger than those of QENS investigations of methane in silicalite by Jobic and co-workers. Unfortunately, we were unable to obtain the exact result values of these QENS investigations to allow a direct comparison to our own QENS and MD figures due to the studies by Jobic only giving the methane D_s values in graphical form.

7.5 Summary:

The diffusion of methane in ZSM5-FR and silicalite has been simulated by molecular dynamics at two different levels of loading and compared with the

results from experimental QENS observations. The diffusion constants calculated from MD simulations above 200 K closely match those reported in the literature for similar systems and produce estimates of mobility which closely match those obtained by experiment, confirming that the molecular force field used in these simulations can accurately describe small C_1 molecules as well as the larger alkanes and olefins whose simulations are reported above. The force field's ability to describe the behaviour of methane in the liquid phase is less accurate owing to the way in which the intermolecular hydrocarbon parameters were derived. Comparison of the simulations in the 200 – 375 K region shows that methane-zeolite interactions are less significant in this temperature range than methane-methane ones due to congestion of the pores. This observation is consistent with the QENS results showing that the methane is fully mobile within the zeolite at these temperatures and no methane remains adsorbed to the pore walls.

Chapter 8: Conclusions and Future Work

The work reported in this thesis has highlighted the ability of neutron scattering methods to supply new insights into systems of interest to catalysis and the ways in which vibrational analysis by INS and the analysis of dynamics by QENS can complement each other. The well-established ability of QENS measurements and MD simulations to validate results and provide insight into the results from each method when used in concert has also been demonstrated. After briefly summarising the key findings reported previously, this chapter will consider areas where this thesis has highlighted obvious potential for additional work of interest to be carried out on catalytic zeolite systems using these techniques, some of which is already underway.

8.1 Conclusions and Key Findings:

The neutron scattering techniques of INS and QENS have been applied to the study of the reactivity of olefins over the acid zeolite catalyst H-ZSM-5. Both techniques have demonstrated the capability to provide new insights into the reaction chemistry and dynamics which occur inside zeolites and exhibit a clear synergy when employed in combination. The INS results provide information on the interactions responsible for changes in mobility and broad-range QENS results, collected through the EFWS method, guiding the assignment of INS measurements to the temperatures of greatest interest.

Investigation of the interactions of olefins in fresh H-ZSM-5 have shown that the extremely high activity of the catalyst causes the olefins to undergo protonation and subsequent oligomerization even at low temperatures, with reactivity for propene commencing at 225 K. Examination of the reaction intermediates made possible through INS, has shown that the reaction proceeds through a hydrogen-bonded intermediate as a first step, and that the subsequent protonation of the olefin to a bonded carbocation represents the rate-limiting stage of the reaction. Examination of the product spectra suggests, that for both propene and 1-octene, pore wall interactions result in reactions at interior acid sites producing linear oligomers which form the bulk of the final product.

This oligomerization activity prevents the measurement of the movement of propene or 1-octene in fresh zeolites by QENS. It is possible to observe the movement of the oligomers themselves, which are trapped within the pore network, but capable of rotating around their long axis within the straight channels of the zeolite. Studies using propane as an inert analogue for propene have found, in concert with MD simulations, that the adsorbed C_3 molecules spend the majority of their time undergoing short jumps within the pore channels of the zeolite. Movement into the pore intersections is disfavoured and longer-range diffusion takes place by longer jumps across the pore channels at intervals too long to be observed by the instruments employed.

Hydrothermal de-alumination plays an important role in determining the activity of zeolite catalysts and occurs rapidly enough in industrial use that studies using fresh materials do not accurately represent the zeolite's activity for the majority of its catalytic lifetime. To study the effect of de-alumination two steam-treated samples were prepared. It was found that differences in the steam treatment protocol do not result in significant changes to the properties of the final zeolite, provided the target level of de-alumination is sufficiently extensive. At low temperatures for hydrocarbon reaction, this de-alumination was found to have the effect of delaying the onset of catalytic activity for oligomerization to higher temperatures and increasing the mobility of hydrocarbons within the zeolite, both due to reduced acid-hydrocarbon interactions. The mobility increase was not found to result from changes in the geometry of the molecular motions, but purely due to them occurring at shorter intervals, indicating that this geometry is defined by structural factors arising from the framework itself, rather than the acid sites.

The techniques developed in these studies have also proven applicable to investigations of reactivity at higher temperatures more typical of catalytic use of zeolites. These have allowed studies of propene conversion and 1-octene cracking to be enhanced by non-destructive analysis of the composition of the coke species which accumulate within the zeolite. Both reactions are found to proceed by a dual-cycle hydrocarbon pool mechanism involving oligomerization, cracking and aromatic formation which requires temperatures of 673 K to operate effectively. Lower temperatures result in excessive coke build-up because of deactivation of certain reactions in the cycle, which can be observed by INS.

In conclusion, neutron techniques have proven to be powerful tools for the analysis of catalytic reactivity in zeolite catalysts where the reactive species have high levels of hydrogen content and thus result in strong incoherent scattering responses. The potential for applying these methods to other questions involving zeolite catalytic chemistry is high.

8.2 Ongoing and Proposed Further Investigations:

The results reported above have highlighted several areas where further work could potentially produce results of catalytic or industrial interest. Some of these areas are simple extensions of the work already reported to provide additional information which it was not possible to collect in the time available. Others are the application of these techniques to additional catalytic systems or new, related techniques to the systems studied here. Each potential line of enquiry will be briefly summarised below, where efforts are already underway to undertake these investigations, these will be highlighted.

8.2.1 Extensions to 1-Octene Cracking Analysis:

For the octene cracking microreactor studies discussed in Section 6.3 the ability to derive useful results from the INS data of the retained coke species is somewhat restricted by the limited resolution of the available spectra, recorded on MAPS. Measurement of the same systems using TOSCA would allow additional information from the higher resolution peaks, including analysis of relative peak position, allow observation of modes below 200 cm^{-1} without interference from the elastic line and permit direct comparability with the propene data in Section 6.2.3. An application to obtain time for such measurements under the ISIS Rapid Access route has been approved, with instrument time at ISIS allocated for April 2021.

In addition to these measurements, NMR has historically been the most widely-used technique for coked zeolite catalyst studies and measurements of the coked catalysts by this measurement would also provide useful data. In particular, ^{27}Al and ^{29}Si measurements would permit us to determine what degree of catalyst steaming has occurred in the catalyst in the course of the reaction, and compare this against acid loss under artificial aging conditions. These measurements are currently underway in collaboration with the Johnson Matthey Technology Centre at Sonning Common, Oxfordshire, UK.

8.2.2 Determining Proton Locations in Zeolites:

One of the aspects of zeolite characterisation of greatest potential industrial interest is the accurate determination of the acid site locations within the framework. Attempts to achieve this through the use of neutron diffraction measurements were reported in Section 3.1.3 and have thus far eluded analysis. However, attempts to refine the fit of the diffraction data are still ongoing at the University of Aberdeen and may result in improved refinements of the ZSM-5 structure. An alternative method which is under consideration is the use of single-crystal studies. ZSM-5 crystals large enough for single-crystal neutron diffraction cannot be practically synthesised but the same is not true for X-ray diffraction and planning for a series of such experiments is currently underway.

8.2.3 QENS Analysis of Slow-Moving Systems:

While QENS has achieved good results in observing the motions of hydrocarbons within the zeolite frameworks in cases where unwanted reactions could be avoided, it is also clear that nearly all the systems investigated have considerable movement occurring which cannot be resolved by the instruments employed in this thesis. This is especially important in the case of octene, where even in the high-mobility steamed sample it was only possible to resolve molecular rotations and not the actual motion of the alkyl chain through the pore network (Section 5.3.2), According to studies of octane diffusion by Jobic, diffusion of C_8 chains takes place on a timescale almost 2 orders of magnitude slower than the equivalent C_3 diffusions.[72] It should, however, be possible to observe octene movements through the application of the spin-echo QENS technique (SE-QENS) which, as discussed in Section 2.1.3.3, can resolve much smaller energy transfer values (and hence longer time-scale processes) than backscattering instruments like OSIRIS and IRIS. The application of SE-QENS to a similar problem, the extremely slow movement of methanol in H-ZSM-5 as discussed in Chapter 7, is currently underway with a series of measurements at the Institut Laue-Langevin, Grenoble, France, which will supply experience with the use of this technique.

Finally, while the attempts to measure movement in silicalite reported in Appendix 2 were unsuccessful, the results do indicate that such studies are worth repeating, if an acceptably pure silicalite material can be sourced for use as the framework. Comparison of movements in silicalite, with those of the steamed samples measured in Chapter 5, will be especially enlightening in showing what residual levels of acid bonding exist in the steamed materials or to what extent mobility has been increased by structural changes. The primary difficulty will lie in obtaining a completely acid-free MFI framework; this may require synthesis of the zeolite material 'in house'. Steam treatment of the low-aluminium sample already tested to attempt to remove the residual acid sites is also a possibility worth investigating.

8.2.4 Improving the Accuracy of MD Force Fields:

Although the MD simulations reported here have provided some useful insight into the geometry of the hydrocarbon motions observed by QENS, it is also clear that the force field parameters, particularly those describing zeolite-alkane interactions, requires modification to more accurately describe the system being modelled under diverse conditions of temperature and chain length. One promising approach to do this is provided by the software package 'molecular dynamics Monte Carlo' (MDMC), currently under development by a number of institutions, including the ISIS Facility.[212] It is possible to simulate QENS spectra from MD trajectory data in order to fit the force field parameters to QENS results by iteratively simulating a system, comparing the simulated QENS spectrum to experimental results and adjusting the force field parameters to bring the two into closer agreement. MDMC is still presently in early development and is predicted to be released for public use in late 2021.

Appendix 1: List of Central Facilities Beam Time Allocations

Table A1-1: Details of beam-time allocations providing data contributing toward the results reported above. Allocations provided by the Science and Technology Facilities Council. All experiments performed at the ISIS Neutron and Muon Source, Oxfordshire. In accordance with ISIS policy on open-access research, these datasets are publically accessible at the provided DOIs after three years from the date of the experiment.

Title (Date)	Type	Samples	DOI
RB1620443 Studies of propene formation by gasoline cracking in steamed ZSM-5 by QENS. (November 2016)	**QENS** (OSIRIS)	**ZSM5-FR** Unloaded, 5 – 375 K. + 1-octene (loaded at 293 K), 5 – 375 K. + propene (loaded at 293 K), 5 – 375 K.	10.5286/ISIS.E.RB1620443
RB1620408 Studies of propene formation by gasoline cracking in steamed ZSM-5 by INS. (December 2016)	**INS** (MAPS + TOSCA)	**ZSM5-FR** Unloaded. + 1-octene (loaded at 293 K). + propene (loaded at 293 K). + propene (loaded at 140 K). **Propene** **1-octene** **Polyethylene**	10.5286/ISIS.E.RB1620408
RB1720047 INS studies of the interaction of propene with ZSM-5. (December 2017)	**INS** (TOSCA)	**ZSM5-FR** Unloaded. + propene (loaded at 140 K), 140 – 293 K.	10.5286/ISIS.E.RB1720047
RB1720048 QENS studies of the interaction of propene with ZSM-5. (October 2017)	**QENS** (OSIRIS)	**ZSM5-ST(873K)** + propene (loaded at 140 K), 5 – 370 K (EFWS only).	10.5286/ISIS.E.RB1720048
RB1810123 Studies of the effect of steaming on catalyst-substrate interactions in ZSM-5 cracking catalysts. (April 2018)	**INS** (TOSCA)	**ZSM5-ST(873K)** Unloaded. + propene (loaded at 140 K), 140 K, 270 K, 293 K. **ZSM5-ST(873K)** Unloaded. + 1-octene (loaded at 200 K), 200 K, 293 K.	10.5286/ISIS.E.RB1810123

RB1820118 Studies of catalyst-substrate interactions in an industrial ZSM-5 cracking catalyst. (November 2018)	**INS** (TOSCA)	**ZSM5-ST(873K)** Unloaded. + propene (loaded at 140 K), 170 K - 325 K.	10.5286/ISIS.E.RB1820118
RB1820119 Diffusion of model hydrocarbon species in a steady-state industrial zeolite cracking catalyst. (December 2018)	**QENS** (OSIRIS)	**ZSM5-ST(873K)** + propene (loaded at 140 K), 5 – 370 K. **ZSM5-ST(1073K)** Unloaded, 5 – 370 K. + 1-octene (loaded at 293 K), 160 – 370 K, 5 K.	10.5286/ISIS.E.RB1820119
RB1910203 INS Studies of Olefin Reactivity in HZSM-5 Zeolite Catalysts. (March 2019)	**INS** (TOSCA)	**ZSM5-FR_Prop _473K** Coked catalyst. **ZSM5-FR_Prop_573K** Coked catalyst. **ZSM5-FR_Prop_673K** Coked catalyst.	10.5286/ISIS.E.RB1910203
RB1920589 Quantification of Brønsted acid site densities in zeolites: an INS investigation. (November 2019)	**INS** (MAPS)	**ZSM5-FR** **Brucite Standards** 54 mg 154 mg 320 mg 620 mg	10.5286/ISIS.E.RB1920589
RB1920592 Separation of factors contributing to the overall diffusion behaviour of olefin species in catalytic zeotype structures. (November 2019)	**QENS** (OSIRIS)	**ZSM5-ST(873K)** Unloaded, 5 – 370 K. + propane (loaded at 140 K), 5 – 375 K. **ZSM5-SIL** Unloaded, 5 – 370 K. + propene (loaded at 140 K), 5 – 375 K + propane (loaded at 140 K), 5 – 375 K.	10.5286/ISIS.E.RB1920592
RB2010486 Studies of 1-octene cracking in ZSM-5 by INS. (November 2020)	**INS** (MAPS)	**ZSM5-FR_Oct_573K** Coked catalyst. **ZSM5-FR_Oct_673K** Coked catalyst. **ZSM5-ST(1073K)_Oct_573K** Coked catalyst. **ZSM5-ST(1073K)_Oct_573K** Coked catalyst.	10.5286/ISIS.E.RB2010486
RB2010522 Additional studies of propane diffusion in MFI zeolite structures. (October 2020)	**QENS** (IRIS)	**ZSM5-FR** + propane (loaded at 140 K), 5 – 375 K. **ZSM5-ST(1073K)** Unloaded, 5 – 375 K. + propane (loaded at 140 K), 5 – 375 K. **1-octene** Bulk, 5-375 K.	10.5286/ISIS.E.RB2010522

Appendix 2: Diffusion and Interactions of Olefins in Non-protonated Zeotype Structures

The majority of industrial zeolites are solid acid catalysts where the active sites are Brønsted acid groups located within the micropore structure. The interactions of the reagent species with these groups and the effect of the pore structure on the diffusion of adsorbates to and from the active sites are what dictate the catalytic mechanism of the zeolite and provide its shape selectivity. Having investigated hydrocarbon mobility in standard H-ZSM-5 in Chapter 4 it has been established that understanding of what proportion of the barriers to diffusion is due to the effect of the acid groups is important to understanding the results of QENS studies and to validating the molecular force field used for MD simulations. This appendix presents the results of our attempts to distinguish the mobility effects arising from the acid site interactions from those due to differences in rigidity and molecular size between alkene and alkane adsorbates. This was carried out by a combined QENS and molecular dynamics study of the mobility of our model compound species in a purely siliceous zeotype framework with the same structure as ZSM-5.

A2.1 Non-Protonated MFI Frameworks:

The work in Chapter 4 has shown that it would be helpful to gain a better understanding of the exact role which interactions with the Brønsted acid groups of H-ZSM-5 play in determining the barriers to diffusion within the zeolite framework. The most obvious way to obtain this information is by comparing the results already obtained against those for a zeolite with the same framework structure, but which has no aluminium substitutions and therefore no acid sites. Technically speaking, 'ZSM-5' refers specifically to MFI structured zeolites with some level of aluminium substitution, while the purely siliceous analogue is referred to as 'silicalite'.[7] The structural and framework properties of silicalite are generally similar to those of H-ZSM-5, with the exception that silicalite frameworks are hydrophobic due to the lack of sites suitable for hydrogen bonding. This arises because, with the interactions of the silanol groups with water being insufficiently strong for adsorption to be more energetically favourable than remaining in the liquid state outside the pores.[7] Silicalite is still capable of adsorbing hydrocarbons smaller than the limiting radius of the pores, meaning that C_3 and C_8 model compounds can be introduced in the same manner employed previously.

A2.1.5 Silicalite Characterisation:

Sourcing silicalite in quantities sufficient for neutron-based analysis is harder than obtaining ZSM-5 because it is not widely used as an industrial catalyst. Owing to the lack of acid-based activity, it is not manufactured in significant quantity. This process is further complicated by the fact that the synthesis process for silicalite will readily, and preferentially, incorporate even trace quantities of alumina contamination, generating an extremely low-aluminium ZSM-5 instead. These investigations were performed using the lowest-aluminium content material which could be sourced from Johnson Matthey. This had a silica:alumina ratio of 1290:1 (Si:Al = 645:1) as assessed by X-ray fluorescence; characterisation studies of ZSM5-FR have shown that XRF habitually overestimates the level of framework aluminium in ZSM-5 samples (Section 3.1.2), thus it is expected that this material will have a nominal level of Brønsted acidity that can serve as a suitable silicalite

analogue. The material as supplied was calcined and dried according to the procedures in Sections 2.4.1 and 2.4.2 and the resulting material assigned the short designation ZSM5-SIL.

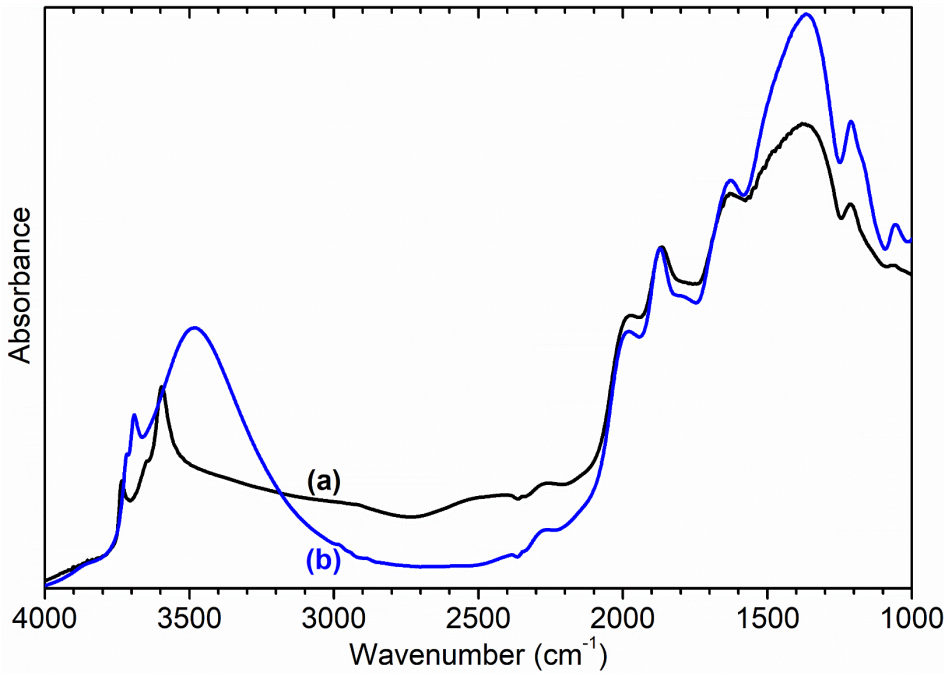

Figure A2-1: Infrared spectra of ZSM5-FR (a) and ZSM5-SIL (b) recorded by DRIFTS. Spectral intensities normalised with respect to the silanol framework peak at 1875 cm^{-1}.

The infrared spectrum of ZSM5-SIL (Figure A2-1) confirms that it is silicalite-like in character. The broad peak centred at 3485 cm^{-1} is characteristic of silicalite-type frameworks and is assigned to silanol hydroxyls interacting by medium-strength hydrogen bonds, as they are located in close proximity in silanol nests.[213] The separate peak at 3692 cm^{-1} is assigned to silanols which are located in isolation at the exterior surface and which therefore are not subject to this hydrogen bonding. The ZSM5-SIL spectrum shows no signs of the peak associated with Brønsted acid O-H groups, observed at 3595 cm^{-1} for ZSM5-FR.

Table A2-1: Comparison of the structural and acid properties of ZSM5-FR and ZSM5-SIL as established by zeolite characterisation measurements.

Sample	^{27}Al NMR		Ammonia TPD	
	Total Relative Intensity (± 0.03)	AlO_4 Relative Intensity (± 0.03)	Silanol (sites /u.c)	Brønsted (sites /u.c)
ZSM5-FR	1.00	0.91	2.62 ± 0.26	2.31 ± 0.12
ZSM5-SIL	0.02	0.02	0.87 ± 0.14	0.01 ± 0.01

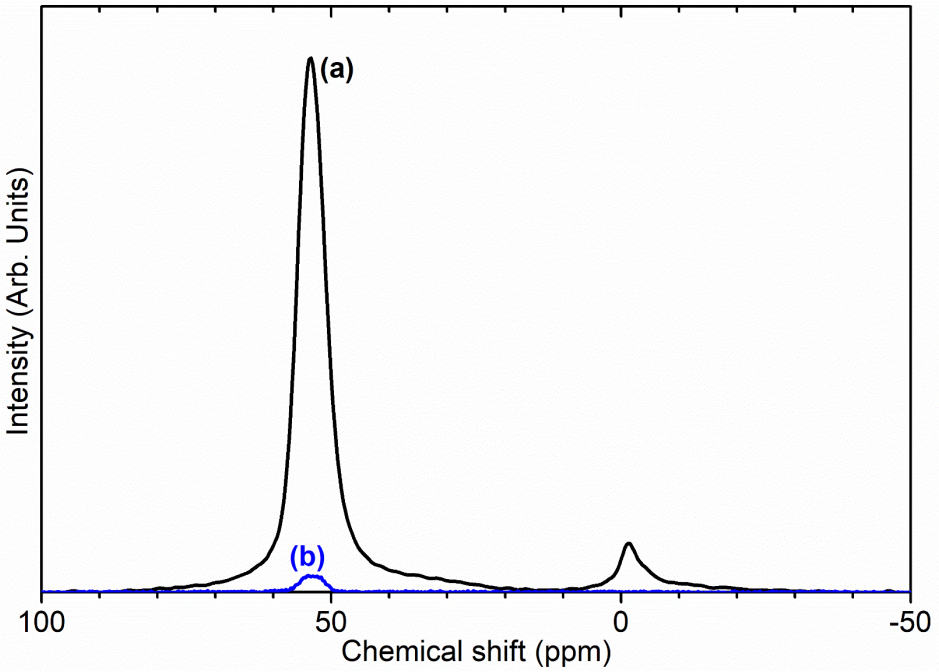

Figure A2-2: Comparison of the ^{27}Al NMR spectra of ZSM5-FR (a), and ZSM5-SIL (b) showing changes reduced framework AlO_4 content.

The results of additional characterisation of ZSM5-SIL are compared with the corresponding values for ZSM5-FR in Table A2-1. ^{27}Al NMR measurements do show a population of AlO_4 nuclei at the chemical shift associated with framework aluminium (Figure A2-2); the intensity of this peak is at the limits of detectability, but is approximately 2 % that of the framework peak in ZSM5-FR suggesting that ZSM5-SIL does contain framework acid sites but with an Si:Al ratio of *ca*. 1300:1, lower than even that predicted by XRF measurement. Ammonia TPD measurements show similar results (Figure A2-3), with a barely-detectable amount of ammonia chemisorbed to Brønsted sites being desorbed between 810 and 860 K. The amount of silanol groups detected by TPD is also reduced, indicating that the large number of silanol nests detected in the DRIFTS spectrum

are not active for ammonia chemisorption. Form these results it can be surmised that ZSM5-SIL is largely siliceous, but contains a very low level of widely-dispersed acid sites, something which proves to have an important effect on the QENS studies discussed below.

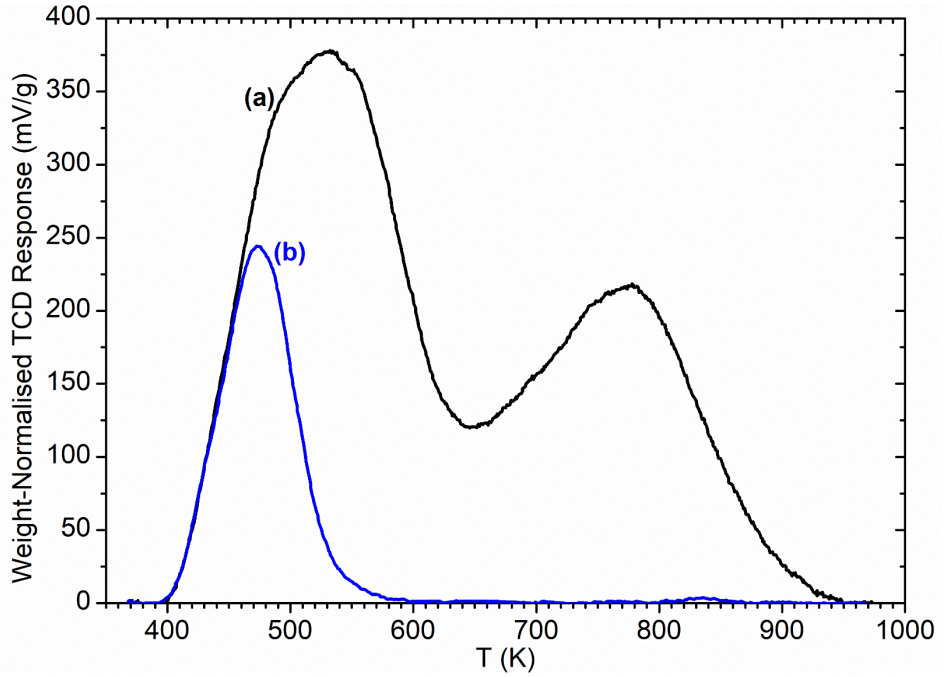

Figure A2-3: Ammonia desorption vs temperature trace for ZSM5-FR (a) and ZSM5-SIL (b). Peaks represent the desorption of ammonia molecules chemisorbed to silanol groups from 400-600 K and those bound to Brønsted acid sites from 650-900 K.[132]

A2.2 QENS Investigations Using Silicalite:

QENS investigations were performed of the mobility of propene and propane in ZSM5-SIL at loading levels of 4.95 and 4.97 molecules per unit cell respectively. The propene sample was loaded at 170 K to prevent reaction, while the inert nature of the propane meant that loading of this sample was carried out at room temperature for simplicity. Measurements used the OSIRIS spectrometer. Both samples were cooled to base temperature and EFWS data collected; propane data was taken at 20 K intervals from 30-370 K, while for the propene sample collection was every 20 K from 30 – 170 K and every 10 K from 180 - 300 K.

For the propene sample, once the sample has entered the liquid propene phase mobility in the silicalite framework is slightly higher than that in ZSM5-FR

(Figure A2-4), a factor which can presumably be attributed to the reduced effect of acid-olefin bonding. Unfortunately, once the sample reaches *ca*. 210 – 225 K it undergoes a large decrease in mobility similar to that observed in the fresh material. It appears from these results that despite ZSM5_SIL only having a minimal level of acidity, this is still sufficient to catalyse the oligomerization of the entire propene dose once the temperature rises above the activation energy of the oligomerization reaction. Hence determining the mobility of olefins in an unaltered MFI framework without effects from acid groups or oligomerization reactions will require the sourcing of a true silicalite material without any trace level of aluminium whatsoever. The lower relative mobility of the final oligomer in the ZSM5-SIL sample does suggest that the product molecule has a larger average size than that in ZSM5-FR, presumably due to the very widely spaced acid sites leaving increased room for oligomer growth.

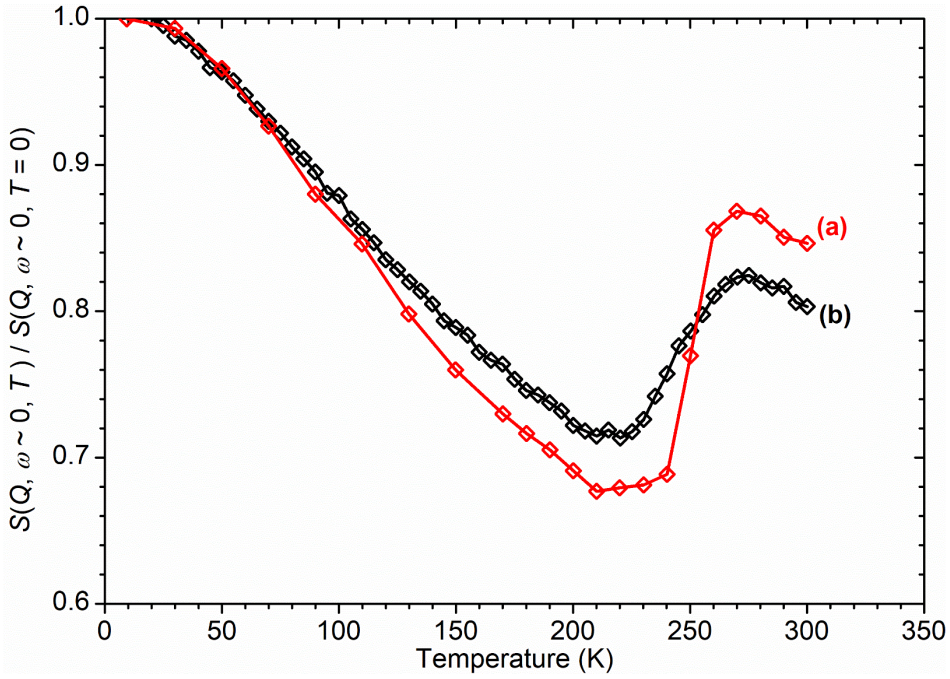

Figure A2-4: Elastic fixed window scan data for propene in ZSM5-SIL (a) compared with equivalent data in ZSM5-FR taken from Figure 4-24 (b). Relative elastic intensities normalised against the value at 20 K to allow comparison between samples.

In contrast, the propane results exhibit anomalous behaviour which indicates the presence of a fault having occurred during the data collection for this sample. Since propane is unreactive, the expected EFWS pattern would be a constant decrease with increasing temperature, with the rate of decrease varying as

determined by the phase changes of the propane, as observed in ZSM5-FR in Figure 4-24. Instead, as shown in Figure A2-5, there is an increase in the relative elastic intensity between 130 and 150 K, following which the rate of mobility increase is considerably less than that observed in ZSM5-FR. This temperature is far too low for this change to be due to a reaction of the sample, even if propane was capable of reacting in such a manner. Furthermore, if the sample is re-cooled with EFWS data being collected during the process it can be seen that this increase in elastic intensity is not permanent (as would be the case if it were due to a reaction of the sample) but does exhibit a hysteresis effect where the trace remains in the 'high' mode until 130 K, following which it returns to the previously observed behaviour over the course of *ca*. 40 K.

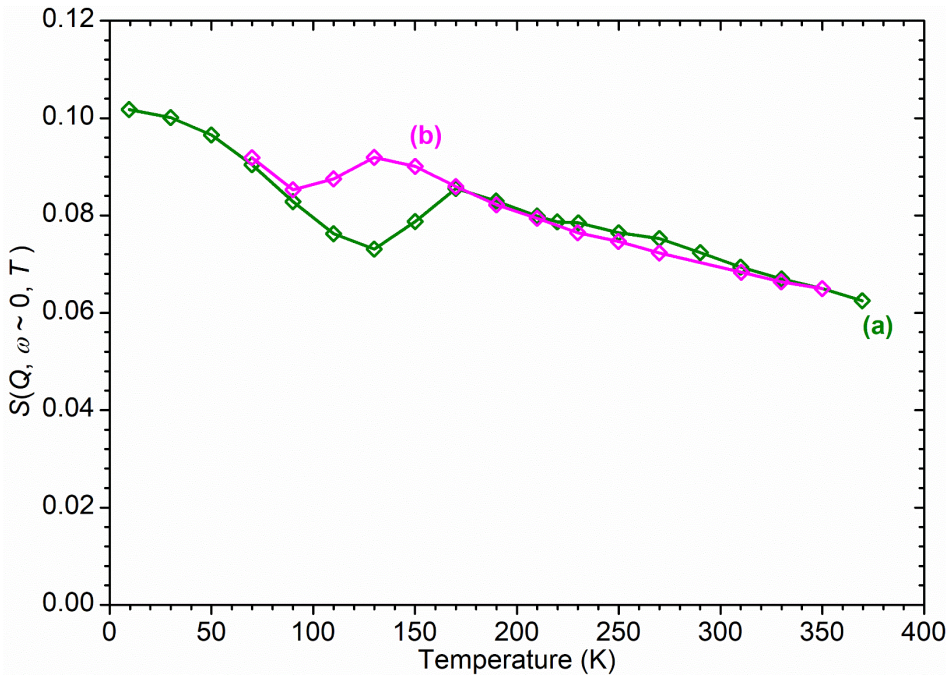

Figure A2-5: Elastic fixed window scan data for propene in ZSM5-SIL from 10 – 370 K (a) and the same sample during re-cooling from 360 – 70 K (b).

Attempts to develop an explanation for this behaviour have so far been unsuccessful. The removal of propane from the sample into the experimental environment is not a suitable explanation for three reasons: the temperature is such that it would have to do so as a liquid, leaving it nowhere to migrate that is not in the instrument beam. Monitoring of the pressure in the gas handling pipework did not indicate an increase in gas pressure consistent with propane migrating out of the sample. In addition, the migration of the hydrocarbon outside

the instrument beam would have the effect of decreasing the overall scattering intensity, an effect which is not observed. Further measurements have established that this behaviour is reproducible, but have not clarified the matter beyond that. Current lines of enquiry centre on possible confinement effects within the zeolite crystals or, as-yet, unidentified errors in the experimental protocol, but a satisfactory explanation remains elusive at present.

Therefore, the attempt to obtain QENS measurements of the movement of C_3 molecules in a non-protonated MFI framework has foundered on a combination of issues with experimental design and the inability to source a suitable silicalite material for testing and cannot be used to derive information on the effect of the acid site interactions on hydrocarbon mobility. Work outside of this project will examine experimental protocols in an attempt to establish whether certain sample handling procedures are compromising the QENS measurement.

A2.3 MD Simulations in Silicalite:

MD simulations of the C_3 and C_8 model compounds in silicalite were performed by removing the Al substitutions and associated acid sites from the frameworks used for the simulations reported in Section 4.3; all other aspects of the simulation procedure were identical to the earlier experiment. The results, given in Table A2-2, show that (with the exception of some anomalous behaviour in the low temperature octane simulations) the simulated hydrocarbons diffuse approximately 8 % faster in silicalite than H-ZSM-5, and thus that the Brønsted acid sites account for this proportion of the overall barriers to diffusion in the simulated system. The activation energies of the motions do not appear to change significantly between the two frameworks. Unfortunately, without experimental data to benchmark these results against it is not possible to assess how accurately they correspond to interactions in actual zeolite-hydrocarbons systems.

Table A2-2: Self-diffusion coefficients (D_s) and activation energies (E_a) for propene, propane, 1-octene and octane in silicalite calculated from MD results. Ratios show the relationship of these values to those from the corresponding simulations in H-ZSM-5 from Chapter 4.

T (K)	D_s (m^2s^{-1})		Ratio Silicalite : ZSM-5	
	Propene	**Propane**	**Propene**	**Propane**
170	9.52×10^{-10}	8.36×10^{-10}	1.08 : 1	1.13 : 1
220	1.32×10^{-9}	1.20×10^{-9}	1.07 : 1	1.10 : 1
270	1.73×10^{-9}	1.53×10^{-9}	1.08 : 1	1.07 : 1
320	2.08×10^{-9}	1.90×10^{-9}	1.06 : 1	1.09 : 1
370	2.42×10^{-9}	2.23×10^{-9}	1.03 : 1	1.07 : 1
D_0 (m^2s^{-1})	4.75×10^{-9}	4.24×10^{-9}	1.07 : 1	0.99 : 1
E_a (kJ/mol)	2.29	2.29	1 : 1	0.92 : 1
T (K)	**D_s (m^2s^{-1})**		**Ratio Silicalite : ZSM-5**	
	1-octene	**Octane**	**1-octene**	**Octane**
170	2.96×10^{-10}	2.85×10^{-10}	1.02 : 1	0.96 : 1
220	4.34×10^{-10}	4.13×10^{-10}	1.00 : 1	0.92 : 1
270	6.13×10^{-10}	6.19×10^{-10}	1.04 : 1	1.07 : 1
320	7.78×10^{-10}	7.76×10^{-10}	1.03 : 1	1.07 : 1
370	9.57×10^{-10}	9.53×10^{-10}	1.07 : 1	1.07 : 1
D_0 (m^2s^{-1})	2.72×10^{-9}	2.93×10^{-9}	1.06 : 1	1.08 : 1
E_a (kJ/mol)	3.26	3.50	1.02 : 1	1.02 : 1

A2.4 Summary:

Attempts have been made to experimentally determine the effect of Brønsted acid groups on adsorbate diffusion through the use of QENS methods. Unfortunately, the derivation of useful insights into diffusion behaviour from the results has been stymied by a variety of experimental factors. MD simulations suggest that these interactions account for approximately 8 % of the energy barriers to diffusion in H-ZSM-5, but in the absence of experimental validation of these results, they cannot be regarded with confidence. Additional QENS measurements correcting the issues identified above, most notably through the

provision of a truly acid-free silicalite catalyst, are required. The results although inconclusive are reported here as it is thought the outcomes observed may be indicating some vulnerability in sample handling procedures. In part, it reveals the care required to examine C3/C5 diffusion characteristics in zeolites and as a function of Brønsted acid site density. At present, a more consistent correlation between experiment and simulation is evasive.

Appendix 3: Additional Mass Spectrometry Data for Reaction Tests

The data presented here represents the full-duration mass spectrometry data recorded for the 1-octene cracking reactions reported in Chapter 6, Section 6.3.2. Averaged data at key reaction points from these traces was used to prepare Figures 6-17 and 6-19. The numbers on each plot represent the atomic mass number of each trace, which are analysed according to the assignments in Table A3-1. All signals are normalised against the flow gas for each reaction.

Table A3-1: Assignment of the expanded array of mass spectroscopy signals in Figures A3-1 – A3-9 to associated molecules. All alkene signals should be interpreted as also including contributions from fragmentation of larger molecules in the mass spectrometer. The 27 amu signal is used to monitor levels of ethene due to the use of N_2 (m/z = 28 amu) as a flow gas in some reactions.

Signal (amu)	Associated Fragment
27	Ethene
41	Propene
44	Propane
55	Butene
58	Butane
70	Pentene
72	Pentane
78	Benzene
79	Dimethyl cyclopentadiene
84	Hexene
86	Hexane
91	Tropylium (subst. benzenes)
112	Octene

Figure A3-1: Eluent mass spectrum from passing 1-octene over a SiO_2 blank at 473 K.

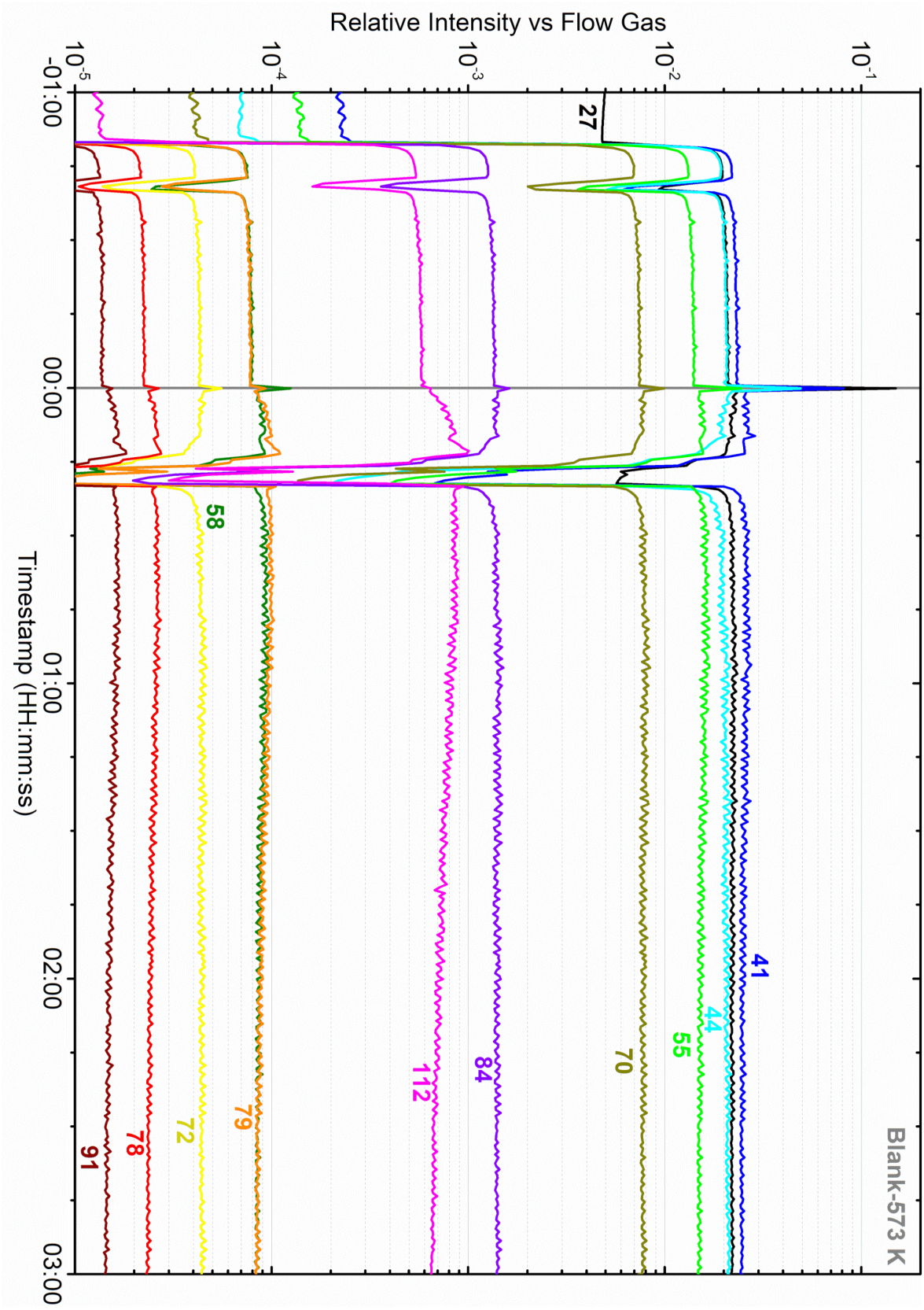

Figure A3-2: Eluent mass spectrum from passing 1-octene over a SiO_2 blank at 573 K.

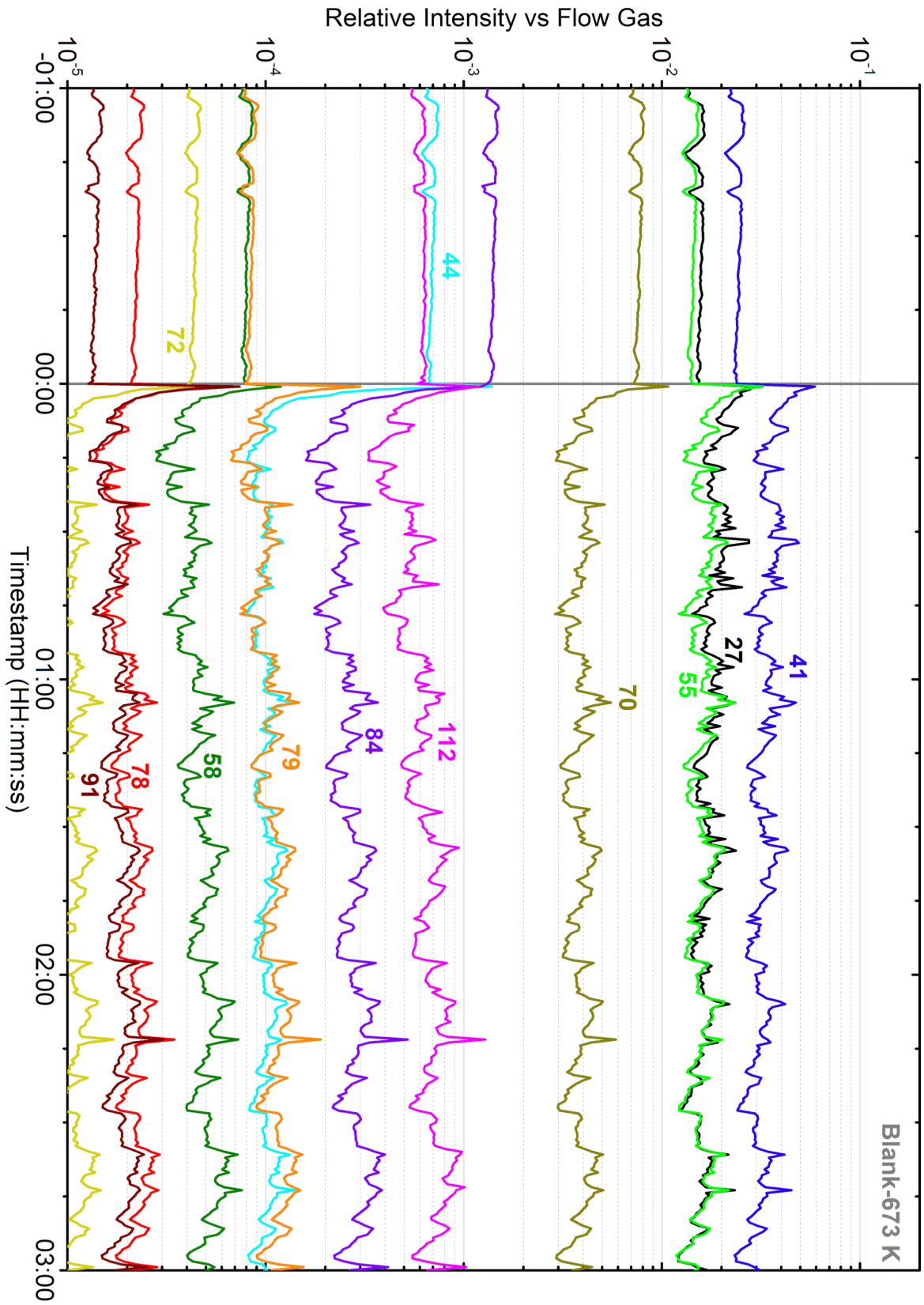

Figure A3-3: Eluent mass spectrum from passing 1-octene over a SiO_2 blank at 673 K.

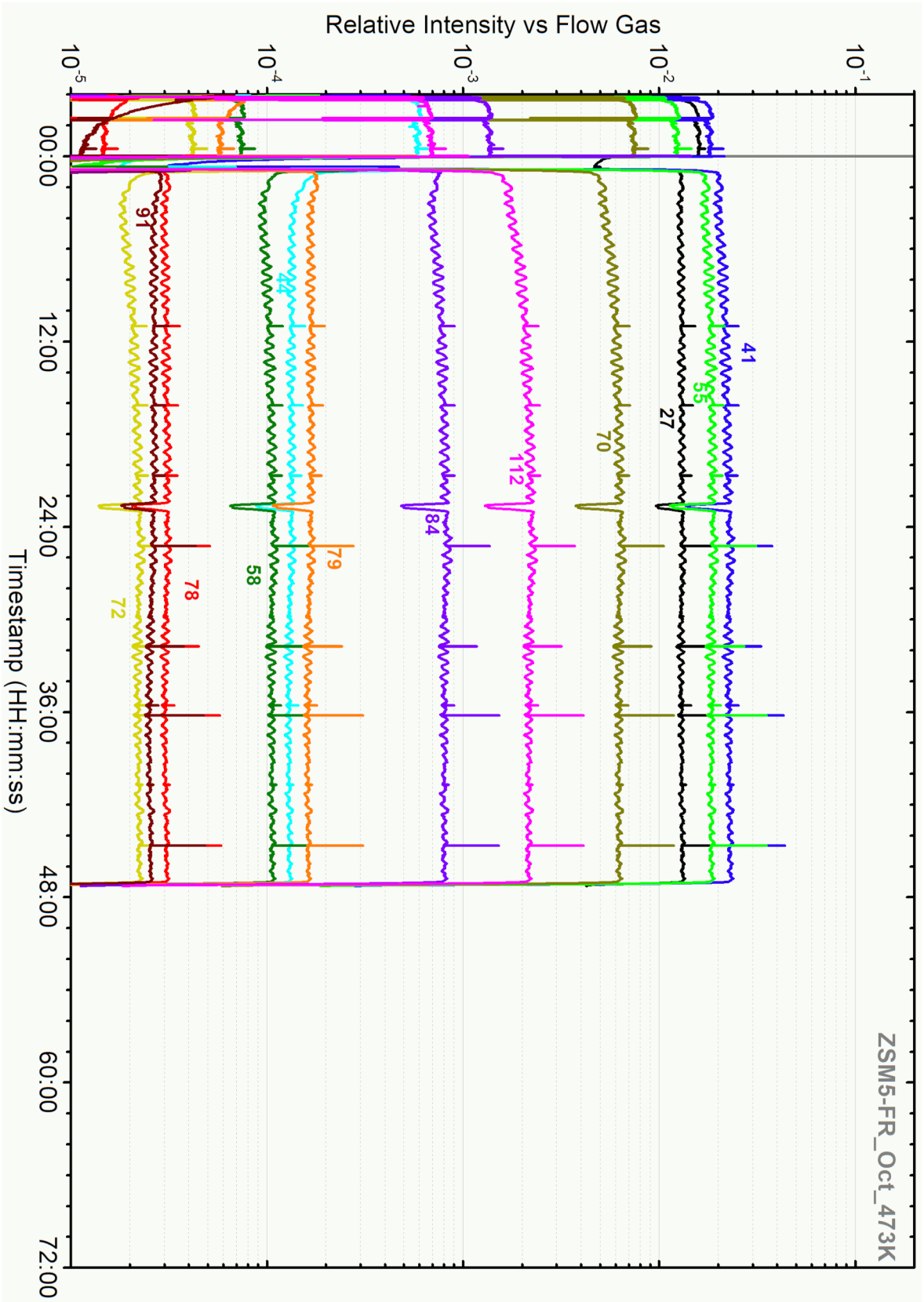

Figure A3-4: Eluent mass spectrum from reacting 1-octene over ZSM5-FR at 473 K.

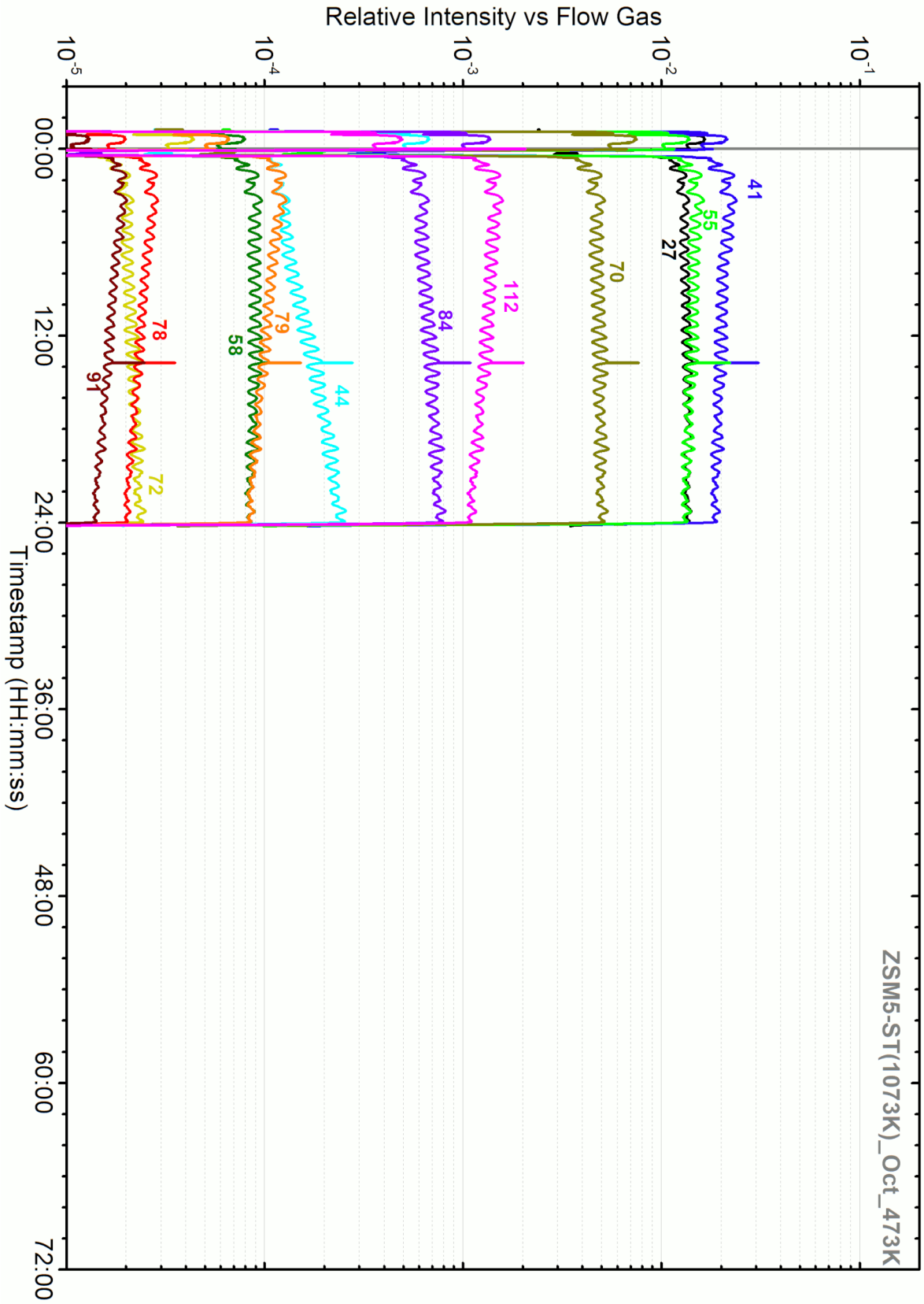

Figure A3-5: Eluent mass spectrum from reacting 1-octene over ZSM5-ST(1073K) at 473 K.

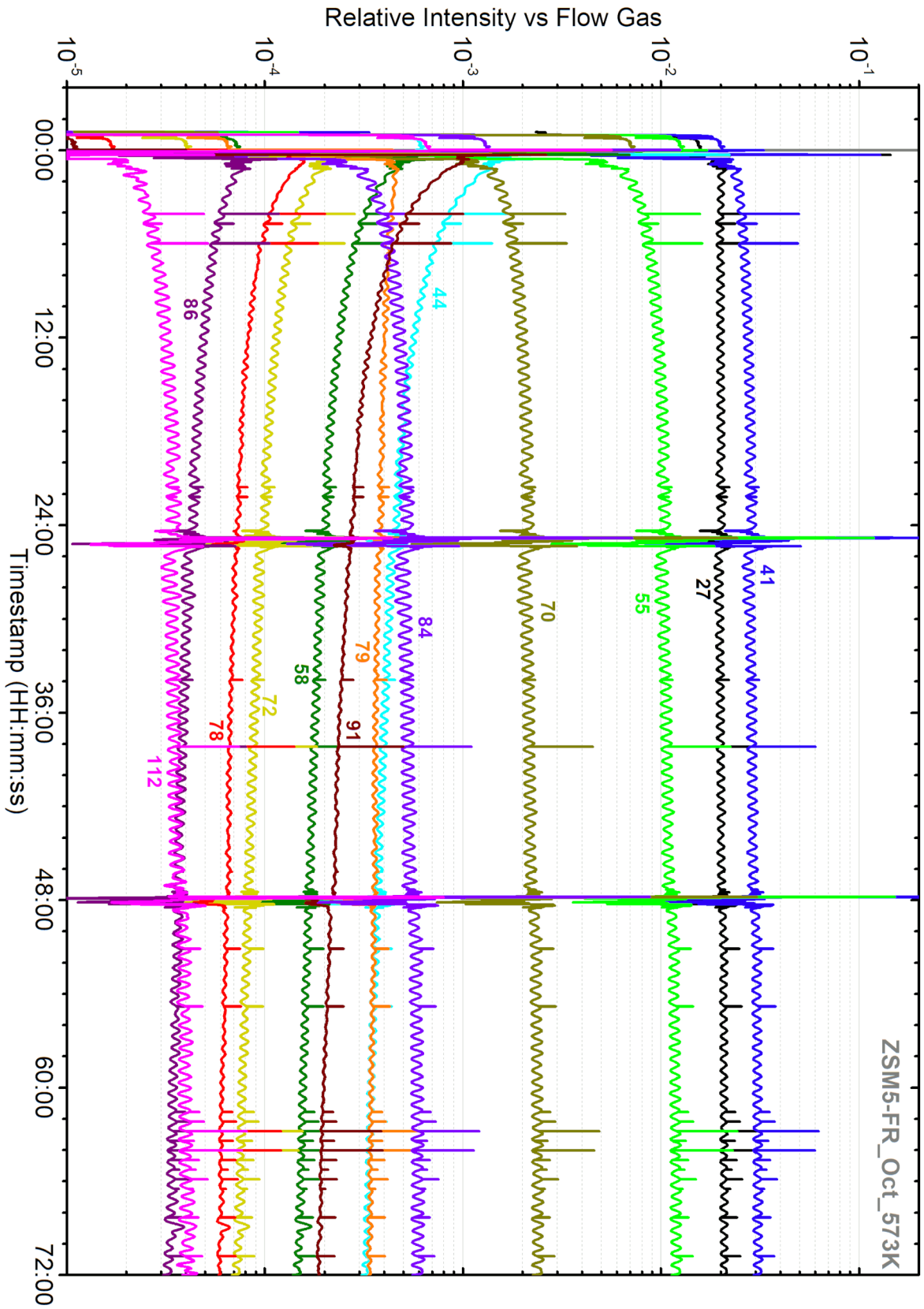

Figure A3-6: Eluent mass spectrum from reacting 1-octene over ZSM5-FR at 573 K.

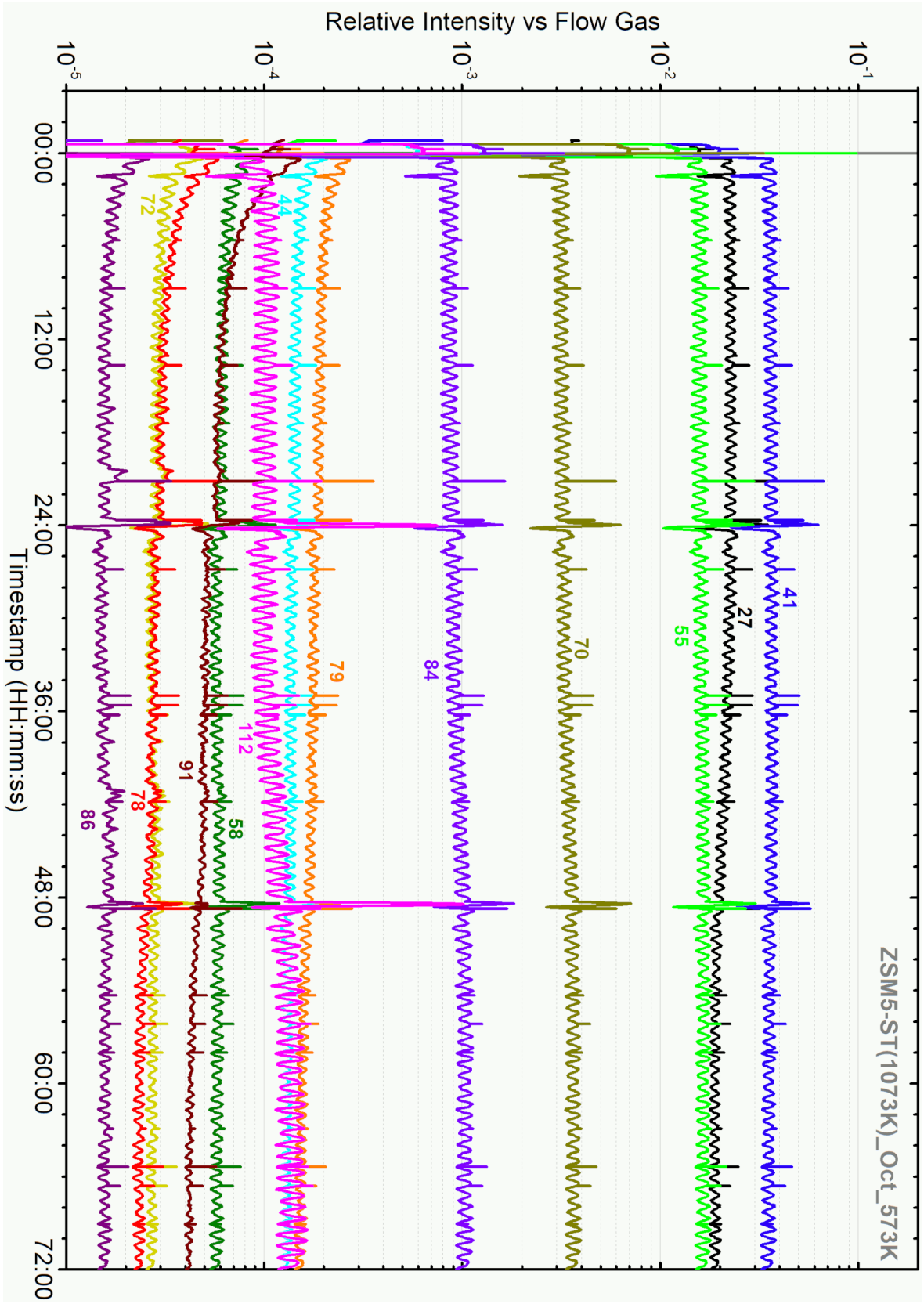

Figure A3-7: Eluent mass spectrum from reacting 1-octene over ZSM5-ST(1073K) at 573 K.

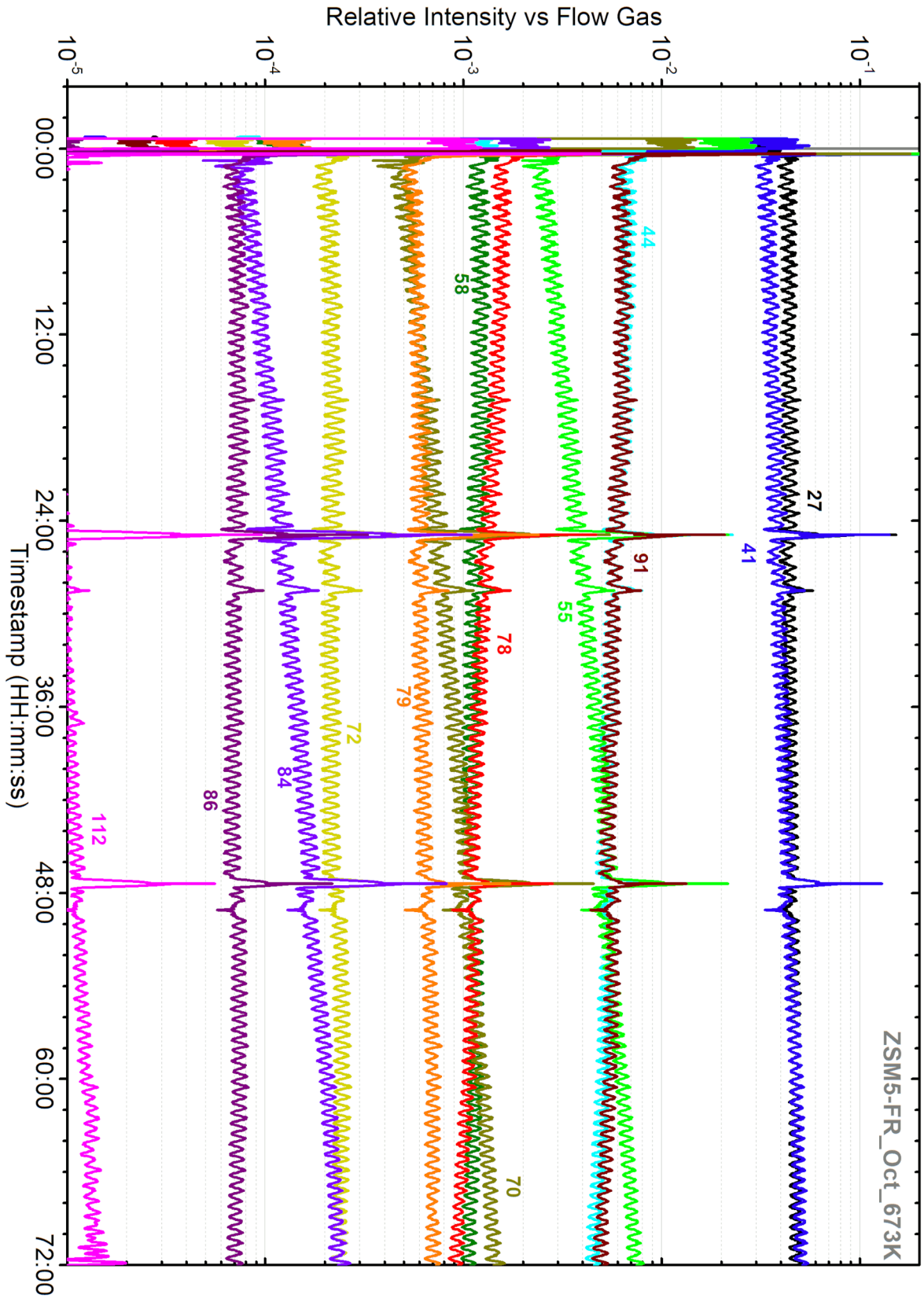

Figure A3-8: Eluent mass spectrum from reacting 1-octene over ZSM5-FR at 673 K.

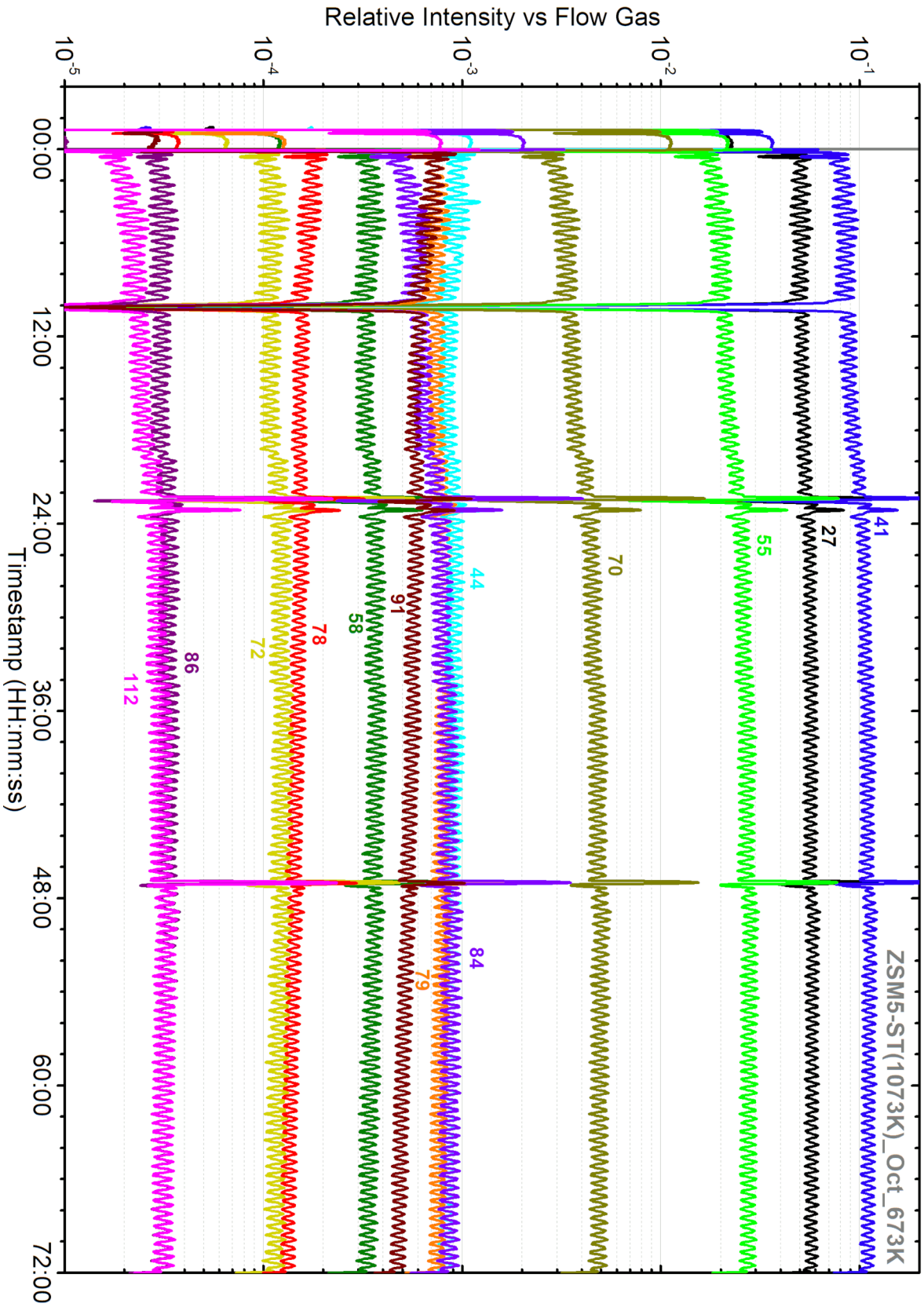

Figure A3-9: Eluent mass spectrum from reacting 1-octene over ZSM5-ST(1073K) at 673 K.

References

1. Chester, A. W.; Derouane, E. G., *Zeolite Characterisation and Catalysis*. Springer: Dordrecht, **2009**, 10.1007/978-1-4020-9678-5.
2. Lourenco, J. P.; Ribeiro, M. F.; Ribeiro, F. R.; Rocha, J.; Onida, B.; Garrone, E.; Gabelica, Z., Synthesis, characterization, and catalytic properties of AlPO4-40, CoAPO-40, and ZnAPO-40. *Zeolites* **1997**, *18* (5-6), 398-407.
3. Hedge, S. G.; Ratnasamy, P.; Kustov, L. M.; Kazansky, V. B., Acidity and catalytic activity of SAPO-5 and AlPO-5 molecular-sieves. *Zeolites* **1988**, *8* (2), 137-141.
4. Patarin, J.; Kessler, H.; Guth, J. L., Iron distribution in iron MFI-type zeolite samples synthesized in fluoride medium: Influence of the synthesis procedure. *Zeolites* **1990**, *10* (7), 674-679.
5. Awate, S. V.; Joshi, P. N.; Shiralkar, V. P.; Kotasthane, A. N., Synthesis and characterization of gallosilicate pentasil (MFI) framework zeolites. *J. Incl. Phenom. Mol. Recogn. Chem.* **1992**, *13* (3), 207-218.
6. Bhaumik, A.; Kumar, R., A new As^{3+}-silicate molecular-sieve with MFI structure. *J. Chem. Soc., Chem. Commun.* **1995**, *8*, 869-870.
7. Flanigen, E. M.; Bennett, J. M.; Grose, R. W.; Cohen, J. P.; Patton, R. L.; Kirchner, R. M.; Smith, J. V., Silicalite, a new hydrophobic crystalline silica molecular-sieve. *Nature* **1978**, *271* (5645), 512-516.
8. Baerlocher, C.; McCusker, L. Database of Zeolite Structures. http://www.iza-structure.org/databases/ (accessed December 2020).
9. Lee, H.; Choi, W.; Choi, H. J.; Hong, S. B., PST-33: A Four-Layer ABC-6 Zeolite with the Stacking Sequence AABC. *ACS Mater. Lett.* **2020**, *2* (8), 981-985.
10. Colella, C.; Gualtieri, A. F., Cronstedt's zeolite. *Microporous Mesoporous Mater.* **2007**, *105* (3), 213-221.
11. Barrer, R. M., Syntheses and reactions of mordenite. *J. Chem. Soc.* **1948**, 2158-2163.

12. Argauer, R. J.; Landolt, G. R. Crystalline zeolite ZSM-5 and method of preparing the same. U.S. Patent 3,702,886, November 14, **1972**.
13. Barrer, R. M., Chemical nomenclature and formulation of compositions of synthetic and natural zeolites. *Pure Appl. Chem.* **1979**, *51* (5), 1091-1100.
14. Breck, D. W. Crystalline zeolite Y. US Patent 3130007A, April 21st, **1964**.
15. Olson, D. H.; Kokotailo, G. T.; Lawton, S. L.; Meier, W. M., Crystal-structure and structure-related properties of ZSM-5. *J. Phys. Chem.* **1981**, *85* (15), 2238-2243.
16. Youngs, T. G. A., Aten—An application for the creation, editing, and visualization of coordinates for glasses, liquids, crystals, and molecules. *J. Comput. Chem.* **2010**, *31* (3), 639-648.
17. Corma, A., Inorganic solid acids and their use in acid-catalyzed hydrocarbon reactions. *Chem. Rev.* **1995**, *95* (3), 559-614.
18. den Hollander, M. A.; Wissink, M.; Makkee, M.; Moulijn, J. A., Gasoline conversion: reactivity towards cracking with equilibrated FCC and ZSM-5 catalysts. *Appl. Catal., A* **2002**, *223* (1-2), 85-102.
19. Clough, M.; Pope, J. C.; Lin, L. T. X.; Komvokis, V.; Pan, S. S.; Yilmaz, B., Nanoporous materials forge a path forward to enable sustainable growth: Technology advancements in fluid catalytic cracking. *Microporous Mesoporous Mater.* **2017**, *254*, 45-58.
20. Degnan, T. F.; Chitnis, G. K.; Schipper, P. H., History of ZSM-5 fluid catalytic cracking additive development at Mobil. *Microporous Mesoporous Mater.* **2000**, *35-6*, 245-252.
21. Sadrameli, S. M., Thermal/catalytic cracking of liquid hydrocarbons for the production of olefins: A state-of-the-art review II: Catalytic cracking review. *Fuel* **2016**, *173*, 285-297.
22. Akah, A.; Al-Ghrami, M., Maximizing propylene production via FCC technology. *Appl. Petrochem. Res.* **2015**, *5* (4), 377-392.
23. Awayssa, O.; Al-Yassir, N.; Aitani, A.; Al-Khattaf, S., Modified HZSM-5 as FCC additive for enhancing light olefins yield from catalytic cracking of VGO. *Appl. Catal., A* **2014**, *477*, 172-183.

24. Bessell, S.; Seddon, D., The Conversion of Ethene and Propene to Higher Hydrocarbons over ZSM-5. *J. Catal.* **1987**, *105* (1), 270-275.
25. Corma, A.; Martinez, C.; Doskocil, E., Designing MFI-based catalysts with improved catalyst life for C-3(=) and C-5(=) oligomerization to high-quality liquid fuels. *J. Catal.* **2013**, *300*, 183-196.
26. Chen, C. S. H.; Bridger, R. F., Shape-selective oligomerization of alkenes to near-linear hydrocarbons by zeolite catalysis. *J. Catal.* **1996**, *161* (2), 687-693.
27. Song, C.; Garcés, J. M.; Sugi, Y., *Shape-Selective Catalysis: Chemicals Synthesis and Hydrocarbon Processing*. ACS Symp. Ser., **2000**, Vol. 738.
28. Chen, N. Y.; Kaeding, W. W.; Dwyer, F. G., Para-directed aromatic reactions over shape-selective molecular sieve zeolite catalysts. *J. Am. Chem. Soc.* **1979**, *101* (22), 6783-6784.
29. den Hollander, M. A.; Wissink, M.; Makkee, M.; Moulijn, J. A., Synergy effects of ZSM-5 addition in fluid catalytic cracking of hydrotreated flashed distillate. *Appl. Catal., A* **2002**, *223* (1-2), 103-119.
30. Guo, Y. H.; Pu, M.; Wu, J. Y.; Zhang, J. Y.; Chen, B. H., Theoretical study of the cracking mechanisms of linear alpha-olefins catalyzed by zeolites. *Appl. Surf. Sci.* **2007**, *254* (2), 604-609.
31. Ong, L. H.; Dömök, M.; Olindo, R.; van Veen, A. C.; Lercher, J. A., Dealumination of HZSM-5 via steam-treatment. *Microporous Mesoporous Mater.* **2012**, *164*, 9-20.
32. Hoff, T. C.; Thilakaratne, R.; Gardner, D. W.; Brown, R. C.; Tessonnier, J.-P., Thermal Stability of Aluminum-Rich ZSM-5 Zeolites and Consequences on Aromatization Reactions. *J. Phys. Chem. C* **2016**, *120* (36), 20103-20113.
33. Triantafyllidis, K. S.; Vlessidis, A. G.; Nalbandian, L.; Evmiridis, N. P., Effect of the degree and type of the dealumination method on the structural, compositional and acidic characteristics of H-ZSM-5 zeolites. *Microporous Mesoporous Mater.* **2001**, *47* (2-3), 369-388.
34. Gusev, A. A.; Psarras, A. C.; Triantafyllidis, K. S.; Lappas, A. A.; Diddams, P. A., Effect of Steam Deactivation Severity of ZSM-5 Additives on LPG Olefins Production in the FCC Process. *Molecules* **2017**, *22* (10).

35. Ibáñez, M.; Epelde, E.; Aguayo, A. T.; Gayubo, A. G.; Bilbao, J.; Castaño, P., Selective dealumination of HZSM-5 zeolite boosts propylene by modifying 1-butene cracking pathway. *Appl. Catal., A* **2017**, *543*, 1-9.
36. Stocker, M., Methanol-to-hydrocarbons: catalytic materials and their behavior. *Microporous Mesoporous Mater.* **1999**, *29* (1-2), 3-48.
37. Chang, C. D.; Silvestri, A. J., Conversion of methanol and other o-compounds to hydrocarbons over zeolite catalysts. *J. Catal.* **1977**, *47* (2), 249-259.
38. Luo, G. Q.; McDonald, A. G., Conversion of methanol and glycerol into gasoline via ZSM-5 catalysis. *Energy Fuels* **2014**, *28* (1), 600-606.
39. Ilias, S.; Bhan, A., Mechanism of the Catalytic Conversion of Methanol to Hydrocarbons. *ACS Catal.* **2013**, *3* (1), 18-31.
40. Olsbye, U.; Svelle, S.; Lillerud, K. P.; Wei, Z. H.; Chen, Y. Y.; Li, J. F.; Wang, J. G.; Fan, W. B., The formation and degradation of active species during methanol conversion over protonated zeotype catalysts. *Chem. Soc. Rev.* **2015**, *44* (20), 7155-76.
41. Dahl, I. M.; Kolboe, S., On the reaction-mechanism for propene formation in the MTO reaction over SAPO-34. *Catal. Lett.* **1993**, *20* (3-4), 329-336.
42. Yarulina, I.; Chowdhury, A. D.; Meirer, F.; Weckhuysen, B. M.; Gascon, J., Recent trends and fundamental insights in the methanol-to-hydrocarbons process. *Nat. Catal.* **2018**, *1* (6), 398-411.
43. Yamazaki, H.; Shima, H.; Imai, H.; Yokoi, T.; Tatsumi, T.; Kondo, J. N., Direct Production of Propene from Methoxy Species and Dimethyl Ether over H-ZSM-5. *J. Phys. Chem. C* **2012**, *116* (45), 24091-24097.
44. Li, J.; Wei, Z.; Chen, Y.; Jing, B.; He, Y.; Dong, M.; Jiao, H.; Li, X.; Qin, Z.; Wang, J.; Fan, W., A route to form initial hydrocarbon pool species in methanol conversion to olefins over zeolites. *J. Catal.* **2014**, *317*, 277-283.
45. Vandichel, M.; Lesthaeghe, D.; Mynsbrugge, J. V. d.; Waroquier, M.; Van Speybroeck, V., Assembly of cyclic hydrocarbons from ethene and propene in acid zeolite catalysis to produce active catalytic sites for MTO conversion. *J. Catal.* **2010**, *271* (1), 67-78.

46. Allotta, P. M.; Stair, P. C., Time-Resolved Studies of Ethylene and Propylene Reactions in Zeolite H-MFI by In-Situ Fast IR Heating and UV Raman Spectroscopy. *ACS Catal.* **2012**, *2* (11), 2424-2432.
47. Minova, I. B.; Matam, S. K.; Greenaway, A.; Catlow, C. R. A.; Frogley, M. D.; Cinque, G.; Wright, P. A.; Howe, R. F., Elementary Steps in the Formation of Hydrocarbons from Surface Methoxy Groups in HZSM-5 Seen by Synchrotron Infrared Microspectroscopy. *ACS Catal.* **2019**, *9* (7), 6564-6570.
48. Spoto, G.; Bordiga, S.; Ricchiardi, G.; Scarano, D.; Zecchina, A.; Borello, E., IR study of ethene and propene oligomerization on H-ZSM-5: hydrogen-bonded precursor formation, initiation and propagation mechanisms and structure of the entrapped oligomers. *J. Chem. Soc., Faraday Trans.* **1994**, *90* (18), 2827-2835.
49. Geobaldo, F.; Spoto, G.; Bordiga, S.; Lamberti, C.; Zecchina, A., Propene oligomerization on H-mordenite: Hydrogen-bonding interaction, chain initiation, propagation and hydrogen transfer studied by temperature-programmed FTIR and UV–VIS spectroscopies. *J. Chem. Soc., Faraday Trans.* **1997**, *93* (6), 1243-1249.
50. Bjørgen, M.; Lillerud, K. P.; Olsbye, U.; Bordiga, S.; Zeechina, A., 1-Butene oligomerization in Bronsted acidic zeolites: mechanistic insights from low-temperature in situ FTIR spectroscopy. *J. Phys. Chem. B* **2004**, *108* (23), 7862-7870.
51. Campbell, S. M.; Jiang, X. Z.; Howe, R. F., Methanol to hydrocarbons: spectroscopic studies and the significance of extra-framework aluminium. *Microporous Mesoporous Mater.* **1999**, *29* (1-2), 91-108.
52. Palumbo, L.; Bonino, F.; Beato, P.; Bjørgen, M.; Zecchina, A.; Bordiga, S., Conversion of Methanol to Hydrocarbons: Spectroscopic Characterization of Carbonaceous Species Formed over H-ZSM-5. *J. Phys. Chem. C* **2008**, *112* (26), 9710-9716.
53. Lezcano-Gonzalez, I.; Campbell, E.; Hoffman, A. E. J.; Bocus, M.; Sazanovich, I. V.; Towrie, M.; Agote-Aran, M.; Gibson, E. K.; Greenaway, A.; De Wispelaere, K.; Van Speybroeck, V.; Beale, A. M., Insight into the effects of confined hydrocarbon species on the lifetime

of methanol conversion catalysts. *Nat. Mater.* **2020**, *19* (10), 1081-1087.

54. Bauer, F.; Karge, H. G., Characterization of Coke on Zeolites. In *Molecular Sieves, Vol. 5: Characterization II*, Karge, H. G.; Weitkamp, J., Eds. Springer Berlin: Heidelburg, **2007**; pp 249-264.
55. Magnoux, P.; Roger, P.; Canaff, C.; Fouche, V.; Gnep, N. S.; Guisnet, M., New technique for the characterization of carbonaceous compounds responsible for zeolite deactivation. *Stud. Surf. Sci. Catal.* **1987**, *34*, 317-330.
56. Albers, P. W.; Lennon, D.; Parker, S. F., Catalysis. In *Neutron Scattering - Applications in Biology, Chemistry, and Materials Science*, Fernandez-Alonso, F.; Price, D. L., Eds. Elsevier Academic Press Inc: San Diego, **2017**; pp 279-348.
57. Mitchell, P. C. H.; Parker, S. F.; Ramirez-Cuesta, A. J.; Tomkinson, J., *Vibrational Spectroscopy With Neutrons: With Applications in Chemistry, Biology, Materials Science and Catalysis*. World Scientific: Hackensack, NJ, **2005,** Vol. 3.
58. Warringham, R.; Bellaire, D.; Parker, S. F.; Taylor, J.; Ewings, R. A.; Goodway, C. M.; Kibble, M.; Wakefield, S. R.; Jura, M.; Dudman, M. P.; Tooze, R. P.; Webb, P. B.; Lennon, D., Sample environment issues relevant to the acquisition of inelastic neutron scattering measurements of heterogeneous catalyst samples. *J. Phys.: Conf. Ser.* **2014**, *554* (1), 012005.
59. Albers, P. W.; Parker, S. F., Inelastic Incoherent Neutron Scattering in Catalysis Research. In *Advances in Catalysis, Vol 51*, Gates, B. C.; Knozinger, H., Eds. Elsevier Academic Press Inc: San Diego, **2007**; pp 99-132.
60. Parker, S. F.; Lennon, D.; Albers, P. W., Vibrational Spectroscopy with Neutrons: A Review of New Directions. *Appl. Spectrosc.* **2011**, *65* (12), 1325-1341.
61. Parker, S. F.; Ramirez-Cuesta, A. J.; Daemen, L., Vibrational spectroscopy with neutrons: Recent developments. *Spectrochim. Acta, Part A* **2018**, *190*, 518-523.

62. Howe, R. F.; McGregor, J.; Parker, S. F.; Collier, P.; Lennon, D., Application of Inelastic Neutron Scattering to the Methanol-to-Gasoline Reaction Over a ZSM-5 Catalyst. *Catal. Lett.* **2016**, *146* (7), 1242-1248.
63. Suwardiyanto; Howe, R. F.; Gibson, E. K.; Catlow, C. R. A.; Hameed, A.; McGregor, J.; Collier, P.; Parker, S. F.; Lennon, D., An assessment of hydrocarbon species in the methanol-to-hydrocarbon reaction over a ZSM-5 catalyst. *Faraday Discuss.* **2017**, *197*, 447-471.
64. Jobic, H.; Theodorou, D. N., Quasi-elastic neutron scattering and molecular dynamics simulation as complementary techniques for studying diffusion in zeolites. *Microporous Mesoporous Mater.* **2007**, *102* (1-3), 21-50.
65. O'Malley, A. J.; Catlow, C. R. A., Sorbate Dynamics in Zeolite Catalysts. In *Experimental Methods in the Physical Sciences*, Fernandez-Alonso, F.; Price, D. L., Eds. Academic Press: **2017**; pp 349-401.
66. Vasenkov, S.; Bohlmann, W.; Galvosas, P.; Geier, O.; Liu, H.; Karger, J., PFG NMR study of diffusion in MFI-type zeolites: Evidence of the existence of intracrystalline transport barriers. *J. Phys. Chem. B* **2001**, *105* (25), 5922-5927.
67. Jobic, H.; Bée, M.; Caro, J.; Bülow, M.; Kärger, J., Molecular self-diffusion of methane in zeolite ZSM-5 by quasi-elastic neutron scattering and nuclear magnetic resonance pulsed field gradient technique. *J. Chem. Soc., Faraday Trans. 1* **1989**, *85* (12), 4201-4209.
68. Caro, J.; Bülow, M.; Schirmer, W.; Kärger, J.; Heink, W.; Pfeifer, H.; Ždanov, S. P., Microdynamics of methane, ethane and propane in ZSM-5 type zeolites. *J. Chem. Soc., Faraday Trans. 1* **1985**, *81* (10), 2541-2550.
69. Jobic, H.; Bée, M.; Kearley, G. J., Dynamics of ethane and propane in zeolite ZSM-5 studied by quasi-elastic neutron scattering. *Zeolites* **1992**, *12* (2), 146-151.
70. Jobic, H., Molecular Motions In Zeolites. *Spectrochimica Acta Part A-Molecular and Biomolecular Spectroscopy* **1992**, *48* (3), 293-312.
71. Jobic, H.; Theodorou, D. N., Diffusion of Long n-Alkanes in Silicalite. A Comparison between Neutron Scattering Experiments and Hierarchical Simulation Results. *J. Phys. Chem. B* **2006**, *110* (5), 1964-1967.

72. Jobic, H., Diffusion of linear and branched alkanes in ZSM-5. A quasi-elastic neutron scattering study. *J. Mol. Catal. A: Chem.* **2000**, *158* (1), 135-142.
73. O'Malley, A. J.; Catlow, C. R. A.; Monkenbusch, M.; Jobic, H., Diffusion of Isobutane in Silicalite: A Neutron Spin-Echo and Molecular Dynamics Simulation Study. *J. Phys. Chem. C* **2015**, *119* (48), 26999-27006.
74. O'Malley, A. J.; Catlow, C. R. A., Molecular dynamics simulations of longer n-alkanes in silicalite: state-of-the-art models achieving close agreement with experiment. *Phys. Chem. Chem. Phys.* **2015**, *17* (3), 1943-1948.
75. O'Malley, A. J.; Catlow, C. R. A., Molecular dynamics simulations of longer n-alkanes in silicalite: a comparison of framework and hydrocarbon models. *Phys. Chem. Chem. Phys.* **2013**, *15* (43), 19024-19030.
76. Anderson, J. R.; Chang, Y. F.; Western, R. J., Retained and desorbed products from reaction of 1-octene over H-ZSM-5 zeolite. *Appl. Catal.* **1991**, *75* (1), 87-91.
77. Zhang, P. Q.; Xu, J. G.; Wang, X. S.; Guo, H. C., Catalytic performance of nanocrystallite HZSM-5 catalysts for transformation of normal C-8 hydrocarbons. *Chin. J. Catal.* **2005**, *26* (3), 216-222.
78. Pynn, R., Neutron Scattering: A Primer. *Los Alamos Sci.* **1990**, *19*, 1-31.
79. Sears, V. F., Neutron scattering lengths and cross sections. *Neutron News* **1992**, *3* (3), 26-37.
80. Institut Laue-Langevin. https://www.ill.eu (accessed December 2020).
81. ISIS. http://www.isis.stfc.ac.uk/ (accessed December 2020).
82. Pinna, R. S.; Rudić, S.; Parker, S. F.; Armstrong, J.; Zanetti, M.; Škoro, G.; Waller, S. P.; Zacek, D.; Smith, C. A.; Capstick, M. J.; McPhail, D. J.; Pooley, D. E.; Howells, G. D.; Gorini, G.; Fernandez-Alonso, F., The neutron guide upgrade of the TOSCA spectrometer. *Nucl. Instrum. Methods Phys. Res., Sect. A* **2018**, *896*, 68-74.
83. Parker, S. F.; Fernandez-Alonso, F.; Ramirez-Cuesta, A. J.; Tomkinson, J.; Rudic, S.; Pinna, R. S.; Gorini, G.; Castañon, J. F., Recent and future developments on TOSCA at ISIS. *J. Phys.: Conf. Ser.* **2014**, *554* (1), 012003.

84. Colognesi, D.; Celli, M.; Cilloco, F.; Newport, R. J.; Parker, S. F.; Rossi-Albertini, V.; Sacchetti, F.; Tomkinson, J.; Zoppi, M., TOSCA neutron spectrometer: The final configuration. *Appl. Phys. A: Mater. Sci. Process.* **2002**, *74* (1), 64-66.

85. Bee, M., *Quasielastic Neutron Scattering: Principles and Applications in Solid State Chemistry, Biology and Materials Science*. Adam Hilger: Bristol and Philadelphia, **1988**.

86. Telling, M. T. F., *A Practical Guide to Quasi-elastic Neutron Scattering*. The Royal Society of Chemistry: **2020**.

87. Einstein, A., Über die von der molekularkinetischen Theorie der Wärme geforderte Bewegung von in ruhenden Flüssigkeiten suspendierten Teilchen. *Ann. Phys.* **1905**, *322* (8), 549-560.

88. Van Hove, L., Correlations in Space and Time and Born Approximation Scattering in Systems of Interacting Particles. *Phys. Rev.* **1954**, *95* (1), 249-262.

89. Chudley, C. T.; Elliott, R. J., Neutron scattering from a liquid on a jump diffusion model. *Proc. Phys. Soc., London* **1961**, *77* (494), 353-361.

90. García-Sakai, V.; Adams, M. A.; Howells, W. S.; Telling, M. T. F.; Demmel, F.; Fernandez-Alonso, F., *The IRIS User Guide*. 3rd ed.; **2011**. http://purl.org/net/epubs/work/54579.

91. Carlile, C. J.; Adams, M. A., The design of the IRIS inelastic neutron spectrometer and improvements to its analysers. *Phys. B.* **1992**, *182* (4), 431-440.

92. Telling, M. T. F.; Andersen, K. H., Spectroscopic characteristics of the OSIRIS near-backscattering crystal analyser spectrometer on the ISIS pulsed neutron source. *Phys. Chem. Chem. Phys.* **2005**, *7* (6), 1255-1261.

93. Burton, A. W., Powder Diffraction in Zeolite Science. In *Zeolite Characterisation and Catalysis*, Chester, A. W.; Derouane, E. G., Eds. Springer: Dordrecht, **2009**; pp 1-64.

94. Czjzek, M.; Jobic, H.; Fitch, A. N.; Vogt, T., Direct determination of proton positions in D-Y and H-Y zeolite samples by neutron powder diffraction. *J. Phys. Chem.* **1992**, *96* (4), 1535-1540.

95. Smith, R. I.; Hull, S.; Tucker, M. G.; Playford, H. Y.; McPhail, D. J.; Waller, S. P.; Norberg, S. T., The upgraded Polaris powder diffractometer at the ISIS neutron source. *Rev. Sci. Instrum.* **2019**, *90* (11), 115101.

96. Campbell, S. M.; Bibby, D. M.; Coddington, J. M.; Howe, R. F.; Meinhold, R. H., Dealumination of HZSM-5 Zeolites: I. Calcination and Hydrothermal Treatment. *J. Catal.* **1996**, *161* (1), 338-349.

97. Arnold, O.; Bilheux, J. C.; Borreguero, J. M.; Buts, A.; Campbell, S. I.; Chapon, L.; Doucet, M.; Draper, N.; Ferraz Leal, R.; Gigg, M. A.; Lynch, V. E.; Markvardsen, A.; Mikkelson, D. J.; Mikkelson, R. L.; Miller, R.; Palmen, K.; Parker, P.; Passos, G.; Perring, T. G.; Peterson, P. F.; Ren, S.; Reuter, M. A.; Savici, A. T.; Taylor, J. W.; Taylor, R. J.; Tolchenov, R.; Zhou, W.; Zikovsky, J., Mantid—Data analysis and visualization package for neutron scattering and μSR experiments. *Nucl. Instrum. Methods Phys. Res., Sect. A* **2014**, *764*, 156-166.

98. Mslice. http://mslice.isis.rl.ac.uk/Main_Page (accessed December 2020).

99. Azuah, R. T.; Kneller, L. R.; Qiu, Y. M.; Tregenna-Piggott, P. L. W.; Brown, C. M.; Copley, J. R. D.; Dimeo, R. M., DAVE: A Comprehensive Software Suite for the Reduction, Visualization, and Analysis of Low Energy Neutron Spectroscopic Data. *J. Res. Natl. Inst. Stand. Technol.* **2009**, *114* (6), 341-358.

100. Toby, B. H.; Von Dreele, R. B., GSAS-II: the genesis of a modern open-source all purpose crystallography software package. *J. Appl. Crystallogr.* **2013**, *46* (2), 544-549.

101. Born, M.; Oppenheimer, R., Zur Quantentheorie der Molekeln. *Ann. Phys.* **1927**, *389* (20), 457-484.

102. Hohenberg, P.; Kohn, W., Inhomogeneous Electron Gas. *Phys. Rev.* **1964**, *136* (3B), B864-B871.

103. Becke, A. D., Density-functional thermochemistry .3. the role of exact exchange. *J. Chem. Phys.* **1993**, *98* (7), 5648-5652.

104. Lee, C. T.; Yang, W. T.; Parr, R. G., Development of the colle-salvetti correlation-energy formula into a functional of the electron-density. *Phys. Rev. B* **1988**, *37* (2), 785-789.

105. Wong, M. W., Vibrational frequency prediction using density functional theory. *Chem. Phys. Lett.* **1996**, *256* (4-5), 391-399.

106. Ramirez-Cuesta, A. J., aCLIMAX 4.0.1, The new version of the software for analyzing and interpreting INS spectra. *Comput. Phys. Commun.* **2004**, *157* (3), 226-238.

107. Dymkowski, K.; Parker, S. F.; Fernandez-Alonso, F.; Mukhopadhyay, S., AbINS: The modern software for INS interpretation. *Phys. B.* **2018**, https://doi.org/10.1016/j.physb.2018.02.034.

108. Frisch, M. J.; Trucks, G. W.; Schlegel, H. B.; Scuseria, G. E.; Robb, M. A.; Cheeseman, J. R.; Montgomery, J., J. A.; Vreven, T.; Kudin, K. N.; Burant, J. C.; Millam, J. M.; Iyengar, S. S.; Tomasi, J.; Barone, V.; Mennucci, B.; Cossi, M.; Scalmani, G.; Rega, N.; Petersson, G. A.; Nakatsuji, H.; Hada, M.; Ehara, M.; Toyota, K.; Fukuda, R.; Hasegawa, J.; Ishida, M.; Nakajima, T.; Honda, Y.; Kitao, O.; Nakai, H.; Klene, M.; Li, X.; Knox, J. E.; Hratchian, H. P.; Cross, J. B.; Bakken, V.; Adamo, C.; Jaramillo, J.; Gomperts, R.; Stratmann, R. E.; Yazyev, O.; Austin, A. J.; Cammi, R.; Pomelli, C.; Ochterski, J. W.; Ayala, P. Y.; Morokuma, K.; Voth, G. A.; Salvador, P.; Dannenberg, J. J.; Zakrzewski, V. G.; Dapprich, S.; Daniels, A. D.; Strain, M. C.; Farkas, O.; Malick, D. K.; Rabuck, A. D.; Raghavachari, K.; Foresman, J. B.; Ortiz, J. V.; Cui, Q.; Baboul, A. G.; Clifford, S.; Cioslowski, J.; Stefanov, B. B.; Liu, G.; Liashenko, A.; Piskorz, P.; Komaromi, I.; Martin, R. L.; Fox, D. J.; Keith, T.; Al-Laham, M. A.; Peng, C. Y.; Nanayakkara, A.; Challacombe, M.; Gill, P. M. W.; Johnson, B.; Chen, W.; Wong, M. W.; Gonzalez, C.; Pople, J. A. *Gaussian 03W*, Version 6.0; Gaussian Inc.: Wallingford CT, United States, **2004**.

109. Stephens, P. J.; Devlin, F. J.; Chabalowski, C. F.; Frisch, M. J., Ab-initio calculation of vibrational absorption and circular-dichroism spectra using density-functional force-fields. *J. Phys. Chem.* **1994**, *98* (45), 11623-11627.

110. O'Malley, A. J.; Parker, S. F.; Catlow, C. R. A., Neutron spectroscopy as a tool in catalytic science. *Chem. Commun.* **2017**, *53* (90), 12164-12176.

111. Todorov, I. T.; Smith, W., *The DL_POLY_4 User Manual [online]*. Science and Technology Facilities Council: **2018**. https://www.scd.stfc.ac.uk/Pages/DL_POLY.aspx (accessed December 2020).
112. Ewald, P. P., Die Berechnung optischer und elektrostatischer Gitterpotentiale. *Ann. Phys.* **1921**, *369* (3), 253-287.
113. Swope, W. C.; Andersen, H. C.; Berens, P. H.; Wilson, K. R., A computer simulation method for the calculation of equilibrium constants for the formation of physical clusters of molecules: Application to small water clusters. *The Journal of Chemical Physics* **1982**, *76* (1), 637-649.
114. Berendsen, H. J. C.; Postma, J. P. M.; Vangunsteren, W. F.; Dinola, A.; Haak, J. R., Molecular dynamics with coupling to an external bath. *J. Chem. Phys.* **1984**, *81* (8), 3684-3690.
115. Dempsey, W.; Kuhl, G. H.; Olson, D. H., Variation of lattice parameter with aluminum content in synthetic sodium faujasites; evidence for ordering of framework ions. *J. Phys. Chem.* **1969**, *73* (2), 387-390.
116. Jackson, R. A.; Catlow, C. R. A., Computer simulation studies of zeolite structure. *Mol. Simul.* **1988**, *1* (4), 207-U27.
117. Schröder, K. P.; Sauer, J.; Leslie, M.; Catlow, C. R. A.; Thomas, J. M., Bridging hydroxyl-groups in zeolitic catalysts - a computer-simulation of their structure, vibrational properties and acidity in protonated faujasites (H-Y zeolites). *Chem. Phys. Lett.* **1992**, *188* (3-4), 320-325.
118. Raj, N.; Sastre, G.; Catlow, C. R. A., Diffusion of octane in silicalite: A molecular dynamics study. *J. Phys. Chem. B* **1999**, *103* (50), 11007-11015.
119. Banks, J. L.; Beard, H. S.; Cao, Y. X.; Cho, A. E.; Damm, W.; Farid, R.; Felts, A. K.; Halgren, T. A.; Mainz, D. T.; Maple, J. R.; Murphy, R.; Philipp, D. M.; Repasky, M. P.; Zhang, L. Y.; Berne, B. J.; Friesner, R. A.; Gallicchio, E.; Levy, R. M., Integrated modeling program, applied chemical theory (IMPACT). *J. Comput. Chem.* **2005**, *26* (16), 1752-1780.
120. Kiselev, A. V.; Lopatkin, A. A.; Shulga, A. A., Molecular statistical calculation of gas-adsorption by silicalite. *Zeolites* **1985**, *5* (4), 261-267.

121. Vetrivel, R.; Catlow, C. R. A.; Colbourn, E. A., Simulation studies of reactive molecules in zeolites. *J. Chem. Soc., Faraday Trans.* **1989**, *85*, 497-503.

122. Catlow, C. R. A.; Freeman, C. M.; Vessal, B.; Tomlinson, S. M.; Leslie, M., Molecular dynamics studies of hydrocarbon diffusion in zeolites. *J. Chem. Soc., Faraday Trans.* **1991**, *87* (13), 1947-1950.

123. O'Malley, A. J.; Sakai, V. G.; Silverwood, I. P.; Dimitratos, N.; Parker, S. F.; Catlow, C. R. A., Methanol diffusion in zeolite HY: a combined quasielastic neutron scattering and molecular dynamics simulation study. *Phys. Chem. Chem. Phys.* **2016**, *18* (26), 17294-17302.

124. Todorov, I. T.; Smith, W.; Trachenko, K.; Dove, M. T., DL_POLY_3: new dimensions in molecular dynamics simulations via massive parallelism. *J. Mater. Chem.* **2006**, *16* (20), 1911-1918.

125. Glasgow HPCC. https://www.gla.ac.uk/myglasgow/it/hpcc/ (accessed December 2020).

126. Yong, C. W., Descriptions and Implementations of DL_F Notation: A Natural Chemical Expression System of Atom Types for Molecular Simulations. *J. Chem. Inf. Model.* **2016**, *56* (8), 1405-1409.

127. Hoover, W. G., Canonical dynamics: Equilibrium phase-space distributions. *Phys. Rev. A* **1985**, *31* (3), 1695-1697.

128. Goret, G.; Aoun, B.; Pellegrini, E., MDANSE: An Interactive Analysis Environment for Molecular Dynamics Simulations. *J. Chem. Inf. Model.* **2017**, *57* (1), 1-5.

129. Zhao, Z.; Xu, S.; Hu, M. Y.; Bao, X.; Peden, C. H. F.; Hu, J., Investigation of Aluminum Site Changes of Dehydrated Zeolite H-Beta during a Rehydration Process by High-Field Solid-State NMR. *J. Phys. Chem. C* **2015**, *119* (3), 1410-1417.

130. Brunauer, S.; Emmett, P. H.; Teller, E., Adsorption of gases in multimolecular layers. *J. Am. Chem. Soc.* **1938**, *60*, 309-319.

131. de Boer, J. H.; Lippens, B. C.; Linsen, B. G.; Broekhoff, J. C. P.; van den Heuvel, A.; Osinga, T. J., The *t*-curve of multimolecular N_2-adsorption. *J. Colloid Interface Sci.* **1966**, *21* (4), 405-414.

132. Niwa, M.; Katada, N., New Method for the Temperature-Programmed Desorption (TPD) of Ammonia Experiment for Characterization of Zeolite Acidity: A Review. *Chem. Rec.* **2013**, *13* (5), 432-455.
133. Arena, F.; Di Chio, R.; Trunfio, G., An experimental assessment of the ammonia temperature programmed desorption method for probing the surface acidic properties of heterogeneous catalysts. *Appl. Catal. A-Gen.* **2015**, *503*, 227-236.
134. Mintova, S.; Barrier, N., *Verified synthesis of zeolytic materials*. 3rd Revised ed.; Published on behalf of the Synthesis Commission of the International Zeolite Association: **2016**.
135. Kliewer, C. E., Electron Microscopy and Imaging. In *Zeolite Characterisation and Catalysis*, Chester, A. W.; Derouane, E. G., Eds. Springer: Dordrecht, **2009**; pp 169-196.
136. Sing, K. S. W., Reporting physisorption data for gas/solid systems with special reference to the determination of surface area and porosity (Recommendations 1984). *Pure Appl. Chem.* **1985**, *57* (4), 603-619.
137. Emdadi, L.; Wu, Y.; Zhu, G.; Chang, C.-C.; Fan, W.; Pham, T.; Lobo, R. F.; Liu, D., Dual Template Synthesis of Meso- and Microporous MFI Zeolite Nanosheet Assemblies with Tailored Activity in Catalytic Reactions. *Chem. Mater.* **2014**, *26* (3), 1345-1355.
138. Topsoe, N. Y.; Pedersen, K.; Derouane, E. G., Infrared and temperature-programmed desorption study of the acidic properties of ZSM-5-type zeolites. *J. Catal.* **1981**, *70* (1), 41-52.
139. Fyfe, C. A.; Feng, Y.; Grondey, H.; Kokotailo, G. T.; Gies, H., One- and two-dimensional high-resolution solid-state NMR studies of zeolite lattice structures. *Chem. Rev.* **1991**, *91* (7), 1525-1543.
140. Malicki, N.; Mali, G.; Quoineaud, A.-A.; Bourges, P.; Simon, L. J.; Thibault-Starzyk, F.; Fernandez, C., Aluminium triplets in dealuminated zeolites detected by ^{27}Al NMR correlation spectroscopy. *Microporous Mesoporous Mater.* **2010**, *129* (1), 100-105.
141. Silverwood, I. P.; Hamilton, N. G.; Laycock, C. J.; Staniforth, J. Z.; Ormerod, R. M.; Frost, C. D.; Parker, S. F.; Lennon, D., Quantification of surface species present on a nickel/alumina methane reforming catalyst. *Phys. Chem. Chem. Phys.* **2010**, *12* (13), 3102-3107.

142. Kosslick, H.; Fricke, R., Chemical Analysis of Aluminosilicates, Aluminophosphates and Related Molecular Sieves. In *Molecular Sieves, Vol. 5: Characterization II*, Karge, H. G.; Weitkamp, J., Eds. Springer Berlin: Heidelburg, **2007**; pp 1-66.

143. Perea, D. E.; Arslan, I.; Liu, J.; Ristanović, Z.; Kovarik, L.; Arey, B. W.; Lercher, J. A.; Bare, S. R.; Weckhuysen, B. M., Determining the location and nearest neighbours of aluminium in zeolites with atom probe tomography. *Nat. Commun.* **2015**, *6* (1), 7589.

144. Xing, B.; Ma, J.; Li, R.; Jiao, H., Location, distribution and acidity of Al substitution in ZSM-5 with different Si/Al ratios – a periodic DFT computation. *Catal. Sci. Technol.* **2017**, *7* (23), 5694-5708.

145. Van der Mynsbrugge, J.; Janda, A.; Lin, L.-C.; Van Speybroeck, V.; Head-Gordon, M.; Bell, A. T., Understanding Brønsted-Acid Catalyzed Monomolecular Reactions of Alkanes in Zeolite Pores by Combining Insights from Experiment and Theory. *ChemPhysChem* **2018**, *19* (4), 341-358.

146. Mentzen, B. F., Crystallographic determination of the positions of the monovalent H, Li, Na, K, Rb, and Tl cations in fully dehydrated MFI type zeolites. *J. Phys. Chem. C* **2007**, *111* (51), 18932-18941.

147. Hawkins, A. P.; Zachariou, A.; Collier, P.; Ewings, R. A.; Howe, R. F.; Parker, S. F.; Lennon, D., Low-temperature studies of propene oligomerization in ZSM-5 by inelastic neutron scattering spectroscopy. *RSC Adv.* **2019**, *9* (33), 18785-18790.

148. Hawkins, A. P.; Zachariou, A.; Parker, S. F.; Collier, P.; Silverwood, I. P.; Howe, R. F.; Lennon, D., Onset of propene oligomerization reactivity in ZSM-5 studied by Inelastic Neutron Scattering spectroscopy. *ACS Omega* **2020**, *5* (14), 7762-7770.

149. Fateley, W. G.; Miller, F. A., Torsional frequencies in the far infrared—III: The form of the potential curve for hindered internal rotation of a methyl group. *Spectrochim. Acta,* **1963**, *19* (3), 611-628.

150. Ghosh, A. K.; Kydd, R. A., A Fourier-transform infrared spectral study of propene reactions on acidic zeolites. *J. Catal.* **1986**, *100* (1), 185-195.

151. Lennon, D.; McNamara, J.; Phillips, J. R.; Ibberson, R. M.; Parker, S. F., An inelastic neutron scattering spectroscopic investigation of the adsorption of ethene and propene on carbon. *Phys. Chem. Chem. Phys.* **2000**, *2* (19), 4447-4451.

152. Hawkins, A. P.; O'Malley, A. J.; Zachariou, A.; Collier, P.; Ewings, R. A.; Silverwood, I. P.; Howe, R. F.; Parker, S. F.; Lennon, D., Investigation of the Dynamics of 1-Octene Adsorption at 293 K in a ZSM-5 Catalyst by Inelastic and Quasielastic Neutron Scattering. *J. Phys. Chem. C* **2018**, *123* (1), 417-425.

153. Fraser, G. T.; Suenram, R. D.; Lugez, C. L., Investigation of conformationally rich molecules: Rotational spectra of fifteen conformational isomers of 1-octene. *J. Phys. Chem. A* **2001**, *105* (43), 9859-9864.

154. Bower, D. I.; Maddams, W. F., *The Vibrational Spectroscopy of Polymers*. Cambridge University Press: Cambridge, **1989**, DOI: 10.1017/CBO9780511623189.

155. Braden, D. A.; Parker, S. F.; Tomkinson, J.; Hudson, B. S., Inelastic neutron scattering spectra of the longitudinal acoustic modes of the normal alkanes from pentane to pentacosane. *J. Chem. Phys.* **1999**, *111* (1), 429-437.

156. Demmel, F.; McPhail, D.; French, C.; Maxwell, D.; Harrison, S.; Boxall, J.; Rhodes, N.; Mukhopadhyay, S.; Silverwood, I.; Sakai, V. G.; Fernandez-Alonso, F., ToF-Backscattering spectroscopy at the ISIS Facility: Status and Perspectives. *J. Phys.: Conf. Ser.* **2018**, *1021*, 012027.

157. Weber, D.; Sederman, A. J.; Mantle, M. D.; Mitchell, J.; Gladden, L. F., Surface diffusion in porous catalysts. *Phys. Chem. Chem. Phys.* **2010**, *12* (11), 2619-2624.

158. Stepanov, A. G.; Luzgin, M. V.; Romannikov, V. N.; Zamaraev, K. I., Carbenium ion properties of octene-1 adsorbed on zeolite H-ZSM-5. *Catal. Lett.* **1994**, *24* (3), 271-284.

159. ISIS INS Database. https://edata.stfc.ac.uk/handle/edata/18 (accessed February 2021).

160. Parker, S. F., Inelastic neutron scattering spectra of polyethylene. *J. Chem. Soc., Faraday Trans.* **1996**, *92* (11), 1941-1946.

161. Ardit, M.; Martucci, A.; Cruciani, G., Monoclinic–Orthorhombic Phase Transition in ZSM-5 Zeolite: Spontaneous Strain Variation and Thermodynamic Properties. *J. Phys. Chem. C* **2015**, *119* (13), 7351-7359.

162. Eder, F.; Lercher, J. A., On the role of the pore size and tortuosity for sorption of alkanes in molecular sieves. *J. Phys. Chem. B* **1997**, *101* (8), 1273-1278.

163. Chiu, C. C.; Vayssilov, G. N.; Genest, A.; Borgna, A.; Rosch, N., Predicting Adsorption Enthalpies on Silicalite and HZSM-5: A Benchmark Study on DFT Strategies Addressing Dispersion Interactions. *J. Comput. Chem.* **2014**, *35* (10), 809-819.

164. Peterlin-Neumaier, T.; Springer, T., Investigation of relaxation processes in linear polyethylene in the 10^{-9} sec region by means of high-resolution neutron spectroscopy. *J. Polym. Sci., Polym. Phys. Ed.* **1976**, *14* (8), 1351-1359.

165. Norton, C. J., Olefin Polymerization over Synthetic Molecular Sieves. *Ind. Eng. Chem. Process Des. Dev.* **1964**, *3* (3), 230-236.

166. Tabak, S. A.; Krambeck, F. J.; Garwood, W. E., Conversion of propylene and butylene over ZSM-5 catalyst. *AIChE J.* **1986**, *32* (9), 1526-1531.

167. Sarazen, M. L.; Doskocil, E.; Iglesia, E., Catalysis on solid acids: Mechanism and catalyst descriptors in oligomerization reactions of light alkenes. *J. Catal.* **2016**, *344*, 553-569.

168. Sarazen, M. L.; Doskocil, E.; Iglesia, E., Effects of Void Environment and Acid Strength on Alkene Oligomerization Selectivity. *ACS Catal.* **2016**, *6* (10), 7059-7070.

169. Oliveira, P.; Borges, P.; Pinto, R. R.; Lemos, M. A. N. D. A.; Lemos, F.; Védrine, J. C.; Ribeiro, F. R., Light olefin transformation over ZSM-5 zeolites with different acid strengths – A kinetic model. *Appl. Catal., A* **2010**, *384* (1), 177-185.

170. Parker, S. F., unpublished work from ISIS, Chilton, UK.

171. Kazansky, V.; Subbotina, I.; Jentoft, F., Intensities of combination IR bands as an indication of the concerted mechanism of proton transfer

from acidic hydroxyl groups in zeolites to the ethylene hydrogen-bonded by protons. *J. Catal.* **2006**, *240* (1), 66-72.

172. Bernauer, M.; Tabor, E.; Pashkova, V.; Kaucky, D.; Sobalik, Z.; Wichterlova, B.; Dedecek, J., Proton Proximity - New Key Parameter Controlling Adsorption, Desorption and Activity in Propene Oligomerization over H-ZSM-5 Zeolites. *J. Catal.* **2016**, *344*, 157-172.
173. Vandenberg, J. P.; Wolthuizen, J. P.; Clague, A. D. H.; Hays, G. R.; Huis, R.; Vanhooff, J. H. C., Low-Temperature Oligomerization of Small Olefins on Zeolite H-ZSM-5 - an Investigation with High-Resolution Solid-State ^{13}C-NMR. *J. Catal.* **1983**, *80* (1), 130-138.
174. Silverwood, I. P.; Sakai, V. G., Propane diffusion in ZSM-5 pores measured by quasielastic neutron scattering under macroscopic flow. *Chem. Eng. Sci.* **2018**, *186*, 116-121.
175. Nowak, A. K.; Den Ouden, C. J. J.; Pickett, S. D.; Smit, B.; Cheetham, A. K.; Post, M. F. M.; Thomas, J. M., Mobility of adsorbed species in zeolites: methane, ethane, and propane diffusivities. *J. Phys. Chem.* **1991**, *95* (2), 848-854.
176. Leroy, F.; Rousseau, B.; Fuchs, A. H., Self-diffusion of n-alkanes in silicalite using molecular dynamics simulation: A comparison between rigid and flexible frameworks. *Phys. Chem. Chem. Phys.* **2004**, *6* (4), 775-783.
177. Singwi, K. S.; Sjölander, A., Diffusive motions in water and cold neutron scattering. *Phys. Rev.* **1960**, *119* (3), 863-871.
178. Williams, B. A.; Babitz, S. M.; Miller, J. T.; Snurr, R. Q.; Kung, H. H., The roles of acid strength and pore diffusion in the enhanced cracking activity of steamed Y zeolites. *Appl. Catal. A-Gen.* **1999**, *177* (2), 161-175.
179. Silaghi, M. C.; Chizallet, C.; Sauer, J.; Raybaud, P., Dealumination mechanisms of zeolites and extra-framework aluminum confinement. *J. Catal.* **2016**, *339*, 242-255.
180. Campbell, S. M.; Bibby, D. M.; Coddington, J. M.; Howe, R. F., Dealumination of HZSM-5 Zeolites: II. Methanol to Gasoline Conversion. *J. Catal.* **1996**, *161* (1), 350-358.

181. Cabral de Menezes, S. M.; Lam, Y. L.; Damodaran, K.; Pruski, M., Modification of H-ZSM-5 zeolites with phosphorus. 1. Identification of aluminum species by 27Al solid-state NMR and characterization of their catalytic properties. *Microporous Mesoporous Mater.* **2006**, *95* (1), 286-295.

182. Van Bokhoven, J. A.; Roest, A. L.; Koningsberger, D. C.; Miller, J. T.; Nachtegaal, G. H.; Kentgens, A. P. M., Changes in structural and electronic properties of the zeolite framework induced by extraframework Al and la in H-USY and La(x)NaY: A29Si and27AI MAS NMR and27A1 MQ MAS NMR study. *J. Phys. Chem. B* **2000**, *104* (29), 6743-6754.

183. Sanz, J.; Fornés, V.; Corma, A., Extraframework aluminium in steam- and SiCl4-dealuminated Y zeolite. A 27Al and 29Si nuclear magnetic resonance study. *J. Chem. Soc., Faraday Trans. 1* **1988**, *84* (9), 3113-3119.

184. Wulfers, M. J.; Jentoft, F. C., The Role of Cyclopentadienium Ions in Methanol-to-Hydrocarbons Chemistry. *ACS Catal.* **2014**, *4* (10), 3521-3532.

185. Mosley, J. D.; Young, J. W.; Agarwal, J.; Schaefer, H. F.; Schleyer, P. V. R.; Duncan, M. A., Structural Isomerization of the Gas-Phase 2-Norbornyl Cation Revealed with Infrared Spectroscopy and Computational Chemistry. *Angew. Chem.-Int. Edit.* **2014**, *53* (23), 5888-5891.

186. Hernandez, E. D.; Jentoft, F. C., Spectroscopic Signatures Reveal Cyclopentenyl Cation Contributions in Methanol-to-Olefins Catalysis. *ACS Catal.* **2020**, *10* (10), 5764-5782.

187. Hawkins, A. P.; Zachariou, A.; Parker, S. F.; Collier, P.; Howe, R. F.; Lennon, D., Studies of propene conversion over H-ZSM-5 demonstrate the importance of propene as an intermediate in methanol-to-hydrocarbons chemistry. *Catal. Sci. Technol.* **2021**, *11* (8), 2924-2938.

188. Lin-Vien, D.; Colthup, N. B.; Fateley, W. G.; Grasselli, J. G., *The Handbook of Infrared and Raman Characteristic Frequencies of Organic Molecules*. Academic Press: San Diego, **1991**.

189. Müller, S.; Liu, Y.; Vishnuvarthan, M.; Sun, X.; van Veen, A. C.; Haller, G. L.; Sanchez-Sanchez, M.; Lercher, J. A., Coke formation and deactivation pathways on H-ZSM-5 in the conversion of methanol to olefins. *J. Catal.* **2015**, *325*, 48-59.

190. Song, W.; Nicholas, J. B.; Haw, J. F., Acid−Base Chemistry of a Carbenium Ion in a Zeolite under Equilibrium Conditions: Verification of a Theoretical Explanation of Carbenium Ion Stability. *J. Am. Chem. Soc.* **2001**, *123* (1), 121-129.

191. Jacobs, P. A.; Von Ballmoos, R., Framework hydroxyl groups of H-ZSM-5 zeolites. *J. Phys. Chem.* **1982**, *86* (15), 3050-3052.

192. Vedrine, J. C.; Auroux, A.; Coudurier, G., Combined physical techniques in the characterization of zeolite ZSM-5 and ZSM-11 acidity and basicity. *ACS Symp. Ser.* **1984**, *248*, 253-273.

193. Mlinar, A. N.; Zimmerman, P. M.; Celik, F. E.; Head-Gordon, M.; Bell, A. T., Effects of Brønsted-acid site proximity on the oligomerization of propene in H-MFI. *J. Catal.* **2012**, *288*, 65-73.

194. Haw, J. F.; Marcus, D. M., Well-defined (supra)molecular structures in zeolite methanol-to-olefin catalysis. *Top. Catal.* **2005**, *34* (1), 41-48.

195. Haw, J. F.; Nicholas, J. B.; Song, W.; Deng, F.; Wang, Z.; Xu, T.; Heneghan, C. S., Roles for Cyclopentenyl Cations in the Synthesis of Hydrocarbons from Methanol on Zeolite Catalyst HZSM-5. *J. Am. Chem. Soc.* **2000**, *122* (19), 4763-4775.

196. Mores, D.; Stavitski, E.; Kox, M. H. F.; Kornatowski, J.; Olsbye, U.; Weckhuysen, B. M., Space- and Time-Resolved In-situ Spectroscopy on the Coke Formation in Molecular Sieves: Methanol-to-Olefin Conversion over H-ZSM-5 and H-SAPO-34. *Chem. - Eur. J.* **2008**, *14* (36), 11320-11327.

197. Zhang, W.; Zhang, M.; Xu, S.; Gao, S.; Wei, Y.; Liu, Z., Methylcyclopentenyl Cations Linking Initial Stage and Highly Efficient Stage in Methanol-to-Hydrocarbon Process. *ACS Catal.* **2020**, *10* (8), 4510-4516.

198. Yuen, L.-T.; Zones, S. I.; Harris, T. V.; Gallegos, E. J.; Auroux, A., Product selectivity in methanol to hydrocarbon conversion for

isostructural compositions of AFI and CHA molecular sieves. *Microporous Mater.* **1994**, *2* (2), 105-117.

199. Westgård Erichsen, M.; Svelle, S.; Olsbye, U., The influence of catalyst acid strength on the methanol to hydrocarbons (MTH) reaction. *Catal. Today* **2013**, *215*, 216-223.
200. Arora, S. S.; Bhan, A., The critical role of methanol pressure in controlling its transfer dehydrogenation and the corresponding effect on propylene-to-ethylene ratio during methanol-to-hydrocarbons catalysis on H-ZSM-5. *J. Catal.* **2017**, *356*, 300-306.
201. Bhaskar, G. V.; Do, D. D., Toluene disproportionation reaction over HZSM-5 zeolites: kinetics and mechanism. *Ind. Eng. Chem. Res.* **1990**, *29* (3), 355-361.
202. Albahar, M.; Li, C.; Zholobenko, V. L.; Garforth, A. A., The effect of ZSM-5 zeolite crystal size on p-xylene selectivity in toluene disproportionation. *Microporous Mesoporous Mater.* **2020**, *302*, 110221.
203. Zachariou, A.; Hawkins, A. P.; Parker, S. F.; Lennon, D.; Howe, R. F., Neutron spectroscopy studies of methanol to hydrocarbons catalysis over ZSM-5. *Catal. Today* **2020**, 10.1016/j.cattod.2020.05.030.
204. Zachariou, A.; Hawkins, A. P.; Suwardiyanto; Collier, P.; Barrow, N.; Howe, R. F.; Parker, S. F.; Lennon, D., New Spectroscopic Insight into the Deactivation of a ZSM‐5 Methanol‐to‐Hydrocarbons Catalyst. *ChemCatChem* **2021**, 10.1002/cctc.202100286.
205. Matam, S. K.; O'Malley, A. J.; Catlow, C. R. A.; Suwardiyanto; Collier, P.; Hawkins, A. P.; Zachariou, A.; Lennon, D.; Silverwood, I. P.; Parker, S. F.; Howe, R. F., The Effects of MTG Catalysis on Methanol Mobility in ZSM-5. *Catal. Sci. Technol.* **2018**, *8* (13), 3304-3312.
206. Omojola, T.; Silverwood, I. P.; O'Malley, A. J., Molecular behaviour of methanol and dimethyl ether in H-ZSM-5 catalysts as a function of Si/Al ratio: a quasielastic neutron scattering study. *Catal. Sci. Technol.* **2020**, *10* (13), 4305-4320.
207. Jobic, H.; Bée, M.; Kearley, G. J., Translational and rotational dynamics of methane in ZSM-5 zeolite: A quasi-elastic neutron scattering study. *Zeolites* **1989**, *9* (4), 312-317.

208. Silverwood, I. P.; Agote-Arán, M.; Lezcano-Gonzalez, I.; Kroner, A.; Beale, A. M., QENS study of methane diffusion in Mo/H-ZSM-5 used for the methane dehydroaromatisation reaction. *AIP Conference Proceedings* **2018**, *1969* (1), 030002.

209. López, F.; Pérez, R.; Ruette, F.; Medina, E., Interplay of entropic and memory effects in diffusion of methane in silicalite zeolites. *Phys. Rev. E* **2005**, *72* (6), 061111.

210. Smit, B.; Maesen, T. L. M., Molecular simulations of zeolites: Adsorption, diffusion, and shape selectivity. *Chem. Rev.* **2008**, *108* (10), 4125-4184.

211. Jobic, H., Diffusion studies using quasi-elastic neutron scattering. In *Membrane Science and Technology*, Kanellopoulos, N. K., Ed. Elsevier: **2000**; pp 109-137.

212. Molecular Dynamics Monte Carlo. http://mdmcproject.org (accessed January 2021).

213. Bordiga, S.; Ugliengo, P.; Damin, A.; Lamberti, C.; Spoto, G.; Zecchina, A.; Spanò, G.; Buzzoni, R.; Dalloro, L.; Rivetti, F., Hydroxyls nests in defective silicalites and strained structures derived upon dehydroxylation: vibrational properties and theoretical modelling. *Top. Catal.* **2001**, *15* (1), 43-52.